frontiers | Research Topics

How animals see: Structure and function of light sensory tissues along evolution

Edited by
Marta Agudo-Barriuso, Francisco M. Nadal-Nicolás, Isabel Pinilla and Nicolás Cuenca

Published in
Frontiers in Neuroanatomy

ISSN 1664-8714
ISBN 978-2-83251-966-0
DOI 10.3389/978-2-83251-966-0

About Frontiers

Frontiers is more than just an open access publisher of scholarly articles: it is a pioneering approach to the world of academia, radically improving the way scholarly research is managed. The grand vision of Frontiers is a world where all people have an equal opportunity to seek, share and generate knowledge. Frontiers provides immediate and permanent online open access to all its publications, but this alone is not enough to realize our grand goals.

Frontiers journal series

The Frontiers journal series is a multi-tier and interdisciplinary set of open-access, online journals, promising a paradigm shift from the current review, selection and dissemination processes in academic publishing. All Frontiers journals are driven by researchers for researchers; therefore, they constitute a service to the scholarly community. At the same time, the *Frontiers journal series* operates on a revolutionary invention, the tiered publishing system, initially addressing specific communities of scholars, and gradually climbing up to broader public understanding, thus serving the interests of the lay society, too.

Dedication to quality

Each Frontiers article is a landmark of the highest quality, thanks to genuinely collaborative interactions between authors and review editors, who include some of the world's best academicians. Research must be certified by peers before entering a stream of knowledge that may eventually reach the public - and shape society; therefore, Frontiers only applies the most rigorous and unbiased reviews. Frontiers revolutionizes research publishing by freely delivering the most outstanding research, evaluated with no bias from both the academic and social point of view. By applying the most advanced information technologies, Frontiers is catapulting scholarly publishing into a new generation.

What are Frontiers Research Topics?

Frontiers Research Topics are very popular trademarks of the *Frontiers journals series*: they are collections of at least ten articles, all centered on a particular subject. With their unique mix of varied contributions from Original Research to Review Articles, Frontiers Research Topics unify the most influential researchers, the latest key findings and historical advances in a hot research area.

Find out more on how to host your own Frontiers Research Topic or contribute to one as an author by contacting the Frontiers editorial office: frontiersin.org/about/contact

How animals see: Structure and function of light sensory tissues along evolution

Topic editors

Marta Agudo-Barriuso — Biomedical Research Institute of Murcia (IMIB), Spain

Francisco M. Nadal-Nicolás — Retinal Neurophysiology Section, National Eye Institute (NIH), United States

Isabel Pinilla — Hospital Clinico Universitario, Spain

Nicolás Cuenca — University of Alicante, Spain

Citation

Agudo-Barriuso, M., Nadal-Nicolás, F. M., Pinilla, I., Cuenca, N., eds. (2023). *How animals see: Structure and function of light sensory tissues along evolution*. Lausanne: Frontiers Media SA. doi: 10.3389/978-2-83251-966-0

Table of contents

05 Characterization of the Canine Retinal Vasculature With Optical Coherence Tomography Angiography: Comparisons With Histology and Fluorescein Angiography
Ana Ripolles-Garcia, Gordon Ruthel, Gui-Shuang Ying, Yineng Chen, Nicolas Cuenca, Gustavo D. Aguirre and William A. Beltran

19 The Functional Anatomy of the Cornea and Anterior Chamber in Lampreys: Insights From the Pouched Lamprey, *Geotria australis* (Geotriidae, Agnatha)
H. Barry Collin, Julian Ratcliffe and Shaun P. Collin

36 Asymmetric Distributions of Achromatic Bipolar Cells in the Mouse Retina
Zachary J. Sharpe, Angela Shehu and Tomomi Ichinose

48 Type II Opsins in the Eye, the Pineal Complex and the Skin of *Xenopus laevis*: Using Changes in Skin Pigmentation as a Readout of Visual and Circadian Activity
Gabriel E. Bertolesi, Nilakshi Debnath, Hannan R. Malik, Lawrence L. H. Man and Sarah McFarlane

65 Morphological Plasticity of the Retina of Viperidae Snakes Is Associated With Ontogenetic Changes in Ecology and Behavior
Juliana H. Tashiro, Dora F. Ventura and Einat Hauzman

84 Immunohistochemical Characterisation of the Whale Retina
Noelia Ruzafa, Xandra Pereiro and Elena Vecino

100 The Evolution of Visual Roles – Ancient Vision Versus Object Vision
Dan-Eric Nilsson

106 An EvoDevo Study of Salmonid Visual Opsin Dynamics and Photopigment Spectral Sensitivity
Mariann Eilertsen, Wayne Iwan Lee Davies, Dharmeshkumar Patel, Jonathan E. Barnes, Rita Karlsen, Jessica Kate Mountford, Deborah L. Stenkamp, Jagdish Suresh Patel and Jon Vidar Helvik

121 Expression of Opsins of the Box Jellyfish *Tripedalia cystophora* Reveals the First Photopigment in Cnidarian Ocelli and Supports the Presence of Photoisomerases
Anders Garm, Jens-Erik Svaerke, Daniela Pontieri and Todd H. Oakley

134 Corrigendum: Expression of opsins of the box jellyfish *Tripedalia cystophora* reveals the first photopigment in cnidarian ocelli and supports the presence of photoisomerases
Anders Garm, Jens-Erik Svaerke, Daniela Pontieri and Todd H. Oakley

136 The retina of the lab rat: focus on retinal ganglion cells and photoreceptors
Caridad Galindo-Romero, María Norte-Muñoz, Alejandro Gallego-Ortega, Kristy T. Rodríguez-Ramírez, Fernando Lucas-Ruiz, María Josefa González-Riquelme, Manuel Vidal-Sanz and Marta Agudo-Barriuso

144 Scribble basal polarity acquisition in RPE cells and its mislocalization in a pathological AMD-like model
Alicia Segurado, Alba Rodríguez-Carrillo, Bárbara Castellanos, Emiliano Hernández-Galilea, Almudena Velasco and Concepción Lillo

frontiers in Neuroanatomy

ORIGINAL RESEARCH
published: 13 December 2021
doi: 10.3389/fnana.2021.785249

Characterization of the Canine Retinal Vasculature With Optical Coherence Tomography Angiography: Comparisons With Histology and Fluorescein Angiography

*Ana Ripolles-Garcia[1], Gordon Ruthel[2], Gui-Shuang Ying[3], Yineng Chen[3], Nicolas Cuenca[4], Gustavo D. Aguirre[1] and William A. Beltran[1]**

[1] Division of Experimental Retinal Therapies, Department of Clinical Sciences & Advanced Medicine, School of Veterinary Medicine, University of Pennsylvania, Philadelphia, PA, United States, [2] Department of Pathobiology, School of Veterinary Medicine, University of Pennsylvania, Philadelphia, PA, United States, [3] Department of Ophthalmology, Scheie Eye Institute, Perelman School of Medicine, University of Pennsylvania, Philadelphia, PA, United States, [4] Department of Physiology, Genetics and Microbiology, University of Alicante, Alicante, Spain

OPEN ACCESS

Edited by:
Enrica Strettoi, Institute of Neuroscience, Consiglio Nazionale delle Ricerche (CNR), Italy

Reviewed by:
Miruna G. Ghinia-Tegla, City College of New York (CUNY), United States
Michael Kalloniatis, University of New South Wales, Australia

***Correspondence:**
William A. Beltran
wbeltran@vet.upenn.edu

Received: *28 September 2021*
Accepted: *23 November 2021*
Published: *13 December 2021*

Citation:
Ripolles-Garcia A, Ruthel G, Ying G-S, Chen Y, Cuenca N, Aguirre GD and Beltran WA (2021) Characterization of the Canine Retinal Vasculature With Optical Coherence Tomography Angiography: Comparisons With Histology and Fluorescein Angiography. Front. Neuroanat. 15:785249. doi: 10.3389/fnana.2021.785249

Purpose: To present a methodology for quantification of the canine retinal vasculature imaged by optical coherence tomography angiography (OCTA) and validate this approach by comparison with fluorescein angiography (FA) and confocal imaging of retinal wholemounts labelled by immunohistochemistry (IHC).

Methods: Six normal adult dogs underwent retinal OCTA imaging in both eyes. The images extracted from the different microvascular plexuses at eight retinal locations spanning the central and mid-peripheral fundus were analyzed using the AngioTool software. FA was performed in one eye and was compared to the OCTA images. Six eyes from three dogs were processed by IHC to examine the retinal vasculature.

Results: A total of four retinal plexuses were identified by OCTA in the canine retina, and their density and topographical pattern varied with eccentricity. OCTA offered improved resolution over FA with the advantage of allowing imaging of the individual plexuses. Detection by OCTA of small vessels within the deep capillary plexus was possible and approached the level of resolution achieved with *ex vivo* imaging of the retinal vasculature by confocal microscopy/IHC. The plexuses herein described are analogous to human retinal vasculature.

Conclusion: OCTA can be used to image and quantify non-invasively the vascular retinal networks of the canine retina. We provide normative data in eight different retinal locations that can be imaged non-invasively with this technology. This could support analysis of retinal vascular changes associated with disease and following therapeutic intervention.

Keywords: OCTA, canine retinal vasculature, vasculature quantification, vessel density (VD), vascular plexuses

INTRODUCTION

The retina is a complex and highly metabolic extracranial part of the central nervous system that requires a continuous and self-regulated blood supply (Harris et al., 1998; Yu and Cringle, 2001). In vascularised retinas, oxygenation is ensured by a well-organised retinal and choroidal vascular network. The choriocapillaris, a network of capillary vessels located under the retinal pigmented epithelium, is the main source of oxygen for the outer retina, and retinal vessels are the main supply for the inner retina (Michaelson, 1954). While choroidal vasculature has been maintained throughout evolution in vertebrates, the retinal vasculature pattern differs widely between species (Rochon-Duvigneaud, 1943). Based on the presence and distribution of this vasculature, four patterns have been described: euangiotic/holangiotic, merangiotic, paurangiotic and anangiotic (Leber, 1875; Schaepdrijver et al., 1989). The canine retina is classified as holangiotic as its blood vessels extend from the optic nerve head to the far periphery. In the temporally located *area centralis*, they converge toward the highly specialized fovea-like area (Peichl, 1992; Beltran et al., 2014).

However, the vasculature of the canine retina has not been thoroughly studied, and the location of the different vascular networks, as well as their nomenclature, remains unclear (Leber, 1875; Barrett, 1886; Mutlu and Leopold, 1964). In dogs, previous studies have imprecisely identified the presence of radially distributed blood vessels surrounding the optic nerve papilla, parallel to the nerve fibre layer (NFL) (Parry, 1953; Mutlu and Leopold, 1964). A second vascular network composed of major arterioles and venules has also been described and identified within the ganglion cell layer (GCL) (Parry, 1953; Mutlu and Leopold, 1964). Additionally, two capillary beds have been identified in the inner plexiform layer (IPL) (Schaepdrijver et al., 1989) and inner half of the outer plexiform layer (OPL) (Barrett, 1886; Parry, 1953; Mutlu and Leopold, 1964; Engerman et al., 1966; Schaepdrijver et al., 1989). However, the techniques used to describe the canine retinal microvasculature to date, such as vascular corrosion casting (Fischer and Slatter, 1978; Schaepdrijver et al., 1989), do not include structural analysis of the exact location of the vasculature in relation to the retinal layers. Furthermore, there are discrepancies between studies in the number of plexuses described (Michaelson, 1954). In contrast, four vascular plexuses have been identified and extensively described in the human retina (Chan et al., 2012).

Evaluation and quantification of the retinal vasculature is a valuable method to diagnose and monitor the progression of many retinal diseases that can result in blindness. This information serves as an essential diagnostic, prognostic, and therapeutic tool (Yao et al., 2020). Fluorescein angiography (FA) is currently the most widely applied technique in human and veterinary medicine for evaluation of retinal vessels *in vivo* (Gelatt et al., 1976; Cavallerano, 1996). Conventional FA has several disadvantages such as: suboptimal resolution in visualization of deeper retinal capillaries, and the need to use an intravenous contrast agent which may cause adverse systemic reactions (Kwiterovich et al., 1991; López-Sáez et al., 1998). Nonetheless, FA can detect increased vessel permeability evidenced by dye leakage, which is pathognomonic of blood-retinal barrier breakdown.

Optical coherence tomography angiography (OCTA) is a novel non-invasive technology that allows detailed visualization of retinal circulation, enabling the study of the vascular plexuses separately using their intrinsic motion decorrelation. The OCTA probabilistic full-spectrum amplitude decorrelation algorithm generates images based on the motion signal between a series of OCT b-scans acquired at the same position. The differences between the images acquired are due to erythrocyte movement in the blood vessels. By focusing on the movement, the algorithm is able eliminate all static sections of the scan area in order to generate a resulting image. This image is then further processed to produce the final *en face* angiogram (Coscas et al., 2016). Hence, it is able to detect vessel networks using their intrinsic motion decorrelation, thus avoiding the need for an intravenous dye (Jia et al., 2012).

While there are many different techniques and parameters utilized to quantify retinal vasculature, vessel density (VD) is the most widely used across studies (Pechauer et al., 2015). VD is generally defined as the percent area of an image that is occupied by blood vessels. However, the absolute values can vary widely between studies and there is a need for validation of novel OCTA-based approaches in canine retinas. Currently, the most recognized method of validating OCTA images is via direct comparison with retinal wholemounts processed for detection of the retinal vasculature by immunohistochemistry (IHC) (Yu et al., 2021). Ultimately, in order to be considered a reliable imaging technique, OCTA must recognize the majority of the vessels that are visualized by IHC.

The main objective of this study was to establish a methodology and normative data for retinal vasculature quantification by OCTA in canine eyes. We also aimed to validate our proposed methodology by comparison with FA and IHC. In order to achieve these goals, we investigated the anatomic features of the different retinal plexuses, their interconnections, and how their specific topographic patterns vary as a function of eccentricity from the optic nerve head.

MATERIALS AND METHODS

Study Animals

The animals enrolled in the study were part of the Retinal Diseases Studies Facility research colony at the University of Pennsylvania. All the procedures were approved by the Institutional Animal Care and Use Committee of the University of Pennsylvania (IACUC# 804956).

The study population consisted of 6 normal, mesocephalic, mongrel dogs (12 eyes) with a mean age of 4.5 $\pm$ 1.3 years of age, and both genders were equally represented. All the animals underwent OCTA imaging in both eyes (OCTA module, Spectralis HRA + OCT2, version 6.9.4.0, Heidelberg Engineering Inc., Franklin, MA, United States) prior to FA being performed in one eye at the end of the procedure.

Three animals, with both genders represented, where humanely euthanized with an overdose of a pentobarbital-based euthanasia solution (Euthasol, Virbac, Westlake, TX, United States) administered via intravenous injection, and their retinas were processed for IHC analysis, as previously described (Beltran et al., 2014).

For the *in vivo* imaging, the pupils were dilated with atropine sulfate 1%, tropicamide 1% (both drugs from Akorn Inc., Lake Forest, IL, United States) and phenylephrine 10% (Paragon Biotech, Portland, OR, United States). The dogs were anesthetised by intravenous propofol induction (2–6 mg/kg, Zoetis, Kalamazoo, MI, United States) and maintained with gas inhalation (isoflurane 2–3%, Akorn Inc., Lake Forest, IL, United States). Once positioned in sternal recumbency, the eyelids were kept open with an eye speculum and two stay sutures (Vicryl 4-0, Ethicon Inc., Somerville, NJ, United States). The stay sutures were placed in the conjunctiva 1–2 mm away from the limbus at the 2 and 10 o'clock position in order to gently manipulate the orientation of the visual axis as required to image the entire retina. The ocular surface was lubricated frequently with saline (Sodium Chloride 0.9%, ICU Medical, Inc., Lake Forest, IL, United States) and the anaesthetic plane was closely monitored via heart and respiratory rate, electrocardiography, blood pressure and oxygen saturation measurements.

Optical Coherence Tomography Angiography Characterisation of the Retinal Vasculature

The retinal vascular characteristics were studied and quantified by obtaining 10-degree square OCTA images along the superior, inferior, temporal, and nasal retinal quadrants. For study purposes, 8 areas were preselected within the central and mid-peripheral retina (see **Table 1**). The mid-periphery scans corresponded to the most eccentric locations that could be reliably imaged with the OCTA unit. Indeed, the position of the globes in the orbit, and the shape of the canine skull precluded imaging of the peripheral retina. An additional area centered on the optic nerve head (ONH) was included for qualitative analysis only. The first scan was acquired in the *area centralis* and centered on the canine fovea-like area whose exact location was confirmed by anatomical features previously described including ONL thinning and a centrally converging vascular pattern (**Supplementary Figure S1**) (Beltran et al., 2014). Additionally, the orientation of the NFL on *en face* OCT shows a particular pattern bending around the very center of this cone-rich region (**Supplementary Figure S1A**), and this newly identified feature was used to accurately position the OCTA scanning window.

Each imaged area was composed of volumetric scans that included 512 a-scans and 512 b-scans with 6 μm distance in between b-scans. This provided a lateral resolution of 5.75 μm/pixel and a depth resolution of 3.87 μm/pixel. In order to account for curvature bias, we calculated the retinal magnification factor based on the individual axial globe length and the following formula RMF = 2*π*(0.59*AGL)/360, as previously described (Beltran et al., 2014). The axial globe length was measured in all 12 eyes after each imaging session by ultrasound (Sonomed A-scan A1500, Sonomed-Escalon, Lake Success, NY, United States), and the mean ± SD was 21.2 ± 0.5 mm. By using this approach, we calculated that the 10 × 10 degree OCTA images corresponded in these dogs to a 2.2 ± 0.05 mm^2 area. The exact area for each eye, was used to calibrate the AngioTool software (see below) and obtain accurate quantifications.

TABLE 1 | Location of the areas of interest and their distance from the optic nerve.

Area of interest	Distance from optic nerve (mm) Mean ± SD
Optic nerve head	0
Area centralis	4.8 ± 0.18
Temporal mid-periphery	7.7 ± 1.49
Nasal centre	4.6 ± 0.59
Nasal mid-periphery	9.6 ± 1.05
Superior centre	5.9 ± 0.80
Superior mid-periphery	10.2 ± 1.27
Inferior centre	4.0 ± 0.63
Inferior mid-periphery	6.8 ± 1.33

In order to individually image the vascular networks, the boundaries of the plexuses were identified and selected by adjusting the location where the algorithm is applied on the OCT b-scan, with the designated software (Heidelberg Eye Explorer, HEYEX). In order to define the most superficial individual retinal plexus the first boundary of the slab was placed on the ILM and the second segmentation line was manually displaced in depth until no vessels were captured on the *en face* OCTA. The upper boundary was then displaced to the endpoint of the previous one, and the same process was repeated to define the following plexus. In this way, we not only identified different plexuses but also described their location based on the retinal lamination seen by OCT.

Quantitative analysis was performed in all the areas of interest, with the exception of the ONH scan (**Table 1**). The OCT angiograms were extracted as .tiff files and then imported into the semiautomated vessel-analysis program AngioTool (Zudaire et al., 2011). This is a validated software, accessible in the public domain[1] (0.6a version, National Cancer Institute, Bethesda, MD, United States). AngioTool processes images in order to obtain a set of quantitative parameters and has previously been used to quantify retinal vasculature in other species (Zudaire et al., 2011; Giannakaki-Zimmermann et al., 2016; Liu et al., 2017; Munk et al., 2017; Sun et al., 2021; Told et al., 2021). Once the angiogram is uploaded into AngioTool, the program allows adjustments to the vessel diameter and intensity to ensure that the resulting image matches the correct vessel profile. Once the analysis is completed, the program extracts the results in a working spreadsheet. For each analyzed slab, we selected among the AngioTool parameters: VD, Junction Density (JD), Average Vessels Length (AVL), and Lacunarity (LC). For more details, see **Table 2**.

[1]https://ccrod.cancer.gov/confluence/display/ROB2/Downloads

TABLE 2 | AngioTool parameters used to characterise the retinal vasculature.

Vascular parameter	Unit	Definition and interpretation
Vessel density (Vessels% area)	Vessels area /total area	Percentage of the sampled area that is covered by blood vessels. The values range from 0 to 100. Represents how densely vascularised a tissue is.
Junction density (Branching index)	Junctions /mm^2	Number of vessel junctions normalised per unit area. Informs if there is angiogenesis or vessel loss over time.
Average Vessels length	mm	Mean length of all the vessels in the image. Represents the mean length of the vessels before they branch.
Lacunarity		Index for vascular structural non-uniformity. The higher the value, the more heterogeneous is the area analyzed. Low lacunarity indicates homogeneity in the sampled area.

Validation of Optical Coherence Tomography Angiography Quantifications by Comparison With Fluorescein Angiography and Immunohistochemistry

Fluorescein angiography images were obtained from the last eye evaluated (left eye) in all dogs. The FA images were obtained via fluorescein injection into the cephalic vein (20 mg/kg of Fluorescein sodium 10%, AK-FLUOR, Akorn, Lane Forest, IL, United States). Several cSLO fundus photographs were acquired with a short wavelength laser (488 nm, Spectralis Blue Autofluorescence mode) at the completion of the venous phase defined by a homogeneous and complete filling of the retinal venules (Schaepdrijver et al., 1996). The images were acquired with a 30 degrees lens that provided a lateral resolution of 5.60 μm/pixel.

For wholemount preparation, the retinas were prepared as previously described (Beltran et al., 2014). Briefly, after 15 min of fixation in 4% paraformaldehyde, the neuroretina was separated from the RPE and the fixation continued for 4 h at 4°C. The tissues were incubated for 4 days at 4°C in a solution containing primary antibodies directed against Collagen IV (1:100, Millipore Sigma AB769, Burlington, MA, United States). Fluorochrome-labelled secondary antibodies (Alexa Fluor 488 and 568 dyes; 1:200, Thermo Scientific) and DAPI nuclear stain were applied for 24 h at 4°C. The retinas were imaged using a 2-photon confocal microscope (Leica SP8 Multiphoton, Leica Microsystems, Wetzlar, Germany) with a 20x (HCX APO L, 1.0 NA) water immersion objective lens. The captured images studied were composed of individual 0.5 mm^2 fields, acquired from z stacks spanning from the ILM to the ONL. Z-stacks were acquired at 1.5 μm Z-steps in 1024 × 1024 pixel format at 400 Hz with a line average of 2. These settings offered a lateral resolution of 0.541 μm/pixel and axial resolution of 1.5 μm/pixel. The images were acquired, merged, and analyzed with Leica Application Suite (LAS X, 3D Visualisation Module).

The evaluation of the anatomical features of the plexuses by IHC was performed in three eyes by stitching tiled z-stacks, covering an area that extended from the ONH to the *ora serrata* in all four retinal quadrants. Using the 3D representation module of the Leica Application Suite, we measured the distance from the optic nerve to the area where each of the retinal vascular plexuses was no longer present, to identify the topographical distribution of each vascular network.

For quantitative analysis, the OCTA images were matched with those obtained with FA and IHC using a graphic editing software (Adobe Photoshop CC, Adobe Systems Inc., CA, United States) and by matching vascular landmarks in the areas of interest. For this purpose, the individual 0.5 mm^2 fields on IHC were stitched to cover the same squared area that was previously imaged on OCTA in the eight areas of interest. From this merged three-dimensional stack, the plexuses were extracted by cropping the subset of data that contained the same vascular networks defined by OCTA. Once the individual stacks were extracted, the mass projection image was exported as a .tif file and used for quantification using AngioTool, as previously described.

Statistical Analysis

All statistical analyses were performed using SAS v9.4 (SAS Institute, Cary, NC, United States). For all tests, two-sided $p \leq 0.05$ was considered statistically significant.

The mean (standard deviation, SD) of each OCTA measurements from the different locations within each quadrant was calculated, and 95% normal limits were derived as mean ± 1.96*SD. For the statistical comparison of each OCTA measures between mid-periphery vs. central areas, generalised linear models were fitted and generalised estimating equations (GEE) were used to account for the inter-eye correlation for measures from two eyes of the same dog and correlation of measures at different locations from the same eye. In the GEE, the unstructured covariance structure was used.

For comparison of measures between imaging techniques (OCTA vs. FA and OCTA vs. IHC) that were measured in one eye per dog, paired *t*-tests were used to test their statistical significance.

RESULTS

Optical Coherence Tomography Angiography Enables Identification of Four Vascular Plexuses in the Canine Retina

Manual segmentation in the OCTA module of the HEYEX software enabled precise localisation of individual retinal vascular plexuses within the retinal layers by concurrent visualisation of both the OCTA b-scan and the *en face* view of the angiogram (**Figure 1**). The most inner vascular network found within the NFL extended only into the peripapillary region and did not reach

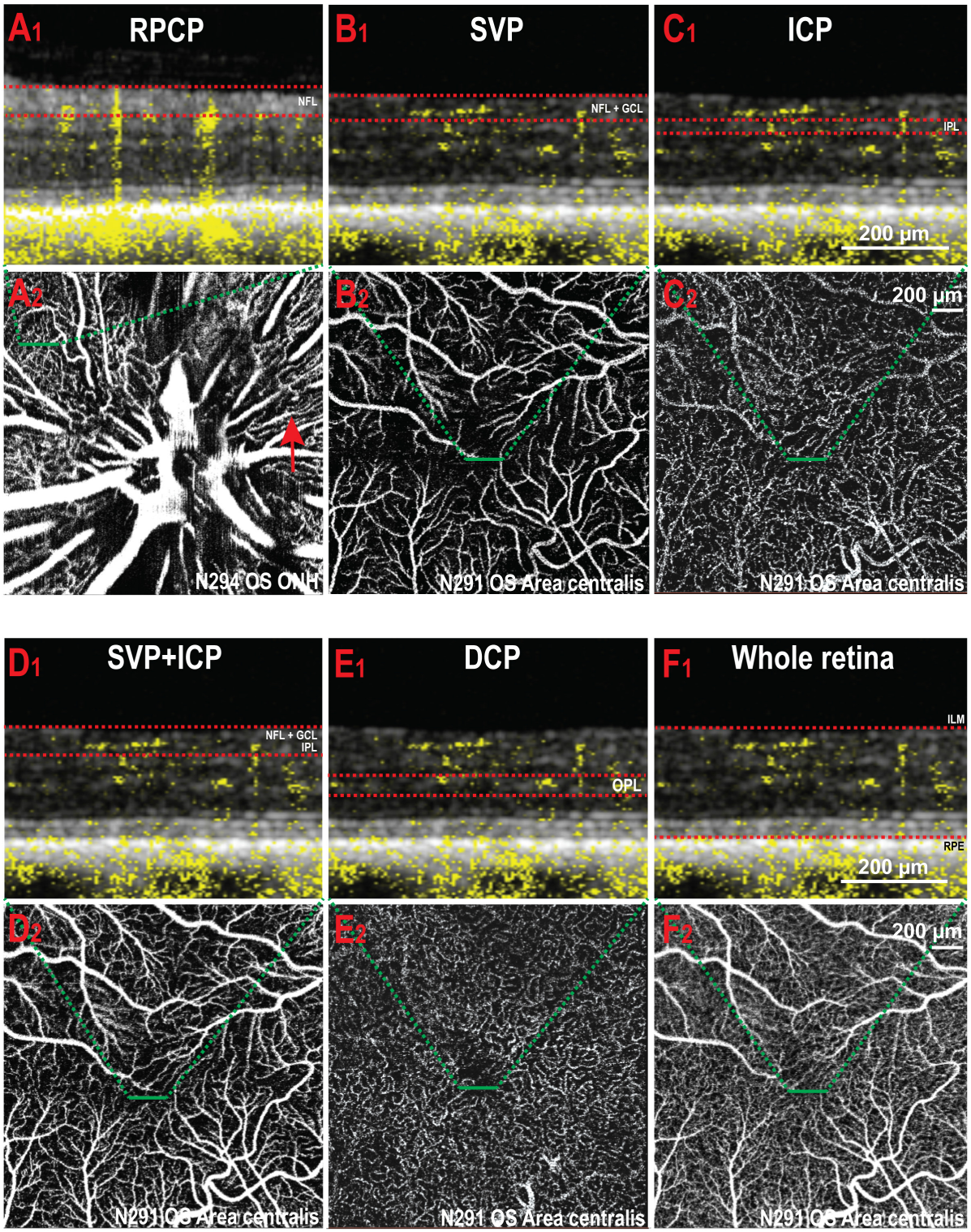

FIGURE 1 | Illustration of the vascular plexuses of the canine retina imaged by OCTA. **(A1,2)** Radial peripapillary capillary plexus (RPCP). This plexus is only seen within the NFL (red arrow) around the optic nerve head. **(B1,2)** Superficial vascular plexus (SVP) in the *area centralis*. **(C1,2)** Intermediate capillary plexus (ICP) in the same area. **(D1,2)** SVP and ICP extracted together. **(E1,2)** Deep capillary plexus (DCP). **(F1,2)** OCT angiogram containing all the retinal vascular networks (= whole retina thickness). The red dotted lines in panels **(A1–F1)** delineate the inner and outer boundaries of the slab selected to extract the angiograms shown in panels **(A2–F2)** (green dashed lines). NFL, nerve fibre layer; OS, left eye; ONH, optic nerve head; GCL, ganglion cell layer; IPL, inner plexiform layer; OPL, outer plexiform layer; ILM, inner limiting membrane; RPE, retinal pigment epithelium.

central areas. This plexus shared similarities with the human Radial Peripapillary Capillary Network (RPCP; **Figures 1A1,2**). The second vascular network spanned from the ILM to the GCL/IPL border, was formed by large arterioles, venules and their connecting capillaries, and branched from the ONH to the mid-periphery (most eccentric areas scanned by OCTA). It was analogous to the Superficial Vascular Plexus described in human retinas (SVP; **Figures 1B1,2**). We did not find an avascular zone in the canine SVP at the corresponding location of the canine fovea-like area, as is commonly seen in species with a foveal pit. The third vascular network was located within the IPL in proximity with the INL and contained capillaries which formed a homogeneous mesh. This vascular network was defined as the Intermediate Capillary Plexus (ICP; **Figures 1C1,2**). The SVP and ICP were seen in very close proximity, and they were frequently extracted together (**Figures 1C1,2**). The fourth and outermost plexus was located within the inner half of the OPL and formed a dense network of capillaries. This plexus was similar to the human Deep Capillary Plexus (DCP; **Figures 1E1,2**).

A previously undescribed feature seen in 9 out of 12 eyes consisted of a small focal area with a lower density of vessels in the DCP at the centre of the canine fovea-like area (**Supplementary Figure S2A**). We confirmed by IHC that this same anatomical feature was visible on retinal wholemounts in the DCP but not in the SVP (**Supplementary Figure S2B**).

Vessel Density and Other Vascular Optical Coherence Tomography Angiography Parameters Vary With Retinal Eccentricity

Due to the presence of large vessels in the SVP that occasionally invade the ICP, individual differentiation and segmentation of these two plexuses was challenging. Consequently, both plexuses were extracted together in the same imaging slab to be quantified as a single image (**Figures 1D1,2**). The DCP was extracted next, and then the last slab, whose limitations were set at the ILM and RPE (whole retina, WR; **Figures 1F1,2**). Representative images from each area and slabs used for quantification are compiled in **Figure 2**.

The 95% confidence intervals of OCTA parameters for each slab (SVP + ICP, DCP and WR) were calculated, providing a range of reference values for this adult dog cohort (**Table 3**).

Along each quadrant, the VD was consistently lower in the mid-periphery in comparison to more central areas. This was observed for both the SVP + ICP and the DCP, although not always reaching statistical significance (**Figures 3A1,B1,C1**). JD values followed a similar topographical pattern, being higher in the more central areas than in the mid-periphery. This reached statistical significance in all four quadrants of the DCP (**Figures 3A2,B2,C2**). AVL results also showed a similar

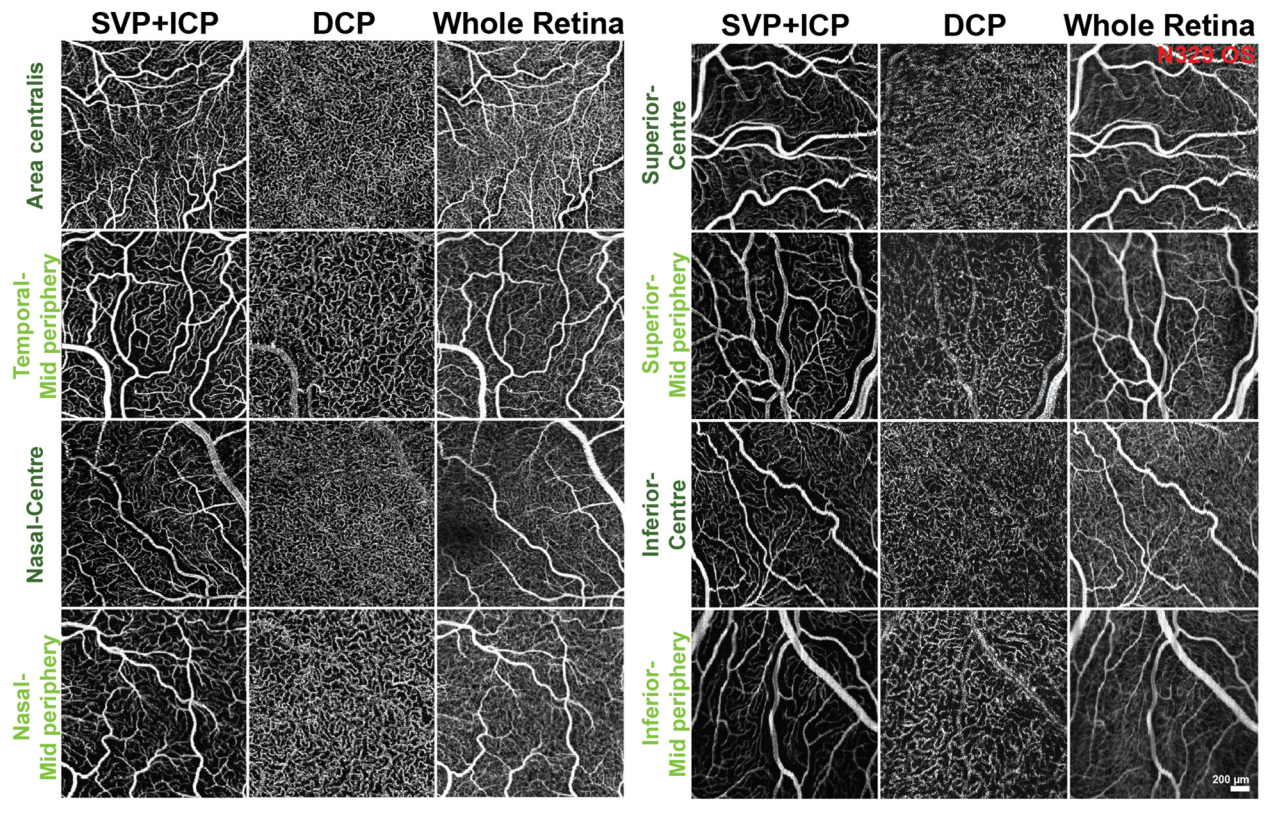

FIGURE 2 | Representative OCTA images of the areas and slabs used for quantification. SVP, superficial vascular plexus; ICP, intermediate capillary plexus; DCP, deep capillary plexus.

TABLE 3 | Normal range of the vascular parameters in each retinal area.

Right eye ($N = 6$)									
95% Confidence limits		***Area centralis***	**Temporal mid-periphery**	**Nasal centre**	**Nasal mid-periphery**	**Superior centre**	**Superior mid-periphery**	**Inferior centre**	**Inferior mid-periphery**
SVP + ICP	VD	28.5–45.1	28.6–43.7	22.2–51.4	24.5–46.1	23.4–44.4	27.5–38.3	22.2–60.8	24.9–43.7
	JD	39.7–179.3	38.5–126.0	50.7–137.7	34.1–117.3	21.8–145.6	30.8–106.3	29.7–152.9	24.9–123.8
	AVL	0.10–0.66	0.17–0.58	0.12–0.66	0.08–0.68	0.01–0.80	0.15–0.64	–0.38 to 2	0.12–0.73
	LC	0.04–0.13	0.05–0.16	0.03–0.16	0.04–0.18	0.01–0.22	0.07–0.15	0.01–0.17	0.06–0.16
DCP	VD	39.1–49.8	35.6–51.0	30.4–49.6	26.0–50.3	27.0–53.8	34.1–47.1	38.4–47.5	27.8–43.2
	JD	125.9–262.0	81.3–280.2	87.8–231.8	40.3–224.6	60.8–279.7	52.7–217.6	121.5–214.0	70.6–146.6
	AVL	0.15–1.26	–0.3 to 1.66	0.06–0.77	–0.28 to 1.19	–0.33 to 1.55	0.10–0.84	0.09–1.22	0.05–0.57
	LC	0.03–0.07	0.03–0.09	0.03–0.11	0.01–0.16	0.00–0.15	0.04–0.09	0.05–0.07	0.05–0.14
WR	VD	39.0–47.5	32.0–48.8	32.8–45.3	33.8–44.6	27.8–47.1	25.9–59.4	31.2–46.9	25.8–48.5
	JD	129.5–258.0	93.2–210.9	110.0–210.1	103.3–209.7	47.0–227.9	89.0–220.3	106.2–187.0	60.9–219.7
	AVL	0.21–1.00	0.19–0.60	0.15–0.67	0.15–0.69	–0.01 to 0.75	–1.57 to 3.45	0.17–0.66	0.01–0.76
	LC	0.04–0.07	0.04–0.10	0.04–0.10	0.05–0.11	0.04–0.13	0.02–0.12	0.05–0.11	0.03–0.15
Left eye ($N = 6$)									
95% Confidence limits		***Area centralis***	**Temporal mid-periphery**	**Nasal centre**	**Nasal mid-periphery**	**Superior centre**	**Superior mid-periphery**	**Inferior centre**	**Inferior mid-periphery**
SVP + ICP	VD	35.1–46.5	31.7–44.2	30.2–49.3	32.0–40.2	21.7–62.2	31.9–42.4	31.7–43.2	24.1–46.3
	JD	81.7–216.0	55.6–117.6	37.1–141.4	77.9–109.2	62.3–144.7	72.6–116.3	52.8–142.1	18.9–112.6
	AVL	0.18–0.84	0.21–0.82	–0.06 to 1.19	0.17–0.72	–0.31 to 1.77	0.24–0.74	0.32–0.75	0.09–0.98
	LC	0.04–0.09	0.07–0.11	0.06–0.11	0.07–0.12	0.03–0.14	0.08–0.10	0.06–0.12	0.03–0.22
DCP	VD	42.1–49.0	33.3–49.6	35.4–51.8	30.8–50.6	39.8–48.4	37.8–45.9	38.5–48.3	27.9–44.6
	JD	139.5–281.7	81.3–221.6	65.3–333.9	51.6–254.2	140.3–232.2	125.3–177.5	114.7–235.3	68.0–162.1
	AVL	–0.09 to 1.74	–0.21 to 1.45	–0.36 to 1.77	–0.58 to 1.92	0.18–1.06	0.31–0.83	0.41–0.81	0.08–0.67
	LC	0.04–0.06	0.03–0.10	0.03–0.08	0.03–0.11	0.04–0.07	0.05–0.08	0.04–0.08	0.04–0.14
WR	VD	40.7–48.6	33.0–47.9	36.8–43.7	35.5–49.0	29.3–48.8	36.6–48.2	30.7–48.5	27.8–45.6
	JD	144.3–278.9	96.1–207.6	133.7–206.9	117.2–245.6	72.5–193.5	109.0–251.7	96.7–220.4	69.0–210.8
	AVL	0.28–1.14	0.26–0.63	0.34–0.49	0.22–0.92	0.09–0.71	0.27–0.82	0.15–0.79	0.06–0.64
	LC	0.04–0.06	0.03–0.12	0.06–0.08	0.03–0.10	0.04–0.13	0.04–0.09	0.03–0.11	0.03–0.17

SVP, superficial vascular plexus; ICP, intermediate capillary plexus; DCP, deep capillary plexus; WR, whole retina; VD, vessel density (%); JD, junction density (number of junctions/mm^2); AVL, average vessel length (mm); LC, lacunarity.

topographical trend, with mid-peripheral vessels being shorter due to decreased tortuosity (**Figures 3A3,B3,C3**). Finally, LC values were found to be higher in mid-peripheral than in central areas, suggesting increased vascular heterogeneity toward the periphery (**Figures 3A4,B4,C4**).

Analysis of the quality of the OCTA scans using signal to noise ratio values provided by the Spectralis software (HEYEX) showed that the best images were acquired in the *area centralis* and the poorest in the inferior mid-periphery. For more details see **Supplementary Table S1**.

Optical Coherence Tomography Angiography Supersedes Fundus Fluorescein Angiography at Detecting Small Vascular Networks

Fluorescein angiography images were acquired at the late venous phase, which was seen at 18 ± 4.7 s after contrast agent injection. Since FA does not allow visualisation of individual vascular networks, the images were compared to the OCTA image extracted from the combination of all the slabs (WR). Qualitatively, OCT angiograms had a greater ability to resolve smaller vascular branches and capillaries than FA (**Supplementary Figure S3A**) and this was confirmed quantitatively when values of vascular parameters (VD, JD, AVL, and LC) were compared between the two techniques (**Supplementary Figure S3B**).

Immunohistochemistry Validates Optical Coherence Tomography Angiography as a Reliable Technique to Image Retinal Vessels

To confirm the presence of the four plexuses identified by OCTA, retinal wholemounts from three previously OCTA-imaged eyes were processed for IHC with an antibody (Collagen IV) that labels vessels and imaged by 2-photon/confocal microscopy (**Figure 4**). A pan-retinal three-dimensional representation of the plexuses and their inter-connections was evaluated, in regions that extended from the ONH to the periphery (*ora serrata*) in

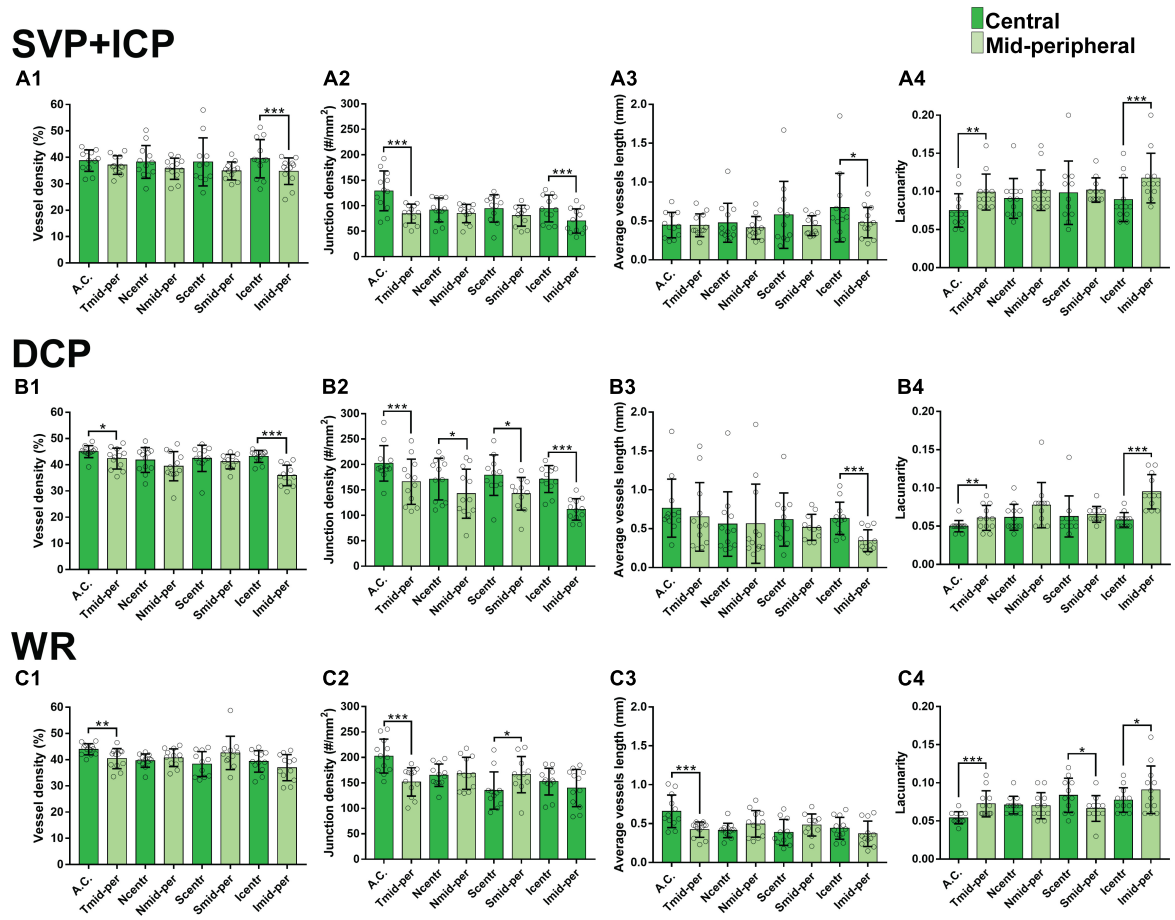

FIGURE 3 | Topographical quantification of vascular plexuses by OCTA in the canine retina. The vessel density **(A1,B1,C1)**, junction density **(A2,B2,C2)**, average vessel length **(A3,B3,C3)** and lacunarity **(A4,B4,C4)** values are provided for the superficial vascular plexus and intermediate capillary plexus (SVP+ICP, **A1–4**), deep capillary plexus (DCP, **B1–4**) and whole retina slabs (WR, **C1–4**). A.C., *area centralis*; T, temporal; N, nasal; S: superior; I, inferior; mid-per, mid-periphery. Results are shown as a mean ± SD ($n = 12$). Paired *t*-test: $*p \leq 0.05$, $**p \leq 0.01$, $***p \leq 0.001$.

each quadrant (**Figure 5A** and **Supplementary Video S1**). The SVP contained large arterioles and venules that radiated from the ONH and diverged off, creating tangential branches above and below to form the closely related ICP and RPCP (**Figure 5A1**). The vessels in the ICP were also seen to branch out and cross through the INL forming the DCP (**Figure 5A1,2**, white arrows). The DCP is a dense plexus of capillaries and the closest vascular supply to the photoreceptors somatas in the ONL (**Figure 4A5**). The DCP approaches the SVP towards the periphery (**Figure 5A3**) to finally merge with it near the ora serrata (**Figure 5A4**). In the two dense capillary networks (ICP and DCP), intercapillary bridging cells were identified and positively labelled with Collagen IV (**Supplementary Video S1**). No vascular structures were found beyond the ONL (**Figure 4A6**).

It is noteworthy that, these four plexuses were not identified in all locations of the retina (**Figure 5B1**). Peripapillary, the RPCP was only found to extend within 4–5.3 mm from the center of the ONH (**Figure 5B2** and **Table 4**). Although easily identifiable in the central retina, the ICP becomes closer to the SVP in the periphery, precluding its independent visualisation. It was found to merge with the SVP within 9–15.6 mm from the centre of the ONH (**Figure 5B** and **Table 4**). In the far periphery, the DCP merged with the SVP (**Figure 5B**).

Qualitative comparison of both imaging techniques showed that small capillaries that were well resolved by confocal microscopy/IHC could also be detected by OCTA, albeit with a lower resolution (**Figure 6**). Images of the SVP + ICP obtained by IHC showed more precisely the smaller capillaries within the ICP, thus resulting in higher VD and JD values in all retinal quadrants, although statistical significance was not always reached, likely due to the small sample size (**Supplementary Figure S4**). Since the homogeneous ICP was better imaged by IHC than OCTA, LC values were lower in IHC images of the SVP + ICP (**Supplementary Figure S4**). It is worth noting that small vessels within the DCP were overall well detected with OCTA, and VD values were not found to be significantly different when comparing the two imaging approaches (**Supplementary Figure S4**). Images from the "Whole retina" slab followed the same trend described for SVP + ICP (**Supplementary Figure S4**) with a higher VD detected by IHC.

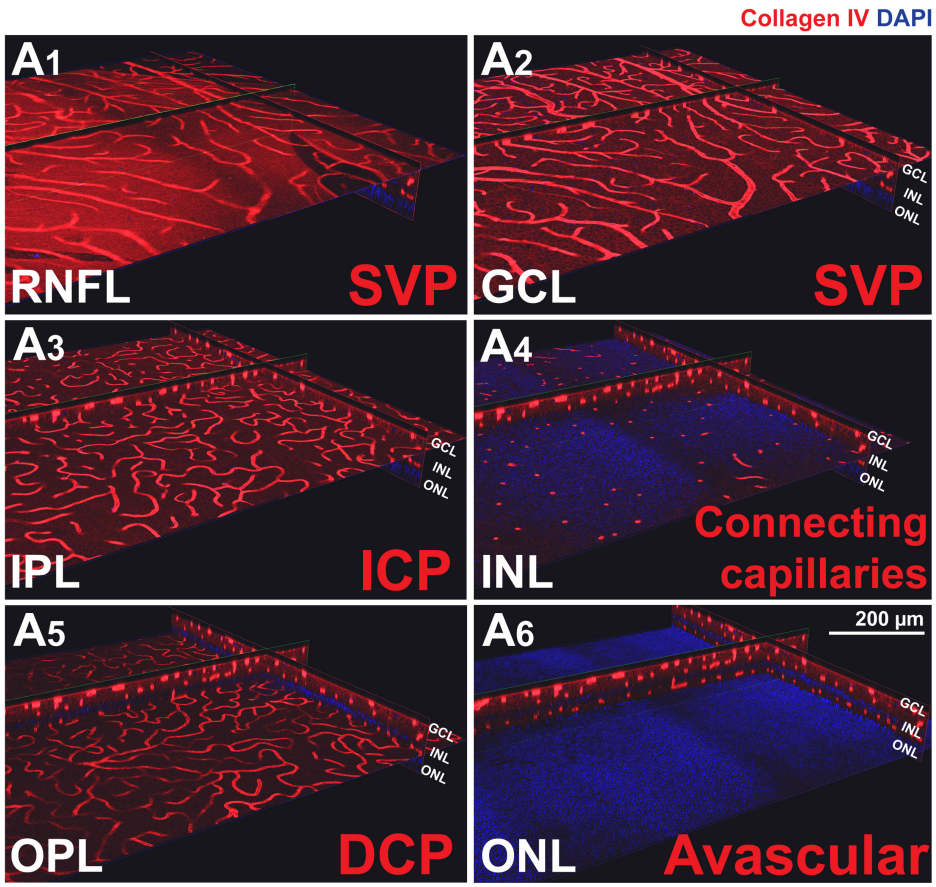

FIGURE 4 | Canine retinal vascular plexuses imaged by 2-photon/confocal microscopy/IHC. **(A1,2)** *En face* and cross-sectional visualisation of the superficial vascular plexus (SVP), **(A3)** the intermediate capillary plexus (ICP), and **(A5)** the deep capillary plexus (DCP). **(A4)** The INL contains connecting capillaries from the ICP to the DCP. **(A6)** The ONL is avascular.

DISCUSSION

Optical Coherence Tomography Angiography Reveals Four Vascular Plexuses in the Canine Retina That Share Similarities With Vascular Networks Reported in Human

The retinal distribution of the main arterioles, venules and capillary networks has been previously, albeit imprecisely, described in dogs through the use of vascular corrosion casting combined with light and electron microscopy (Engerman et al., 1966; Flower et al., 1985; Schaepdrijver et al., 1989). However, the number of plexuses, as well as their nomenclature, differs between canine studies (Engerman et al., 1966; Schaepdrijver et al., 1989). With the use of modern imaging techniques, this work has confirmed the presence of four distinct canine retinal plexuses. Since the topographical pattern and location of these plexuses within the retinal layers is analogous to that found in human retinas, we propose that the same nomenclature (RPCP, SVP, ICP, and DCP) outlined by Campbell et al. (2017) be used in all future description of canine retinas (Cuenca et al., 2020).

Similar to the human retinal vasculature, the holangiotic canine retina has a dual blood supply, with oxygenation of the inner retinal layers provided by the four vascular plexuses, and the outer retina relying on the choriocapillaris (Michaelson, 1954). This contrasts with the vascularisation of other vertebrates in which the entire retina relies quasi exclusively on choroidal blood supply (Rochon-Duvigneaud, 1943). Although no studies have reported measurements of intraretinal oxygen tension levels in the dog, it is likely that it shares a similar profile as that of other holangiotic species (Braun et al., 1995). In holangiotic retinas, the outer retinal oxygen levels gradually decrease as a function of distance from the choriocapillaris, and in the inner retina higher levels are found in close proximity to the retinal plexuses, reflecting the dual blood supply. In contrast, in anangiotic or avascular areas of merangiotic retinas, the oxygen values decrease rapidly as the distance from the choriocapillaris increases, reaching very low levels across the majority of the inner retina (Yu and Cringle, 2001). Our detailed analysis of the canine retinal vasculature, particularly the description of the exact location of each plexus within retinal layers, will help improve further understanding of the physiologic and pathologic intraretinal oxygen tension distribution as well as the energy

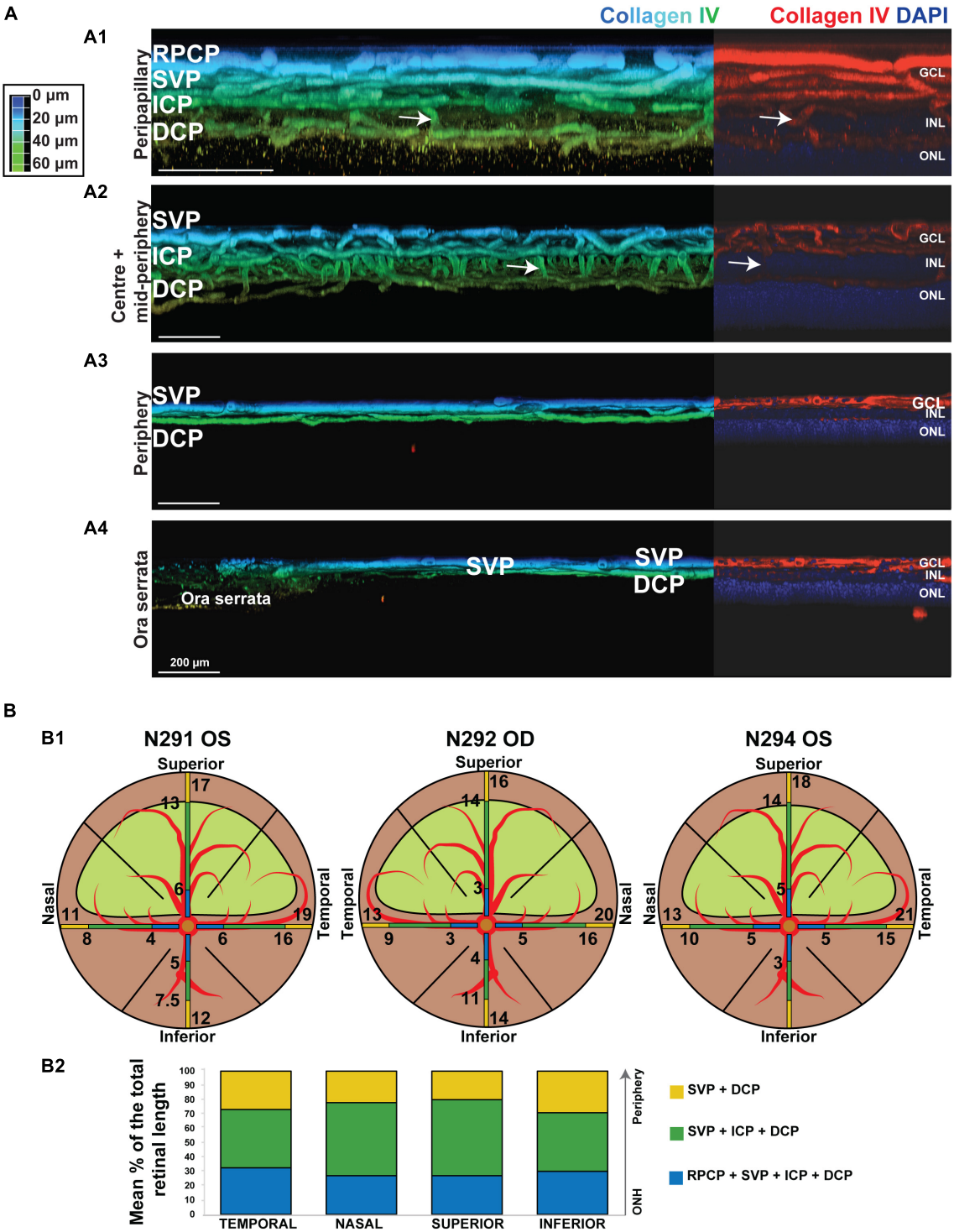

FIGURE 5 | Topographical analysis by IHC of the vascular networks on canine retinal wholemounts. **(A)** Pseudocolored three-dimensional representation of the vascular plexuses imaged by 2 photon/confocal microscopy at four locations extending from the peripapillary region to the *ora serrata*. In the peripapillary region **(A1)**, all four plexuses are identified (RPCP, radial peripapillary capillary plexus; SVP, superficial vascular plexus; ICP, intermediate capillary plexus; DCP, deep capillary plexus). In the central and mid-peripheral retina **(A2)**, the RPCP is no longer seen. At the periphery **(A3)** only the SVP and DCP remain, and both merge at the far periphery close to the *ora serrata* **(A4)**. The right-side portion of each panel shows localisation of the Collagen IV vascular marker (in red) and DAPI (in blue) for improved visualisation of the retinal layers in which the plexuses are located. **(B)** Graphic representation of the topographical extension from the ONH of each vascular plexus measured in three individual retinal wholemounts **(B1)** and averaged as percentage of retinal length (ONH to *ora serrata* distance) in **(B2)**. Numerical values shown on the retinal diagrams **(B1)** represent the distance from the centre of the ONH to the point where a change in the number of plexuses in seen **(B2)**.

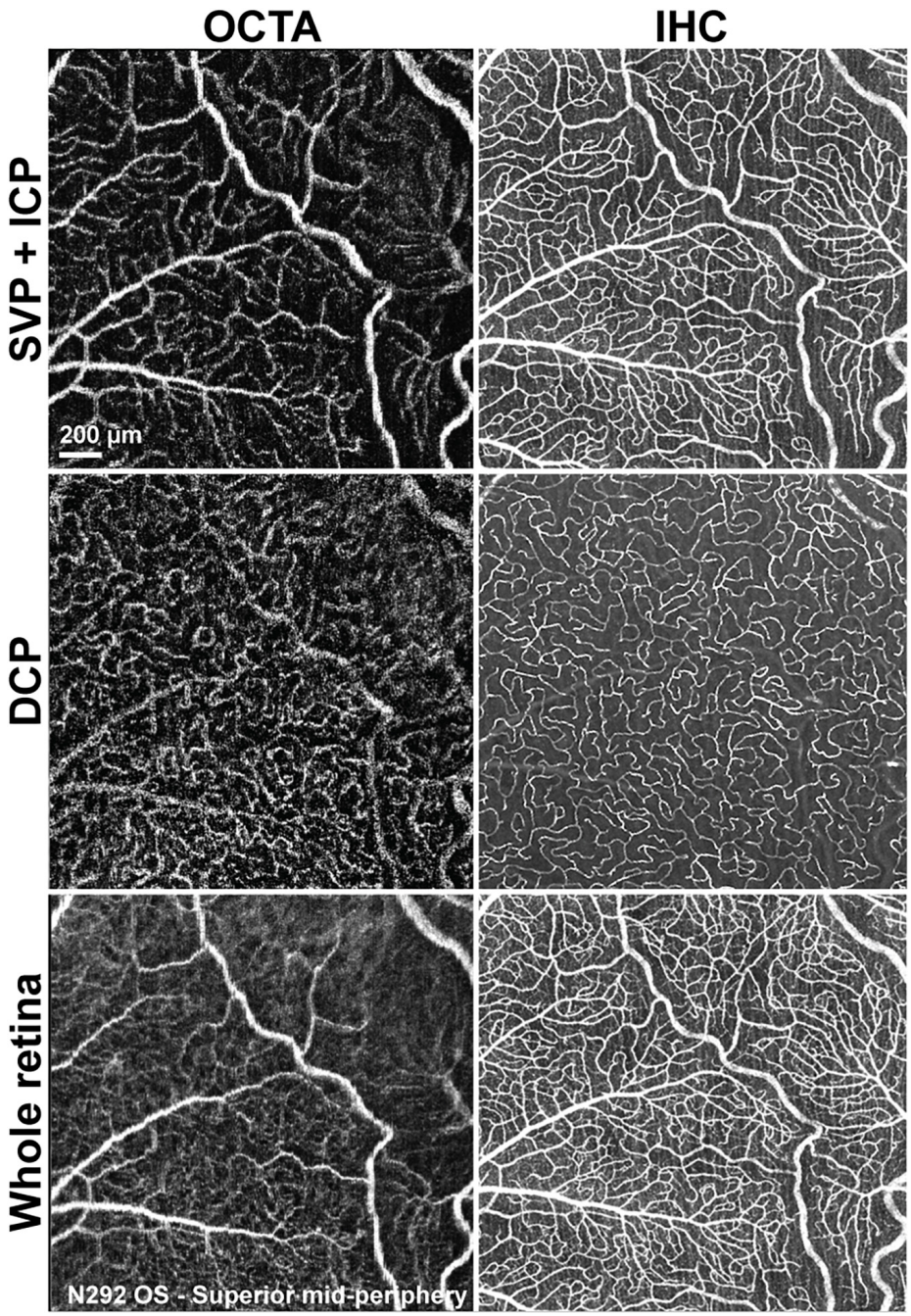

FIGURE 6 | Qualitative comparison of retinal vascular network imaging in dogs by OCTA and IHC. *In vivo* OCTA **(A1,B1,C1)** approaches the level of resolution seen with confocal microscopy/IHC on retinal wholemounts for detection of small capillaries **(A2,B2,C2)**. SVP, superficial vascular plexus; ICP, intermediate capillary plexus; DCP, deep capillary plexus; OS, left eye.

demand and metabolic pathways throughout the various retinal layers in this species.

It is worth noting that while dogs possess a fovea-like region that contains a density of cones comparable to that of primates (Beltran et al., 2014), we did not identify a well-defined foveal avascular zone (FAZ) as described in human eyes (Chui et al., 2012). Nevertheless, in our small cohort of dogs, a poorly defined area with a lower density of vessels was seen in the DCP. Interestingly, this closely resembles the vascular pattern seen in people with a fovea plana. In this condition, the lack of a FAZ and the absence of foveal pit do not affect vision (Marmor et al., 2008; Dolz-Marco et al., 2016; Cicinelli et al., 2017; Chatzistergiou et al., 2021). Hence, the lack of a FAZ in dogs is likely associated with the anatomy of the canine fovea-like area that lacks a foveal pit.

TABLE 4 | Variation in the number of plexuses per quadrant, imaged by 2-photon confocal microscopy.

Plexuses	Temporal		Nasal		Superior		Inferior	
	Mean (*SD*) mm from ONH	Percentage of the total length	Mean (*SD*) mm from ONH	Percentage of the total length	Mean (*SD*) mm from ONH	Percentage of the total length	Mean (*SD*) mm from ONH	Percentage of the total length
RPCP + SVP + ICP + DCP	0–4 (0.5)	33	0–5.3 (0.5)	27	0–4.6 (0.69)	27	0–4 (1)	30
SVP + ICP + DCP	4 (0.5)–9 (1)	41	5.3 (0.5)–15.6 (0.5)	51	4.6 (0.69)–13.6 (0.5)	53	4 (1)–9.5 (1.32)	41
SVP + DCP	9 (1)–12.3 (1.01)	26	15.6 (0.5)–20 (1)	22	13.6 (0.5)–17 (0.6)	20	9.5 (1.32)–13.3 (1.01)	29
Total length	12.3 (1.01)		20 (1)		17 (0.6)		13.3 (1.01)	

RPCP, radial peripapillary capillary plexus; SVP, superficial vascular plexus; ICP, intermediate capillary plexus; DCP, deep capillary plexus.

Optical Coherence Tomography Angiography Can Be Used to Quantify Vascular Parameters in Dogs

Although many studies have reported quantitative data for OCTA images in human retinas, no canine vascular parameters have been described. This study provides normative data for the SVP + ICP, DCP, and WR, successfully establishing a reference range that can be consulted and compared in future studies.

In human eyes, the number of retinal plexuses and their densities diminish toward the periphery (Campbell et al., 2017; Cuenca et al., 2020; Park et al., 2021), and this is similar to what Engerman et al. (1966) previously described in dogs. Our work not only confirms this finding, but now provides quantitative data for four parameters that are frequently used to characterise vascular networks.

Interestingly, we found the VD, JD, and homogeneity (lowest LC) of the DCP to be highest within the *area centralis*. This is very similar to what occurs in the human fovea and this finding indicates that this region of the central canine retina shares closer homology to the primate fovea than previously described (Chan et al., 2012).

Optical coherence tomography angiography signal strength affects the detection of smaller vessels, and Yu et al. (2019) confirmed that a low signal strength can underestimate VD. This highlights the importance of including signal strength or quality parameters when reporting quantitative data (Al-Sheikh et al., 2017). Straightforward ways to optimise quality include, frequently lubricating the ocular surface as well as minimising eye movements through adjustment of the anaesthetic plane to minimise projection and motion artefacts.

Optical Coherence Tomography Angiography Is a Valid Method for Non-invasive *in vivo* Characterisation of Retinal Vascular Networks in Dogs

We validated the OCTA results by comparison with two other imaging techniques, FA, and IHC (acquired with two-photon/confocal microscopy). The lateral resolution differed between techniques: 5.75 μm/pixel for OCTA (Rocholz et al., 2018), 5.6 μm/pixel for FA and 0.541 μm/pixel for confocal microscopy. The axial resolution of OCTA and confocal microscopy images was 3.87 μm/pixel and 1.5 μm/pixel respectively (Rocholz et al., 2018). All three techniques had sufficient resolution to enable detection of the smallest capillaries, which in our samples had a diameter of approximately 8 μm, similar to that reported in human retinas (Tan et al., 2012). Limitations inherent to each technique explained the differences in image quality but did not affect the quantitative comparison of vascular parameters measured by OCTA and IHC/confocal microscopy.

In our evaluation, OCTA angiograms were of higher resolution when compared to FA images at the same location. Similar to what is reported in humans (Spaide et al., 2015), OCTA in dogs enabled identification of capillary beds (ICP and DCP) that were not identified with FA. However, FA provided a larger

field of view and the artefacts that were found in some of the OCTA scans (motion artefacts and decorrelation abnormalities due to projection artefact) were not seen in FA images.

When compared to the images obtained by IHC on retinal wholemounts, our study confirms that OCTA provides good visualisation of the SVP and the DCP. We also found that there was an underrepresentation of small calibre vessels on OCTA, especially those located in highly reflective layers (ICP). These findings have also been reported when evaluating OCTA in *ex vivo* pig eyes (Yu et al., 2021). When compared to images acquired at the same locations by confocal microscopy/IHC, our results suggest that OCTA is a valuable technique for visualising and quantifying retinal vasculature in dogs, especially for analysis of VD in the DCP. Additionally, by IHC we found that the ICP merges with the SVP but not with the DCP as it occurs in human retinas (Chan et al., 2012).

There are some limitations to be considered, such as the small number of eyes that were used for quantitative validation of the OCTA by histology analysis. Additionally, there was minimal misalignment between the images obtained by OCTA and IHC, likely due to shrinkage/expansion due to fixation and distortion of the retinal tissue during the flatmounting process.

CONCLUSION

Our study confirmed the feasibility of using OCTA in dogs, providing depth-resolved images from different segmented retinal layers that allow evaluation of individual plexuses. This paves the way for further *in vivo* analyses of canine retinal vasculature in a wide number of retinal pathologies with a vascular phenotype.

DATA AVAILABILITY STATEMENT

The original contributions presented in the study are included in the article/**Supplementary Material**, further inquiries can be directed to the corresponding author/s.

ETHICS STATEMENT

The animal study was reviewed and approved by IACUC of the University of Pennsylvania.

AUTHOR CONTRIBUTIONS

AR-G conducted all the *in vivo* imaging in the animals, performed the immunohistochemical examination, conceived the project, and wrote the original draft. GR acquired the confocal microscopy images of immunolabeled cryosections. G-SY and YC performed the statistical analysis. NC conceived the project. GA acquired the funding and provided the animal resources. WB conceived the project, acquired the funding, provided the animal resources, supervised the project, reviewed and edited the original graft. All the authors contributed to the article and approved the submitted version.

FUNDING

This study was supported by NIH grants U24EY029890, RO1EY017549, RO1EY06855, P30EY001583, S10 OD021633-01, Foundation Fighting Blindness, Fighting Blindness Canada.

ACKNOWLEDGMENTS

The authors would like to thank Lydia Melnyk for research coordination. Also, Terry Jordan, Jacqueline Wivel, Nanci Newsom, Mayra Quiroz, and the staff of the RDSF for anaesthesia and animal care support. And finally, Tahira Akala and Dr. Alexa P. Gray for help with manuscript editing.

SUPPLEMENTARY MATERIAL

The Supplementary Material for this article can be found online at: https://www.frontiersin.org/articles/10.3389/fnana.2021.785249/full#supplementary-material

REFERENCES

Al-Sheikh, M., Ghasemi Falavarjani, K., Akil, H., and Sadda, S. R. (2017). Impact of image quality on OCT angiography based quantitative measurements. *Int. J. Retina Vitreous* 3:13. doi: 10.1186/s40942-017-0068-9

Barrett, J. W. (1886). The distribution of blood vessels in the retinae of mammals. *J. Physiol.* 7, 230–239. doi: 10.1113/jphysiol.1886.sp000218

Beltran, W. A., Cideciyan, A. V., Guziewicz, K. E., Iwabe, S., Swider, M., Scott, E. M., et al. (2014). Canine retina has a primate fovea-like bouquet of cone photoreceptors which is affected by inherited macular degenerations. *PLoS One* 9:e90390. doi: 10.1371/journal.pone.0090390

Braun, R. D., Linsenmeier, R. A., and Goldstick, T. K. (1995). Oxygen consumption in the inner and outer retina of the cat. *Invest. Ophthalmol. Vis. Sci.* 36, 542–554.

Campbell, J. P., Zhang, M., Hwang, T. S., Bailey, S. T., Wilson, D. J., Jia, Y., et al. (2017). Detailed vascular anatomy of the human retina by projection-resolved optical coherence tomography angiography. *Sci. Rep.* 7:42201. doi: 10.1038/srep42201

Cavallerano, A. A. (1996). Ophthalmic fluorescein angiography. *Optom. Clin.* 5, 1–23.

Chan, G., Balaratnasingam, C., Yu, P. K., Morgan, W. H., Mcallister, I. L., Cringle, S. J., et al. (2012). Quantitative morphometry of perifoveal capillary networks in the human retina. *Invest. Ophthalmol. Vis. Sci.* 53, 5502–5514. doi: 10.1167/iovs.12-10265

Chatzistergiou, V., Cilliers, H., Pournaras, J. A., and Ambresin, A. (2021). Foveaplana on optical coherence tomography angiography: new perspectives. *Retina* 41, 1541–1546. doi: 10.1097/IAE.0000000000003046

Chui, T. Y., Zhong, Z., Song, H., and Burns, S. A. (2012). Foveal avascular zone and its relationship to foveal pit shape. *Optom. Vis. Sci.* 89, 602–610. doi: 10.1097/OPX.0b013e3182504227

Cicinelli, M. V., Carnevali, A., Rabiolo, A., Querques, L., Zucchiatti, I., Scorcia, V., et al. (2017). Clinical Spectrum of Macular-Foveal Capillaries Evaluated with Optical Coherence Tomography Angiography. *Retina* 37, 436–443. doi: 10.1097/IAE.0000000000001199

Coscas, G., Lupidi, M., and Coscas, F. (2016). "Heidelberg Spectralis optical coherence tomography angiography: technical aspects," in *OCT Angiography in Retinal and Macular Diseases. Developments in Ophthalmology*, eds F. Bandello, E. H. Souied, and G. Querques (Basel: Karger), 1–5. doi: 10.1159/000442768

Cuenca, N., Ortuno-Lizaran, I., Sanchez-Saez, X., Kutsyr, O., Albertos-Arranz, H., Fernandez-Sanchez, L., et al. (2020). Interpretation of OCT and OCTA images from a histological approach: clinical and experimental implications. *Prog. Retin. Eye Res.* 77:100828. doi: 10.1016/j.preteyeres.2019.100828

Dolz-Marco, R., Phasukkijwatana, N., Sarraf, D., and Freund, K. B. (2016). Optical coherence tomography angiography in fovea plana. *Ophthalmic Surg. Lasers Imaging Retina* 47, 670–673. doi: 10.3928/23258160-20160707-10

Engerman, R. L., Molitor, D. L., and Bloodworth, J. M. Jr. (1966). Vascular system of the dog retina: light and electron microscopic studies. *Exp. Eye Res.* 5, 296–301. doi: 10.1016/s0014-4835(66)80039-8

Fischer, M. W., and Slatter, D. H. (1978). Preparation and orientation of canine Retinal vasculature: a modified trypsin digestion technique. *Aust. J. Ophthalmol.* 6, 46–50. doi: 10.1111/j.1442-9071.1978.tb00252.x

Flower, R. W., Mcleod, D. S., Lutty, G. A., Goldberg, B., and Wajer, S. D. (1985). Postnatal retinal vascular development of the puppy. *Invest. Ophthalmol. Vis. Sci.* 26, 957–968.

Gelatt, K. N., Henderson, J. D. Jr., and Steffen, G. R. (1976). Fluorescein angiography of the normal and diseased ocular fundi of the laboratory dog. *J. Am. Vet. Med. Assoc.* 169, 980–984.

Giannakaki-Zimmermann, H., Kokona, D., Wolf, S., Ebneter, A., and Zinkernagel, M. S. (2016). Optical Coherence Tomography Angiography in Mice: comparison with Confocal Scanning Laser Microscopy and Fluorescein Angiography. *Transl. Vis. Sci. Technol.* 5:11. doi: 10.1167/tvst.5.4.11

Harris, A., Ciulla, T. A., Chung, H. S., and Martin, B. (1998). Regulation of retinal and optic nerve blood flow. *Arch. Ophthalmol.* 116, 1491–1495. doi: 10.1001/archopht.116.11.1491

Jia, Y., Tan, O., Tokayer, J., Potsaid, B., Wang, Y., Liu, J. J., et al. (2012). Split-spectrum amplitude-decorrelation angiography with optical coherence tomography. *Opt. Express* 20, 4710–4725. doi: 10.1364/oe.20.004710

Kwiterovich, K. A., Maguire, M. G., Murphy, R. P., Schachat, A. P., Bressler, N. M., Bressler, S. B., et al. (1991). Frequency of Adverse Systemic Reactions after Fluorescein Angiography. *Ophthalmology* 98, 1139–1142. doi: 10.1016/s0161-6420(91)32165-1

Leber, T. (1875). *Die Circulations-und Ernährungsverhältnisse des Auges*. Canada: AbeBooks Inc

Liu, W., Luisi, J., Liu, H., Motamedi, M., and Zhang, W. (2017). OCT-Angiography for non-Invasive monitoring of neuronal and Vascular structure in mouse retina: implication for characterization of retinal neurovascular coupling. *EC Ophthalmol.* 5, 89–98.

López-Sáez, M. P., Ordoqui, E., Tornero, P., Baeza, A., Sainza, T., Zubeldia, J. M., et al. (1998). Fluorescein-induced allergic reaction. *Ann. Allergy Asthma Immunol.* 81, 428–430. doi: 10.1016/s1081-1206(10)63140-7

Marmor, M. F., Choi, S. S., Zawadzki, R. J., and Werner, J. S. (2008). Visual insignificance of the foveal pit: reassessment of foveal hypoplasia as fovea plana. *Arch. Ophthalmol.* 126, 907–913. doi: 10.1001/archopht.126.7.907

Michaelson, I. C. (1954). *Retinal Circulation in Man and Animals*. Springfield, Illinois: Charles C Thomas Publisher.

Munk, M. R., Giannakaki-Zimmermann, H., Berger, L., Huf, W., Ebneter, A., Wolf, S., et al. (2017). OCT-angiography: a qualitative and quantitative comparison of 4 OCT-A devices. *PLoS One* 12:e0177059. doi: 10.1371/journal.pone.0177059

Mutlu, F., and Leopold, I. H. (1964). Structure of the retinal vascular system of the dog, monkey, rat, mouse and cow. *Am. J. Ophthalmol.* 58, 261–270. doi: 10.1016/0002-9394(64)91575-2

Park, M. M., Young, B. K., Shen, L. L., Adelman, R. A., and Del Priore, L. V. (2021). Topographic Variation of Retinal Vascular Density in Normal Eyes Using Optical Coherence Tomography Angiography. *Transl. Vis. Sci. Technol.* 10, 15–15. doi: 10.1167/tvst.10.12.15

Parry, H. B. (1953). Degenerations of the dog retina. I. Structure and development of the retina of the normal dog. *Br. J. Ophthalmol.* 37, 385–404. doi: 10.1136/bjo.37.7.385

Pechauer, A. D., Jia, Y., Liu, L., Gao, S. S., Jiang, C., and Huang, D. (2015). Optical coherence tomography angiography of peripapillary retinal blood flow response to hyperoxia. *Invest. Ophthalmol. Vis. Sci.* 56, 3287–3291. doi: 10.1167/iovs.15-16655

Peichl, L. (1992). Topography of ganglion cells in the dog and wolf retina. *J. Comp. Neurol.* 324, 603–620. doi: 10.1002/cne.903240412

Rocholz, R., Teussink, M., Dolz-Marco, R., Holzhey, C., Dechent, J., Tafreshi, A., et al. (2018). *SPECTRALIS optical coherence tomography angiography (OCTA): principles and clinical applications*. Germany: Heidelberg Engineering Academy, 1–10.

Rochon-Duvigneaud, A. (1943). *Les yeux et la vision des vertébrés*. Paris: Masson.

Schaepdrijver, L. D., Simoens, P., and Lauwers, H. (1996). Fluorescein angiography of the canine retina. *Vet. Comp. Ophthalmol.* 6, 111–119.

Schaepdrijver, L. D., Simoens, P., Lauwers, H., and Geest, J. P. D. (1989). Retinal vascular patterns in domestic animals. *Res. Vet. Sci.* 47, 34–42. doi: 10.1016/s0034-5288(18)31228-1

Spaide, R. F., Klancnik, J. M. Jr., and Cooney, M. J. (2015). Retinal vascular layers imaged by fluorescein angiography and optical coherence tomography angiography. *JAMA Ophthalmol.* 133, 45–50. doi: 10.1001/jamaophthalmol.2014.3616

Sun, M. T., Huang, S., Chan, W., Craig, J. E., Knight, L. S. W., Sanders, P., et al. (2021). Impact of cardiometabolic factors on retinal vasculature: A 3 x 3, 6 x 6 and 8 x 8-mm ocular coherence tomography angiography study. *Clin. Exp. Ophthalmol.* 49, 260–269. doi: 10.1111/ceo.13913

Tan, P. E., Yu, P. K., Balaratnasingam, C., Cringle, S. J., Morgan, W. H., Mcallister, I. L., et al. (2012). Quantitative confocal imaging of the retinal microvasculature in the human retina. *Invest. Ophthalmol. Vis. Sci.* 53, 5728–5736. doi: 10.1167/iovs.12-10017

Told, R., Reiter, G. S., Schranz, M., Reumueller, A., Hacker, V., Mittermueller, T. J., et al. (2021). Correlation of retinal thickness and swept-source optical coherence tomography angiography derived vascular changes in patients with neovascular age-related macular degeneration. *Curr. Eye Res.* 46, 1002–1009. doi: 10.1080/02713683.2020.1849734

Yao, X., Alam, M. N., Le, D., and Toslak, D. (2020). Quantitative optical coherence tomography angiography: a review. *Exp. Biol. Med.* 245, 301–312. doi: 10.1177/1535370219899893

Yu, D. Y., and Cringle, S. J. (2001). Oxygen distribution and consumption within the retina in vascularised and avascular retinas and in animal models of retinal disease. *Prog. Retin. Eye Res.* 20, 175–208. doi: 10.1016/s1350-9462(00)00027-6

Yu, J. J., Camino, A., Liu, L., Zhang, X., Wang, J., Gao, S. S., et al. (2019). Signal strength reduction effects in OCT angiography. *Ophthalmol. Retina* 3, 835–842. doi: 10.1016/j.oret.2019.04.029

Yu, P. K., Mehnert, A., Athwal, A., Sarunic, M. V., and Yu, D. Y. (2021). Use of the retinal vascular histology to validate an optical coherence tomography angiography technique. *Transl. Vis. Sci. Technol.* 10:29. doi: 10.1167/tvst.10.1.29

Zudaire, E., Gambardella, L., Kurcz, C., and Vermeren, S. (2011). A computational tool for quantitative analysis of vascular networks. *PLoS One* 6:e27385. doi: 10.1371/journal.pone.0027385

Conflict of Interest: The authors declare that the research was conducted in the absence of any commercial or financial relationships that could be construed as a potential conflict of interest.

Publisher's Note: All claims expressed in this article are solely those of the authors and do not necessarily represent those of their affiliated organizations, or those of the publisher, the editors and the reviewers. Any product that may be evaluated in this article, or claim that may be made by its manufacturer, is not guaranteed or endorsed by the publisher.

frontiers in Neuroanatomy

ORIGINAL RESEARCH
published: 23 December 2021
doi: 10.3389/fnana.2021.786729

The Functional Anatomy of the Cornea and Anterior Chamber in Lampreys: Insights From the Pouched Lamprey, *Geotria australis* (Geotriidae, Agnatha)

H. Barry Collin[1], *Julian Ratcliffe*[2] *and Shaun P. Collin*[3,4]*

[1] Department of Optometry and Vision Science, University of New South Wales, Kensington, NSW, Australia, [2] La Trobe Bioimaging Platform, La Trobe University, Bundoora, VIC, Australia, [3] Oceans Graduate School and Oceans Institute, The University of Western Australia, Crawley, WA, Australia, [4] School of Life Sciences, La Trobe University, Bundoora, VIC, Australia

Extant lampreys (Petromyzontiformes) are one of two lineages of surviving jawless fishes or agnathans, and are therefore of critical importance to our understanding of vertebrate evolution. Anadromous lampreys undergo a protracted lifecycle, which includes metamorphosis from a larval ammocoete stage to an adult that moves between freshwater and saltwater with exposure to a range of lighting conditions. Previous studies have revealed that photoreception differs radically across the three extant families with the Pouched lamprey *Geotria australis* possessing a complex retina with the potential for pentachromacy. This study investigates the functional morphology of the cornea and anterior chamber of *G. australis*, which is specialised compared to its northern hemisphere counterparts. Using light microscopy, scanning and transmission electron microscopy and microcomputed tomography, the cornea is found to be split into a primary spectacle (dermal cornea) and a scleral cornea (continuous with the scleral eyecup), separated by a mucoid layer bounded on each side by a basement membrane. A number of other specialisations are described including mucin-secreting epithelial cells and microholes, four types of stromal sutures for the inhibition of stromal swelling, abundant anastomosing and branching of collagen lamellae, and a scleral endothelium bounded by basement membranes. The structure and function of the cornea including an annular and possibly a pectinate ligament and iris are discussed in the context of the evolution of the eye in vertebrates.

Keywords: lamprey, cornea, spectacle, iris, stroma, sutures, annular ligament, pectinate ligament

OPEN ACCESS

Edited by:
Nicolás Cuenca,
University of Alicante, Spain

Reviewed by:
M. Carmen Acosta,
Miguel Hernández University of Elche, Spain
Adolfo Aracil-Marco,
Miguel Hernández University of Elche, Spain

***Correspondence:**
Shaun P. Collin
s.collin@latrobe.edu.au
orcid.org/0000-0001-6236-0771

Received: *30 September 2021*
Accepted: *30 November 2021*
Published: *23 December 2021*

Citation:
Collin HB, Ratcliffe J and Collin SP (2021) The Functional Anatomy of the Cornea and Anterior Chamber in Lampreys: Insights From the Pouched Lamprey, Geotria australis (Geotriidae, Agnatha). Front. Neuroanat. 15:786729. doi: 10.3389/fnana.2021.786729

INTRODUCTION

Lampreys (Petromyzontiformes) and hagfishes (Myxiniformes) are the extant representatives of the agnathan (jawless) stage in vertebrate evolution. There are 42 known extant species of lamprey; 37 species belonging to the family Petromyzontidae restricted to the northern hemisphere (Hubbs and Potter, 1971; Potter et al., 2015) and five species separated into two families in the southern hemisphere, with Mordaciidae containing three species and Geotriidae represented by two species,

Geotria australis and the recently reinstated *Geotria macrostoma* (Potter and Strahan, 1968; Riva-Rossi et al., 2020). Phylogenetic analyses suggest that northern hemisphere lampreys are the most derived and of the two southern hemisphere genera (*Geotria* and *Mordacia*), *Mordacia* is the most basal (i.e., most similar to the ancestral stock; Potter et al., 2015), but the issue is not fully resolved (Evans et al., 2018).

Lampreys have a protracted larval phase, where the larvae are microphagous and photophobic (Hardisty and Potter, 1971a,b), burrowing in freshwater rivers for many years, before they undergo a radical metamorphosis to become adults. Anadromous species such as the Pouched lamprey, *Geotria australis* then migrate downstream to enter their marine phase, where they are found in high numbers throughout the austral summer in the cold and clear waters surrounding South Georgia (Potter et al., 1979; Prince, 1980). *G. australis* form a substantial component of the diet of the grey-headed albatross, *Diomedea chrysostoma* (Prince, 1980), which forage on parasitised teleost fishes (Hardisty, 1979; Potter et al., 1980) in the brightly-lit surface waters. As a means of camouflage, both downstream and marine phase *G. australis* adopt a countershading colouration with a luminance gradient from dark (blue) dorsal to pale (silver) ventral pigmentation to enhance the match between the radiance of the body and that of the background from different viewing angles. Upon reaching maturity, *G. australis* then return to their natal freshwater river and migrate upstream, where they spawn and ultimately die (Potter et al., 1983).

The image-forming eyes of *G. australis* have been found to be the most specialised of all lampreys examined, at least with respect to photoreception. In contrast to the northern hemisphere (holarctic) lampreys and members of the only other southern hemisphere family of lampreys (Mordaciidae), the pouched lamprey possesses five types of photoreceptors (based on both morphology, spectral sensitivity and visual opsin expression, Collin et al., 2003a,b; Warrington et al., 2020), providing the potential for pentachromatic vision under some light conditions throughout its protracted life cycle. The eyes of members of the holarctic Petromyzontidae possess two photoreceptor types (a cone-like and a rod-like, Holmberg et al., 1977; Ishikawa et al., 1987), while the Mordaciidae possess only a single type of rod-like photoreceptor (Collin and Potter, 2000). Although a non-spherical lens to mediate variable focus and a split cornea have previously been reported in *G. australis* (Collin et al., 1999), there are no detailed analyses of the cornea in any southern hemisphere species of lampreys.

Both Walls (1942) and Duke-Elder (1958) describe the eyes of many species of northern hemisphere (holarctic) lampreys to be flattened antero-posteriorly with the cornea split into dermal and scleral components separated by a delicate layer of mucoid tissue. A prominent feature of these eyes is a transparent "window" in the dermis overlying the eye that forms the dermal cornea. The mucoid layer allows the eye to rotate beneath the dermal goggle. The arrangement of a "fixed transparent structure separate from the globe underneath which the eye is free to rotate" is defined as a primary spectacle (Treviranus, 1820; Franz, 1934), which is derived from the surface ectoderm. This arrangement is different from a secondary spectacle, which is formed by the development of a transparent area of the eyelids by the edge to edge fusion of two lids that have become transparent to form a fixed spectacle (Hein, 1913; Franz, 1934; Walls, 1942). The lens is close to the scleral cornea, which is continuous with the sclera of the eyecup. The tendon of a large cornealis muscle located outside and caudal to the eyecup inserts into the posterior edge of the dermal cornea, which, upon contraction, pulls the dermal and scleral corneas and the lens, toward the retina to accommodate from myopia to emmetropia (Walls, 1942).

The split corneas of the Northern hemisphere lampreys including the Sea lamprey, *Petromyzon marinus* (Van Horn et al., 1969a,b**;** Pederson et al., 1971) and the European river lamprey, *Lampetra fluviatilis* (Dickson and Graves, 1981) have previously been described. The dermal cornea is thick with a layer of stratified squamous epithelial cells overlying a stroma of collagen lamellae, many of which are linked by sutural fibres that inhibit swelling and prevent the loss of transparency during environmental changes (Van Horn et al., 1969b; Pederson et al., 1971). A mucoid layer bounded by mesodermal layers of cells, overlies a scleral cornea with a stroma that lacks fibroblasts and a posterior layer of endothelial cells. Dickson and Graves (1981) also provide an ultrastructural description of the eye in the Sea lamprey, *P. marinus* including the anterior chamber, iris and lens.

There are only a few studies of the cornea in southern hemisphere lampreys, namely, the Pouched lamprey, *Geotria australis* (Collin et al., 1999; Collin and Collin, 2000a, 2006) and the Shorthead lamprey, *Mordacia mordax* (Collin and Collin, 2000a, 2006; Collin and Potter, 2000), with these studies focussing only on light and scanning electron microscopical examination of the ultrastructure of the corneal epithelial surface. One publication used transmission electron microscopy to briefly describe the ultrastructure of the cornea of the ammocoete larva of *Geotria australis* (Meyer-Rochow and Stewart, 1996).

The aim of this study is to describe the functional morphology of the cornea and anterior chamber in the Pouched lamprey, *Geotria australis*. This anadromous species represents one of only two species in the family Geotriidae and, compared to the other two families of lampreys, possesses a specialised visual system with the potential for pentachromacy over a range of light conditions throughout its lifecycle. It is hoped that this study will improve our understanding of the evolution of the cornea and its role in vision.

MATERIALS AND METHODS

Source of Animals

Ten recently-metamorphosed, downstream migrating young adults of *Geotria australis* (Gray, 1851) (75–110 mm in total length) were collected from streams and rivers in south-western Australia using an electric fish shocker. All collection, holding and experimental procedures followed the guidelines of the National Health and Medical Research Council (NHMRC) - Australian Code of Practice for the Care and Use of Animals for Scientific Purposes, in accordance with The University of Western Australia Animal Local Ethics protocol (Approval Numbers: RA/3/100/917 and RA/3/100/1220). Three upstream

migrants of *G. australis* at approximately 2–3 months after they had commenced their spawning run (50–60 cm in total length) were also captured using fish traps at Meadowbank dam in the Derwent River, Tasmania (Inland Fisheries Service Permit Number: 2011-32) and transported to The University of Western Australia (Department of Fisheries Translocation Permit Number: 871/11). Animals were kept in aquaria in a temperature-controlled room that was maintained at 10–14°C with a 12 h:12 h light:dark cycle. While maintained in aquaria, the head and eyes of both downstream and upstream migrants were photographed using a Nikon digital camera (D5600) (Collin and Collin, 2021b).

Animals were euthanised by immersion in a 0.5 mg ml^{-1} solution of tricaine methanesulfonate (MS-222; Sigma-Aldrich, Australia) buffered with an equal concentration of $NaHCO_3$ (Ajax Finechem, Australia) in the light phase of the light/dark cycle.

Light and Electron Microscopy

Enucleated eyes, including the dermal cornea, were immersion-fixed in Karnovsky's fixative (2.5% (w/v) glutaraldehyde (ProSciTech, Australia), 2% (w/v) PFA and 1% dimethyl sulphoxide (DMSO; Sigma-Aldrich, Australia) in 0.1 M sodium cacodylate buffer (ProSciTech, Australia), pH 7.4) and stored at 4°C. Eyes were post-fixed in 1% (w/v) osmium tetroxide (Sigma-Aldrich, Australia) in 0.13M Sorenson's buffer (0.13M Na_2HPO_4 (Millipore Sigma, Australia), 0.13 M KH_2PO_4 (Sigma-Aldrich, Australia), pH 7.4) for about 2 h. The tissue was rinsed in 0.13 M Sorenson's buffer, dehydrated through a graded series of ethanols (25, 50, 70, 80, 95, and 100%) followed by treatment with propylene oxide (VWR, Australia), before infiltration with araldite (ProSciTech, Australia) or Spurrs (Sigma-Aldrich) resin using a tissue processor (Leica-Reichert Lynx). The samples were then cured at 60°C overnight.

Transverse and tangential (semi-thin) sections (1–2 μm) were cut using an American Optical rotary microtome and a glass knife. Sections were mounted on subbed slides, stained with Toluidine blue, examined using a BH-2 Olympus compound light microscope and photographed on an Olympus DP-30 digital camera fitted with a trinocular C mount. Ultrathin sections (70–90 nm) were cut using a diamond knife (DiATOME 45°), collected on copper grids with 200 mesh or rectangular 75/300 mesh (ProSciTech, Australia) and stained using lead citrate (Reynolds, 1963) and uranyl acetate according to Collin et al. (1999). Sections were examined on a Philips 410 transmission electron microscope operated at 80 kV and photographed using Kodak Technical Pan black and white film rated at 100 ASA, or on a Jeol JEM-2100 LaB_6 TEM operated at 80 kV and photographed on a Gatan Orius SC 200 CCD.

Following post-fixation of the eyes in osmium tetroxide in 0.1 M cacodylate buffer and dehydration in a graded series of alcohols (30, 50, 70, 90, 95, and 100%), ocular tissue was critical point-dried in either a Polaron (Watford, United Kingdom) or a Tousimis (Labtech, United Kingdom) critical point dryer and mounted on 10-mm aluminium stubs with double-sided tape. Once the two corneas were dissected free of the globe at the limbus, they were carefully separated under a dissecting microscope (Nikon SMZ745T). Both corneas were then hemisected so that half of the cornea was inverted and both sides were displayed in order to ensure both anterior and posterior surfaces were differentiated. Selected mounted corneal pieces were examined using one of two methods: (1) Corneal tissue was coated with 12–15 nm of gold-palladium in a Polaron sputter coater, placed in an oven at 40°C overnight before being examined using a JEOL field emission scanning electron microscope operated at an accelerating voltage of 3 kV; and (2) Corneal tissue was coated with 5 nm platinum in a Safematic CCU-010 HV sputter coater (Microscopy Solutions, Australia) and examined using a Hitachi SU7000 field emission SEM operated at an accelerating voltage of 5 kV, equipped with backscattering secondary electron and STEM detectors. Results were recorded both on 35 mm film and digitally. The Hitachi SU7000 FESEM multi zig-zag function was used for automated wide area montaging in order to examine the extent of the insertion of the annular ligament into the scleral cornea.

Micro Computed Tomography

A block containing the eye of a downstream migrant, prepared as above for TEM imaging was used for microCT imaging. Micro X-ray Computed Tomography (μXCT) measurements were carried out using an Xradia© micro XCT200 (Carl Zeiss X-ray Microscopy, Inc.). This uses a microfocus X-ray source with a rotating sample holder and an imaging detector system consisted of coupling objective lens and CCD camera. The source consists of a closed x-ray tube with the tube voltage of 40 kV and a peak power of 10W. One data acquisition set consisted of 361 equiangular projections over 180 degrees. The exposure time was 1 s for each projection. The tomographic scan involved rotating the sample whilst recording transmission images on the CCD. Each projection image was corrected for the non-uniform illumination in the imaging system, determined by taking a reference image of the beam without sample. A cone beam filtered back-projection algorithm is used to obtain the 3D reconstructed image. The final three-dimensional reconstructed image size was 512 × 512 × 512 voxels with the voxel size of 7 μm along each side and Field of View (FOV) of $(3.5\ mm)^3$. A lateral image of the eye is presented to show the location and size of the annular ligament with respect to other ocular features.

Quantitative Analyses

Measurements of both surface (using SEM) and internal (using TEM) corneal features in left and right eyes were performed on digital images using the Photoshop calibration tool (Version 20.0.4). Although all features of the cornea and anterior chamber were examined in both phases (downstream and upstream migrants), all morphometric measurements presented are only for the downstream individuals. The ultrastructure of the cornea and anterior chamber was examined in both downstream and upstream stages in order to assess whether there were any major morphological changes during the anadromous adult phase of the lifecycle of this species, other than overall changes in eye size. Since there were no major changes, we restricted our morphometric analyses to only the eyes of downstream migrants. For statistical reasons, we targetted downstream

migrants, since they were all captured just prior to entering the marine phase and had a comparable eye size. Between 20 and 50 examples of each corneal feature were measured (± standard deviation) and dimensions were compared using a two-tailed t-test for independent variables. Measurements were performed on both left (n = 3) and right (n = 4) eyes of seven individual downstream migrants, but all features were not found to be significantly different, as has been found for corneal features in a range of other vertebrate eyes (Nam et al., 2006; Werther et al., 2017; Collin and Collin, 2021b). Therefore, the data for left and right eyes were pooled. The mean and standard deviation for each corneal component are presented in **Table 1**. No attempt was made to assess the degree of shrinkage in our study in order to allow direct comparison to be made with measurements derived using previously published electron micrographs using similar methods. However, due to the different methods of histological processing, it is expected that the same corneal features measured using scanning and transmission electron microscopy may differ slightly. Shrinkage of around 30–40% is expected following fixation and resin embedding for transmission electron microscopy (Hayat, 1986). Therefore, a correction factor should be applied to the data presented to give an estimate of the *in vivo* tissue and cell dimensions. All comparisons of the arrangement and morphometric analyses of components of the cornea and anterior chamber in other species are with comparable adult phases unless otherwise indicated.

TABLE 1 | Summary of the components of the dermal and scleral corneas and their dimensions in the Pouched lamprey, *Geotria australis* listed from anterior to posterior.

Corneal Region	Central	Peripheral
Dermal cornea		
Epithelium	24.4 ± 4.1 μm	61.9 ± 16.1 μm
Basement membrane	140 ± 31 nm	140 ± 31 nm
Bowman's layer	Not present	Not present
Stroma (∼100 lamellae)	24.4 ± 3.1 μm	110.1 ± 34.7 μm
Basement membrane	Not present	Not present
Monocellular layer	885 ± 68 nm	885 ± 68 nm
Basement membrane	20.7 ± 7 nm	20.7 ± 7 nm
Total dermal cornea	49.85 μm	173.05 μm
Mucoid layer	Present	Present
Scleral cornea		
Basement membrane	25 ± 3 nm	25 ± 3 nm
Monocellular layer	978 ± 29 nm	978 ± 29 nm
Basement membrane	Not present	Not present
Stroma (∼20 lamellae)	4.75 ± 0.64 μm	15.6 ± 4.5 μm
Basement membrane	86 ± 15 nm	86 ± 15 nm
Monocellular layer (endothelium)	707 ± 45 nm	707 ± 45 nm
Basement membrane	37 ± 12 nm	37 ± 12 nm
Total scleral cornea	6.58 μm	17.83 μm
Annular ligament	Not present	Zero to 135 μm

RESULTS

Dermal Cornea

The cornea of the Pouched lamprey (*Geotria australis*) possesses a primary spectacle (dermal cornea) and a scleral cornea separated by a narrow mucoid layer, which widens toward the periphery (**Figure 1**). Using light and transmission electron microscopy, the thickness of the dermal cornea was 49.85 μm in the centre with the epithelium (24.4 ± 4.1 μm) and stroma (24.4 ± 3.1 μm) being of equal thickness (**Figure 1G**). In the periphery, there is a three-fold increase in thickness to 173.05 μm, with the dermal stroma occupying almost two thirds of the total corneal thickness (**Table 1**). In the caudal periphery of the dermal cornea, there is a dorso-ventral seam of connective tissue, which indicates the insertion of the tendon of the caudal cornealis muscle. The cornealis muscle is located extra-orbitally and just beneath the dermis of the head. A suspensory ligament and an intraocular retractor muscle are absent, leaving the lens to be supported only by the vitreous humour, the iris, scleral cornea and a thin fibrous membrane extending from the lens equator to the ora retinalis (Gustafsson et al., 2010).

Viewed using scanning electron microscopy (SEM), the surface of the dermal cornea is covered by polygonal, mainly rounded hexagonal and pentagonal epithelial cells (**Figure 2**). The superficial epithelial cells are covered by numerous microprojections (both microvilli and interweaving microplicae) with a mean width of 115 ± 6 nm and a density of 5,511 ± 2,025 cells/mm^{-2} (density previously published by Collin and Collin, 2000a, 2006). Between the microplicae, are numerous holes or pits (microholes), which vary in size up to 660 nm in diameter, with a previously published mean diameter of 395 ± 15 nm (Collin and Collin, 2006). However, we remeasured the diameter of the corneal holes using SEM and found that the size (diameter) of the holes was dependent on the size of the cell, with the smallest cells having the largest holes and the larger cells having the smallest holes, while the largest cells had no holes (**Table 2** and **Figures 2A–C**). In addition, the microhole maximum diameter as a percentage of the cell maximum diameter decreased from 11.34 ± 1.84% for the small cells (up to 8 μm) to 1.38 ± 0.45% for the large cells (15–19 μm) (**Table 2**).

Viewed using transmission electron microscopy (TEM), the superficial epithelium has five or six layers of stratified squamous cells (**Figure 3A**). The shape and arrangement of these cells appears to fit the criteria for scutoids as presented by Gómez-Gálvez et al. (2018). The intermediate (wing) epithelial cells immediately below the superficial cells are flatter and wider (up to 14.5 μm) with elongated nuclei, and contain high numbers of vacuoles, which are almost exclusively aggregated on the side of the nucleus nearer to the epithelial (anterior) surface (**Figure 3B**). The mean diameter of these intracellular vacuoles (430 ± 191 nm) is not significantly different (p = 0.463) from the diameter of the surface holes. These vacuoles contain amorphous material, presumably mucus and are arranged in cylindrical formations extending up to 2 μm beneath the surface of the epithelium and are separated by cell cytoplasm containing fine filaments (**Figure 3B**). The mean diameter of the surface holes is 403 ± 128 nm, which is not significantly different from the mean diameter of the surface holes observed using SEM. Adjacent

TABLE 2 | A comparison between the diameter of the holes in the epithelial cells of the cornea of the Pouched lamprey, *Geotria australis* and the diameter of the corneal epithelial cells.

	Diameter of holes	Comparison	Significance	% of cell diameter*
Small cells (up to 8 μm)	457 ± 89 nm	Small versus medium	$p < 0.00001$	11.34 ± 1.84
Medium cells (9–14 μm)	317 ± 55 nm	Medium versus large	$p < 0.00001$	3.25 ± 1.70
Large cells (15–19 μm)	196 ± 38 nm	Small versus large	$p < 0.00001$	1.38 ± 0.45
Largest cells (>20 μm)	No holes		All significant	

**Microhole maximum diameter as a percentage of the cell maximum diameter.*

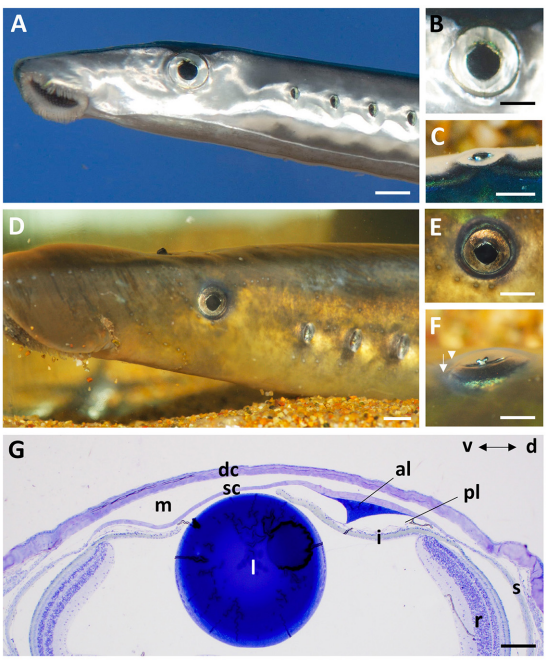

FIGURE 1 | The eye and anterior chamber of the pouched lamprey, *Geotria australis* in the downstream **(A–C)** and upstream **(D–F)** migrant stages. The eyes are laterally-placed in both stages with a near-circular pupil **(A,B,D,E)**, an iris with a ruffled edge on the dorsal border **(B,E)** and a y-shaped iridial operculum that projects laterally **(C,F)**. Note the differentiation of the dermal (arrowhead) and scleral (arrow) corneas in panel **(F)**. **(G)** Transverse section of the cornea and anterior chamber of the eye of a downstream migrant showing the close proximity of the lens (l) to the scleral cornea (sc) and the prominent annular ligament (al) in the dorsal (d) region. dc, dermal cornea; i, iris; m, region occupied by a mucoid layer; pl, possible pectinate ligament; r, retina, s, sclera; v, ventral. Scale bars: 2 mm **(A)**; 1 mm **(B)**; 2 mm **(C)**; 5 mm **(D)**; 3 mm **(E)**; 2 mm **(F)**; 0.2 mm **(G)**.

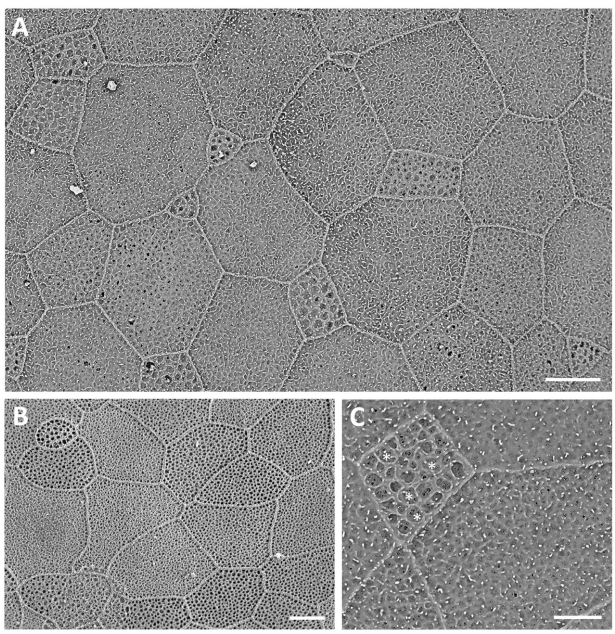

FIGURE 2 | Surface ultrastructure of the dermal cornea viewed using scanning electron microscopy **(A–C)**. The surface of the cornea shows an array of polygonal epithelial cells, which range in size. Projecting from the surface of the epithelial cells are microridges and microvilli, which surround mucus-filled microholes. Note the largest holes occur within the smallest cells, each of which contains a dense accumulation of mucous [asterisks in panel **(C)**]. Scale bars: 6 μm **(A)**; 5 μm **(B)**; 2.5 μm **(C)**.

to these holes, and above the surface of the epithelium, sit many small globules of mucus, with some globules appearing to be in the process of release through the surface epithelial holes. There are also some thin flattened cells up to 25 μm in width, with elongated nuclei, cytoplasm devoid of vacuoles and a surface with small microvilli but without holes. All epithelial cells interdigitate with one another and are bound together with desmosomes with a density of around 7.5 desmosomes per square micron (**Figure 4A**). In the limbal region and continuing into the skin, the epithelial cells are large (up to 24 μm in diameter), each containing a round nucleus with a nucleolus and up to 20 vesicles containing an amorphous material resembling lipid (**Figure 3C**). When observed using transmission electron microscopy, the basal epithelial cells are tall and columnar with large round nuclei, cytoplasm devoid of vacuoles and a diameter of 5.4–6.5 μm. The basal epithelial cells are attached to a dense basement membrane (with a thickness of 140 ± 31 nm) by numerous hemidesmosomes. There are some areas where the basement membrane is less dense or absent and these gaps are 98.2 ± 11.4 nm wide (**Figure 4A**).

The dermal stroma does not possess a Bowman's layer and there is no evidence of anchoring fibrils or anchoring plaques in the region of the basement membrane (**Figure 4A**). The stroma consists of approximately 100 lamellae of collagen fibrils, which have a mean diameter of 28.5 ± 4 nm and a D-periodicity of 59.6 ± 3.3 nm. The direction of the collagen fibrils in each lamella is approximately at right angles to the adjacent

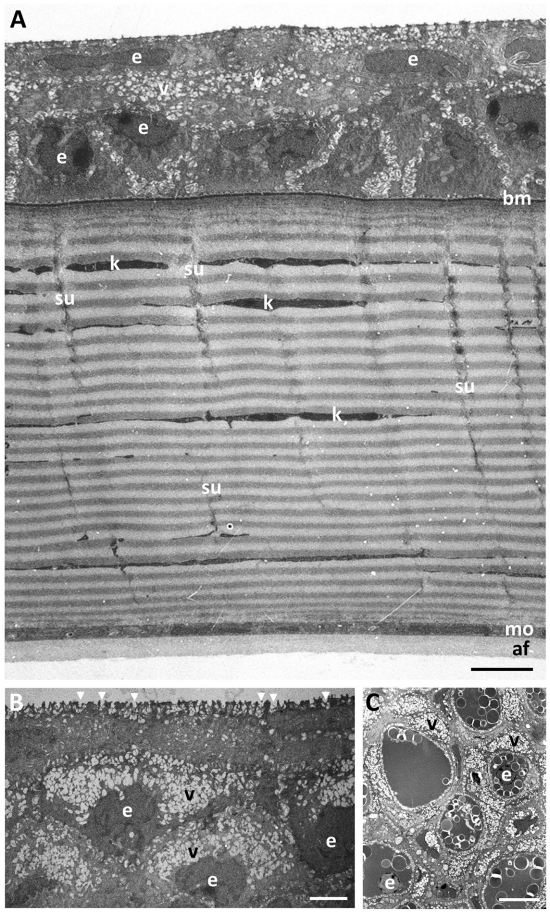

FIGURE 3 | Ultrastructure of the dermal cornea. **(A)** Transverse section of the full thickness of the dermal cornea showing the layers of stratified squamous epithelial cells (e) overlying a basement membrane (bm), a stroma comprised of up to 100 lamellae of collagen fibrils, and a monolayer of cells (mo). The posterior surface of the dermal cornea is lined with an amorphous aggregation of fibres (af). Note the gradation of cytoplasmic vacuoles (v) with the highest concentration in the more superficial epithelial cells with the high number of microholes at the surface (arrowheads) **(B)**. Individual collagen lamellae are interrupted by keratocytes (k) and vertically-oriented sutures (su). **(C)** Transverse section through the limbal region of the dermis showing large epithelial cells containing aggregations of spherical vesicles resembling lipids and high concentrations of vacuoles. Scale bars: 10 μm **(A)**; 2.5 μm **(B)**; 10 μm **(C)**.

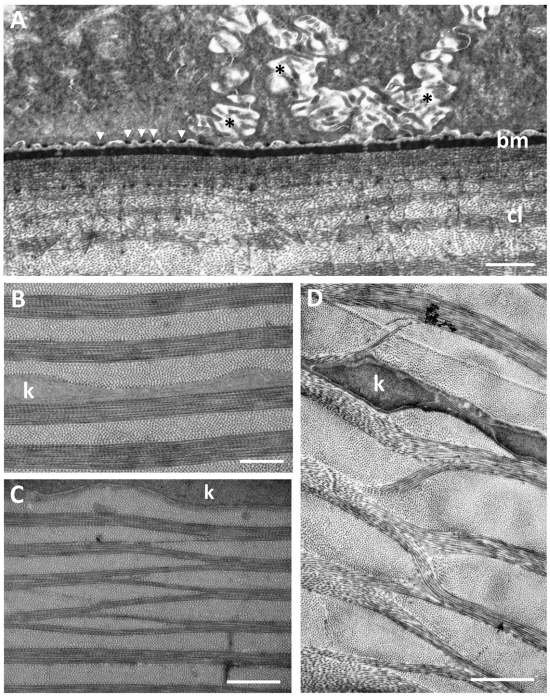

FIGURE 4 | (A) Posterior region of the corneal epithelium showing the dense basement membrane attached to the basal epithelial cells via hemidesmosomes (arrowheads). Note the complex interdigitations of the adjacent cell membranes (asterisks). The anterior region of the corneal stroma is comprised of a series of corneal lamellae (cl) containing only one collagen fibril. Bowman's layer is absent. **(B)** Middle region of the stroma of the central dermal cornea showing the collagen lamellae with bundles of collagen fibrils with alternating orientations. **(C,D)** Branching and anastomosing of the collagen lamellae in the peripheral cornea showing bundles of collagen fibrils running obliquely between lamellae with the same orientation, interrupted by keratocytes (k). Scale bars: 6 μm **(A)**; 0.5 μm **(B)**; 1 μm **(C)**; 2 μm **(D)**.

lamellae (**Figures 3A**, **4B**). However, the lamellae are not of equal thickness. In the anterior stroma, each lamella consists of only one collagen fibril, while each lamella in the middle and posterior regions of the stroma contain around 10 and 3 collagen fibrils, respectively (**Figures 3A**, **4A**). The variation in mean lamellar thickness throughout the depth of the stroma is 47.0 ± 4.8 nm (anterior 10 lamellae), 337.5 ± 44.4 nm (the central 10 lamellae) and 99.9 ± 16.1 nm (the posterior 10 lamellae). There are a few flattened cells (keratocytes) scattered throughout the stroma and these lie between the lamellae (**Figure 4B**). No polymorphonuclear leucocytes or pigment cells are present within the stroma.

The stroma of the dermal cornea possesses several types of specialisation with respect to the arrangement of collagen fibrils, namely extensive branching and anastomosing of the collagen lamellae and several types of vertical sutures. With respect to collagen branching, this may consist of single or multiple collagen fibrils running obliquely between two collagen lamellae with the same orientation of fibrils (**Figures 4C,D**). Although present in some central areas of the dermal cornea, branching and anastomosing is predominantly in the peripheral cornea. There are several types of "vertical sutures" present in the dermal corneal stroma, although they appear to be present only in the central cornea (**Figure 3A**).

Four (sub) types of suture are characterised on the basis of the number of collagen fibrils, their orientation and stromal depth: (1) *Amorphous vertical sutures*, consisting of collections of amorphous material, probably proteoglycans (Alanazi et al., 2015), and occasional collagen fibrils, extending over two or more collagen lamellae (**Figures 5A,B**); (2) *Small vertical sutures*, consisting of single collagen fibrils, approximately 25 nm wide and 75 nm long, extending between two lamellae of the same collagen fibril orientation

(**Figures 5C,D**). These sutures appear to occur in only the most superficial lamellae, where each lamella consists of only one or two collagen fibrils. The position of these sutures appears to correspond with the periodic darkly-stained regions of the collagen fibrils (**Figure 5D**). Collectively, they resemble a "picket fence"; (3) *Single fibre vertical sutures*, consisting of individual collagen fibrils running vertically or at random angles across two or several collagen lamellae, up to 2.2 μm in length but probably extend over greater distances in other planes (**Figure 5C**). These sutures occur only in the anterior region of the central cornea and do not constitute a Bowman's layer; (4) *Large vertical sutures*, consisting of large bundles of collagen fibrils extending vertically through most (perhaps all) of the dermal stroma. The bundles of fibrils appear to weave their way through the corneal lamellae (**Figure 5E**). Associated with the collagen bundles are large deposits of usually darkly-staining amorphous material, probably proteoglycans (Alanazi et al., 2015). When observed using the light microscope, these large sutures may take on a square saw-toothed appearance (**Figures 3A**, **5A,B**).

Posterior to the dermal stroma is a single layer of cells (endothelium) with large nuclei and an overall thickness of 885 ± 68 nm (**Figures 6A,C**). There is a continuous basement membrane (20.7 ± 7 nm thick) extending over the internal (mucoid) side of the posterior cellular monolayer, with no microprojections or cilia. There is no basement membrane between the stroma and the posterior cellular layer.

Mucoid Layer

Between the dermal and the scleral corneas, there is a mucoid layer consisting of amorphous material with scattered fibres resembling thin collagen fibrils, each having a diameter of 21.5 ± 3.7 nm, which is significantly less ($p < 0.00001$) than the diameter of the dermal corneal collagen fibrils (28.4 ± 4.0 nm). When viewed using scanning electron microscopy, these fibrils appear to be accumulated mainly on the posterior surface of the basement membrane of the central region of the dermal cornea, as shown in **Figures 6A,B**, although there are fewer fibrils seen adhering to the basement membrane in the peripheral region of the dermal cornea (**Figures 6C,D**).

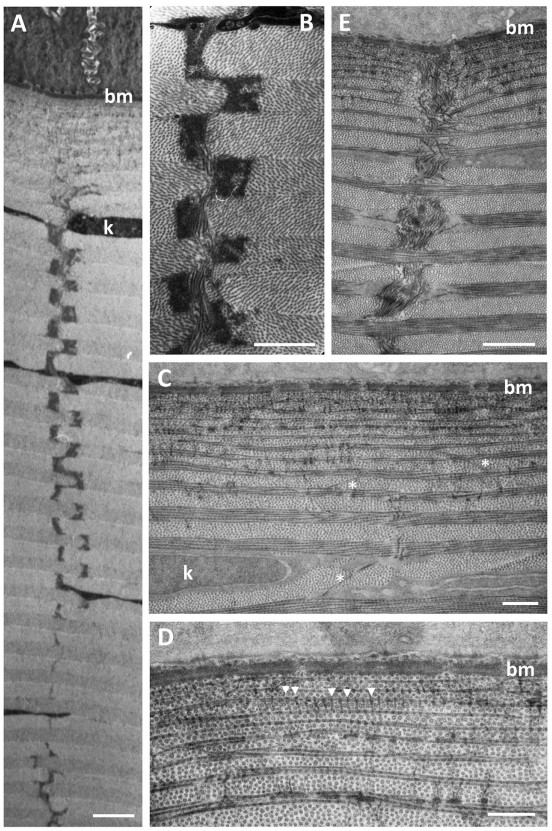

FIGURE 5 | Ultrastructure of vertical sutures in *G. australis*. **(A,B)** Type 1 Amorphous vertical sutures showing the alternating osmiophilic plaques of presumably proteoglycans piercing many collagen lamellae throughout the depth of the dermal corneal stroma. **(C,D)** Anterior region of the dermal stroma showing Type 2 (single collagen fibrils extending between two collagen lamellae of the same orientation, between arrowheads) and 3 (single collagen fibrils extending vertically or at random angles across two or more collagen lamellae, asterisks) vertical sutures. **(E)** A Type 4 vertical suture, which consists of a large bundle of collagen fibrils extending vertically through multiple collagen lamellae. Scale bars: 10 μm **(A)**; 7 μm **(B)**; 0.5 μm **(C)**; 0.5 μm **(D)**; 15 μm **(E)**.

Scleral Cornea

The scleral cornea is continuous with the sclera of the globe and has a thickness of 6.58 μm at the centre and 17.83 μm in the periphery (**Table 1** and **Figures 1G**, **7A**). The scleral stroma is 4.75 ± 0.64 μm thick in the centre and 15.6 ± 4.5 μm in the periphery and contains 19 or 20 lamellae of collagen fibrils with each lamella oriented at right angles to the adjacent lamellae (**Figure 7A**). The collagen fibrils have a diameter of 24.2 ± 1.2 nm, which is significantly different from the collagen in the dermal cornea ($p < 0.00001$) and mucoid layer ($p = 0.0022$). No cells, i.e., keratocytes or inflammatory cells, are present within the stroma of the scleral cornea. No branching and anastomosing of collagen lamellae or any vertical sutures are present in the scleral cornea (Collin and Collin, 2021b).

The scleral stroma is bounded by two monolayers of cells, one anteriorly and one posteriorly, where the posterior layer may be considered to be a corneal endothelium. On the mucoid side of the anterior monocellular layer, which has a thickness of 978 ± 29 nm, there is a continuous basement membrane with a thickness of 25 ± 3 nm (**Figure 6E**) that is covered in dense fibrils (**Figure 6F**). There is no basement membrane on the stromal side of the anterior monolayer. The posterior monocellular layer (707 ± 45 nm thick) of the scleral stroma has a well-formed continuous basement membrane, with a thickness of 37 ± 12 nm, on the posterior (anterior chamber) side and a more diffuse basement membrane with a thickness of 86 ± 15 nm on the stromal side (**Figures 7A,B**). The basement membrane (on the stromal side) does not represent a true Desçemet's membrane, as it does not have any obvious structure and there is no periodic banding. No microvilli or cilia are present extending into the anterior chamber but loose amorphous material and fibres are located in between the scleral cornea and the lens (**Figures 7C,D**). A summary of the dimensions of the corneal components is presented in **Table 1**.

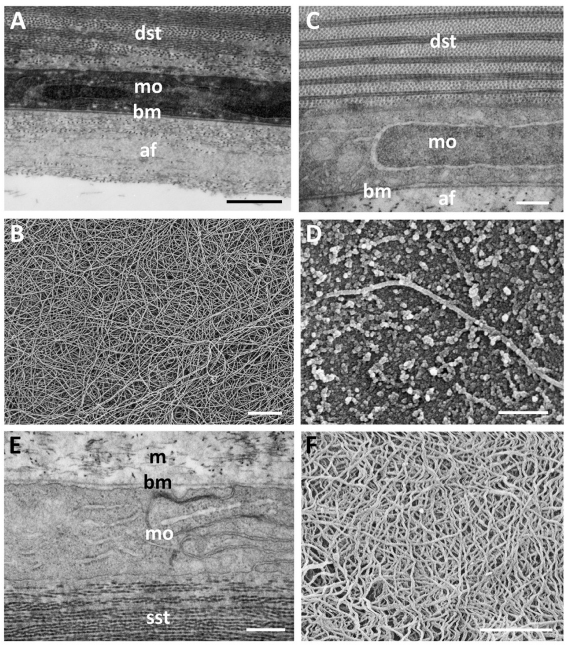

FIGURE 6 | Ultrastructure of the lining of the mucoid layer separating the dermal and scleral corneas. **(A)** Transmission electron micrograph of the posterior region of the central dermal cornea, which consists of the stroma (dst), a monolayer of cells (mo) and a basement membrane (bm). Posterior to the basement membrane lies a collection of amorphous material with scattered fibres (af) resembling thin collagen fibrils, which are shown using scanning electron microscopy (SEM) in panel **(B)**. In peripheral cornea, the scattered fibres of the mucoid layer are less dense **(C)**, where the surface of the basement membrane is revealed using SEM **(D)**. **(E)** The anterior surface of the scleral cornea underlying the mucoid layer (m) is covered by a basement membrane and another monolayer of cells, which in turn overlies the scleral stroma (sst). The anterior surface of the scleral cornea is covered by a dense tangle of fibres as viewed using SEM **(F)**. Scale bars: 1 μm **(A)**; 1 μm **(B)**; 0.5 μm **(C)**; 0.25 μm **(D)**; 0.5 μm **(E)**; 0.8 μm **(F)**.

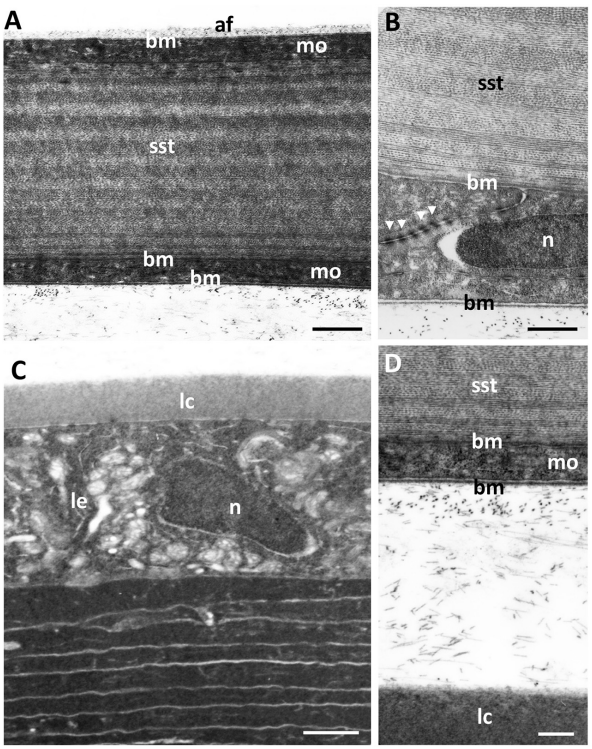

FIGURE 7 | Transverse section of the scleral stroma and the anterior region of the lens. **(A)** The scleral cornea is bounded by monolayer of cells (mo), with the anterior monolayer covered by a basement membrane (bm) and the posterior monolayer (or endothelium) surrounded by basement membranes on both sides. The scleral stroma (sst) comprises collagen lamellae. The scleral cornea is separated from the lens by scattered fibres. The anterior lens is bordered by a capsule (lc) and an epithelial cell layer (le), which surround the concentric layers of lens cells. **(B)** Posterior of the scleral cornea showing the anterior and posterior basement membranes bordering two opposing endothelial cells linked by tight junctions (arrowheads). **(C)** Scattered fibres between the scleral cornea and lens. n, nucleus. **(D)** The anterior chamber between the posterior scleral cornea and the lens capsule, showing the scattered collagen fibrils. Scale bars: 2 μm **(A)**; 0.3 μm **(B)**; 1.5 μm **(C)**; 0.7 μm **(D)**.

Annular Ligament

In the periphery of the scleral cornea, between the basement membrane of the scleral stroma and the corneal endothelium (posterior cellular layer) is an "annular ligament" (**Figures 1G**, **8**). However, the "annular ligament" is not truly annular or ligamentous, since it is only well-developed dorsally, tapering laterally (rostrally) to be much thinner (and even non-existent) caudally and ventrally (**Figure 8A**). It is triangular in cross-section being thickest (up to 135 μm) in the peripheral cornea and tapering to the angle of the anterior chamber for a distance of up to 500 μm and also tapering toward the central cornea, for up to 300 μm, terminating well before reaching the central cornea. At its peak thickness, the annular ligament spans the anterior chamber angle and is reflected onto the anterior surface of the iris (**Figures 8B,C,E**). The annular ligament consists of large cells, 4.2–29.1 μm in their longest dimension (mean 13.84 ± 5.01 μm) with large oval nuclei (**Figure 8D**). The majority of the cytoplasm is filled with a darkly-staining (osmiophilic) amorphous material, with few organelles. When viewed in both fixed and living animals, the annular ligament is thickest and most well-developed i.e., dense, when viewed using micro-computed tomography (**Figure 8A**) in the dorsal region of the eye, "filling" or overlying the gap produced by a dorsal notch in the iris, where a region of irideal tissue is deflected dorsally (**Figures 1B,C,E,F**).

At the corneal apex of the annular ligament, the posterior monocellular layer (endothelium) of the scleral cornea becomes duplicated. The endothelial cells maintain some of their characteristics, in that the nuclei are irregular compared with the oval-shaped nuclei of the "ligament" cells, the cytoplasm is more lightly-stained, there are more organelles and the cells are attached to each with occasional desmosomes. Desmosomes are not present between the cells of the annular ligament, which are frequently separated by large spaces. An additional feature is that the cell membranes of the endothelial cells stain black (osmiophilic) using the methods indicted, while the cell membranes of the annular ligament are not osmiophilic, where

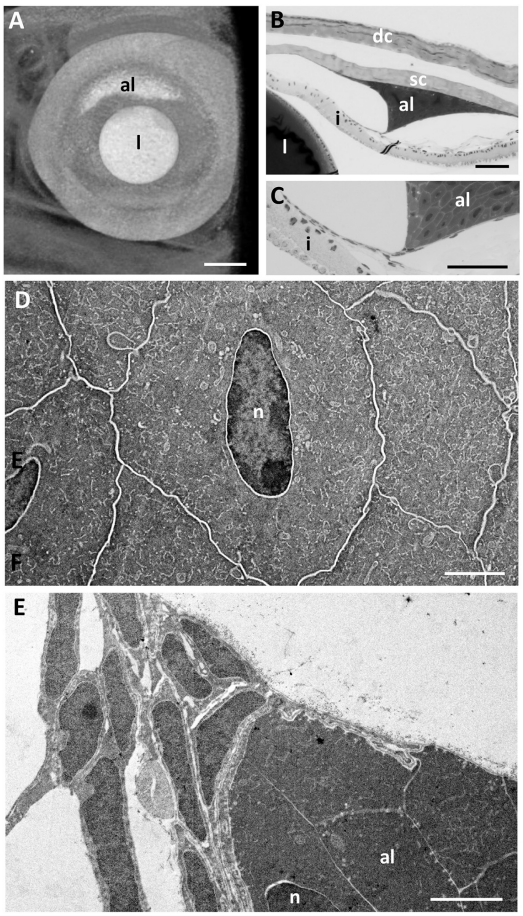

FIGURE 8 | The annular ligament. **(A)** Micro-computed tomography image of the eye of *G. australis* clearly showing the location of the dorsal annular ligament (al). Rostral is toward the left. **(B,C)** Light micrographs of the anterior chamber of the eye showing the triangular annular ligament confluent with the posterior edge of the scleral cornea **(B)** and tapering and joining the anterior iris **(C)**. **(D)** Electron micrograph showing the ultrastructure of the cells comprising the annular ligament with darkly-stained cytoplasm but cell membranes that are not osmiophilic. **(E)** Tapering of the annular ligament as it projects centrally and joins the iris [as in panel **(C)**]. dc, dermal cornea; i, iris; l, lens; n, nucleus; sc, scleral cornea. Scale bars: 0.5 mm **(A)**; 0.1 mm **(B)**; 0.1 mm **(C)**; 2.5 μm **(D)**; 2.5 μm **(E)**.

the cell borders appear as white lines (**Figures 8D,E**). About 200 μm from its corneal origin, the endothelial cells stop, although the basement membrane is still present on the anterior chamber side of the annular ligament cells.

At the apex of the triangular annular ligament nearest the iris, there are additional cells, each of which is separated from the annular ligament cells and from each other by a basement membrane. These cells resemble endothelial cells, in that they have large elongated nuclei and very little cytoplasm (**Figure 8E**), in marked contrast to the cells of the annular ligament, which are predominantly composed of cytoplasm (**Figure 8D**). These cells continue along the surface of the iris for up to 200 μm, as double or multiple layers of cells with an irregular basement membrane on both sides. Endothelial cells are also present on the surface of the iris peripheral to the annular ligament extending toward the anterior chamber angle (**Figures 8B,C**).

In some specimens, there is a large mass of cellular tissue (up to 175 μm long and 30 μm wide), which extends within the anterior chamber from the apex of the annular ligament toward the pupil. It appears to be present where the "annular ligament" is well developed, although its dimensions vary. In the vicinity of these masses, the extensions of the annular ligament onto the iris surface appear to be missing, indicating that these masses may represent artefactual separation of the annular ligament tissue from the surface of the iris.

Within the anterior chamber angle, there are also some strands of cellular tissue forming a loose network attached to the annular ligament and to the trabecular meshwork. These may be related to the pectinate ligament described by other authors, although since they are attached to the annular ligament, they may be additional extensions of that structure. However, some of this network may be due to an artefactual separation of the annular ligamentous tissue from the iris surface (**Figure 8B**).

Iris

In life, the iris appears silvery, with a non-mobile, slightly asymmetric pupil with the ventral radius of curvature of the iris being only two-thirds of the dorsal radius (**Figures 1A,B,D,E**). The superior margin of the pupil has two indentations or notches, giving rise to a small and bifurcated flap (or operculum) with extensions anteriorly (70 μm) and caudally (55 μm), that is deflected dorsally to lie approximately perpendicular to the plane of the iris (**Figures 1C,F**, **9A**). Structurally, the iris has an anterior single epithelial cell layer, a fibrovascular stroma with large blood vessels and two posterior layers of pigment epithelium (**Figures 9B–D**). The fibrovascular stroma is around 18 μm thick in the periphery, tapering to a thickness of 2–3 μm near the pupil. The anterior pigment epithelial layer (posterior to the stroma) consists of large densely-pigmented cuboidal cells, 17.9–20.5 μm thick in the periphery and 10.3–12.0 μm centrally. The posterior pigment epithelial layer has a thickness of approximately 7.7–8.5 μm peripherally (and is non-pigmented) and 5.5–6.1 μm more centrally, where it contains scattered pigment granules (**Figure 9D**). Aggregations of stacks of what may have contained guanine crystals are located in the anterior of the iris, which would give rise to the silvery appearance of the iris in life (**Figures 9C,D**).

DISCUSSION

The Evolution of Lamprey Cornea

The eyes of humans, mammals and birds have only one cornea, while some other vertebrates possess two corneas. A primary spectacle (or dermal cornea) and a scleral cornea are found in lampreys (Walls, 1942), including, *G. australis* (this study), the Sea lamprey, *Petroymyzon marinus* (Van Horn et al., 1969a,b; Pederson et al., 1971), the European river lamprey, *Lampetra fluviatilis* (Dickson and Graves, 1981; Dickson et al., 1982) and tadpoles and aquatic adult amphibians (Walls, 1942). The formation of a primary spectacle occurs when

the superficial layers of the cornea derived from the surface ectoderm (primary spectacle) do not fuse with the deeper layers of mesodermal origin (scleral cornea) (Pederson et al., 1971). A similar arrangement may also occur in bottom-dwelling fishes, where dermal and scleral corneas have been reported, i.e., in the Salamanderfish *Lepidogalalaxias salamandroides* (Collin and Collin, 1996) and the Pipefish, *Corythoichthyes paxtoni* (Collin and Collin, 1995) and both mudskippers (*Periophthalmus* spp.) and lungfishes (*Protopterus* spp.) (Walls, 1942). However, the corneal arrangement in these species may be considered to be secondary spectacles, which occur when a transparent area of the lower lids develops or when there is fusion of the upper and lower lids, forming a true cavity lined with epithelial cells, as found in some fishes and reptiles (Franz, 1934; Walls, 1942). However, further work is needed to differentiate the embryological origins of primary and secondary spectacles in fishes.

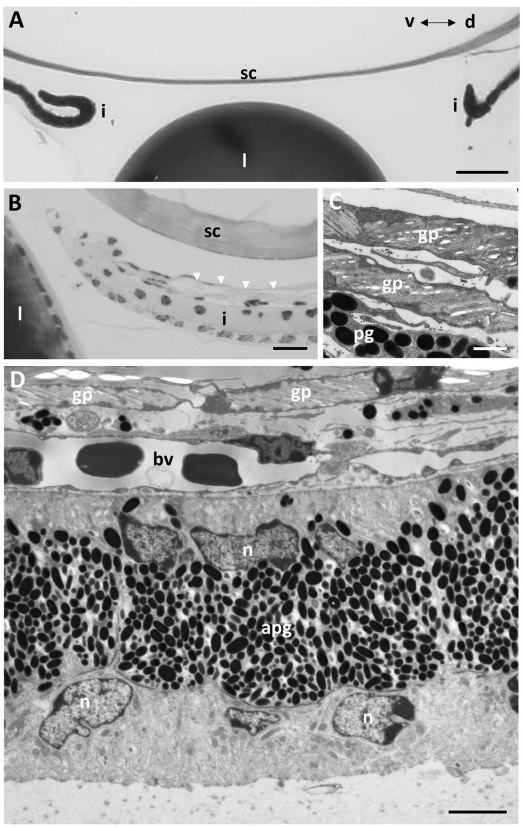

FIGURE 9 | Iris structure. **(A)** Light micrograph of the anterior chamber showing the lens (l) and scleral cornea (sc) and the two limits of the dorsal and ventral profiles of the iris (i). Note the split end of the dorsal iris and the outward curve in the ventral iris. **(B)** Light micrograph showing the dorsal limit of the iris and the anterior location of the guanine plates shown in C (arrowheads). **(C)** Electron micrograph of the guanine plates (gp) covering the anterior iris with scattered pigment granules (pg). **(D)** Electron micrograph of the iris in transverse section showing the anterior guanine plates, a layer of blood vessels (bv) within the fibrovascular stroma and the dense anterior aggregation of pigment granules (apg) within the peripheral region of the iris. The posterior epithelial cells are devoid of pigment granules in the peripheral iris. n, nucleus. Scale bars: 0.1 μm **(A)**; 8 μm **(B)**; 8 μm **(C)**; 30 μm **(D)**.

The Structure and Function of Corneal Surface Holes

The surface holes in the epithelium of the dermal cornea of *Geotria australis* appear to be a characteristic feature in high abundance with an inverse relationship between the size of the holes and the size of the epithelial cells. The presence of these holes has been previously reported for the Pouched lamprey *Geotria australis* (Collin and Collin, 2000a, 2006), the Shorthead lamprey, *Mordacia mordax* (Collin and Collin, 2006), the ammocoete stage (Dickson et al., 1982), but not the adult stage, of the Sea lamprey (*Petromyzon marinus*) (Van Horn et al., 1969a; Pederson et al., 1971; Dickson et al., 1982), the Black shark, *Dalatias licha* (Collin and Collin, 2000b, 2006), and the Australian lungfish, *Neoceratodus forsteri* (Collin and Collin, 2006). Surface holes also occur in the pre-metamorphic Axolotl, *Ambystoma mexicanum* (Collin and Collin, 2000b, 2006, 2021a) but have almost completely disappeared in the post-metamorphic stage (Collin and Collin, 2021a). The inverse correlation between the surface cell diameter and the width of the holes found in the Pouched lamprey has also been reported for the pre-metamorphic axolotl, *A. mexicanum* (Collin and Collin, 2021a). A statistical comparison of the diameter of the microholes in the two species reveals that the small, medium and large epithelial cells in *G. australis* possess microholes with a diameter of 457 ± 89 nm, 317 ± 55 and 196 ± 38 nm, respectively. A similar relationship exists for the axolotl, where the small, medium and large epithelial cells in *A. mexicanum*, possess microholes with a diameter of 597 ± 212 nm, 400 ± 184 nm and 187 ± 81 nm, respectively.

The presence of high numbers of cytoplasmic vacuoles aggregated on the superficial side of the wing cells of the dermal epithelium has been reported in both the ammocoete larva (Dickson et al., 1982) and the adult (Van Horn et al., 1969a) of the Sea lamprey, *P. marinus*. However, the slender mucus-filled channels containing membrane-bound vesicles are present in the superficial epithelial cells of the ammocoete Sea lamprey (Dickson et al., 1982) but are not found in the adult animal (Van Horn et al., 1969a). From this ultrastructural study on adult *G. australis*, it is now apparent that the wing cells migrate to the surface of the dermal cornea, where they appear as small cells and release their mucus-filled vesicles through large holes. As the cells spread out onto the surface and the majority of the vesicles have been released, the holes become smaller. When the cytoplasm is eventually devoid of mucus vesicles, the cells become large and flattened and the holes disappear as a prelude to the cell being sloughed off. In humans, the cell turnover is about 7 days (Edelhauser et al., 1994) but the turn-over time is unknown in *G. australis*. The mucus protects the surface of the corneal epithelium, especially as a barrier to pathogens, helps maintain hydration of the ocular surface and is an important component of the corneal tear film (Hodges and Dartt, 2013).

Differences in Corneal Thickness

The thickness of the central cornea of downstream adult *Geotria australis* was previously measured by Collin et al. (1999) and was reported to be 120 ± 20 μm, which is much greater than

our combined finding of a thickness of 56.43 μm in this study. However, their measurements were made on unfixed, fast-frozen eyes (with no histological shrinkage) and included the dermal and scleral corneas including the mucoid layer, the thickness of which we were unable to accurately assess. The difference between these two measurements (63.57 μm) may be an indication of the central thickness of the mucoid layer. The central thickness of the cornea (dermal plus scleral plus mucoid layer) of another southern hemisphere lamprey (*Mordacia mordax*) is 240 μm (Collin and Potter, 2000). It is difficult to compare the central thickness of the dermal cornea of *G. australis* (49.85 μm) with other species, which do not have a primary spectacle. However, the structure of the primary spectacle (dermal cornea) of the *G. australis* is similar to that of the secondary spectacle of snakes, in that there is an epithelium, stroma and endothelium (Da Silva et al., 2016), but among 14 species of snakes, the central thickness of the stroma varies from 9.0 to 132.3 μm, compared with 24.4 μm for the *G. australis*.

The greater thickness of the dermal cornea in the periphery (173.05 μm) compared with the centre (49.85 μm) in *G. australis* appears not to have been reported in other lampreys, but is common in jawed fishes including the Florida garfish, *Lepisosteus platyrhincus*, in which the dorsal (390 μm) and ventral (310 μm) limbal corneal thicknesses are greater than the central thickness (240 μm) (Collin and Collin, 1993). In mammals and most other vertebrates, the cornea is thin in the centre compared with the periphery, which is approximately 50% thicker (Gipson, 1994). Known exceptions are the Sandlance *Limnichthyes fasciatus*, in which the central thickness is more than four times that of the periphery, primarily due to the presence of a refractive autochthonous layer (Collin and Collin, 1988; Pettigrew and Collin, 1995) and both the Trout, *Salmo fario* (Tripathi, 1974) and the Pipefish *Corythoichthyes paxtoni* (Collin and Collin, 1995), in which the centre thickness is roughly twice that of the periphery. The epithelium of the dermal cornea in *G. australis* is 5–6 layers deep, which is similar to *P. marinus* (4–5 layers) (Van Horn et al., 1969a) and *L. salamandroides* (4–5 layers) (Collin and Collin, 1996) but more than *C. paxtoni* (2 layers) (Collin and Collin, 1995) and less than *L. platyrhincus* (10 layers)(Collin and Collin, 1993). Epithelial thickness is a function of the level of corneal transparency and protection required, both of which would be vital for vision in brightly-lit, shallow water and repeated dives into the substrate during the downstream phase of the lifecycle of *G. australis*.

The Lack of Bowman's Layer

Specialisation of the anterior corneal stroma into Bowman's layer with randomly-arranged collagen fibrils occurs in humans and primates (Collin and Collin, 2001), although its appearance in other species of vertebrates appears to be somewhat random (Wilson, 2020). Bowman's layer was not observed in the dermal cornea of the Pouched lamprey *Geotria australis* (this study), and both the Sea lamprey, *Petromyzon marinus* and the European river lamprey, *Lampetra fluviatilis* (Rochon-Duvigneaud, 1943). However, this is in contrast to the findings of Van Horn et al. (1969a), who described a Bowman's layer in the dermal cornea of *P. marinus*. It has been reported in some elasmobranchs, i.e., Spiny dogfish (*Squalus acanthias)* (Goldman and Benedek, 1967; Alanazi et al., 2015), the Stingray, *Dasyatis Americana* (10–20 μm thick, Alanazi et al., 2015) and the Clearnose skate, *Raja eglanteria* (Conrad et al., 1994) and some species of teleosts, i.e., the Brown trout (*Salmo trutta*), the Brook trout (*Salmo gairdneri*) and the Rainbow trout (*Salvelinus fontinalis*) constituting about 12.5% of the stroma (Edelhauser and Siegesmund, 1968). However, the collagen fibrils of Bowman's layer in all these species appear to be oriented in a horizontal pattern and are not randomly distributed as observed in mammals (Edelhauser and Siegesmund, 1968). Although the function of Bowman's layer is unknown these randomly-oriented collagen fibrils within the anterior region of the corneal stroma fail to modulate the passage of moderate- to large-sized proteins and therefore signify a reduction in barrier function (Wilson, 2020). It is unknown why this is important in *G. australis*.

The Dermal Stroma and the Structure and Function of Vertical Sutures

The stroma of the dermal cornea of the Pouched lamprey *Geotria australis* has a number of specialised features. In addition to the absence of a Bowman's layer, the anterior lamellae are very thin (0.047 μm) and comprise only one collagen fibre, compared with the central (0.337 μm) and posterior (0.100 μm) lamellae. A similar variation has been shown in several species of vertebrates (**Table 3**) but in the majority, the central lamellae are the thickest, while in humans, the opposite is true. The anterior lamellae of *G. australis* consist of only one collagen fibril, which is much narrower than all other reported species of vertebrates except the Pipefish, *Corythoichthyes paxtoni* (3 collagen fibrils) (Collin and Collin, 1995). The diameter of the collagen fibrils has been reported in many aquatic species and all fall within the range between 17 and 40 nm and, although some of these differences may be due to a range of processing techniques, regional differences in collagen fibril diameter are common within a species, i.e., dermal versus scleral stromal lamellae (**Table 4**). In snakes, the thickness of the collagen lamellae appears constant (Da Silva et al., 2016). Differences in collagen fibril diameter are directly related to the mechanical properties of the tissue, whereby large collagen fibrils are predicted to have a greater tensile strength and small diameter fibrils increase surface area and improve the probability of interfibrillar cross links between collagen fibrils and the components of the matrix (Parry et al., 1978).

Our findings of extensive branching and anastomosing of collagen lamellae in the spectacle of the Pouched lamprey, *Geotria australis* is not consistent with the claims that branching is comparatively rare in fishes (Winkler et al., 2015) and that there is a progressive increase in the branching of the collagen lamellae moving from lowest in fishes, increased in amphibians, higher in reptiles and highest in birds (Winkler et al., 2015; Koudouna et al., 2018). Branching of lamellae is present in the central region of the dermal cornea of the Sea lamprey *Petromyzon marinus* (Van Horn et al., 1969a), however, in *G. australis*, the branching is almost entirely in the peripheral cornea, which is consistent with reports of branching

TABLE 3 | The thickness of collagen lamellae in different regions of the stroma of the dermal cornea in *Geotria australis* compared to the corneas of other vertebrates.

Species	Anterior stroma	Middle stroma	Posterior stroma	Number of lamellae	References
Pouched lamprey *Geotria australis*	0.047 μm	0.337 μm	0.100 μm	100	This study
Stingray *Dasyatis americana*	2.62 μm	8.65 μm	4.80 μm	25	Alanazi et al., 2015
Stingray *Dasyatis americana*	7.6 μm	8.9 μm	5.2 μm		Alibrahim et al., 2011
Spiny dogfish *Squalus acanthias*	12.14 μm	18.3 μm	13 μm		Alibrahim et al., 2011
Spiny dogfish *Squalus acanthias*	1.456 μm	5.82 μm	5.535 μm	24–25	Goldman and Benedek, 1967
Dhub lizard *Uromastyx aegyptia*	0.36 μm	1.47 μm	0.79 μm		Akhtar et al., 2016
Florida garfish *Lepisosteus platyrhinchus*	∼3.0 μm	∼3.0 μm	0.20 μm	55–65	Collin and Collin, 1993
Humans *Homo sapiens*	1.75 μm	0.68 μm	2.63 μm	242	Bergmanson et al., 2005

The totals are the sum of the components for the dermal and scleral corneas.

TABLE 4 | Collagen fibril diameter in the cornea of a range of aquatic vertebrates.

Species		Region	Fibril diameter	Source
Pouched lamprey	*Geotria australis*	Primary spectacle	28.5 ± 4 nm	This study
		Mucoid layer	23.5 ± 4.0 nm	This study
		Scleral cornea	24.2 ± 1.2 nm	This study
Sea Lamprey	*Petromyzon marinus*	Scleral cornea	39.26 nm	Van Horn et al., 1969a
Dogfish	*Koinga lebruni*	Cornea	25.2 nm	Craig and Parry, 1981
Elephant fish	*Callorhynchus milii*	Cornea	25.5 nm	Craig and Parry, 1981
Stingray	*Bathytoshia brevicaudata*	Cornea	24.5 nm	Craig and Parry, 1981
Stingray	*Dasyatis americana*	Cornea	22.13 nm	Alanazi et al., 2015
Shark	*Squalis acanthias*	Cornea	24.25 nm	Alanazi et al., 2015
Shark	*Squalis acanthias*	Cornea	26.9–32.7 nm	Goldman and Benedek, 1967
Salamanderfish	*Lepidogalaxias salamandroides*	Secondary spectacle	30–40 nm	Collin and Collin, 1996
Pacific tomcod	*Microgadus proximus*	Dermal cornea	26 ± 4 nm	Collin and Collin, 1998
		Ant. scleral cornea	22 ± 5 nm	Collin and Collin, 1998
		Post. scleral cornea	22 ± 5 nm	Collin and Collin, 1998
Rattail	*Nezumia aequalis*	Dermal cornea	20 ± 3 nm	Collin and Collin, 1998
		Ant. scleral cornea	25 ± 3 nm	Collin and Collin, 1998
		Post. scleral cornea	20 ± 3 nm	Collin and Collin, 1998
Armoured grenadier	*Coryphanoides amartus*	Dermal cornea	27 ± 6 nm	Collin and Collin, 1998
		Ant. scleral cornea	22 ± 6 nm	Collin and Collin, 1998
		Post. scleral cornea	21 ± 2 nm	Collin and Collin, 1998
Pipefish	*Corythoichthyes paxtoni*	Dermal corneal	17–20 nm	Collin and Collin, 1995
		Scleral corneal	22–24 nm	Collin and Collin, 1995
Florida garfish	*Lepisosteus platyrhincus*	Cornea	20–40 nm	Collin and Collin, 1993

in the skin of the Sea lamprey *P. marinus* (Van Horn et al., 1969a). Branching is also present in the Holostei, i.e., the Sturgeon, *Acipenser sturio*, the Chondrichthyes, i.e., the Great white shark *Carcharodon carcharias* (Koudouna et al., 2018), and the Teleostei, i.e., the Trout *Salmo trutta* (Edelhauser and Siegesmund, 1968), the Pacific tomcod, *Microgadus proximus*, the Rattail, *Nezumia aequalis* and the Armoured grenadier, *Coryphanoides (Nematonurus) armatus* (Collin and Collin, 1998). The function of branching and anastomosing may be to modulate the shear strength of the cornea (Smolek and McCarey, 1990) and to stabilise the corneal shape necessary for the development of a refractive lens (Winkler et al., 2015). As branching and anastomosing are common in birds, which move between different aerial atmospheric pressures and withstand increased pressure on the cornea due to high speed diving, and aquatic vertebrates, which move between different hydrostatic pressures associated with different depths of the water column, it is appropriate that their corneas should have additional structural adaptations compared with terrestrial vertebrates. In mammals and humans, branching is restricted to a single plane in the superficial layers of the cornea (Winkler et al., 2015), which is associated with Bowman's layer (Winkler et al., 2011).

Four structural subtypes of vertical sutures are described in the Pouched lamprey *Geotria australis*, showing a heightened level of species-specific complexity not yet observed in the vertebrate cornea. Considered to be an adaptation for maintaining corneal transparency by inhibiting stromal swelling as a result of extreme cold (Fisher and Zadunaisky, 1977), exposure to large changes in pH (Christianson, 1982) and/or when moving between freshwater and seawater (Conrad et al., 1981; Wheaton and Edelhauser, 1983; Menasche et al., 1988; Collin and Collin, 2001), vertical sutures consist of collagen fibrils, which perpendicularly traverse stromal collagen lamellae. Vertical

sutures are predominantly found in the dermal stroma in species possessing a primary spectacle, which may be associated with maintaining optical transparency in the protective "goggle" directly exposed to changing environmental conditions. This would appear to be critical for *G. australis*, which is anadromous, moving between freshwater and seawater and back to freshwater during its protracted lifecycle, and spends much of its adult marine phase in the cold waters off South Georgia (Potter et al., 1979; Prince, 1980). Sutures have been described previously in the stroma of the spectacle of the Sea lamprey *Petromyzon marinus* (Van Horn et al., 1969a,b; Pederson et al., 1971), which appear to be of our Type 4. It is unknown how these vertical sutures develop but they may originate as extensions of the fibroblasts (keratocytes), running across lamellae (Dickson and Graves, 1981; Dickson et al., 1982), which are in the process of producing the vertically arranged collagen fibrils.

Thick vertical sutures (Type 4 in this study) are also found in chondrichthyans i.e., the Spiny dogfish *Squalus acanthias* (Goldman and Benedek, 1967; Conrad et al., 1981; Alanazi et al., 2015), the Stingray *Dasyatis americana* (Alanazi et al., 2015) and the Clearnose skate, *Raja eglanteria* (Conrad et al., 1994) and elephant shark, *Hydrolagus colliei* (Collin and Collin, 2001) and teleosts i.e., Salamander fish *Lepidogalaxias salamandroides* (Collin and Collin, 1996) and the deep-sea teleost *Cataetyx laticeps* (Collin and Collin, 2001), in which they may traverse as many as ten adjacent collagen lamellae or span the full depth of the cornea, originating in the basal lamina of the epithelium and terminating in Desçemet's membrane. Vertical sutures do not appear to be present in terrestrial species, including snakes, birds and mammals (Da Silva et al., 2016).

The Mucoid Layer

The mucoid layer between the dermal and scleral corneas, consisting of amorphous material with scattered fibres resembling thin collagen fibrils in *Geotria australis*, appears to be a common feature in all vertebrates with split corneas. Thought to allow the eye to rotate beneath the protective goggle provided by the dermal cornea (which is continuous with the surrounding skin), the collagen fibrils appear to be very dense centrally, providing a heightened level of adherence, thereby enabling the action of the caudal cornealis muscle in retracting the lens to be more effective and accounting for the variation in the thickness of this layer centro-peripherally. The findings of endothelial basement membranes on both surfaces facing the mucoid layer and, in particular, on the anterior chamber side of the scleral corneal endothelium are very unusual features of *G. australis*, which are shared by the Sea lamprey *Petromyzon marinus* (Van Horn et al., 1969a; Dickson et al., 1982).

Desçemet's Membrane and an Endothelial Basement Membrane

The Pouched lamprey *Geotria australis* does not possess a Desçemet's membrane but has a diffuse basement membrane with a thickness of 86 ± 15 nm situated between the stroma and the posterior endothelium of the scleral cornea. This is in agreement with the finding of Rochon-Duvigneaud (1943), who found a non-homogenous layer between the stroma and posterior endothelium of the scleral cornea of both the Sea lamprey *Petromyzon marinus* and the European river lamprey *Lampetra fluviatilis* but not a Desçemet's membrane. A Desçemet's membrane was also found to be lacking in *P. marinus* by Van Horn et al. (1969a) and Pederson et al. (1971), where only a thin, discontinuous layer of electron dense material was found to separate the endothelial cells from the stroma.

A Desçemet's membrane has been claimed to be present in the elasmobranch cornea i.e., in the Stingray *Dasyatis americana* (Goldman and Benedek, 1967; Alanazi et al., 2015), the Spiny dogfish *Squalus acanthias* (Alanazi et al., 2015), where it is described as very fine, loosely-woven microfibrils (Alanazi et al., 2015) or as a very thin (0.3–4.4 μm) homogeneous layer of fine fibrils (Goldman and Benedek, 1967), and the teleost cornea i.e., in the Pipefish *Corythoichthyes paxtoni* (2 μm thick, Collin and Collin, 1995), the Zebrafish *Danio rerio* (0.15 μm, Zhao et al., 2006), the Salamanderfish, *Lepidogalaxias salamandroides* (∼75 to 100 nm in centre and ∼200 nm in the periphery, Collin and Collin, 1996) and in three species of deep-sea fishes (0.1–0.23 nm, Collin and Collin, 1998). However, in a number of species of trout, Edelhauser and Siegesmund (1968) found only a poorly-defined endothelial basement membrane.

It is apparent that differentiating Desçemet's membrane from a normal endothelial basement membrane can be difficult and should not be based only upon the thickness of the membrane. In humans, Descemet's membrane continues to grow throughout life and has a thickness of around 3 μm at birth (Murphy et al., 1984) and may reach a thickness of up to 12 μm in adults (Gipson, 1994) or even 18 to 19 μm in the elderly (Murphy et al., 1984). It has a structure with an anterior (embryonic) banded portion with a periodicity of between 110 and 120 nm (Murphy et al., 1984; Gipson, 1994) and a less dense, non-banded portion. A similar structure has been reported in the aquatic Little penguin (*Eudyptula minor*) (Collin and Collin, 2021b) and in numerous mammals, including, the rat (3.5 μm thick with a periodicity of 120 nm), the mouse (ddY strain) (2.5 μm thick with a periodicity of 120 nm), the mouse (C3H strain) (5 μm thick with a periodicity of 120 nm), the guinea pig (13 μm thick with a periodicity of 120 nm), the cat (periodicity of 100 nm), the rabbit (5.6 μm thick) and various species of cattle (20 μm thick, periodicity 120 nm) (Hayaski et al., 2020).

Desçemet's membrane or the posterior elastic lamina has been described as the basement membrane of the corneal endothelium (Gipson, 1994) or as a dense, thick, relatively transparent and cell-free matrix that separates the corneal stroma from the endothelium (de Oliviera and Wilson, 2020). Murphy et al. (1984) describe the three major processes, necessary to form a Desçemet's membrane; namely growth in the prenatal period, differentiation into a striated basement membrane and an increase in thickness in the postnatal period, giving rise to an extraordinarily thick and multilayered structure. Jakus (1956) states that Desçemet's membrane has a hexagonal structure and is banded (107 μm) in transverse section.

If we adopt the descriptions of Gipson (1994) and de Oliviera and Wilson (2020), almost all vertebrates possess a Desçemet's membrane. However, if we adopt the definitions of Jakus (1956) and Murphy et al. (1984), all of the vertebrates with thin, incomplete, irregular collections of loosely-woven fine fibrils would be better described as having a basement membrane rather than a Desçemet's membrane and this includes the lampreys. Further differentiation may be possible as a result of tissue analysis of the membranes, e.g., using monoclonal antibodies to label components such as collagen (Cheng et al., 2021) and laminin (Leung et al., 2000). Collagen Type IV and laminin are major components of basement membranes (Kefalides et al., 1979; Kühn et al., 1981; Sanes et al., 1990), while Desçemet's membrane, a morphologically unique basement membrane, is rich in collagen Type VIII (Kapoor et al., 1986; Illidge et al., 2001), in addition to some collagen Type IV (Leung et al., 2000), although, in rabbits, Desçemet's membrane does not contain laminin (Leung et al., 2000).

The Structure, Evolution and Function of the "Annular Ligament"

The "annular ligament" of the Pouched lamprey *Geotria australis* is situated in the periphery of the scleral cornea, between the basement membrane of the scleral stroma and the corneal endothelium. Composed of large cells with amorphous cytoplasm, this triangular tissue appears to be restricted to the dorsal region of the eye in *G. australis* with its apex attached to the anterior iris. An "annular ligament" has also been described briefly in the Sea lamprey, *Petromyzon marinus* (Rochon-Duvigneaud, 1943; Dickson and Graves, 1981) and the European river lamprey, *Lampetra fluviatilis* (Walls, 1942; Rochon-Duvigneaud, 1943) but in several studies of the ultrastructure of the cornea in Sea lamprey, *Petromyzon marinus*, there is no mention of an "annular ligament" (Van Horn et al., 1969a; Pederson et al., 1971; Dickson et al., 1982) suggesting that it is also not annular in these species of lampreys. There have been no previous detailed descriptions of the "annular ligament" in any southern hemisphere lampreys.

The structure of the "annular ligament" in *G. australis* is similar to that described for what may be a homologous structure in the Goldfish *Carassius auratus,* i.e., tissue comprised of large polyhedral cells, with few mitochondria and indistinct cristae (Tripathi, 1974) and in the Zebrafish, *Danio rerio* i.e., with a cytoplasm, which contains an abundant accumulation of glycoproteins, including keratocan and lumican (Chen et al., 2008). Walls (1942) described the "annular ligament" in *L. fluviatilis* as a conspicuous thickening composed of epithelioid cells, which may represent a "piling up" of Desçemet's mesothelium. Based on its structure and chemical composition, the term "annular ligament" appears inappropriate, as previously pointed out by Rochon-Duvigneaud (1943), who termed this the "vesioculo-hyaline tissue of the angle" and Tripathi (1974), as collagen is not present within the structure or its cellular components (Collin and Collin, 1996). Chen et al. (2008) described the "annular ligament" of *D. rerio* as a "prominent ligament-like fibrous meshwork" but then reported that the cells contained abundant accumulations of the glycoproteins, keratocan and lumican, with no mention of collagen. The "annular ligament" also lacks the characteristic alignment of parallel bundles of collagen fibrils and fibroblasts observed in the ligaments of mammals (Redler et al., 2019; Kaku et al., 2020).

The origin of the "annular ligament" has been debated but our findings indicate that it is derived from the scleral corneal endothelium, which persists until the annular ligament markedly increases in thickness. The continuation of the basement membrane without an obvious endothelium implies that the cells still maintain this membrane-producing ability in *G. australis*. From an evolutionary perspective, the "annular ligament" may have been present in the last common ancestor of lampreys given it has been retained in at least some species of Chondrichthyes (Elasmobranchii), i.e., the Dogfish *Squalus acanthias* (Tripathi, 1974), although it is not described in the eyes of the Stingray *Dasyatis americana* (Alanazi et al., 2015), the Clearnose skate *Raja eglanteria* (Conrad et al., 1994) or non-actinopterygian early ray-finned fishes including the Chondrostei. It is poorly developed in *Polypterus* spp. (Duke-Elder, 1958) and the Holostei, but particularly well-developed in the dorsal region of the cornea in the Florida garfish *Lepidosteus platyrhincus* (Duke-Elder, 1958; Tripathi, 1974; Collin and Collin, 1993) and the Teleostei, i.e., where it is common and well-developed in cyprinids (Rochon-Duvigneaud, 1943), extending across most of the surface of the iris (Oppel and Franz, 1913), a species of trout *Salmo trutta* (Edelhauser and Siegesmund, 1968), the Goldfish *Carassius auratus* (Rochon-Duvigneaud, 1943; Tripathi, 1974), the Gudgeon, *Gobio fluviatilis* (Rochon-Duvigneaud, 1943), the Salamanderfish *Lepidogalaxias salamandroides* (Collin and Collin, 1996) and the Zebrafish *Danio rerio* (Yoshikawa et al., 2007; Chen et al., 2008). The "annular ligament" appears to be absent in the Dipnoi (lungfishes) (Duke-Elder, 1958; Tripathi, 1974). The function of the annular ligament is unknown (Walls, 1942; Duke-Elder, 1958) but is suggested to be secretive (Baecker, 1931) or refractive (Collin and Collin, 1996), although due to its location in *G. australis,* it may help to support the suspension of the opercular flap in the dorsal iris (see below).

Pectinate Ligament

Similar to the debate over the name of the "annular ligament" the term "pectinate ligament" is also thought to be misleading (Wolff, 1948). According to official gross-anatomical nomenclature, "pectinatum ligamentum" is a synonym or a substitute for the trabecular meshwork ("reticulum trabeculare") (Simoens et al., 1996), although most veterinary ophthalmologists attribute the term pectinate ligament to the anterior-most strands of the meshwork at the iridocorneal angle, whereas the more peripheral parts of the meshwork are called the trabecular meshwork (Simoens et al., 1996).

The strands of the "pectinate ligament" are defined as being comprised of a central collagen core, surrounded by mesothelium (Walls, 1942; Allen et al., 1955; Duke-Elder, 1958). However, the loose network in the eye of the Pouched lamprey *Geotria australis*

appears to be cellular, lacking a collagen core and is attached to the "annular ligament," and thereby is thought to be an extension of that structure. Walls (1942) and Duke-Elder (1958) both claim that in the lamprey eye, delicate strands, perhaps coated with mesothelium, cross from the end of the annular ligament to the periphery of the iris, like a "pectinate ligament." These strands are prominent in *Lampetra fluviatilis*, but practically non-existent (except superiorly) in the brook lamprey *Ichthyomyzon fossor* (Walls, 1942). The "pectinate ligament" is developed to varying degrees in different species but is absent in the selachians (Elasmobranchii) (Oppel and Franz, 1913; Duke-Elder, 1958) and rudimentary or vestigal in lower placentals and humans (Allen et al., 1955; Duke-Elder, 1958). The function of the "pectinate ligament" is unknown.

The Iris

The pupil of *Geotria australis* is bounded by a highly-reflective, silvery iris (produced by stacks of presumably guanine crystals (Dickson and Graves, 1981), which appears to be almost circular in shape in both downstream and upstream migrants. However, along the superior margin of the iris are two indentations or notches, giving rise to a small and bifurcated flap (or operculum) that is deflected dorsally. Although other regions of the superior margin of the iris are raised slightly above the pupillary plane, the flap appears to be suspended to sit perpendicular to the pupil and parallel to the surface of the head. This is an unusual feature, which has not been observed in any other species of lamprey, although it bears some resemblance to the irideal operculum of the iris in batoids (McComb and Kajiura, 2008) and catfishes (Douglas et al., 2002; Collin, 2003). Its function is unknown but may serve to reduce bright light entering the eye from above, thereby reducing intraocular flare, given that *G. australis* spends appreciable amounts of time in the surface waters of the open ocean (in its marine phase).

DATA AVAILABILITY STATEMENT

The raw data supporting the conclusions of this article will be made available by the authors, without undue reservation.

ETHICS STATEMENT

The animal study was reviewed and approved by The University of Western Australia Animal Ethics Committee.

AUTHOR CONTRIBUTIONS

All authors contributed to the design of the study, the acquisition of data, data analysis, and interpretation and writing the manuscript.

FUNDING

This study was funded by the Australian Research Council (DP110103294), The University of Western Australia and La Trobe University, Australia.

ACKNOWLEDGMENTS

Thank you to Ian Potter and David Morgan for assistance in accessing animals and discussions on the importance of this group of agnathans. We would like to thank Michael Archer for technical assistance in electron microscopy and histology, Benedicta Arhatari for assistance with the microcomputed tomography, and Caroline Kerr for assistance with permits, ethics and maintenance of lampreys.

REFERENCES

Akhtar, S., Alkhalaf, M., Khan, A. A., and Almubrad, T. M. (2016). Ultrastructure features and three-dimensional transmission electron tomography of Dhub lizard (*Uromastyx aegyptia*) cornea and its adaptation to a desert environment. *Microsc. Microanal.* 22, 922–932. doi: 10.1017/S1431927616011466

Alanazi, S. A., Almubrad, T., Alibrahim, A. I. A., Khan, A. A., and Akha, S. (2015). Ultrastructure organisation of collagen fibrils and proteoglycans of stingray and shark corneal stroma. *J. Ophthalmol.* 2015:686914. doi: 10.1155/2015/686914

Alibrahim, A., Almubrad, T., and Akhar, S. (2011). Ultrastructure of stingray and shark corneal stroma. *Acta Ophthalmol.* 89:215. doi: 10.1111/j.1755-3768.2011.215.x

Allen, L., Burian, H. M., and Braley, A. E. (1955). The anterior border ring of Schwalbe and the pectinate ligament. *AMA Arch. Ophthalmol.* 53, 799–806. doi: 10.1001/archopt.1955.00930010807003

Baecker, R. (1931). The chamber rim tissue (ligament annular) and the changing behavior of the corneal margin of the fish cellulofibrous. *Z. Mikr. Anat. Forsch.* 26, 412–533.

Bergmanson, J. P. G., Horne, J., Doughty, M. J., Garcia, M., and Gondo, M. (2005). Assessment of the number of lamellae in the central region of the normal human corneal stroma at the resolution of the transmission electron microscope. *Eye Contact Lens* 31, 281–287. doi: 10.1097/01.ICL.0000165280.94927.0D

Chen, C.-C., Yeh, L.-K., Liu, C.-Y., Kao, W. W.-Y., Samples, J. R., Lin, S.-J., et al. (2008). Morphological differences between the trabecular meshworks of zebrafish and mammals. *Curr. Eye Res.* 33, 59–72. doi: 10.1080/02713680701795026

Cheng, Y.-X., Ziao, L., Yang, Y.-L., Liu, X.-D., Zhou, X.-R., Bu, Z.-F., et al. (2021). Collagen type VIII alpha 2 chain (COL8A2), an important component of the basement membrane of the corneal endothelium, facilitates the malignant development of glioblastoma cells via inducing EMT. *J. Bioenerg. Biomembr.* 53, 49–59. doi: 10.1007/s10863-020-09865-1

Christianson, P. (1982). The distribution of *Lepidogalaxias salamandroides* and other freshwater fishes in the lowest southwest of Western Australia. *J. R. Soc. West. Aust.* 65, 131–141.

Collin, H. B., and Collin, S. P. (1988). The cornea of the sandlance, *Limnichthyes fasciatus* (Creeiidae). *Cornea* 7, 190–203.

Collin, H. B., and Collin, S. P. (1995). Ultrastructure and organisation of the cornea, lens and iris in the pipefish, *Corythoichthyes paxoni* (Syngathidae, teleostei). *Histol. Histopathol.* 10, 313–323.

Collin, H. B., and Collin, S. P. (1996). The fine structure of the cornea of the salamanderfish, *Lepidogalaxias salamandroides* (Lepidogalaxiidae, Teleostei). *Cornea* 15, 414–426. doi: 10.1097/00003226-199607000-00012

Collin, H. B., and Collin, S. P. (2000a). The corneal surface of aquatic vertebrates: microstructures with optical and nutritional function? *Philos. Trans. R. Soc. Lond. B* 355, 1171–1176. doi: 10.1098/rstb.2000.0661

Collin, S. P. (2003). "Vision in catfishes," in *Catfishes*, eds B. G. Kapoor, G. Arratia, M. Chardon, and R. Diogo (Oxford: New Delhi), 669–700.

Collin, S. P., and Collin, H. B. (1993). The visual system of the Florida garfish, *Lepisosteus platyrhincus* (Ginglymodi). II Cornea and lens. *Brain Behav. Evol.* 42, 98–115. doi: 10.1159/000114143

Collin, S. P., and Collin, H. B. (1998). The deep-sea teleost cornea: a comparative study of gadiform fishes. *Histol. Histopathol.* 13, 325–336. doi: 10.14670/HH-13.325

Collin, S. P., and Collin, H. B. (2000b). A comparative SEM study of the vertebrate corneal epithelium. *Cornea* 19, 218–230. doi: 10.1097/00003226-200003000-00017

Collin, S. P., and Collin, H. B. (2001). "The fish cornea: sensory adaptations for different aquatic environments," in *Sensory Biology of Jawed Fishes - New Insights*, eds B. G. Kapoo, Y. N. Andrianov, J. Falcon, S. P. Collin, M. A. Barry, and T. J. Hara (New Delhi: Oxford and IBH Publishing Co), 57–96.

Collin, S. P., and Collin, H. B. (2006). The corneal epithelial surface in the eyes of vertebrates: environmental and evolutionary influences on structure and function. *J. Morphol.* 267, 273–291. doi: 10.1002/jmor.10400

Collin, S. P., and Collin, H. B. (2021b). Functional morphology of the cornea of the Little Penguin *Eudyptula minor* (Aves). *J. Anat.* 239, 732–746. doi: 10.1111/joa.13438

Collin, S. P., and Collin, H. B. (2021a). A comparison of the ultrastructure of the cornea of the pre- and post-metamorphic axolotl (*Ambystoma mexicanu*m, Amphibia). *Exp. Eye Res.* 202:108396. doi: 10.1016/jexer.2020.108396

Collin, S. P., Hart, N. S., Shand, J., and Potter, I. C. (2003a). Morphology and spectral absorption characteristics of retinal photoreceptors in the southern hemisphere lamprey (*Geotria australis*). *Vis. Neurosci.* 20, 119–130. doi: 10.1017/s0952523803202030

Collin, S. P., Knight, M. A., Davies, W. L., Potter, I. C., Hunt, D. M., and Trezise, A. E. O. (2003b). Ancient colour vision: multiple opsin genes in the ancestral vertebrates. *Curr. Biol.* 13, R864–R865. doi: 10.1016/j.cub.2003.10.044

Collin, S. P., and Potter, I. C. (2000). The ocular morphology of the southern hemisphere lamprey *Mordacia mordax* Richardson with special reference to a single class of photoreceptor and a retinal tapetum. *Brain Behav. Evol.* 55, 120–138. doi: 10.1159/000006647

Collin, S. P., Potter, I. C., and Braekevelt, C. R. (1999). The ocular morphology of the southern hemisphere lamprey *Geotria australis* Gray, with special reference to optical specialisations and the characterisation and phylogeny of photoreceptor types. *Brain Behav. Evol.* 54, 96–118. doi: 10.1159/000006616

Conrad, G. W., Kelly, P. T., von, der Mark, K., and Edelhauser, H. F. (1981). A comparative study of elasmobranch corneal and scleral collagens. *Exp. Eye Res.* 32, 659–672. doi: 10.1016/0014-4835(81)90015-4

Conrad, G. W., Paulsen, A. Q., and Luer, C. A. (1994). Embryonic development of the cornea in the eye of the Clearnose skate, *Raja eglanteri*, I. Stromal development in the absence of an endothelium. *J. Exp. Zool.* 296, 263–276. doi: 10.1002/jez.1402690311

Craig, A. S., and Parry, D. A. (1981). Collagen fibrils of the vertebrate corneal stroma. *J. Ultrastruct. Res* 74, 232–239. doi: 10.1016/s0022-5320(81)80081-0

Da Silva, M.-A. O., Bertelsen, M. F., Wang, T., Prause, J. U., Svahn, T., and Heegardt, S. (2016). Comparative morphology of the snake spectacle using light and transmission electron microscopy. *Vet. Ophthalmol.* 19, 285–290. doi: 10.1111/vop.12281

de Oliviera, R. C., and Wilson, S. E. (2020). Descemet's membrane development, structure, function and regeneration. *Exp. Eye Res.* 197:108090. doi: 10.1016/j.exer.2020.108090

Dickson, D. H., and Graves, D. A. (1981). "The ultrastructure and development of the eye," in *The Biology of Lampreys*, Vol. 3, eds M. W. Hardisty and I. C. Potter (London: Academic Press), 43–94.

Dickson, D. H., Graves, D. A., and Moyles, M. R. (1982). Corneal splitting in the developing lamprey *Petromyzon marinus* L. eye. *Am. J. Anat.* 165, 83–98. doi: 10.1002/aja.1001650108

Douglas, R. H., Collin, S. P., and Corrigan, J. (2002). The eyes of suckermouth armoured catfish (Loricariidae, subfamily Hypostomus): pupil response, lenticular spherical aberration and retinal topography. *J. Exp. Biol.* 205, 3425–3433.

Duke-Elder, S. (1958). "The eye in evolution," in *System of Ophthalmology*, Vol. I, eds S. Duke-Elder and D. Abrams (London: Henry Kimpton).

Edelhauser, H. F., Geroski, D. H., and Ubels, J. L. (1994). "Physiology," in *The Cornea*, 3rd Edn, eds G. Smolin and R. Thoft (Boston, MA: Little, Brown and Co), 25–46.

Edelhauser, H. F., and Siegesmund, K. A. (1968). The localization of sodium in the teleost cornea. *Invest. Ophthalmol.* 7, 147–155.

Evans, T. M., Janvier, P., and Docker, M. F. (2018). The evolution of lamprey (Petromyzontida) life history and the origin of metamorphosis. *Rev. Fish Biol. Fish.* 28, 825–838. doi: 10.1007/s11160-018-9536-z

Fisher, F. H., and Zadunaisky, J. A. (1977). Electrical and hydrophilic properties of fish corneal. *Exp. Eye Res.* 25, 149–161. doi: 10.1016/0014-4835(77)90127-0

Franz, V. (1934). "Vergleichende Anatomie des Wirbeltierauges," in *Handbuch der Vergleichenden Anatomie der Wirbeltiere Bd. 2 III Höhere Sinnesorgane)*, eds L. Bolk, E. Göppert, E. Kallius, and W. Lubosch (Berlin: Urbane und Schwatzenberg), 989–1292.

Gipson, I. K. (1994). "The anatomy of the conjunctiva, cornea and limbus," in *The Cornea*, 3rd Edn, eds G. Smolin and R. Thoft (Boston, MA: Little, Brown and Co), 3–24.

Goldman, J. N., and Benedek, G. B. (1967). The relationship between morphology and transparency in the non-swelling corneal stroma of the shark. *Invest. Ophthalmol.* 6, 574–600.

Gómez-Gálvez, P., Vincente-Munuera, P., Tagua, A., Forga, C., Castro, A. M., Letrán, M., et al. (2018). Scutoids are a geometrical solution to three-dimensional packing of epithelia. *Nat. Commun.* 9:2960.

Gustafsson, O. S. E., Ekström, P., and Kröger, H. H. (2010). A fibrous membrane suspends the multifocal lens in the eyes of lampreys and African lungfishes. *J. Morphol.* 271, 980–989. doi: 10.1002/jmor.10849

Hardisty, M. W. (1979). "Ecology and behaviour," in *Biology of the Cyclostomes*, ed. M. W. Hardisty (London: Chapman and Hall), 51–75.

Hardisty, M. W., and Potter, I. C. (1971a). "The behaviour, ecology and growth of larval lampreys," in *The Biology of Lampreys*, eds M. W. Hardisty and I. C. Potter (London: Academic Press), 85–125.

Hardisty, M. W., and Potter, I. C. (1971b). "The general biology of adult lampreys," in *The Biology of Lampreys*, eds M. W. Hardisty and I. C. Potter (London: Academic Press), 127–206.

Hayaski, S., Osawa, T., and Tohyama, K. (2020). Comparative observations on corneas, with special reference to Bowman's layer and Descemet's membrane in mammals and amphibians. *J. Morphol.* 254, 247–258. doi: 10.1002/jmor.100.30

Hayat, M. A. (1986). *Basic Techniques for Transmission Electron Microscopy*. Orlando, FL: Academic Press.

Hein, S. A. A. (1913). Over oogleden en fornices conjunctivae bij teleostomi. *Tijds. D. Nederl. Dierk. Vereen Ser.* 12, 238–280.

Hodges, R. R., and Dartt, D. A. (2013). Tear film mucins: front line defenders of the ocular surface: comparison with airway and gastrointestinal tract mucins. *Exp. Eye Res.* 117, 62–78. doi: 10.1016/j.exer.2013.07.027

Holmberg, K., Öhman, P., and Dreyfert, T. (1977). ERG-recordings from the retina of the river lamprey (*Lampetra fluviatilis*). *Vis. Res.* 17, 715–717. doi: 10.1016/s0042-6989(77)80008-4

Hubbs, C. L., and Potter, I. C. (1971). "Distribution, phylogeny and taxonomy," in *The Biology of Lampreys*, eds M. W. Hardisty and I. C. Potter (London: Academic Press), 1–65.

Illidge, C., Kielty, C., and Shuttleworth, A. (2001). Type VIII collagen: heterotrimeric chain association. *Int. J. Biochem. Cell Biol.* 33, 31–329. doi: 10.1016/s1357-2725(01)00013-9

Ishikawa, M., Takao, M., Washioka, H., Tokunaga, F., Watanabe, H., and Tonosaki, A. (1987). Demonstration of rod and cone photoreceptors in the lamprey retina by freeze-replication and immunofluorescence. *Cell Tissue Res.* 249, 241–246. doi: 10.1007/BF00215506

Jakus, M. A. (1956). Studies of the cornea. II. The fine structure of Descemet's membrane. *J. Biophys. Biochem. Cytol.* 2, 243–252. doi: 10.1083/jcb.2.4.243

Kaku, N., Shimada, T., Tanaka, A., Ando, T., Tabata, T., and Tagomori, H. (2020). Ultrastructure and three dimensional architecture of the anterior cruciate ligament in the knee joints of young and old monkeys. *Med. Mol. Morphol.* 53, 7–14. doi: 10.1007/s00795-019-00224-7

Kapoor, R., Bornstein, P., and Sage, H. (1986). Type VIII collagen from bovine Descemet's membrane: structural characterization of a triple-helical domain. *Biochemistry* 25, 3930–3937. doi: 10.1021/bi00361a029

Kefalides, N. A., Alper, R., and Clark, C. C. (1979). Biochemistry and metabolism of basement membranes. *Int. Rev. Cytol.* 61, 167–228. doi: 10.1016/s0074-7696(08)61998-1

Koudouna, E., Winkler, M., Mikula, E., Juhasz, T., and Brown, D. J. (2018). Evolution of the vertebrate corneal stroma. *Prog. Ret. Eye Res.* 64, 65–76. doi: 10.1016/jpreteyeres.2018.01.002

Kühn, K., Weidermann, H., Timpl, R., Ristelli, J., Dieringer, H., Voss, T., et al. (1981). Macromolecular structure of basement membrane collagens. Identification of 7 S collagen as a crosslinking domain of type IV collagen. *FEBS Lett.* 125, 123–128. doi: 10.1016/0014-5793(81)81012-5

Leung, E. W., Rife, L., Smith, R. E., and Kay, E. P. (2000). Extracellular matrix components in retrocorneal fibrous membrane in comparison to corneal endothelium and Descemet's membrane. *Mol. Vis.* 6, 15–23.

McComb, M. D., and Kajiura, S. M. (2008). Visual fields of four batoid fishes: a comparative study. *J. Exp. Biol.* 211, 482–490. doi: 10.1242/jeb.014506

Menasche, M., Dagonet, F., Waegenner, M. J., and Pouliquen, Y. (1988). Swelling evaluation of "Scyliorhinus canicula L" cornea. *Cornea* 7, 204–209.

Meyer-Rochow, V. B., and Stewart, D. (1996). Review of larval and postlarval eye ultrastructure in the lamprey (Cyclostomata) with special emphasis on *Geotria australis* (Gray). *Micros. Res. Technol.* 35, 431–444. doi: 10.1002/(SICI)1097-0029(19961215)35:6<431::AID-JEMT3>3.0.CO;2-L

Murphy, C., Alvarado, J., and Juster, R. (1984). Prenatal and postnatal growth of the human Descemet's membrane. *Invest. Ophthalmol. Vis. Sci.* 25, 1402–1415.

Nam, S. M., Lee, H. K., Kim, E. K., and Seo, K. Y. (2006). Comparison of corneal thickness after the installation of topical anesthetics; proparacaine versus oxybuprocaine. *Cornea* 25, 51–54. doi: 10.1097/01.ico.0000179929.97651.59

Oppel, A., and Franz, V. (1913). *Lehrbuch der Vergleichenden Mikroskopischen Anatomie der Wirbeltiere*. Jena: Verlag von Gustav Fischer.

Parry, D. A. D., Barnes, G. R. G., and Craig, A. S. (1978). A comparison of the size distribution of collagen fibrils in connective tissues as a function of age and a possible relation between fibril size distribution and mechanical properties. *Proc. R. Soc. B Biol. Sci.* 203, 305–321. doi: 10.1098/rspb.1978.0107

Pederson, H. J., Van Horn, D. L., and Edelhauser, H. F. (1971). Ultrastructural changes associated with loss of transparency in the primary spectacle and cornea of the spawning Sea lamprey. *Exp. Eye Res.* 12, 147–150. doi: 10.1016/0014-4835(71)90139-4

Pettigrew, J. D., and Collin, S. P. (1995). Terrestrial optics in an aquatic eye: the sandlance, *Limnichthyes fasciatus* (Creediidae, Teleostei). *J. Comp. Physiol. A* 177, 397–408.

Potter, I. C., Gill, H. S., Renaud, C. B., and Haoucher, D. (2015). "The taxonomy, phylogeny, and distribution of lampreys," in *Lampreys: Biology, Conservation and Control*, ed. M. F. Docker (Berlin: Springer), 35–73.

Potter, I. C., Hilliard, R. W., and Bird, D. J. (1980). Metamorphosis in the southern hemisphere lamprey, *Geotria australis*. *J. Zool.* 190, 405–430. doi: 10.1111/j.1469-7998.1980.tb01435.x

Potter, I. C., Hilliard, R. W., Bird, D. J., and Macey, D. J. (1983). Quantitative data on morphology and organ weights during the protracted spawning-run period of the southern hemisphere lamprey *Geotria australis*. *J. Zool.* 200, 1–20.

Potter, I. C., Prince, P. A., and Croxall, J. P. (1979). Data on the adult marine and migratory phases in the life cycle of the southern hemisphere lamprey, *Geotria australis* Gray. *Environ. Biol. Fish.* 4, 65–69. doi: 10.1007/bf00005929

Potter, I. C., and Strahan, R. (1968). The taxonomy of the lampreys Geotria and Mordacia and their distribution in Australia. *Proc. Linn. Soc. Lond.* 179, 229–240. doi: 10.1111/j.1095-8312.1968.tb00980.x

Prince, P. A. (1980). The food and feeding ecology of grey-headed albatross *Diomedea chrysostoma* and black-browed albatross *D. melanophris*. *Ibis* 122, 476–488. doi: 10.1111/j.1474-919x.1980.tb00902.x

Redler, A., Miglietta, S., Monaco, E., Matassa, R., Relucenti, M., Daggett, M., et al. (2019). Ultrastructural assessment of the anterolateral ligament. *Orthop. J. Sports Med.* 7:10.1177/2325967119887920. doi: 10.1177/2325967119887920

Reynolds, E. S. (1963). The use of lead citrate at high pH as an electronopaque stain in electron microscopy. *J. Cell Biol.* 17, 208–212. doi: 10.1083/jcb.17.1.208

Riva-Rossi, C., Barrasso, D. A., Baker, C., Quiroga, A. P., Baigún, C., and Basso, N. G. (2020). Revalidation of the Argentinian pouched lamprey *Geotria macrostoma* (Burmeister, 1868) with molecular and morphological evidence. *PLoS One* 15:e0233792. doi: 10.1371/journal.pone.0233792

Rochon-Duvigneaud, A. (1943). *Les Yeux et la Vision des Vertébrés*. Paris: Masson et Cie.

Sanes, J. R., Engvall, E., and Hunter, D. D. (1990). Molecular heterogeneity of basal laminae: Isoforms of laminin and collagen IV at the neuromuscular junction and elsewhere. *J. Cell Biol.* 11, 1685–1699. doi: 10.1083/jcb.111.4.1685

Simoens, P., de Geest, J.-P., and Lauwers, H. (1996). Comparative morphology of the pectinate ligament of domestic mammals, as observed under the dissecting microscope and the scanning electronmicroscope. *J. Vet. Med. Sci.* 58, 977–982. doi: 10.1292/jvms.58.10_977

Smolek, M. K., and McCarey, B. E. (1990). Interlamellar adhesive strength in human eyebank corneas. *Invest. Ophthalmol. Vis. Sci.* 31, 1087–1095.

Treviranus, G. R. (1820). "Über die Verschiedenheiten der Gestalt und Lage der Hirnorgane in den verschiedenen Classen des Thierreichs," in *Untersuchungen über den Bau und die Functionen des Gehirns, der Nerven. (und)der Sinneswerkzeuge in den verschiedenen Classen und Familien des Thierreichs* (Bremen: Johann Georg Heyse).

Tripathi, R. C. (1974). "Comparative physiology and anatomy of the aqueous outflow pathway," in *The Eye. Comparative Physiology*, eds H. Davson and L. T. Graham (New York, NY: Academic Press), 163–356.

Van Horn, D. L., Edelhauser, H. F., and Schultz, R. O. (1969a). Ultrastructure of the primary spectacle and cornea of the Sea lamprey. *J. Ultrastruct. Res.* 26, 454–464. doi: 10.1016/s0022-5320(69)90051-3

Van Horn, D. L., Edelhauser, H. F., and Schultz, R. O. (1969b). A comparative study of stromal swelling in Sea lamprey spectacle and Brook trout cornea. *J. Ultrastruct. Res.* 28, 452–461. doi: 10.1016/s0022-5320(69)80033-x

Walls, G. (1942). *The Vertebrate Eye and Its Adaptive Radiation*. New York, NY: Hafner.

Warrington, R. E., Davies, W. I. L., Hemmi, J. M., Hart, N. S., Potter, I. C., Collin, S. P., et al. (2021). Visual opsin expression and morphological characterisation of retinal photoreceptors in the pouched lamprey (*Geotria australis*, Gray). *J. Comp. Neurol.* 529, 2265–2282. doi: 10.1002/cne.25092

Werther, K., Candioto, C. G., and Korbel, R. (2017). Ocular histomorphometry of free-living common kestrels (*Falco tinnunculus*). *J. Avian Med. Surg.* 31, 319–326. doi: 10.1647/2014-039

Wheaton, D. J., and Edelhauser, H. F. (1983). Measurement of the stromal pressure in elasmobranch and sculpin cornea. *Bull. Mt. Desert Isl. Biol. Lab.* 23, 30–31.

Wilson, S. E. (2020). Bowman's layer in the cornea – structure and function and regeneration. *Exp. Eye Res.* 195:108033. doi: 10.1016/j.exer.2020.108033

Winkler, M., Chai, D., Kriling, S., Nien, C. J., Brown, D. J., Jester, B., et al. (2011). Nonlinear optical macroscopic assessment of 3-D corneal collagen organization and axial biomechanics. *Invest. Ophthalmol. Vis. Sci.* 52, 8818–8827. doi: 10.1167/iovs.11-8070

Winkler, M., Shoa, G., Tran, S. T., Xie, Y., Thomasy, S., Raghunathan, V. K., et al. (2015). A comparative study of vertebrate corneal structure: the evolution of a refractive lens. *Invest. Ophthalmol. Vis. Sci.* 56, 2764–2772. doi: 10.1167/iovs.15-16584

Wolff, E. (1948). *The Anatomy of the Eye and Orbit*, 3rd Edn. London: H. K. Lewis & Co.

Yoshikawa, S., Norcom, E., Nakamura, H., Yee, R. M., and Zhoa, X. C. (2007). Transgenic analysis of the anterior eye-specific enhancers of the zebrafish gelsolin-like 1 (gsn/1) gene. *Am. J. Anat.* 236, 1929–1938. doi: 10.1002/dvdy.21197

Zhao, X. C., Yee, R. W., Norcom, E., Burgess, H., Avanesov, A. S., Barrish, J. P., et al. (2006). The Zebrafish cornea: structure and development. *Invest. Ophthalmol. Vis. Sci.* 47, 4341–4348. doi: 10.1167/iovs.05-1611

Conflict of Interest: The authors declare that the research was conducted in the absence of any commercial or financial relationships that could be construed as a potential conflict of interest.

Publisher's Note: All claims expressed in this article are solely those of the authors and do not necessarily represent those of their affiliated organizations, or those of the publisher, the editors and the reviewers. Any product that may be evaluated in this article, or claim that may be made by its manufacturer, is not guaranteed or endorsed by the publisher.

frontiers in Neuroanatomy

ORIGINAL RESEARCH
published: 13 January 2022
doi: 10.3389/fnana.2021.786142

Asymmetric Distributions of Achromatic Bipolar Cells in the Mouse Retina

*Zachary J. Sharpe, Angela Shehu and Tomomi Ichinose**

Department of Ophthalmology, Visual and Anatomical Sciences, Wayne State University School of Medicine, Detroit, MI, United States

In the retina, evolutionary changes can be traced in the topography of photoreceptors. The shape of the visual streak depends on the height of the animal and its habitat, namely, woods, prairies, or mountains. Also, the distribution of distinct wavelength-sensitive cones is unique to each animal. For example, UV and green cones reside in the ventral and dorsal regions in the mouse retina, respectively, whereas in the rat retina these cones are homogeneously distributed. In contrast with the abundant investigation on the distribution of photoreceptors and the third-order neurons, the distribution of bipolar cells has not been well understood. We utilized two enhanced green fluorescent protein (EGFP) mouse lines, Lhx4-EGFP (Lhx4) and 6030405A18Rik-EGFP (Rik), to examine the topographic distributions of bipolar cells in the retina. First, we characterized their GFP-expressing cells using type-specific markers. We found that GFP was expressed by type 2, type 3a, and type 6 bipolar cells in the Rik mice and by type 3b, type 4, and type 5 bipolar cells in the Lhx4 mice. All these types are achromatic. Then, we examined the distributions of bipolar cells in the four cardinal directions and three different eccentricities of the retinal tissue. In the Rik mice, GFP-expressing bipolar cells were more highly observed in the nasal region than those in the temporal retina. The number of GFP cells was not different along with the ventral-dorsal axis. In contrast, in the Lhx4 mice, GFP-expressing cells occurred at a higher density in the ventral region than in the dorsal retina. However, no difference was observed along the nasal-temporal axis. Furthermore, we examined which type of bipolar cells contributed to the asymmetric distributions in the Rik mice. We found that type 3a bipolar cells occurred at a higher density in the temporal region, whereas type 6 bipolar cells were denser in the nasal region. The asymmetricity of these bipolar cells shaped the uneven distribution of the GFP cells in the Rik mice. In conclusion, we found that a subset of achromatic bipolar cells is asymmetrically distributed in the mouse retina, suggesting their unique roles in achromatic visual processing.

Keywords: retina, GFP, immunohistochemistry, bipolar cells, topography

OPEN ACCESS

Edited by:
Nicolás Cuenca,
University of Alicante, Spain

Reviewed by:
Ulrike Grünert,
The University of Sydney, Australia
Patrick W. Keeley,
University of California,
Santa Barbara, United States
Yoshihiko Tsukamoto,
Hyogo College of Medicine, Japan

***Correspondence:**
Tomomi Ichinose
tichinos@med.wayne.edu

Received: *29 September 2021*
Accepted: *13 December 2021*
Published: *13 January 2022*

Citation:
Sharpe ZJ, Shehu A and Ichinose T (2022) Asymmetric Distributions of Achromatic Bipolar Cells in the Mouse Retina. Front. Neuroanat. 15:786142. doi: 10.3389/fnana.2021.786142

INTRODUCTION

The eyes of vertebrates contain a single lens and retina, which evolutionarily split from the compound eyes of arthropods millions of years ago (Peterson et al., 2004; Jones, 2014). Since the separation, the structure of the retinas of vertebrates has evolved similarly among species, from fish to primates. The structure consists of five major neurons: photoreceptors, bipolar cells, ganglion cells, horizontal cells, and amacrine cells (Kolb, 2011). However, adaptational changes are recognized among animals with different body heights and habitats through the distinct topographies of retinal neurons. The topography of photoreceptors has been well investigated among species. Most non-primate mammals have two types of cones: short-wavelength sensitive cones (S-cones) and middle/long-wavelength sensitive cones (M/L-cones). However, some rodents lack S-cones, potentially due to their nocturnality (Peichl and Moutairou, 1998). Furthermore, the distribution of M- and S-cones in the retina is diverse depending on the height and habitat of the animals. The shape of the visual streak is longitudinal along the nasal-temporal axis for short-height animals, while the visual streak of taller animals exhibits dorsal extension (Peichl, 2005; Schiviz et al., 2008).

In the mouse retina, two types of photoreceptors, S- and M-cones, are heterogeneously distributed in the ventral and dorsal retinas, respectively (Szel et al., 1992). The inhomogeneous distributions of the two cones suggest that S-cones in the ventral retina enable the mouse to look up at the sky and M-cones in the dorsal regions support looking down at the grass. However, the dual opsin-expressing cones exist in the ventral retina (Haverkamp et al., 2005), and the color recognition of these two regions appears to be more complicated (Denman et al., 2018). Color vision by two wavelength-opponency primarily occurs in the ventral retina, which supports the upper visual field, by involving rod photoreceptors (Szatko et al., 2020) or by concentrated S-cones in the ventral retina (Nadal-Nicolas et al., 2020).

In addition to photoreceptors, the heterogeneous distributions of other retinal neurons have been gradually reported in the mouse retina. The M1-type melanopsin ganglion cells are asymmetrically distributed along the ventral-dorsal axis (Sondereker et al., 2017). Furthermore, OFF-alpha transient ganglion cells (OFF-α T RGCs) exhibit functional heterogeneous distributions; their light-evoked responses are transient in the ventral retina but are sustained in the dorsal retina (Warwick et al., 2018). This might be attributed to a distinct inhibitory network (Warwick et al., 2018) or the distinct locations and lengths of the initial segment of OFF-α T RGCs in two different retinal regions (Werginz et al., 2020).

Bipolar cells consist of approximately 15 types of chromatic and achromatic cells (Wässle et al., 2009; Breuninger et al., 2011). Type-dependent, diverse functional architecture is suggested for achromatic cells, such as motion detection (Euler et al., 2014; Hellmer et al., 2021). Bipolar cell topography was investigated by Camerino et al. (2021), which revealed that many types of OFF bipolar cells occurred at a higher density in the ventral retina than in the dorsal retina. However, the topography of other types of bipolar cells has not been investigated. To examine the topography of bipolar cells, we used two mouse lines that express the green fluorescent protein (GFP) in some types of bipolar cells. We found a heterogeneous distribution of some types of bipolar cells in the retina, suggesting their unique functions.

MATERIALS AND METHODS

Ethical Approval

All animal procedures were approved by the Institutional Animal Care and Use Committee at the Wayne State University (protocol no. 20-10-2909). All the necessary steps were taken to minimize animal suffering. The tissues were harvested immediately after the animal was euthanized by CO_2 inhalation and cervical dislocation.

Mice

The 6030405A18Rik-EGFP (RRID:MMRRC_030515-UCD) and Lhx4-EGFP (RRID:MMRRC_030699-UCD) mouse lines, henceforth referred to as Rik and Lhx4, respectively, were obtained. The Rik line expresses enhanced green fluorescent protein (EGFP) under the control of the serine-rich and transmembrane domain-containing 1 (*Sertm1*) promoter. The Lhx4 line expresses GFP under the control of the LIM homeobox protein 4 (*Lhx4*) promoter. After they were received from the MMRRC, mice were crossed with C57BL6/J mice (Jackson Lab, Stock #000664) for more than 5 generations before being used for this study. Mice were maintained on a 12-h light/dark cycle and provided with free access to food and water. Litters were routinely genotyped for transgenes using PCR and gel electrophoresis and only those that tested positive were used for further experimentation. For this study, both male and female mice aged 1–6 months were used.

Retinal Preparation

After euthanasia, the ventral side of the cornea was marked by a heat rod before enucleation. Eyes were enucleated and dissected in HEPES buffer solution composed of (in mM) 115 NaCl, 2.5 KCl, 2.5 $CaCl_2$, 1.0 $MgCl_2$, 10 HEPES, and 28 glucose, adjusted to pH 7.4 with NaOH. The dissection buffer was continuously bubbled with 100% oxygen during the procedure. The cauterization landmark was used to make a large incision in the ventral retina for the orientation of cardinal directions. Detailed dissection steps were previously described (Hellmer and Ichinose, 2015). Retinal preparations were kept in an oxygenated dark box until fixation. Whole retinas were fixed using incubation in 4% paraformaldehyde (PFA) in 0.1 M phosphate buffer (PB) for 1 h at room temperature. For transverse slice sections, retinas were fixed in 4% PFA for 30 min at room temperature. Both types of preparations were then washed with PB three times for 15 min each after fixation. Slice sections were then cryoprotected in 30% sucrose in PB overnight at 4°C. Samples were immersed in a 3:1 mixture of 30% sucrose in PB for 1 h at room temperature, embedded in 100% tissue freezing medium (Electron Microscopy Sciences #72592, Hatfield, PA, United States), and rapidly frozen in a dry ice/acetone bath. Slices were cut at 14 μm using a

Cryotome cryostat (Thermo Fisher Scientific, Waltham, MA, United States) and dried in an oven at 55°C for 1 h.

Immunostaining

Preparations were blocked for 1 h before staining by incubation at room temperature in 10% normal donkey serum (NDS) with 0.5% Triton X-100 in 0.01 M PBS (PBS-T). Primary antibodies were prepared in 3% NDS in PBS-T. Bipolar cells were identified by antibody staining. Anti-synaptotagmin-2 (Syt2) was used for type 2 bipolar cell soma staining and type 6 axon terminals, anti-hyperpolarization-activated cyclic-nucleotide gated channels (HCN4) for type 3a, anti-protein kinase A, regulatory subunit IIβ (PKARIIβ) for type 3b, anti-calsenilin (Csen) for type 4, and anti-protein kinase Cα (PKCα) for rod bipolar cells (RBCs) in accordance with previously characterized markers (Ghosh et al., 2004; Wässle et al., 2009). Starburst amacrine cells (SACs) were identified using antibodies against choline acetyltransferase (ChAT). Staining against s-opsin, highly expressed in the ventral retina, was used to validate the accuracy of the dissection marking method. A detailed list of primary antibodies can be found in **Table 1**. Slice preparations were incubated with primary antibody overnight at room temperature. Whole mounts were incubated with primary antibody for 48 h at 4°C. Phosphate-buffered saline (PBS) at a concentration of 0.01 M was used to wash the preparations three times for 15 min each. Secondary antibodies included donkey anti-rabbit Alexa 568, anti-mouse Alexa 568, anti-goat Alexa 633, and anti-mouse Alexa 647 (Thermo Fisher Scientific, Waltham, MA, United States). Secondary antibodies were dissolved in 3% NDS in PBS-T. Preparations were incubated with secondary antibody for 2 h at room temperature followed by washing in PBS three times for 15 min each. Preparations were placed on glass slides with ProLong Gold antifade reagent (Thermo Fisher Scientific) and a glass coverslip.

Imaging

Both slice preparations and whole mounts were imaged on a TCS SP8 confocal microscope (Leica, Germany) using an HC PL APO CS2 40 × water immersion objective. Slices were imaged at 1,024 × 512 pixels with a step size of 0.3 microns. For whole mounts, a total of 12 fields were imaged per retina, corresponding to four cardinal directions and three eccentricities each. Three eccentricities were defined as a center, approximately 500 μm away from the optic nerve head, middle, 1,000 μm away from the optic nerve head, and peripheral, 1,500 μm away from the optic nerve head. If the targeted region was free of damage, it was imaged. If damage or large vasculature was present, an adjacent field was imaged. Each field was imaged at 512 × 512 pixels and one-micron step size. The large ventral incision made during dissection was used for orientation, which was confirmed by the s-opsin staining ($n = 1$ eye). Each field was imaged as a z-stack encompassing the inner nuclear layer (INL) using GFP-labeled somas as a landmark. Central regions were noted as being in the central one-third of the retina near the optic nerve, middle regions the middle third, and peripheral regions the outer third.

Image Analysis, Cell Counting, and Statistics

Colocalization analysis of GFP and bipolar cell subtype markers was performed using Leica Application Suite X imaging software (version 3.5.5., Leica). Cells were counted in 100 μm × 100 μm regions of interest. Counting of cells in the region of interest was performed independently by two to four people under the condition that the origin of tissue, region, and eccentricity were blinded. We used a manual cell counter plugin included with the Fiji distribution of ImageJ (Schindelin et al., 2012). We counted GFP-expressing bipolar cells only if the somas resided in the outer half of the INL. For antibody-stained cells, bipolar cells were determined and counted if their somas resided in the outer half of the INL and dendrites extending to the outer plexiform layer (OPL). All statistical analysis and graph preparation were performed using GraphPad Prism (version 9, GraphPad Software, La Jolla, CA, United States). Two-way ANOVA was used to analyze the bipolar cell topography data for orientation and eccentricity with Tukey's multiple comparisons test. Linear regression was used to evaluate density gradients along the ventral-dorsal and nasal-temporal axes. Differences were considered significant if $p < 0.05$. SigmaPlot (version 14, Systat Software, San Jose, CA) was used to make color-coded heat maps using coordinates of counted fields and calculated densities.

RESULTS

Two Strains of Mice Expressed Green Fluorescent Protein by Bipolar Cells in the Retina

First, we investigated the types of GFP-expressing cells in the Rik and Lhx4 mice, which were characterized as bipolar cell GFP strains (Siegert et al., 2009). For both strains, GFP-expressing somas were observed in the outer to the middle region of the INL, and processes extended both to the OPL and the inner plexiform layer (IPL) (**Figure 1**). After capturing the images in the slice preparations using a confocal microscope, we examined how the processes of each cell extended. A large majority of the cells that we examined were bipolar cells with dendrites extending to the OPL and axons extending toward the IPL (Rik, 511/575 cells, $n = 5$ mice; Lhx4, 524/551 cells, $n = 4$ mice), confirming that these are bipolar cell GFP mouse lines.

Approximately 15 subtypes of bipolar cells of the retina are identified in many species across the vertebrates, including humans, primates, rodents, fish, and salamander (Wu et al., 2000; Haverkamp et al., 2003; Connaughton et al., 2004; Ghosh et al., 2004; MacNeil et al., 2004). In the mouse retina, bipolar cell types have been characterized by their distinct patterns of axon terminal ramification in the IPL, particularly about the two cholinergic bands (**Figure 1A**; Ghosh et al., 2004; Ichinose et al., 2014; Ichinose and Hellmer, 2016). Axon terminals of the GFP-expressing bipolar cells in the Rik and Lhx4 mice ramified differently in the IPL (**Figure 1**). Bipolar cells in the Rik mice ramified either on the outer side of the OFF ChAT band or on the inner side of the ON ChAT band (**Figure 1B**), suggesting that

TABLE 1 | Primary antibodies.

Antibody	Immunogen	Source, Cat.#, Species	RRID	Dilution
Calsenilin/DREAM, clone40A5	Full-length GST fusion protein of human Calsenilin	EMD Millipore, 05-756 Mouse monoclonal	AB_2313634	1:1,000
ChAT	Human placental enzyme	EMD Millipore, AB144P Goat monoclonal	AB_2079751	1:200
HCN4	GST fusion protein with amino acids 119-155 of human HCN4	Alomone Labs, APC-052, Rabbit polyclonal	AB_2039906	1:500
Opnsw1	Recombinant human blue opsin	EMD Millipore, AB5407, Rabbit polyclonal	AB_177457	1:100
PKARIIβ	Amino acids 1-418 of human PKARIIβ	BD Biosciences, 610625, Mouse monoclonal	AB_397957	1:3,000
PKCα	Amino acids 645-672 at C-terminus of human PKCα	Santa Cruz Biotechnology, sc-8393 Mouse monoclonal	AB_628142	1:500
Synaptotagmin-2	Zebrafish Syt2	Zebrafish International Resource Center, znp1, Mouse monoclonal	AB_10013783	1:200

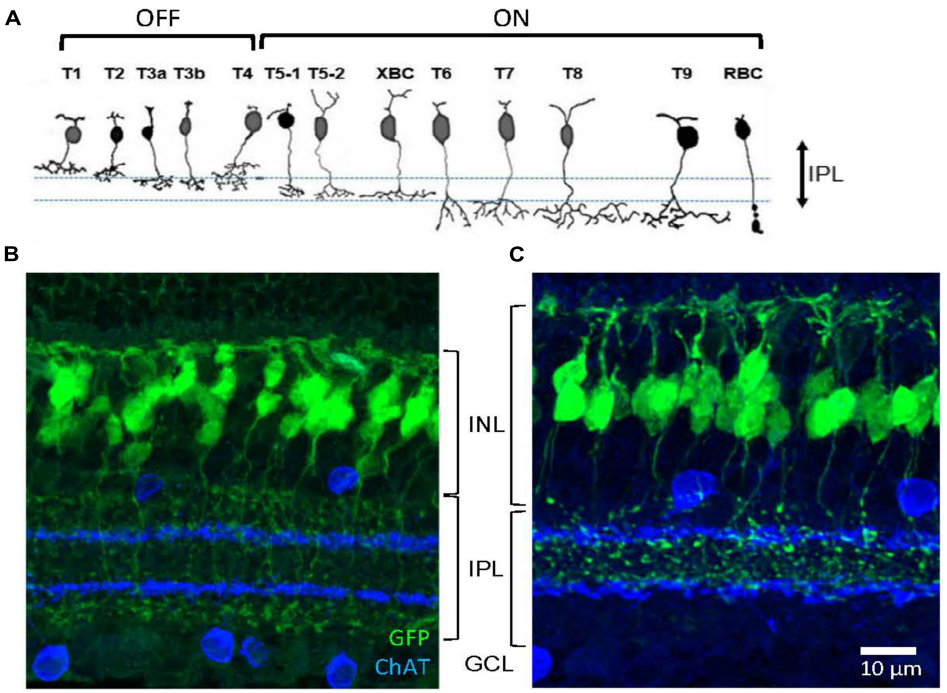

FIGURE 1 | Two bipolar cell GFP strains. **(A)** Schematic showing 13 types of bipolar cells. Each type of cell ramifies differently on the OFF (upper) and ON ChAT bands (lower). **(B)** A transverse section shows GFP-expressing bipolar cells in the Rik mouse. Axon terminals of these cells ramified either outer to the OFF ChAT band or inner to the ON ChAT band in the IPL. **(C)** A transverse section shows GFP-expressing cells in the Lhx4 mice. Axon terminals ramified between two ChAT bands in the IPL. IPL, inner plexiform layer; INL, inner nuclear layer; GCL, ganglion cell layer.

these are types 1, 2, 6, 7, 8, 9, or rod bipolar cells. In contrast, bipolar cells in the Lhx4 mice ramified between two ChAT bands (**Figure 1C**), suggesting that these are type 3a, 3b, 4, or 5 bipolar cells. Bipolar cell types in the mouse retina are well investigated and their unique molecular expression has been revealed (Wässle et al., 2009; Shekhar et al., 2016). We used the type-specific antibodies to examine the bipolar cell types in these mouse lines.

By conducting immunohistochemistry, we labeled as type 2 (Syt2), type 3a (HCN4), type 3b (PKARII), type 4 (Csen), type 6 (Syt2), and rod bipolar cells (PKCα) and analyzed whether these cells colocalized with GFP-expressing bipolar cells. As shown in **Figure 2**, we found that Syt2-positive cells expressed GFP in the Rik mice (76/77 cell somas, 98.7% and 58/58 axon terminals in the sublaminae b, 100%). Notably, Syt2 labels type 2 cells from the soma to axon in the sublaminae a and the axon terminals of type 6 cells that ramify in sublaminae b. GFP-expressing axon terminals in the S1 IPL (outermost layer) and the S4–S5 IPL (innermost layer) completely colocalized with Syt2, indicating that GFP was expressed by type 2 and 6 bipolar cells and not by type 1, 7, 8, 9, or rod bipolar cells. Also, HCN4-positive cells expressed GFP (56/57 cells, 98.3%), indicating that the Rik mice expressed type 3a bipolar cells. However, GFP was not expressed by PKARIIβ-positive cells (0/23 cells), Csen (0/26 cells), and PKCα (0/92 cells). The number of cells was counted across 5 Rik mice. These results indicate that the GFP-expressing cells are a combination of type 2, 3a, and 6 bipolar cells.

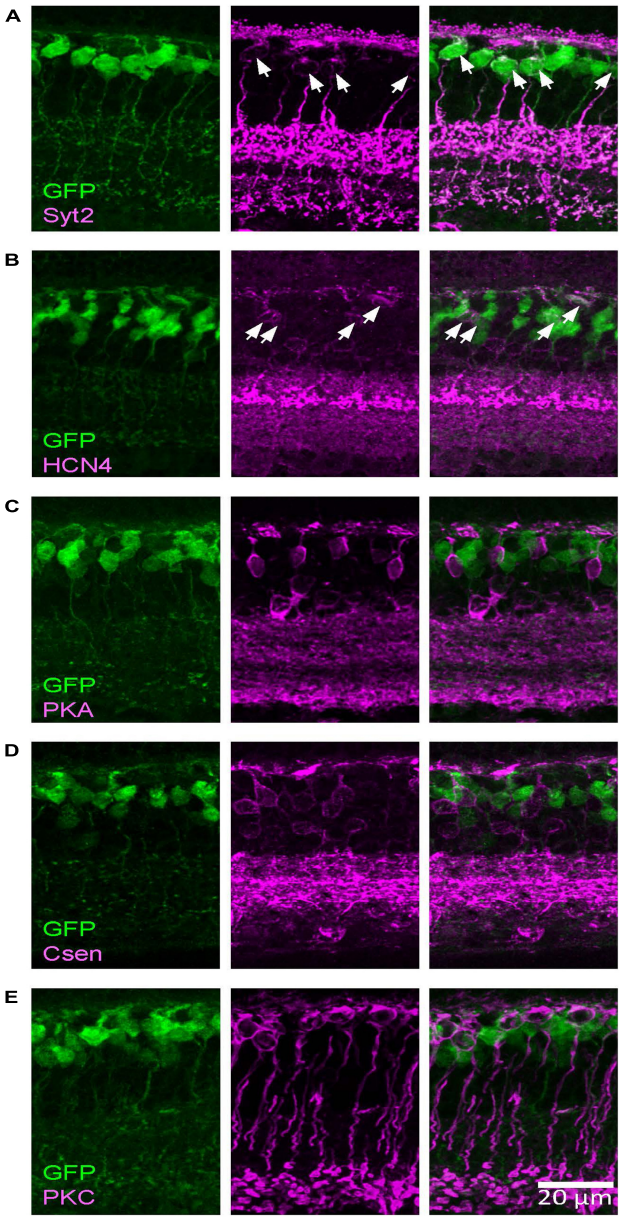

FIGURE 2 | The Rik mouse GFP-expressing cells were type 2 and 3a bipolar cells. Images were taken from a single *z* section. **(A)** A type 2 bipolar cell marker, Syt2, colocalized with GFP-expressing cells. Asterisks indicate somas labeled both with Syt2 and GFP. **(B)** A type 3a marker, HCN4, colocalized with GFP cells. Asterisks indicate colocalized cells. **(C)** A type 3b marker, PKARIIβ, did not colocalize with GFP cells. **(D)** A type 4 marker, Csen, did not colocalize with GFP cells. **(E)** A rod bipolar cell marker, PKCα, did not colocalized with GFP cells.

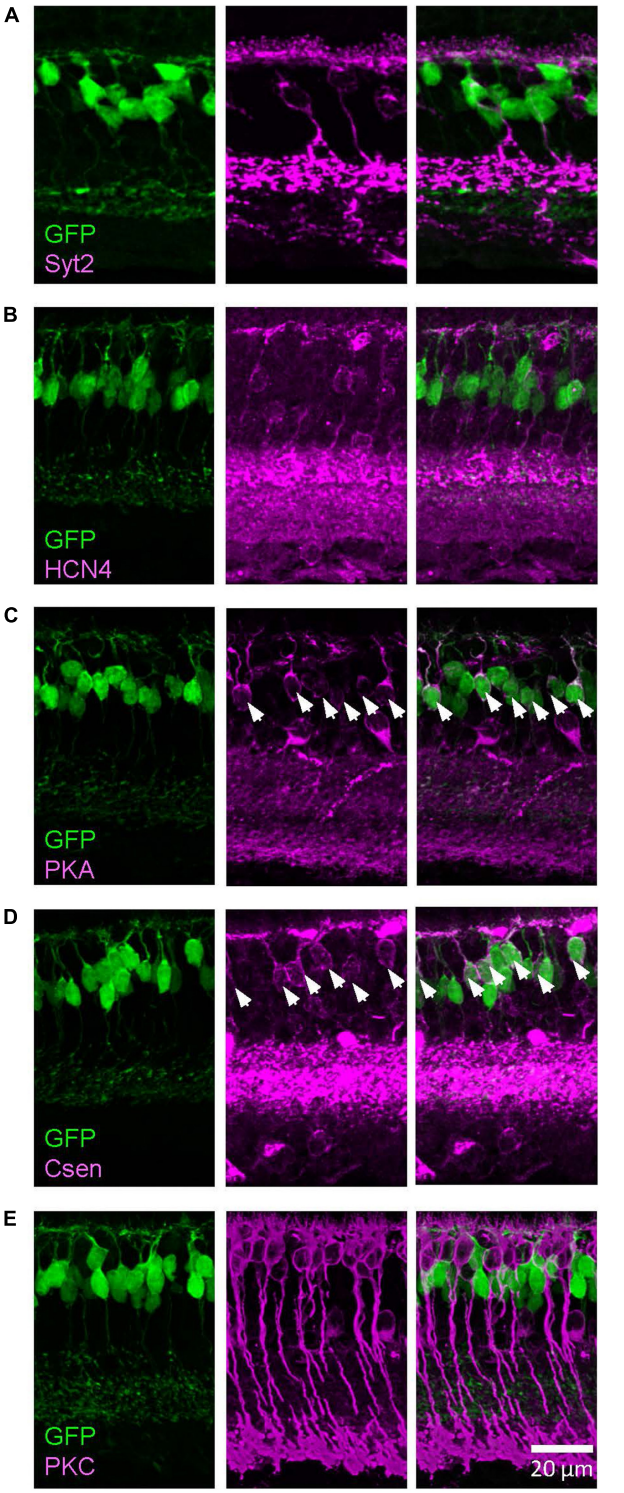

FIGURE 3 | The Lhx4 mouse GFP-expressing cells were type 3b and 4 bipolar cells. Images were taken from a single *z* section. **(A)** A type 2 bipolar cell marker, Syt2, did not colocalize with GFP-expressing cells. **(B)** A type 3a marker, HCN4, did not colocalize with GFP cells. **(C)** A type 3b marker, PKARIIβ, colocalized with GFP cells, indicated by asterisks. **(D)** A type 4 marker, Csen, colocalized with GFP cells, indicated by asterisks. **(E)** A rod bipolar cell marker, PKCα, did not colocalize with GFP cells.

Similarly, we examined the GFP-expressing cells in the Lhx4 mice with the colocalization of markers (**Figure 3**). We found that PKARIIβ-positive cells expressed GFP in the Lhx4 mice (116/120 cells, 97%) and also Csen-positive cells (30/31 cells, 97%). GFP was not expressed by Syt2-positive cells (0/60 cells), HCN4 (0/34 cells), and PKCα (0/43 cells). The number of cells was counted

across 4 Lhx4 mice. In addition, axon terminals of a subset of the GFP cells ramified near the ON ChAT band (**Figure 1B**), suggesting that they are type 5 ON bipolar cells (Hellmer et al., 2016). We did not observe the XBC, one of the type 5 bipolar cells with widely spread axon terminals (Helmstaedter et al., 2013; Hellmer et al., 2016). However, we could not distinguish other subsets. Therefore, GFP-expressing cells in the Lhx4 mice are a combination of type 3b, 4, and 5 bipolar cells. A summary of bipolar cell types expressing GFP in Rik and Lhx mice is shown in **Figure 4**.

Topography of Green Fluorescent Protein-Expressing Cells in the Rik and Lhx4 Mice

Using these two mouse lines, we examined the distribution of bipolar cells in the wholemount retina. There is a heterogeneous distribution of distinct opsin-expressing photoreceptors on the retinal surface (Szel et al., 1992; Haverkamp et al., 2005; Peichl, 2005; Schiviz et al., 2008). The distinct distributions occur in the four retinal directions (ventral, dorsal, nasal, and temporal) and eccentricities from the optic nerve head. Therefore, we measured the density of GFP-expressing bipolar cells in three different eccentricities (central, intermediate, and peripheral retinas) in the four cardinal directions.

Wholemount preparations were made from the Rik mouse eyes. After capturing cellular images using a confocal microscope, GFP-expressing cells were counted in 12 different locations (**Figure 5A**). On average, the density of GFP-expressing bipolar cells in the Rik mice was 8,486 ± 687 cells/mm^2 ($n = 5$ retinas), which was comparable with the data suggested by Wässle et al. (2009) (total of type 2, 3a, and 6 was 8,457 cells/mm^2). The cell densities for each region were plotted accordingly on the retinal locations ($n = 5$ retinas, **Figure 5B**), which suggested that cellular density was higher in the nasal region. We first examined the bipolar cell density as a function of the retinal eccentricity (**Figure 5C**), which revealed no difference among the distinct areas. Then, we analyzed the density as a function of the cardinal directions. We found that the cellular density was significantly higher in the nasal retina than in the temporal and dorsal retinas (**Figure 5D**, $p = 0.038$: nasal vs. temporal, $p = 0.027$: nasal vs. dorsal, $n = 5$ retinas, 2-way ANOVA). We also compared the densities along the nasal-temporal and the ventral-dorsal axes. The bipolar cell density in the Rik-GFP mice was higher in the nasal region along the nasal-temporal axis ($n = 5$ retinas, $R^2 = 0.19$, $p = 0.018$) (**Figure 5E**). In contrast, the cellular density was not different along the ventral-dorsal axis ($R^2 = 0.06$, $p = 0.21$) (**Figure 5F**). For these panels, data points from individual mice are color-coded, demonstrating the consistency across retinas.

Similarly, the cellular density of the Lhx4 mouse eyes was measured (**Figure 6**). The overall average density of GFP-expressing bipolar cells in the Lhx mice was 12,100 ± 1,373 cells/mm^2 ($n = 5$ retinas), which was comparable with the data suggested by Wässle et al. (2009) (total of type 3b, 4, and 5 was 11,260 cells/mm^2). The density plot shown in **Figure 6B** suggested that GFP cells occurred at a higher density in the ventral and nasal regions. We first analyzed the bipolar cell density as a function of the eccentricity (**Figure 6C**), which revealed that the density was significantly lower in the central retina than in the middle retina ($p = 0.005$, $n = 5$ retinas, 2-way ANOVA). Then, we compared the density as a function of the four cardinal directions, which showed no significant effect (**Figure 6D**). The regression analysis revealed that there was no density difference along the nasal-temporal axis ($R^2 = 0.06$, $p = 0.20$) (**Figure 6E**); however, the density in the ventral region was significantly higher along the ventral-dorsal axis ($R^2 = 0.21$, $p = 0.011$) (**Figure 6F**). Taken together, results suggested that some types of bipolar cells exhibit a heterogeneous distribution along the retinal axes.

Bipolar Cell Type-Dependent Asymmetric Distributions

Asymmetric distribution of OFF bipolar cells in the retina has been shown by Camerino et al. (2021). They reported that five types of bipolar cells occurred at a higher density in the ventral retina than in the dorsal retina. The bipolar cells in the Lhx4 mice, containing type 3b and 4 OFF bipolar cells, showed similar distribution patterns. However, cells in the Rik mice, containing type 2 and 3a OFF and type 6 ON bipolar cells, occurred at a higher density in the nasal region, which is not consistent with their findings. Therefore, we examined the distribution of each bipolar cell type in the Rik mice using the type-specific markers.

Immunohistochemistry was conducted using the type 2 (Syt2) and 3a (HCN4) markers using three retinas representing three different Rik mice (**Figure 7A**). We analyzed 6 regions in each retina along the nasal-temporal axis. Bipolar cells that showed colocalization with antibody staining were counted; GFP showed high rates of colocalization with both Syt2 (602/607 cells, 99.2%) and HCN4 (416/422 cells, 98.6%). The distribution of Syt2-positive, type 2 bipolar cells is similar along the nasal-temporal axis (**Figure 7B**), and no difference was observed between temporal and nasal regions (**Figure 7B**, $n = 3$ retinas, $p = 0.205$, linear regression analysis). Interestingly, HCN4-positive, type 3a cells occurred at a higher density in the temporal region than in the nasal regions (**Figure 7C**, $n = 3$ retinas, $R^2 = 0.23$, $p = 0.045$, linear regression analysis). Furthermore, we analyzed GFP-only cells that were neither labeled with Syt2 nor HCN4 and were type 6 ON bipolar cells (GFP + /Syt2-/HCN4-) (**Figure 2**). Notably, type 6 bipolar cells are positive with Syt2 only at the axon terminals but negative at the soma (**Figure 2**; Wässle et al., 2009). The GFP + /Syt2-/HCN4- cells occurred at a higher density in the nasal region along with the nasal-temporal axis (**Figure 7D**, $n = 3$ retinas, $R^2 = 0.44$, $p = 0.003$, linear regression analysis).

Figure 5D shows that bipolar cell density is higher in the nasal retina than in the temporal retina. On average, the GFP cell density was 640 cells/mm^2 higher in the nasal region (**Figure 5**). **Figure 7** shows that HCN4 cell density was slightly higher in the temporal regions by 550 cells/mm^2, on average. However, GFP + /Syt2-/HCN4- cell density was 1,030 cells/mm^2 higher in the nasal region. Therefore, the net increase in the nasal regions was approximately 500 cells/mm^2, which may explain the overall

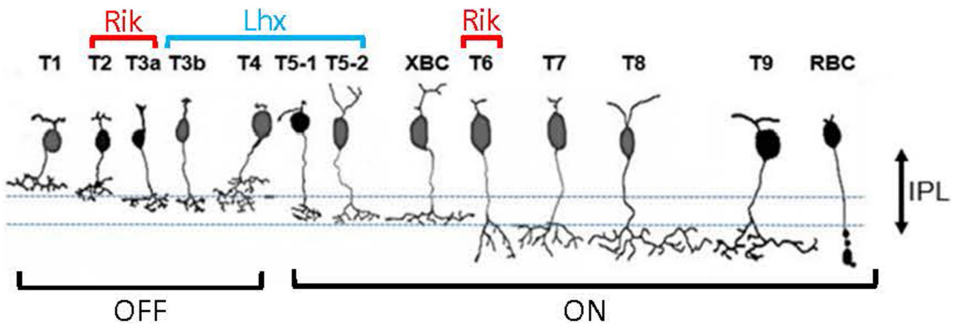

FIGURE 4 | A summary panel showing bipolar cell types that are contained by the Rik and Lhx mice.

GFP staining results (**Figure 5D**). In conclusion, we found that type 6 bipolar cells occur at a higher density in the nasal retina than in the temporal retina. In contrast, type 3a cell density was higher in the temporal region.

DISCUSSION

Summary of Results

We investigated the two GFP mouse lines and found that GFP was expressed by a unique set of achromatic bipolar cells. We found that GFP was expressed by type 2, 3a, and 6 bipolar cells in the Rik mice, whereas GFP was expressed by type 3b, 4, and 5 bipolar cells in the Lhx4 mice. Then, we examined the distributions of these bipolar cells in the retina. We found that GFP-expressing bipolar cells in the Rik mice occurred at a higher density in the nasal retina, whereas GFP cells in the Lhx4 mice occurred at a higher density in the ventral retina. It has been reported that OFF bipolar cells occur at a higher density in the ventral region, which explained the Lhx4 mice results. However, the Rik mouse distribution pattern was not consistent with their finding. Therefore, we used type-specific antibodies to examine which types contributed to the asymmetric distributions in the Rik mouse. We found that the density of HCN4-labeled type 3a cells was higher in the temporal region. Also, GFP + /Syt2- / HCN4-, type 6 bipolar cells occurred at a higher density in the nasal region.

Physiological Significance of Each Type of Bipolar Cell

Bipolar cells are second-order neurons that receive visual signaling from photoreceptors, which initiate multiple, parallel processing pathways (Wässle, 2004; Euler et al., 2014). Approximately 15 types of bipolar cells have been identified in the vertebrate retina, from fish and amphibians to mammals and primates (Wu et al., 2000; Haverkamp et al., 2003; Connaughton et al., 2004; Ghosh et al., 2004; MacNeil et al., 2004), which are thought to encode distinct components of image signals to support parallel processing. Among the 15 types of bipolar cells in the mouse retina, unique functions of some bipolar cells have been characterized; rod bipolar cells are the only type of bipolar cells mediating rod signaling. Other bipolar cells from type 1 through type 9 transmit cone-mediated signaling. Chromatic bipolar cells, also identified as type 9 bipolar cells, exclusively transmit UV-cone signaling (Haverkamp et al., 2005; Breuninger et al., 2011), and type 1 bipolar cells transmit M-cone signaling (Breuninger et al., 2011).

Type 2 through type 8 are achromatic cone bipolar cells. Their unique molecular expression has been reported (Wässle et al., 2009; Shekhar et al., 2016), indicating their unique roles in visual signaling. Although their distinct temporal processing has been demonstrated (Baden et al., 2013; Borghuis et al., 2013; Ichinose et al., 2014; Ichinose and Hellmer, 2016), unique roles of each type in image processing have not been understood. Because bipolar cells provide synaptic inputs to the third-order neurons, recent connectomic studies offer some clues.

Connectomic reconstruction of bipolar cells using serial block-face electron microscopy (SBEM) was first reported by Helmstaedter et al. (2013). They found that each type of bipolar cells exhibited distinct connectivity to SACs and to direction-selective ganglion cells (DSGCs), which are key neurons for motion detection (Euler et al., 2002; Lee and Zhou, 2006). Detailed connectivity of the SACs of bipolar cells was further revealed (Kim et al., 2014; Ding et al., 2016; Greene et al., 2016). These reports similarly found that type 2 and type 7 bipolar cells provide synaptic inputs at proximal dendrites of OFF and ON SACs, respectively, whereas type 3 and type 5 cells connect at more distal portions of OFF and ON SAC dendrites. DSGCs receive synaptic inputs directly from type 3, 4, and 5 bipolar cells (Helmstaedter et al., 2013; Yonehara et al., 2013). Collectively, these reports indicate that type 2, 3, 4, 5, and 7 bipolar cells play a role in motion detection.

Type 6 bipolar cells show unique longitudinally extended axon terminals (**Figure 1A**), and they are not primarily involved in the motion detection circuits. Instead, their roles in rod signaling have been reported. AII amacrine cells convey rod signaling, which receives synaptic inputs from rod bipolar cells and transmits the signal to ON cone bipolar cells through gap junctions. Although all types of ON cone bipolar cells are thought to have couplings, type 6 bipolar cells have a significantly large area of gap junctions with AII amacrine cells (Tsukamoto and Omi, 2017). Furthermore, type 6 bipolar cells provide inputs to dopaminergic amacrine cells *via* ectopic processes in the OFF sublamina of the IPL (Dumitrescu et al., 2009). These facts suggest that type 6 bipolar cells are one of the crucial components in light adaptation.

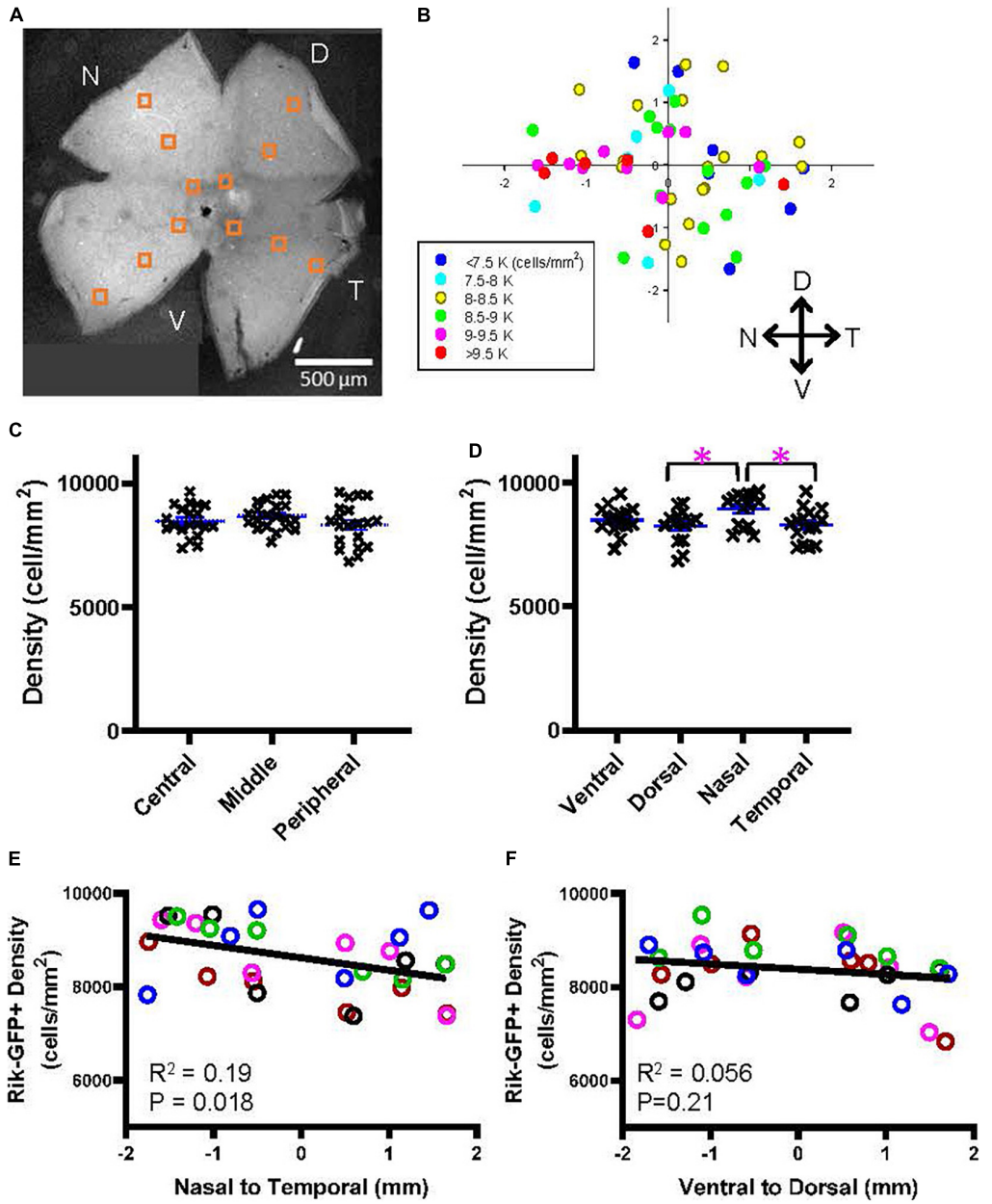

FIGURE 5 | A heterogeneous distribution of GFP cells in the Rik mouse. **(A)** A wholemount retinal tissue from a Rik mouse eye. Boxes on the tissue indicate the region of interest (ROI), where cells were counted and analyzed. **(B)** A heatmap shows all ROI densities from 5 Rik retinas. GFP cells were highly distributed in the nasal region. **(C)** GFP cells at three eccentricities were plotted as a function of their density. Central, middle, and peripheral regions were defined by an approximate distance of 500, 100, and 1,500 µm away from the optic nerve head, respectively. No difference was observed between three groups. **(D)** All GFP cells were divided into four groups based on their cardinal directions. The cell density was significantly higher in the nasal direction than in the temporal and dorsal directions. Asterisks indicate statistical significance among the groups ($p = 0.027$: dorsal vs. nasal, $p = 0.038$: nasal vs. temporal, $n = 5$ retinas, 2-way ANOVA). **(E)** A linear regression analysis revealed that the GFP cell density was higher in the nasal direction along with the nasal-temporal axis. For this panel and all other linear regression analyses, data points from individual retinal tissues are color coded. **(F)** A linear regression analysis of GFP cell density along with the ventral-dorsal axis did not show uneven distributions.

Implication of Our Results

We used two GFP mouse strains to examine the distribution of bipolar cells in the different regions of the retina. We found that these strains contain GFP-expressing bipolar cells, which are thought to be achromatic types (Haverkamp et al., 2005; Breuninger et al., 2011). The GFP expression occurred almost entirely for the particular bipolar cell types (>98%, "Results" section), demonstrating that these mouse lines can be new bipolar cell markers. The distributions of these achromatic bipolar cells were relatively homogeneous compared with the topographic

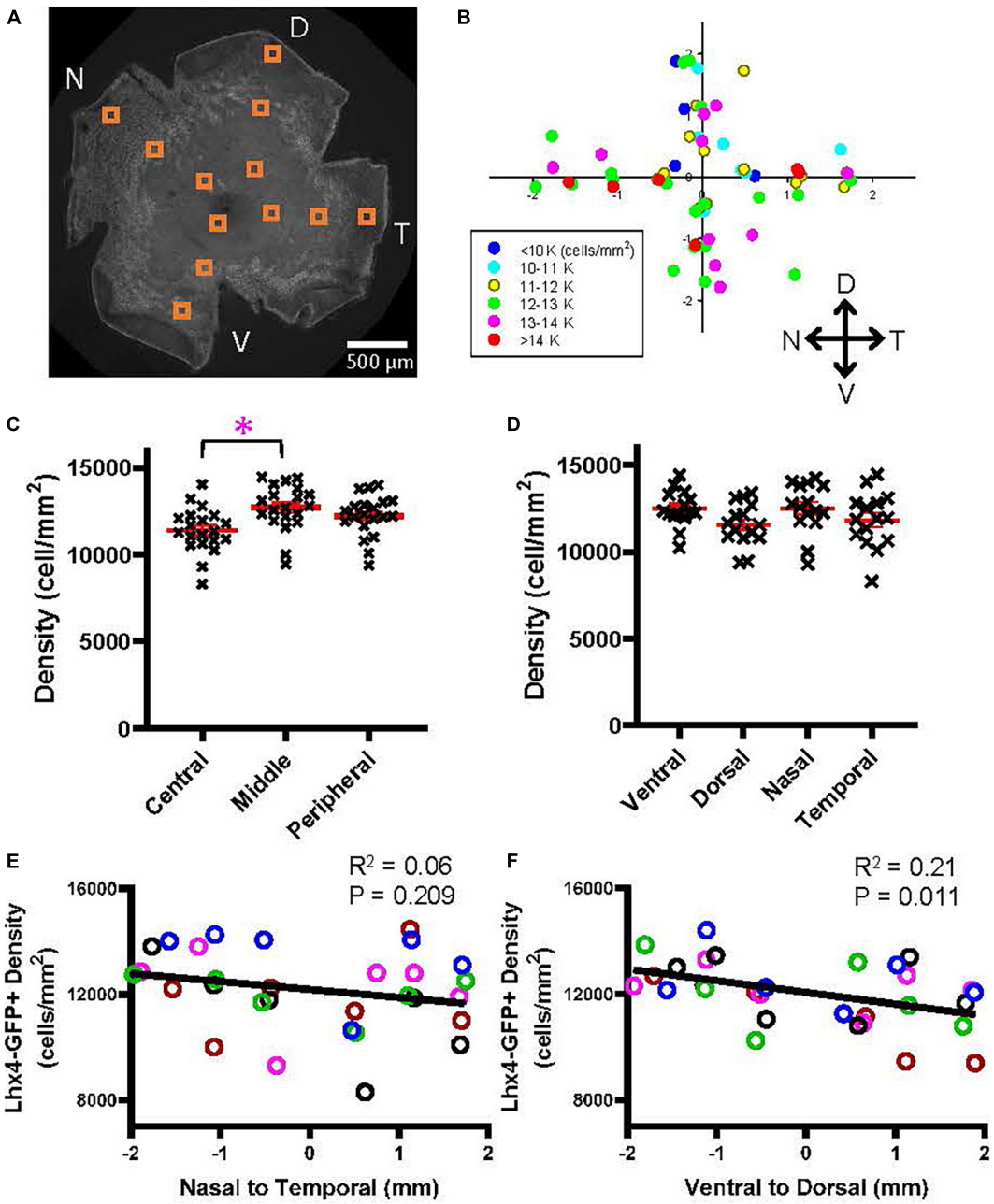

FIGURE 6 | A heterogeneous distribution of the GFP cells in the Lhx4 mouse. **(A)** A wholemount retinal tissue from a Lhx4 mouse eye. Boxes on the tissue indicate the ROI, where cells were counted and analyzed. **(B)** A heatmap shows all ROI densities from 5 Lhx4 retinas. GFP cells were highly distributed in the ventral region. **(C)** GFP cells at three eccentricities were plotted as a function of their density. The middle eccentricity showed significantly higher cell density than the central retina ($p = 0.005$, $n = 5$ retinas, 2-way ANOVA). **(D)** All GFP cells were divided into four groups based on their cardinal directions. No significant difference in density was found between directions (2-way ANOVA). **(E)** A linear regression analysis revealed that the GFP cell density showed no difference along the nasal-temporal axis. An asterisk indicates statistical significance. **(F)** A linear regression analysis of GFP cell density along the ventral-dorsal axis showed a significant decrease going from the ventral to dorsal regions.

separation of two distinct opsin-expressing cones (Szel et al., 1992; Haverkamp et al., 2005). However, we found heterogeneity in the distributions of type 3a and 6 bipolar cells.

We found that type 3a bipolar cells occurred at a higher density in the temporal retina (**Figure 7**). Axon terminals of type 3 cells ramify in the OFF ChAT band, which are thought to be one of the key players for motion detection. When a mouse walks forward, the scenery runs backward, which would activate direction-selective neurons for the posterior toward the temporal direction. DSGCs for the posterior direction were

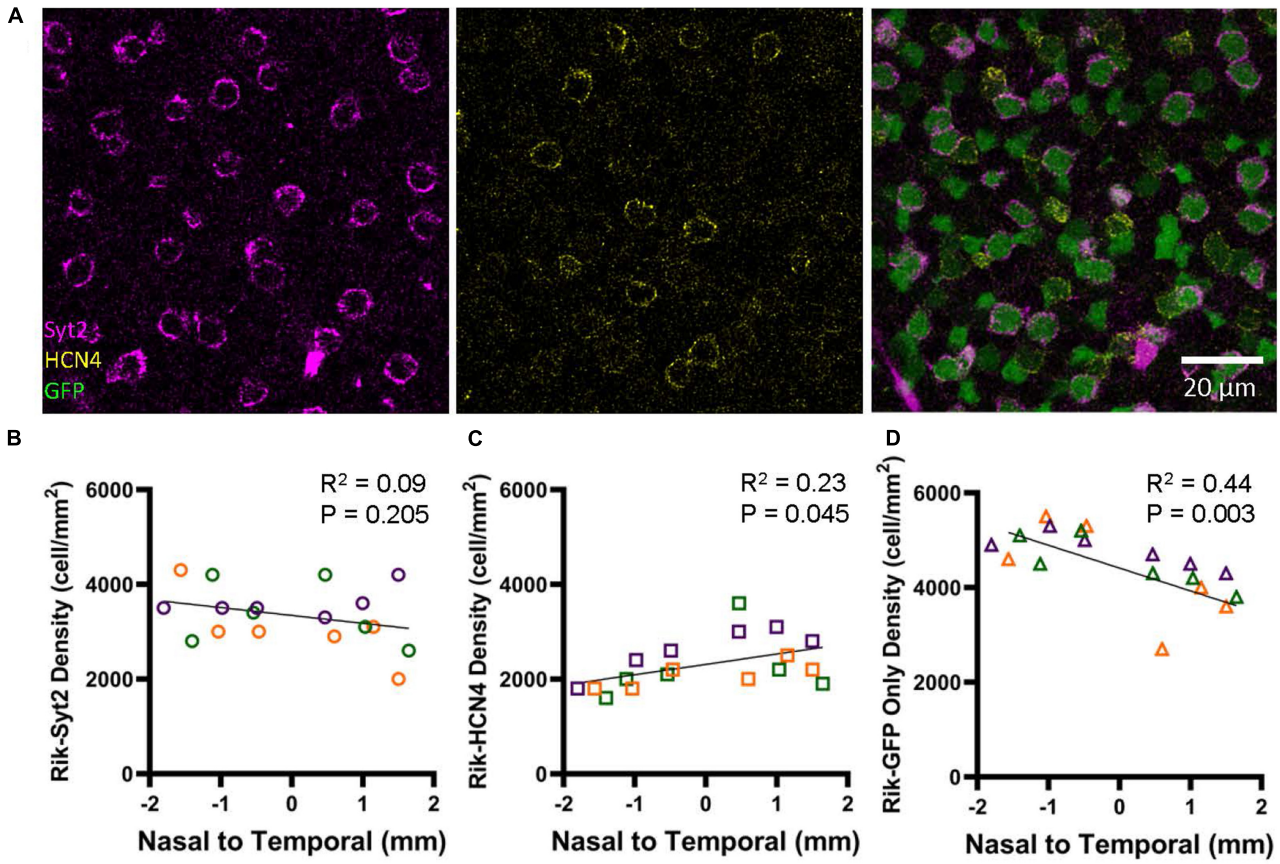

FIGURE 7 | Bipolar cell type-dependent asymmetricity in the Rik mouse. **(A)** Subsets of GFP cells were colocalized with Syt2 and HCN4 antibodies, which revealed three different types of bipolar cells in the wholemount retinal tissues. **(B)** The density of Syt2-positive GFP cells did not show asymmetric distributions along the nasal-temporal axis (linear regression analysis). Each color on the graphs in B-D represent a different mouse. **(C)** The density of HCN4-positive, type 3a cells was higher along with the nasal-temporal axis (linear regression analysis). **(D)** The density of GFP+/Syt2-/ HCN4-, type 6 bipolar cells, was found to show a gradient of decreasing density moving from the nasal region to the temporal region (linear regression analysis).

genetically identified as DRD4 and TRHR ganglion cells (Rivlin-Etzion et al., 2011). According to the report provided by Rivlin-Etzion et al. (2011) TRHR-marked ON-OFF ganglion cells were slightly higher in the temporal retinal region. This may relate to our observation of the heterogeneous distribution of type 3a bipolar cells. Type 5 bipolar cells are similarly important for motion detection. However, in the Lhx4 mice, we did not observe the differential distribution of GFP cells along the nasal-temporal axis. Type 5 bipolar cells consist of multiple subsets (Helmstaedter et al., 2013; Hellmer et al., 2016), and not all subsets might play a role in motion detection. Therefore, unlike the type 3a cells in the Rik mice, type 5 cells in the Lhx4 mice did not contribute to the heterogeneous distribution along the temporal-nasal axis.

We also found that type 6 bipolar cells occurred at a higher density in the nasal region than in the temporal region (**Figure 7**). As mentioned above, type 6 bipolar cells are crucial for light adaptation rather than motion detection. However, light adaptation does not seem to require heterogeneity of their responsible networks. Rather than their functional requirement, it might relate to the cone expression, which occurs at a higher distribution in the nasal-ventral region (Ortin-Martinez et al., 2014).

CONCLUSION

We used two bipolar cell GFP mouse strains to examine the distributions of achromatic bipolar cells. The heterogeneous distribution occurred in the axes of ventral-dorsal or nasal-temporal rather than the eccentricity (e.g., **Figures 5C**, **6C**). Even though the distribution of bipolar cells was more homogeneous than the distribution of photoreceptors, we found the differential distribution of a couple of bipolar cell types along with the nasal-temporal axis. We will need further investigation of the functional significance of the heterogeneity.

DATA AVAILABILITY STATEMENT

The original contributions presented in the study are included in the article/supplementary material, further inquiries can be directed to the corresponding author/s.

ETHICS STATEMENT

The animal study was reviewed and approved by the Institutional Animal Care and Use Committee at Wayne State University (protocol #20-10-2909).

AUTHOR CONTRIBUTIONS

TI designed the study. ZS and AS collected experimental data and performed statistical analysis. ZS and TI wrote the manuscript. All authors read, revised, and approved the submitted version of the text.

FUNDING

This study was supported by the National Institutes of Health (NIH) research project grant (R01 EY028915 and R01 EY032917) to TI, the Vision Core grant to the Department (P30 EY004068), and by the Research to Prevent Blindness (RPB).

ACKNOWLEDGMENTS

We thank A. Chakraborty for conducting the initial phase of this study and J. Bohl for technical assistance.

REFERENCES

Baden, T., Berens, P., Bethge, M., and Euler, T. (2013). Spikes in mammalian bipolar cells support temporal layering of the inner retina. *Curr. Biol.* 23, 48–52. doi: 10.1016/j.cub.2012.11.006

Borghuis, B. G., Marvin, J. S., Looger, L. L., and Demb, J. B. (2013). Two-photon imaging of nonlinear glutamate release dynamics at bipolar cell synapses in the mouse retina. *J. Neurosci.* 33, 10972–10985. doi: 10.1523/JNEUROSCI.1241-13.2013

Breuninger, T., Puller, C., Haverkamp, S., and Euler, T. (2011). Chromatic bipolar cell pathways in the mouse retina. *J. Neurosci.* 31, 6504–6517. doi: 10.1523/JNEUROSCI.0616-11.2011

Camerino, M. J., Engerbretson, I. J., Fife, P. A., Reynolds, N. B., Berria, M. H., Doyle, J. R., et al. (2021). OFF bipolar cell density varies by subtype, eccentricity, and along the dorsal ventral axis in the mouse retina. *J. Comp. Neurol.* 529, 1911–1925. doi: 10.1002/cne.25064

Connaughton, V. P., Graham, D., and Nelson, R. (2004). Identification and morphological classification of horizontal, bipolar, and amacrine cells within the zebrafish retina. *J. Comp. Neurol.* 477, 371–385. doi: 10.1002/cne.20261

Denman, D. J., Luviano, J. A., Ollerenshaw, D. R., Cross, S., Williams, D., Buice, M. A., et al. (2018). Mouse color and wavelength-specific luminance contrast sensitivity are non-uniform across visual space. *Elife* 7:e31209. doi: 10.7554/eLife.31209

Ding, H., Smith, R. G., Poleg-Polsky, A., Diamond, J. S., and Briggman, K. L. (2016). Species-specific wiring for direction selectivity in the mammalian retina. *Nature* 535, 105–110. doi: 10.1038/nature18609

Dumitrescu, O. N., Pucci, F. G., Wong, K. Y., and Berson, D. M. (2009). Ectopic retinal ON bipolar cell synapses in the OFF inner plexiform layer: contacts with dopaminergic amacrine cells and melanopsin ganglion cells. *J. Comp. Neurol.* 517, 226–244. doi: 10.1002/cne.22158

Euler, T., Detwiler, P. B., and Denk, W. (2002). Directionally selective calcium signals in dendrites of starburst amacrine cells. *Nature* 418, 845–852. doi: 10.1038/nature00931

Euler, T., Haverkamp, S., Schubert, T., and Baden, T. (2014). Retinal bipolar cells: elementary building blocks of vision. *Nat. Rev. Neurosci.* 15, 507–519. doi: 10.1038/nrn3783

Ghosh, K. K., Bujan, S., Haverkamp, S., Feigenspan, A., and Wässle, H. (2004). Types of bipolar cells in the mouse retina. *J. Comp. Neurol.* 469, 70–82.

Greene, M. J., Kim, J. S., Seung, H. S., and EyeWirers. (2016). Analogous convergence of sustained and transient inputs in parallel on and off pathways for retinal motion computation. *Cell Rep.* 14, 1892–1900. doi: 10.1016/j.celrep.2016.02.001

Haverkamp, S., Haeseleer, F., and Hendrickson, A. (2003). A comparison of immunocytochemical markers to identify bipolar cell types in human and monkey retina. *Vis. Neurosci.* 20, 589–600. doi: 10.1017/s0952523803206015

Haverkamp, S., Wässle, H., Duebel, J., Kuner, T., Augustine, G. J., Feng, G., et al. (2005). The primordial, blue-cone color system of the mouse retina. *J. Neurosci.* 25, 5438–5445. doi: 10.1523/JNEUROSCI.1117-05.2005

Hellmer, C. B., and Ichinose, T. (2015). Recording light-evoked postsynaptic responses in neurons in dark-adapted, mouse retinal slice preparations using patch clamp techniques. *J. Visualiz. Exp.* 2015:52422. doi: 10.3791/52422

Hellmer, C. B., Hall, L. M., Bohl, J. M., Sharpe, Z. J., Smith, R. G., and Ichinose, T. (2021). Cholinergic feedback to bipolar cells contributes to motion detection in the mouse retina. *Cell Rep.* 37:110106. doi: 10.1016/j.celrep.2021.110106

Hellmer, C. B., Zhou, Y., Fyk-Kolodziej, B., Hu, Z., and Ichinose, T. (2016). Morphological and physiological analysis of type-5 and other bipolar cells in the Mouse Retina. *Neuroscience* 315, 246–258. doi: 10.1016/j.neuroscience.2015.12.016

Helmstaedter, M., Briggman, K. L., Turaga, S. C., Jain, V., Seung, H. S., and Denk, W. (2013). Connectomic reconstruction of the inner plexiform layer in the mouse retina. *Nature* 500, 168–174. doi: 10.1038/nature12346

Ichinose, T., and Hellmer, C. B. (2016). Differential signalling and glutamate receptor compositions in the OFF bipolar cell types in the mouse retina. *J. Physiol.* 594, 883–894. doi: 10.1113/JP271458

Ichinose, T., Fyk-Kolodziej, B., and Cohn, J. (2014). Roles of ON cone bipolar cell subtypes in temporal coding in the mouse retina. *J. Neurosci.* 34, 8761–8771. doi: 10.1523/JNEUROSCI.3965-13.2014

Jones, B. W. (2014). "Evolution of sight in the animal kingdom," in *Webvision*. Available online at: https://webvision.med.utah.edu/2014/07/evolution-of-sight-in-the-animal-kingdom/ (accessed August 25, 2021).

Kim, J. S., Greene, M. J., Zlateski, A., Lee, K., Richardson, M., Turaga, S. C., et al. (2014). Space-time wiring specificity supports direction selectivity in the retina. *Nature* 509, 331–336. doi: 10.1038/nature13240

Kolb, H. (2011). "Simple anatomy of the retina," in *Foundation*, eds H. Kolb, R. Nelson, and B. W. Jones. Available online at: http://webvision.med.utah.edu/ (accessed August 25, 2021).

Lee, S., and Zhou, Z. J. (2006). The synaptic mechanism of direction selectivity in distal processes of starburst amacrine cells. *Neuron* 51, 787–799. doi: 10.1016/j.neuron.2006.08.007

MacNeil, M. A., Heussy, J. K., Dacheux, R. F., Raviola, E., and Masland, R. H. (2004). The population of bipolar cells in the rabbit retina. *J. Comp. Neurol.* 472, 73–86.

Nadal-Nicolas, F. M., Kunze, V. P., Ball, J. M., Peng, B. T., Krishnan, A., Zhou, G., et al. (2020). True S-cones are concentrated in the ventral mouse retina and wired for color detection in the upper visual field. *Elife* 9:e56840. doi: 10.7554/eLife.56840

Ortin-Martinez, A., Nadal-Nicolas, F. M., Jimenez-Lopez, M., Alburquerque-Bejar, J. J., Nieto-Lopez, L., Garcia-Ayuso, D., et al. (2014). Number and distribution of mouse retinal cone photoreceptors: differences between an albino (Swiss) and a pigmented (C57/BL6) strain. *PLoS One* 9:e102392. doi: 10.1371/journal.pone.0102392

Peichl, L. (2005). Diversity of mammalian photoreceptor properties: adaptations to habitat and lifestyle? *Anat. Rec. A Discov. Mol. Cell Evol. Biol.* 287, 1001–1012. doi: 10.1002/ar.a.20262

Peichl, L., and Moutairou, K. (1998). Absence of short-wavelength sensitive cones in the retinae of seals (Carnivora) and African giant rats (Rodentia). *Eur. J. Neurosci.* 10, 2586–2594. doi: 10.1046/j.1460-9568.1998.00265.x

Peterson, K. J., Lyons, J. B., Nowak, K. S., Takacs, C. M., Wargo, M. J., and McPeek, M. A. (2004). Estimating metazoan divergence times with a molecular clock. *Proc. Natl. Acad. Sci. U.S.A.* 101, 6536–6541. doi: 10.1073/pnas.0401670101

Rivlin-Etzion, M., Zhou, K., Wei, W., Elstrott, J., Nguyen, P. L., Barres, B. A., et al. (2011). Transgenic mice reveal unexpected diversity of on-off direction-selective retinal ganglion cell subtypes and brain structures involved in motion processing. *J. Neurosci.* 31, 8760–8769. doi: 10.1523/JNEUROSCI.0564-11.2011

Schindelin, J., Arganda-Carreras, I., Frise, E., Kaynig, V., Longair, M., Pietzsch, T., et al. (2012). Fiji: an open-source platform for biological-image analysis. *Nat. Methods* 9, 676–682. doi: 10.1038/nmeth.2019

Schiviz, A. N., Ruf, T., Kuebber-Heiss, A., Schubert, C., and Ahnelt, P. K. (2008). Retinal cone topography of artiodactyl mammals: influence of body height and habitat. *J. Comp. Neurol.* 507, 1336–1350. doi: 10.1002/cne.21626

Shekhar, K., Lapan, S. W., Whitney, I. E., Tran, N. M., Macosko, E. Z., Kowalczyk, M., et al. (2016). Comprehensive classification of retinal bipolar neurons by single-cell transcriptomics. *Cell* 166, 1308–1323.e1330. doi: 10.1016/j.cell.2016.07.054

Siegert, S., Scherf, B. G., Del Punta, K., Didkovsky, N., Heintz, N., and Roska, B. (2009). Genetic address book for retinal cell types. *Nat. Neurosci.* 12, 1197–1204. doi: 10.1038/nn.2370

Sondereker, K. B., Onyak, J. R., Islam, S. W., Ross, C. L., and Renna, J. M. (2017). Melanopsin ganglion cell outer retinal dendrites: morphologically distinct and asymmetrically distributed in the mouse retina. *J. Comp. Neurol.* 525, 3653–3665. doi: 10.1002/cne.24293

Szatko, K. P., Korympidou, M. M., Ran, Y., Berens, P., Dalkara, D., Schubert, T., et al. (2020). Neural circuits in the mouse retina support color vision in the upper visual field. *Nat. Commun.* 11:3481. doi: 10.1038/s41467-020-17113-8

Szel, A., Rohlich, P., Caffe, A. R., Juliusson, B., Aguirre, G., and Van Veen, T. (1992). Unique topographic separation of two spectral classes of cones in the mouse retina. *J. Comp. Neurol.* 325, 327–342. doi: 10.1002/cne.903250302

Tsukamoto, Y., and Omi, N. (2017). Classification of mouse retinal bipolar cells: type-specific connectivity with special reference to rod-driven AII amacrine pathways. *Front. Neuroanat.* 11:92. doi: 10.3389/fnana.2017.00092

Warwick, R. A., Kaushansky, N., Sarid, N., Golan, A., and Rivlin-Etzion, M. (2018). Inhomogeneous encoding of the visual field in the mouse retina. *Curr. Biol.* 28, 655–665.e653. doi: 10.1016/j.cub.2018.01.016

Wässle, H. (2004). Parallel processing in the mammalian retina. *Nat. Rev. Neurosci.* 5, 747–757. doi: 10.1038/nrn1497

Wässle, H., Puller, C., Muller, F., and Haverkamp, S. (2009). Cone contacts, mosaics, and territories of bipolar cells in the mouse retina. *J. Neurosci.* 29, 106–117. doi: 10.1523/JNEUROSCI.4442-08.2009

Werginz, P., Raghuram, V., and Fried, S. I. (2020). Tailoring of the axon initial segment shapes the conversion of synaptic inputs into spiking output in OFF-alpha T retinal ganglion cells. *Sci. Adv.* 6:eabb6642. doi: 10.1126/sciadv.abb6642

Wu, S. M., Gao, F., and Maple, B. R. (2000). Functional architecture of synapses in the inner retina: segregation of visual signals by stratification of bipolar cell axon terminals. *J. Neurosci.* 20, 4462–4470. doi: 10.1523/JNEUROSCI.20-12-04462.2000

Yonehara, K., Farrow, K., Ghanem, A., Hillier, D., Balint, K., Teixeira, M., et al. (2013). The first stage of cardinal direction selectivity is localized to the dendrites of retinal ganglion cells. *Neuron* 79, 1078–1085. doi: 10.1016/j.neuron.2013.08.005

Conflict of Interest: The authors declare that the research was conducted in the absence of any commercial or financial relationships that could be construed as a potential conflict of interest.

Publisher's Note: All claims expressed in this article are solely those of the authors and do not necessarily represent those of their affiliated organizations, or those of the publisher, the editors and the reviewers. Any product that may be evaluated in this article, or claim that may be made by its manufacturer, is not guaranteed or endorsed by the publisher.

frontiers in Neuroanatomy

REVIEW
published: 21 January 2022
doi: 10.3389/fnana.2021.784478

Type II Opsins in the Eye, the Pineal Complex and the Skin of *Xenopus laevis*: Using Changes in Skin Pigmentation as a Readout of Visual and Circadian Activity

Gabriel E. Bertolesi, Nilakshi Debnath, Hannan R. Malik, Lawrence L. H. Man and Sarah McFarlane*

Department of Cell Biology and Anatomy, Hotchkiss Brain Institute and Alberta Children's Hospital Research Institute, University of Calgary, Calgary, AB, Canada

The eye, the pineal complex and the skin are important photosensitive organs. The African clawed frog, *Xenopus laevis,* senses light from the environment and adjusts skin color accordingly. For example, light reflected from the surface induces camouflage through background adaptation while light from above produces circadian variation in skin pigmentation. During embryogenesis, background adaptation, and circadian skin variation are segregated responses regulated by the secretion of α-melanocyte-stimulating hormone (α-MSH) and melatonin through the photosensitivity of the eye and pineal complex, respectively. Changes in the color of skin pigmentation have been used as a readout of biochemical and physiological processes since the initial purification of pineal melatonin from pigs, and more recently have been employed to better understand the neuroendocrine circuit that regulates background adaptation. The identification of 37 type II opsin genes in the genome of the allotetraploid *X. laevis,* combined with analysis of their expression in the eye, pineal complex and skin, is contributing to the elucidation of the role of opsins in the different photosensitive organs, but also brings new questions and challenges. In this review, we analyze new findings regarding the anatomical localization and functions of type II opsins in sensing light. The contribution of *X. laevis* in revealing the neuroendocrine circuits that regulate background adaptation and circadian light variation through changes in skin pigmentation is discussed. Finally, the presence of opsins in *X. laevis* skin melanophores is presented and compared with the secretory melanocytes of birds and mammals.

Keywords: melanophore, melanocyte, background adaptation, circadian rhythm, evolution, pigment cell, light response, photosensitive

OPEN ACCESS

Edited by:
Francisco M. Nadal-Nicolas, National Eye Institute (NIH), United States

Reviewed by:
Diego García-González, Biotech Research and Innovation Center, University of Copenhagen, Denmark
Elise Cau, CNRS Délégation Occitanie, France

****Correspondence:***
Gabriel E. Bertolesi
gbertole@ucalgary.ca

Received: *27 September 2021*
Accepted: *13 December 2021*
Published: *21 January 2022*

Citation:
Bertolesi GE, Debnath N, Malik HR, Man LLH and McFarlane S (2022) Type II Opsins in the Eye, the Pineal Complex and the Skin of Xenopus laevis: Using Changes in Skin Pigmentation as a Readout of Visual and Circadian Activity. Front. Neuroanat. 15:784478. doi: 10.3389/fnana.2021.784478

INTRODUCTION

Physiologically, color change of the skin is a critical process for survival in ectothermic amphibians. For example, during camouflage through background adaptation, the light reflected from the surface is sensed and the skin undergoes a color change to avoid detection by potential predators or prey (Hoekstra, 2006). The environmental light is also perceived in a circadian manner and the skin adjusts its color for heat retention and/or for light/ultraviolet (UV) protection

(Filadelfi and Castrucci, 1996; Rudh and Qvarnström, 2013). Several physiological processes associated with skin color change are regulated by the neuroendocrine system. The skin itself also functions as a photosensitive organ, and distribution and synthesis of colored pigment also occur in cultures of skin cells (Oshima, 2001). For more than a century, the African clawed frog *Xenopus laevis* has been employed as a model organism to understand cellular and developmental biology (Dawid and Sargent, 1988). The changes in skin color are an important tool for revealing the neuroendocrine circuits that regulate background adaptation and circadian variations. The *Xenopus* model allowed elucidation of the "effectors" that change pigmentation, with the dispersing agent alpha-melanocyte stimulating hormone (α-MSH) darkening the skin during background adaptation, and melatonin lightening the skin at night (Filadelfi and Castrucci, 1996; Roubos et al., 2010; Bertolesi and McFarlane, 2018). Unknown, however, is the identity of the "initiators" that trigger the physiological color response; molecules that sense light in photosensitive organs such as the eye, the pineal complex (named here as the frontal organ plus the pineal gland) and the skin. Fortunately, two critical events in the last decade positioned *Xenopus laevis* as an excellent model organism to unveil the initiating components: (1) Full sequencing of the genome (Session et al., 2016), and (2) Discovery of a remarkable number and diversity of type II opsin photopigments which were originally detected in zebrafish (Davies et al., 2015) and compared with other species, including *Xenopus laevis* (Davies et al., 2015; Bertolesi et al., 2020).

Anurans (frogs), the amphibian order to which *Xenopus laevis* belongs, offer additional advantages in both broadening our understanding of the evolutionary processes that may have occurred during the transition to land, and providing information about the mechanisms of sensing light that produce changes in skin pigmentation. During evolution, the transition from aquatic to terrestrial life occurred together with dramatic changes in anatomical structures, sensory systems, and the skin. For example, developing limbs transformed the swimming locomotive organs to structures better adapted to land (Dickson et al., 2021), while the eye increased in size and moved from a lateral to a dorsal position characteristic of the early amphibian Tetrapod (Nilsson, 2021). Interestingly, the "buena vista" theory, recently suggested by MacIver et al. (2017), postulates that a contributing factor to the further evolution of limbs and the emergence of novel neurological circuits was the evolution of a sensory system capable of "seeing" over longer distances, which preceded the evolution of fully terrestrial limbs. The formation of limbs during metamorphosis from swimming tadpoles to land-adapted froglets, the change in the anatomical position of the eye from a lateral to dorsal position, and the generation of novel neuronal circuits are important features of Anuran development that show certain similarities with the evolutionary processes. These evolutionary-developmental similarities are evident in Anurans of the other two orders of living amphibians: the Caudata (salamanders) and Gymnophiona (caecilians). The evolution and photoreception of the three orders of amphibians were reviewed recently (Mohun and Davies, 2019). In this review we focus on *Xenopus laevis* and emphasize skin pigmentation changes that occur during early development (see section "Changes in Skin Pigmentation During Early Development. Background Adaptation and Circadian Variation in Skin Response Are Segregated and Driven by Photosensitivity of the Eye and the Pineal Complex, Respectively"). The evolutionary origin of this allotetraploid species, and the variability of type II opsins and their anatomical expression in the eye, the pineal complex, and the skin are discussed in section "Origin of *Xenopus laevis* and Genetics of Type II Opsins."

Using changes in skin pigmentation as a readout of light-sensing mechanisms is simple in *Xenopus*, at least during early development, in that the eye and the pineal complex are both photosensitive, and the neuroendocrine circuits that induce skin color variation are segregated (Bertolesi et al., 2020). Mammals are more complicated when it comes to understanding the light-regulated pigmentation processes, since their ancestors lost an external photosensitive pineal complex as it became incorporated into the brain. In mammals, neuroendocrine light-mediated changes in skin pigmentation are under the control of eye photosensitivity alone (Klein, 2006), which prevents the separate analysis of skin color changes triggered by visual (e.g., background adaptation) and non-visual (e.g., circadian) processes. The extensive nocturnal period which mammalian ancestors embraced in order to avoid competing with the diurnal and dominant reptiles [nocturnal bottleneck theory (Gerkema et al., 2013)] may have been the selective force for the loss of an external photosensitive pineal complex. Additionally, the evolution of insulation systems that appeared independently during the advent of thermoregulation in avian-reptile and mammalian lineages induced dramatic changes in the characteristics of the integument, by transforming intracellular pigment-dispersing melanophores into pigment-secretory melanocytes (Haslam et al., 2014; Lovegrove, 2017). Thus, *Xenopus* possess a pigmentation system that responds to signals from several photosensitive organs. In section "Function of Type II Opsins in *Xenopus* eye. The Role of Intrinsically Photosensitive Horizontal Cells (ipHCs) and Pinopsin-Expressing Photoreceptors" we analyze the structure of the *Xenopus* eye, its activation during development, and the expression of type II opsins in the context of their visual role to regulate background adaptation. The anatomy of the pineal complex as a photosensor of environmental light is discussed in section "Structure of the Pineal Complex, Expression of Type II Opsins and Melatonin Secretion." Finally, in section "Type II Opsins in the Skin. From the Ectothermic *Xenopus* to Endothermic Mammals," the presence of opsins in *X. laevis* skin melanophores is compared to our current knowledge of the involvement of opsins in secretory melanocytes of mammals.

Changes in Skin Pigmentation During Early Development. Background Adaptation and Circadian Variation in Skin Response Are Segregated and Driven by Photosensitivity of the Eye and the Pineal Complex, Respectively

The integument of amphibians, such as the frog *Xenopus laevis*, non-avian reptiles, and fish, is exposed to light and rapidly adapts

its pigmentation color to the local environment. Conversely, avian reptiles and mammals possess an integument protected by feathers and fur, respectively, and display markedly slower color changes. In *Xenopus* larvae, color change is fast, with two physiological responses observed in minutes or hours if the larvae are raised initially on a white background with light shining from above: (1) Background adaptation, and (2) Circadian variation in skin color. Switching the larvae from a white to a black background darkens the skin by the dispersion of melanosomes (melanin-filled vesicles) residing in dermal pigment cells called melanophores (**Figure 1A**). This cryptic physiological response, termed background adaptation, increases survival by reducing detection by natural predators. The response was described in *Xenopus* in some detail almost a century ago by Hogben and Slome (1931, 1936). Indeed, the authors were the first to indicate that background adaptation is mediated by a neuroendocrine circuit that requires a functional hypophysis, specifically the pars intermedia. Work, years later, demonstrated that synthesis and secretion of the pigment dispersing agent α-MSH from the hypophysis is responsible for background adaptation in amphibians (Jenks et al., 1977; Kramer et al., 2003).

In contrast to black background adaptation, when tadpoles are switched to dark conditions melanosomes aggregate and lighten the skin (**Figure 1A**). Although the skin lightening response in dark conditions was known for several years (McCord and Allen, 1917), it was not until the mid 20th century when a "chemical substance" released from the pineal gland was recognized as an "effector" that induces melanosome aggregation (Bagnara, 1960a). Melatonin was biochemically purified from pig pineal glands, helped by the lightening of tadpole skin as a readout (Lerner et al., 1958). It is worth noting that all vertebrates, independent of whether they are diurnal or nocturnal, release melatonin into the bloodstream at night. In *Xenopus*, the circadian whitening of skin by melatonin is thought to contribute to thermoregulation (Filadelfi and Castrucci, 1996).

To understand the neuroendocrine circuits responsible for background adaptation and the circadian variation in skin color, our laboratory and others focused on the early developmental window and determined when the responses initiate (Jenks et al., 1977; Verburg-van Kemenade et al., 1984; Bertolesi et al., 2017). An advantage of *Xenopus laevis* is the simplicity of the pigmentation system in that of the eight different types of colored pigmented chromatophore described in vertebrates (brown melanophores, red erythrophoros, blue cyanophores, yellow xanthophores, white leucophores, reflective iridophore and the dichromatic erythro-iridophore and erythro-cyanophore) (Schartl et al., 2016), only brown, melanin-containing melanophores are present at early developmental times (Fukuzawa, 2000; Kumasaka et al., 2005). Pigment cells are derived from the neural crest, which proliferate and differentiate–with pigment cells being visible by the naked eye over the dorsal head, belly and tail by stage 32–33/34 (day 3 at 16°C) in *Xenopus* tadpoles. Slight differences in pigmentation are observed that depend on the level between different hatches. The response to black background emerges at stage 39/40 (**Figure 1A**; day 4 at 16°C), immediately after the eye circuits becomes functional (stage 37; see section "Function of Type II Opsins in *Xenopus* eye. The Role of Intrinsically Photosensitive Horizontal Cells (ipHCs) and Pinopsin-Expressing Photoreceptors") (Verburg-van Kemenade et al., 1984; Bertolesi et al., 2014, 2017). The change in pigmentation induced by black background becomes more apparent within 2 days (**Figure 1A**, day 5 and 6 at 16°C; stage 42 and 43/44). Skin lightening triggered by dark also initiates at stage 39, but only if embryos are raised on a light/dark cycle (**Figure 1A**). Raising tadpoles in continuous

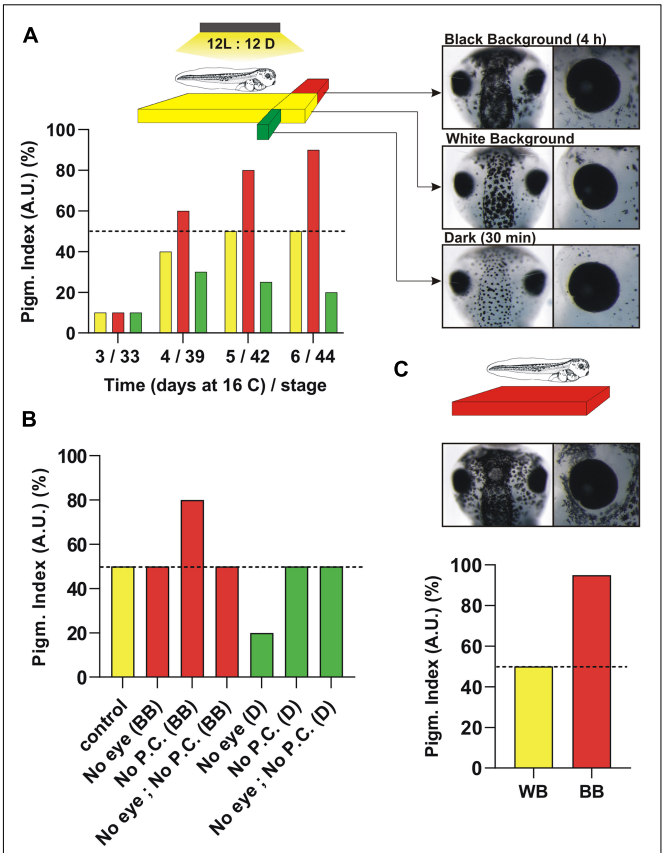

FIGURE 1 | Pigmentation response induced by reflected light from the substrate (background adaptation) or environmental light (dark/light) over *Xenopus laevis* development. **(A)** Pigmentation levels at different developmental times represented approximately (50%; day 5/6) from embryos raised on a white background (WB) (yellow column). The light shines from above in cycles of 12 h ON/12 h OFF and the pigmentation is measured at the middle of the light cycle. The timeline in days (*X*-axis) of embryos maintained at 16°C until stage 43/44 is assigned to the approximate developmental stage. Tadpoles raised on a white substrate (WB) are switched either to a black background for 4 h (BB; red columns) or dark for 30 min (D; green columns) (see schematic). The pigmentation response is measured in the dorsal head (see pictures). **(B)** Pigmentation response of stage 43/44 embryos compared to enucleation (No eye), pinealectomy (No P.C) or both (No eye, No P.C.). The surgery is performed 24 h before pigmentation measurement. **(C)** Morphological pigmentation of embryos induced by raising tadpoles on a black background from early stages. Note the difference in the "morphological" pigmentation (increase in melanophore number mainly around the eye) when tadpoles are raised on a BB vs. the quick "physiological" responses seen in tadpoles raised on a WB. See text for additional details.

light or dark delays the onset of the circadian light response (Bertolesi et al., 2017), likely because of lack of entrainment of the pineal complex.

Two important questions that needed addressing were whether: (1) background adaptation and circadian skin color variation are developmentally segregated, and (2) skin pigmentation can be used as a readout of both of the photosensitive circuits. The schematic in **Figure 1** shows the relative skin pigmentation of embryos developed on a white background with light shining down from above in light cycles of 12 h ON: 12 h OFF which produces an "intermediate" level of skin pigmentation when measured at the middle of the light cycle (**Figures 1A–C**, exemplified as 50% pigmentation level). This intermediate pigmentation level is an advantage as it allows quantifiable darkening and lightening responses to changes in background and environmental light, respectively. Thus, when tadpoles are switched to either a black background for approximately 3–4 h, or dark conditions for 30 min, the skin darkens or lightens, respectively (**Figure 1A**, schematic). These numbers correspond to the amount of time required to induce the maximum response (Bertolesi et al., 2017). When embryos reach stage 43/44, both neuroendocrine circuits are functional and both darkening and lightening are easily measurable – mainly in the dorsal head (**Figure 1A**, pictures). Pigmentation changes are also detectable in the belly and the tail (Bertolesi et al., 2015). Of note, the process of aggregation/dispersion of pigment over short time periods described here is known as "physiological color change" and differs from the "morphological" variation in pigmentation. The latter response comprises a slow change in color that occurs generally by varying the number of pigment cells and/or the type of pigment (Sugimoto, 2002; Bertolesi et al., 2016a). Morphological variation in skin pigmentation is detectable in *Xenopus* larvae raised on a black background from early stages when compared to larvae raised on a white background, with the black background increasing the number of melanophores (Bertolesi et al., 2016a; **Figure 1C**, morphological pigmentation; see the increased number of melanophores around the eye).

We recently showed that both neuroendocrine circuits are functional by stage 43/44 (Bertolesi et al., 2020). At this stage, the circuits are independent of each other, with background light being sensed by the eye and environmental light detected by the photosensitive pineal complex. Indeed, with eye enucleation the melanosome dispersion triggered by 4 h on a black background disappears, while the lightening induced by dark exposure remains similar to that of sham controls (**Figure 1B**). In contrast, pinealectomy abolishes the lightening triggered by dark conditions, but not the background adaptation response (**Figure 1B**; Bertolesi et al., 2020). Of note, pinealectomy in young embryos removes the secretory structure responsible for systemic melatonin (see section "Structure of the Pineal Complex, Expression of Type II Opsins and Melatonin Secretion"), so a simple experiment, where the pineal complex was covered with a small piece of aluminum foil, was used to show that the organ is photosensitive and responsible for the skin lightening induced by dark (Bertolesi et al., 2020).

An additional aspect to consider when skin pigmentation is used as a readout is the capacity of melanophores themselves to sense light and trigger either the dispersion or aggregation of melanosomes. This process, discussed in section "Type II Opsins in the Skin. From the Ectothermic *Xenopus* to Endothermic Mammals," is known as the "primary color response" and occurs when photosensitive molecules, like type II opsins, initiate a signal transduction cascade that affects the distribution of melanosomes (Oshima, 2001). *Xenopus* melanophores *in vitro* exhibit primary responses (Seldenrijk et al., 1979; Daniolos et al., 1990; Rollag, 1996). The fact that pigmentation in the enucleated and pinealectomized larvae is similar to that of sham controls (**Figure 1B**; Bertolesi et al., 2020), however, indicates that the primary response *in vivo* has a minimal role when compared to the pigmentation changes induced by the "secondary" responses triggered by hormones; α-MSH for background adaptation and melatonin for environmental light.

Since background adaptation and circadian responses are segregated at the circuit level, and the primary response of melanophores provides a negligible contribution, changes in skin pigmentation can be used to distinguish signals that originate independently in the eye and the pineal complex. Interesting questions remain: Are these results applicable to older developmental stages of *Xenopus*, and further, to other species? Unfortunately, experiments that compare simultaneously the pigmentation response with enucleation or pinealectomy have not been performed in older post-metamorphic froglets. Neural circuits are known to change over development, and so it is not a given that the pigmentation response would be controlled similarly in embryos and adults. For instance, new neuronal connections are made by the eye just prior to metamorphosis, as per the generation of the axons of ipsilateral retinal ganglion cells to complement the contralateral axon projection formed at earlier developmental times (Larsson, 2011; von Uckermann et al., 2016). Ipsilateral and contralateral connections from both eyes provide stereoscopic vision. Little is known with respect to neuronal interactions between the photosensitive pineal complex and the eye in adult *Xenopus*, although new connections are not unexpected.

In considering whether other species have similar pigmentation responses to *Xenopus* it is important to bear in mind the dramatic changes that occurred during evolution in the mechanisms that regulate skin pigmentation. For example, background adaptation in Tetrapoda is regulated by a "uni-hormonal" mechanism, where changes in the systemic levels of the dispersing hormone α-MSH alter pigmentation color. In contrast, teleosts exhibit "dual hormonal" control, mediated by α-MSH and a second pituitary hormone with melanosome-aggregating ability known as melanin-concentrating hormone like (MCHL) (previously known as MCH) (Kawauchi et al., 1983; Bertolesi et al., 2019; Diniz and Bittencourt, 2019; Bertolesi and McFarlane, 2020). Additionally, the evolution of systems of insulation during the advent of thermoregulation modified the integument of avian-reptiles and mammals in such a way that places them in a different integument class relative to amphibians and non-avian reptiles (Lovegrove, 2017). Thus, additional species with mechanisms and observable color changes in the

skin similar to those found in *Xenopus laevis* should likely be present within the amphibian and/or the reptile lineages.

Origin of *Xenopus laevis* and Genetics of Type II Opsins

Xenopus laevis is an allotetraploid species that arose *via* the interspecific hybridization of diploid progenitors with 2n = 18, with the subsequent stabilization of the duplicated genome to restore meiotic paring. Thus, its total chromosome number (2n = 36) nearly doubles that of the Western clawed frog *Xenopus tropicalis* (2n = 20) [used as a reference genome (Session et al., 2016)] and the existent species in the *Xenopus* taxonomic genus known today (29 species). The full genome sequence is accessible through Xenbase[1], and the chromosomal localization of genes is found in any of the pairs co-orthologous to the corresponding *X. tropicalis* chromosome, denoting an L and S for the longer and shorter homolog, respectively. The sex chromosome (Z/W) corresponds to 2L which includes the sex determinant gene, *dmw* (W-linked DM-domain), presented as a single allele but absent in males (Yoshimoto and Ito, 2011). In evolutionary terms, *X. laevis* is a relatively recent species in that the diploid progenitor diverged around 34 million years ago (mya) and combined to form the allotetraploid ancestor around 17–18 mya (Session et al., 2016).

Our laboratory has focused on the identification of type II opsins in an effort to determine the light sensors that trigger changes in skin pigmentation. Of note, type II opsins possess a different evolutionary origin than the type I (microbial) opsins, although some similarities at the molecular level exist. Common to both opsin types are the seven transmembrane domains and the capacity to sense light to trigger an intracellular signal. However, type II opsins belong to a family of G-protein-coupled receptors (GPCRs) that likely derived from the melatonin receptor approximately 711–700 mya, before the appearance of vertebrates (approximately 540 mya) (Feuda et al., 2012; Porter et al., 2012). An amino acid switch to a lysine in the seventh transmembrane domain allowed the binding of a chromophore ("photosensor"; generally retinal) to trigger a conformational change and a G-protein-associated signal transduction cascade upon light stimulation (Lamb, 2013). We identified a total of 37 opsin genes in the *X. laevis* genome, most of which correspond to duplicated forms present in the L and S chromosomes, while others are single copies generated as a result of pseudogenization (Bertolesi et al., 2020; **Figures 2A,B**). Without considering duplicated genes, a total of 22 opsins are present, and we recently reported their expression in the stage 43/44 tadpole eye (Bertolesi et al., 2021) and pineal complex (Bertolesi et al., 2020; **Figure 2B**). As an approximation of opsins expressed by skin melanophores, we show here the RT-PCR analysis of opsins detected in isolated tails from stage 43/44 tadpoles, using similar PCR conditions to those published previously (Bertolesi et al., 2020, 2021; **Figure 2A**). We also analyzed the expression of opsins in a stable melanophore cell line generated from stage 30 to 35 tadpoles, MEX cells (Kashina et al., 2004; **Figure 2A**). The 22 opsins are classified in six phylogenetically related groups, named based on their tissue localization as identified in initial expression analyses, although current knowledge indicates a more complex scenario (**Figure 2B**): (1) the "**visual opsins**" [rhodopsin (*opn2*; Rh1); low wavelength sensitive opsin (*opn1lw*; Lws); short wavelength sensitive opsin 1 (*opn1sw1*; Sws1) and short wavelength sensitive opsin 2 (*opnsw2*; Sws2); (2) the "**pineal opsins,**" also known as "non-visual opsins" as they were identified in extraocular tissues of non-mammalian vertebrates [pinopsin (*opnp*); vertebrate ancient opsin (*opnva*), parapinopsin (*opnpp*) and pareietopsin (*opnpt*)]; (3) the "**non-visual opsins**" [encephalopsin (*opn3*) and several teleost multiple tissues opsins (*tmtops*; *tmtopsb* and *tmtops2*)]; (4) the "**neuropsins**" [opsin5 (*opn5;* is the only neuropsin gene present in mammals), and several paralogs identified in non-mammalian vertebrates (*opn6, 7,* and *8*); in this group, additional duplications occurred in *opn6* and *7* in *Xenopus* (*opn6a* and *opn6b*, and *opn7a* and *opn7b*)]; 5) the "**photoisomerases**" [the retinal G-protein coupled receptor (*rgr*) and retinal pigment epithelium (RPE)-derived rhodopsin homolog (*rrh*; a.k.a. peropsin)]; and (6) the "**melanopsins**" [*Xenopus* contains two paralogous genes, the mammalian-like *opn4* (a.k.a. *opn4m*) and the *Xenopus*-like *opn4b* (a.k.a. *opn4x*)]. Of the type II opsins described in vertebrates, those absent from the *Xenopus* genome are *exorhodopsin* and *opn9*, which appeared during evolution only in the teleost lineage, and the rhodopsin-like 2 gene (*rh2*) that was lost in amphibians and mammals (Davies et al., 2015).

Both the identification of type II opsins and analysis of their expression is proving helpful in determining their functional roles in regulating skin pigmentation. The genome duplication, however, remains an important consideration in that the two "subgenomes" have evolved asymmetrically, with one showing more intrachromosomal rearrangement, gene loss by deletion and pseudogenization than the other (Session et al., 2016). Indeed, expression of type II opsin genes varies between photosensitive organs and between the subgenomes as suggested by RNAseq analysis (**Figure 2C**). Of note, data regarding gene expression (RNAseq) and chromatin data (Chip-seq) are now integrated and available in Xenbase (Fortriede et al., 2020).

The anatomical localization of the Type II opsins in the eye, pineal complex and skin are discussed in the next three sections and provide important information for understanding the molecular mechanisms that regulate changes in skin pigmentation.

Function of Type II Opsins in *Xenopus* Eye, the Role of Intrinsically Photosensitive Horizontal Cells and Pinopsin-Expressing Photoreceptors

The *X. laevis* eye is well studied and the structure of the retina is similar to that found in all vertebrates. Within the retina, there are five classes of neurons distributed in three different layers: photoreceptors, horizontal, bipolar, amacrine, and retinal ganglion cells (Lamb, 2013). Anurans exhibit two types of classical photoreceptors, rods and cones, with specific characteristics regarding the expression of type II opsins (see below). Light entering the eye stimulates photoreceptors located

[1]http://www.xenbase.org/entry/

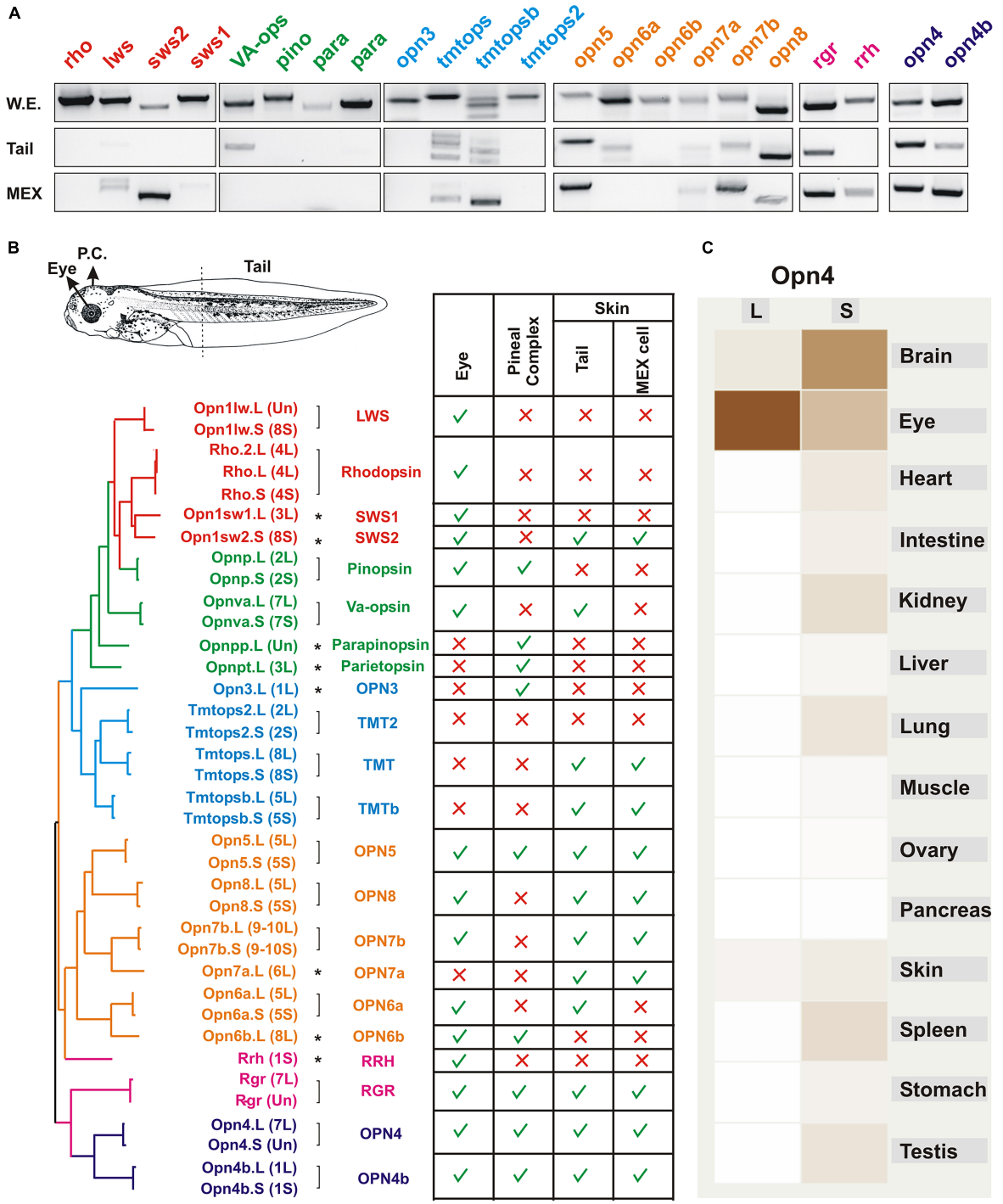

FIGURE 2 | Expression of opsins in the *Xenopus* larval eye, pineal complex, and skin. **(A)** RT-PCR analysis showing mRNA expression of the indicated opsins at stage 43/44 in the whole embryo and isolated tails, and in a melanophore cell line (MEX) obtained from stage 30–35 *X. laevis* tadpoles (Kashina et al., 2004). RT-PCR conditions are similar to those published previously (Bertolesi et al., 2020, 2021). **(B)** Opsins identified in the *X. laevis* genome and their expression in the pineal complex, eye and tails. The putative amino acid sequences were compared, and a molecular phylogenetic analysis performed by the maximum-likelihood method is shown (not to scale). Type II opsins are grouped according to what was initially considered as their tissue localization: visual opsins (red); pineal opsins (green); non-visual opsins (blue); neuropsins (orange); photoisomerases (pink) and melanopsins (purple). Groups are also approximately reflected in the phylogenetic tree. Brackets denote genes duplicated and maintained on the long (L) and short (S) chromosomes, with single copy genes indicated with an asterisk. The table show the summary of expression of opsins in the eye (Bertolesi et al., 2021), the pineal complex (Bertolesi et al., 2020), and the tails and MEX cells as determined by RT-PCR as in **A. (C)** A comparative expression analysis determined by RNAseq of *opn4* in different organs from both genes (L and S) is reproduced from Xenbase (http://www.xenbase.org/, RRID:SCR_003280). Darker color reflects higher mRNA expression.

in the outer nuclear layer (ONL), which transmit signals to bipolar cells and then retinal ganglion cells. The axons of retinal ganglion cells exit out of the eye and target the brain. Horizontal and amacrine cells sit in the inner nuclear layer (INL) and function to regulate signals within the retina (**Figure 3A**).

Rods and cones express type II opsins, and are almost equally represented and evenly distributed between the central and the peripheral retina of adults and young *Xenopus* larvae (Gábriel and Wilhelm, 2001; Bertolesi et al., 2021; **Figure 3A**). Intriguingly, in the majority of vertebrates there is only one kind of rod – the red rod - with the rest of the photoreceptors being cones. Anurans are unique in this respect for having both "red" and "green" rods. Rods constitute half of the total photoreceptors, and approximately 97–98% are the classical "red rods" which express the photopigment rhodopsin (Rh1) (Gábriel and Wilhelm, 2001), with the "green rods" expressing the short wavelength sensitive 2 (Sws2) opsin (Darden et al., 2003; **Figure 3A**). As for the cones, 85% contain the long-wavelength-sensitive opsin (Lws) and the remaining the short-wavelength-sensitive opsin 1 (Sws1) (Gábriel and Wilhelm, 2001; Bertolesi et al., 2021; **Figure 3A**). The Sws2 photopigment found in *Xenopus* green rods contributes to color vision (Kojima et al., 2017; Patel et al., 2020). While it is traditionally accepted that rods mediate night vision due to their high sensitivity to light, the Sws2 photopigment may contribute to both night sensitivity and color vision; Indeed, the isomerization characteristics of Sws2 allows the Sws2 rods to work together with red rods for low-light vision, while also providing color discrimination between gray and blue (Kojima et al., 2017). A third class of cones, "miniature" cones, were also detected in adult frogs that constitute less than 4% of the total percentage of all cones. UV sensitivity was intimated for these miniature cones based on a similar morphology of the *Xenopus* cones with those in the retina of salamanders (Zhang et al., 1994). However, we did not detect miniature cones or UV-sensitive opsins in photoreceptors of young *Xenopus* larvae (Bertolesi et al., 2021). Instead, we find a few cones (less than 5%) that express pinopsin, a pigment sensitive to blue wavelength light. Pinopsin was initially discovered in the pineal gland (Okano et al., 1994) and is postulated to regulate melatonin production (Natesan et al., 2002) (see section "Structure of the Pineal Complex, Expression of Type II Opsins and Melatonin Secretion"). Interestingly, in *X. laevis* larvae, pinopsin is co-expressed in approximately 50% of the *sws1* positive cells, mainly in the dorsal retina (Bertolesi et al., 2021; **Figure 3A**). In adult *X. tropicalis, sws1* positive cells as well as a small fraction of *rh1* positive cells co-express pinopsin (Sato et al., 2018a). Of note, pinopsin is found in other vertebrates, including non-avian reptiles (Taniguchi et al., 2001) and avian-reptiles, but only in the pineal complex for the latter (Okano et al., 1994). Pinopsin was lost during evolution in mammals and teleosts (Davies et al., 2015). Together, these data show that *Xenopus laevis* tadpoles exhibit several different photoreceptors that express distinctive type II opsins, including *rh1* or *sws*2 (rods), *lws*1 or *sws*1 (cones) and *sws1-pino* (co-expressing cones) (**Figure 3A**).

Melanopsin, another blue-sensitive opsin encoded by two paralogous genes (*opn4* and *opn4b*), was originally found in *Xenopus*, with expression reported in the eye, pineal complex, and melanophores (Provencio et al., 1998; Koyanagi et al., 2005). In the *Xenopus* retina, *opn4* and *opn4b* are co-expressed in a subset of horizontal and retinal ganglion cells (Bertolesi et al., 2015, 2021; Bertolesi and McFarlane, 2018; **Figure 3A**). Melanopsin confers these cells with photosensitivity, a fact that led to their being named intrinsically photosensitive horizontal (ipHCs) and retinal ganglion (ipRGCs) cells. In *Xenopus*, the ipHCs are located in the dorsal retina and are 6-7 times more abundant than the ipRGCs in the central retina, which constitute only 2% of the total ganglion cells (Bertolesi et al., 2014, 2015; **Figure 3A**). The L and S copies of the two melanopsin genes remain in the *Xenopus* genome. Of note, *opn4* and *opn4b* paralogs arose originally from a gene duplication 600 mya, but *opn4b* was lost in mammals due to unknown pressures of selection (Bellingham et al., 2006). Thus, during mammalian evolution both the *opn4b* gene as well as the ipHCs were lost, while ipRGCs remained.

The role of the ipHCs is not fully understood, but horizontal cells (HCs) as a general class have been studied extensively in many animal models including *Xenopus*. Studies pointed to the existence of ipHCs prior to their actual discovery. For instance, in Anurans HCs are classified based on their response to light: "Luminosity" HCs and "Chromaticity" HCs (Gábriel and Wilhelm, 2001). Luminosity HCs, like mammalian HCs, hyperpolarize to stimuli of all wavelengths, and provide inhibitory feedback to photoreceptors (Hassin and Witkovsky, 1983; Gábriel and Wilhelm, 2001). The feedback mechanism aids in fine-tuning contrast and color vision. Therefore, luminosity HCs likely correspond to melanopsin-negative HCs. Conversely, Anuran "chromaticity" HCs differentially respond to a variety of wavelengths and exhibit depolarizing responses (Stone et al., 1990). Interestingly, electrophysiological recordings from isolated ipHCs from teleosts and birds also indicate a light-induced depolarization response (Cheng et al., 2009; Sun et al., 2014; Morera et al., 2016), suggesting that the "chromaticity" HCs correspond to ipHCs (**Figure 3A**). Interestingly, we find differences between HCs and ipHCs with respect to the expression of the immediate gene marker, *c-fos,* in that the classical HCs turn on *c-fos* expression in response to light, while the ipHCs do not (Bertolesi et al., 2014). Melanopsin expression in ipHCs should make them light sensitive and give them a photosensing role. Evolutionarily, this is the most plausible scenario considering *opn4b* positive ipHCs in chicken act as photoreceptors (Morera et al., 2016). Further study is required, however, to understand the differences and the functional role of HCs and ipHCs in *Xenopus.*

In mammals, the only melanopsin gene, *opn4*, is expressed in 2% of retinal ganglion cells found primarily located in the dorsal retina, where it plays key roles in both visual and non-visual responses. Entrainment of the circadian rhythm and sleep latency are examples of non-visual functions (Hannibal et al., 2002; Hattar et al., 2002; Lupi et al., 2008). Melanopsin also has a visual role in the recognition of background light intensity and image representation (Storchi et al., 2017; Allen et al., 2019). Thus, it is possible that with the evolutionary loss in mammals of both the ipHCs and a photosensitive pineal gland, the ipRGCs, together with additional retinal circuits, took control of important visual and non-visual physiological functions.

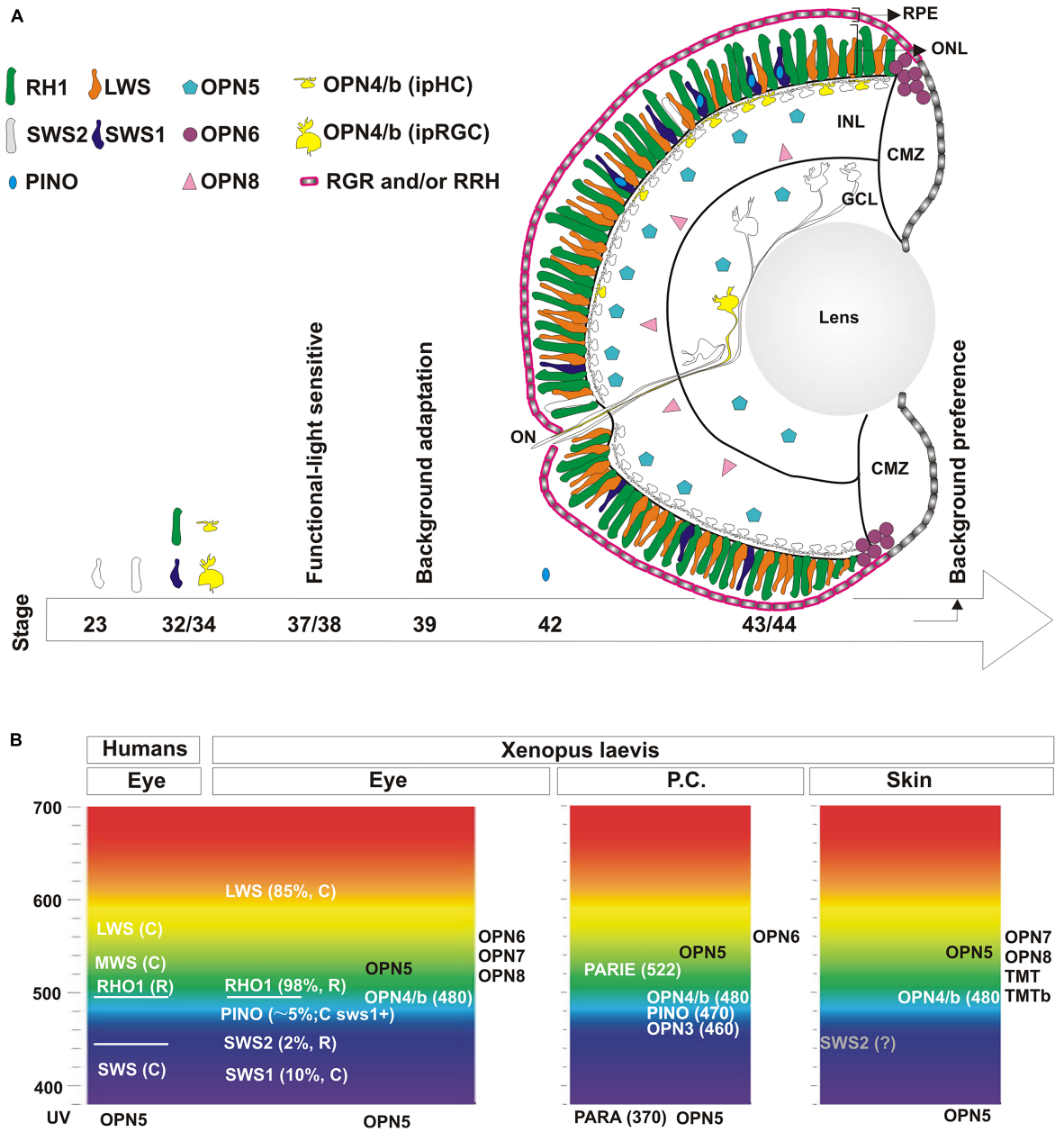

FIGURE 3 | Localization and developmental expression of opsins in the eye. **(A)** Schematic of the central retina showing the expression of opsins in photoreceptors in the outer nuclear layer (ONL) in rods (Rh1; green and Sws2; white) and cones (Lws; orange and Sws1, blue). Pinopsin (light blue) is always co-expressed dorsally with a few *sws1* positive cells. Melanopsin (yellow) is expressed both by intrinsically photosensitive horizontal cells (ipHC) located dorsally in the retina in the inner nuclear layer (INL), and a minor population of retinal ganglion cells in the ganglion cell layer (GCL) (RGCs; 2% of total), called the intrinsically photosensitive RGCs (ipRGC). *opn5* mRNA (magenta) is expressed by cells in the outer portion of the INL and in the GCL, while *opn8* mRNA (pink) is present in cells in the inner part of the INL, likely amacrine cells. *opn6* (purple) expressing cells sit at the boundary of the proliferative CMZ and the ONL. *rgr* and *rrh* mRNAs (pink) are expressed by the RPE but excluded from the CMZ. A developmental timeline is schematized with an arrow at the bottom, with the emergence of opsin expression or specific behavioral responses indicated. **(B)** Opsins expressed in the eye, the pineal complex, and the skin (tails or MEX cells) of *Xenopus laevis* are shown at the approximate absorbance peak of their spectral sensitivity, and compared to the spectral sensitivity of human visual opsins. See text for additional details.

Several neuropsins are expressed in the eye of *Xenopus*, although their physiological roles are not completely understood. Opn5, a UV sensitive photopigment, is the best studied, mainly because it is the only neuropsin found in mammals. In *Xenopus*, *opn5* is present in cells of the inner nuclear and ganglion cell layers (**Figure 3A**; Yamashita et al., 2014; Bertolesi et al., 2021), as well as deep in the brain (Currie et al., 2016). Assuming some evolutionary conservation in Opn5 function, its presence in the *Xenopus* retina likely involves non-visual roles. In support, mammalian OPN5 regulates the photoentrainment

of the retina (Buhr et al., 2015), with *Opn5* null mice showing impaired photoentrainment and phase shifting to UVA light (Ota et al., 2018). Of note, the deep brain diencephalic neurons that express *opn5* may participate in motor/behavioral responses. For instance, a role for Opn5 in light-dependent swimming, independent of the eye and the pineal complex, was suggested in *Xenopus*, although genetic support is lacking (Currie et al., 2016). In birds, hypothalamic *opn5* positive cells are thought to contribute to migration and seasonal reproduction (Nakane et al., 2014). The role of other retinal-expressed neuropsins, such as Opn6 and Opn8, is unknown. *opn8* is expressed by INL cells of the *Xenopus* retina, likely amacrine cells, while *opn5* mRNA may be present in bipolar cells (Bertolesi et al., 2021; **Figure 3A**). Finally, *opn6* is expressed by newly born photoreceptors in the ONL of the peripheral retina bordering the proliferative ciliary marginal zone (CMZ) (**Figure 3A**; Bertolesi et al., 2021).

Most of the opsins, including all of the photoreceptor opsins, bind 11-*cis* retinal in their resting state. 11-*cis* retinal is isomerized to all-trans retinal following light activation. Thus, a functional retina requires a continuous supply of new 11-*cis* retinal. The RPE functions as the supplier for the reconversion of all-*trans* to 11-*cis* retinal, which is mediated by two photoisomerases, RGR and RRH (Bellingham et al., 2003; Davies et al., 2015). In *Xenopus* larvae, both photoisomerases are expressed by the RPE outside of the CMZ (Bertolesi et al., 2021; **Figure 3A**) as befits their supplier role to photoreceptors. Yet, it is unclear if RGR and RRH are expressed by the same or different RPE cells. An interesting yet controversial issue is the source of 11-*cis* retinal for opsins present in cells located at a distance from the RPE. A possible explanation is provided by the biochemical characteristics of Opn5 of *Xenopus* and birds. In these species, the Opn5 protein binds 11-*cis*-retinal to produce a UV light-absorbing form, but also binds all-trans-retinal to produce a visible light-absorbing form that generates 11-*cis* retinal. Cycling between UV- and yellow light reconverts one form to the other repeatedly (Yamashita et al., 2014; Sato et al., 2018b). Further studies are necessary to determine if Opn5, 6, 7, and 8 may work as bidirectional forms of opsins, or function to provide 11-*cis* retinal to other opsins located away from the RPE.

The maximum absorption peaks of the *Xenopus* opsins as compared with human visual opsins is shown in **Figure 3B**. The rods include those that express either green-sensitive Rhodopsin (λ max $\sim$ 500–523 nm) (Dartnall, 1956; Batni et al., 1996) or blue-sensitive Sws2 (λ max $\sim$ 434 nm) (Darden et al., 2003). The most abundant cone, expressing Lws, is red sensitive (λ max $\sim$ 611 nm) (Witkovsky et al., 1981) and shows peak sensitivity at a longer wavelength than its human counterpart, while the Sws1 cone is blue-violet sensitive (λ max $\sim$ 425 nm) (Starace and Knox, 1998; **Figure 3B**). Pinopsin and melanopsins (Opn4 and Opn4b) have maximum absorbances at 470 nm and approximately 480 nm, respectively (Shirzad-Wasei and DeGrip, 2016; Sato et al., 2018a). It is important to note that the absorbance spectrum of opsins changes depending on the chromophore used (Vitamin A1 or A2). For example, *Xenopus* Rh1 shifts from 500 to 523 nm and Sws2 from 434 to 443 nm with the use of Vitamin A1 or A2, respectively (Dartnall, 1956; Witkovsky et al., 1981; Darden et al., 2003). The mammalian chromophore, Vitamin A1, is the form used primarily in experiments analyzing the physicochemical properties of type II opsins. In amphibians, however, the main chromophore is Vitamin A2, which shifts the spectrum to a longer absorbance. Indeed, adult *Xenopus* retina contains only 5–12% Vitamin A1 (Wald, 1955) and Vitamin A2 is almost exclusively detected in stage 43/44 retinas (Bridges et al., 1977).

The onset of retinal function, which requires the developmental expression of type II opsins, contributes to our understanding of the mechanism that regulates changes in skin pigmentation. Cones are both born and determined before the first rods appear (Chang and Harris, 1998). Interestingly, while both rods and red cones begins to emerge early in development (stage 23; 1.5 day at 16°C), the expression of the classical type II opsins initiates in most photoreceptors only a day later at stage 32, and becomes pronounced by stage 35/36 (**Figure 3A**). Melanopsin expression in both ipHCs and ipRGCs, like opsins in classical photoreceptors, initiates by stage 32 and is readily detectable at stage 33/34 (Bertolesi et al., 2014; **Figure 3A**). Our understanding of when opsin expression initiates is based on the more abundant rods and cones: Rh1- and Lws- expressing, respectively (Stiemke et al., 1994; Chang and Harris, 1998). Likely the timetable for generating photoreceptors expressing other opsins is similar, with the exception of pinopsin-expressing cones that emerge at stage 42/43 (Bertolesi et al., 2021). Photoreceptors first form synapses at stage 37/38 (Witkovsky, 2000), and this is when the retina becomes light sensitive. Using light-induced *c-fos* expression, we defined functional 'unit circuits' at stage 37/38 that consist of two to three *c-fos* positive INL cells and one RGC, which increase over time (Bertolesi et al., 2014). How do these results correspond with the emergence of the eye-dependent background adaptation response? The initial studies of background adaptation performed by Hogben and Slome (1936) suggest a differential activation of the retina, with the dorsal part capturing light reflected from the surface. Interestingly, pinopsin and melanopsin are both located in the dorsal retina (**Figure 3A**). The onset of pinopsin expression in the eye, however, occurs a day after background adaptation is detected (stage 39/40) (day 4 in **Figures 1A**, **3A**; Bertolesi et al., 2021). Thus, pinopsin is eliminated from a list of potential light sensors for background adaptation. Instead, melanopsin (ipHCs or ipRGC) may be involved; Indeed, melanopsin mRNA appears prior to the phenotypic response (Bertolesi et al., 2014), and pharmacological inhibition of melanopsin (AA92593) in the eye induces the synthesis and release of α-MSH and consequent skin darkening (Bertolesi et al., 2015, 2016b). Together, the data support a model where the dorsally located melanopsin-expressing cells are the photosensors for background adaptation. The circuit that links light sensitivity in the eye to the release of α-MSH from the pars intermedia pituitary involves an intermediary, the suprachiasmatic melanotrope inhibitory neuron (SMIN) (Ubink et al., 1998). The model proposes that with a white background the dorsal retina receives more light than the ventral retina, because of the reflected light from the surface. Activation of the ipHCs and/or ipRGCs, and subsequently the intermediary SMIN neurons, blocks the synthesis and release of α-MSH from melanotropes located in the hypophysis. Conversely, with a black background

the ipHCs/ipRGCs are inactive, releasing the inhibition on α-MSH secretion and inducing melanosome dispersion and skin darkening (Bertolesi and McFarlane, 2018). An open question is if ipHCs and/or ipRGCs have similar or different roles in the background adaptation process. Both cell types are preferentially located in the dorsal retina. The ipHCs are seven time more abundant than ipRGCs (Bertolesi et al., 2014), however, and in birds ipHCs act as photoreceptors (Morera et al., 2016). Nonetheless, more studies are necessary to identify the melanopsin expressing cell that serves as photoreceptor during background adaptation.

The delayed developmental expression of pinopsin relative to visual opsins suggests a role in a behavioral response associated with background recognition. Indeed, older tadpoles (stage 45/46) are able to discriminate different colors and intensities of light, including those generated by different substrates (Rothman et al., 2016; Hunt et al., 2020). Interestingly, young tadpoles adapted to a white background prefer this surface, while froglets choose a black background irrespective of their previous adaptation (Moriya et al., 1996a; Bertolesi et al., 2021). Changes in pinopsin retinal expression during development correlates with this behavioral response (Bertolesi et al., 2021). Together, these data suggest that opsins like melanopsin (Opn4 and Opn4b) and pinopsin that are linked classically to non-visual roles in mammals (sleep and circadian rhythm) and birds (melatonin secretion) also function in background recognition in young tadpoles *via* the eye.

Structure of the Pineal Complex, Expression of Type II Opsins and Melatonin Secretion

In *Xenopus,* type II opsins expressed in the pineal complex sense light that regulates melatonin secretion, and therefore, a non-visual response in skin pigmentation. The first evidence for this pathway was that 'pineal gland' extracts caused lightening in amphibian tadpoles (McCord and Allen, 1917). This pigmentation response was then used as a biological readout during melatonin purification from the mammalian pineal gland (Lerner et al., 1958). Structurally, the pineal gland is integrated in the brains of mammals. In amphibians, the gland is referred to as the pineal complex as it consists of two components: (1) the pineal gland, which is the neuroendocrine-secretory organ, and (2) the frontal organ, an accessory photosensitive structure (Charlton, 1968; Korf et al., 1981; Sapède and Cau, 2013). Of note, the frontal organ is present in many non-mammalian vertebrates, although it is given different names, such as the parapineal organ in teleosts and lamprey, and parietal eye in non-avian reptiles (Sapède and Cau, 2013). The pineal complex displays a simpler structure than the retina, containing only two neuronal types, photoreceptors and projection neurons. These two cells are generated from the same pool of floating head precursors and represent the functional homologs of retinal photoreceptors and retinal ganglion cells, respectively (Arendt, 2003; Sapède and Cau, 2013). In adult frogs, the pineal gland is located intracranially, at the top of the brain, while the frontal organ sits extracranially in close proximity (Charlton, 1968; Korf et al., 1981; Sapède and Cau, 2013). Anatomically, the pineal complex can be visualized in stage 42 *Xenopus* larvae, with the photosensitive frontal organ located under the skin and the pineal gland sitting immediately beside it in a dorsal position between the habenular and posterior commissures (Bertolesi et al., 2020). *in situ* hybridization and immunohistochemistry analyses reveal that the pineal complex is functional in *Xenopus* larvae by stage 43, with both the frontal and pineal organ displaying phenotypic characteristics of sensory and secretory tissues (Bertolesi et al., 2020). It is worth noting that at stage 43/44 the two structures are not completely separated. Additionally, the intra- and extra-cranial tissues are not yet evident, since the formation of bony-skull structure initiates at stage 52 (Slater et al., 2009).

The pineal complex primarily regulates sleep and wake cycles by transducing light and dark information and subsequently melatonin secretion. Light establishes the pattern by which melatonin is secreted by the pineal gland, with melatonin at low levels during the day and peaking at night (Coomans et al., 2015). The release of melatonin also influences both thermoregulation and the control of daily and seasonal rhythmic processes (Filadelfi and Castrucci, 1996; Simonneaux and Ribelayga, 2003; Nisembaum et al., 2015). Interestingly, recent studies show that type II opsins detect not only light, but thermal energy can act *via* the opsins to induce cellular activity (reviewed by Moraes et al., 2021). The thermal contribution of type II opsins to melatonin secretion, and thus skin pigmentation, has not yet been investigated and is not addressed in this review.

In vertebrates, melatonin synthesis occurs in four enzymatic steps, with the third one critical for light-regulated rhythmicity (Falcón et al., 2009). The third step is the conversion of serotonin to *N*-acetylserotonin by aryl alkylamine *N*-acetyltransferase (AANAT), and then a final *O*-methylation of *N*-acetylserotonin by hydroxyindole-*O*-methyltransferase to produce melatonin (Falcón et al., 2009). Interestingly, AANAT plays a significant role both in the synthesis of melatonin and in driving the rhythmic activity of melatonin release from both the pineal gland and the eye (Klein, 2006). Indeed, this key enzyme itself is regulated at the transcriptional and post-translational levels in a circadian manner, as levels are low during the day with activity peaking at night (Klein, 2006). In frogs, Aanat is expressed in retinal photoreceptors as well as in the pineal epithelium where pineal photoreceptors reside. Aanat labeling is concentrated in the inner segment in contact with the cerebrospinal fluid in the pineal lumen (Isorna et al., 2006), suggesting that the pineal photoreceptors possess both secretory and photoreceptor functions. In concordance with Aanat being present in both the *Xenopus* eye and pineal complex, melatonin is synthesized in both structures (Wiechmann and Sherry, 2012). Retinal melatonin may exert physiologically insignificant effects on pigmentation, however, given its rapid degradation (Green et al., 1999). Indeed, retinal melatonin behaves as a local neuromodulator, while pinealectomy results in a significant decrease in or complete abolition of plasma melatonin (Cahill and Besharse, 1989). In agreement, pinealectomy, but not enucleation, affects pigment aggregation induced by dark (**Figure 1B**).

Developmentally, *Xenopus* embryos express the enzymes necessary for melatonin biosynthesis, and 'pineal' *in vitro*

explants show melatonin production as early as stage 26 (approximately 30 h post-fertilization), despite the pineal complex itself evaginating from the diencephalon on the second day of embryogenesis (Green et al., 1999). Interestingly, differentiation of neurons in the habenular nuclei, a paired structure anterior to the pineal organ, is upregulated by light exposure and reduced by melatonin treatment in early development (36 h post fertilization) of zebrafish (de Borsetti et al., 2011). At an equivalent developmental time in *Xenopus*, Bsx, a transcription factor that controls pineal progenitor proliferation and the photoreceptor fate, is also expressed with light rhythmicity (D'Autilia et al., 2010). This raises the question as to what photosensor/s senses the light that induces both the expression of Bsx and the melatonin-synthesizing Aanat enzyme? Additionally, when does expression of the photosensor initiate? In contrast to what is known of roles for type II opsins in the *Xenopus* retina, our understanding of pineal opsins is limited. mRNAs of type II opsins such as *opnp, opnpp*, *opnpt*, *opn3*, *opn4*, *opn4b*, *opn5*, *opn6b,* and *rgr* (**Figure 2**) are detected in the *Xenopus* pineal complex at stage 43/44 (Bertolesi et al., 2020). Data from our laboratory suggests that the pineal complex becomes fully functional to induce skin lightening at stage 39 (**Figure 1A**). Cells of the pineal complex in stage 43/44 *Xenopus* larvae exhibit sensitivity to environmental light conditions, with lightening of the skin occurring 30 min after a piece of tin foil is placed atop the pineal to prevent light from reaching the complex (Bertolesi et al., 2020). It is possible that while melatonin-synthesizing cells can produce melatonin at early developmental times, as suggested by the *in vitro* studies in *Xenopus* (Green et al., 1999), and zebrafish (de Borsetti et al., 2011), it is not until later that the cells produce sufficient melatonin to affect skin pigmentation. The opsin sensor expressed at early stages is currently unknown and further studies are necessary to determine the onset of pineal opsin expression.

A comparative analysis of opsins expressed by the *Xenopus* pineal complex with other species, as well as their wavelength sensitivity, has proven helpful for understanding the evolutionary functionalization of opsins and their possible role in regulating melatonin secretion, and therefore skin pigmentation. The nerves of the frontal organ in adult *X. laevis* show light sensitivity with both achromatic and chromatic responses. Two separate mechanisms underlie the chromatic response: The inhibitory response is maximally sensitive at approximately 360 nm (UV) while the excitatory response peaks at 520 nm. In comparison, the action spectrum of the achromatic response of the pineal and frontal organs peaks between 500 and 520 nm (Korf et al., 1981). A plethora of opsins are expressed in the stage 43/44 pineal complex (**Figure 2**). Of these, parapinopsin (Opnpp) and Opn5 likely function as absorbers of UV light in *Xenopus* and other vertebrates (Wada et al., 2012; Yamashita et al., 2014), and therefore could drive the inhibitory response at 360 nm. However, none of the UV-sensitive opsins are likely involved in the lightening of skin pigmentation, in that such a response in *Xenopus* is inhibited by visible-light (maximum inhibition between 470 and 650 nm) (Bertolesi et al., 2020). In teleosts, melatonin release from a perfused pineal is inhibited maximally at 520 nm but is not impacted by UV light (Ziv et al., 2007). Only one parapinopsin gene exists in *Xenopus* with the second lost likely by pseudogenization. In the teleost lineage, however, the parapinospin gene was duplicated during the teleost specific genome duplication. The spectral sensitivity and expression pattern of the paralogs differ, with one remaining as UV-sensitive (PP1) while the other became a blue-light sensitive opsin (PP2) (Koyanagi et al., 2015), reflecting the functionalization of parapinopsins during teleost evolution. Additionally, parietopsin (Opnpt) has a maximum absorbance (522 nm) corresponding to the peak of the achromatic excitatory signal in frogs (Su et al., 2006). Interestingly, the parapinopsin and the parietopsin genes disappeared in avian reptiles and turtles concomitant with the loss of the parietal eye in these lineages (Emerling, 2017), reinforcing the idea of a role for these opsins exclusively as frontal organ sensors. As in *Xenopus*, contraposed achromatic responses are described for the pineal complex of lamprey and teleosts, with an inhibitory response mediated by UV-light and an excitatory one by visible light (520 to 560 nm), and assigned to parapinopsin and parietopsin sensitivity, respectively (Koyanagi et al., 2015, 2017; Wada et al., 2021). Within the pineal complex, the encephalopsin (Opn3) as well as the melanopsins (Opn4 and Opn4b) function as blue light-sensitive opsins, while Opn4 acts as a light sensor in the mammalian eye that regulates melatonin secretion and circadian rhythm entrainment (Prayag et al., 2019). The role of the neuropsin Opn6b remains poorly understood, while the retinal G-protein coupled receptor Rgr functions as a photoisomerase in the pineal complex, binding trans-retinal for chromophore conversion. Taken together, several opsins sensitive in the visual range of the light spectrum may serve as the photosensors that mediate skin lightening by the pineal complex. However, a complete understanding of their roles in skin pigmentation still remains to be determined.

Type II Opsins in the Skin. From the Ectothermic *Xenopus* to Endothermic Mammals

In addition to the eye and the pineal complex, the skin/integument of animals is an essential light sensor as it is exposed directly to environmental light. While the role that photosensation plays in different skin cells is not well understood, in general, UV protection and circadian regulation are considered the two most important functions (Slominski et al., 2004; Sapède and Cau, 2013; Bertolesi and McFarlane, 2018). A better understanding of how type II opsins regulate melanosome movements in *Xenopus laevis* melanophores will contribute to our knowledge of how the only pigment producing cells of human skin, the melanocytes, respond directly to sunlight, in that melanocytes derive evolutionarily from melanophores of the amphibian ancestors (Ligon and Mccartney, 2016; Schartl et al., 2016; McNamara et al., 2021). Evolutionary, human skin has conserved a cell-autonomous mechanism to regulate the expression of circadian clock genes (Hardman et al., 2015). Melanocytes secrete melanin-containing vesicles to neighboring cells, keratinocytes, which retain the melanin. The secretory phenotype of the melanocytes likely emerged when fur and feathers evolved as insulation systems

for thermoregulation. Two important observations support this idea: (1) The number and diversity of melanosomes detected in well-preserved fossils of avian reptiles and mammalian lineages increase in correlation with the emergence of thermoregulation (Lindgren et al., 2015; Lovegrove, 2017). These phenotypic differences remain in existent melanophores and melanocytes of amphibians and mammals, respectively; and (2) Pheomelanin, a derivative of melanin, is synthesized in melanocytes of birds and mammals, but not fish (Kottler et al., 2015; McNamara et al., 2021). Interestingly, pheomelanin is also detected in amphibian fossils (Colleary et al., 2015). Of note, similar to other ectotherms, *Xenopus laevis* has additional types of chromatophores, including iridophores that reflect light and give the skin a shiny appearance, and xanthophores, which appear yellow or orange due to the presence of pteridines (Nakajima et al., 2021). However, these cell types appear later in development than melanophores (Droin, 1992).

Opsin proteins expressed by skin cell melanophores relay environmental light information to the cell. With the physiological regulation of skin color change in *Xenopus* tadpoles (discussed above), the primary response mediated by direct action of light is not as important as the secondary response mediated by the neuroendocrine system. However, direct responses to light and dark through melanosome aggregation and dispersion are present in some amphibian species, including *X. laevis* (Moriya et al., 1996b; Oshima, 2001). Interestingly, while three different melanophore cell lines established from *Xenopus laevis* show a common dispersing and aggregating response to α-MSH and melatonin (secondary response), respectively, they exhibit distinct responses to direct light. Two cell lines were established by isolating melanophores from stage 30 to 35 *Xenopus* tadpoles. These cell lines, named MEL (Daniolos et al., 1990) and MEX (Kashina et al., 2004), aggregate melanosomes in the dark and disperse them with light. In MEL cells, light induces melanosome dispersion at 460 nm in the presence of all-trans retinal (Daniolos et al., 1990; Rollag, 1996), suggesting an opsin-mediated response. At least two opsins, Opn4 and Opn4b, are present in MEL cells (Moraes et al., 2015), while several opsin genes are expressed in MEX cells, including the melanopsins (**Figure 2**). Interestingly, Opn4 and Opn4b show a distinct subcellular localization, with Opn4b found in the cell membrane and cytoplasm, and Opn4 in the nucleus (Moraes et al., 2015). While we know by RT-PCR analysis which opsin genes are expressed in the skin (**Figure 2**), we do not know in which cell types the genes are transcribed and whether protein is present. The MEX cells allow us to directly assess expression of opsins by melanophores: RT-PCR analysis indicates mRNA for *sws2, tmtops, tmtopsb, opn5*, *opn7a/b, opn8*, *opn4, and opn4b*. Given the diversity of opsin expression in melanophores, assigning a function to melanopsin or any other opsin as a physiological sensor during the light-induced dispersion of melanosomes in MEL and MEX is not yet possible. The third melanophore cell line was generated from isolated tail fins of *Xenopus* tadpoles between stages 51–54 (Seldenrijk et al., 1979). These cells also show melanosome dispersion in response to α-MSH. In contrast to MEL and MEX cell lines, however, these tail fin melanophores aggregate their melanosomes in light and disperse then in the dark, with approximately half of the melanophores in the dish exhibiting light sensitivity (Seldenrijk et al., 1979). This light-mediated aggregation response concurs with that observed in isolated tail fins from *Xenopus* larvae at the same developmental stage (Moriya et al., 1996b). Similarly, melanosome aggregation mediated by light is observed during tail regeneration in stage 49 and older tadpoles (Bagnara, 1960b). The differences in the primary response to light of these cultured melanophores obtained at different developmental stages may be due to the differential expression of opsins in melanophores. Of note, our RT-PCR analysis of opsins from MEX cells (stage 30–35) and isolated tails from stage 43/44 indicate differences (**Figure 2**), suggesting that dynamic opsin expression occurs over development. Why there are changes in the primary light response as the tadpoles age, and which opsins are expressed by the melanophores of pre-metamorphic tadpoles, still needs answering.

Initial studies performed in isolated fin tails or cultured melanophores from *Xenopus laevis* allowed authors to suggest a possible role of the visual opsins, particularly rhodopsin, in pigment cells (Daniolos et al., 1990; Miyashita et al., 1996; Moriya et al., 1996a). These studies identified rhodopsin by immunolabeling and by spectral analysis of the melanophore response to light. The extent of the diversity of opsins, however, was not known at that time, and brings into question the specificity of the antibodies that were used to recognize the visual rhodopsin. Indeed, our analysis of opsin gene expression by RT-PCR in tails isolated from stage 43/44 *Xenopus* shows no expression of the classical visual opsins (**Figures 2A,B**). In agreement, in MEX cells only *sws2* is consistently detectable (**Figures 2A,B**). Melanopsin *opn4* and *opn4b*, and the *opn5* neuropsin are thought to be critical for circadian regulation and UV protection in mammalian melanocytes. For example, OPN5 induces clock gene expression and circadian photoentrainment in mouse melanocytes (Buhr et al., 2019), and participates in UV-mediated melanogenesis in human melanocytes *in vitro* (Lan et al., 2021). OPN4 also participates in melanogenesis of mammalian melanocytes, as well as controlling melanocyte proliferation (de Assis et al., 2018, 2020). The presence of Opn4 protein (Provencio et al., 1998) and *opn5* mRNA in tail skin and melanophores (**Figures 2A,B**) indicates that these proteins may play comparable roles in *Xenopus*. *Opn7a/b* and *opn8* do not exist in avian reptiles and mammals, but are expressed in the *Xenopus* tadpole tail and MEX cells (**Figure 2**), though with unknown function. There are no reports of pineal opsins regulating mammalian melanocytes. Thus, it was not surprising that, with the exception of low expression of VA-opsin in the tail, we did not detect pineal opsin expression in the tail or MEX cells (**Figure 2**). *Opn3* is absent from *Xenopus* tails and MEX cells at early developmental times (**Figure 2**), but expression may occur later during development, as OPN3 regulates pigmentation of mammalian melanocytes (Ozdeslik et al., 2019; Olinski et al., 2020) Alternatively, through evolution the expression of *opn3* may have been lost in *Xenopus* melanophores. Finally, a family of opsins, whose ubiquitous expression in zebrafish gave them the name of *teleost multiple tissue opsins* (tmtops), regulate the entrainment

of the peripheral circadian clock (Moutsaki et al., 2003). Of the three *tmt* opsins found in the *Xenopus* genome (*tmtops*, *tmtops2,* and *tmtopsb*), two of them, *tmtops* and *tmtopnb*, are expressed in the tail and in MEX cells (**Figure 2**). Interestingly, genes of the *tmt* family remain in almost all vertebrate genomes, including avian reptiles and mammals (monotremes and marsupials). *tmt* genes did disappear recently in the eutherians (Davies et al., 2015), suggesting that the evolutionary selection of *tmt genes* was unaffected by thermoregulation and the melanophore/melanocyte transition. Together, these data show that many but not all of the opsins present in *Xenopus* melanophores remain in mammalian melanocytes with an assigned role either in the cell autonomous peripheral entrainment of the skin cell cycle or as a UV/light regulator of melanogenesis.

CONCLUSION

In *Xenopus laevis* tadpoles, light sensed by the eye, the pineal complex and the skin produces specific physiological responses that include changes in skin pigmentation. For example, the color of the background surface is sensed by the eye to produce changes in skin pigmentation to prevent the tadpoles from being detected by predators. This cryptic response, named background adaptation, increases survival. In contrast, detection of environmental day light by the pineal complex is used to alter skin pigmentation levels to adjust for thermoregulation or UV protection. The photosensors for these physiological responses are type II opsins, with their roles just beginning to be elucidated. A large number of diverse type II opsins exist in vertebrates, which are expressed in different organs. In *X. laevis* we identified 22 separate opsin genes, after removal of the duplicated forms characteristic of the allotetraploid nature of this species. In the last few years, we analyzed the expression of these type II opsins. These expression data we combined with skin pigmentation assays to establish for distinct pigmentation responses the participating light-sensitive organ and type II opsin(s) that works as the light sensor.

In the Anuran eye, the classical visual opsins are expressed by two rods (*rh1* and *sws2*) and two cones (*lws* and *sws1).* Additionally, *pinopsin* is co-expressed with *sws1* in a few dorsally located cone photoreceptors. The melanopsin genes (*opn4* and *opn4b*) are also expressed dorsally in ipHCs. These ipHCs likely act as "photoreceptors" to regulate background adaptation, with pharmacological inhibition of melanopsin increasing α-MSH release from the pars intermedia pituitary to darken the skin. In contrast, we propose that pinopsin transduces the surface color to initiate a behavioral response where the organism chooses a specific background surface (background preference). A role for ipHCs as "photoreceptors," and the expression of more than one opsin in eye classical photoreceptors (e.a. *pino* + *sws1*+) (Morera et al., 2016; Sato et al., 2018a; Bertolesi et al., 2021), are novel discoveries that likely will push *Xenopus laevis* forward on a new retinal research journey. Additional opsins, such as the neuropsins, *opn5*, *6,* and *8*, are expressed in the eye, although their function is not known.

Xenopus tadpoles lighten the skin in the dark because at night the pineal complex increases its secretion of melatonin into the circulation. Skin lightening and melatonin release are inhibited maximally by 520 nm visible light, which alongside the expression data, points to the involvement of candidate opsins. Several opsins expressed in the pineal complex absorb light at this wavelength, including Opn4, Opn4b, Opn3, Pinopsin (*opnp*) and Parietopsin (*opnpt*). Interestingly, *parapinopsin* (*opnpp*) and *parietopsin* are expressed in the frontal organ, and their UV and blue/green light sensitivities, respectively, correlate with the inhibitory and stimulatory electrophysiological recordings detected in the nerve of the adult frontal organs (Korf et al., 1981). During evolution, *parapinopsin* and *parietopsin* genes disappeared in avian reptiles and turtles concomitant with the loss of the parietal eye in these lineages (Emerling, 2017). The use of CRISPR/Cas9 technology to knock out different opsins in F0 generation *Xenopus* (Blitz and Nakayama, 2021), in combination with pigmentation assays, will help provide an answer to the question as to whether one or more pineal complex-expressed opsins regulate melatonin secretion.

Finally, we analyzed the mRNA expression of *Xenopus* opsins in the tail and in a melanophore cell line (MEX cells) and compared the expression with what we currently know of their role in mammalian melanocytes. Several opsins, such as Opn4 and Opn5, have been evolutionarily selected as a sensor for either the cell autonomous entrainment of the melanocyte cell cycle or for UV/light regulation of melanogenesis. These genes are conserved between melanophores and melanocytes.

Studying the regulation of skin pigmentation in *Xenopus laevis* has proven extremely insightful for our understanding of photosensory organs (eye, pineal complex, and skin) and their evolution. The recent full sequencing of the *Xenopus laevis* genome, the discovery of several type II opsin photopigments, and novel technologies have established this model organism for new fields of investigation.

AUTHOR CONTRIBUTIONS

GB and ND performed the RT-PCR study from tails and MEX cells. GB, ND, HM, LM, and SM wrote the manuscript and critically revised the manuscript. All authors contributed to the article and approved the submitted version.

FUNDING

This work was supported by a Discovery grant from the Natural Sciences and Engineering Research Council of Canada (NSERC) to SM, NSERC Undergraduate Research Awards (LM, ND), and NSERC Canada Graduate Scholarship-Master's (HM).

ACKNOWLEDGMENTS

The MEX cell line was kindly provided by Dr. Vladimir Rodionov. We thank Carrie Hehr for excellent technical assistance.

REFERENCES

Allen, A. E., Martial, F. P., and Lucas, R. J. (2019). Form vision from melanopsin in humans. *Nat. Commun.* 10:2274. doi: 10.1038/s41467-019-10113-3

Arendt, D. (2003). Evolution of eyes and photoreceptor cell types. *Int. J. Dev. Biol.* 47, 563–571.

Bagnara, J. T. (1960a). Pineal regulation of the body lightening reaction in amphibian larvae. *Science* 132, 1481–1483.

Bagnara, J. T. (1960b). Tail melanophores of *Xenopus* in normal development and regeneration. *Biol. Bull.* 118, 1–8. doi: 10.2307/1539050

Batni, S., Scalzetti, L., Moody, S. A., and Knox, B. E. (1996). Characterization of the *Xenopus rhodopsin* gene. *J. Biol. Chem.* 271, 3179–3186. doi: 10.1074/jbc.271.6.3179

Bellingham, J., Chaurasia, S. S., Melyan, Z., Liu, C., Cameron, M. A., Tarttelin, E. E., et al. (2006). Evolution of melanopsin photoreceptors: discovery and characterization of a new melanopsin in nonmammalian vertebrates. *PLoS Biol.* 4:e254. doi: 10.1371/journal.pbio.0040254

Bellingham, J., Wells, D. J., and Foster, R. G. (2003). *In silico* characterisation and chromosomal localisation of human RRH (peropsin)–implications for opsin evolution. *BMC Genomics* 4:3. doi: 10.1186/1471-2164-4-3

Bertolesi, G. E., Atkinson-Leadbeater, K., Mackey, E. M., Song, Y. N., Heyne, B., and McFarlane, S. (2020). The regulation of skin pigmentation in response to environmental light by pineal type II opsins and skin melanophore melatonin receptors. *J. Photochem. Photobiol. B Biol.* 212, 112024. doi: 10.1016/j.jphotobiol.2020.112024

Bertolesi, G. E., Debnath, N., Atkinson-Leadbeater, K., Niedzwiecka, A., and McFarlane, S. (2021). Distinct type II opsins in the eye decode light properties for background adaptation and behavioural background preference. *Mol. Ecol.* 30, 6659–6676. doi: 10.1111/MEC.16203

Bertolesi, G. E., Hehr, C. L., and McFarlane, S. (2014). Wiring the retinal circuits activated by light during early development. *Neural Dev.* 9:3. doi: 10.1186/1749-8104-9-3

Bertolesi, G. E., Hehr, C. L., and McFarlane, S. (2015). Melanopsin photoreception in the eye regulates light-induced skin colour changes through the production of α-MSH in the pituitary gland. *Pigment Cell Melanoma Res.* 28, 559–571. doi: 10.1111/pcmr.12387

Bertolesi, G. E., Hehr, C. L., Munn, H., and McFarlane, S. (2016a). Two light-activated neuroendocrine circuits arising in the eye trigger physiological and morphological pigmentation. *Pigment Cell Melanoma Res.* 29, 688–701. doi: 10.1111/pcmr.12531

Bertolesi, G. E., Vazhappilly, S. T., Hehr, C. L., and Mcfarlane, S. (2016b). Pharmacological induction of skin pigmentation unveils the neuroendocrine circuit regulated by light. *Pigment Cell Melanoma Res.* 29, 186–198. doi: 10.1111/pcmr.12442

Bertolesi, G. E., and McFarlane, S. (2018). Seeing the light to change colour: an evolutionary perspective on the role of melanopsin in neuroendocrine circuits regulating light-mediated skin pigmentation. *Pigment Cell Melanoma Res.* 31, 354–373. doi: 10.1111/pcmr.12678

Bertolesi, G. E., and McFarlane, S. (2020). Melanin-concentrating hormone like and somatolactin. A teleost-specific hypothalamic-hypophyseal axis system linking physiological and morphological pigmentation. *Pigment Cell Melanoma Res.* 34, 564–574. doi: 10.1111/pcmr.12924

Bertolesi, G. E., Song, Y. N., Atkinson-Leadbeater, K., Yang, J.-L. J., and McFarlane, S. (2017). Interaction and developmental activation of two neuroendocrine systems that regulate light-mediated skin pigmentation. *Pigment Cell Melanoma Res.* 30, 413–423. doi: 10.1111/pcmr.12589

Bertolesi, G. E., Zhang, J. Z., and McFarlane, S. (2019). Plasticity for colour adaptation in vertebrates explained by the evolution of the genes pomc, pmch and pmchl. *Pigment Cell Melanoma Res.* 32, 510–527. doi: 10.1111/pcmr.12776

Blitz, I., and Nakayama, T. (2021). CRISPR-Cas9 mutagenesis in *Xenopus tropicalis* for phenotypic analyses in the F_0 generation and beyond. *Cold Spring Harb. Protoc.* doi: 10.1101/PDB.PROT106971 [Epub ahead of print].

Bridges, C., Hollyfield, J., Witkovsky, P., and Gallin, E. (1977). The visual pigment and vitamin A of *Xenopus laevis* embryos, larvae and adults. *Exp. Eye Res.* 24, 7–13. doi: 10.1016/0014-4835(77)90279-2

Buhr, E., Vemaraju, S., Diaz, N., Lang, R., and Van Gelder, R. (2019). Neuropsin (OPN5) mediates local light-dependent induction of circadian clock genes and circadian photoentrainment in exposed murine skin. *Curr. Biol.* 29, 3478–3487.e4. doi: 10.1016/J.CUB.2019.08.063

Buhr, E. D., Yue, W. W. S., Ren, X., Jiang, Z., Liao, H.-W. R., Mei, X., et al. (2015). Neuropsin (OPN5)-mediated photoentrainment of local circadian oscillators in mammalian retina and cornea. *Proc. Natl. Acad. Sci. U.S.A.* 112, 13093–13098. doi: 10.1073/pnas.1516259112

Cahill, G., and Besharse, J. (1989). Retinal melatonin is metabolized within the eye of *Xenopus laevis*. *Proc. Natl. Acad. Sci. U.S.A.* 86, 1098–1102. doi: 10.1073/PNAS.86.3.1098

Chang, W. S., and Harris, W. A. (1998). Sequential genesis and determination of cone and rod photoreceptors in *Xenopus*. *J. Neurobiol.* 35, 227–244. doi: 10.1002/(SICI)1097-4695(19980605)35:3<227::AID-NEU1<3.0.CO;2-0

Charlton, H. M. (1968). The pineal gland of *Xenopus laevis*, Daudin: a histological, histochemical, and electron microscopic study. *Gen. Comp. Endocrinol.* 11, 465–480. doi: 10.1016/0016-6480(68)90062-2

Cheng, N., Tsunenari, T., and Yau, K.-W. (2009). Intrinsic light response of retinal horizontal cells of teleosts. *Nature* 460, 899–903. doi: 10.1038/nature08175

Colleary, C., Dolocan, A., Gardner, J., Singh, S., Wuttke, M., Rabenstein, R., et al. (2015). Chemical, experimental, and morphological evidence for diagenetically altered melanin in exceptionally preserved fossils. *Proc. Natl. Acad. Sci. U.S.A.* 112, 12592–12597. doi: 10.1073/pnas.1509831112

Coomans, C. P., Ramkisoensing, A., and Meijer, J. H. (2015). The suprachiasmatic nuclei as a seasonal clock. *Front. Neuroendocrinol.* 37, 29–42. doi: 10.1016/j.yfrne.2014.11.002

Currie, S. P., Doherty, G. H., and Sillar, K. T. (2016). Deep-brain photoreception links luminance detection to motor output in *Xenopus* frog tadpoles. *Proc. Natl. Acad. Sci. U.S.A.* 113, 6053–6058. doi: 10.1073/pnas.1515516113

Daniolos, A., Lerner, A. B., and Lerner, M. R. (1990). Action of light on frog pigment cells in culture. *Pigment Cell Res.* 3, 38–43. doi: 10.1111/j.1600-0749.1990.tb00260.x

Darden, A. G., Wu, B. X., Znoiko, S. L., Hazard, E. S., Kono, M., Crouch, R. K., et al. (2003). A novel *Xenopus* SWS2, P434 visual pigment: structure, cellular location, and spectral analyses. *Mol. Vis.* 9, 191–199.

Dartnall, H. (1956). Further observations on the visual pigments of the clawed toad, *Xenopus laevis*. *J. Physiol.* 134, 327–338. doi: 10.1113/JPHYSIOL.1956.SP005646

D'Autilia, S., Broccoli, V., Barsacchi, G., and Andreazzoli, M. (2010). *Xenopus* Bsx links daily cell cycle rhythms and pineal photoreceptor fate. *Proc. Natl. Acad. Sci. U.S.A.* 107, 6352–6357. doi: 10.1073/pnas.1000854107

Davies, W. I. L., Tamai, T. K., Zheng, L., Fu, J. K., Rihel, J., Foster, R. G., et al. (2015). An extended family of novel vertebrate photopigments is widely expressed and displays a diversity of function. *Genome Res.* 25, 1666–1679. doi: 10.1101/gr.189886.115

Dawid, I., and Sargent, T. (1988). *Xenopus laevis* in developmental and molecular biology. *Science* 240, 1443–1448. doi: 10.1126/SCIENCE.3287620

de Assis, L., Mendes, D., Silva, M., Kinker, G., Pereira-Lima, I., Moraes, M., et al. (2020). Melanopsin mediates UVA-dependent modulation of proliferation, pigmentation, apoptosis, and molecular clock in normal and malignant melanocytes. *Biochim. Biophys. Acta Mol. Cell Res.* 1867:118789. doi: 10.1016/J.BBAMCR.2020.118789

de Assis, L., Moraes, M., Magalhães-Marques, K., and Castrucci, A. (2018). Melanopsin and rhodopsin mediate UVA-induced immediate pigment darkening: unravelling the photosensitive system of the skin. *Eur. J. Cell Biol.* 97, 150–162. doi: 10.1016/J.EJCB.2018.01.004

de Borsetti, N. H., Dean, B. J., Bain, E. J., Clanton, J. A., Taylor, R. W., and Gamse, J. T. (2011). Light and melatonin schedule neuronal differentiation in the habenular nuclei. *Dev. Biol.* 358, 251–261. doi: 10.1016/J.YDBIO.2011.07.038

Dickson, B., Clack, J., Smithson, T., and Pierce, S. (2021). Functional adaptive landscapes predict terrestrial capacity at the origin of limbs. *Nature* 589, 242–245. doi: 10.1038/S41586-020-2974-5

Diniz, G. B., and Bittencourt, J. C. (2019). The melanin-concentrating hormone (MCH) system: a tale of two peptides. *Front. Neurosci.* 13:1280. doi: 10.3389/fnins.2019.01280

Droin, A. (1992). Genetic and experimental studies on a new pigment mutant in *Xenopus laevis*. *J. Exp. Zool.* 264, 196–205. doi: 10.1002/JEZ.1402640212

Emerling, C. A. (2017). Archelosaurian color vision, parietal eye loss, and the crocodylian nocturnal bottleneck. *Mol. Biol. Evol.* 34, 666–676. doi: 10.1093/molbev/msw265

Falcón, J., Besseau, L., Fuentès, M., Sauzet, S., Magnanou, E., and Boeuf, G. (2009). Structural and functional evolution of the pineal melatonin system in vertebrates. *Ann. N. Y. Acad. Sci.* 1163, 101–111. doi: 10.1111/J.1749-6632.2009.04435.X

Feuda, R., Hamilton, S. C., McInerney, J. O., and Pisani, D. (2012). Metazoan opsin evolution reveals a simple route to animal vision. *Proc. Natl. Acad. Sci. U.S.A.* 109, 18868–18872. doi: 10.1073/pnas.1204609109

Filadelfi, A. M., and Castrucci, A. M. (1996). Comparative aspects of the pineal/melatonin system of poikilothermic vertebrates. *J. Pineal Res.* 20, 175–186. doi: 10.1111/j.1600-079x.1996.tb00256.x

Fortriede, J. D., Pells, T. J., Chu, S., Chaturvedi, P., Wang, D., Fisher, M. E., et al. (2020). Xenbase: deep integration of GEO & SRA RNA-seq and ChIP-seq data in a model organism database. *Nucleic Acids Res.* 48, D776–D782. doi: 10.1093/NAR/GKZ933

Fukuzawa, T. (2000). Melanophore lineage and clonal organization of the epidermis in *Xenopus* embryos as revealed by expression of a biogenic marker, GFP. *Pigment Cell Res.* 13, 151–157. doi: 10.1034/J.1600-0749.2000.130306.X

Gábriel, R., and Wilhelm, M. (2001). Structure and function of photoreceptor and second-order cell mosaics in the retina of *Xenopus*. *Int. Rev. Cytol.* 210, 77–120. doi: 10.1016/s0074-7696(01)10004-5

Gerkema, M. P., Davies, W. I. L., Foster, R. G., Menaker, M., and Hut, R. A. (2013). The nocturnal bottleneck and the evolution of activity patterns in mammals. *Proc. Biol. Sci.* 280:20130508. doi: 10.1098/rspb.2013.0508

Green, C. B., Liang, M. Y., Steenhard, B. M., and Besharse, J. C. (1999). Ontogeny of circadian and light regulation of melatonin release in *Xenopus laevis* embryos. *Brain Res. Dev. Brain Res.* 117, 109–116. doi: 10.1016/s0165-3806(99)00109-1

Hannibal, J., Hindersson, P., Nevo, E., and Fahrenkrug, J. (2002). The circadian photopigment melanopsin is expressed in the blind subterranean mole rat, *Spalax*. *Neuroreport* 13, 1411–1414. doi: 10.1097/00001756-200208070-00013

Hardman, J., Tobin, D., Haslam, I., Farjo, N., Farjo, B., Al-Nuaimi, Y., et al. (2015). The peripheral clock regulates human pigmentation. *J. Invest. Dermatol.* 135, 1053–1064. doi: 10.1038/JID.2014.442

Haslam, I. S., Roubos, E. W., Mangoni, M. L., Yoshizato, K., Vaudry, H., Kloepper, J. E., et al. (2014). From frog integument to human skin: dermatological perspectives from frog skin biology. *Biol. Rev.* 89, 618–655. doi: 10.1111/brv.12072

Hassin, G., and Witkovsky, P. (1983). Intracellular recording from identified photoreceptors and horizontal cells of the *Xenopus retina*. *Vis. Res.* 23, 921–931. doi: 10.1016/0042-6989(83)90001-9

Hattar, S., Liao, H. W., Takao, M., Berson, D. M., and Yau, K. W. (2002). Melanopsin-containing retinal ganglion cells: architecture, projections, and intrinsic photosensitivity. *Science* 295, 1065–1070. doi: 10.1126/science.1069609

Hoekstra, H. E. (2006). Genetics, development and evolution of adaptive pigmentation in vertebrates. *Heredity* 97, 222–234. doi: 10.1038/sj.hdy.6800861

Hogben, L., and Slome, D. (1931). The pigmentary effector system. VI. The dual character of endocrine co-ordination in amphibian colour change. *Proc. R. Soc. B* 108, 10–54. doi: 10.1086/303379

Hogben, L., and Slome, D. (1936). The pigmentary effector system. VIII. The dual receptive mechanism of the amphibian background response. *Proc. R. Soc. B* 120, 158–173. doi: 10.1098/rspb.1936.0029

Hunt, J. E., Bruno, J. R., and Pratt, K. G. (2020). An innate color preference displayed by *Xenopus* tadpoles is persistent and requires the tegmentum. *Front. Behav. Neurosci.* 14:71. doi: 10.3389/fnbeh.2020.00071

Isorna, E., Besseau, L., Boeuf, G., Desdevises, Y., Vuilleumier, R., Alonso-Gómez, A., et al. (2006). Retinal, pineal and diencephalic expression of frog arylalkylamine N-acetyltransferase-1. *Mol. Cell. Endocrinol.* 252, 11–18. doi: 10.1016/J.MCE.2006.03.032

Jenks, B. G., VanOverbeeke, A. P., and McStay, B. F. (1977). Synthesis, storage, and release of MSH in the pars intermedia of the pituitary gland of *Xenopus laevis* during background adaptation. *Can. J. Zool.* 55, 922–927. doi: 10.1139/z77-120

Kashina, A. S., Semenova, I. V., Ivanov, P. A., Potekhina, E. S., Zaliapin, I., and Rodionov, V. I. (2004). Protein kinase A, which regulates intracellular transport, forms complexes with molecular motors on organelles. *Curr. Biol.* 14, 1877–1881. doi: 10.1016/J.CUB.2004.10.003

Kawauchi, H., Kawazoe, I., Tsubokawa, M., Kishida, M., and Baker, B. I. (1983). Characterization of melanin-concentrating hormone in chum salmon pituitaries. *Nature* 305, 321–323. doi: 10.1038/305321a0

Klein, D. C. (2006). Evolution of the vertebrate pineal gland: the AANAT hypothesis. *Chronobiol. Int.* 23, 5–20. doi: 10.1080/07420520500545839

Kojima, K., Matsutani, Y., Yamashita, T., Yanagawa, M., Imamoto, Y., Yamano, Y., et al. (2017). Adaptation of cone pigments found in green rods for scotopic vision through a single amino acid mutation. *Proc. Natl. Acad. Sci. U.S.A.* 114, 5437–5442. doi: 10.1073/pnas.1620010114

Korf, H. W., Liesner, R., Meissl, H., and Kirk, A. (1981). Pineal complex of the clawed toad, *Xenopus laevis* Daud.: structure and function. *Cell Tissue Res.* 216, 113–130. doi: 10.1007/bf00234548

Kottler, V. A., Künstner, A., and Schartl, M. (2015). Pheomelanin in fish? *Pigment Cell Melanoma Res.* 28, 355–356. doi: 10.1111/pcmr.12359

Koyanagi, M., Kawano-Yamashita, E., Wada, S., and Terakita, A. (2017). Vertebrate bistable pigment parapinopsin: implications for emergence of visual signaling and neofunctionalization of non-visual pigment. *Front. Ecol. Evol.* 5:23. doi: 10.3389/fevo.2017.00023

Koyanagi, M., Kubokawa, K., Tsukamoto, H., Shichida, Y., and Terakita, A. (2005). Cephalochordate melanopsin: evolutionary linkage between invertebrate visual cells and vertebrate photosensitive retinal ganglion cells. *Curr. Biol.* 15, 1065–1069. doi: 10.1016/j.cub.2005.04.063

Koyanagi, M., Wada, S., Kawano-Yamashita, E., Hara, Y., Kuraku, S., Kosaka, S., et al. (2015). Diversification of non-visual photopigment parapinopsin in spectral sensitivity for diverse pineal functions. *BMC Biol.* 13:73. doi: 10.1186/s12915-015-0174-9

Kramer, B. M. R., Claassen, I. E. W. M., Westphal, N. J., Jansen, M., Tuinhof, R., Jenks, B. G., et al. (2003). Alpha-melanophore-stimulating hormone in the brain, cranial placode derivatives, and retina of *Xenopus laevis* during development in relation to background adaptation. *J. Comp. Neurol.* 456, 73–83. doi: 10.1002/cne.10513

Kumasaka, M., Sato, S., Yajima, I., Goding, C. R., and Yamamoto, H. (2005). Regulation of melanoblast and retinal pigment epithelium development by *Xenopus laevis* Mitf. *Dev. Dyn.* 234, 523–534. doi: 10.1002/DVDY.20505

Lamb, T. D. (2013). Evolution of phototransduction, vertebrate photoreceptors and retina. *Prog. Retin. Eye Res.* 36, 52–119. doi: 10.1016/j.preteyeres.2013.06.001

Lan, Y., Zeng, W., Dong, X., and Lu, H. (2021). Opsin 5 is a key regulator of ultraviolet radiation-induced melanogenesis in human epidermal melanocytes. *Br. J. Dermatol.* 185, 391–404. doi: 10.1111/BJD.19797

Larsson, M. (2011). Binocular vision and ipsilateral retinal projections in relation to eye and forelimb coordination. *Brain. Behav. Evol.* 77, 219–230. doi: 10.1159/000329257

Lerner, A. B., Case, J. D., Takahashi, Y., Lee, T. H., and Mori, W. (1958). Isolation of melatonin, the pineal gland factor that lightnes melanocytes. *J. Am. Chem. Soc.* 80, 2587–2587. doi: 10.1021/ja01543a060

Ligon, R. A., and Mccartney, K. L. (2016). Biochemical regulation of pigment motility in vertebrate chromatophores: a review of physiological color change mechanisms. *Curr. Zool.* 62, 237–252.

Lindgren, J., Moyer, A., Schweitzer, M. H., Sjövall, P., Uvdal, P., Nilsson, D. E., et al. (2015). Interpreting melanin-based coloration through deep time: a critical review. *Proc. R. Soc. B Biol. Sci.* 282:20150614. doi: 10.1098/rspb.2015.0614

Lovegrove, B. G. (2017). A phenology of the evolution of endothermy in birds and mammals. *Biol. Rev.* 92, 1213–1240. doi: 10.1111/brv.12280

Lupi, D., Oster, H., Thompson, S., and Foster, R. G. (2008). The acute light-induction of sleep is mediated by OPN4-based photoreception. *Nat. Neurosci.* 11, 1068–1073. doi: 10.1038/nn.2179

MacIver, M., Schmitz, L., Mugan, U., Murphey, T., and Mobley, C. (2017). Massive increase in visual range preceded the origin of terrestrial vertebrates. *Proc. Natl. Acad. Sci. U.S.A.* 114, E2375–E2384. doi: 10.1073/PNAS.1615563114

McCord, C. P., and Allen, F. P. (1917). Evidences associating pineal gland function with alterations in pigmentation. *J. Exp. Zool.* 23, 207–224. doi: 10.1002/jez.1400230108

McNamara, M., Rossi, V., Slater, T., Rogers, C., Ducrest, A., Dubey, S., et al. (2021). Decoding the evolution of melanin in vertebrates. *Trends Ecol. Evol.* 36, 430–443. doi: 10.1016/J.TREE.2020.12.012

Miyashita, Y., Moriya, T., Yokosawa, N., Hatta, S., Arai, J., Kusunoki, S., et al. (1996). Light-sensitive response in melanophores of *Xenopus laevis*: II.Rho is involved in light-induced melanin aggregation. *J. Exp. Zool.* 276, 125–131. doi: 10.1002/(SICI)1097-010X(19961001)276:2<125::AID-JEZ5<3.0.CO;2-Q

Mohun, S. M., and Davies, W. I. L. (2019). The evolution of amphibian photoreception. *Front. Ecol. Evol.* 7:321. doi: 10.3389/fevo.2019.00321

Moraes, M. N., de Assis, L. V. M., Provencio, I., Castrucci, A. M., and de, L. (2021). Opsins outside the eye and the skin: a more complex scenario than originally thought for a classical light sensor. *Cell Tissue Res.* 385, 519–538. doi: 10.1007/s00441-021-03500-0

Moraes, M. N., Ramos, B. C., Poletini, M. O., and Castrucci, A. M. L. (2015). Melanopsins: localization and phototransduction in *Xenopus laevis* melanophores. *Photochem. Photobiol.* 91, 1133–1141. doi: 10.1111/php.12484

Morera, L. P., Díaz, N. M., and Guido, M. E. (2016). Horizontal cells expressing melanopsin x are novel photoreceptors in the avian inner retina. *Proc. Natl. Acad. Sci. U.S.A.* 113, 13215–13220. doi: 10.1073/pnas.1608901113

Moriya, T., Kito, K., Miyashita, Y., and Asami, K. (1996a). Preference for background color of the *Xenopus laevis* tadpole. *J. Exp. Zool.* 276, 335–344. doi: 10.1002/(SICI)1097-010X(19961201)276:5<335::AID-JEZ4<3.0.CO;2-P

Moriya, T., Miyashita, Y., Arai, J., Kusunoki, S., Abe, M., and Asami, K. (1996b). Light-sensitive response in melanophores of *Xenopus laevis*: I. Spectral characteristics of melanophore response in isolated tail fin of *Xenopus* tadpole. *J. Exp. Zool.* 276, 11–18. doi: 10.1002/(SICI)1097-010X(19960901)276:1<11::AID-JEZ2<3.0.CO;2-8

Moutsaki, P., Whitmore, D., Bellingham, J., Sakamoto, K., David-Gray, Z. K., and Foster, R. G. (2003). Teleost multiple tissue (tmt) opsin: a candidate photopigment regulating the peripheral clocks of zebrafish? *Brain Res. Mol. Brain Res.* 112, 135–145.

Nakajima, K., Shimamura, M., and Furuno, N. (2021). Generation of no-yellow-pigment *Xenopus tropicalis* by slc2a7 gene knockout. *Dev. Dyn.* 250, 1420–1431. doi: 10.1002/DVDY.334

Nakane, Y., Shimmura, T., Abe, H., and Yoshimura, T. (2014). Intrinsic photosensitivity of a deep brain photoreceptor. *Curr. Biol.* 24, R596–R597. doi: 10.1016/J.CUB.2014.05.038

Natesan, A., Geetha, L., and Zatz, M. (2002). Rhythm and soul in the avian pineal. *Cell Tissue Res.* 309, 35–45.

Nilsson, D.-E. (2021). The diversity of eyes and vision. *Annu. Rev. Vis. Sci.* 7, 19–41. doi: 10.1146/annurev-vision-121820

Nisembaum, L., Besseau, L., Paulin, C., Charpantier, A., Martin, P., Magnanou, M., et al. (2015). In the heat of the night: thermo-TRPV channels in the salmonid pineal photoreceptors and modulation of melatonin secretion. *Endocrinology* 156, 4629–4638. doi: 10.1210/EN.2015-1684

Okano, T., Yoshizawa, T., and Fukada, Y. (1994). Pinopsin is a chicken pineal photoreceptive molecule. *Nature* 372, 94–97. doi: 10.1038/372094a0

Olinski, L. E., Lin, E. M., and Oancea, E. (2020). Illuminating insights into opsin 3 function in the skin. *Adv. Biol. Regul.* 75:100668. doi: 10.1016/j.jbior.2019.100668

Oshima, N. (2001). Direct reception of light by chromatophores of lower vertebrates. *Pigment Cell Res.* 14, 312–319. doi: 10.1034/j.1600-0749.2001.140502.x

Ota, W., Nakane, Y., Hattar, S., and Yoshimura, T. (2018). Impaired circadian photoentrainment in Opn5-null mice. *iScience* 6, 299–305. doi: 10.1016/j.isci.2018.08.010

Ozdeslik, R., Olinski, L., Trieu, M., Oprian, D., and Oancea, E. (2019). Human nonvisual opsin 3 regulates pigmentation of epidermal melanocytes through functional interaction with melanocortin 1 receptor. *Proc. Natl. Acad. Sci. U.S.A.* 116, 11508–11517. doi: 10.1073/PNAS.1902825116

Patel, D., Barnes, J., Davies, W., Stenkamp, D., and Pate, J. (2020). Short-wavelength-sensitive 2 (Sws2) visual photopigment models combined with atomistic molecular simulations to predict spectral peaks of absorbance. *PLoS Comput. Biol.* 16:e1008212. doi: 10.1371/JOURNAL.PCBI.1008212

Porter, M. L., Blasic, J. R., Bok, M. J., Cameron, E. G., Pringle, T., Cronin, T. W., et al. (2012). Shedding new light on opsin evolution. *Proc. Biol. Sci.* 279, 3–14. doi: 10.1098/rspb.2011.1819

Prayag, A. S., Najjar, R. P., and Gronfier, C. (2019). Melatonin suppression is exquisitely sensitive to light and primarily driven by melanopsin in humans. *J. Pineal Res.* 66:e12562. doi: 10.1111/jpi.12562

Provencio, I., Jiang, G., De Grip, W. J., Hayes, W. P., and Rollag, M. D. (1998). Melanopsin: an opsin in melanophores, brain, and eye. *Proc. Natl. Acad. Sci. U.S.A.* 95, 340–345. doi: 10.1073/pnas.95.1.340

Rollag, M. D. (1996). Amphibian melanophores become photosensitive when treated with retinal. *J. Exp. Zool.* 275, 20–26. doi: 10.1002/(SICI)1097-010X(19960501)275:1<20::AID-JEZ4<3.0.CO;2-C

Rothman, G. R., Blackiston, D. J., and Levin, M. (2016). Color and intensity discrimination in *Xenopus laevis* tadpoles. *Anim. Cogn.* 19, 911–919. doi: 10.1007/s10071-016-0990-5

Roubos, E. W., Van Wijk, D. C. W. A., Kozicz, T., Scheenen, W. J. J. M., and Jenks, B. G. (2010). Plasticity of melanotrope cell regulations in *Xenopus laevis*. *Eur. J. Neurosci.* 32, 2082–2086. doi: 10.1111/j.1460-9568.2010.07526.x

Rudh, A., and Qvarnström, A. (2013). Adaptive colouration in amphibians. *Semin. Cell Dev. Biol.* 24, 553–561. doi: 10.1016/j.semcdb.2013.05.004

Sapède, D., and Cau, E. (2013). The pineal gland from development to function. *Curr. Top. Dev. Biol.* 106, 171–215. doi: 10.1016/B978-0-12-416021-7.00005-5

Sato, K., Yamashita, T., Kojima, K., Sakai, K., Matsutani, Y., Yanagawa, M., et al. (2018a). Pinopsin evolved as the ancestral dim-light visual opsin in vertebrates. *Commun. Biol.* 1:156. doi: 10.1038/s42003-018-0164-x

Sato, K., Yamashita, T., Ohuchi, H., Takeuchi, A., Gotoh, H., Ono, K., et al. (2018b). Opn5L1 is a retinal receptor that behaves as a reverse and self-regenerating photoreceptor. *Nat. Commun.* 9:1255. doi: 10.1038/s41467-018-03603-3

Schartl, M., Larue, L., Goda, M., Bosenberg, M. W., Hashimoto, H., and Kelsh, R. N. (2016). What is a vertebrate pigment cell? *Pigment Cell Melanoma Res.* 29, 8–14. doi: 10.1111/pcmr.12409

Seldenrijk, R., Hup, D., de Graan, P., and van de Veerdonk, F. (1979). Morphological and physiological aspects of melanophores in primary culture from tadpoles of *Xenopus laevis*. *Cell Tissue Res.* 198, 397–409. doi: 10.1007/BF00234185

Session, A. M., Uno, Y., Kwon, T., Chapman, J. A., Toyoda, A., Takahashi, S., et al. (2016). Genome evolution in the allotetraploid frog *Xenopus laevis*. *Nature* 538, 336–343. doi: 10.1038/nature19840

Shirzad-Wasei, N., and DeGrip, W. J. (2016). Heterologous expression of melanopsin: present, problems and prospects. *Prog. Retin. Eye Res.* 52, 1–21. doi: 10.1016/j.preteyeres.2016.02.001

Simonneaux, V., and Ribelayga, C. (2003). Generation of the melatonin endocrine message in mammals: a review of the complex regulation of melatonin synthesis by norepinephrine, peptides, and other pineal transmitters. *Pharmacol. Rev.* 55, 325–395. doi: 10.1124/pr.55.2.2

Slater, B., Liu, K., Kwan, M., Quarto, N., and Longaker, M. (2009). Cranial osteogenesis and suture morphology in *Xenopus laevis*: a unique model system for studying craniofacial development. *PLoS One* 4:e3914. doi: 10.1371/JOURNAL.PONE.0003914

Slominski, A., Tobin, D. J., Shibahara, S., and Wortsman, J. (2004). Melanin pigmentation in mammalian skin and its hormonal regulation. *Physiol. Rev.* 84, 1155–1228.

Starace, D. M., and Knox, B. E. (1998). Cloning and expression of a *Xenopus* short wavelength cone pigment. *Exp. Eye Res.* 67, 209–220. doi: 10.1006/exer.1998.0507

Stiemke, M., Landers, R., Al-Ubaidi, M., Rayborn, M., and Hollyfield, J. (1994). Photoreceptor outer segment development in *Xenopus laevis*: influence of the pigment epithelium. *Dev. Biol.* 162, 169–180. doi: 10.1006/DBIO.1994.1076

Stone, S., Witkovsky, P., and Schütte, M. (1990). A chromatic horizontal cell in the *Xenopus* retina: intracellular staining and synaptic pharmacology. *J. Neurophysiol.* 64, 1683–1694. doi: 10.1152/JN.1990.64.6.1683

Storchi, R., Bedford, R. A., Martial, F. P., Allen, A. E., Wynne, J., Montemurro, M. A., et al. (2017). Modulation of fast narrowband oscillations in the mouse retina and dLGN according to background light intensity. *Neuron* 93, 299–307. doi: 10.1016/j.neuron.2016.12.027

Su, C.-Y., Luo, D.-G., Terakita, A., Shichida, Y., Liao, H.-W., Kazmi, M. A., et al. (2006). Parietal-eye phototransduction components and their potential evolutionary implications. *Science* 311, 1617–1621. doi: 10.1126/science.1123802

Sugimoto, M. (2002). Morphological color changes in fish: regulation of pigment cell density and morphology. *Microsc. Res. Tech.* 58, 496–503. doi: 10.1002/jemt.10168

Sun, L., Kawano-Yamashita, E., Nagata, T., Tsukamoto, H., Furutani, Y., Koyanagi, M., et al. (2014). Distribution of mammalian-like melanopsin in cyclostome retinas exhibiting a different extent of visual functions. *PLoS One* 9:e108209. doi: 10.1371/journal.pone.0108209

Taniguchi, Y., Hisatomi, O., Yoshida, M., and Tokunaga, F. (2001). Pinopsin expressed in the retinal photoreceptors of a diurnal gecko. *FEBS Lett.* 496, 69–74. doi: 10.1016/S0014-5793(01)02395-X

Ubink, R., Tuinhof, R., and Roubos, E. W. (1998). Identification of suprachiasmatic melanotrope-inhibiting neurons in *Xenopus laevis*: a confocal laser-scanning microscopy study. *J. Comp. Neurol.* 397, 60–68.

Verburg-van Kemenade, B. M., Willems, P. H., Jenks, B. G., and van Overbeeke, A. P. (1984). The development of the pars intermedia and its role in the regulation of dermal melanophores in the larvae of the amphibian *Xenopus laevis*. *Gen. Comp. Endocrinol.* 55, 54–65. doi: 10.1016/0016-6480(84)90128-x

von Uckermann, G., Lambert, F. M., Combes, D., Straka, H., and Simmers, J. (2016). Adaptive plasticity of spino-extraocular motor coupling during locomotion in metamorphosing *Xenopus laevis*. *J. Exp. Biol.* 219, 1110–1121. doi: 10.1242/jeb.136168

Wada, S., Kawano-Yamashita, E., Koyanagi, M., and Terakita, A. (2012). Expression of UV-sensitive parapinopsin in the iguana parietal eyes and its implication in UV-sensitivity in vertebrate pineal-related organs. *PLoS One* 7:e39003. doi: 10.1371/journal.pone.0039003

Wada, S., Kawano-Yamashita, E., Sugihara, T., Tamotsu, S., Koyanagi, M., and Terakita, A. (2021). Insights into the evolutionary origin of the pineal color discrimination mechanism from the river lamprey. *BMC Biol.* 19:188. doi: 10.1186/S12915-021-01121-1

Wald, G. (1955). Visual pigments and vitamins A of the clawed toad, *Xenopus laevis*. *Nature* 175, 390–391. doi: 10.1038/175390A0

Wiechmann, A. F., and Sherry, D. M. (2012). Melatonin receptors are anatomically organized to modulate transmission specifically to cone pathways in the retina of *Xenopus laevis*. *J. Comp. Neurol.* 520, 1115–1127. doi: 10.1002/cne.22783

Witkovsky, P. (2000). Photoreceptor classes and transmission at the photoreceptor synapse in the retina of the clawed frog, *Xenopus laevis*. *Microsc. Res. Tech.* 50, 338–346. doi: 10.1002/1097-0029(20000901)50:5<338::AID-JEMT3>3.0.CO;2-I

Witkovsky, P., Levine, J., Engbretson, G., Hassin, G., and MacNichol, E. (1981). A microspectrophotometric study of normal and artificial visual pigments in the photoreceptors of *Xenopus laevis*. *Vis. Res.* 21, 867–873. doi: 10.1016/0042-6989(81)90187-5

Yamashita, T., Ono, K., Ohuchi, H., Yumoto, A., Gotoh, H., Tomonari, S., et al. (2014). Evolution of mammalian Opn5 as a specialized UV-absorbing pigment by a single amino acid mutation. *J. Biol. Chem.* 289, 3991–4000. doi: 10.1074/jbc.M113.514075

Yoshimoto, S., and Ito, M. (2011). A ZZ/ZW-type sex determination in *Xenopus laevis*. *FEBS J.* 278, 1020–1026. doi: 10.1111/J.1742-4658.2011.08031.X

Zhang, J., Kleinschmidt, J., Sun, P., and Witkovsky, P. (1994). Identification of cone classes in *Xenopus* retina by immunocytochemistry and staining with lectins and vital dyes. *Vis. Neurosci.* 11, 1185–1192. doi: 10.1017/S0952523800006982

Ziv, L., Tovin, A., Strasser, D., and Gothilf, Y. (2007). Spectral sensitivity of melatonin suppression in the zebrafish pineal gland. *Exp. Eye Res.* 84, 92–99. doi: 10.1016/j.exer.2006.09.004

Conflict of Interest: The authors declare that the research was conducted in the absence of any commercial or financial relationships that could be construed as a potential conflict of interest.

frontiers in Neuroanatomy

ORIGINAL RESEARCH
published: 26 January 2022
doi: 10.3389/fnana.2021.770804

Morphological Plasticity of the Retina of Viperidae Snakes Is Associated With Ontogenetic Changes in Ecology and Behavior

*Juliana H. Tashiro, Dora F. Ventura and Einat Hauzman**

Department of Experimental Psychology, Psychology Institute, University of São Paulo, São Paulo, Brazil

Snakes of the Viperidae family have retinas adapted to low light conditions, with high packaging of rod-photoreceptors containing the rhodopsin photopigment (RH1), and three types of cone-photoreceptors, large single and double cones with long-wavelength sensitive opsins (LWS), and small single cones with short-wavelength sensitive opsins (SWS1). In this study, we compared the density and distribution of photoreceptors and ganglion cell layer (GCL) cells in whole-mounted retinas of two viperid snakes, the lancehead *Bothrops jararaca* and the rattlesnake *Crotalus durissus*, and we estimated the upper limits of spatial resolving power based on anatomical data. The ground-dwelling *C. durissus* inhabits savannah-like habitats and actively searches for places to hide before using the sit-and-wait hunting strategy to ambush rodents. *B. jararaca* inhabits forested areas and has ontogenetic changes in ecology and behavior. Adults are terrestrial and use similar hunting strategies to those used by rattlesnakes to prey on rodents. Juveniles are semi-arboreal and use the sit-and-wait strategy and caudal luring to attract ectothermic prey. Our analyses showed that neuronal densities were similar for the two species, but their patterns of distribution were different between and within species. In adults and juveniles of *C. durissus*, cones were distributed in poorly defined visual streaks and rods were concentrated in the dorsal retina, indicating higher sensitivity in the lower visual field. In adults of *B. jararaca*, both cones and rods were distributed in poorly defined visual streaks, while in juveniles, rods were concentrated in the dorsal retina and cones in the ventral retina, enhancing sensitivity in the lower visual field and visual acuity in the upper field. The GCL cells had peak densities in the temporal retina of *C. durissus* and adults of *B. jararaca*, indicating higher acuity in the frontal field. In juveniles of *B. jararaca*, the peak density of GCL cells in the ventral retina indicates better acuity in the upper field. The estimated visual acuity varied from 2.3 to 2.8 cycles per degree. Our results showed interspecific differences and suggest ontogenetic plasticity of the retinal architecture associated with changes in the niche occupied by viperid snakes, and highlight the importance of the retinal topography for visual ecology and behavior of snakes.

Keywords: visual ecology, opsins, visual acuity, stereology, *Crotalus durissus*, *Bothrops jararaca*, retinal topography

OPEN ACCESS

Edited by:
Nicolás Cuenca,
University of Alicante, Spain

Reviewed by:
Marta Agudo-Barriuso,
Biomedical Research Institute of Murcia (IMIB), Spain
Peter Ahnelt,
Medical University of Vienna, Austria

****Correspondence:***
Einat Hauzman
hauzman.einat@gmail.com

Received: *04 September 2021*
Accepted: *27 December 2021*
Published: *26 January 2022*

Citation:
Tashiro JH, Ventura DF and Hauzman E (2022) Morphological Plasticity of the Retina of Viperidae Snakes Is Associated With Ontogenetic Changes in Ecology and Behavior. Front. Neuroanat. 15:770804. doi: 10.3389/fnana.2021.770804

INTRODUCTION

The highly diverse group of Snakes, with more than 3,800 species (Uetz et al., 2020) has a fascinating diversity of retinal morphology, especially regarding the photoreceptor types (Walls, 1942; Underwood, 1967a, 1970; Caprette, 2005; Hauzman et al., 2017; Hauzman, 2020). This group represents a valuable model to test hypotheses of correlation between the types of retinal specialization and species ecology and behavior. The vertebrate retina is formed by layers of cells and nerve plexuses organized in a highly conserved fashion that allows the vertical flow of luminous information from the photoreceptors in the outermost retina toward the ganglion cells in the innermost retina (Ramón y Cajal, 1983). The photoreceptors contain the visual pigments that absorb photons and trigger an enzymatic cascade within the cell. The light energy is converted into neural signals that are transmitted to bipolar cells and from those to the ganglion cells (GCs) that conduct the information to the brain (Ramón y Cajal, 1983).

The density and distribution of cells in the retinas are highly variable among species. Specific regions of higher cell density, the retinal specializations, reflect areas of the visual field that have greater importance for photon uptake, spatial resolution, or other visual functions depending on the cell type (Baden et al., 2020). Two main types of retinal specializations, visual streak and *area centralis*, were described in many vertebrates and are usually associated with the habitat occupied by the species (Hughes, 1977; Moore et al., 2017). Visual streaks are elongated regions of higher cell density that allow a wide screening of the surroundings without the constant need for head and eye movements and are usually associated with the use of open environments. *Areae centrales* are concentric regions of higher cell density usually found in species that occupy closed environments such as forests, where the horizon is obstructed by vegetation (Hughes, 1977; Collin, 2008; Moore et al., 2017).

In Snakes, despite the ecological diversity of the group, a very limited number of studies investigated the organization of neurons in the retinas (Wong, 1989; Hart et al., 2012; Hauzman et al., 2014, 2018). Different types of specializations were described even among sympatric and closely related species. In marine Elapidae snakes the GCs are arranged in horizontal streaks that might enable a better view of the open ocean environment (Hart et al., 2012), and in two out of three marine species analyzed by Hart et al. (2012), an additional *area centralis* in the ventral retina was associated with specific foraging strategies. In the arboreal Dipsadidae snake *Philodryas olfersii*, the photoreceptors and GC are arranged in horizontal streaks, while in the close-related ground-dwelling *Philodryas patagoniensis*, these neurons are concentrated in a ventral *area centralis*, indicating better spatial resolution of the upper visual field (Hauzman et al., 2014). In a comparative study of the distribution of GCs of diurnal and nocturnal Dipsadidae snakes, it was suggested that the type of specialization may also be associated with daily activity patterns and foraging strategies (Hauzman et al., 2018), in which diurnal species that actively forage during the day display visual streaks, while nocturnal species or those that feed on slow-moving prey have *area centralis* in different regions of the retinas (Hauzman et al., 2018). These studies revealed the variability of adaptations of the visual structures of snakes, and indicate that different selective forces may shape the retinal architecture irrespective of phylogenetic blueprints.

The Viperidae family represents a valuable model for investigating adaptations of the visual structures due to the diversity of species and habitats occupied, predation strategies with accurate strike performances (Reiserer, 2002; Chen et al., 2017; Schraft and Clark, 2019), and an elaborate thermosensitive sensory system in pitviper species (subfamily Crotalinae) integrated with inputs from visual neurons in the tectum (Hartline et al., 1978). Additionally, some viperid species have ontogenetic changes in the niche occupied and thus, represent a unique opportunity to explore how morphological adaptations of the retina might be associated with their visual ecology. Viperids are primarily nocturnal or crepuscular, and their retinas have a predominance of rods, highly sensitive photoreceptors adapted to low light (scotopic) conditions, and three types of cones, photoreceptors responsible for daylight (photopic) vision. The rods contain the typical rhodopsin (RH1) photopigment, and cones are classified as single cones and double cones sensitive to medium/long wavelengths, with the LWS photopigment, and single cones sensitive to short wavelengths, with the SWS1 photopigment (Bittencourt et al., 2019; Gower et al., 2019).

In this study, we compared the density and distribution of photoreceptors and ganglion cell layer (GCL) cells in the retinas of two pitvipers. The rattlesnake, *Crotalus durissus* (**Figure 1**), is a terrestrial snake that inhabits open fields of the Cerrado, a Brazilian savannah-like habitat, and actively search for places to hide before using the sit-and-wait hunting strategy to ambush rodents (Salomão et al., 1995; Sawaya et al., 2008; Tozetti and Martins, 2008, 2013). The lancehead, *Bothrops jararaca* (**Figure 1**), inhabits predominantly forested areas of the Atlantic Rain Forest and has ontogenetic changes in niche occupied and in behavior. Adults are terrestrial and use similar hunting strategies as rattlesnakes to prey on mammals. Juveniles are semi-arboreal and use the sit-and-wait strategy and caudal luring to attract ectothermic vertebrates, mainly anurans (Sazima, 1991, 1992, 2006; Marques and Sazima, 2004). We hypothesized that the differences in behavior and niche occupied by juveniles and adults of *B. jararaca* might be associated with rearrangements of the retinal architecture according to specific visual needs. With a stereological approach to quantify neurons in whole-mounted retinas, we observed differences in the density and distribution of cells between species, especially regarding the proportion and distribution of rods and cones, and differences in the retinal topography of juveniles and adults of *B. jararaca* that might reflect ontogenetic changes in the visual ecology. This study demonstrates that the habitat occupied by snakes and their foraging strategies are associated with different patterns of neuron distribution in the retina, which highlights the importance of their retinal specializations for visually guided behaviors.

FIGURE 1 | Photographs of adults (upper images) and juveniles (lower images) of *Bothrops jararaca* and *Crotalus durissus*. The whitetail observed in the juvenile of *B. jararaca* (lower left) is used for caudal luring. Photographs: Marcio Roberto Costa Martins.

MATERIALS AND METHODS

Snakes

Snakes (n = 33) were provided by the Butantan Institute, São Paulo, Brazil, and were euthanized with a lethal injection of sodium thiopental (100 mg/kg). Animal procedures were in accordance with ethical principles of animal management and experimentation established by the Brazilian Animal Experiment College (COBEA). The project was approved by the Ethics Committee of Animal Research of the Psychology Institute, University of São Paulo, Brazil. Individuals were classified as adults or juveniles based on the snout-vent length (SVL) and body mass (**Supplementary Table 1**; Sazima and Abe, 1991; Almeida-Santos, 2005; de Moraes, 2008; Barros, 2011; Fiorillo et al., 2020a).

Tissue Processing

Following euthanasia, the eyes were enucleated, their axial lengths were measured, and a small radial incision was made in the dorsal region for later orientation. The corneas were removed and the eyecups were fixed in 4% paraformaldehyde (PFA) diluted in phosphate buffer (PB) 0.1 M, for 3 h. The retinas were carefully dissected and maintained in PB 0.1 M at 4°C. When needed, the retinas were bleached in 10% hydrogen peroxide diluted in PB 0.1 M, for 24–48 h, at room temperature, prior to immunohistochemistry or Nissl procedures.

Immunohistochemistry

For immunohistochemistry, free-floating retinas were preincubated in 10% normal goat serum (Jackson ImmunoResearch, West Grove, United States) or 10% normal donkey serum (Sigma-Aldrich, St. Louis, MO, EUA), diluted in PB 0.1 M with 0.3% Triton X-100, for 1 h, at room temperature. The retinas were incubated with primary antibodies (**Table 1**) diluted in PB 0.1 M with 0.3% Triton X-100, for 3 days, at 4°C. The following antibodies were used: rabbit anti-SWS1 opsin (Sigma-Aldrich, AB5407; 1:200), rabbit anti-LWS opsin (Sigma-Aldrich, AB5405; 1:200), and for double immunofluorescence labeling, a mixture of the antibodies goat anti-SWS1 opsin (Santa Cruz Biotechnology, sc-14363; 1:200) and rabbit anti-LWS opsin (Sigma-Aldrich; AB5407; 1:200). The retinas were washed in PB 0.1 M with 0.3% Triton X-100 and incubated for 2 h with the secondary antibodies, at room temperature, protected from light: tetramethylrhodamine (TRITC)-conjugated goat anti-rabbit (immunoglobulin G, whole molecules; Jackson Immunoresearch Laboratories; 1:200), and for double-labeled retinas, a combination of TRITC-conjugated donkey anti-goat with Alexa Fluor® 488-conjugated donkey anti-rabbit (immunoglobulin G, whole molecule; Jackson Immunoresearch Laboratories; 1:200). The retinas were rinsed in 0.1 M PB, flat-mounted on glass slides with the photoreceptor layer facing up, mounted with Vectashield (Vector Laboratories Inc. California, United States), and observed under a fluorescent microscope (Leica DM5500B), with a set of filters for TRITC (excitation

TABLE 1 | Primary and secondary antibodies used to label cones in retinas of snakes.

Antibody	Immunogen	Source, host and catalog no.
Primary antibody		
Blue opsin (OPN1SW)	Human (*Homo sapiens*) blue-sensitive opsin NKQFQACIMKMVCG KAMTDESDTCSSQKTEV STVSSTQVGPN	Merck Millipore (Germany). Rabbit polyclonal. Cat#AB5407
Blue opsin (OPN1SW)	Human (*Homo sapiens*) blue-sensitive opsin EFYLFKNISSVGP WDGPQYH	Santa Cruz Biotech. (Germany). Goat polyclonal. Cat#sc14363
Red/Green opsin (OPN1LW)	Human (*Homo sapiens*) red/green–sensitive opsin RQFRNCILQLFGKK VDDGSELSSASKTEV SSVSSVSPA	Merck Millipore (Germany). Rabbit polyclonal. Cat#AB5405
Secondary antibody		
Goat anti-rabbit IgG + TRITC	Heavy and light chains of gamma immunoglobulins	Jackson Immunoresearch Lab. (EUA). Goat. Cat#AB2337926
Donkey anti-goat IgG + Alexa Fluor® 488	Heavy and light chains of gamma immunoglobulins	Jackson Immunoresearch Lab. (EUA). Donkey. Cat#AB2340400
Donkey anti-rabbit IgG + TRITC	Heavy and light chains of gamma immunoglobulins	Jackson Immunoresearch Lab. (EUA). Donkey. Cat#AB2340588

green, emission red) and Alexa Fluor® 488 (excitation blue, emission green).

Antibody Characterization and Specificity

Immunohistochemistry procedures were performed with polyclonal antibodies raised in rabbits against the last 42 amino acids of the C-terminal of human blue opsin (Sigma-Aldrich; AB5407), against the last 38 amino acids of the C-terminal of human red/green opsins (Sigma-Aldrich; AB5405), or raised in goats against a synthetic peptide with 20 amino acids of human blue opsin (Santa Cruz Biotechnology; sc-14363) (**Table 1**). The specificity of the antibodies for snakes was described previously (Hauzman et al., 2014, 2017; Bittencourt et al., 2019; Gower et al., 2019). Double labeling with the antibodies against SWS1 and against LWS opsins showed differential labeling of distinct photoreceptor populations (**Figure 2**), further indicating the specificity of both antibodies for particular types of cones. We also assessed the specificity of the two anti-SWS1 antibodies, by incubating 12 μm retinal sections of *B. jararaca* and *C. durissus* obtained at −25°C with a cryostat (Leica, CM1100; Nussloch, Germany), with a mixture of both antibodies, rabbit anti-SWS1 (AB5407; 1:200) and goat anti-SWS1 (sc14363; 1:200). Immunofluorescence visualization showed a small number of small single cones labeled by both antibodies (data not shown), indicating the specificity of both antibodies against SWS1 cones.

Nissl Staining

We used Nissl staining technique in whole-mounted retinas to analyze the population of GCL cells. Small radial incisions were made in the dissected retinas to allow them to be flat-mounted onto gelatinized glass slides, with the GCL facing up. The retinas were incubated with paraformaldehyde vapors overnight, at room temperature, for enhancing the adherence to the slide and to increase the differentiation of ganglion cells during staining (Coimbra et al., 2006). The tissues were rehydrated in decreasing ethanol series (95, 70, 50%), rinsed in distilled water acidified with glacial acetic acid, stained in aqueous solution of 2% cresyl violet for approximately 1 min, dehydrated in increasing concentrations of ethanol, cleared in xylene, and coverslipped with DPX (Sigma-Aldrich. St. Louis, MO, EUA).

To analyze the density and distribution of GCL cells, we used the cytological criteria proposed by Wong (1989) to distinguish ganglion cells from amacrine and glial cells. The ganglion cells

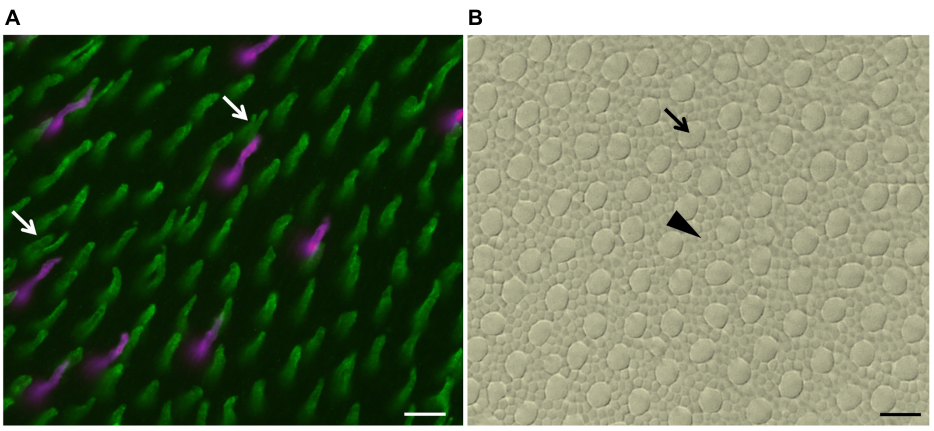

FIGURE 2 | Images of a counting field of a whole-mounted retina of *B. jararaca* double-labeled with anti-SWS1 opsin and anti-LWS opsin antibodies. **(A)** Outer segments of LWS cones (green), including single cones and double cones (white arrows), and of SWS1 cones (magenta). **(B)** Mosaic of photoreceptors of the same field shown in **(A)**, viewed under bright light: inner segments of rods (black arrowhead) and cones (black arrow). Scale bars 10 μm.

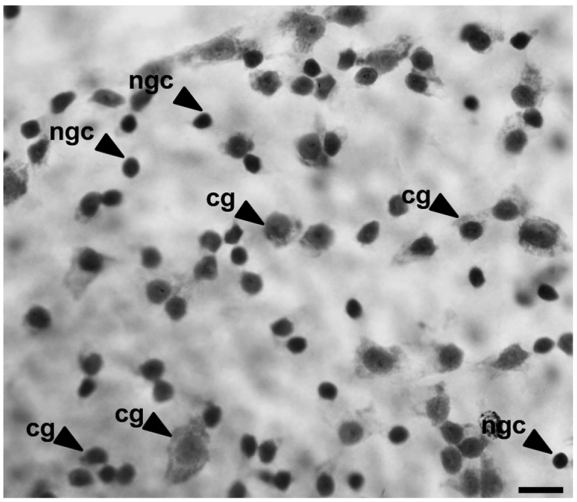

FIGURE 3 | Image of the GCL cells of *B. jararaca* indicating the morphological criteria used to distinguish ganglion cells (gc), with polygonal cell bodies, from other cell populations (ngc, non-ganglion cell), with a well-defined circular shape and dense nucleus. Scale bar: 10 μm.

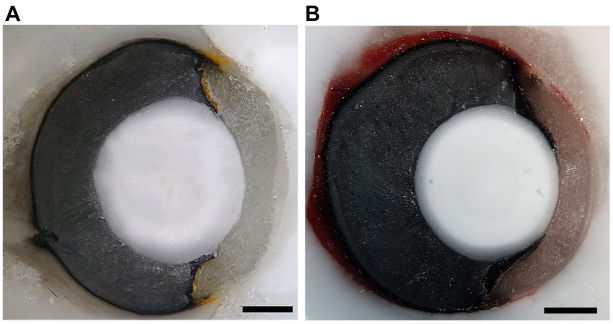

FIGURE 4 | Cryosectioned eye from adults of **(A)** *B. jararaca* and **(B)** *C. durissus*. Scale bars: 1 mm.

were differentiated by their larger polygonal soma, abundant Nissl substance in the cytoplasm, and a prominent nucleolus (**Figure 3**; Hart et al., 2012). Glial cells were differentiated by smaller soma size and a round and darkly stained profile, and amacrine cells were identified by a smaller and circular profile with a more darkly stained nucleus compared to ganglion cells (Hart et al., 2012). The glial and amacrine cells were not counted.

Stereological Assessment of the Density and Distribution of Retinal Neurons

The density and distribution of retinal neurons were accessed using a stereological approach based on the optical fractionator method (West et al., 1991), modified for retinal whole-mounts (Coimbra et al., 2009, 2012), using a motorized microscope (DM5500B, Leica Microsystems, Germany), connected to a computer running the Stereo Investigator software (MicroBrightField, Colchester, VT). The coordinates of the outer edges of the retinas were obtained using a 5x/NA 0.15 objective. Approximately 200 counting frames were positioned in a random fashion covering the entire area of the retina. Cells were counted when laying entirely within the counting frame or when intersected the acceptance lines, without touching the rejection lines (Gundersen, 1997). The area of the counting frame and the sampling grids varied according to the cell types and the retinal area, and were defined in pilot experiments, in order to obtain an acceptable Scheaffer coefficient of error (CE) (<0.10) (Scheaffer et al., 1996). The stereological parameters used to estimate the number of photoreceptors and GCL cells of each retina are described in **Supplementary Tables 2, 3**. To estimate the total population of neurons (N_{total}), we considered the area of sampling fraction (asf) according to the algorithm: $N_{total} = \sum Q \times 1/asf$, where $\sum Q$ is the sum of the total number of neurons counted and the area of sampling fraction is the ratio between the counting frame and the sampling grid (Coimbra et al., 2009).

Anatomical Estimates of the Visual Acuity

We estimated the upper limits of spatial resolving power based on the peak density of GCL cells and the presumed focal distance of the eyes. The focal lengths were estimated by freezing and sectioning eyes from one adult and one juvenile individual of each species. The fresh eyes were enucleated and rapidly frozen, embedded in Tissue-Tek OCT compound (Sakura Finetechnical Co., Tokyo, Japan), and the blocks were sectioned at −25°C on a cryostat (Leica CM1100; Nussloch, Germany). Photographs of the blocks were taken every 12 μm, with a camera (Axio CamMR, Carl ZeissVision, Germany) coupled to a stereomicroscope (SMZ775-T, NIKON, Japan), and a computed running the Axio Vision 4.1 software (Carl Zeiss, Germany). The areas of the lens and eyes were measured using the ImageJ software (NIH, Bethesda, United States) and the photographs that had the larger lens diameters were identified and used for optical measurements. Measurements of the axial length of the eye, lens axial diameter, and posterior nodal distance (PND) that represents the focal length and corresponds to the distance from the center of the lens to the retina-choroid border were taken along the optical axis, which was located by connecting the geometric centers of the optical components (Lisney and Collin, 2008). In *B. jararaca*, the focal length corresponded to 50% of the adult eye axial length of the adult (**Figure 4A**) and 67% of the juvenile. In *C. durissus* the focal distance corresponded to 60% of eyes axial length of both adult (**Figure 4B**) and juvenile. Those values were used to estimate the focal distance of the eyes used for GCL cell counts.

We estimated the upper limits of spatial resolution considering two possible arrangements of the ganglion cells, a hexagonal and a square array. The distance d subtended as 1 degree on the retina was determined from the PND and the equation $d = (2\pi PND)/360$ (Pettigrew et al., 1998). Considering a hexagonal array, we estimated the average spacing between cells (S) using the formula $S^2 = 2/(D\sqrt{3})$, where D is the peak density of GCL cells in cells/mm^2. The maximum spatial

TABLE 2 | Stereological assessment of total photoreceptors, rods and cones in retinas of adults and juveniles of *B. jararaca* and *C. durissus*.

Species		Total photoreceptors					Rods						Cones					
	Retinal area (mm^2)	Estimated population	CE	Mean density cells/mm^2	Max. density cells/mm^2	Min. density cells/mm^2	Estimated population	CE	Mean density cells/mm^2	Max. density cells/mm^2	Min. density cells/mm^2	% of rods	Estimated population	CE	Mean density cells/mm^2	Max. density cells/mm^2	Min. density cells/mm^2	% of cones
B. jararaca																		
Bj-A#3-RE	46.7	3,636,618	0.03	77,872	114,400	12,400	3,371,110	0.03	72,187	105,600	9,600	92.7	264,878	0.02	5,672	9,200	400	7.3
Bj-A#4-LE	31.2	2,869,378	0.04	91,967	148,800	12,400	2,709,182	0.04	86,833	141,200	10,400	94.4	158,654	0.04	5,085	10,800	400	5.5
Bj-A#5-RE	53.2	3,807,837	0.03	71,576	109,600	18,400	3,546,488	0.03	66,663	104,400	16,400	93.1	260,680	0.02	4,900	8,000	800	6.8
Bj-A#6-LE	54.0	2,851,821	0.04	52,909	89,200	11,200	2,817,263	0.01	52,268	84,400	6,800	98.8	206,879	0.02	3,838	5,600	400	7.3
Mean ± sd	46.3 ± 10.6	3,291,413 ± 502,399	0.04 ± 0.01	73,581 ± 16,205	115,500 ± 24,743	13,600 ± 3,250	3,111,011 ± 410,304	0.03 ± 0.01	69,488 ± 14,290	108,900 ± 23,627	10,800 ± 4,040	94.8 ± 2.8	264,878 ± 50,245	0.03 ± 0.01	4,874 ± 765	8,400 ± 2,191	500 ± 200	6.7 ± 0.8
Bj-J#2-RE	21.2	3,584,610	0.03	169,085	220,800	32,800	3,354,150	0.03	158,215	210,000	26,000	93.6	230,245	0.01	10,864	15,200	2,800	6.4
Bj-J#3-RE	23.8	3,055,351	0.03	128,376	176,400	48,400	2,842,807	0.03	119,446	167,600	42,800	93.0	212,322	0.02	8,921	12,800	2,400	6.9
Bj-J#4-LE	24.4	2,796,266	0.04	114,601	196,800	26,400	2,633,346	0.04	107,924	186,000	23,200	94.2	257,634	0.01	10,559	16,400	2,000	9.2
Mean ± sd	23.1 ± 1.7	3,145,409 ± 401,814	0.03 ± 0.01	137,354 ± 28,330	198,000 ± 22,224	35,867 ± 11,316	2,943,434 ± 370,788	0.03 ± 0.01	128,528 ± 26,347	187,867 ± 21,262	30,667 ± 10,601	93.6 ± 0.6	233,400 ± 22,820	0.01 ± 0.00	10,113 ± 1,044	14,800 ± 1,833	2,400 ± 400	7.5 ± 1.5
C. durissus																		
Cd-A#1-LE	55.1	3,585,315	0.03	65,069	113,600	21,200	3,249,205	0.03	58,969	103,600	18,000	90.6	335,662	0.02	6,092	11,600	1,200	9.4
Cd-A#2-RE	49.7	3,364,254	0.04	67,691	102,000	20,400	3,005,135	0.04	60,465	93,200	18,000	89.3	359,130	0.02	7,226	11,200	1,600	10.7
Cd-A#3-LE	48.3	3,648,600	0.04	75,540	123,600	14,800	3,296,354	0.04	68,248	112,800	12,800	90,3	369,688	0.04	7,654	12,400	1,200	10.1
Cd-A#4-LE	41.8	3,637,157	0.03	87,013	124,000	23,600	3,267,345	0.03	78,166	112,400	20,800	89.8	369,717	0.02	8,845	13,600	1,200	10.2
Cd-A#5-RE	39.5	3,402,368	0.03	87,128	131,200	29,600	3,095,653	0.03	78,371	121,200	23,200	91.0	343,716	0.02	8,702	13,600	1,600	10.1
Mean ± sd	46.9 ± 6.3	3,527,539 ± 134,480	0.03 ± 0.01	76,488 ± 10,400	118,880 ± 11,326	21,920 ± 5,370	3,182,738 ± 126,107	0.03 ± 0.01	68,844 ± 9,297	108,640 ± 10,642	18,560 ± 3,884	90.2 ± 0.7	355,582 ± 15,403	0.02 ± 0.01	7,704 ± 1,132	12,480 ± 1,110	1,360 ± 219	10.1 ± 0.5
Cd-J#1-RE	23.3	3,432,051	0.03	147,298	197,600	32,000	3,085,128	0.03	132,409	190,000	29,600	89.9	351,105	0.03	15,069	23,200	2,400	10.2
Cd-J#5-RE	22.4	2,761,716	0.03	125,533	220,000	41,600	2,503,403	0.04	111,759	198,000	13,200	90.6	312,409	0.01	13,947	22,800	2,000	11.3
Cd-J#6-LE	25.0	3,084,595	0.03	123,384	188,800	26,800	2,751,033	0.03	110,041	173,200	22,000	89.2	344,946	0.01	13,798	19,600	1,200	11.2
Mean ± sd	23.6 ± 1.3	3,092,787 ± 335,242	0.03 ± 0.00	132,071 ± 13,230	202,133 ± 16,086	33,467 ± 7,508	2,779,855 ± 291,932	0.03 ± 0.00	118,070 ± 12,448	187,067 ± 12,658	21,600 ± 8,207	89.9 ± 0.7	336,153 ± 20,793	0.02 ± 0.01	14,471 ± 695	21,867 ± 1,973	1,867 ± 611	10.9 ± 0.6

CE, Scheaffer's coefficient of error; sd, standard deviation; RE, right eye; LE, left eye.

TABLE 3 | Stereological assessment of SWS1 and LWS cones in retinas of adults and juveniles of *B. jararaca* and *C. durissus*.

Species	SWS1 cones							LWS cones					
	Retinal area (mm^2)	Estimated population	CE	Mean density cells/mm^2	Max. density cells/mm^2	Min. density cells/mm^2	% of SWS1 cones	Estimated population	CE	Mean density cells/mm^2	Max. density cells/mm^2	Min. density cells/mm^2	% of LWS cones
B. jararaca													
Bj-A#3-RE	46.7	16,977	0.03	364	833	31	6.4	238,939	0.03	5,116	8,549	154	90.2
Bj-A#4-LE	31.2	–	–	–	–	–		100,325	0.04	3,216	6,844	133	63.2
Bj-A#5-RE	53.2	29,468	0.03	554	1,142	62	11.3	216,110	0.03	4,062	6,358	370	82.9
Bj-A#6-LE	54.0	17,529	0.04	325	741	31	8.5	–	–	–	–	–	
Mean ± sd	46.3 ± 10.6	21,325 ± 7,058	0.04 ± 0.01	414 ± 123	905 ± 210	41 ± 18	8.7 ± 2.5	185,125 ± 74,321	0.03 ± 0.01	4,131 ± 952	7,250 ± 1,151	219 ± 131	78.8 ± 14.0
Bj-J#2-RE	21.2	25,644	0.04	1,210	2,400	300	11.1	199,050	0.03	9,389	12,900	1,100	86.5
Bj-J#3-RE	23.8	17,303	0.04	727	1,500	200	8.1	194,195	0.03	8,159	11,700	2,200	91.5
Bj-J#4-LE	24.4	23,007	0.03	943	2,300	100	8.9	191,516	0.03	7,849	13,200	2,400	74.3
Mean ± sd	23.1 ± 1.7	21,985 ± 4,263	0.03 ± 0.00	960 ± 242	2.067 ± 493	200 ± 100	9.4 ± 1.5	194,920 ± 3,819	0.03 ± 0.00	8,466 ± 814	12,600 ± 794	1,900 ± 700	84.1 ± 8.8
C. durissus													
Cd-A#1-LE	55.1	36,898	0.03	670	1,296	216	11.0	–	–	–	–	–	–
Cd-A#2-RE	49.7	–	–	–	–	–	–	322,641	0.03	6,492	10,370	1,574	89.9
Cd-A#3-LE	48.3	–	–	–	–	–	–	290,315	0.04	6,011	9,599	1,080	78.5
Cd-A#4-LE	41.8	33,563	0.03	803	1,451	247	9.1	313,665	0.03	7,504	11,512	1,636	84.8
Cd-A#5-RE	39.5	32,502	0.03	823	1,605	93	9.5	265,604	0.03	6,724	10,247	1,142	77.4
Mean ± sd	46.9 ± 6.3	34,321 ± 2,294	0.03 ± 0.00	765 ± 83	1,451 ± 155	185 ± 81	9.8 ± 1.0	298,056 ± 25,568	0.04 ± 0.01	6,683 ± 623	10,432 ± 795	1,358 ± 287	82.6 ± 5.8
Cd-J#1-RE	23.3	37,023	0.03	1,589	3,800	200	10.5	294,591	0.04	12,643	19,700	2,200	83.9
Cd-J#5-RE	22.4	30,016	0.05	1,340	2,900	500	9.6	269,625	0.03	12,037	19,400	1,600	86.3
Cd-J#6-LE	25.0	30,126	0.04	1,205	2,600	100	8.7	255,124	0.04	10,205	17,100	1,100	74.0
Mean ± sd	23.5 ± 1.3	32,388 ± 44,014	0.04 ± 0.01	1,378 ± 195	3,100 ± 624	267 ± 208	9.6 ± 0.9	273,113 ± 19,964	0.04 ± 0.00	11,628 ± 1,270	18,733 ± 1,422	1,567 ± 451	81.4 ± 6.5

CE, Scheaffer's coefficient of error; sd, standard deviation; RE, right eye; LE, left eye.

frequency (v) (Nyquist) of a sinusoidal grating (Snyder and Miller, 1977) that has resolution with this cellular arrangement was calculated as $v = 1/S\sqrt{3}$. This value was multiplied by the distance d, to obtain the spatial resolution in cycles per degree (cpd). In a second approach, considering that the ganglion cells might be organized in a square distribution, we estimated the linear density of GCL cells (cells/mm^2) from the square root of the peak density (D), and divided the linear cell density by 2 (because at least 2 cells are required to detect 1 cycle of a given spatial frequency). The resulting value was multiplied by the distance d to obtain the visual acuity in cpd (Pettigrew et al., 1998; Coimbra et al., 2013).

To infer the behavioral significance of the estimated visual acuity in an ecological context, we predicted the minimum size of objects that the viperid snakes can spatially resolve (Coimbra et al., 2017). To do so, we estimated the angular distance in the retina that corresponds to one cycle by calculating the inverse of the spatial resolving power (cycles/degree). This value was divided by 2 to obtain the minimum angle of resolution (MAR), which represents the angular distance of the smallest resolvable detail on the retina. Subsequently, using the trigonometric relationship between the MAR and a presumed distance (D), relevant, for instance, for foraging a prey or for predator detection, we estimated the minimum object size (obj), according to the equation: $D = obj/tanMar$. According to the Nyquist sampling theorem, because an object needs to be twice the threshold to be spatially resolved, we multiplied the minimum object size by 2 (Marshall, 2000).

Statistical Analysis

Statistical analyzes were performed with R (version 4.0.2)[1] and the RStudio software (1.3.959), to compare the total population and mean densities of retinal neurons among the four sampled groups, adults and juveniles of *B. jararaca* and of *C. durissus*, as well as the retinal area, eyes axial length and visual acuity. The normality of the distribution of values in each group was checked using the Shapiro-Wilk test, and homogeneities among groups were analyzed using the Levene test. The non-parametric test of Mann-Whitney for independent samples was applied for comparisons, even when values had normal distribution, due to the low sampling size in each group. Differences were considered significant when $p < 0.05$.

RESULTS

We analyzed the density and distribution of photoreceptors and GCL cells in 18 retinas of *B. jararaca* (adults: $n = 8$; juveniles: $n = 10$) and 17 retinas of *C. durissus* (adults: $n = 9$; juveniles: $n = 8$) (**Tables 2–4**). The different populations of cones were identified

[1]https://cran.r-project.org/

TABLE 4 | Stereological assessment of the population of GCL cells of adults and juveniles of *B. jararaca* and *C. durissus* and anatomical parameters used to estimate the upper limit of spatial resolution.

Species	Retinal area (mm^2)	Total cells in the GCL	CE	Mean density (cells/mm^2)	Peak density (cells/mm^2)	Minimum density (cells/mm^2)	asf	Eye axial length (mm)	PND mm	Spatial resolution (cpd)	
										Square array	Hexagonal array
B. jararaca											
Bj-A#1-RE	47.8	181,812	0.02	3,804	7,111	533	0.034	5.4	2.7	2.0	2.1
Bj-A#2-RE	39.6	187,201	0.04	4,680	10,489	356	0.029	5.0	2.5	2.3	2.4
Bj-A#4-RE	32.6	152,918	0.04	4,634	9,956	533	0.039	5.1	2.6	2.2	2.4
Bj-A#7-RE	31.8	204,869	0.01	6,402	10,311	533	0.044	4.2	2.1	1.8	2.0
Mean ± sd	38.0 ± 7.4	181,700 ± 21,568	0.03 ± 0.01	4,880 ± 1,092	9,467 ± 1,586	489 ± 89	0.037 ± 0.006	4.9 ± 0.5	2.5 ± 0.3	2.1 ± 0.2	2.2 ± 0.2
Bj-J#1-RE	16.9	157,709	0.03	9,331	17,956	356	0.062	3.2	1.2	2.6	2.7
Bj-J#5-LE	16.6	155,611	0.02	9,374	15,822	533	0.088	2.8	1.1	2.1	2.2
Bj-J#6-LE	19.1	188,770	0.03	9,883	15,487	889	0.060	3.4	1.3	2.4	2.6
Bj-J#7-RE	17.0	161,431	0.02	9,496	16,000	178	0.089	2.7	1.0	2.0	2.2
Bj-J#8-LE	15.5	187,434	0.02	11,715	18,133	533	0.087	3.0	1.1	2.4	2.5
Bj-J#9-LE	15.6	163,733	0.03	10,233	16,711	178	0.082	2.7	1.0	2.0	2.2
Bj-J#10-RE	19.3	172,298	0.02	9,068	14,933	533	0.062	3.0	1.1	2.1	2.3
Mean ± sd	17.1 ± 1.5	169,569 ± 13,730	0.02 ± 0.00	9,871 ± 900	16,435 ± 1,224	457 ± 248	0.076 ± 0.014	3.0 ± 0.2	1.1 ± 0.1	2.2 ± 0.2	2.4 ± 0.2
C. durissus											
Cd-A#3-RE	49.2	221,415	0.03	4,500	9,778	178	0.034	5.2	2.2	2.7	2.9
Cd-A#6-LE	37.5	182,861	0.03	4,876	9,778	356	0.034	5.3	2.2	2.8	3.0
Cd-A#7-RE	49.0	222,181	0.05	4,534	11,022	356	0.021	4.4	1.8	2.4	2.6
Cd-A#8-RE	61.5	234,109	0.03	3,807	7,289	711	0.018	6.1	2.6	2.7	2.9
Mean ± sd	49.3 ± 9.8	215,141 ± 22,291	0.03 ± 0.01	4,429 ± 448	9,467 ± 1,566	400 ± 224	0.027 ± 0.008	5.3 ± 0.7	2.2 ± 0.3	2.6 ± 0.2	2.8 ± 0.2
Cd-J#2-RE	19.6	222,188	0.02	11,336	16,356	2,133	0.060	3.3	1.4	2.2	2.4
Cd-J#3-RE	21.5	193,436	0.03	8,997	14,400	1,422	0.045	3.8	1.6	2.1	2.2
Cd-J#4-LE	21.9	217,938	0.03	9,951	16,178	2,489	0.045	–	–	–	–
Cd-J#7-LE	19.2	192,725	0.03	10,038	16,711	2,489	0.058	3.2	1.4	2.2	2.4
Cd-J#8-LE	23.9	204,274	0.03	8,547	13,156	1,067	0.043	3.2	1.3	1.9	2.1
Mean ± sd	21.2 ± 1.9	206,112 ± 13,616	0.03 ± 0.00	9,774 ± 1,078	15,360 ± 1,522	1,920 ± 646	0.050 ± 0.008	3.4 ± 0.3	1.4 ± 0.1	2.1 ± 0.1	2.3 ± 0.1

sd, standard deviation; CE, Scheaffer's coefficient of error; PND, posterior nodal distance; cpd, cycles per degree; RE, right eye; LE, left eye.

by immunohistochemistry labeling with antibodies against SWS1 and LWS opsins (**Figure 2A**). The total photoreceptor population was viewed under bright light and by adjusting the focus of the microscope into the photoreceptor's inner segments level (**Figure 2B**). Cones and rods were differentiated by the larger diameters of the inner segments of cones compared to the small and highly packed inner segments of rods (Gower et al., 2019; **Figure 2B**). For cell counting in each sampling field, the photoreceptors labeled by the antibodies were counted first, then all photoreceptors (cones and rods) were counted under bright light to analyze the proportion of each photoreceptor type (rods, LWS, and SWS1 cones). Single and double LWS cones were not always easily differentiated from each other and were quantified together (**Figure 2A**).

Population of Photoreceptors

The total population of photoreceptors was estimated from the whole-mounted retinas of *B. jararaca* ($n = 7$) and *C. durissus* ($n = 8$). Adults and juveniles of both species had similar average total photoreceptors values, ranging from 3,092,787 ± 335,242 (median: 3,084,595) to 3,527,539 ± 134,480 (median: 3,585,315) cells in juveniles and adults of *C. durissus*, respectively (**Figure 5** and **Table 2**). The mean density of photoreceptors, however, was higher in juveniles of both species (137,354 ± 28,330 cells/mm^2; median: 128,376 cells/mm^2 in *B. jararaca* and 132,071 ± 13,230 cells/mm^2; median: 125,533 cells/mm^2 in *C. durissus*) compared to adults (73,581 ± 16,205 cells/mm^2; median: 74,724 cells/mm^2 in *B. jararaca* and 76,488 ± 10,400 cells/mm^2; median: 75,540 cells/mm^2 in *C. durissus*) (**Figure 5** and **Table 2**).

Rods were predominant and accounted for approximately 90% of the photoreceptors in retinas of both species (**Table 2**). The total population of rods was similar between adults and juveniles, varying from 2,779,855 ± 291,932 (median: 2,751,033) cells in juveniles of *C. durissus* and 3,182,738 ± 126,107 (median: 3,249,205) cells in adults (**Figure 5** and **Table 2**). The average density of rods was higher in juveniles (128,528 ± 26,347 cells/mm^2; median: 119,446 cells/mm^2 in *B. jararaca* and 118,070 ± 12,448 cells/mm^2; median: 111,759 cells/mm^2 in *C. durissus*) compared to adults (69,488 ± 14,290 cells/mm^2; median: 69,425 cells/mm^2 in *B. jararaca* and 68,844 ± 9,297 cells/mm^2; median: 68,248 cells/mm^2 in *C. durissus*) (**Figure 5** and **Table 2**).

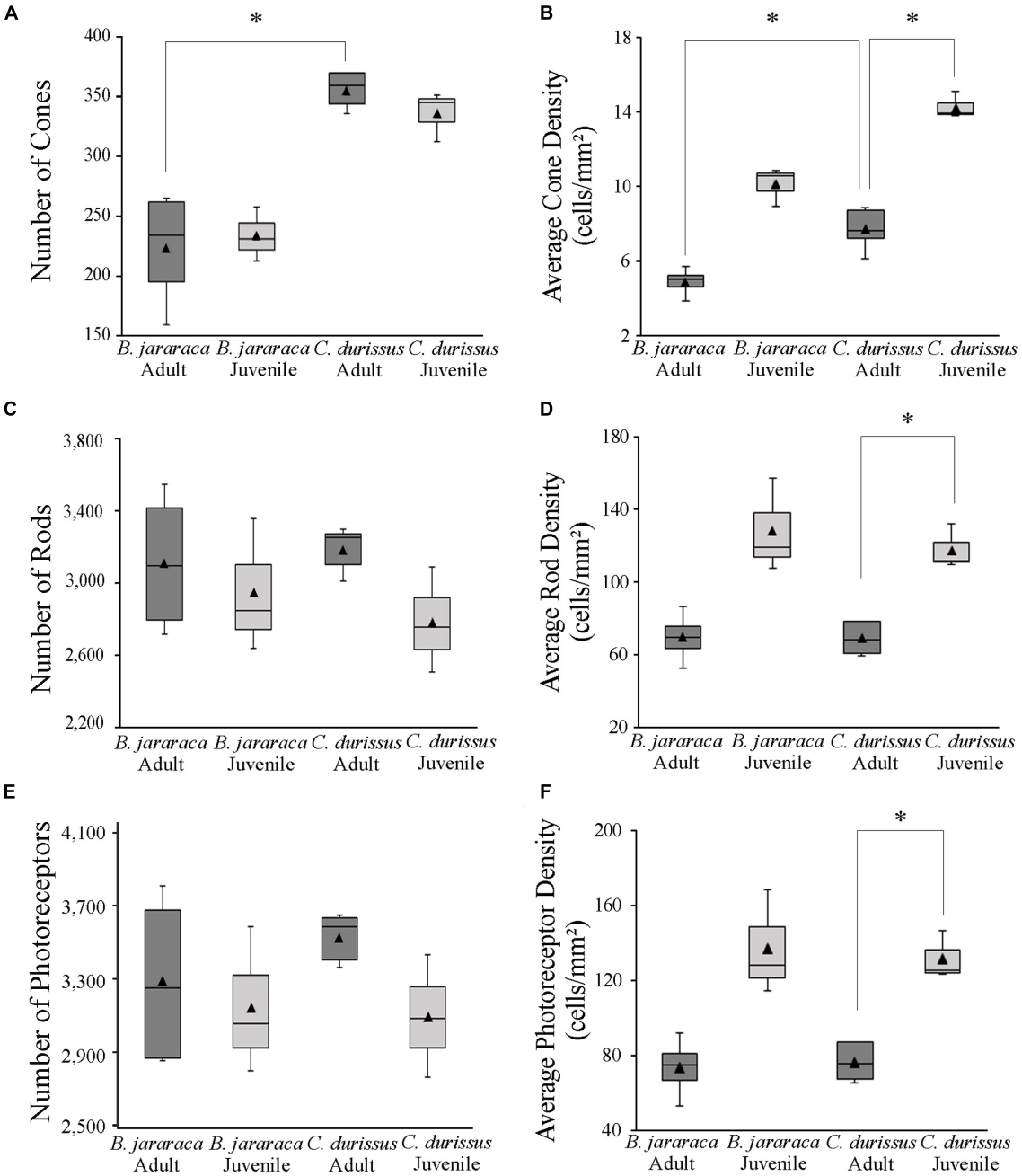

FIGURE 5 | Boxplot representations of the medians (thick black lines) and quartiles (boxes) of the total number and mean density of **(A,B)** cones, **(C,D)** rods, and **(E,F)** photoreceptors in retinas of adults and juveniles of *B. jararaca* and *C. durissus*. Mean density values are represented by the triangles. The values should be multiplied by 10^3. Groups with statistically significant differences are indicated by asterisk (*$p < 0.05$).

The total population of cones represented about 7% of the photoreceptors in *B. jararaca*, and about 10% in *C. durissus* (**Table 2**), and was similar between adults and juveniles, varying from 233,400 ± 22,82 (median: 230,245) cells in juveniles of *B. jararaca* and 355,582 ± 15,403 (median: 359,130) cells in adults of *C. durissus* (**Figure 5** and **Table 2**). The average density of cones was higher in juveniles (10,113 ± 1,044 cells/mm^2; median: 10,559 cells/mm^2 in *B. jararaca* and 14,471 ± 695 cells/mm^2; median: 13,947 cells/mm^2 in *C. durissus*) compared to adults (4,874 ± 765 cells/mm^2; median: 4,993 cells/mm^2 in *B. jararaca* and 7,704 ± 1,132 cells/mm^2; median: 7,654 cells/mm^2 in *C. durissus*) (**Figure 5** and **Table 2**). The mean density of cones was significantly higher in adults of *C. durissus* compared with adults of *B. jararaca* (**Figure 5**).

The population of SWS1 cones accounted for approximately 10% of the cones in retinas of both species (**Table 3**). The

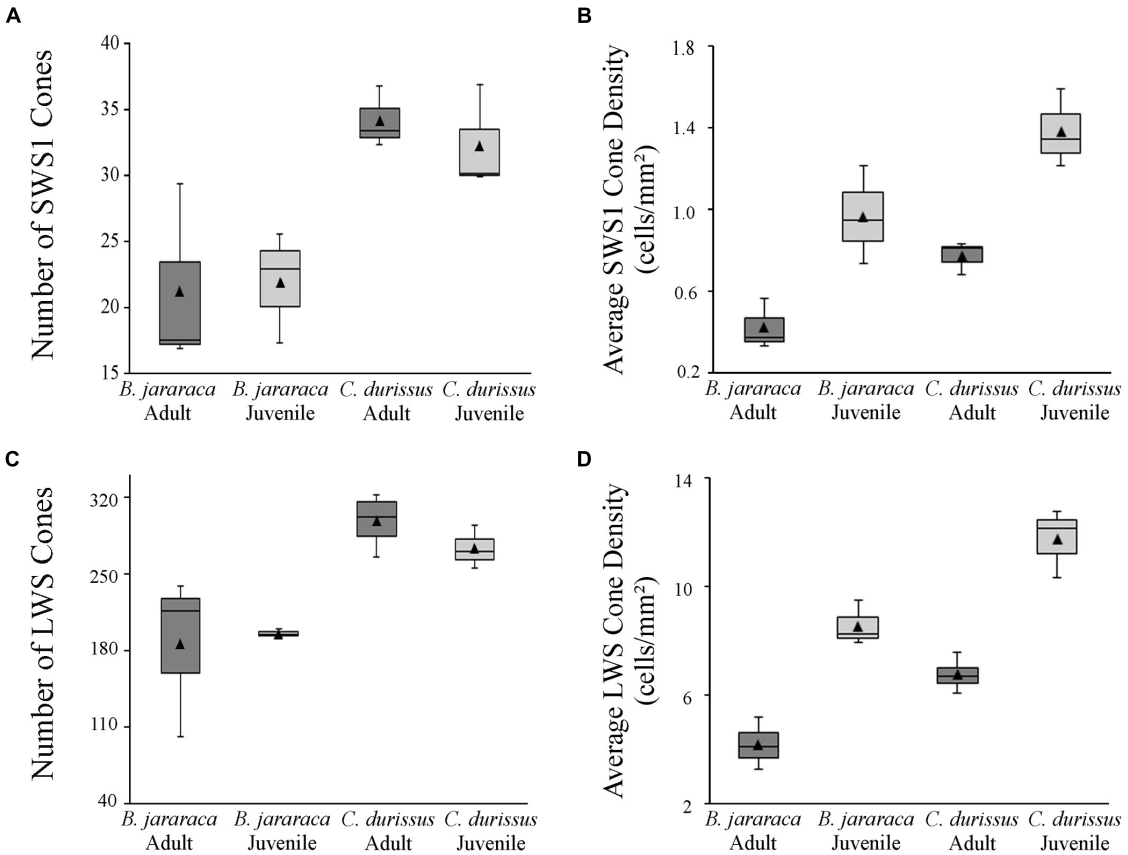

FIGURE 6 | Boxplot representations of the medians (thick black lines) and quartiles (boxes) of the total number and mean density of **(A,B)** small single SWS1 cones and **(C,D)** large single and double LWS cones, in retinas of adults and juveniles of *B. jararaca* and *C. durissus*. The mean density values are represented by the triangles. The values should be multiplied by 10^3.

total population of SWS1 cones was similar between adults and juveniles, and lower in *B. jararaca* (21,655 ± 0,466 cells; adults median: 17,529 cells; juveniles median: 23,007 cells) compared with *C. durissus* (33,354 ± 1,366 cells; adults median: 33,563 cells; juveniles median: 30,126 cells) (**Figure 6** and **Table 3**). The average density was higher in juveniles (960 ± 242 cells/mm^2; median: 943 cells/mm^2 in *B. jararaca* and 1,378 ± 195 cells/mm^2; median: 1,340 cells/mm^2 in *C. durissus*) compared with adults (414 ± 123 cells/mm^2; median: 364 cells/mm^2 in *B. jararaca* and 765 ± 83 cells/mm^2; median: 803 cells/mm^2 in *C. durissus*) (**Figure 6** and **Table 3**).

The LWS cones accounted for approximately 85% of the cones (**Table 3**). The total population of LWS cones was similar between adults and juveniles of both species, and lower in *B. jararaca* (190,022 ± 6,927 cells; adults median: 216,110 cells; juveniles median: 194,195 cells) compared with *C. durissus* (292,585 ± 17,63 cells; adults median: 301,990 cells; juveniles median: 269,625 cells) (**Figure 6** and **Table 3**). In both species the mean density of LWS cones was higher in juveniles (8,466 ± 814 cells/mm^2; median: 8,159 cells/mm^2 in *B. jararaca* and 11,628 ± 1,207 cells/mm^2; median: 12,037 cells/mm^2 in *C. durissus*) compared with adults (4,131 ± 952 cells/mm^2; median: 4,062 cells/mm^2 in *B. jararaca* and 6,683 ± 623 cells/mm^2; median: 6,608 cells/mm^2 in *C. durissus*) (**Figure 6** and **Table 3**).

Photoreceptors Topography

The distribution of photoreceptors showed differences between and within species. In adults of *B. jararaca*, rods and cones were distributed in poorly defined horizontal streaks (**Figure 7** and **Supplementary Figures 1, 2**). In juveniles, rods were concentrated in an anisotropic *area centralis* in the dorsal retina, while cones were concentrated in the ventral retina (**Figure 7** and **Supplementary Figures 1, 2**). Mean density values were estimated from retinal sectors (dorsal, ventral, temporal, and nasal). In adults and juveniles of *B. jararaca*, higher densities of rods were located in the temporal retina. Higher density of cones were located in the ventral retina of juveniles and in the temporal region in adults (**Supplementary Figure 3** and **Supplementary Table 4**). In *C. durissus*, the isodensity maps of rods and cones were similar between adults and juveniles. Rods were concentrated in the dorsal retina in an anisotropic *area centralis*, and cones were organized in poorly defined visual streaks (**Figure 7** and **Supplementary Figures 1, 2**). Density estimates of retinal sectors indicated higher density of rods in the temporal retina of juveniles and in the dorsal retina of adults.

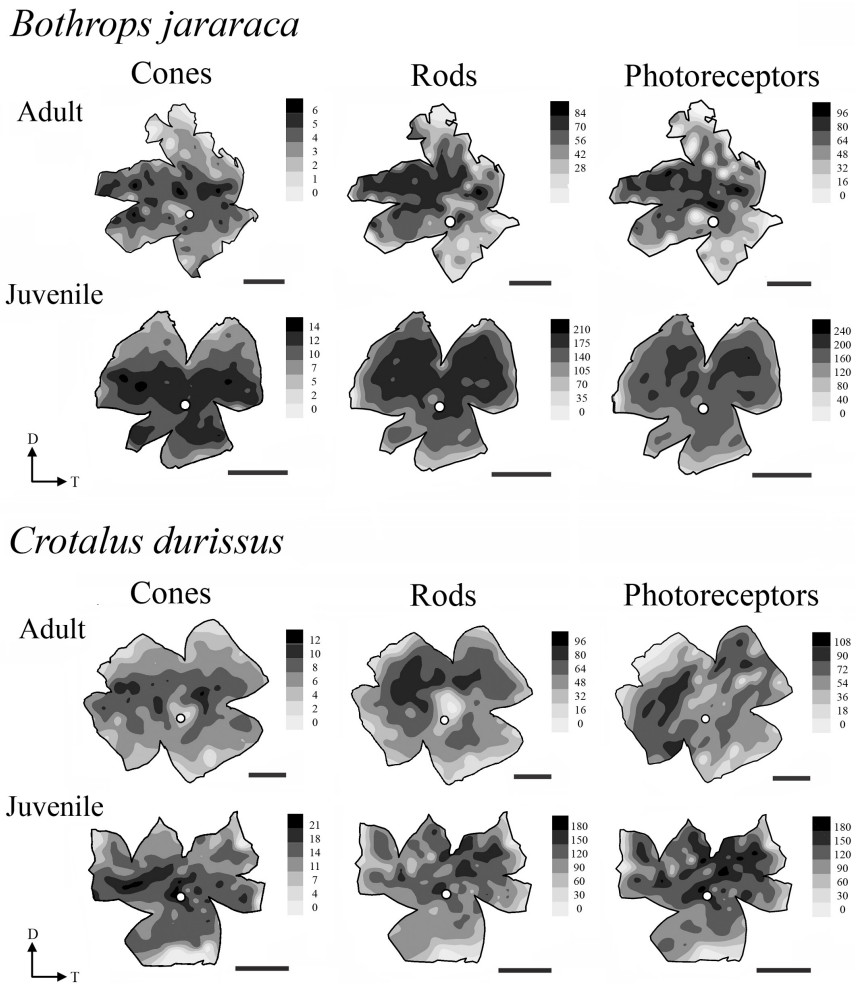

FIGURE 7 | Representative topographic maps of the retinas of *B. jararaca* and *C. durissus*, showing the distribution of cones, rods, and photoreceptors in adults and juveniles. In adults of *B. jararaca*, both rods and cones form poorly defined visual streaks. In juveniles, rods are concentrated in a dorsal *area* and cones in a ventral *area*. In retinas of adults and juveniles of *C. durissus* rods are concentrated in anisotropic *area centralis* in the dorsal retina, and cones are arranged in poorly defined visual streaks. Gray bars indicate the density of cells per mm^2, and the values should be multiplied by 10^3. The optic nerve head is depicted as a white circle. D, dorsal; T, temporal. Scale bars 2 mm.

Cones had higher densities in the temporal region in adults and in the nasal region in juveniles (**Supplementary Figure 3** and **Supplementary Table 4**). In both species, the SWS1 cones showed diffuse distributions, with peak densities located in the central or ventral retina (**Figure 8** and **Supplementary Figure 4**). The distribution of LWS cones in the retinas of adults and juveniles of both species was similar to that observed for the distribution of total cones, with poorly defined visual streaks in adults of both species and in juveniles of *C. durissus*, and a higher concentration of LWS cones in the central and ventral retina of juveniles of *B. jararaca* (**Figure 8** and **Supplementary Figure 5**).

Ganglion Cell Layer Cells and Estimates of the Spatial Resolving Power

The population of GCL cells was estimated from 11 retinas of *B. jararaca* (adults: $n = 4$, juveniles: $n = 7$) and 9 retinas of *C. durissus* (adults: $n = 4$, juveniles: $n = 5$) (**Table 4**). The total population of GCL cells was similar between adults and juveniles of both species, ranging from 169,569 ± 13,730 (median: 163,733) cells in juveniles of *B. jararaca* and 215,141 ± 22,291 (median: 221,798) cells in adults of *C. durissus* (**Figure 9** and **Table 4**). The average density of GCL cells was significantly higher in retinas of juveniles (9,871 ± 900 cells/mm^2; median: 9,496 cells/mm^2 in *B. jararaca* and 9,774 ± 1,078 cells/mm^2; median: 9,951 cells/mm^2 in *C. durissus*) compared with adults (4,880 ± 1,092 cells/mm^2; median: 4,657 cells/mm^2 in *B. jararaca* and 4,429 ± 448 cells/mm^2; median: 4,517 cells/mm^2 in *C. durissus*) (**Figure 9** and **Table 4**). In the four groups analyzed, the isodensity maps of GCL cells did not show defined distribution patterns (**Figure 10** and **Supplementary Figure 6**). In retinas of adults and juveniles of *C. durissus* and adults of *B. jararaca*, we observed diffuse distributions and peak density of cells in the temporal retina (**Figure 10** and

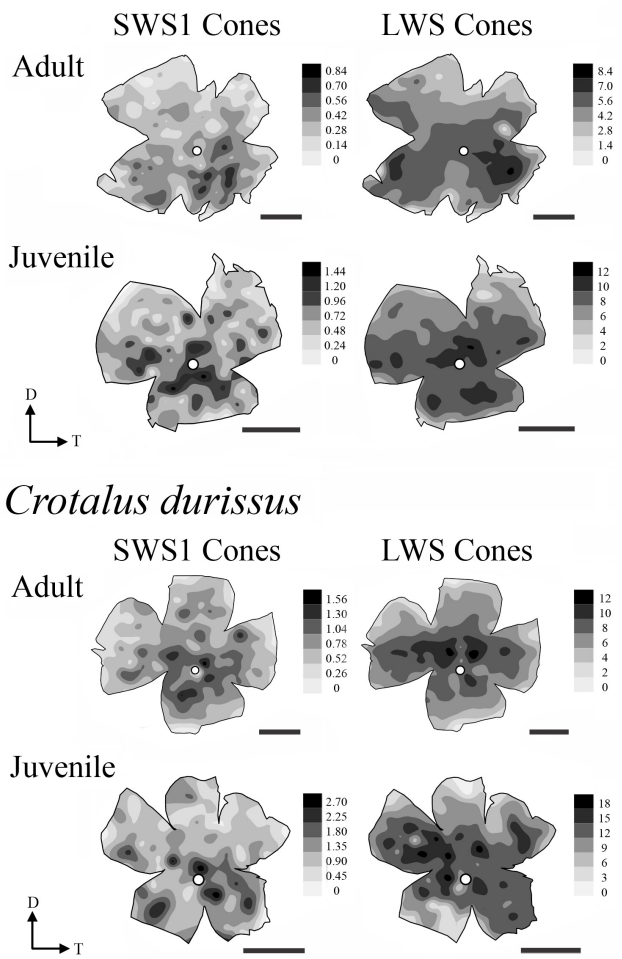

FIGURE 8 | Representative retinal topographic maps of small single SWS1 cones and large single and double LWS cones of adults and juveniles of *B. jararaca* and *C. durissus*. Gray bars indicate the density of cells per mm^2, and values should be multiplied by 10^3. The optic nerve head is depicted as a white circle. D, dorsal; T, temporal. Scale bars 2 mm.

Supplementary Figure 6). In juveniles of *B. jararaca* the GCL cells were concentrated in the ventral retina with a decreasing ventral-dorsal gradient and peak density located in the ventral area (**Figure 10** and **Supplementary Figure 6**). Density estimates in retinal sectors showed higher values in the temporal retina of adults and juveniles of *C. durissus* and adults of *B. jararaca* (**Supplementary Figure 3** and **Supplementary Table 5**). In juveniles of *B. jararaca*, higher densities were located in the ventral retinas (**Supplementary Figure 3** and **Supplementary Table 5**), in agreement with the observed isodensity maps (**Figure 10** and **Supplementary Figure 6**).

The theoretical upper limits of spatial resolving power were estimated based on the ganglion cell peak densities using two approaches, one considering that the ganglion cells are organized in a hexagonal array and the other considering a square array. Adults and juveniles of *B. jararaca* had similar estimated visual acuity values, with 2.2 ± 0.2 cycles per degree (cpd) (median: 2.3 cpd) and 2.4 ± 0.2 cpd (median: 2.3 cpd), respectively (**Figure 9** and **Table 4**). In *C. durissus* the estimated visual acuity was significantly higher in adults, with 2.8 ± 0.2 cpd (median: 2.9 cpd), compared to juveniles, with 2.3 ± 0.1 cpd (median: 2.3 cpd) (**Figure 9** and **Table 4**). The estimated acuity values of adults of *C. durissus* were also significantly higher than of adults of *B. jararaca* (**Figure 9** and **Table 4**).

From the estimated visual acuity values we calculated the minimum angle of resolution. The estimated distance relevant for predatory behavior was calculated considering the tangent of the minimum angle of resolution and minimum target size. For species with the lowest (2.2 cpd) and highest (2.8 cpd) spatial resolving power, we estimated a minimum angle of resolution of 0.45° and 0.36°. In an ecological context, snakes with lower estimated spatial resolution can observe an object with a minimum size of 10 cm, such as a small mammal, at a distance of approximately 13 m. Snakes with the higher presumed spatial resolution might be able to observe an object of the same size at a distance of about 17 m. These estimates indicate that at these predicted distances objects larger than the minimum target size can be spatially detected.

DISCUSSION

In this study, we analyzed the density and distribution of neurons in whole-mounted retinas of Viperidae snakes, considering an ontogenetic approach. Our analyzes revealed a predominance of rods in the outer retinas of *Bothrops jararaca* and *Crotalus durissus*, and three distinct populations of cones: single and double cones containing the LWS photopigment and single cones containing the SWS1 photopigment, as previously described for viperids (Walls, 1942; Underwood, 1967b; Bittencourt et al., 2019; Gower et al., 2019). Our results showed that the two species have similar density values of photoreceptors and GCL cells. However, the distribution of these neurons differed between species and between juveniles and adults of *B. jararaca*, pointing to a reorganization of the retinal architecture that might be associated with the ontogenetic changes in the niche occupied and hunting strategies, as summarized in **Figure 11**.

Photoreceptor Population

The retinas of *B. jararaca* and *C. durissus* had a high proportion of rods (about 90% of the photoreceptors) (**Figure 5** and **Table 2**), which indicates high sensitivity to light, in agreement with their nocturnal or crepuscular activity pattern (Martins et al., 2001; Fiorillo et al., 2020b). Previous studies described the predominance of rods in retinas of viperid snakes based on analysis of retinal sections (Walls, 1934, 1942; Underwood, 1967b; Bittencourt et al., 2019; Gower et al., 2019) and fragments of flat-mounted retinas (Gower et al., 2019). Snakes stand out among vertebrates by their highly variable patterns of photoreceptor morphology (Walls, 1942). In the Caenophidia group ("advanced" snakes), nocturnal species from different families, including viperids, have four types of photoreceptors,

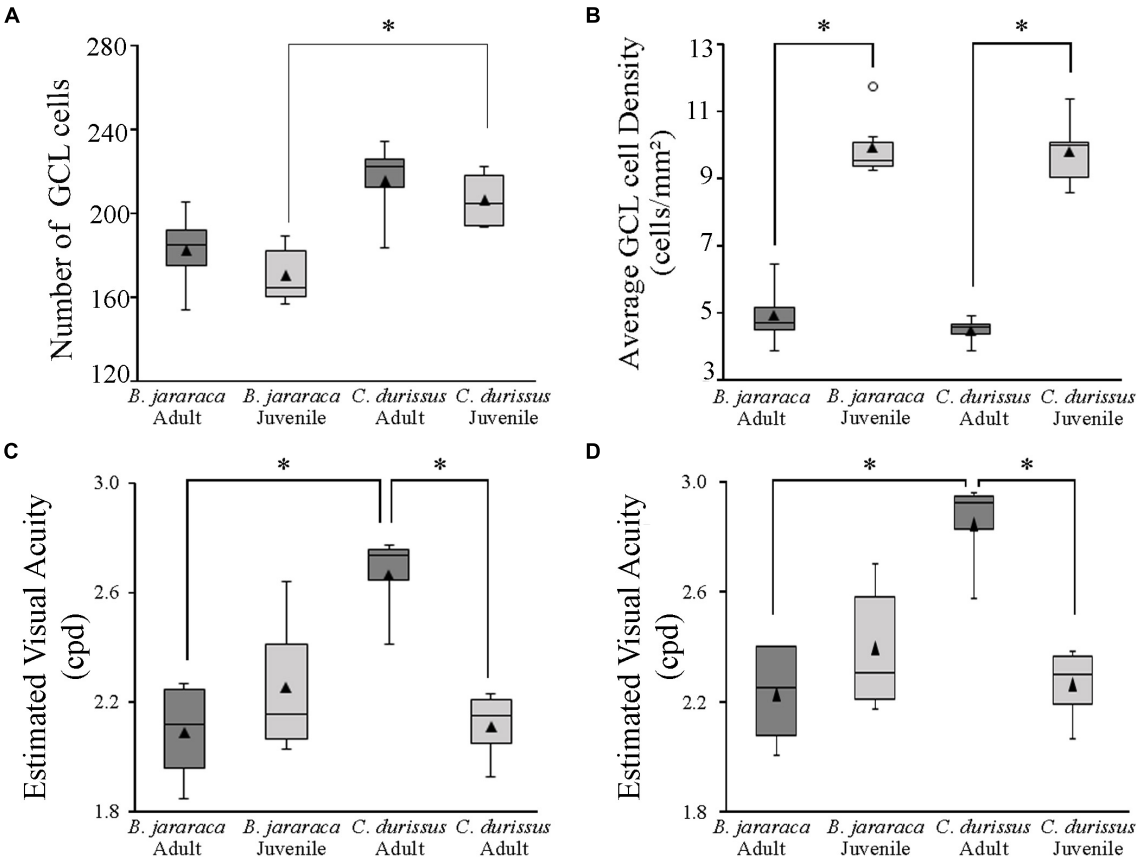

FIGURE 9 | Boxplot representations of the medians (thick black lines) and quartiles (boxes) of **(A)** the total number of GCL cells and **(B)** the mean density of GCL cells in adults and juveniles of *B. jararaca* and *C. durissus*. The values in **(A,B)** should be multiplied by 10^3. The open circle in **(B)** indicates an outlier value. Boxplots showing the estimated visual acuity considering **(C)** a square array of the ganglion cells, and **(D)** a hexagonal array of ganglion cells, in adults and juveniles of *B. jararaca* and *C. durissus*. The mean densities are represented by the triangles. Groups with statistically significant differences are indicated by asterisk (*$p < 0.05$).

with a unique type of double cone that differs from double cones of other vertebrates, with a large principal member and an extremely slender and attached accessory member (Walls, 1942). On the other hand, diurnal caenophidian snakes have "pure-cone" retinas, with the absence of typical rods, the presence of a transmuted cone-like rod, and lower photoreceptor density compared to nocturnal species (Walls, 1942; Schott et al., 2016; Hauzman et al., 2017; Hauzman, 2020).

The comparison of the populations of cones and rods in *B. jararaca* and *C. durissus* showed a higher proportion of cones in retinas of *C. durissus* (10% in juveniles and adults) compared to *B. jararaca* (7.5% in juveniles and 6.5% in adults) (**Figure 5** and **Table 2**). This difference, although subtle, might reflect functional differences in temporal and spatial resolution between both species, which agree with the habitat occupied. *C. durissus* inhabit predominantly open areas of the Cerrado, with higher incidence of light (Miranda et al., 1997) compared to the closed forested areas predominantly occupied by *B. jararaca* (McWilliam et al., 1993; de Paula and Lemos Filho, 2001). In both species, the population of cones is dominated by large single cones and double cones that contain the LWS photopigment (about 80–90%) (**Figure 6** and **Table 3**), with spectral sensitivity peak (λ_{max}) predicted at 555 nm (Bittencourt et al., 2019). Small single cones with the SWS1 photopigment comprise about 10% of the cone population (**Figure 6** and **Table 3**), with λ_{max} predicted at the UV range (360–370 nm) in both species (Bittencourt et al., 2019). Gower et al. (2019) identified double cones with the SWS1 photopigment in retinas of two viperid snakes, *Echis coloratus* and *C. durissus*, a unique type of photoreceptor described for the first time in vertebrates. However, in our analysis of whole-mounted retinas, this type of cone was not identified, and all double cones observed were found to contain only the LWS photopigment (**Figure 2**).

The distribution of photoreceptors differed between *C. durissus* and *B. jararaca* and between juveniles and adults of *B. jararaca* (**Figure 7**). In *C. durissus*, the visual streak formed by cones might reflect a better panoramic view of the environment under photopic conditions (**Figure 7**). This specialization might benefit scanning of the environment while searching for shelters for body temperature control during the day, a frequent behavior of snakes that occupy open environments where they are subject to overheating (Tozetti and Martins, 2008). On the other hand, the higher density of rods in the dorsal retina (**Figure 7**) might improve light sensitivity in the lower

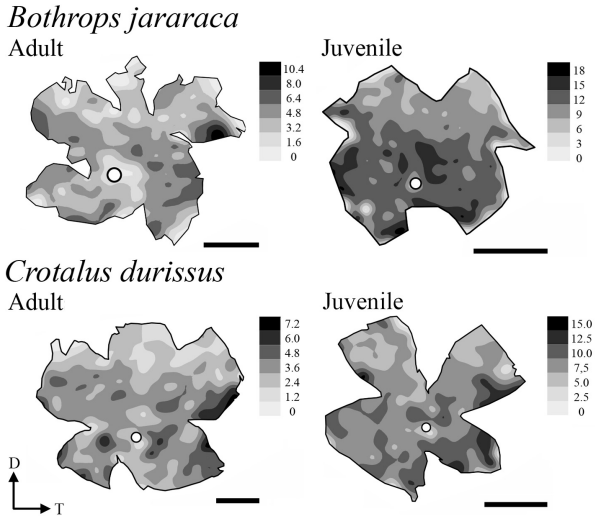

FIGURE 10 | Representative retinal topographic maps of the GCL cells of adults and juveniles of *B. jararaca* and *C. durissus*. Gray bars indicate the density of cells per mm^2, and the values should be multiplied by 10^3. The optic nerve head is depicted as a white circle. D, dorsal; T, temporal. Scale bars 2 mm.

visual field, possibly favoring foraging behavior and searching for rodents during twilight and at night. These patterns of distribution of cones and rods were found in both, juveniles and adults of *C. durissus* (**Figures 7**, **11**).

In *B. jararaca*, ontogenetic changes in the niche occupied seem to be associated with plasticity of the retinal architecture. In juveniles, a higher density of cones was observed in the ventral retina (**Figures 7**, **11**), a specialization that might provide higher acuity in the upper visual field. Oppositely, a higher density of rods in the dorsal retina might benefit the view of the lower visual field under scotopic conditions (**Figure 7**). Juveniles of *B. jararaca* occupy the arboreal stratum and use sit-and-wait and caudal luring as hunting strategies. Therefore, it is plausible to speculate that the difference in the distribution of cones and rods might be associated with the direction of predation pressure. Cones located in a ventral *area* might favor the view of aerial predators, such as diurnal birds approaching from above during the day (**Figure 11**) (Sazima, 1992; Costa et al., 2014). Higher concentration of rods in the dorsal retina might benefit the view of terrestrial predators, such as marsupials, approaching from below, during the night (**Figure 11**) (Emmons, 1990; Sazima, 1992; Jared et al., 1998; Oliveira and Santori, 1999). Compared to terrestrial snakes, arboreal species display a higher number of defensive tactics, which is likely associated with greater exposure to predators approaching from a variety of directions (Martins et al., 2008).

Adults of *B. jararaca* occupy terrestrial environments, lose the caudal luring, and actively forage for endothermic prey (Sazima, 1992, 2006). Their retinas have cones and rods distributed in poorly defined visual streaks, a specialization that benefits the panoramic view of the terrestrial forested stratum under photopic and scotopic conditions (**Figures 7**, **11**). A similar distribution of cones was described in terrestrial, arboreal and semiaquatic colubrids (Hauzman, 2014; Hauzman et al., 2014), indicating that this specialization is widely observed in snakes and might contribute to active foraging behavior in different environments. As far as we are aware, this is the first description of a horizontal streak formed by rods in the retinas of snakes.

The distribution of LWS cones (single and double) was similar to the distribution of total cones in both species, as expected based on their high proportion (**Figure 8**). The distribution of SWS1 cones did not show a defined pattern of specialization. Higher densities of SWS1 cones were found in the ventral and central retina in adults and juveniles of both species (**Figure 8**), as described for diurnal colubrid snakes (Hauzman et al., 2014). This distribution might favor the view of potential aerial predators approaching from the upper visual field, as many bird species are important predators of snakes (Martins and Oliveira, 1998; Tozetti, 2006; Specht et al., 2008; Costa et al., 2014). Higher densities of UV cones were also described in the ventral retina of mammals (Szél et al., 1992, 1994; Famiglietti and Sharpe, 1995; Peichl et al., 2005; Huber et al., 2010). In mice, UV cones contribute to chromatic discrimination of the upper visual field (Szatko et al., 2020), and might be relevant for visualizing the silhouette of aerial predators against the blue sky background (Calderone and Jacobs, 1995; Szél et al., 1992).

Density and Topography of Ganglion Cell Layer Cells and Estimates of the Visual Acuity

The mean density of GCL cells was similar between *B. jararaca* and *C. durissus*. However, juveniles had higher average density values compared to adults (**Figure 9** and **Table 4**). This difference can be attributed to the increase in the area of the retina. Juveniles have smaller retinas and thus, higher cell packaging. As the animals grow, the eye increases, such as the retinal area, but the cell population remains constant, resulting in lower density values. A higher GCL cell density in juveniles compared to adults was also described in fish (Hagedorn and Fernald, 1992; Bailes et al., 2006), birds (Straznicky and Chehade, 1987), amphibians (Nguyen and Straznicky, 1989), and mammals (Robinson et al., 1989). Considering there is no neuron loss or additional generation of cells in the GCL, we suggest the increase of retinal area followed by the decrease of cell density is associated with interstitial growth, as described for chicken retinas (Straznicky and Chehade, 1987). It is notable that in *Bothrops jararaca* these changes in cell density are associated with rearrangements of the cell distribution.

The distribution of GCL cells was similar between adults and juveniles of *C. durissus*, with no defined type of specialization, and with peak density of cells in the temporal retina (**Figures 10**, **11**). This specialization might benefit the view of the frontal field and favor strike performance of endothermic prey. The same topographic pattern of GCL cells was found in retinas of adults of *B. jararaca* (**Figures 10**, **11**). The visual information arriving in the midbrain, from the projections of this temporal specialization might be combined with infrared information from the loreal pit, a thermosensory organ of Crotalinae snakes located between the eyes and the nostrils (Noble and Schmidt, 1973). The nerve

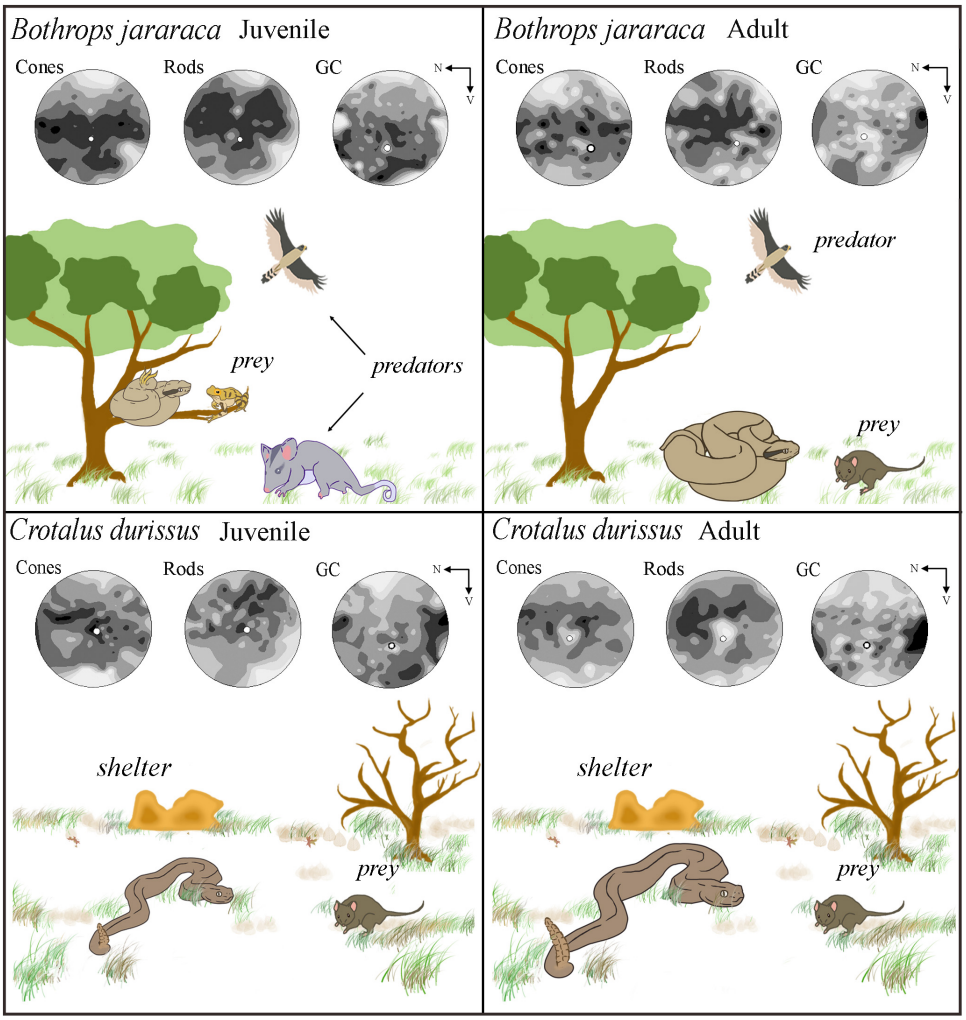

FIGURE 11 | Schematic diagram illustrating the niche occupied by adults and juveniles of *Bothrops jararaca* and *Crotalus durissus*, and the distribution of neurons in the retinas of each species. **(Upper panel)** *B. jararaca* inhabits forested areas and has ontogenetic changes in diet, behavior, and microhabitat occupied. Juveniles are arboreal, feed on ectothermic prey (attracted by caudal luring), and are susceptible to predation pressure coming from different directions. A higher density of cones and GCL cells in the ventral retina might benefit the view of aerial predators under photopic conditions. A higher density of rods in the ventral retina might favor the view of terrestrial predators in the lower visual field under scotopic conditions. Adults are terrestrial and actively hunt for endothermic prey. Cones and rods are distributed in poorly defined visual streaks, and GCL cells have higher densities in the temporal retina. These specializations might benefit the panoramic view of the environment under photopic and scotopic conditions and of strike performances. **(Lower panel)** Adults and juveniles of *C. durissus* occupy open environments (Cerrado) and feed on endothermic prey. In both, cones form poorly defined visual streaks that might benefit scanning the environment to search for shelters for body temperature control during the day to avoid overheating, a usual behavior in snakes that occupy open areas. The higher density of rods in the dorsal retina might favor foraging behavior at scotopic conditions. The peak density of GCL cells in the temporal retina might benefit the view of the frontal field and favor strike performances. N, nasal; V, ventral.

terminals of the loreal pit cells project to the optic tectum in the midbrain (Newman and Hartline, 1982), where the visual and thermosensory inputs are combined, allowing an integrated perception from ultra-violet to infrared wavelengths (Newman and Hartline, 1981; Moiseenkova et al., 2003; Goris, 2011), important in both scotopic and photopic conditions. During the night, thermal detection enables the perception of temperature changes. During the day, discrimination of infrared information may be compromised due to higher temperatures (Chen et al., 2012), yielding predominance of perceptual information to visual inputs.

In juveniles of *B. jararaca* the higher density of GCL cells in the ventral retina is in agreement with the distribution of cones (**Figures 8**, **10**, **11**), which indicates a higher convergence from cones to GCs in this region (from approximately 4:1 in the periphery, to ∼1:1 in the *area centralis*), enabling higher spatial resolution in the upper visual field. A similar distribution pattern of GCL cells, with higher density in the ventral retina was observed in the dipsadid snakes *Dipsas albifrons* and *Sibynomorphus neuwiedi* (Hauzman et al., 2018). Both species are nocturnal, semi-arboreal, and feed on ectothermic prey (gooeaters) (Maia et al., 2011; Sazima and Muscat, 2016), such as

juveniles of *B. jararaca*. Thus, we suggest that this type of specialization might be associated with the niche occupied by snakes, the direction of predatory threats, and particularities of hunting strategies, which do not involve active foraging of fast moving prey (**Figure 11**). Reorganization of the distribution of GCL cells according to ontogenetic changes in ecology and behavior was also described in frogs (Dunlop and Beazley, 1981) and in fish (Shand, 1997; Bozzano and Catalan, 2002; Miyazaki et al., 2011). In the fish *Acanthopagrus butcheri*, the retinas of juveniles have a temporal *area centralis*, which favors object detection in the frontal visual field and might be important for feeding on plankton in pelagic waters. On the other hand, adults occupy the benthic environment. This ecological switch is accompanied by a displacement of the *area* toward the dorsal or dorso-temporal retina, which might increase acuity in the lower-frontal visual field and benefit their hunting strategies for the capture of small fish, polychaete worms and detritus obtained from the benthos (Shand et al., 2000).

The estimated upper limits of spatial resolving power based on the peak cell density of GCL cells of the viperid snakes varied from 2 to 3 cpd (**Table 4**). These values were similar to those estimated for diurnal dipsadid snakes of the genus *Philodryas* spp. (Hauzman et al., 2014) and for the marine elapid *Aipysurus laevis* (Hart et al., 2012), with spatial resolution between 2.3 and 2.6 cpd, and were higher than the values estimated for nocturnal dipsadids, with about 1.3 cpd (Hauzman et al., 2018). Our comparisons showed slightly higher estimated visual acuity in adults of *C. durissus* compared to the other groups analyzed (**Figure 9**). We predicted that the estimated visual acuity of ∼2.3 cpd of adults and juveniles of *B. jararaca* and juveniles of *C. durissus* would allow the view of potential prey such as rodents, at a minimum size of 10 cm, at a distance of about 13 m. On the other hand, adults of *C. durissus* with estimated visual acuity at ∼2.8 cpd, might be able to detect the same minimum object size at a higher distance, about 17 m. These estimates also indicate that these snakes can have a high capability to observe potential predators such as birds of prey (Martins and Oliveira, 1998; Tozetti, 2006; Specht et al., 2008; Costa et al., 2014) at longer distances. However, behavioral analyzes are necessary to confirm if the estimated values of spatial resolution based on anatomical data are reached, and to ascertain whether the differences imply functional significance, relevant to the species ecology and visual behavior.

CONCLUSION

Interspecific differences in the density and distribution of retinal neurons were identified in the viperid snakes *B. jararaca* and *C. durissus*. Rod-dominated retinas represent a functional advantage associated with the nocturnal activity pattern of both species. The higher proportion of cones in *C. durissus* might represent an adaptation to the open and brighter Cerrado environment. This study showed for the first time in snakes that ontogenetic changes in ecology and behavior are associated with morphological plasticity of the retinas. We suggest that the differences in the niche occupied, hunting strategies, prey type, and direction of approach of predatory threats are reflected in reorganizations of the distribution of retinal neurons between juveniles and adults of *B. jararaca*. In comparison, the absence of variation in neuron distribution patterns in retinas of *C. durissus* throughout life agrees with the maintenance of the same ecological and behavioral traits in juveniles and adults. These results highlight the importance of retinal specializations for the performance of visually guided behaviors, and how habitat use and hunting strategies might represent relevant ecological forces that shape the retinal architecture in snakes. Future behavioral studies should be applied to verify functional implications of the retinal organizations as well as the estimated upper limits of spatial resolving power, between 2 and 3 cpd. In addition, the patterns of neuronal connections in the retina rely on a highly intricate network for visual processing. The results of this study open up a new avenue for future analysis on the connectivity patterns of the inner retina of Viperidae snakes.

DATA AVAILABILITY STATEMENT

The original contributions presented in the study are included in the article/**Supplementary Material**, further inquiries can be directed to the corresponding author/s.

ETHICS STATEMENT

The animal study was reviewed and approved by the Ethics Committee of Animal Research of the Psychology Institute, University of São Paulo, Brazil.

AUTHOR CONTRIBUTIONS

EH conceived the study. DV obtained the funding. JT and EH performed the research and wrote the manuscript. JT, EH, and DV analyzed the data. All authors contributed to manuscript revision and approved the submitted version.

FUNDING

This work was supported by the São Paulo Research Foundation (FAPESP) with grants to JT (2018/13910-9), EH (2014/25743-9, 2018/09321-8), and DV (2014/26818-2), the Brazilian National Research Council (CNPq), with a grant to DV (309409/2015-2) and EH (163302/2020), and the Coordination for the Improvement of Higher Education Personnel (CAPES), with a grant to JT (88887.601346/2021-00).

ACKNOWLEDGMENTS

We thank Giuseppe Puorto, Felipe Gobbi Grazziotin, Adriana Mezini, Karina Banci, and Kathleen Fernandes Grego for animals' provision, and Kalena Barros da Silva and Valdir Germano for assistance with snakes' handling. We thank Dania Emi

Hamasaki for providing reagents. We are grateful to Carola A. M. Yovanovich and Marcio R. C. Martins for valuable discussions, and Fernando A. F. Rocha and Marcelo F. Costa for methodological contributions. We also acknowledge the two reviewers for their valuable suggestions.

SUPPLEMENTARY MATERIAL

The Supplementary Material for this article can be found online at: https://www.frontiersin.org/articles/10.3389/fnana.2021.770804/full#supplementary-material

REFERENCES

Almeida-Santos, S. M. (2005). *Modelos Reprodutivos Em Serpentes: Estocagem De Esperma E Placentação Em Crotalus Durissus E Bothrops Jararaca. Ph. D, Thesis*. Universidade de São Paulo.

Baden, T., Euler, T., and Berens, P. (2020). Understanding the retinal basis of vision across species. *Nat. Rev. Neurosci.* 21, 5–20. doi: 10.1038/s41583-019-0242-1

Bailes, H. J., Trezise, A. N., and Collin, S. P. (2006). The number, morphology, and distribution of retinal ganglion cells and optic axons in the *Australian lungfish Neoceratodus forsteri* (krefft 1870). *Vis. Neurosci.* 23, 257–273. doi: 10.1017/S0952523806232103

Barros, V. A. (2011). *Biologia Reprodutiva De Três Espécies De Serpentes Da Família Viperidae Da Região Neotropical São José Do Rio Preto. Ph. D, Thesis*. Universidade Estadual Paulista "Júlio de Mesquita Filho".

Bittencourt, G. B., Hauzman, E., Bonci, D. M. O., and Ventura, D. F. (2019). Photoreceptors morphology and genetics of the visual pigments of *Bothrops jararaca* and *Crotalus durissus* terrificus (serpentes, viperidae). *Vis. Res.* 158, 72–77. doi: 10.1016/j.visres.2019.02.006

Bozzano, A., and Catalan, I. A. (2002). Ontogenetic changes in the retinal topography of the European hake, *Merluccius merluccius*: implications for feeding and depth distribution. *Mar. Biol.* 141, 549–559. doi: 10.1007/s00227-002-0840-7

Calderone, J. B., and Jacobs, G. H. (1995). Regional variations in the relative sensitivity to uv light in the mouse retina. *Vis. Neurosci.* 12, 463–468. doi: 10.1017/S0952523800008361

Caprette, C. L. (2005). *Conquering The Cold Shudder: The Origin and Evolution of Snakes Eyes Ph. D, Thesis*. The Ohio State University.

Chen, Q., Deng, H., Brauth, S. E., Ding, L., and Tang, Y. (2012). Reduced performance of prey targeting in pit vipers with contralaterally occluded infrared and visual senses. *PLoS One* 7:1–8. doi: 10.1371/journal.pone.0034989

Chen, Q., Liu, Y., Brauth, S. E., Fang, G., and Tang, Y. (2017). The thermal background determines how the infrared and visual systems interact in pit vipers. *J. Exp. Biol.* 220, 3103–3109. doi: 10.1242/jeb.155382

Coimbra, J. P., Hart, N. S., Collin, S. P., and Manger, P. R. (2013). Scene from above: Retinal ganglion cell topography and spatial resolving power in the giraffe (giraffa camelopardalis). *J. Comp. Neurol.* 521, 2042–2057. doi: 10.1002/cne.23271

Coimbra, J. P., Nolan, P. M., Collin, S. P., and Hart, N. S. (2012). Retinal ganglion cell topography and spatial resolving power in penguins. *Brain. Behav. Evol.* 80, 254–268. doi: 10.1159/000341901

Coimbra, J. P., Pettigrew, J. D., Kaswera-Kyamakya, C., Gilissen, E., Collin, S. P., and Manger, P. R. (2017). Retinal ganglion cell topography and spatial resolving power in African megachiropterans: influence of roosting microhabitat and foraging. *J. Comp. Neurol.* 525, 186–203. doi: 10.1002/cne.24055

Coimbra, J. P., Trévia, N., Marceliano, M. L. V., Andrade-Da-Costa, B. L., da, S., Picanço-Diniz, C. W., et al. (2009). Number and distribution of neurons in the retinal ganglion cell layer in relation to foraging behaviors of tyrant flycatchers. *J. Comp. Neurol.* 514, 66–73. doi: 10.1002/cne.21992

Coimbra, J. P., Videira Marceliano, M. L., Da Silveira Andrade-Da-Costa, B. L., and Yamada, E. S. (2006). The retina of tyrant flycatchers: topographic organization of neuronal density and size in the ganglion cell layer of the great kiskadee *Pitangus sulphuratus* and the rusty margined flycatcher *Myiozetetes cayanensis* (aves: tyrannidae). *Brain. Behav. Evol.* 68, 15–25. doi: 10.1159/000092310

Collin, S. P. (2008). A web-based archive for topographic maps of retinal cell distribution in vertebrates: invited paper. *Clin. Exp. Optom.* 91, 85–95. doi: 10.1111/j.1444-0938.2007.00228.x

Costa, H. C., Lopes, L. E., Marçal, B. D. F., and Zorzin, G. (2014). The reptile hunter's menu: a review of the prey species of laughing falcons, *Herpetotheres cachinnans* (aves: falconiformes). *North. West. J. Zool.* 10, 445–453.

de Moraes, R. A. (2008). *Variações Em Caracteres Morfológicos E Ecológicos Em Populações De Bothrops Jararaca (Serpentes: Viperidae) No Estado De São Paulo Ph. D, Thesis*. Universidade de São Paulo.

de Paula, S. A., and Lemos Filho, J. P. (2001). Dinâmica do dossel em mata semidecídua no perímetro urbano de belo horizonte, MG. *Rev. Bras. Botânica* 24, 545–551. doi: 10.1590/s0100-84042001000500009

Dunlop, S. A., and Beazley, L. D. (1981). Changing retinal ganglion cell distribution in the frog heleioporus eyrei. *J. Comp. Neurol.* 202, 221–236. doi: 10.1002/cne.902020208

Emmons, L. H. (1990). *Neotropical Rainforest Mammals*. Chicago: The University of Chicago Press.

Famiglietti, E. V., and Sharpe, S. J. (1995). Regional topography of rod and immunocytochemically characterized " blue " and " green " cone photoreceptors in rabbit retina. *Vis. Neurosci.* 12, 1151–1175. doi: 10.1017/s0952523800006799

Fiorillo, B. F., Tozetti, A. M., and Martins, M. (2020a). Habitat use by five species of sympatric pitvipers (bothrops, crotalus) in a brazilian savannah. *Herpetol. Notes* 13, 951–960.

Fiorillo, B. F., da Silva, B. R., Menezes, F. A., Marques, O. A. V., and Martins, M. (2020b). Composition and natural history of snakes from etá farm region, sete barras, south-eastern brazil. *Zookeys* 931, 115–153. doi: 10.3897/zookeys.931.46882

Goris, R. C. (2011). Infrared organs of snakes: an integral part of vision. *J. Herpetol.* 45, 2–14. doi: 10.1670/10-238.1

Gower, D. J., Sampaio, F. L., Peichl, L., Wagner, H. J., Loew, E. R., McLamb, W., et al. (2019). Evolution of the eyes of vipers with and without infrared-sensing pit organs. *Biol. J. Linn. Soc.* 126, 796–823. doi: 10.1093/biolinnean/blz003

Gundersen, H. J. G. (1997). Notes on the estimation of the numerical density of arbitrary profiles: the edge efect. *J. Microsc.* 111, 219–223. doi: 10.1039/AN9244900130

Hagedorn, M., and Fernald, R. D. (1992). Retinal growth and cell addition during embryogenesis in the teleost, haplochromis burtoni. *J. Comp. Neurol.* 321, 193–208. doi: 10.1002/cne.903210203

Hart, N. S., Coimbra, J. P., Collin, S. P., and Westhoff, G. (2012). Photoreceptor types, visual pigments, and topographic specializations in the retinas of hydrophiid sea snakes. *J. Comp. Neurol.* 520, 1246–1261. doi: 10.1002/cne.22784

Hartline, P., Kass, L., and Loop, M. (1978). Merging of modalities in the optic tectum: infrared and visual integration in rattlesnakes. *Science* 199, 1225–1229. doi: 10.1126/science.628839

Hauzman, E. (2014). *Ecologia e Evolução do Sistema Visual De Serpentes Caenophidia: Estudos Comparativos da Morfologia Retiniana e Genética de Opsinas Ph. D, Thesis*. Universidade de São Paulo.

Hauzman, E. (2020). Adaptations and evolutionary trajectories of the snake rod and cone photoreceptors. *Semin. Cell Dev. Biol.* 106, 86–93. doi: 10.1016/j.semcdb.2020.04.004

Hauzman, E., Bonci, D. M. O., Grotzner, S. R., Mela, M., Liber, A. M. P., Martins, S. L., et al. (2014). Comparative study of photoreceptor and retinal ganglion cell topography and spatial resolving power in dipsadidae snakes. *Brain Behav. Evol.* 84, 197–213. doi: 10.1159/000365275

Hauzman, E., Bonci, D. M. O., Suárez-Villota, E. Y., Neitz, M., and Ventura, D. F. (2017). Daily activity patterns influence retinal morphology, signatures of selection, and spectral tuning of opsin genes in colubrid snakes. *BMC Evol. Biol.* 17:1–14. doi: 10.1186/s12862-017-1110-0

Hauzman, E., Bonci, D. M. O., and Ventura, D. F. (2018). "Retinal topographic maps: a glimpse into the animals' visual world," in *Sensory Nervous System*, Vol. 1, ed. T. Heinbockel (London: IntechOpen), 101–126. doi: 10.5772/intechopen.74645

Huber, G., Heynen, S., Imsand, C., vom Hagen, F., Muehlfriedel, R., Tanimoto, N., et al. (2010). Novel rodent models for macular research. *PLoS One* 5:403. doi: 10.1371/journal.pone.0013403

Hughes, A. (1977). "The topography of vision in mammals of contrasting life style: comparative optics and retinal organisation," in *The Visual System in Vertebrates*, ed. F. Crescitelli (New York: Springer-Verlag), 613–756. doi: 10.1007/978-3-642-66468-7_11

Jared, C., Antoniazzi, M. M., and Almeida-Santos, S. M. (1998). Predation of snakes by the young of opossum (*Didelphis marsupialis*) in captivity. *Snake* 28, 68–70.

Lisney, T. J., and Collin, S. P. (2008). Retinal ganglion cell distribution and spatial resolving power in elasmobranchs. *Brain Behav. Evol.* 2008, 59–77. doi: 10.1159/000146082

Maia, T., Dorigo, T. A., Gomes, S. R., Santos, S. B., and Rocha, C. F. D. (2011). *Sibynomorphus neuwiedi* (ihering, 1911) (serpentes; dipsadidae) and *Potamojanuarius lamellatus* (Semper, 1885) (gastropoda; veronicellidae): a trophic relationship revealed. *Biotemas* 25, 211–213. doi: 10.5007/2175-7925.2012v25n1p211

Marques, O. A. V., and Sazima, I. (2004). "História natural dos répteis da estação ecológica juréia," in *Estação Ecológica Juréia-Itatins: Ambiente Físico, Flora e Fauna*, eds W. Marques and O. A. V. Duleba (Holos: Ribeirão Preto), 257–277.

Marshall, N. J. (2000). Communication and camouflage with the same "bright" colours in reef fishes. *Philos. Trans. R. Soc. L B Biol. Sci.* 355, 1243–1248. doi: 10.1098/rstb.2000.0676

Martins, M. and Oliveira, M. E. (1998). Natural history of snakes in forests of the Manaus region, Central Amazonia, Brazil, *Herpetol. Nat. Hist.* 6, 78–150.

Martins, M., Araujo, M. S., Sawaya, R. J., and Nunes, R. (2001). Diversity and evolution of macrohabitat use, body size and morphology in a monophyletic group of neotropical pitvipers (bothrops). *J. Zool.* 254, 529–538. doi: 10.1017/S0952836901001030

Martins, M., Marques, O. A. V., and Sazima, I. (2008). How to be arboreal and diurnal and still stay alive: microhabitat use, time of activity, and defense in neotropical forest snakes. *South Am. J. Herpetol.* 3, 58–67.

McWilliam, A. L. C., Roberts, J. M., Cabral, O. M. R., Leitao, M. V. B. R., de Costa, A. C. L., Maitelli, G. T., et al. (1993). Leaf area index and above-ground biomass of terra firme rain forest and adjacent clearings in Amazonia. *Funct. Ecol.* 7, 310–317.

Miranda, A. C., Miranda, H. S., Lloyd, J., Grace, J., Francey, R. J., Mcintyre, J. A., et al. (1997). Fluxes of carbon, water and energy over brazilian cerrado: an analysis using eddy covariance and stable isotopes. *Plant Cell Envinoment* 20, 315–328. doi: 10.1046/j.1365-3040.1997.d01-80.x

Miyazaki, T., Iwami, T., and Meyer-Rochow, V. B. (2011). The position of the retinal area centralis changes with age in *Champsocephalus gunnari* (channichthyidae), a predatory fish from coastal Antarctic waters. *Polar Biol.* 34, 1117–1123. doi: 10.1007/s00300-011-0969-2

Moiseenkova, V., Bell, B., Motamedi, M., Wozniak, E., and Christensen, B. (2003). Wide-band spectral tuning of heat receptors in the pit organ of the copperhead snake (Crotalinae). *Am. J. Physiol. Regul. Integr. Comp. Physiol.* 284, 598–606. doi: 10.1152/ajpregu.00024.2002

Moore, B. A., Tyrrell, L. P., Kamilar, J. M., Collin, S. P., Dominy, N. J., Hall, M. I., et al. (2017). "Structure and function of regional specializations in the vertebrate retina," in *Evolution of Nervous Systems*, 2nd Edn. ed. J. H. Kaas, and G. Striedter (Amsterdam: Elsevier), 149–172. doi: 10.1016/b978-0-12-804042-3.00008-7

Newman, E. A., and Hartline, P. H. (1981). Integration of visual and infrared information in bimodal neurons of the rattlesnake optic tectum. *Science* 213, 789–791. doi: 10.1126/science.7256281

Newman, E. A., and Hartline, P. H. (1982). The infrared "vision" of snakes. *Sci. Am.* 246, 116–127. doi: 10.1038/scientificamerican0382-116

Nguyen, V. S., and Straznicky, C. (1989). The development and the topographic organization of the retinal ganglion cell layer in *Bufo marinus*. *Exp. Brain Res.* 75, 345–353. doi: 10.1007/BF00247940

Noble, G. K., and Schmidt, A. (1973). The structure and function of the facial and labial pits of snakes. *Am. Philos. Soc.* 77, 263–288.

Oliveira, M. E., and Santori, R. T. (1999). Predatory behavior of the opossum didelphis albiventris on the pitviper bothrops jararaca. *Stud. Neotrop Fauna Environm* 34, 72–75.

Peichl, L. E. O., Chavez, A. E., Ocampo, A., Mena, W., Bozinovic, F., and Palacios, A. G. (2005). Eye and vision in the subterranean rodent cururo (spalacopus cyanus, octodontidae). *J. Comput. Neurol.* 208, 197–208. doi: 10.1002/cne.20491

Pettigrew, J. D., Dreher, B., Hopkins, C. S., McCall, M. J., and Brown, M. (1998). Peak density and distribuition of ganglion cells in the retinae of microchiropteran bats: implications for visual acuity. *Brain Behav. Evol.* 32, 39–56. doi: 10.1159/000116531

Ramón y Cajal, S. (1983). La rétine des vertebrés. *Cellule* 9, 17–257.

Reiserer, R. S. (2002). Stimulus control of caudal luring and other feeding responses: a program for research on visual perception in vipers. *Biol. Vipers* 132, 361–383.

Robinson, S. R., Dreher, B., and McCall, M. J. (1989). Nonuniform retinal expansion during the formation of the rabbit's visual streak: implications for the ontogeny of mammalian retinal topography. *Vis. Neurosci.* 2, 201–219. doi: 10.1017/S0952523800001139

Salomão, M. D. G., Almeida Santos, S. M., and Puorto, G. (1995). Activity pattern of crotalus durissus (viperidae, crotalinae): feeding, reproduction and snakebite. *Stud. Neotrop. Fauna Environ.* 30, 101–106. doi: 10.1080/01650529509360946

Sawaya, R. J., Marques, O. A. V., and Martins, M. (2008). Composition and natural history of a cerrado snake assemblage at itirapina, são paulo state, southeastern Brazil. *Biota Neotrop.* 8, 127–149. doi: 10.1590/S1676-06032008000200015

Sazima, I. (1991). Caudal luring in two neotropical pitvipers, *Bothrops Jararaca and B. Jararacacussu*. *Copeia* 1991, 245–248.

Sazima, I. (1992). Natural history of jararaca pitviper, *Bothrops jararaca* in southeastern, Brazil. *Syst. Biol.* 42, 596. doi: 10.2307/2992495

Sazima, I. (2006). Theatrical frogs and crafty snakes: predation of visually-signalling frogs by tail-luring and ambushing pitvipers. *Aqua (Miradolo Terme)* 11, 117–124.

Sazima, I., and Abe, A. S. (1991). Habits of five brazilian snakes with coral-snake pattern, including a summary of defensive tactics. *Stud. Neotrop. Fauna Environ.* 26, 159–164. doi: 10.1080/01650529109360848

Sazima, I., and Muscat, E. (2016). Shelled baby food: newly hatched goo-eating snakes of the genus dipsas (squamata: dipsadidae) prey on snails in nature. *Herpetol. Bras.* 85, 63–64. doi: 10.1186/1471

Scheaffer, R., Mendenhall, W., and Ott, L. (1996). *Elementary Survey Sampling*, 5th Edn. Boston: PWS-Kent.

Schott, R. K., Müller, J., Yang, C. G. Y., Bhattacharyya, N., Chan, N., Xu, M., et al. (2016). Evolutionary transformation of rod photoreceptors in the all-cone retina of a diurnal garter snake. *Proc. Natl. Acad. Sci. U.S.A.* 113, 356–361. doi: 10.1073/pnas.1513284113

Schraft, H. A., and Clark, R. W. (2019). Sensory basis of navigation in snakes: the relative importance of eyes and pit organs. *Anim. Behav.* 147, 77–82. doi: 10.1016/j.anbehav.2018.11.004

Shand, J. (1997). Ontogenetic changes in retinal structure and visual acuity: a comparative study of coral-reef teleosts with differing post-settlement lifestyles. *Environ. Biol. Fishes* 49, 307–322. doi: 10.1023/A:1007353003066

Shand, J., Chin, S. M., Harman, A. M., Moore, S., and Collin, S. P. (2000). Variability in the location of the retinal ganglion cell area centralis is correlated with ontogenetic changes in feeding behavior in the black bream, acanthopagrus butcheri (sparidae, teleostei). *Brain Behav. Evol.* 55, 176–190. doi: 10.1159/000006651

Snyder, A. W., and Miller, W. H. (1977). Photoreceptor diameter and spacing for highest resolving power. *J. Opt. Soc. Am.* 67, 227–244. doi: 10.1364/josa.67.000696

Specht, G., Mesquita, E. P., and Santos, F. A. (2008). Breeding biology of laughing falcon herpetotheres cachinnans (linnaeus, 1758) (falconidae) in southeastern Brazil. *Rev. Bras. Ornitol.* 16, 155–159.

Straznicky, C., and Chehade, M. (1987). The formation of the area centralis of the retinal ganglion cell layer in the chick. *Development* 100, 411–420. doi: 10.1242/dev.100.3.411

Szatko, K. P., Korympidou, M. M., Ran, Y., Berens, P., Dalkara, D., Schubert, T., et al. (2020). Neural circuits in the mouse retina support color vision in the upper visual field. *Nat. Commun.* 11:3481. doi: 10.1038/s41467-020-17113-8

Szél, Á, Csorba, G., Caffé, A. R., Szél, G., Röhlich, P., and van Veen, T. (1994). Different patterns of retinal cone topography in two genera of rodents, mus and apodemus. *Cell Tissue Res.* 276, 143–150. doi: 10.1007/bf00354793

Szél, R. P., Gaffé, A. R., Juliusson, B., Aguirre, G., and Van Veen, T. (1992). Unique topographic separation of two spectral classes of cones in the mouse retina. *J. Comp. Neurol.* 325, 327–342. doi: 10.1002/cne.903250302

Tozetti, A. M. (2006). *Uso Do Ambiente, Atividade E Ecologia Alimentar Da Cascavel (Crotalus Durissus) Em Área De Cerrado Na Região De Itirapina, SP. Ph. D, Thesis*. Universidade de São Paulo.

Tozetti, A. M., and Martins, M. (2008). Habitat use by the south-American rattlesnake (crotalus durissus) in south-eastern Brazil. *J. Nat. Hist.* 42, 1435–1444. doi: 10.1080/00222930802007823

Tozetti, A. M., and Martins, M. (2013). Daily and seasonal activity patterns of free range south-American rattlesnake (crotalus durissus). *An. Acad. Bras. Cienc.* 85:43. doi: 10.1590/S0001-37652013005000043

Uetz, P., Freed, P., and Hošek, J. (2020). *The Reptile Database*. Available online at: reptile-database.org. (accessed July 1, 2020).

Underwood, G. (1967a). A Comprehensive approach to the classification of higher snakes. *Herpetologica* 23, 161–168.

Underwood, G. (1967b). *A Contribution to the Classification of Snakes*. London: Trust. Br. Museum.

Underwood, G. (1970). "The eye," in *Biology of the Reptilia: morphology*, eds C. Gans and T. S. Parsons (New York: Academic Press), 97.

Walls, G. L. (1934). The reptilian retina. I. a new concept of visual-cell evolution. *Am. J. Ophthalmol.* 17, 892–915. doi: 10.1016/S0002-9394(34)93309-2

Walls, G. L. (1942). The vertebrate eye and its adaptive radiation. *Optom. Vis. Sci.* 151:236.

West, M. J., Slomianka, L., Gundersen, H. J. G., West, M. J., Slomianka, L., and Gundersen, H. J. G. (1991). Unbiased stereological estimation of the total number of neurons in the subdivisions of the rat hippocampus using the optical using the optical fractionator. *Anat. Rec.* 231, 482–497. doi: 10.1002/ar.1092310411

Wong, R. O. (1989). Morphology and distribution of neurons in the retina of the American garter snake thamnophis sirtalis. *J. Comput. Neurol.* 283, 587–601. doi: 10.1002/cne.902830412

Conflict of Interest: The authors declare that the research was conducted in the absence of any commercial or financial relationships that could be construed as a potential conflict of interest.

Publisher's Note: All claims expressed in this article are solely those of the authors and do not necessarily represent those of their affiliated organizations, or those of the publisher, the editors and the reviewers. Any product that may be evaluated in this article, or claim that may be made by its manufacturer, is not guaranteed or endorsed by the publisher.

frontiers in Neuroanatomy

ORIGINAL RESEARCH
published: 04 February 2022
doi: 10.3389/fnana.2022.813369

Immunohistochemical Characterisation of the Whale Retina

Noelia Ruzafa[1,2], Xandra Pereiro[1,2] and Elena Vecino[1,2]**

[1] Experimental Ophthalmo-Biology Group (GOBE), Department of Cell Biology and Histology, University of Basque Country UPV/EHU, Leioa, Spain, [2] Begiker-Ophthalmology Research Group, Biocruces Health Research Institute, Cruces Hospital, Bilbao, Spain

The eye of the largest adult mammal in the world, the whale, offers a unique opportunity to study the evolution of the visual system and its adaptation to aquatic environments. However, the difficulties in obtaining cetacean samples mean these animals have been poorly studied. Thus, the aim of this study was to characterise the different neurons and glial cells in the whale retina by immunohistochemistry using a range of molecular markers. The whale retinal neurons were analysed using different antibodies, labelling retinal ganglion cells (RGCs), photoreceptors, bipolar and amacrine cells. Finally, glial cells were also labelled, including astrocytes, Müller cells and microglia. Thioflavin S was also used to label oligomers and plaques of misfolded proteins. Molecular markers were used to label the specific structures in the whale retinas, as in terrestrial mammalian retinas. However, unlike the retina of most land mammals, whale cones do not express the cone markers used. It is important to highlight the large size of whale RGCs. All the neurofilament (NF) antibodies used labelled whale RGCs, but not all RGCs were labelled by all the NF antibodies used, as it occurs in the porcine and human retina. It is also noteworthy that intrinsically photosensitive RGCs, labelled with melanopsin, form an extraordinary network in the whale retina. The M1, M2, and M3 subtypes of melanopsin positive-cells were detected. Degenerative neurite beading was observed on RGC axons and dendrites when the retina was analysed 48 h post-mortem. In addition, there was a weak Thioflavin S labelling at the edges of some RGCs in a punctuate pattern that possibly reflects an early sign of neurodegeneration. In conclusion, the whale retina differs from that of terrestrial mammals. Their monochromatic rod vision due to the evolutionary loss of cone photoreceptors and the well-developed melanopsin-positive RGC network could, in part, explain the visual perception of these mammals in the deep sea.

Keywords: retina, whale, cetacean, visual system, evolutionary neuroscience, glia, neuron, retinal ganglion cell (RGC)

OPEN ACCESS

Edited by:
Marta Agudo-Barriuso, Biomedical Research Institute of Murcia (IMIB), Spain

Reviewed by:
Lies De Groef, KU Leuven, Belgium
Matthew Alan Smith, Northeast Ohio Medical University, United States

****Correspondence:***
Noelia Ruzafa
noelia.ruzafa@ehu.eus
Elena Vecino
elena.vecino@ehu.eus

Received: *11 November 2021*
Accepted: *10 January 2022*
Published: *04 February 2022*

Citation:
Ruzafa N, Pereiro X and Vecino E (2022) Immunohistochemical Characterisation of the Whale Retina. Front. Neuroanat. 16:813369. doi: 10.3389/fnana.2022.813369

INTRODUCTION

Cetaceans are a mammalian group that contains some of the largest animals on Earth and they offer a unique opportunity to investigate the adaptations of the visual system to the aquatic environment. However, despite its importance, the cetacean visual system has been little studied, and the morphological and anatomical characteristics of the eyes and retina of various cetacean

species remain completely unknown. We assume that studying the structure and morphological features of the retina of these large mammals may help us to understand the adaptation of their vision to the deep sea.

The analysis of retinal ganglion cells (RGCs), the neurons that transmit visual information from the retina to the brain, has been analysed in a variety of cetacean species in order to estimate their visual acuity. The visual acuity appear to be similar in most marine cetaceans and the retinal resolving power is lower than in terrestrial mammals (Murayama et al., 1992; Murayama and Somiya, 1998). Moreover, it is noteworthy to point out that the RGCs named giant cells, the cell body reaches up to 75 μm in diameter (Dawson et al., 1982; Mengual et al., 2015). Due to the enormous size of these cetaceans, their giant RGCs and their very long axons, it was deemed necessary to analyse the neurofilament (NF) expression in the RGCs. The NFs are the predominant intermediate filament proteins in neurons, and they are assemblies of three subunits that form heteropolymeric filaments that are running along the length of the axon, and in the soma, primarily serving a structural function. Not all neurons have the same combination of NF subunits and there are clear differences between species (Ruiz-Ederra et al., 2004). Here, the expression of different RGC markers, including NFs, has been analysed for the first time in the largest animals in the world.

Melanopsin is the visual pigment expressed by a small subset of RGCs, intrinsically photosensitive retinal ganglion cells (ipRGCs). These ipRGCs are mainly implicated in non-image forming functions such as regulation of circadian rhythms or activation of the pupillary light reflex (Lax et al., 2019). Genetic analyses, coupled with molecular modelling, predict that cetacean melanopsin possesses a nearly identical absorption spectra to that of terrestrial mammals (Fasick and Robinson, 2016). However, relatively little is known of the role of melanopsin and ipRGCs in cetaceans.

In addition to RGCs, photoreceptors respond to light, and they have also been studied in cetacean retinas. Most terrestrial mammals have colour vision based on the different visual pigments in the cone photoreceptors. Among terrestrial mammals, the absence of cone-based colour vision is rare and is generally restricted to nocturnal animals. However, a range of marine mammals have consistently demonstrated the absence of S-cones, including toothed whales. However, unlike the terrestrial cone monochromats, these marine mammals have phases of daylight activity. Thus, the evolutionary convergent loss of S-cones in marine species may offer an adaptive advantage in the marine environment (Peichl et al., 2001).

Understanding the visual system of cetaceans is of great interest in comparative anatomy and physiology. Thus, here we present a complete morphological analysis of the retina of two Balaenoptera species. In addition to studying their RGCs and photoreceptors, other retinal cells were also analysed, including ipRGCs, as well as bipolar and amacrine cells. In addition, the glial cells that support and protect the retinal neurons were also analysed, including astrocytes, Müller cells, and microglia. In addition, rat and pig retinas were used to compare the whale retina with that of terrestrial mammals to obtain a more complete characterisation of cetacean retinas.

MATERIALS AND METHODS

Eye Samples and Tissue Collection

The eyes of beached *Balaenoptera physalus* and *Balaenoptera borealis* whales ($n = 2$, one eye from each whale), were extracted and studied for 24 and 48 h post-mortem, respectively. The ocular globes, after extraocular muscles were removed, weigh approximately 1 kg. The eyes were cut down to half and were fixed overnight in 4% paraformaldehyde (PFA) prepared in 0.1 M phosphate buffer (PB, pH 7.4) at 4°C. The retinas were extracted after fixation. Most of the results presented here were obtained from *B. physalus* retina, which was in better condition, although these results were corroborated with the *B. borealis* retina.

The whale retinas were divided into four different disc shaped areas at different distances from the optic nerve: centre (a 2-cm thick band near the optic nerve), middle-centre (a 2.5 cm thick band outside the centre band), middle-periphery (a 2.5 cm thick band adjacent to the middle-centre band), and periphery (a 2 cm thick band at the edge of the retina and the furthest from the optic nerve; **Figure 1**). At least three pieces of each region that were taken along the dorsal axis were analysed. The different retinal regions were then cut into pieces of approximately 1 cm^2 for immunostaining and analysis. To obtain the sections, the retinal tissue, from the four retinal areas described in **Figure 1**, was cryoprotected for 24 h in 30% sucrose in 0.1 M PB at 4°C and embedded in Tissue-Tek O.C.T. compound (Sakura, Netherlands), and the cryosections (14 μm thick) were then stored at −20°C.

Adult porcine eyes were obtained from a local slaughterhouse and transported to the laboratory in cold CO_2-independent

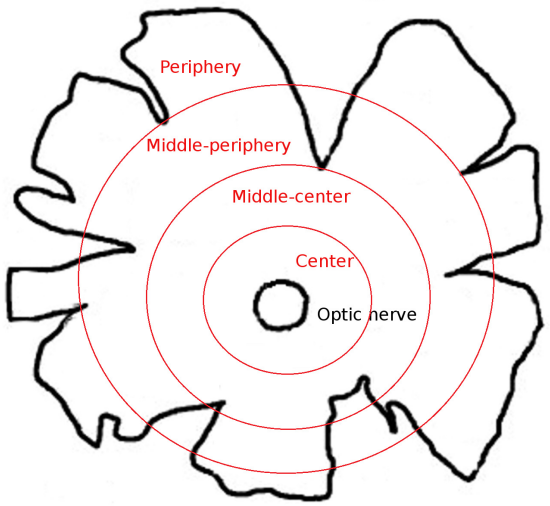

FIGURE 1 | Scheme of the whale retinal areas. Scheme of a whale retina in which the four different areas of the retina are represented as concentric circles in red. The areas were classified based on their distance from the optic nerve: center, a 2-cm thick band near the optic nerve; middle-center, a 2.5-cm thick band outside the center band; middle-periphery, a 2.5-cm thick band adjacent to the middle-center band; and periphery, a 2-cm thick band at the edge of the retina and the furthest from the optic nerve.

medium (Life Technologies, Carlsbad, CA, United States) plus 0.1% gentamicin. Adult Sprague Dawley rat eyes were obtained from animals that were housed under a 12-h light–dark cycle with *ad libitum* access to food and water and were humanely sacrificed by exposure to CO_2. To obtain the whole-mount retina, the eyes were dissected, the entire retina was isolated, and the retinas were fixed in 4% PFA. To obtain the sections, whole eyes were fixed in 4% PFA overnight and cryoprotected for 24 h in 30% sucrose in 0.1 M phosphate buffer at 4°C, finally the eyes were embedded in OCT medium. Cryosections (14 μm thick) were obtained and stored at –20°C.

Animal experimentation adhered to the association for research in vision and ophthalmology (ARVO) Statement for the Use of Animals in Ophthalmic and Vision Research. Moreover, all the experimental protocols complied with the European (2010/63/UE) and Spanish (RD53/2013) regulations regarding the protection of experimental animals, and they were approved by the Ethics Committee for Animal Welfare at the University of the Basque Country.

Immunochemistry and Image Capture

Whole mount retinas were immunostained as described previously (Ruzafa et al., 2018), with minor modifications. The flat fixed retinal tissue was washed in phosphate-buffered saline (PBS, pH 7.4) and non-specific binding was blocked by incubating them overnight at 4°C with shaking in a solution of PBS-Tx + BSA (0.25% Triton-X 100 and 1% bovine serum albumin in PBS). The retina was then incubated for 1 day at 4°C with the primary antibodies (**Table 1**) diluted in PBS-Tx + BSA, after which they were washed three times in PBS for 15 min, and antibody binding was detected over 5 h at room temperature (RT) with shaking using secondary antibodies diluted 1:1,000 in PBS + BSA (1%): Alexa Fluor 555 or 488 conjugated goat anti-mouse, goat anti-rabbit, or donkey anti-goat antibodies (Invitrogen, Eugene, OR, United States). Finally, the retinal tissue was washed three times for 10 min in PBS, flat-mounted onto slides in PBS:glycerol (1:1) and cover slipped.

Retinal cryostat sections were immunostained as described previously (Ruzafa et al., 2017). The sections were washed twice with PBS-Tx for 10 min, and then incubated overnight with primary antibodies diluted in PBS-Tx + BSA. After two washes with PBS, antibody binding was detected for 1 h with aforementioned secondary antibodies (Invitrogen) diluted 1:1,000 in PBS + BSA (1%). The sections were then washed twice with PBS for 10 min, mounted in PBS: glycerol (1:1), and cover slipped.

Thioflavin S (ThS) staining was also performed on these retinas after their incubation with the secondary antibodies. The ThS (Sigma–Aldrich, St. Louis, MO, United States) was kindly provided by Estibaliz Capetillo, and it was diluted 1:250 in PB (pH 7.4) and filtered. The retinas were incubated with ThS for 15 min and then washed three times with PB for 5 min with shaking. Finally, the retinas were washed three times with PBS for 10 min, mounted on slides in PBS: glycerol (1:1) and cover slipped.

Images were acquired with a digital camera (Zeiss Axiocam MRM, Zeiss, Jena, Germany), coupled to an epifluorescence microscope (Zeiss) using the Zen software (Zeiss). Approximately 10X and 20X objectives were used. For cell quantification, the contour of the retina was measured and the retinal surface area was calculated using an automated multi-image acquisition using a motorised microscope stage and the Zen software. In the same piece of retina, at least three different areas between 10 and 15 mm^2 were analysed and different pieces of retina for each region were used. The number of RGCs was counted manually and the cell density was calculated (RGCs/mm^2, represented as the mean of the different analysed areas). The total retinal area was calculated measuring the retina after its extraction and the total RGC density was estimated after the quantified RGC density in different areas. In addition, the longest diameter of RGCs was measured using the Zen software, after taking pictures of at least 25 RGCs from each region. In order to quantify the different subtypes of melanopsin, whole-mount retinas of RGCs were used, the fine adjustment knob of the microscope was continually used during the manual quantification in order to determine the dendrites stratification of these cells. For that, RNA-binding protein with multiple splicing (RBPMS) labelling was used as reference for the ganglion cell layer (GCL).

TABLE 1 | Primary antibodies used.

Antigen	Target	Host	Dilution	Supplier
βIII Tubulin	RGCs	Mouse	1:2,000	Promega
Brn3a	RGCs	Goat	1:1,000	Santa Cruz Biotechnology
Calbindin	Amacrine cells	Mouse	1:1,000	Swant
Calretinin	Amacrine cells	Rabbit	1:1,000	Sigma
CRALBP	Müller cells	Rabbit	1:1,000	Abcam
GFAP	Astrocytes	Mouse	1:1,000	Sigma
Glutamine synthetase	Müller cells	Rabbit	1:10,000	Abcam
Human Cone arrestin	Cones	Rabbit	1:10,000	William Beltran's Lab
Iba-1	Microglia	Rabbit	1:2,000	Wako
Melanopsin	ipRGCs	Rabbit	1:1,000	Thermo Scientific
NF-L	RGCs	Rabbit	1:5,000	Sigma
NF-M	RGCs	Mouse	1:1,000	Sigma
NF-H	RGCs	Rabbit	1:500	Sigma
NF-HP	RGCs	Mouse	1:500	Merck Millipore
Opsin S	Cones (blue)	Rabbit	1:1,000	Merck Millipore
Opsin M/L	Cones (red/green)	Rabbit	1:1,000	Merck Millipore
p75NTR	Müller cells	Rabbit	1:2,000	Abcam
PKC-α	Bipolar cells	Mouse	1:2,000	Santa cruz Biotechnology
Rat Cone arrestin	Cones	Rabbit	1:1,000	Merck Millipore
RBPMS	RGCs	Rabbit	1:4,000	PhosphoSolutions
Rhodopsin	Rods	Mouse	1:1,000	Abcam
S100	Müller cells	Rabbit	1:500	Dako
Vimentin	Müller cells	Mouse	1:10,000	Dako

RESULTS

Retinal Ganglion Cell Analysis

The Retinal Ganglion Cells (RGCs) in the whale retinas were studied by labelling them with specific antibodies. Whale RGCs

were labelled for βIII tubulin, Brn3a, RBPMS, and NFs. It is remarkable that the Brn3a labelling in the whale RGCs was not restricted to the nucleus, as the standard labelling pattern of this marker. In whale RGCs, Brn3a staining was more diffused, and it spread into the soma (see **Figure 2**). A combination of different molecular markers were used to the quantification of RGCs, in particular, the different subunits of NFs and RBPMS. The density of the RGCs in the retina was 36 RGCs/mm^2. The highest RGC density was detected in the middle-periphery of the retina (61 RGCs/mm^2) and the lowest concentration of RGCs was in the center of the retina, close to the optic nerve (14 RGCs/mm^2: **Figure 3**). Moreover, the total number of RGCs in the fin whale retina was estimated based on the RGC density and the total area of the whale retina (8,800 mm^2), giving an estimated total number of RGCs in the fin whale retina of 3,25,000 (**Table 2**). In addition, it is important to note that the large size of the whale RGCs were between 26.5 and 112.9 μm in diameter, with an average size of 52.5 μm in the center and 65.3 μm in the periphery of the retina, reflecting a mild trend in the increase of the soma size toward periphery.

The RGC subtypes were also analysed using different antibodies against NFs: heavy (H), heavy phosphorylated (HP), medium (M), and low (L). The NFs were distributed widely within the RGC soma, dendrites, and axons, although in some cells NF-H and NF-M staining was more intense in the perinuclear area. Some RGCs do not express all types of NFs, yet a high proportion of RGCs were labelled for at least two NF subunits. The RGCs labelled with antibodies against each type of NF were quantified and the percentage of RGCs were represented (**Figure 4** and **Supplementary Figure 1A**).

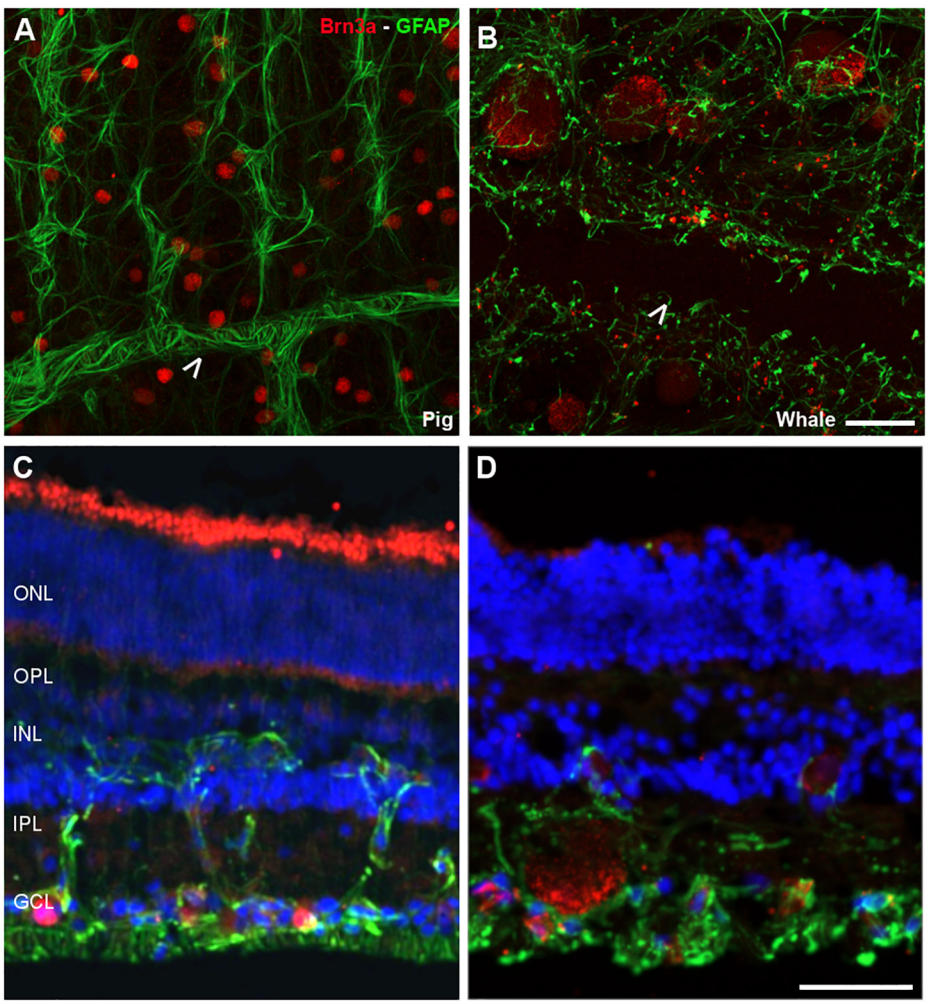

FIGURE 2 | Retinal ganglion cell (RGCs) and astrocytes in the pig and fin whale retina. The cytoskeleton of astrocytes (green) was labelled with an antibody against GFAP and the nuclei of the RGCs (red) with an antibody against Brn3a in both pig **(A,C)** and fin whale **(B,D)** retinas. Whole mount retinas **(A,B)** and sections **(C,D)** are shown. Whale astrocytes do not completely surround the vessels in the whale retina as they do in pigs (white arrowheads **A,B**). The nuclei in the retinal sections were labelled with DAPI (blue **C,D**): ONL, outer nuclear layer; OPL, outer plexiform layer; INL, inner nuclear layer; IPL, inner nuclear layer; GCL, ganglion cell layer. Scale bar = 50 μm.

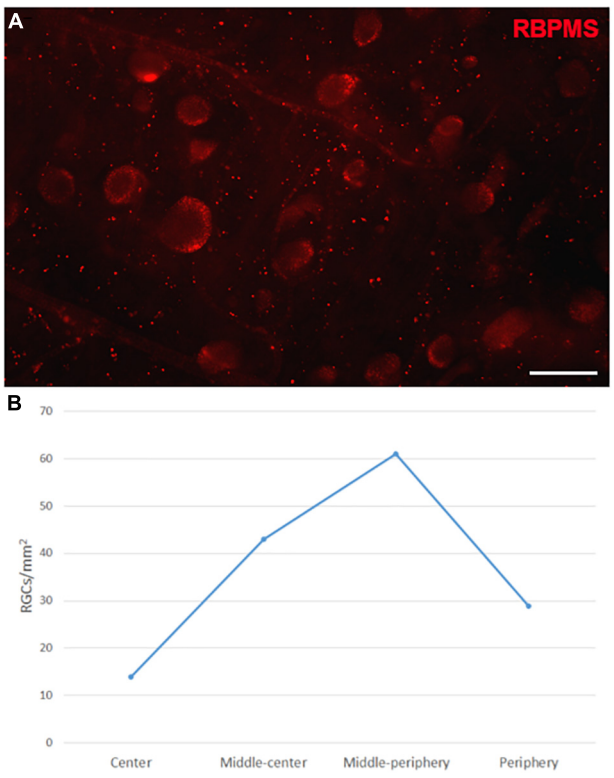

FIGURE 3 | Retinal ganglion cell quantification in the fin whale retina. Image of a whole mount whale retina labelled with an antibody against RBPMS (red) to label RGCs **(A)**. The densities of RGCs (RGCs/mm^2) in different regions of the whale retina are shown in a histogram **(B)**. Scale bar = 100 μm.

TABLE 2 | Comparison of retinal ganglion cells (RGCs) analysis published for whales and human retinas.

Species	RGC density (cells/mm^2)	Total number of RGCs	Retinal area (mm^2)	References
Pilot whale	267.3	203,000	–	Mengual et al., 2015
Grey whale	70	174,000	2,520	Mass, 1996
Killer whale	290	199,000	1,655	Mass et al., 2013
Fin whale	14–61	325,000	8,800	Present study
Human	32,000–38,000	700,000–1,500,000	1,094	Watson, 2014

Intrinsically Photosensitive Retinal Ganglion Cells Analysis

The ipRGCs in the retina were labelled with an antibody against melanopsin and these cells formed an extraordinary network covering the surface of the whale retina. The ipRGCs were more abundant in the center of the retina, at a density of 1.03 melanopsin positive cells/mm^2 close to the optic nerve, which diminished to 0.5 cells/mm^2 toward the periphery (**Figure 5B** and **Supplementary Figure 1B**). In addition, melanopsin cells can be classified depending on the location of their soma and their dendrite stratification. M1 cells have their soma located in the ganglion cell layer (GCL) and their dendrites stratified in the outermost layer of the inner plexiform layer (IPL). The M2 cells have their cell body in the GCL and their dendrites stratified in the innermost layer of the IPL, close to the GCL. The M3 cells have their cell body in the GCL and with dendrites stratified in both the outermost and innermost layer of the IPL. The M1, M2, and M3 melanopsin positive cells were identified in the whale retina (**Supplementary Figure 2**), although most of them were M2. The proportion of M1 cells increased from the centre to the periphery, whereas the percentage of M2 and M3 cells diminished toward the periphery. The percentage of each subtype of ipRGCs in each retinal region are represented (**Figure 5D**). Moreover, melanopsin positive ipRGCs were not labelled with other specific molecular markers for RGCs, such as βIII tubulin, Brn3a, or NFs (**Figure 6**).

Photoreceptors

Photoreceptors were labelled using different antibodies, such as rhodopsin for rods and M/L opsin, S opsin, rat cone arrestin, and human cone arrestin for cones. Rat and pig retinas were used to check the antibody labelling. Rods from the three species were stained with the antibody against rhodopsin, yet unlike the rat and porcine retina, whale cones did not express any of the cone markers (**Figure 7**). Labelling for M/L and S opsin was observed in the rat and pig retina but not in the whale retina. As rat cone arrestin only labelled the rat retina and human cone arrestin only the pig retina, the specificity of this species of the cone arrestin protein, it would mean that we cannot determine if the whale retina expresses arrestin or whether the antibodies used simply fail to recognise whale cone arrestin.

Bipolar and Amacrine Cells

Bipolar cells were also studied in the whale retinas through the abundant expression of Protein kinase C α (PKC-α) by rod bipolar cells. The labelling of these cells was similar to that in the rat and pig retina (**Figure 8**).

Most amacrine cells contain calretinin, calbindin or both, although other retinal cells may contain one or other protein. Using antibodies against these proteins, amacrine cells were labelled in the whale retina consistent with their distribution in the inner nuclear layer (**Figure 9**).

Glial Cells

Glial cells were also analysed in the whale retina, first labelling astrocytes with an antibody against GFAP. We assumed that some Müller cell processes were also stained. Moreover, the relationship between the RGCs and these glial cells was analysed using an antibody against Brn3a to label the nuclei of RGCs. The whale astrocytes adopted a different pattern to other mammalian retinas (e.g., pig astrocytes). The GFAP labelling in the whale retina was punctuate and the astrocytes seemed smaller than in the pig retina. The blood vessels were not completely surrounded by astrocytes, as occurs in other mammalian retinas (**Figure 2**). This lack of labelling could be due to the large size of the blood vessels; thus, the focus plane of image is in the lumen of the vessel. However, the astrocytes network that surround the blood

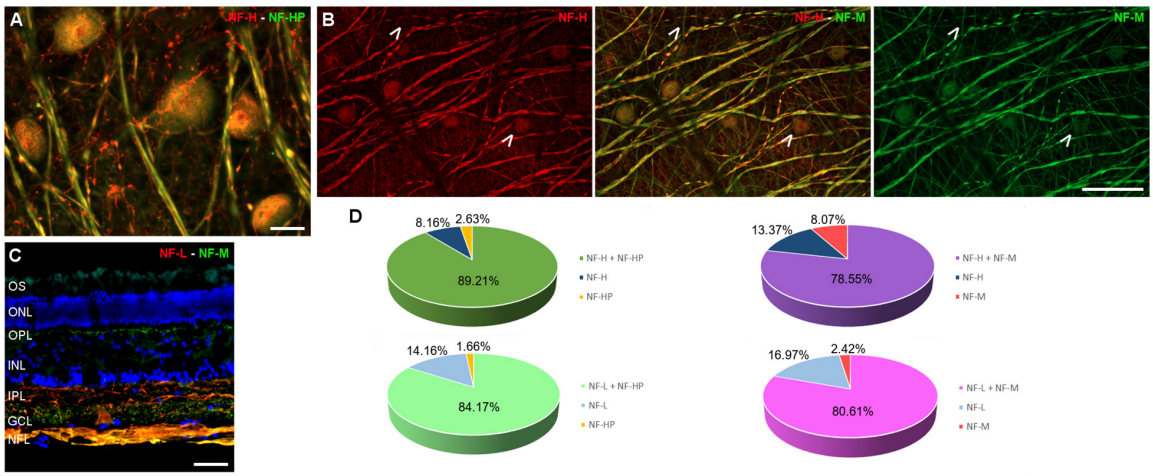

FIGURE 4 | Neurofilament analysis of RGCs in the fin whale retina. Images of whole mount whale retinas **(A,B)**, and retinal sections **(C)** labelled with antibodies against different types of neurofilaments: NF-H (red) and NH-HP (green) **(A)**; NF-H (red) and NH-M (green) **(B)**; and NF-L (red), NH-M (green), and DAPI **(C)**. Note that each type of NF has a specific labelling pattern and not all the neuron structures were labelled with each NF (arrows). The percentage of RGCs labelled with each type of NF was quantified **(D)**. Scale bar = 50 μm.

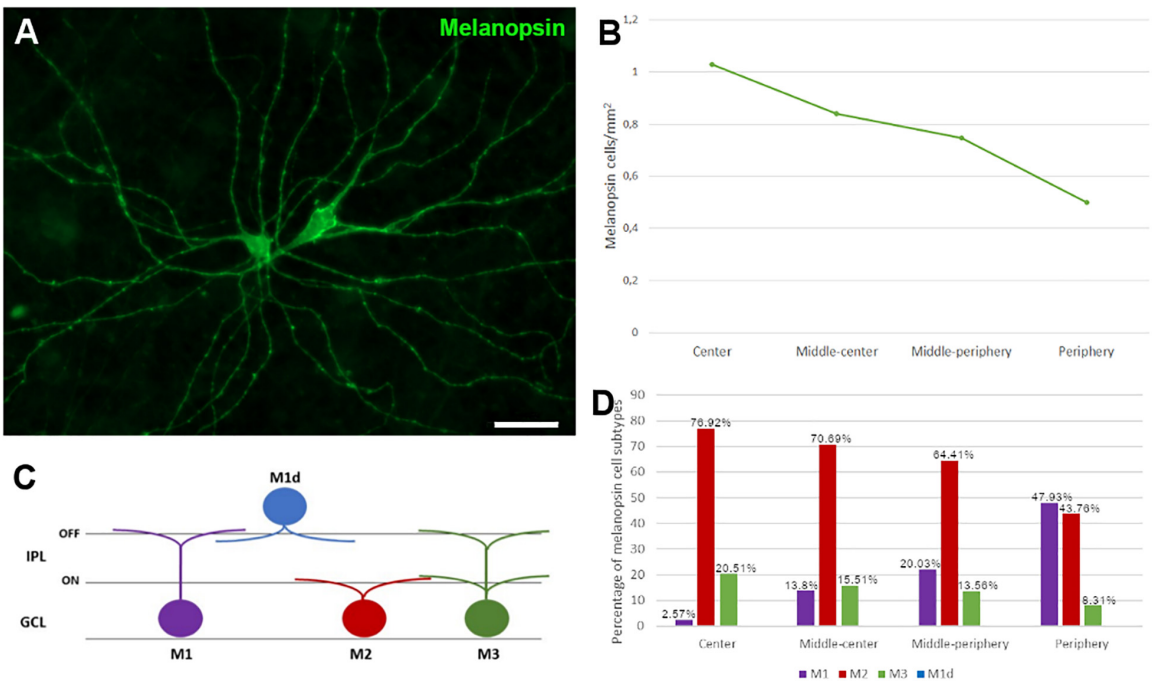

FIGURE 5 | Melanopsin positive cell quantification and classification in the fin whale retina. Melanopsin positive RGCs (green) in the whole mount whale retina **(A)**. Histogram of the total number of melanopsin positive cells/mm^2 in different regions of the whale retina **(B)**. Melanopsin cells can be classified based on their soma location, typically in the ganglion cell layer (GCL), while their dendrites stratify in the inner plexiform layer (IPL) **(C)**. The proportion of M1, M2, and M3 subtypes of melanopsin positive cells, and their distribution is represented in a histogram **(D)**. Scale bar = 100 μm.

vessels in the pig retina seems to be more complex than in the whale retina.

Müller cells were also studied using different antibodies specific to these cells, such as CRALBP, glutamine synthetase (GS), p75NTR, S100, and vimentin. All markers were expressed in the whale Müller cells, which were characteristically radially oriented cells that traverse the retina. In comparison with pig Müller cells, whale Müller cells appeared more robust with thicker end-feet (**Figure 10**).

Microglial cells were analysed in the whale retina using an antibody against Iba1, and assessing their morphology in whole mount retinas at different levels. When the whale retina was

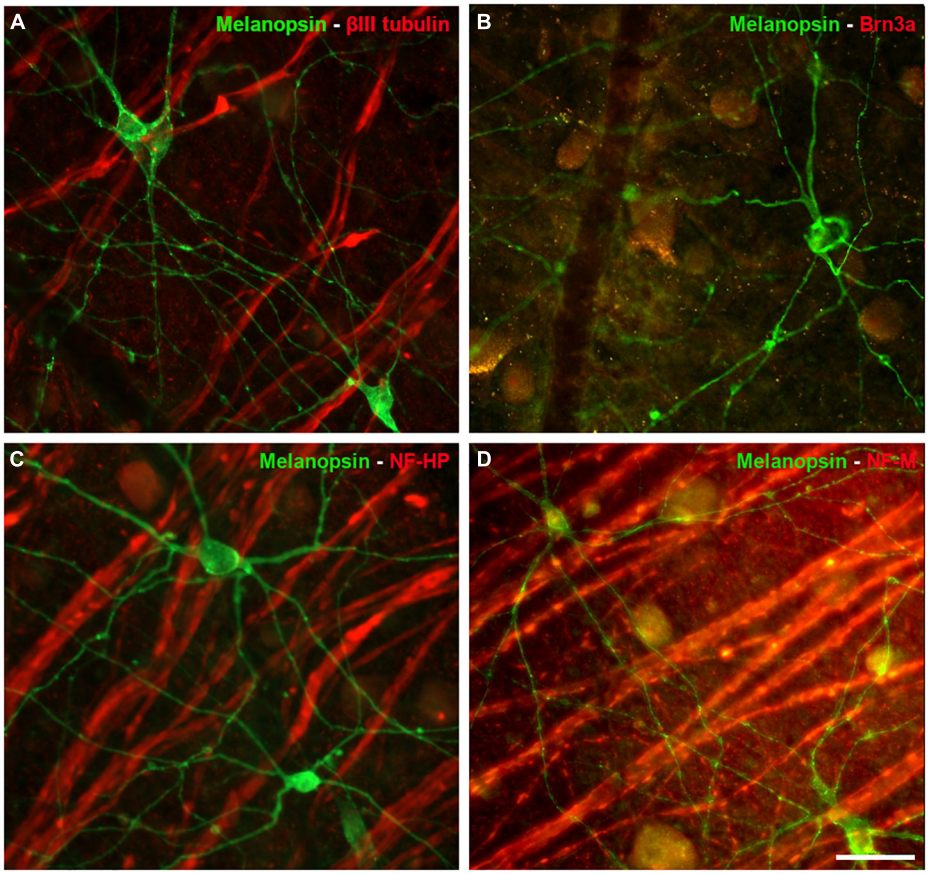

FIGURE 6 | Other RGC markers expressed by Melanopsin positive cells in the whale retina. Images of whole mount whale retinas labelled with antibodies against melanopsin (green) and other specific RGC markers (red): βIII tubulin **(A)**, Brn3a **(B)**, NF-HP **(C)**, and NH-M **(D)**. Note that the melanopsin positive ipRGCs, were not stained with any of the other markers. Scale bar = 100 μm.

compared with the rat retina, whale microglial cells seemed to be more abundant and larger in size. In addition, the limits of the microglial cells were difficult to identify in comparison with rat microglial cells (**Figure 11**).

Neurodegeneration in the Whale Retina

The exact causes of death of the whales were unknown and therefore, signs of neurodegeneration were assessed. The staining of some RGC markers differed in the two whale retinas, whereby the retinas analysed 24 h post-mortem displayed a standard staining pattern while some signs of degeneration were evident in the retinas fixed 48 h post-mortem. Thus, signs of degeneration could be due to the time between the animal death and the time tissues were processed. A distinct distribution of RBPMS was found, shifting from the RGC somas to the axons. In addition, degenerative neurite beading was observed in RGC axons and dendrites with three different markers: RBPMS, NF-H, and melanopsin (**Figure 12**). The remaining cells of the sei whale retina are similar to those of fin whale (**Supplementary Figure 3**).

Thioflavin S (ThS) is commonly used to stain oligomers and plaques of misfolded proteins, as occurs in Alzheimer and Parkinson's diseases. The well-preserved *B. physalus* retina was stained with ThS and weak punctuate labelling was detected at the edges of some RGCs. This labelling on *B. borealis* retina was not included because the ThS staining could be attributable to the bad conservation of the post-mortem tissue and not to the neurodegeneration state of the whale before death. We confirmed that ThS staining was present in RGCs though it was co-localised with βIII tubulin labelling (**Figure 13**).

DISCUSSION

As cetaceans are one of the few mammals that adopt an aquatic lifestyle during evolution, they offer a unique opportunity to study the evolution of the visual system. Our current understanding of the cetacean visual system is rather limited. The study of the extracellular matrix and in particular, the cornea and collagen fibres distribution in relation to their organ size has been performed by our group (Vecino et al., 2021), even though there is abundant evidence that vision plays an important role in their life (Herman, 1990).

Several morphological features of the cetacean eye differ from those of other mammalian eyes. For example, the cetacean eye

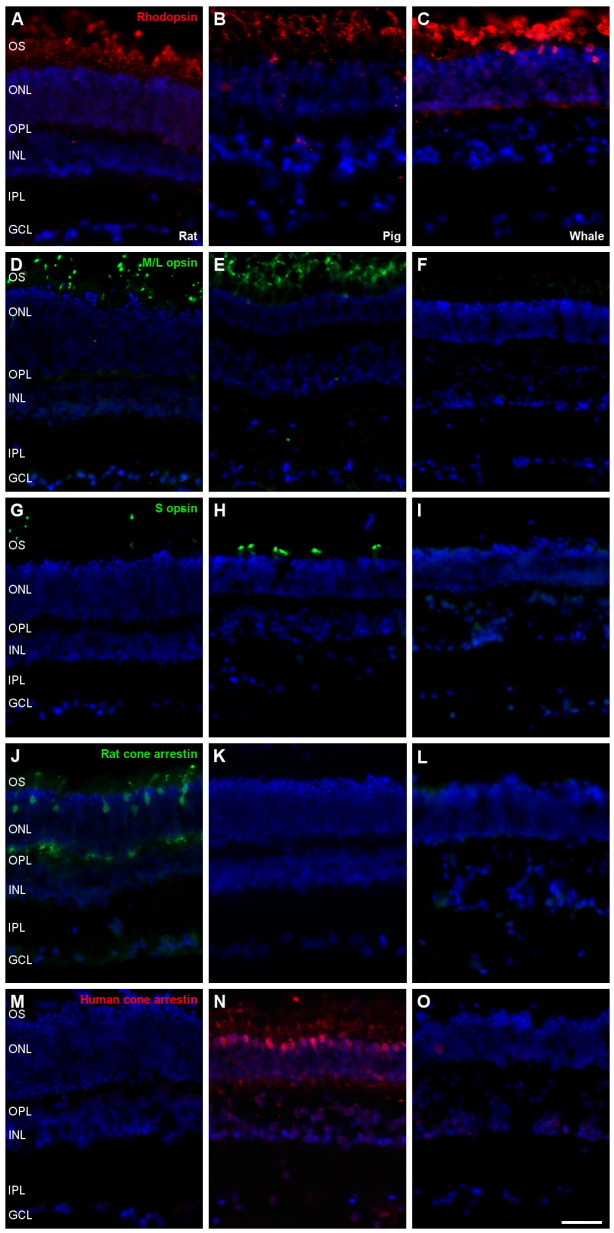

FIGURE 7 | Photoreceptors the in rat, pig and fin whale retina. Sections of rat **(A,D,G,J,M)**, pig **(B,E,H,K,N)**, and whale **(C,F,I,L,O)** retinas. The retinas were labelled with antibodies against rhodopsin (red, **A–C**), M/L opsin (green, **D–F**), S opsin (green, **G–I**), rat cone arrestin (green, **J–L**), and human cone arrestin (red, **M–O**). The nuclei were labelled with DAPI (blue): OS, outer segment; ONL, outer nuclear layer; OPL, outer plexiform layer; INL, inner nuclear layer; IPL, inner nuclear layer; GCL, ganglion cell layer. Scale bar = 50μm.

has well developed extraocular muscles, as well as a thick cornea and sclera to protect against high pressures (Mengual et al., 2015). Collecting the eyes of whales, such as mysticetes (including the genus Balaenoptera), in a sufficiently well-preserved state for histological analysis can be problematic (Lisney and Collin, 2018), although several studies have described morphological characteristics of the cetacean retina, including one of the largest, the fin whale (*Balaenoptera physalus*: Pilleri and Wandeler, 1964). The topographic organisation of RGCs has been analysed in a variety of cetacean species in order to estimate their visual acuity and to compare visual specialisation. Indeed, the density and distribution of RGCs in different whale species has been compared to that in the human retina (**Table 2**). In addition to the estimation of the total number of RGCs, the number of optic fibres was also quantified in some whales, for example: 420,000 in *B. borealis* (Morgane and Jacobs, 1972); 326,000 in *Balaenoptera acutorostrata* (Jansen and Jansen, 1969); and 252,000 in *Balaenoptera physalis* (Jacobs and Jensen, 1964). The total number of RGCs estimated here, analysing from the center to the periphery of the retina, is similar to that of other odontocetes (as pilot whale) and mysticetes (as grey whale) cetacean species. In addition, the values are similar to the total number of RGCs reported for other artiodactyls as the river hippopotamus (approximately 243,000). But the retinas of other terrestrial artiodactyls, such as the giraffe, the camel, and the water buffalo have 1 million or more RGCs. Conversely, some odontocete cetaceans as the Amazonian River dolphin and the tucuxi, have much lower numbers (approximately 15,000 and 45,000, respectively; Lisney and Collin, 2018). On the other hand, the low RGC density found in the fin whale could be explained by the large very size of their retina. In addition, the use of different markers may influence the differences found in respect to other cetaceans.

The distribution of RGCs, the number of optic fibres, the retinal resolving power, the field of best vision and the direction of the visual axis appear to be similar in most marine cetaceans. However, the density of the RGCs and the retinal resolving power are lower in cetaceans than in terrestrial mammals. Though the vision of cetaceans is suitable to recognise motion and contrast, other sensory modalities are also used to detect objects, such as hearing due to their acute auditory capacity (Murayama et al., 1992; Murayama and Somiya, 1998). Although RGC densities are low, two specialised areas of high cell density are apparent in the vast majority of cetacean species (Lisney and Collin, 2018). These areas appear to provide higher visual resolution and may be considered as the areas of best vision. In addition, the position of these areas correlates with the shape of the pupil (Mass, 1996). The shape, size, and density of RGCs in these areas are associated with the ecology of the species (Hughes, 1977). Another typical feature of the cetacean retina is the presence of RGCs named giant cells, the cell body reaches up to 75 μm in diameter, and cells are separated by wide intercellular spaces. These cells might help detect contrast and movement in the depths of the ocean (Dawson et al., 1982; Mengual et al., 2015). In conclusion, cetaceans do not have prominent visual streaks but rather small areas of peak RGC density, although they do have some huge RGCs with large dendrites and is consistent with the need to function in a very low light intensity environment. Thus, these features have ecological implications, implying that cetaceans and terrestrial mammals have distinct visual sensitivity and spatial resolution (Mass and Supin, 1997; Mass et al., 2013; Mengual et al., 2015).

Cetaceans have a relatively low RGC density compared to land mammals (**Figure 3**), even in the high density areas of

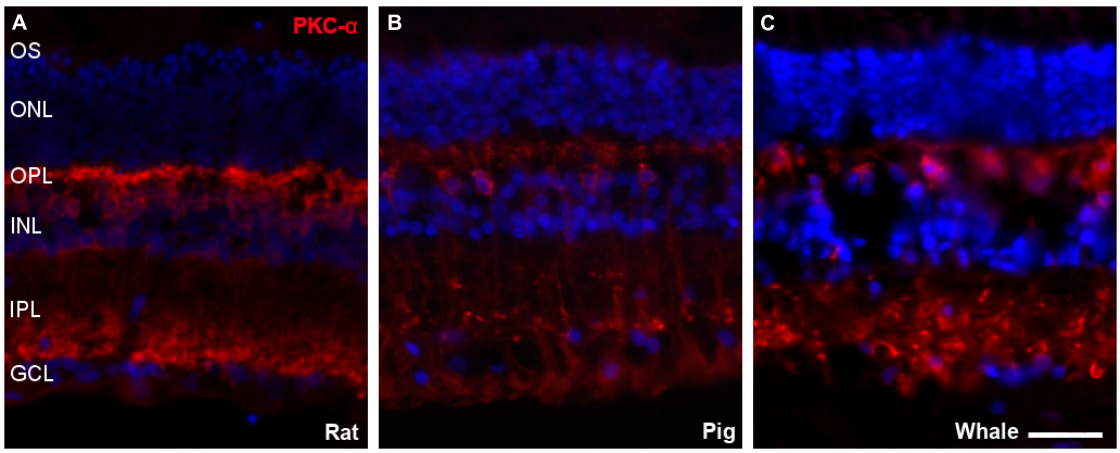

FIGURE 8 | Bipolar cells in the rat, pig, and fin whale retina. Sections from rat **(A)**, pig **(B)**, and whale **(C)** retinas labelled with an antibody against PKC-α (red) to identify bipolar cells. The nuclei were stained with DAPI (blue): OS, outer segment; ONL, outer nuclear layer; OPL, outer plexiform layer; INL, inner nuclear layer; IPL, inner nuclear layer; GCL, ganglion cell layer. Scale bar = 50 μm.

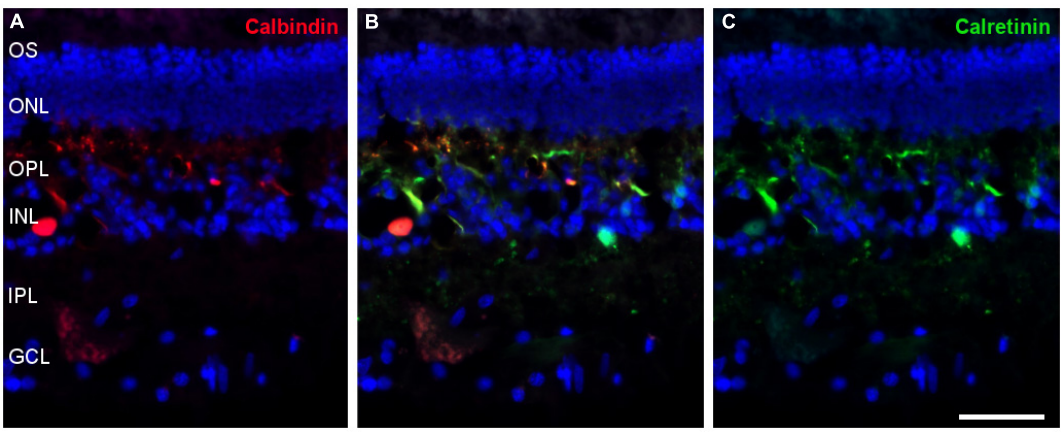

FIGURE 9 | Amacrine cells in the fin whale retina. Sections of whale retinas labelled with antibodies against calbindin (red, **A**) and calretinin (green, **C**) to stain amacrine cells. The merged image of the two antibodies is also shown in panel **(B)**. The nuclei were stained with DAPI (blue): OS, outer segment; ONL, outer nuclear layer; OPL, outer plexiform layer; INL, inner nuclear layer; IPL, inner nuclear layer; GCL, ganglion cell layer. Scale bar = 50 μm.

the retina (Mengual et al., 2015). Irrespective of the brain or body size, the absolute number of neurons is a better predictor of cognitive ability (Herculano-Houzel, 2011). Thus, despite their large size, the retinal resolving power in cetaceans can be generally weaker than that of terrestrial mammals due primarily to their low neurons density (Murayama et al., 1992; Murayama and Somiya, 1998). However, most RGCs are larger in cetaceans than in terrestrial mammals, which has ecological implications given the low light intensity of the cetacean environment. These giant RGCs tend to have larger diameter axons to conduct the visual information to longer distances due to the body length. In addition they might help detect contrasts and movement in the ocean's depths (Mengual et al., 2015). For animals with a large body size like whales, rapid transmission of nerve pulses through the thick axons of large RGCs is important (Dawson et al., 1982). Thus, it has been suggested that the giant RGC-axon systems in the whale retina may be similar to the "Y" cell-axon system (large cell body, broad radiating dendritic tree, and large axon) in terrestrial mammals (Dawson et al., 1982; Mass and Supin, 1997).

Regarding RGC markers, whale RGCs were stained with antibodies against RBPMS, NFs, Brn3a, and βIII tubulin. The NF distribution is similar between whale RGCs and terrestrial mammals, and although not all RGCs express each different type of NF, at least two NF subtypes are detected in a substantial proportion of RGCs. In the porcine and human retina, at least one of each of the three NF subtypes is present in all RGCs, NF-H, and NF-M are distributed widely within all RGC soma and dendrites, whereas NF-L is more restricted to the perinuclear area (Ruiz-Ederra et al., 2004). By contrast, all NFs were distributed widely within the RGC soma in the whale retinas, and NF-H and NF-M were more intensely labelled in the perinuclear area of some cells (**Figure 4**). The analysis of NFs in cetaceans is important

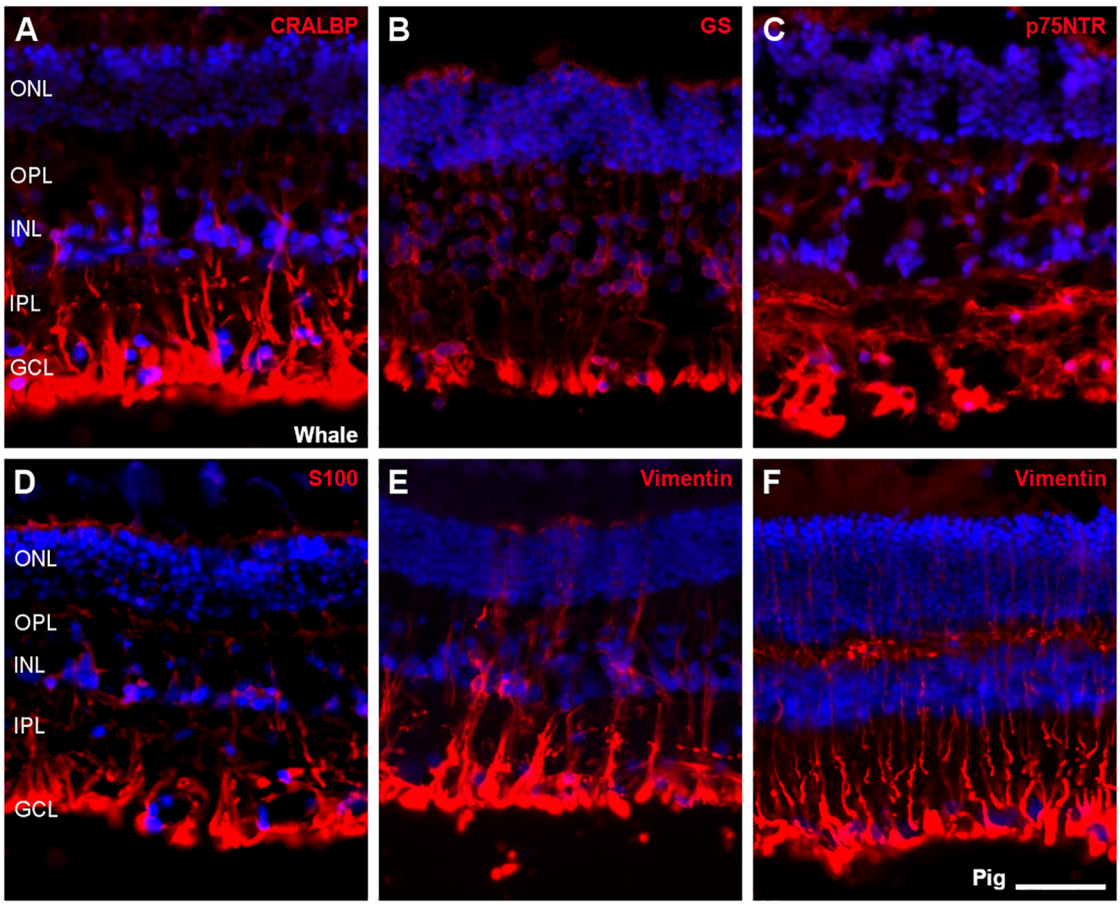

FIGURE 10 | Müller cells in the fin whale and pig retina. Sections from whale retinas labelled with different antibodies to label Müller cells: CRALBP **(A)**, glutamine synthetase (GS, **B**), p75NTR **(C)**, S100 **(D)**, and vimentin **(E)**. A section of the pig retina was also labelled with vimentin **(F)**. The nuclei were stained with DAPI (blue): ONL, outer nuclear layer; OPL, outer plexiform layer; INL, inner nuclear layer; IPL, inner nuclear layer; GCL, ganglion cell layer. Scale bar = 50 μm.

because NFs make up the bulk of the intra-axonal volume in a large axon. The NFs are determinant in generating normal axonal diameters, which is important for normal neuronal activity given that the speed of transmission of the electrical signal along the axon is directly proportional to its diameter: the bigger the diameter, the faster the impulse travels (Lobsiger and Cleveland, 2009). In addition, NFs are more abundant in large RGCs (Ruiz-Ederra et al., 2004) and thus, NFs are crucial for the activity of giant RGCs in whales. Furthermore, while Brn3a is a nuclear marker that serves as a reliable and efficient marker to identify and quantify RGCs (Nadal-Nicolas et al., 2009), Brn3a was not only found in the nucleus but it also spread to the soma in the whale retina.

A small proportion of RGCs express melanopsin, between 1 and 3% in land mammals, and these are ipRGCs (intrinsically photosensitive). These ipRGCs are dedicated to non-image-forming visual functions, including the timing of circadian rhythms and the pupillary light reflex. In the whale, ipRGCs were more abundant in the centre of the retina, diminishing toward the periphery (**Figure 5**). By contrast, ipRGCs are distributed widely throughout the human retina, although a higher density has been observed in the perifoveal area, and a fewer ipRGCs were found in the vicinity of the optic nerve and in the peripheral retina (Lax et al., 2019). Six types of ipRGC (M1 to M6) have been identified, based on morphological and physiological features, and their dendrite morphology. The majority of ipRGCs are of the M1, M2, or M3 subtypes, and they are the easiest to identify as they express more melanopsin. By contrast, the M4, M5, and M6 ipRGCs express very small quantities melanopsin and they are very difficult to identify by standard immunohistochemical techniques (Lax et al., 2019; Vidal-Villegas et al., 2021). Here, M1, M2, and M3 melanopsin ipRGCs were identified in the whale retina, although they were mostly M2. However, the number of M1 cells is higher than that of M2 and M3 cells in the rodent retina, and displaced M1 (M1d, M1 cells with their soma located in the inner nuclear rather than the ganglion cell layer) represent a small group of ipRGCs (Lax et al., 2019). Conversely, M1d is the predominant subtype in the human retina, accounting for about half of all ipRGCs (Ortuno-Lizaran et al., 2018). This difference between species may be due to the different roles of the ipRGCs subtypes. M1 ipRGCs project to approximately 15 brain targets not involved in image forming activities, and M1 cells

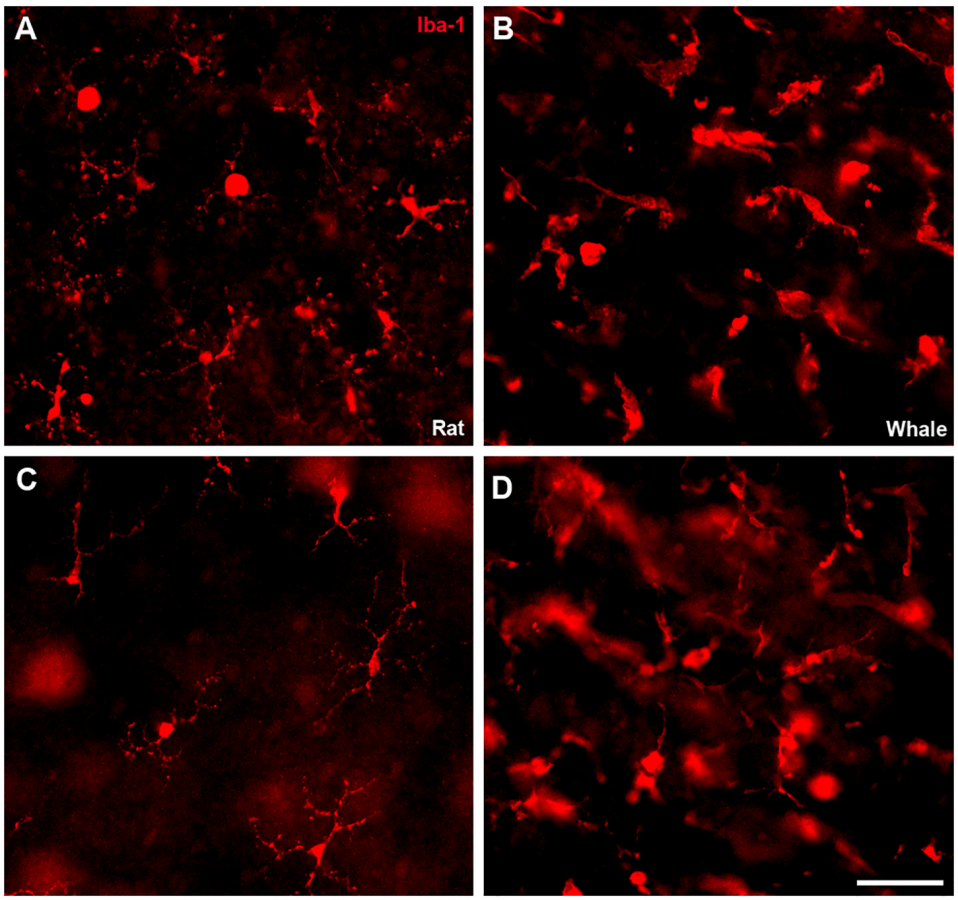

FIGURE 11 | Microglia in the rat and fin whale retina. Microglial cells were labelled with an antibody against Iba1 (red) in rat **(A,C)** and fin whale **(B,D)** whole mount retinas. Images of the microglia were taken close to the ganglion cell layer **(A,B)** and to the inner nuclear layer **(C,D)** in the whole mount retinas. Scale bar = 50 μm.

predominantly project to the suprachiasmatic nucleus (SCN) to control circadian photoentrainment but also to the shell of the olivary pretectal nucleus (OPN) to control the pupillary light reflex and to other mood-regulating regions. By contrast, M2 ipRGCs send few projections to the SCN and they project more strongly to the OPN. In addition, this subtype projects to more traditionally visual areas like the superior colliculus (Schmidt et al., 2011; Lazzerini Ospri et al., 2017). The M2 subtype is predominant in cetaceans, which means that control of the pupillary light reflex is more important to them than controlling the circadian cycle, as in land mammals where M1 subtype is predominant. This is consistent with the fact that they live deep in the ocean where there is barely any light, even during the day.

Surprisingly, ipRGCs were not labelled with classic RGC molecular markers (**Figure 6**). For instance, Brn3a was not expressed by ipRGCs in the mouse retina. Brn3a positive cells project to visual brain centres, supporting the view that melanopsin positive cells are involved exclusively in the non-image forming aspects of vision (Jain et al., 2012). This might explain why Brn3a and melanopsin labelling does not co-localise in the whale retina. In addition, rodent ipRGCs express tubulin but not NFs (Vugler et al., 2008), yet βIII tubulin was not expressed either by ipRGCs in the whale retina. Other ipRGCs melanopsin subtype, M4, has been described to express NF-H or SMI-32 (Schmidt et al., 2014), however, this cell subtype was not identified in the whale retina. IpRGCs are a very complex RGC subtype, and the evolutionary significance of their molecular profile is at present unclear. However, it can be hypothesised that ipRGCs do not express the classical markers of RGCs because they do not fulfil visual functions and they project to different regions of the brain than other RGCs.

Most terrestrial mammals have colour vision based on two spectrally different visual pigments located in two types of cone photoreceptors (M/L and S opsins). Using specific antibodies, we demonstrate an absence of cone opsin in the whale retinas studied here (**Figure 7**), lack of labelling may be due to species specificity of the antibodies used. However, bipolar cell and amacrine immunofluorescence indicate that visual signal transmission is maintained (**Figures 8**, **9**). Studies using electroretinograms in other species, also confirms that their all-rod retinas possess both ON and OFF bipolar cell pathways that are functional (Collin et al., 2009). Previous studies demonstrated rod monochromacy in some cetaceans and several mutations in the opsin gene sequence have been reported in cetaceans, suggesting the

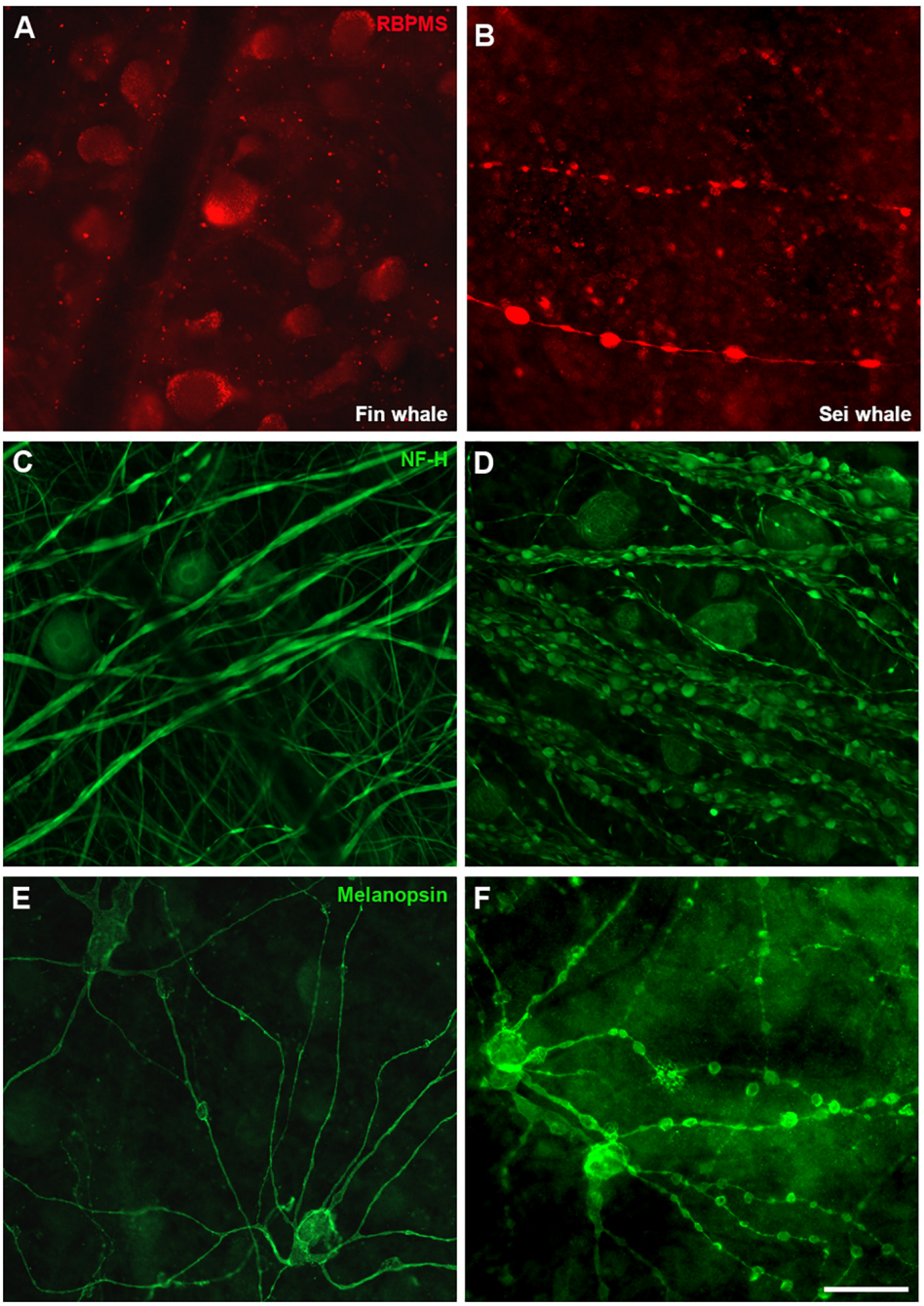

FIGURE 12 | Differences in whale retinas due to tissue conservation. Images of whole mount retinas from fin whale (*Balaenoptera physalus* **A,C,E**) and sei whale (*Balaenoptera borealis* **B,D,F**) fixed 24 and 48 h post-mortem, respectively. The retinas were labelled with antibodies against RBPMS (red, **A,B**), NF-H **(C,D)**, and melanopsin **(E,F)**. Scale bar = 100 μm.

evolutionary complete or partial loss of cone cell function in the retina, while non-photosensitive cones are maintained (Schweikert et al., 2016). Refined histological and advanced microscopy techniques revealed two cone morphologies in cetacean retinas that are not traditional morphologic cone structures, a consequence of genetic modifications influenced by environmental selection pressure (Smith et al., 2021). The discovery of rod monochromacy in whales provides an opportunity to investigate the effects of an evolutionary loss of cone photoreceptors on retinal organisation. Rod photoreceptors are more sensitive detectors of light than cones and they are capable of detecting single photons (Field and Rieke, 2002). Thus, rod-based vision provides better underwater vision in conditions where light intensity is low and light is scattered with

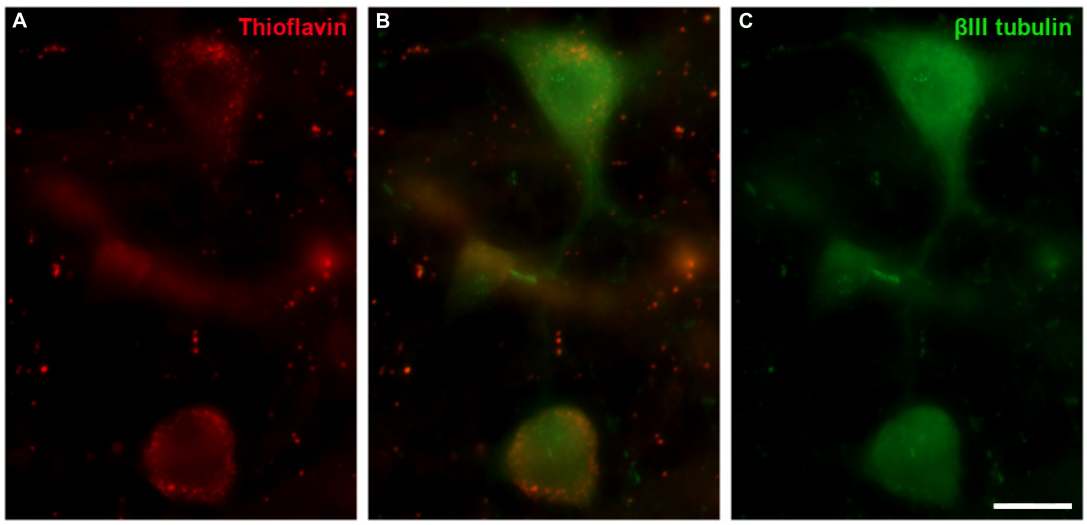

FIGURE 13 | Thioflavin S (ThS) in the fin whale retina. Images of a whole mount whale retina from *Balaenoptera physalus* stained with ThS (red, **A**) and labelled with an antibody against βIII tubulin (green, **B**) to label RGCs. Scale bar = 50 μm.

increasing depth (Smith et al., 2021). In deep-diving species, rod dominance and rapid dark adaptation in particular are traits that indicate these marine mammals use vision primarily in low light levels, where colour vision may be of secondary importance (Peichl et al., 2001).

While whales have adapted to dim light environments and are rod monochromats, the role of ipRGCs could be very important and is not completely understood. Amino acid sequence alignments of cetacean and terrestrial melanopsins reveal very few non-conserved amino acid substitutions, which would result in significant divergence away from this typical absorption maximum. However, the cetacean and land mammalian melanopsins diverge at the carboxy tail, specifically at the sites of phosphorylation that are involved in pigment inactivation (Fasick and Robinson, 2016). Hence, it can be hypothesised that the melanopsin expressed in the retina of rod monochromat cetaceans will have a carboxyl tail that results in slow deactivation kinetics. This slow deactivation of melanopsin will allow these animals to maintain prolonged pupil constriction when they are exposed to bright lights, thereby protecting rod photoreceptors from photo-bleaching (Fasick et al., 2019), and highlighting the importance of the pupillary reflex in cetaceans.

Little is known about the glial cells in the cetacean, with three types of astrocytes identified in the whale brain with distinct thicknesses and lengths of their processes (Pritz-Hohmeier et al., 1994). There were considerably more astroglia in the cetacean optic nerve than in land mammals, with astrocyte processes occupying a higher proportion of the nerve surface and apparently ensheathing every single RGC axon. This high astroglial content in the cetacean nerve could be due to the highly developed metabolic support to CNS neurons required to sustain nervous activity during anaerobic and energy-demanding tasks like prolonged apnoea (Mazzatenta et al., 2001). Surprisingly, there is a punctuate pattern of astrocytes in the whale retina and the identification of individual astrocytes was difficult (**Figure 2**). Moreover, on the blood vessels, the astroglial network seems to be less complex than in other mammal retinas, probably due to the large size of the blood vessels.

Other glial cells in these cetacean retinas appear to be more robust than in land mammal retinas, like Müller cells, for review (Vecino et al., 2016). However, there are considerable morphological variations among related species, both within an individual retina and among different vertebrate groups (Willbold and Layer, 1998). In addition, while the microglia in the whale retina are larger and more diffused, brain microglia seem to be similarly ramified as in other mammals (Pritz-Hohmeier et al., 1994). The large size of these cells (**Figures 10**, **11**) in whales could be related to the large size of their neurons, such as RGCs, and with the large dimensions of the retina. However, more studies will be needed to fully understand glial cells in the cetacean CNS.

Finally, some signs of degeneration were evident in the whale retinas analysed here (**Figure 12**), although the causes of the whales' death were unknown. Some abnormalities were observed, such as a differential distribution of RBPMS in the RGCs. RBPMS was localised to RGC axons rather than RGC somas; this shift in the location of the RBPMS has been observed in other mammalian species as a sign of degeneration (Pereiro et al., 2020). In addition, degenerative neurite beading with focal bead-like swellings on dendrites and axons represents the accumulation of vesicular cargo and transport proteins due to impaired transport, often a neuropathological sign (Takeuchi et al., 2005). However, this neurite beading was observed on RGCs of *B. borealis* probably due to the lag on the fixation and the subsequent degeneration of the tissue.

Thioflavin staining was performed in the retina of the best-preserved whale, *Balaenoptera physalus,* in order to identify if there was any sign of degeneration. In different neurodegenerative diseases, distinct sets of proteins may misfold

and form insoluble fibrillar aggregates to which thioflavin binds and emits fluorescence (Arad et al., 2020). The staining found in this study (**Figure 13**) present a weak labelling mainly in the large RGCs, with a punctuate pattern, and it did not seem to be standard thioflavin staining: a mesh of stained fibrils, a central dense core surrounded by either a corona or compact plaques, with no surrounding material (Bussiere et al., 2004). Thus, although this labelling was not pathological, it could be an early sign of neurodegeneration that may be related to the animal's death.

CONCLUSION

In conclusion, various differences exist between land mammal and whale retinas, such as the low RGC density, the presence of giant RGCs, and the rod-monochromatic vision. While some of the particular characteristics of these cetacean retinas have been studied poorly, their well-developed melanopsin-positive RGC network and characteristic glial cells shown here are features that could be responsible for the special visual perception of these cetaceans.

DATA AVAILABILITY STATEMENT

The original contributions presented in the study are included in the article/**Supplementary Material**, further inquiries can be directed to the corresponding authors.

ETHICS STATEMENT

Ethical review and approval was not required for the animal study because the eyes were collected from beached whales and they were studied post-mortem.

AUTHOR CONTRIBUTIONS

NR and XP: formal analysis. EV: funding acquisition, project administration, and supervision. NR: methodology and writing—original draft of the manuscript. NR, XP, and EV: writing—review and editing, contributed to manuscript revision, read, and approved the submitted version.

FUNDING

We acknowledge the support of ELKARTEK (KK-2019/00086), MINECO-Retos (PID2019-111139RB-I00) and Grupos UPV/EHU (GIU2018/150) to EV, Basque Government postdoctoral grant (POS_2020_2_0031) to XP, and UPV/EHU postdoctoral grant (ESPDOC20/058) to NR.

ACKNOWLEDGMENTS

We would like to thank Estibaliz Capetillo, (Achucarro-Basque Center for Neuroscience), who kindly provided us with thioflavin S and assisted in the discussion of the results obtained. We would also like to thank Nicolás Cuenca and Pedro de la Villa, for the discussion in relation to the classification of the ipRGCs subtypes and Gustavo Aguirre (UPEN), Christian Behl (Mainz University), Keith Martin (Melbourne University), Jonathan Crowston (Singapour University), Don Eric Nilsson (Lunds University), Richard R. Dubielzig (Wisconsin-Madison University), and Sansar C. Sharma (NY Medical College) for the discussion, suggestions, and providing us with very valuable bibliography on the vision of whales.

SUPPLEMENTARY MATERIAL

The Supplementary Material for this article can be found online at: https://www.frontiersin.org/articles/10.3389/fnana.2022.813369/full#supplementary-material

Supplementary Figure 1 | Distribution of RGCs and ipRGCs across the fin whale retina. Images of a large area of a whole mount fin whale retina labelled with antibodies against NF-H (red) and NH-HP (green, **A**) and melanopsin (green, **B**). Scale bar = 250 μm.

Supplementary Figure 2 | M1, M2, and M3 subtypes of melanopsin positive cells in the whale retina. Representative Z-stack images of melanopsin positive RGCs (green) in the whole mount whale retina. The M1 cell with its soma (filled arrowhead) located in the ganglion cell layer (GCL) and with dendrites stratified (unfilled arrowhead) in the outermost (OFF) layer (S1) of the inner plexiform layer (IPL) **(A)**. The M2 cell with its cell body (filled arrowhead) in the GCL and dendrites stratified (unfilled arrowhead) in the innermost (ON) layer of the IPL (S5) **(B)**. The M3 cell with its cell body (filled arrowhead) in the GCL and with dendrites stratified (unfilled arrowhead) in both the S5 and S1 **(C)**. The first photo of each group is the closest to the GCL and the rest of the images were taken every 2 μm in the direction of the inner nuclear layer (IPL), thus, the last photo is the closest to the inner nuclear layer (INL). Scale bar = 100 μm.

Supplementary Figure 3 | Retinal cells in the sei whale retina. Representative pictures of neuron and glial cells of the sei whale (*Balaenoptera borealis*). Although this retina has signs of neurodegeneration, it was useful to analyse RGCs and ipRGCs and to verify that the morphology and distribution of the rest of the cells were similar to that of the fin whale. The retina was labelled with antibodies against rhodopsin (red, **A**) to identify rods, S opsin (green, **B**) and M/L opsin (green, **C**) to identify cones, PKC-α (red, **D**) to identify bipolar cells, GFAP (green, **E**) to identify astrocytes, and vimentin (red, **F**) to identify Müller cells. In addition, images of the microglia labelled with antibody against Iba-1 (red) were taken close to the ganglion cell layer **(G)** and to the inner nuclear layer **(H)** in the whole mount retina. The nuclei were stained with DAPI (blue): ONL, outer nuclear layer; OPL, outer plexiform layer; INL, inner nuclear layer; IPL, inner nuclear layer; GCL, ganglion cell layer. Scale bars = 50 μm.

REFERENCES

Arad, E., Green, H., Jelinek, R., and Rapaport, H. (2020). Revisiting thioflavin T (ThT) fluorescence as a marker of protein fibrillation - the prominent role of electrostatic interactions. *J. Colloid Interface Sci.* 573, 87–95. doi: 10.1016/j.jcis.2020.03.075

Bussiere, T., Bard, F., Barbour, R., Grajeda, H., Guido, T., Khan, K., et al. (2004). Morphological characterization of Thioflavin-S-positive amyloid plaques in

transgenic Alzheimer mice and effect of passive Abeta immunotherapy on their clearance. *Am. J. Pathol.* 165, 987–995. doi: 10.1016/s0002-9440(10)63360-3

Collin, S. P., Davies, W. L., Hart, N. S., and Hunt, D. M. (2009). The evolution of early vertebrate photoreceptors. *Philos. Trans. R. Soc. Lond. B Biol. Sci.* 364, 2925–2940. doi: 10.1098/rstb.2009.0099

Dawson, W. W., Hawthorne, M. N., Jenkins, R. L., and Goldston, R. T. (1982). Giant neural systems in the inner retina and optic nerve of small whales. *J. Comp. Neurol.* 205, 1–7. doi: 10.1002/cne.902050102

Fasick, J. I., Algrain, H., Serba, K. M., and Robinson, P. R. (2019). The retinal pigments of the whale shark (*Rhincodon typus*) and their role in visual foraging ecology. *Vis. Neurosci.* 36:E011. doi: 10.1017/S0952523819000105

Fasick, J. I., and Robinson, P. R. (2016). Adaptations of cetacean retinal pigments to aquatic environments. *Front. Ecol. Evol.* 4:70. doi: 10.3389/fevo.2016.00070

Field, G. D., and Rieke, F. (2002). Nonlinear signal transfer from mouse rods to bipolar cells and implications for visual sensitivity. *Neuron* 34, 773–785. doi: 10.1016/S0896-6273(02)00700-6

Herculano-Houzel, S. (2011). Brains matter, bodies maybe not: the case for examining neuron numbers irrespective of body size. *Ann. N. Y. Acad. Sci.* 1225, 191–199. doi: 10.1111/j.1749-6632.2011.05976.x

Herman, L. M. (1990). "Cognitive performance of dolphins in visually-guided tasks," in *Sensory Abilities of Cetaceans*, eds J. A. Thomas and R. A. Kastelein (Boston, MA: Springer), 455–462. doi: 10.1007/978-1-4899-0858-2_32

Hughes, A. (1977). "The topography of vision in mammals of contrasting life style: comparative optics and retinal organisation," in *The Visual System in Vertebrates*, ed. F. E. A. Crescitelli (Berlin: Springer-Verlag), 613–756. doi: 10.1007/978-3-642-66468-7_11

Jacobs, M. S., and Jensen, A. V. (1964). Gross aspects of the brain and fiber analysis of cranial nerves in the great whale. *J. Comp. Neurol.* 123, 55–72. doi: 10.1002/cne.901230107

Jain, V., Ravindran, E., and Dhingra, N. K. (2012). Differential expression of Brn3 transcription factors in intrinsically photosensitive retinal ganglion cells in mouse. *J. Comp. Neurol.* 520, 742–755. doi: 10.1002/cne.22765

Jansen, J., and Jansen, J. K. S. (1969). "The nervous system of Cetacea," in *The Biology of Marine Mammals*, ed. H. T. Andersen (New York: Academic Press), 175–252.

Lax, P., Ortuno-Lizaran, I., Maneu, V., Vidal-Sanz, M., and Cuenca, N. (2019). Photosensitive melanopsin-containing retinal ganglion cells in health and disease: implications for circadian rhythms. *Int. J. Mol. Sci.* 20:3164. doi: 10.3390/ijms20133164

Lazzerini Ospri, L., Prusky, G., and Hattar, S. (2017). Mood, the circadian system, and melanopsin retinal ganglion cells. *Annu. Rev. Neurosci.* 40, 539–556. doi: 10.1146/annurev-neuro-072116-031324

Lisney, T. J., and Collin, S. P. (2018). Retinal topography in two species of baleen whale (*Cetacea: Mysticeti*). *Brain Behav. Evol.* 92, 97–116. doi: 10.1159/000495285

Lobsiger, C. S., and Cleveland, D. W. (2009). "Neurofilaments: organization and function in neurons," in *Encyclopedia of Neuroscience*, ed. L. Squuire (Amsterdam: Elsevier). doi: 10.1016/B978-008045046-9.00728-2

Mass, A. M. (1996). Regions of increased density of the ganglion cells, and resolution of the retina of the grey whale *Eschrichtius gibbosus*. *Dokl Akad Nauk* 350, 139–142.

Mass, A. M., and Supin, A. Y. (1997). Ocular anatomy, retinal ganglion cell distribution, and visual resolution in the gray whale, *Eschrichtius gibbosus*. *Aquat. Mamm.* 23, 17–28.

Mass, A. M., Supin, A. Y., Abramov, A. V., Mukhametov, L. M., and Rozanova, E. I. (2013). Ocular anatomy, ganglion cell distribution and retinal resolution of a killer whale (*Orcinus orca*). *Brain Behav. Evol.* 81, 1–11. doi: 10.1159/000341949

Mazzatenta, A., Caleo, M., Baldaccini, N. E., and Maffei, L. (2001). A comparative morphometric analysis of the optic nerve in two cetacean species, the striped dolphin (*Stenella coeruleoalba*) and fin whale (*Balaenoptera physalus*). *Vis. Neurosci.* 18, 319–325. doi: 10.1017/s0952523801182155

Mengual, R., García, M., Segovia, Y., and Pertusa, J. F. (2015). Ocular morphology, topography of ganglion cell distributionand visual resolution of the pilot whale (*Globicephala melas*). *Zoomorphology* 134, 339–349. doi: 10.1007/s00435-015-0258-7

Morgane, P. J., and Jacobs, M. S. (1972). "Comparative anatomy of the cetacean nervous system," in *Functional Anatomy of Marine Mammals*, ed. R. J. Harrison (New York: Academic Press), 117–244. doi: 10.1016/j.brainresbull.2005.02.019

Murayama, T., and Somiya, H. (1998). Distribution of ganglion cells and object localizing ability in the retina of three cetaceans. *Fish. Sci.* 64, 27–30. doi: 10.2331/fishsci.64.27

Murayama, T., Somiya, H., Aoki, I., and Ishii, T. (1992). The distribution of ganglion cells in the retina and visual acuity of Minke Whale. *Nippon Suisan Gakkaishi* 56, 1057–1061. doi: 10.2331/suisan.58.1057

Nadal-Nicolas, F. M., Jimenez-Lopez, M., Sobrado-Calvo, P., Nieto-Lopez, L., Canovas-Martinez, I., Salinas-Navarro, M., et al. (2009). Brn3a as a marker of retinal ganglion cells: qualitative and quantitative time course studies in naive and optic nerve-injured retinas. *Invest. Ophthalmol. Vis. Sci.* 50, 3860–3868. doi: 10.1167/iovs.08-3267

Ortuno-Lizaran, I., Esquiva, G., Beach, T. G., Serrano, G. E., Adler, C. H., Lax, P., et al. (2018). Degeneration of human photosensitive retinal ganglion cells may explain sleep and circadian rhythms disorders in Parkinson's disease. *Acta Neuropathol. Commun.* 6:90. doi: 10.1186/s40478-018-0596-z

Peichl, L., Behrmann, G., and Kroger, R. H. (2001). For whales and seals the ocean is not blue: a visual pigment loss in marine mammals. *Eur. J. Neurosci.* 13, 1520–1528. doi: 10.1046/j.0953-816x.2001.01533.x

Pereiro, X., Ruzafa, N., Urcola, J. H., Sharma, S. C., and Vecino, E. (2020). Differential Distribution of RBPMS in pig, rat, and human retina after damage. *Int. J. Mol. Sci.* 21:9330. doi: 10.3390/ijms21239330

Pilleri, G., and Wandeler, A. (1964). Ontogenesis and functional morphology of the eye of the Finback Whale, Balaenoptera Physalus Linnaeus (Cetacea, Mysticeti, Balaenopteridae). *Acta Anat.* 57, 51–74. doi: 10.1159/000142567

Pritz-Hohmeier, S., Hartig, W., Behrmann, G., and Reichenbach, A. (1994). Immunocytochemical demonstration of astrocytes and microglia in the whale brain. *Neurosci. Lett.* 167, 59–62. doi: 10.1016/0304-3940(94)91027-8

Ruiz-Ederra, J., Garcia, M., Hicks, D., and Vecino, E. (2004). Comparative study of the three neurofilament subunits within pig and human retinal ganglion cells. *Mol. Vis.* 10, 83–92.

Ruzafa, N., Pereiro, X., Aspichueta, P., Araiz, J., and Vecino, E. (2018). The Retina of osteopontin deficient mice in aging. *Mol. Neurobiol.* 55, 213–221. doi: 10.1007/s12035-017-0734-9

Ruzafa, N., Rey-Santano, C., Mielgo, V., Pereiro, X., and Vecino, E. (2017). Effect of hypoxia on the retina and superior colliculus of neonatal pigs. *PLoS One* 12:e0175301. doi: 10.1371/journal.pone.0175301

Schmidt, T. M., Alam, N. M., Chen, S., Kofuji, P., Li, W., Prusky, G. T., et al. (2014). A role for melanopsin in alpha retinal ganglion cells and contrast detection. *Neuron* 82, 781–788. doi: 10.1016/j.neuron.2014.03.022

Schmidt, T. M., Chen, S. K., and Hattar, S. (2011). Intrinsically photosensitive retinal ganglion cells: many subtypes, diverse functions. *Trends Neurosci.* 34, 572–580. doi: 10.1016/j.tins.2011.07.001

Schweikert, L. E., Fasick, J. I., and Grace, M. S. (2016). Evolutionary loss of cone photoreception in balaenid whales reveals circuit stability in the mammalian retina. *J. Comp. Neurol.* 524, 2873–2885. doi: 10.1002/cne.23996

Smith, M. A., Waugh, D. A., Mcburney, D. L., George, J. C., Suydam, R. S., Thewissen, J. G. M., et al. (2021). A comparative analysis of cone photoreceptor morphology in bowhead and beluga whales. *J. Comp. Neurol.* 529, 2376–2390. doi: 10.1002/cne.25101

Takeuchi, H., Mizuno, T., Zhang, G., Wang, J., Kawanokuchi, J., Kuno, R., et al. (2005). Neuritic beading induced by activated microglia is an early feature of neuronal dysfunction toward neuronal death by inhibition of mitochondrial respiration and axonal transport. *J. Biol. Chem.* 280, 10444–10454. doi: 10.1074/jbc.M413863200

Vecino, E., Rodriguez, F. D., Ruzafa, N., Pereiro, X., and Sharma, S. C. (2016). Glia-neuron interactions in the mammalian retina. *Prog. Retin. Eye Res.* 51, 1–40. doi: 10.1016/j.preteyeres.2015.06.003

Vecino, E., Ruzafa, N., Pereiro, X., Zulueta, A., Sarmiento, A., and Díez, A. (2021). "The Extracellular matrix of the human and Whale Cornea and Sclera: implications in glaucoma and other pathologies," in *Extracellular Matrix - Developments and Therapeutics*, ed. R. S. Madhurapantula (London: IntechOpen). doi: 10.5772/intechopen.97023

Vidal-Villegas, B., Gallego-Ortega, A., Miralles De Imperial-Ollero, J. A., Martinez De La Casa, J. M., et al. (2021). Photosensitive ganglion cells: a diminutive, yet essential population. *Arch. Soc. Esp. Oftalmol.* 96, 299–315. doi: 10.1016/j.oftale.2020.06.020

Vugler, A. A., Semo, M., Joseph, A., and Jeffery, G. (2008). Survival and remodeling of melanopsin cells during retinal dystrophy. *Vis. Neurosci.* 25, 125–138. doi: 10.1017/S0952523808080309

Watson, A. B. (2014). A formula for human retinal ganglion cell receptive field density as a function of visual field location. *J. Vis.* 14:15. doi: 10.1167/14.7.15

Willbold, E., and Layer, P. G. (1998). Muller glia cells and their possible roles during retina differentiation in vivo and in vitro. *Histol. Histopathol.* 13, 531–552.

Conflict of Interest: The authors declare that the research was conducted in the absence of any commercial or financial relationships that could be construed as a potential conflict of interest.

Publisher's Note: All claims expressed in this article are solely those of the authors and do not necessarily represent those of their affiliated organizations, or those of the publisher, the editors and the reviewers. Any product that may be evaluated in this article, or claim that may be made by its manufacturer, is not guaranteed or endorsed by the publisher.

frontiers in Neuroanatomy

PERSPECTIVE
published: 09 February 2022
doi: 10.3389/fnana.2022.789375

The Evolution of Visual Roles – Ancient Vision Versus Object Vision

*Dan-Eric Nilsson**

Lund Vision Group, Department of Biology, Lund University, Lund, Sweden

Just like other complex biological features, image vision (multi-pixel light sensing) did not evolve suddenly. Animal visual systems have a long prehistory of non-imaging light sensitivity. The first spatial vision was likely very crude with only few pixels, and evolved to improve orientation behaviors previously supported by single-channel directional photoreception. The origin of image vision was simply a switch from single to multiple spatial channels, which improved the behaviors for finding a suitable habitat and position itself within it. Orientation based on spatial vision obviously involves active guidance of behaviors but, by necessity, also assessment of habitat suitability and environmental conditions. These conditions are crucial for deciding when to forage, reproduce, seek shelter, rest, etc. When spatial resolution became good enough to see other animals and interact with them, a whole range of new visual roles emerged: pursuit, escape, communication and other interactions. All these new visual roles require entirely new types of visual processing. Objects needed to be separated from the background, identified and classified to make the correct choice of interaction. Object detection and identification can be used actively to guide behaviors but of course also to assess the over-all situation. Visual roles can thus be classified as either ancient non-object-based tasks, or object vision. Each of these two categories can also be further divided into active visual tasks and visual assessment tasks. This generates four major categories of vision into which I propose that all visual roles can be categorized.

Keywords: vision, visual role, evolution, visual processing, behavior

OPEN ACCESS

Edited by:
Francisco M. Nadal-Nicolas, Retinal Neurophysiology Section, National Eye Institute (NIH), United States

Reviewed by:
Daniel Osorio, University of Sussex, United Kingdom
Manuel Salinas-Navarro, University of Murcia, Spain
Simon B. Laughlin, University of Cambridge, United Kingdom

***Correspondence:**
Dan-Eric Nilsson
dan-e.nilsson@biol.lu.se

Received: *04 October 2021*
Accepted: *20 January 2022*
Published: *09 February 2022*

Citation:
Nilsson D-E (2022) The Evolution of Visual Roles – Ancient Vision Versus Object Vision. Front. Neuroanat. 16:789375. doi: 10.3389/fnana.2022.789375

INTRODUCTION

Imagine you have just bought a sandwich and a paper mug of coffee and are looking for a place to sit and have your lunch. Across the park you see an unoccupied bench in an attractive spot. To get there, you first follow a paved path and then make a shortcut across the lawn. You sit down at the bench and unwrap your sandwich. You remove a piece of lettuce that does not look fresh before you take the first bite.

In this little glimpse of everyday life, you have relied on vision for a range of rather different tasks. You have assessed your environment to find a suitable place and then used visual input to guide your movement along a path and in the direction to a desired place. You have also assessed objects and used vision to guide manipulation of them. As human-oriented as this example is, we still share the very same general roles of vision with other vertebrates, with numerous arthropods, and with cephalopods. Animals of other phyla have less advanced visual systems serving fewer basic types of roles. There are in fact animals that live and prosper with every imaginable intermediate from simple non-visual photoreception to the full set of visual roles found in vertebrates, arthropods and cephalopods. This makes it possible to reconstruct the evolution of vision from the very simplest

forms to the most advanced. Here I will argue that even though vision has evolved many times independently from non-visual photoreception, new roles of vision have, with only few exceptions, been acquired in the same general sequence in all animal groups that have any kind of eyes or vision.

SETTING THE STAGE FOR EVOLUTION OF VISION

As has been argued elsewhere (Nilsson, 2009, 2013, 2020, 2021), the first opsin-based photoreception was likely used to monitor the daily light cycle, to help choose the right activity at the right time. Given the slow changes in daily light levels, the photoreceptors tracking this intensity change would have been slow and non-directional. Much faster intensity changes are caused by the animal moving in or out of shade or into deeper or shallower water, or by clouds. To adapt the behavior to these faster changes, some photoreceptors may have adopted new roles by speeding up their responses or changing their spectral sensitivity. Knowing about intensity changes caused by moving into differently lit parts of the habitat is useful in itself but will also help separate these signals from that of the daily light cycle. Another way to isolate signals arising from the daily light cycle from those arising from natural light disturbances is to employ a biological clock with photoreceptor input (Brown et al., 2014).

Faster photoreceptors also open possibilities for direct control of locomotion, especially if they become directional through an association with screening pigments. Such photoreceptors can actively steer the animal toward brighter or dimmer parts of the environment, and thus be used to seek out suitable habitats or move to optimal positions within a habitat. Positive or negative phototaxis served by a single directional photoreceptor is a common feature of invertebrates, both in adults and larvae (Randel and Jekely, 2016), and would have been a powerful addition to non-directional photoreception in early metazoan evolution. However, even though light-intensity monitoring and directional photoreception have critical and important biological functions, these behaviors can be mediated by a single isolated photoreceptor, and thus do not result from true vision. Instead, true vision relies on the comparison of signals arising from two or more photoreceptors receiving light from different directions.

TRUE VISION FOR HABITAT ORIENTATION

There are two principal limitations to directional photoreception. One is that the animal must turn or scan to find the direction of light or darkness. The other is that it allows orientation only to the overall distribution of light – not to the distribution of spatial structures. Simultaneous comparison of signals from several directional photoreceptors aimed in different directions will remove both limitations and provide true vision (simultaneous spatial resolution). Apart from the obvious multiplication of directional photoreceptors, true vision also requires novel neural circuits for discrimination of spatial intensity differences (contrasts) and their motion. With these in place, even a small number of photoreceptors, and thus a very low resolution, opens for much more efficient orientation in the environment. Specific habitats and locations within habitats can be identified, and vision can actively guide locomotion accordingly (Nilsson, 2013, 2020; Randel and Jekely, 2016).

Interestingly, true spatial vision replaces directional photoreception, but non-directional photoreception remains as important as before vision evolved (**Figure 1**). It may even acquire new roles such as controlling light-dark adaptation of visual photoreceptors (Aranda and Schmidt, 2020). There is an important distinction between the information used by visual photoreceptors and that used for determining the time of day or depth in water (irradiance detectors): visual photoreceptors compare relative intensities within a scene, whereas irradiance detectors measure the absolute light level. For visual photoreceptors, changes in irradiance are a nuisance calling for adaptation mechanisms that dynamically change the gain to match the current irradiance (note that the difference between the darkest and brightest parts of a single scene is 1–2 log units, whereas the daily light cycle covers 8 log units). Consequently, visual photoreception and irradiance monitoring require very different photoreceptor properties. Irradiance detection to support vision may thus be a reason for co-expression of different opsins and signaling pathways, or for different types of photoreceptors in the same eye, such as the melanopsin-expressing retinal ganglion cells that coexist with ciliary rods and cones in vertebrate eyes (Lucas, 2013). This suggests that the major classes of opsins shared by metazoans reflect early divergence of photoreceptive tasks.

Obviously, better spatial resolution (an image of more numerous pixels) improves the ability to orient in the environment, but for most kinds of visual orientation, fine spatial details are of little importance. Comparatively low resolution is sufficient for orientation in relation to visible structures or landmarks (Blevins and Johnsen, 2004; Nilsson et al., 2005; Garm et al., 2007, 2011; Garm and Nilsson, 2014; Nilsson and Bok, 2017; Kirwan et al., 2018; Kirwan and Nilsson, 2019; Sumner-Rooney et al., 2020; Ljungholm and Nilsson, 2021). Any level of spatial resolution can help the animals keep a straight path, find a burrow or shelter (or the way out of one), and it can help find a clear path without collisions. The visual flow field will also provide information about self-motion and the distance to surfaces and structures in the environment (Scholtyssek et al., 2014). The use of global cues, such as the direction of the sun, will allow compass orientation, and learned snapshots can support efficient homing (see Grob et al. (2021) for an excellent classification of orientation behaviors).

The information required for visually guided orientation is not so much the spatial structures themselves as it is their motion. The visual flow-field, looming and motion of spatial structures, are essential for guiding locomotion or any other action. It is the changes over time that carry information about what is going on and provides feedback to motor control systems. Spatial vision and motion vision would thus have evolved in close synchrony because one is largely pointless without the other.

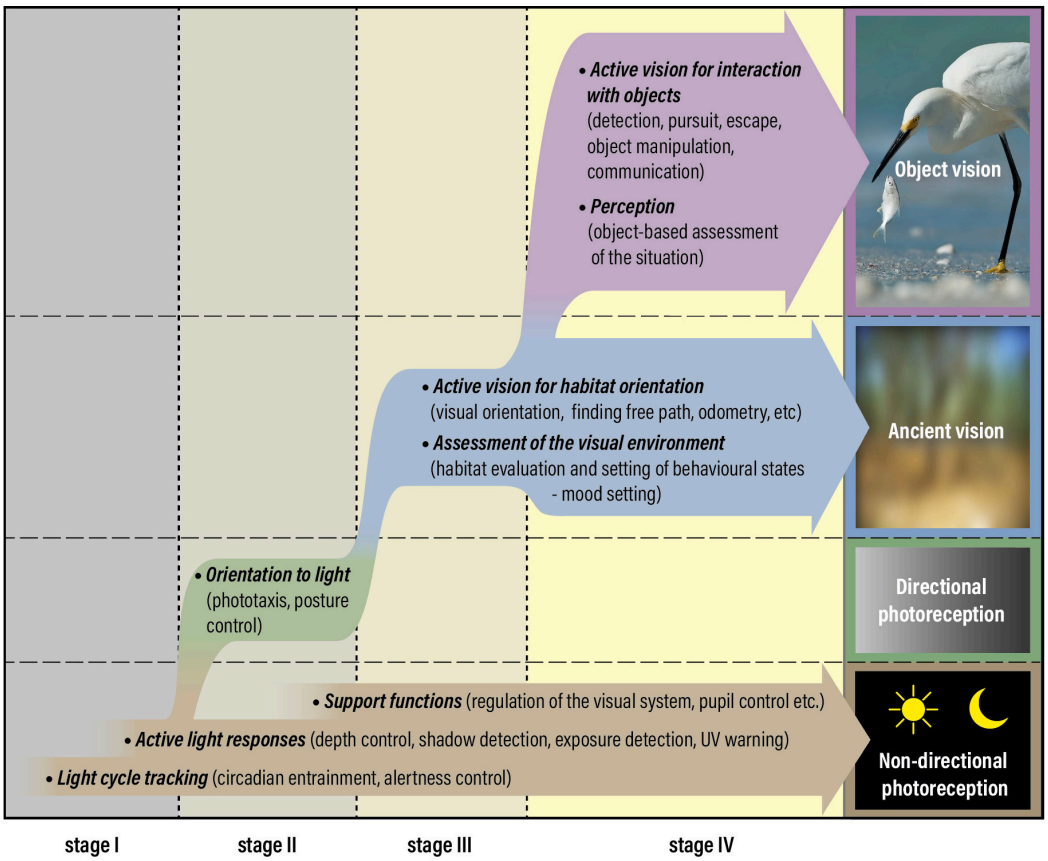

FIGURE 1 | Photoreception and vision have evolved through four distinct stages, starting with *non-directional photoreception* at stage I, acquisition of *directional photoreception* at stage II, which is replaced by *ancient vision* at stage III and complemented by *object vision* at stage IV. True vision and eyes are associated with the introduction of stage III. The figure was originally prepared for a recent review (Nilsson, 2021) but has been adapted to the new concepts of ancient vision and object vision argued for in this manuscript. Ancient vision was not reduced after the introduction of object vision but could massively boost its performance without much additional cost. Consequently, between stages III and IV, vision changed from a minor to a major sensory modality.

Visual orientation may be enhanced by color vision or polarization vision to generate contrasts, but the eyes need not be large or optically sophisticated to provide sufficient resolution for orientation (Nilsson, 2020, 2021). Eyes built to provide spatial resolution are found in about one third of all animal phyla, and in most cases the eyes are small, less than 0.5 mm (Land and Nilsson, 2012; Nilsson, 2021). These eyes are most certainly used to actively guide locomotion toward suitable habitats and to find optimal positions. However, visually guided orientation also requires abilities to assess the environment. Vision can thus be divided into "active vision," i.e., vision used directly to control actions in a closed feedback loop (see and act) and vision used to "assess the environment" for decisions within a wide time frame (Goodale and Milner, 1992). Visually guided locomotion toward a better place must be preceded by a visual assessment resulting in a decision to abandon the current place. Prior to action, and as part of the assessment, there may also be identification of a direction toward a potentially better habitat.

Visual assessment may also contribute substantially to an even more important function: the choice of suitable behaviors. From their complete behavioral repertoire, all animals must continuously select currently suitable behaviors. In a highly species-specific manner, different behaviors are displayed at different times of day, in different seasons, and in different environments. By visually reading the environment, animals may thus get input for setting a behavioral state (mood-setting) that will make them prone to engage in some behaviors but not in others (Berman et al., 2016; Gurarie et al., 2016; Mahoney and Young, 2017; Nässel et al., 2019). The behavioral state thus acts as a master control of behavior and may additionally adjust the animal's physiology to prepare it for specific behaviors. These are essential but sadly neglected visual roles.

The types of visual information used for active vision and for visual assessment differ. Active vision is largely based on the movement of edges, structures, and textures. In contrast, information on the environment and its current state is contained more in the general background, its intensity distribution, and spectral distribution. Because this requires only low spatial and temporal resolution, the information can be carried by relatively small populations of slow large-field neurons. The fact that such neurons have not received much attention probably contributes to our poor understanding of vision involved in assessment tasks.

Based on evolutionary reasoning and the moderate demands on spatial resolution, I have previously used the term "low-resolution vision" to classify orientation tasks and other visual tasks that do not require discrimination of objects (Nilsson, 2009, 2013, 2020, 2021; Land and Nilsson, 2012; Nilsson and Bok, 2017). This term is somewhat misleading because visual orientation, and corresponding visual assessment of the environment, may very well rely on higher spatial frequencies in animals with good eyes. Since the original reason that true vision evolved was to serve orientation in the habitat, I here introduce the term *ancient vision* (non-object-based visual tasks), to distinguish it from all visual roles that involve object discrimination (**Figure 1**). Orientation in the habitat to find suitable locations is the core of ancient vision but it also includes basic visual functions such as measurement of self-motion from optic flow, finding free path, obstacle avoidance, and navigation in relation to landmarks and celestial cues.

OBJECT VISION OPENS A NEW WORLD

With gradually improved spatial resolution, other animals could in principle be detected at distances beyond the immediate vicinity. However, this is not a trivial extension of visual roles. To detect another animal requires that it can be distinguished as an object separate from the background (image segmentation). It further requires that the object can be identified because the world is full of different types of objects that have to be interacted with in very different ways. A prey, a predator, a conspecific, or an inanimate object all call for very different responses. Apart from a reasonably good spatial resolution, visually guided interaction with other animals thus requires image segmentation to isolate objects, as well as object identification and classification. On top of this, novel neural circuits for interactions with objects, with new motor patterns, would also have to evolve, presumably by duplication and modification of pre-existing circuits for orientation in the inanimate world.

How could such a complex set of traits evolve? It seems challenging to find a gradual evolutionary path where not all new traits had to appear simultaneously to make sense. An attractive possibility is that object vision arose from the ability to recognize a shelter, to help find previously used refuges. This is non-object-based orientation and part of ancient vision, but it requires recognition of a learned spatial pattern and comes a long way toward the visual processing required for object recognition. There may be other orientation tasks that involve memory of spatial patterns, which also offer a smooth transition from non-object-based to object-based vision, making the evolutionary transition less challenging.

Advanced visual processing in combination with high spatial resolution (large pixel numbers) also makes for large and energetically expensive brains (Land and Nilsson, 2012). It is thus no wonder that object-based vision is an exclusive feature which has been fully exploited only in three animal groups: the vertebrates, the arthropods, and the cephalopods (octopus, squid, and cuttlefish). Among the arthropods, object-based vision may have evolved independently more than once, as indicated by compound eyes in insects and crustaceans and non-homologous camera-type eyes in spiders [their principal eyes (Nilsson, 2020)]. In arthropods, the situation is complicated by visual systems comprising both lateral and median eyes. In insects and crustaceans the median eyes (dorsal ocelli and nauplius eyes) are not know to be implicated in object discrimination tasks, leaving the lateral compound eyes responsible for their object vision. However, the compound eyes are certainly also involved in orientation and other tasks of ancient vision.

Object vision may be both expensive and neurally demanding, but the benefits are enormous. The ability to detect and identify other animals and food items at some distance offers a tremendous potential for new and advanced behaviors. One of these, visually guided predation, must have led to a major ecological turnover pushing for good vision and swift locomotion in both prey and predator species. The fact that the maximum distance for object recognition is closely related to spatial resolution [visual acuity (Nilsson et al., 2014)], suggests that there were evolutionary arms races in visual performance between competing predators and their prey species, and this would have rapidly led to large eyes and high-performance vision. Other evolutionary responses to the new threat would have been development of protective armor or deep burrowing life-styles to escape visually guided predators. The fossil record reveals that all these features appeared rapidly during the Cambrian explosion, some 540 million years ago. It seems possible, and even likely, that the evolution of object vision and visually guided predation rapidly drove this evolution and generated essentially all modern and swiftly mobile animals from pre-existing small, soft and slow animals.

A huge range of novel visually guided behaviors were made possible by object vision. Apart from its obvious use for catching prey, and for visually guided escape from predators, object vision allows for recognition of conspecifics, visual communication and other visually guided interactions for reproductive and social purposes. Further examples are detection and manipulation of food items.

I analogy with ancient visual roles, object vision can be divided into active tasks of visuomotor control and assessment tasks with both short- and long-term impacts on behavior. Visual perception, which is a central concept in human vision, is largely equivalent to object-based visual assessment. There is no reason to doubt that other vertebrates, arthropods and cephalopods are also capable of visual perception. In contrast to non-object based visual assessment, which informs about habitat quality and current conditions, perception provides information on the current situation and allows for the planning of actions. This too is a major advance from just ancient vision.

Based on human studies, Goodale and Milner (1992) made the important principal distinction between active object-vision and perception. Interestingly, observations of patients with acquired neurological dysfunction suggested that perception is a conscious process whereas active visual tasks in general are not [see also Goodale (2014)]. Whether this also applies to other species among vertebrates, arthropods and cephalopods is difficult to test but fascinating food for speculation.

In the animal groups where object vision has evolved (vertebrates, arthropods, and cephalopods) the ancient visual tasks remain as important as they were before object vision evolved. In fact, ancient vision may exploit the higher resolution required for object vision, resulting in improve performance of general orientation, navigation, path finding, obstacle avoidance, and measurements of self-motion. Large eyes, extensive retinas, and high pixel numbers in neural processing are expensive requirements for object vision (Land and Nilsson, 2012). These costs are offset by the enormous advantages endowed by visual discrimination of objects. Neural circuits for early visual processing and motion detection may be shared by object vision and active ancient vision, making the latter benefit from a major performance boost without much extra cost. Introduction of object vision can thus be expected to result also in major improvements of ancient vision (**Figure 1**).

DISCUSSION

The roles that vision serve can be neatly divided into ancient vision and object vision, where the former must have evolved before the latter. The distinction between active visual tasks for immediate feed-back control of action on the one hand, and assessment tasks, with potentially long time-constants, on the other, applies to both ancient vision and object vision. It is impossible to say whether active vision or assessment vision evolved first. In many ways, the two modes depend on one another: habitat orientation and interaction with objects would normally require a previous assessment of the environment. Likewise, visual assessments make sense only if they lead to behavioral decisions and these may in turn result in visually guided actions.

The overall evolutionary sequence from non-directional photoreception, *via* directional photoreception and ancient vision, to object vision (**Figure 1**), represents a natural increase in the amount of sensory information, eye complexity, and neural complexity. Each step preadapts the sensory system for the next step, implying that it is practically inconceivable to jump any of the steps. The numerous invertebrates at intermediate stages in the sequence offers strong support that the four-step model of visual evolution is not only general but has been followed independently in different animal phyla (Nilsson, 2020). The only groups that are documented to have object vision are vertebrates, arthropods and cephalopods. Many more groups, such as gastropod mollusks, polychetes and jellyfish have stopped at ancient vision, but a few of these groups contain examples that may qualify for object vision (conchs, heteropod snails and alciopid polychetes [see Land, 1981)]. Numerous taxonomic groups have stopped at directional photoreception but it is rare to possess only non-directional photoreception.

There are a few notable exceptions to the general evolutionary sequence of vision. These exceptions are found in sessile or very slow-moving invertebrates where the original eyes for ancient vision have been reduced and new, molecularly different, eyes or dispersed photoreceptors have evolved in novel locations to warn the animal of approaching danger (Bok et al., 2016, 2017; Nilsson, 2021). This has happened in fan worms, bivalves, and chitons, with alarm photoreceptors on the tentacular crown in fan worms, along the mantel edge in bivalves (Morton, 2008; Audino et al., 2020) and over the dorsal shell plates in chitons (Kingston et al., 2018). In fan worms and bivalves, the molecular profile indicates that these photoreceptors and eyes evolved directly from dermal shadow receptors (non-directional photoreception) (Del Pilar Gomez and Nasi, 2000; Bok et al., 2017).

In the past, the evolution of vision has been investigated *via* studies of developmental genes (Arendt, 2003), opsin sequences (Porter et al., 2012; Ramirez et al., 2016) or eye structure (Nilsson, 2009). These studies have added valuable insight into the evolution of vision, but it is important to note that the driving force does not lie at any of these organizational levels. It is the fitness gained by more efficient behaviors that have been the driving force behind the evolution of vision. It should also be emphasized that eyes, brains, and the motile body must evolve in concert to produce a fitness gain through more advanced vision.

DATA AVAILABILITY STATEMENT

The original contributions presented in the study are included in the article/supplementary material, further inquiries can be directed to the corresponding author.

AUTHOR CONTRIBUTIONS

The author confirms being the sole contributor of this work and has approved it for publication.

FUNDING

This study was supported by the Swedish Research Council, Grant No. 2019-04813.

ACKNOWLEDGMENTS

I thank Eric Warrant for constructive comments on the manuscript.

REFERENCES

Aranda, M. L., and Schmidt, T. M. (2020). Diversity of intrinsically photosensitive retinal ganglion cells: circuits and functions. *Cell. Mol. Life Sci.* 78, 889–907. doi: 10.1007/s00018-020-03641-5

Arendt, D. (2003). Evolution of eyes and photoreceptor cell types. *Int. J. Dev. Biol.* 47, 563–571.

Audino, J. A., Serb, J. M., and Rodriguez Marian, J. E. A. (2020). Hard to get, easy to lose: evolution of mantle photoreceptor organs in bivalves (Bivalvia, Pteriomorphia). *Evolution* 7, 2105–2120. doi: 10.1111/evo.14050

Berman, G. J., Bialek, W., and Shaevitz, J. W. (2016). Predictability and hierarchy in *Drosophila* behavior. *Proc. Natl. Aacd. Sci. U.S.A.* 113, 11943–11948.

Blevins, E., and Johnsen, S. (2004). Spatial vision in the echinoid genus *Echinometra*. *J. Exp. Biol.* 207, 4249–4253. doi: 10.1242/jeb.01286

Bok, M. J., Capa, M., and Nilsson, D.-E. (2016). Here, there and everywhere: the radiolar eyes of fan worms (Annelida, Sabellidae). *Integr. Comp. Biol.* 56, 784–795. doi: 10.1093/icb/icw089

Bok, M. J., Porter, M. L., and Nilsson, D.-E. (2017). Phototransduction in fan worm radiolar eyes. *Curr. Biol.* 27, R681–R701. doi: 10.1016/j.cub.2017.05.093

Brown, F. A., Hastings, J. W., and Palmer, J. O. (2014). *The Biological Clock*. New York, NY: Academic Press.

Del Pilar Gomez, M., and Nasi, E. (2000). Light transduction in invertebrate hyperpolarizing photoreceptors: possible involvement of a go-regulated guanylate cyclase. *J. Neurosci.* 20, 5254–5263. doi: 10.1523/JNEUROSCI.20-14-05254.2000

Garm, A., and Nilsson, D.-E. (2014). Visual navigation in starfish: first evidence for the use of vision and eyes in starfish. *Proc. R. Soc. B* 281:20133011. doi: 10.1098/rspb.2013.3011

Garm, A., O'Connor, M., Parkefelt, L., and Nilsson, D.-E. (2007). Visually guided obstacle avoidance in the box jellyfish *Tripedalia cystophora* and *Chiropsella bronzie*. *J. Exp. Biol.* 210, 3616–3623. doi: 10.1242/jeb.004044

Garm, A., Oskarsson, M., and Nilsson, D.-E. (2011). Box jellyfish use terrestrial visual cues for navigation. *Curr. Biol.* 21, 798–803. doi: 10.1016/j.cub.2011.03.054

Goodale, M. A. (2014). How (and why) the visual control of action differs from visual perception. *Proc. Roy. Soc. B* 281:20140337. doi: 10.1098/rspb.2014.0337

Goodale, M. A., and Milner, A. D. (1992). Separate visual pathways for perception and action. *Trends Neurosci.* 15, 20–e25.

Grob, R., El Jundi, B., and Fleischmann, N. (2021). Towards a common terminology for arthropod spatial orientation. *Ethol. Ecol. Evol.* 33, 338–358. doi: 10.1080/03949370.2021.1905075

Gurarie, E., Bracis, C., Delgado, M., Meckley, T. D., Kojola, I., and Wagner, C. M. (2016). What is the animal doing? Tools for exploring behavioural structure in animal movements. *J. Anim. Ecol.* 85, 69–84. doi: 10.1111/1365-2656.12379

Kingston, A. C. N., Chappell, D. R., and Speiser, D. I. (2018). Evidence for spatial vision in *Chiton tuberculatus*, a chiton with eyespots. *J. Exp. Biol.* 221:jeb183632. doi: 10.1242/jeb.183632

Kirwan, J. D., and Nilsson, D.-E. (2019). A millipede compound eye mediating low-resolution vision. *Vis. Res.* 165, 36–44. doi: 10.1016/j.visres.2019.09.003

Kirwan, J. D., Graf, J., Smolka, J., Mayer, G., Henze, M. J., and Nilsson, D.-E. (2018). Low resolution vision in a velvet worm (Onychophora). *J. Exp. Biol.* 221:175802.

Land, M. F. (1981). "Optics and vision in invertebrates," in *Handbook of Sensory Physiology*, Vol. VII, ed. H. Autrum (Berlin: Springer), 471–592.

Land, M. F., and Nilsson, D.-E. (2012). *Animal Eyes*, 2 Edn. Oxford: Oxford University Press, 271.

Ljungholm, M., and Nilsson, D.-E. (2021). Modelling the visual world of a velvet worm. *PLoS Comput. Biol.* 17:e1008808. doi: 10.1371/journal.pcbi.1008808

Lucas, R. J. (2013). Mammalian inner retinal photoreception. *Curr. Biol.* 23, R125–R133. doi: 10.1016/j.cub.2012.12.029

Mahoney, P. J., and Young, J. K. (2017). Uncovering behavioural states from animal activity and site fidelity patterns. *Methods Ecol. Evol.* 8, 174–183.

Morton, B. (2008). The evolution of eyes in the Bivalvia: new insights. *Am. Malacol. Bull.* 26, 35–45.

Nässel, D. R., Pauls, D., and Huetteroth, W. (2019). Neuropeptides in modulation of *Drosophila* behavior: how to get a grip on their pleiotropic actions. *Curr. Opin. Insect Sci.* 36, 1–8. doi: 10.1016/j.cois.2019.03.002

Nilsson, D.-E. (2009). The evolution of eyes and visually guided behaviour. *Philos. Trans. R. Soc. B* 364, 2833–2847. doi: 10.1098/rstb.2009.0083

Nilsson, D.-E. (2013). Eye evolution and its functional basis. *Vis. Neurosci.* 30, 5–20. doi: 10.1017/S0952523813000035

Nilsson, D.-E. (2020). Eye evolution in animals. *Ref. Mod. Neurosci. Biobehav. Psychol.* doi: 10.1016/B978-0-12-805408-6.00013-0

Nilsson, D.-E. (2021). The diversity of eyes and vision. *Annu. Rev. Vis. Sci.* 7, 8.1–8.23.

Nilsson, D.-E., and Bok, M. J. (2017). Low-resolution vision–at the hub of eye evolution. *Integ. Comp. Biol.* 201757, 1066–1070. doi: 10.1093/icb/icx120

Nilsson, D.-E., Gislén, L., Coates, M. M., Skogh, C., and Garm, A. (2005). Advanced optics in a jellyfish eye. *Nature* 435, 201–205. doi: 10.1038/nature03484

Nilsson, D.-E., Warrant, E. J., and Johnsen, S. (2014). Computational visual ecology in the pelagic realm. *Philos. Trans. R. Soc. B* 369:20130038. doi: 10.1098/rstb.2013.0038

Porter, M. L., Blasic, J. R., Bok, M. J., Cameron, E. G., Pringle, T., Cronin, T. W., et al. (2012). Shedding new light on opsin evolution. *Philos. Trans. Roy. Soc. B* 279, 3–14. doi: 10.1098/rspb.2011.1819

Ramirez, M. D., Pairett, A. N., Pankey, M. S., Serb, J. M., Speiser, D. I., Swafford, A. J., et al. (2016). The last common ancestor of most bilaterian animals possessed at least nine opsins. *Genome Biol. Evol.* 8, 3640–3652. doi: 10.1093/gbe/evw248

Randel, N., and Jekely, G. (2016). Phototaxis and the origin of visual eyes. *Philos. Trans. R. Soc. B* 371;20150042. doi: 10.1098/rstb.2015.0042

Scholtyssek, C., Dacke, M., Kröger, R., and Baird, E. (2014). Control of self-motion in dynamic fluids: fish do it differently from bees. *Biol. Lett.* 10:20140279. doi: 10.1098/rsbl.2014.0279

Sumner-Rooney, L., Kirwan, J. D., Lowe, E., and Ullrich-Lüter, E. (2020). Extraocular vision in a brittle star is mediated by chromatophore movement in response to ambient light. *Curr. Biol.* 30, 319–327. doi: 10.1016/j.cub.2019.11.042

Conflict of Interest: The author declares that the research was conducted in the absence of any commercial or financial relationships that could be construed as a potential conflict of interest.

Publisher's Note: All claims expressed in this article are solely those of the authors and do not necessarily represent those of their affiliated organizations, or those of the publisher, the editors and the reviewers. Any product that may be evaluated in this article, or claim that may be made by its manufacturer, is not guaranteed or endorsed by the publisher.

frontiers | Frontiers in Neuroanatomy

ORIGINAL RESEARCH
published: 11 July 2022
doi: 10.3389/fnana.2022.945344

An EvoDevo Study of Salmonid Visual Opsin Dynamics and Photopigment Spectral Sensitivity

*Mariann Eilertsen[1], Wayne Iwan Lee Davies[2,3], Dharmeshkumar Patel[4], Jonathan E. Barnes[4], Rita Karlsen[1], Jessica Kate Mountford[3,5], Deborah L. Stenkamp[6,7], Jagdish Suresh Patel[4,6] and Jon Vidar Helvik[1]**

[1] Department of Biological Sciences, University of Bergen, Bergen, Norway, [2] Umeå Centre for Molecular Medicine, Umeå University, Umeå, Sweden, [3] School of Life Sciences, College of Science, Health and Engineering, La Trobe University, Melbourne, VIC, Australia, [4] Institute for Modeling Collaboration and Innovation (IMCI), University of Idaho, Moscow, ID, United States, [5] Lions Eye Institute, University of Western Australia, Perth, WA, Australia, [6] Department of Biological Sciences, University of Idaho, Moscow, ID, United States, [7] Institute for Bioinformatics and Evolutionary Studies, University of Idaho, Moscow, ID, United States

Salmonids are ideal models as many species follow a distinct developmental program from demersal eggs and a large yolk sac to hatching at an advanced developmental stage. Further, these economically important teleosts inhabit both marine- and freshwaters and experience diverse light environments during their life histories. At a genome level, salmonids have undergone a salmonid-specific fourth whole genome duplication event (Ss4R) compared to other teleosts that are already more genetically diverse compared to many non-teleost vertebrates. Thus, salmonids display phenotypically plastic visual systems that appear to be closely related to their anadromous migration patterns. This is most likely due to a complex interplay between their larger, more gene-rich genomes and broad spectrally enriched habitats; however, the molecular basis and functional consequences for such diversity is not fully understood. This study used advances in genome sequencing to identify the repertoire and genome organization of visual opsin genes (those primarily expressed in retinal photoreceptors) from six different salmonids [Atlantic salmon (*Salmo salar*), brown trout (*Salmo trutta*), Chinook salmon (*Oncorhynchus tshawytcha*), coho salmon (*Oncorhynchus kisutch*), rainbow trout (*Oncorhynchus mykiss*), and sockeye salmon (*Oncorhynchus nerka*)] compared to the northern pike (*Esox lucius*), a closely related non-salmonid species. Results identified multiple orthologues for all five visual opsin classes, except for presence of a single short-wavelength-sensitive-2 opsin gene. Several visual opsin genes were not retained after the Ss4R duplication event, which is consistent with the concept of salmonid rediploidization. Developmentally, transcriptomic analyzes of Atlantic salmon revealed differential expression within each opsin class, with two of the long-wavelength-sensitive opsins not being expressed before first feeding. Also, early opsin expression in the retina was located centrally, expanding dorsally and ventrally as eye development progressed, with rod opsin being the dominant visual opsin post-hatching. Modeling by spectral tuning analysis and atomistic molecular simulation, predicted the greatest variation in the spectral peak

OPEN ACCESS

Edited by:
Marta Agudo-Barriuso, Biomedical Research Institute of Murcia (IMIB), Spain

Reviewed by:
Jack Falcon, Sorbonne Universités, France
K. S. Narayan, Jawaharlal Nehru Centre for Advanced Scientific Research, India

***Correspondence:**
Jon Vidar Helvik
vidar.helvik@uib.no

Received: *16 May 2022*
Accepted: *23 June 2022*
Published: *11 July 2022*

Citation:
Eilertsen M, Davies WIL, Patel D, Barnes JE, Karlsen R, Mountford JK, Stenkamp DL, Patel JS and Helvik JV (2022) An EvoDevo Study of Salmonid Visual Opsin Dynamics and Photopigment Spectral Sensitivity. Front. Neuroanat. 16:945344. doi: 10.3389/fnana.2022.945344

of absorbance to be within the Rh2 class, with a ∼40 nm difference in λ_{max} values between the four medium-wavelength-sensitive photopigments. Overall, it appears that opsin duplication and expression, and their respective spectral tuning profiles, evolved to maximize specialist color vision throughout an anadromous lifecycle, with some visual opsin genes being lost to tailor marine-based vision.

Keywords: photoreception, eye, atomistic molecular simulation, RNA *in situ* hybridization, RNA sequencing, visual opsin, salmonid

INTRODUCTION

Salmonids are a group of closely related teleost species of high economical value with an anadromous lifestyle, inhabiting both freshwater and marine environments as part of their life cycle. These habitats include lakes, rivers, and marine ecosystems from coastal areas to open ocean, all with very different optical characteristics. In the water column, the downwelling light environment changes rapidly with depth as photons are absorbed and scattered by water molecules and components such as dissolved organic matter, chlorophyll in phytoplankton and suspended soil. The concentration of these components varies in fresh and marine waters causing local variations in spectral irradiance (Jerlov, 1976; Levine and MacNichol, 1982; Partridge and Cummings, 1999). In general, the light of shorter and longer wavelengths are limited to the upper water column, while short-wavelengths in the blue part of the light spectrum (around 480 nm) penetrates the deepest (Levine and MacNichol, 1982; Douglas and Djamgoz, 1990). As such, constantly changing lighting conditions (i.e., diurnal variation in both the spectrum and intensity of light environment), place great selective pressure on the visual system of many fishes, especially those that dwell in rivers or near the surface of estuaries and/or oceans, where visual capabilities are likely to change during development, as well as in response to daily and annual fluctuations of light (Evans and Browman, 2004; Carleton et al., 2020).

Visual photoreception is fundamentally dependent on photopigments, which consist of an opsin protein bound to a light-sensitive chromophore, located in the outer membrane of ocular rods and cones (Terakita, 2005). Being sensitive to different wavelengths of light, due in part to the opsin protein sequence present (Carleton et al., 2020), visual photopigments directly translate environmental light information (photons) in the first step of the phototransduction cascade that ultimately leads to a perceived "colored" image of the external world that is generated in the visual centers of the brain. In vertebrates, the cone visual opsins used for color vision are generally divided into four separate classes based on distinct spectral sensitivities with peak absorbance (i.e., λ_{max}) values within the ultraviolet (UV) (SWS1, λ_{max} = 355–445 nm), blue (SWS2, λ_{max} = 400–470 nm), green (RH2, λ_{max} = 460–530 nm) and red (LWS, λ_{max} = 500–575 nm) regions of the light spectrum (Davies et al., 2012). While cones require bright light (i.e., for photopic vision) to function, rods containing RH1 (λ_{max} = 460–530 nm, but is typically ∼500 nm for most shallow water or terrestrial species) are used for dim light or scotopic vision (Yokoyama, 2000).

In general, the photoreceptive or visual possibilities of a species is dependent on the opsin genes existing in the genome and specific spatial and temporal expression patterns. The teleost visual system is particularly diverse among vertebrates, where tandem duplications and whole genome duplications have been characteristically important in shaping the evolution and function of spectrally distinct photoreceptive pathways (Kuraku et al., 2008; Rennison et al., 2012). In the common ancestor of all salmonids, a salmonid-specific fourth whole genome duplication, Ss4R, occurred approximately ∼80 million years ago (mya) (Allendorf and Thorgaard, 1984; Lien et al., 2016). However, genomic analyzes of visual opsins in Atlantic salmon and rainbow trout have revealed that many opsin genes have been lost (Lin et al., 2017; Musilova et al., 2019). For those opsin genes still retained in the genome, it is likely that they have functionally evolved in response to selective pressures such as the external light environment to regulate their expression profiles and/or encode photopigments that exhibit spectrally distinct characteristics *via* changes in amino acids at key tuning sites that spectrally tune these photopigments to different wavelengths (Yokoyama, 2000). In recent years, an increasing number of fish genomes have been sequenced, highlighting the importance of habitat diversity in aqueous environments as a driving force in fish opsin gene evolution (Lin et al., 2017). Based on studies in agnathans, it has been proposed, for many vertebrate classes including teleosts (Davies et al., 2012), that alterations in gene copies and subsequent mutations play an important role in the evolution of color vision and that spectral tuning of visual photopigments often strongly reflects ecology, especially regarding the light environment (Davies et al., 2009).

Unique features of the teleost eye include continued retinal growth and plasticity throughout postembryonic changes and development (Evans and Fernald, 1990). Many marine species, such as Atlantic cod, follow an indirect developmental program, where they hatch with poorly differentiated retinas followed by a long larval period with a pure-cone retina (Balon, 1985). The rods develop during metamorphosis (i.e., the transition to the juvenile stage), supported by a large increase in the expression of rod opsin (Valen et al., 2016). Conversely, salmonids follow a more direct developmental program, with demersal eggs and a large yolk sac, where they hatch at an advanced developmental stage (Kendall et al., 1984). Studies in salmonids show that expression of visual opsins occurs before hatching and that cones expressing *sws1* ("UV"), *rh2* ("green"), and *lws* ("red"), as well as rod opsin, appear embryonically, while cones expressing *sws2* appear after hatching (Cheng et al., 2007). Further, phenotypic plasticity in the visual system of salmonids related to sea-river migration has

been shown by temporal loss and gain of UV cones containing Sws1 photopigments (Allison et al., 2006), as well as a shift from UV to blue sensitivity during salmonid retinal development that is related to a change in lifestyle from rivers with abundant UV light to deeper oceanic waters (Cheng and Flamarique, 2007).

Utilizing recent advances in genome sequencing that provided access to the whole genomes of several salmonids (Macqueen et al., 2017), this study identified the complete complement of visual opsin genes in six salmonids and compared their phylogenetic diversity and rediploidization to that of the northern pike, a sister linage that did not undergo Ss4R (i.e., the salmonid-specific whole genome duplication event) (Rondeau et al., 2014). Developmental opsin expression patterns were monitored, showing differential temporal expression within specific opsin classes. Further, by using a combination of spectral tuning site interrogation and atomistic molecular simulation analyzes, spectral profiles for each Atlantic salmon visual photopigment (i.e., Sws2, Rh2, and Lws classes) were determined and functional consequences discussed within the context of teleost development and visual ecology.

MATERIALS AND METHODS

Animals

Eggs and sperm from Atlantic salmon (*Salmo salar*) were obtained from MOWI, Tveitevågen, Norway. Fertilization took place at an approved laboratory facility at High Technology Center, University of Bergen, Norway, where alevins were raised until the stages, after hatching at 555 day degrees (dd) and just before first feeding at 720 dd. These stages correspond approximately to relative ages 310 and 390 in Gorodilov (1996). The "dd" nomenclature refers to the average temperature per day (6° with a standard deviation of 0.5) multiplied by the number of days. All experiments described followed local animal care guidelines and were given ethical approval by the Norwegian Food Safety Authority. The study complied with ARRIVE guidelines (Percie du Sert et al., 2020).

Molecular Cloning of Visual Opsins

Eyes were collected from Atlantic salmon alevins at the stage just before first feeding, where total RNA was isolated by TRI reagent (Sigma, St. Louis, MO, United States), then treated with DNase I by using a TURBO DNA-free^{TM} Kit (ThermoScientific, Waltham, MA, United States). Complementary DNA (cDNA) was reversely transcribed by using a SuperScript III kit (Invitrogen, Carlsbad, CA, United States) as recommended by the manufacturer's instructions. Initial *in silico* analyzes of the Atlantic salmon genome database ICSASG_v2 (Lien et al., 2016) was conducted by using BLASTP or BLASTN *via* NCBI (Sayers et al., 2019) with zebrafish (*Danio rerio*) visual opsin sequences being used as bait for gene mining. To generate full-length visual opsins, primers were designed that anneal to published or predicted untranslated regions (UTRs) or to regions containing start/stop codons. An Advantage®2 PCR Kit (TaKaRa, Japan) was used to perform amplification reactions by applying PCR or nested PCR approaches (see **Supplementary Table 1**) over 35 cycles. PCR products were extracted from agarose gels using a MinElute®Gel Extraction Kit (Qiagen, Germany), before being cloned into StrataClone PCR Cloning vector pSC-A-amp/kan (Agilent Technologies, LA Jolla, CA, United States). Correct clones were sequenced at the University of Bergen Sequencing Facility, with nucleotide sequences being deposited to the GenBank database with Accession Numbers (ON456431-ON456441).

Sequence and Phylogenetic Analyzes

In silico search in salmonid genome databases [brown trout (*Salmo trutta*), Chinook salmon (*Oncorhynchus tshawytcha*), coho salmon (*Oncorhynchus kisutch*), rainbow trout (*Oncorhynchus mykiss*), sockeye salmon (*Oncorhynchus nerka*)] and in the northern pike (*Esox lucius*) was performed to identify the visual opsins of the respective species. The search was performed by BLASTP or BLASTN on NCBI (Sayers et al., 2019) or Ensembl (Cunningham et al., 2018) using the Atlantic salmon visual opsins in the search. In addition, the sequences used for Atlantic salmon *rh1-2.1* and *rh1-2.2* are from Lin et al. (2017). The coding sequences of annotated or putative opsin genes in the genomes were aligned to the Atlantic salmon visual opsins using Vector NTI9 software (Invitrogen, Carlsbad, CA, United States) and ClustalX2 (Larkin et al., 2007) to evaluate the coding sequence. The genomes of Atlantic salmon, brown trout, Chinook salmon, rainbow trout, coho salmon, and an updated version of northern pike were published on Ensembl (version 104), and recently updated versions of Atlantic salmon and rainbow trout have been published (version 106). The most recent sequences from NCBI and Ensembl have been used in the evaluation of open reading frame (ORF). Sequences determined to yield intact ORFs, cloned sequence for Atlantic salmon and either NCBI or Ensembl sequence for the other species, were used in the phylogenetic analysis, whereas partial sequences and/or sequences derived from pseudogenes were omitted. A codon-matched nucleotide sequence alignment of 90 ray-finned fish opsin coding regions was generated by ClustalW (Higgins et al., 1996) and manually manipulated to refine the accuracy of cross-species comparison. Specifically, the alignment incorporated opsin coding sequences of visual photopigments identified in the genomes of several salmonid species and a phylogenetically related species (i.e., *E. lucius*, northern pike) compared to orthologous visual opsin sequences expressed in the retina of *D. rerio* (zebrafish). All five visual opsin classes (i.e., *lws*, *sws1*, *sws2*, *rh2*, and *rh1*) were included, with zebrafish vertebrate ancient (va) opsin sequences (*va1* and *va2*) used collectively as an outgroup given that this opsin type is a sister clade to all five visual photopigment classes. Phylogenetic analyses of 1,000 replicates were conducted in MEGA11 (Tamura et al., 2021), with evolutionary histories being inferred by using the Maximum Likelihood method and General Time Reversible model (Nei and Kumar, 2000). The percentage of trees in which the associated taxa clustered together is shown next to the branches. Initial trees for the heuristic search were obtained by applying Neighbor-Joining and BioNJ algorithms (Saitou and Nei, 1987) to a matrix of pairwise distances estimated using the Maximum Composite Likelihood (MCL) approach (Tamura and

Nei, 1993). The tree was drawn to scale, with branch lengths measured in the number of substitutions per site. A total of 996 positions was present in the final dataset, with all positions with less than 95% site coverage being eliminated. That is, fewer than 5% alignment gaps, missing data, and ambiguous bases were allowed at any position.

Prediction of λ_{max} Values of Visual Photopigments Expressed in the Eyes of Atlantic Salmon

Currently, it is known that λ_{max} values of vertebrate photopigments are influenced by ∼40 known amino acid tuning sites (Davies et al., 2012; Musilova et al., 2019). Using conventional bovine rod opsin (Accession Number NP001014890) numbering, spectral peak of absorbance values were reliably predicted for Sws1, Rh1, and Lws photopigments using manual interrogation as outlined in Musilova et al. (2019). Particular attention was made at site 86, which is important for UV-sensitivity (UVS) in Sws1 photopigments (Cowing et al., 2002). For Rh1 photopigments, sites 83, 90, 96, 102, 113, 118, 122, 124, 132, 164, 183, 194, 195, 207, 208, 211, 214, 253, 261, 265, 269, 289, 292, 295, 299, 300, and 317 were analyzed as being spectrally important (Sakmar et al., 1991; Chan et al., 1992; Hope et al., 1997; Yokoyama et al., 1999, 2007, 2008; Yokoyama, 2000, 2008; Hunt et al., 2001; Janz and Farrens, 2001; Davies et al., 2007, 2012; Kuraku et al., 2008). Similarly, spectral tuning sites 164, 181, 261, 269, and 292 were investigated to calculate Lws photopigment λ_{max} values (Yokoyama, 2000; Davies et al., 2012). To determine the λ_{max} values of four Rh2 and an Sws2 visual photopigment, molecular dynamics simulations-based modeling approaches were applied (Patel et al., 2018, 2020). In this approach, molecular dynamics simulations were carried out using 3D homology models of vertebrate Rh2 and Sws2-type visual photopigments for which λ_{max} values have been experimentally measured. Molecular simulations were then used to develop simple statistical models using parameters describing conformation and fluctuation of the 11-*cis* retinal chromophore and attached lysine residue, which predicted λ_{max} values with high accuracy. Once determined, representative dark spectra for all visual photopigments were generated using a standard A_1-based rhodopsin template (Govardovskii et al., 2000).

RNA Sequencing Analyzes of Atlantic Salmon Sampled During Development

RNA sequencing reads of the developmental series (whole embryos and alevins) were obtained by downloading from SRA on NCBI (Sayers et al., 2019) (BioProject PRJNA72713, BioSample SAMN02864156-SAMN02864171) associated with the publication of the Atlantic salmon genome (Lien et al., 2016). The developmental stage, day degrees (dd), was identified by calculating the number of days associated with the BioSamples and the incubation temperature (9.4°C) (von Schalburg et al., 2014). The samples were aligned to the published Atlantic salmon genome (GCF_000233375.1) using Bowtie2 (Langmead and Salzberg, 2012), read counts were generated using Samtools (Li et al., 2009) and the reads where normalized to the sample with the lowest number of reads. A heatmap presented by the logfold2 change of individual visual opsin genes was made by pheatmap (Kolde, 2019).

Riboprobes and Localization of Visual Opsin Transcripts by RNA *in situ* Hybridization

Preparation of digoxigenin DIG-labeled riboprobes for the visual opsins of Atlantic salmon were prepared following the manufacturer's instructions (Roche Diagnostics, Germany). In the synthesis of riboprobes, specific PCR products were used as template for the reaction (Thisse and Thisse, 2008), where synthesized probes were precipitated by LiCl and ethanol together with tRNA (Roche Diagnostics, Germany). Nucleotide sequence alignments showed that sequence identity between visual opsin targets was between 50 and 65%, thus ensuring no cross-hybridization between opsin classes. For the four *rh2* genes, the identity in the coding region between the four genes is ∼87% and cross-hybridization was likely to occur. Therefore, the overall Rh2 class expression was analyzed using all four *rh2* as templates in the probe synthesis reaction to generate a probe mix of all genes. For the four *lws* genes, the probe targets the coding region with an overall sequence identity of ∼87%. As such, both *lws*2 and *lws*3 were used as template, however, the probe hybridized to all *lws* genes as the individual probes have a sequence similarity above 90% to paralogues not used during the generation of the probe by PCR. Alevins (555 and 720 dd, hatched Atlantic salmon larvae living on their yolk sac) were euthanized with an overdose of tricaine (MS-222, Sigma, United States) before fixation in 4% paraformaldehyde-buffered PBS and further processed as described in Eilertsen et al. (2014). Cryosectioning of consecutive frontal sections (10 μm) was performed on a Leica CM 3050S cryostat (Leica Biosystems, Germany) and before storage at −20°C, the tissues were air dried for 1 h at room temperature and then incubated for 30 min at 65°C. RNA *in situ* hybridization was carried out as described by Sandbakken et al. (2012). Images were taken with a Leica DFC 320 digital camera (Leica Microsystems, Germany) attached to a Leica DM 6000B microscope (Leica Microsystems, Germany). Adobe Photoshop CC (San Jose, CA, United States) was used to adjust image brightness and contrast, as well as for displaying schematic overviews of visual opsin expression patterns at different developmental stages.

RESULTS

Identification of Visual Opsins in Atlantic Salmon

In silico gene mining of the Atlantic salmon genome and reviewing the literature allowed for the identification of *rh1-1, rh1-2.1, rh1-2.2*, *sws1-1*, *sws1-2*, *sws2*, *rh2-1*, *rh2-2*, *rh2-3*, *rh2-4*, *lws1*, *lws2*, *lws3*, and *lws4* visual opsin genes (**Table 1**, **Supplementary Table 2**, and **Supplementary Figures 1**–**7**). However, *rh1-2.1, rh1-2.2*, and *sws1-2* were evaluated to be pseudogenes by Lin et al. (2017) and this present study (**Supplementary Figures 2**, **6**, **7**). An evaluation of *sws1-2* showed

a 6 base pair (bp) deletion and a premature stop codon, indicating that Sws1-2, if translated, would be truncated. The results of this study show that an additional *lws* gene exists in the salmon genome, here named *lws4*, when compared to the findings of Lin et al. (2017), as indicated in Musilova et al. (2019). Using molecular cloning, the sequence of 11 full-length visual opsins were identified to be expressed in Atlantic salmon.

Identification of Visual Opsins in Other Salmonids and Northern Pike

Using *in silico* analyzes, visual opsins were identified in six additional salmonids as listed above, as well as in the northern pike, a member of the closest related diploid sister-group to salmonids (Rondeau et al., 2014; **Table 1** and **Supplementary Table 2**). In brown trout, *rh1-1*, *rh1-2.1, rh1-2.2*, *sws1-1*, *sws1-2*, *sws2*, *rh2-1*, *rh2-2*, *rh2-3*, *rh2-4*, *lws1*, *lws2*, *lws3*, and *lws4* were identified. Closer inspection showed that *rh1.2.1* and *rh1.2.2* are pseudogenes as it possesses several indels within the ORF, which is consistent with the same gene being a pseudogene in Atlantic salmon (**Supplementary Figure 6**). In addition, *sws1-2* had the same 6 bp deletion as present in Atlantic salmon *sws1-2,* as well as additional indels in the ORF (**Supplementary Figure 7**). As such, these genes were not included in the phylogenetic analyzes. The following genes were identified in Chinook salmon: *rh1-1*, *rh1-2.1*, *sws1-1*, *sws1-2*, *sws2*, *rh2-1*, *rh2-2*, *rh2-3*, *rh2orf-4*, *lws1*, *lws2*, *lws3*, and *lws4*; however, both *lws3* (partial sequence) and *rh1-2.1* contained several indels (**Supplementary Figure 6**) and were not included in the phylogenetic analyzes. In coho salmon, *rh1-1*, *rh1-2.1*, *sws1-1*, *sws1-2*, *sws2*, *rh2-1.1*, *rh2-1.2*, *rh2-2*, *rh2-3*, *rh2-4*, *lws1*, *lws2*, *lws3*, and *lws4* were identified, revealing an additional *rh2* when compared to Atlantic salmon. Closer inspection showed that the ORF of *rh1-2.1* had several indels and is, therefore, a pseudogene as in Atlantic salmon (**Supplementary Figure 6**). The *lws3* gene was not included in the phylogenetic analyzes as it lacks sequence at the 5′ end and contains several indels. In rainbow trout, *rh1-1*, *rh1-2.2*, *sws1-1*, *sws1-2*, *sws2*, *rh2-1.1*, *rh2-1.2*, *rh2-2*, *rh2-3*, *rh2-4*, *lws1*, *lws2*, *lws3*, *lws4*, and *lws4.2* genes were found. As in Atlantic salmon, rainbow trout *rh1-2.2* contained several indels and has become pseudogenized (**Supplementary Figure 6**). In this study, an extra *rh2-1.1* gene was identified compared to Lin et al. (2017) but the *lws*3 gene was evaluated to be a pseudogene, as in Lin et al. (2017), with several indels and a truncated 3′ end. At Ensembl version 106, an extra *lws4* was identified at chromosome 15 (named *lws4.2*). It has a 33 bp deletion in the third transmembrane region and were consider as not functional. In the sockeye salmon genome, the following visual opsin genes were identified: *rh1-1*, *sws1-1*, *sws1-2*, *sws2*, *rh2-1.1*, *rh2-1.2*, *rh2-2*, *rh2-3*, *rh2-4*, *lws1*, *lws2*, and *lws4.* As in coho salmon and rainbow trout, an additional *rh2* gene was also identified. The sockeye salmon genome is currently only hosted by Ensembl Rapid Release, and the search for opsins was done at NCBI, and a search for *rh1-2.1* and *rh1-2.2* genes contained within NCBI databases failed to yield any hits. The *lws4* gene was shown to possess an indel in the ORF and was not included in the phylogenetic analyzes. As revealed in Lin et al. (2017), the northern pike genome contains *rh1-1*, *sws1-1*, *rh2-1*, *rh2-2*, *rh2-3*, *rh2-4*, *lws1*, *lws2*, *lws3*, and *lws4*, and in the updated pike genome at Ensembl database (version 104, Eluc_v4 assembly) a fourth *rh2-4* is included.

Phylogenetic Analyzes of Visual Opsins

A maximum likelihood tree based on a codon-matched alignment of nucleotide sequences was generated to show the putative evolutionary relationship between differing salmonid visual opsin gene copy numbers and related visual opsin genes of the northern pike. Specifically, **Figure 1** shows the presence of several *lws*, *sws1, sws2*, and *rh2* cone opsin genes, with all species having one functional *rh1* gene. All salmonids have an additional *sws1* gene compared to northern pike (**Table 2**); however, the second *sws1-2* sequence was only included in the phylogenetic analyzes for Chinook salmon, coho salmon, rainbow trout, and sockeye salmon since these genes are intact and likely to be functional photopigments. As shown in Lin et al. (2017), northern pike lack a *sws2* gene in the genome, while salmonids all possess one intact *sws2* gene. The *lws1* and *lws2* genes were present for all salmonids and northern pike, while the *lws3* gene was only included for Atlantic salmon, brown trout and northern pike since it was not identified, present as a partial sequence or assigned as a pseudogene in other salmonids. The *lws4* gene was not identified in sockeye salmon but were present for the other species. The maximum likelihood tree of the *rh2* opsin class revealed that salmonids possess 3 to 5 *rh2* genes: coho salmon, rainbow trout, and sockeye salmon all have five *rh2* genes, with phylogenetic analyzes showing that there has been an extra duplication of the *rh2-1* gene in these species. The *rh2* opsin genes in salmonids are tandemly duplicated in a gene array where each gene is located in close proximity to each other on the same chromosome for a particular species (**Supplementary Table 2**). Phylogenetically, *rh2-1/rh2-2* and *rh2-3/rh2-4* appear to branch together.

TABLE 1 | Visual opsin repertoires in six salmonids and northern pike.

Species	*rh1*	*sws1*	*sws2*	*rh2*	*lws*	Not included in the phylogenetic analyses
Atlantic salmon (*Salmo salar*)	3	2	1	4	4	*rh1-2.1*, *rh1-2.2*, *sws1-2*
Brown trout (*Salmo trutta*)	2	2	1	4	4	*rh1-2.1*, *rh1-2.2*, *sws1-2*
Chinook salmon (*Oncorhynchus tshawytcha*)	2	2	1	4	4	*rh1-2.1*, *lws3*
Coho salmon (*Oncorhynchus kisutch*)	2	2	1	5	4	*rh1-2.1*, *lws3*
Northern pike (*Esox lucius*)	1	1	0	4	4	
Rainbow trout (*Oncorhynchus mykiss*)	2	2	1	5	4	*rh2-1.2*, *lws3*, *lws4.2*
Sockeye salmon (*Oncorhynchus nerka*)	1	2	1	5	3	*lws4*

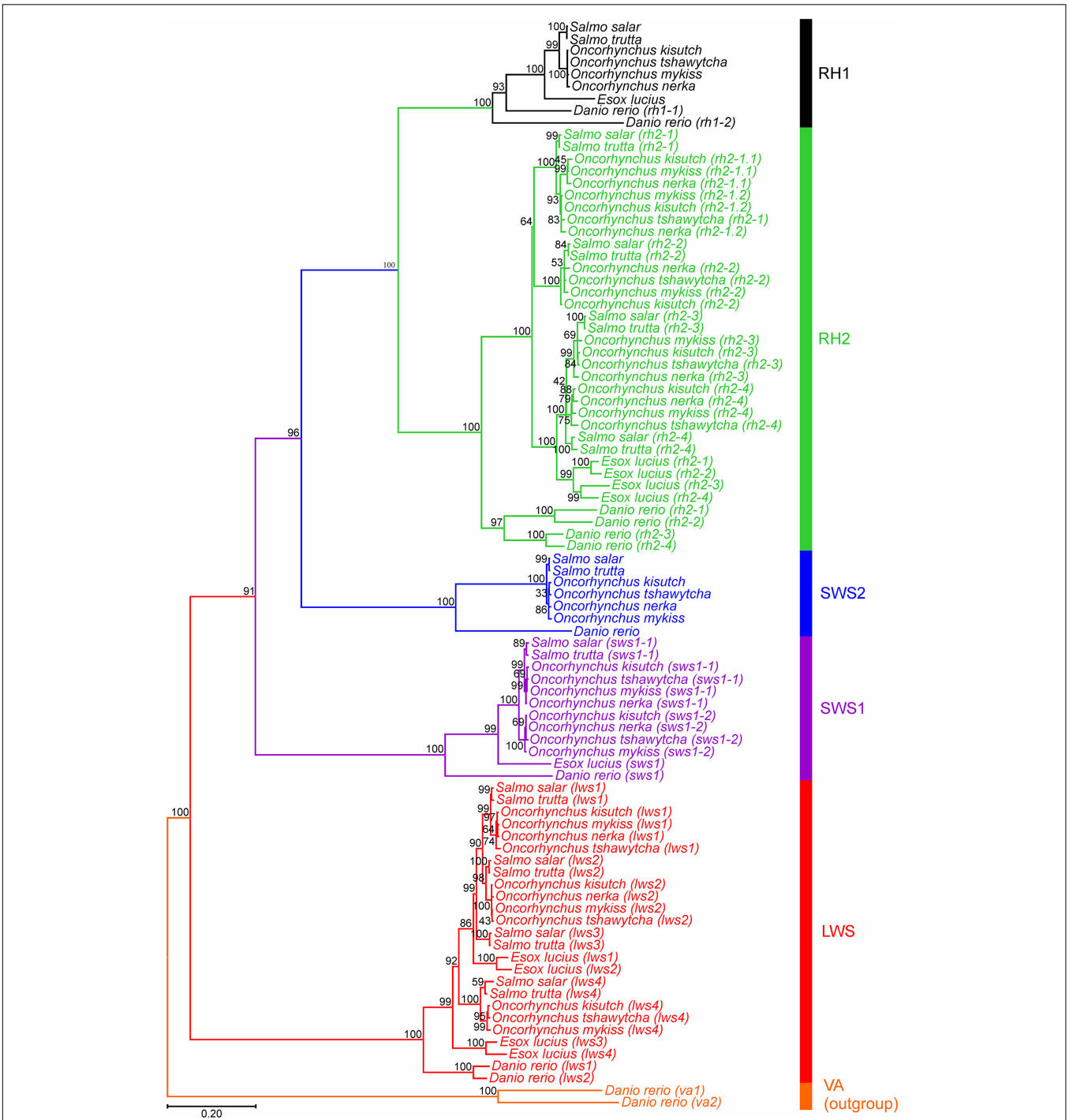

FIGURE 1 | Opsin evolutionary history as inferred by using the Maximum Likelihood method and General Time Reversible model (Nei and Kumar, 2000). The tree with the highest log likelihood (–21,458.16) is shown. The percentage of trees for which the associated taxa clustered together is shown next to the branches. Initial tree(s) for the heuristic search were obtained automatically by applying Neighbor-Join and BioNJ algorithms (Saitou and Nei, 1987), with a bootstrap value of 1,000, to a matrix of pairwise distances estimated using the Maximum Composite Likelihood (MCL) approach (Tamura and Nei, 1993), and then selecting the topology with superior log likelihood value. A discrete Gamma distribution was used to model evolutionary rate differences among sites [5 categories (+*G*, parameter = 1.0379)]. The rate variation model allowed for some sites to be evolutionarily invariable [(+*I*), 8.84% sites]. The tree is drawn to scale, with branch lengths measured in the number of nucleotide substitutions per site (indicated by the scale bar). This analysis involved 90 nucleotide sequences, where photopigment genes from six salmonid species and northern pike across five visual opsin classes (*lws*, *sws1*, *sws2*, *rh2*, and *rh1*) were compared. *Danio rerio* (zebrafish) vertebrate ancient (va) opsin 1 and 2 (*va1* and *va2*) sequences were used as an outgroup. Codon positions included were 1st + 2nd + 3rd + noncoding. All positions with less than 95% site coverage were eliminated, i.e., fewer than 5% alignment gaps, missing data, and ambiguous bases were allowed at any position (partial deletion option). There was a total of 996 positions in the final dataset. Evolutionary analyses were conducted in MEGA11 (Tamura et al., 2021).

TABLE 2 | Area under the RMSF($_{LYS+RET}$) curve and median values of various angles used to predict λ_{max} values for each of the four Atlantic salmon Rh2 photopigments and a single Sws2 visual photopigment using the statistical models.

	Angle 3	Torsion 3	Torsion 12	Predicted λ_{max}
Sws2	132.33	2.14	−5.1	420.04
	Torsion 15	**RMSF($_{LYS + RET}$)**		**Predicted λ_{max}**
Rh2-1	3.64	0.79		471.5
Rh2-2	3.06	0.76		475.5
Rh2-3	0.41	1.12		511.2
Rh2-4	0.84	1.1		506.4

Predicted λ_{max} Values of Visual Photopigments in Atlantic Salmon

For Lws, Sws1, and Rh1 photopigments, it is possible to accurately determine spectral peak of absorbance (λ_{max}) values using manual interrogation (e.g., Davies et al., 2012; Musilova et al., 2019). Specifically, analyses of the ∼40 known amino acid tuning sites showed that Sws1 was predicted to have a λ_{max} value at 360 nm due to the presence of Phe86, (Cowing et al., 2002), whereas the spectral peak of Atlantic salmon Rh1 was determined to be 509 nm (**Figure 2** and **Table 2**), assuming the use of a vitamin A_1-based retinal chromophore in both cases. Similar inspection of the four Lws photopigments in Atlantic salmon predicted a 14 nm span in their respective λ_{max} values based on the presence of spectral tuning sites 164, 181, 261, 269, and 292 (Yokoyama, 2000; Davies et al., 2012). Specifically, these spectral peaks ranged from 546 nm (for Lws3) to 560 nm (for Lws1), whereas the λ_{max} value was predicted to be 553 nm for both Lws2 and Lws4 photopigments (**Figure 2**).

As λ_{max} values for Sws2 and Rh2 photopigment classes are difficult to accurately predict from amino acid sequences alone, molecular dynamics simulations-based modeling approaches were applied (Patel et al., 2018, 2020). A two-term statistical model, 475.628 + (−8.720 ×Torsion 15) + (34.925 ×RMSF$_{(LYS + RET)}$), predicted the λ_{max} values of four Rh2 cone visual photopigments expressed in Atlantic salmon (**Figure 3**). In this model, Torsion 15 was a median value of the dihedral angle formed by C7–C6–C5–C18 atoms of 11-*cis* retinal (**Figure 3C**) and RMSF$_{(LYS + RET)}$ was a value of area under the root mean square fluctuation curve of the chromophore bound to lysine residue in the chromophore binding site (**Figure 3D**; Patel et al., 2018). Conversely, the λ_{max} value of Atlantic salmon Sws2 cone visual photopigment was predicted by a three-term model: 2677.5348 − (−17.052 ×Angle 3) + (5.1634 ×Torsion 3) + (2.3642 ×Torsion 12), where Angle 3 (C3–C7–C8), Torsion 3 (C15–C14–C13–C20), and Torsion 12 (C19–C9–C8–C7) were the median values obtained from molecular dynamics simulations (**Figures 3E–G**; Patel et al., 2020). To do this, molecular dynamics simulations using each visual photopigment homology model were performed as previously described (Patel et al., 2018, 2020). Specifically, 100 ns long molecular dynamics simulation for all five visual photopigment systems were performed using a GROMACS simulation package (Van Der Spoel et al., 2005). RMSF and median values of the angles were then calculated from each 100 ns simulation and these values were applied to the statistical models to predict all λ_{max} values. Modeling results showed that Sws2 had a λ_{max} value at 420 nm, whereas the predicted λ_{max} values of Atlantic salmon Rh2 photopigments span a range of almost 40 nm, from 472 to 511 nm, where Rh2-1/Rh2-2 have λ_{max} values around 475 nm and Rh2-3/Rh2-4 around 510 nm (**Figure 2** and **Table 2**).

Differential Expression of Visual Opsins in Atlantic Salmon Development

The relative expression profiles of visual opsins in whole embryos and alevins are shown in **Figure 4**, where the developmental series ranges from the eye pigmentation stage to first feeding. In addition, **Table 3** shows the mean relative level of expression by normalized counts at each developmental stage, where reads were normalized to the sample with the lowest number of reads (**Supplementary Table 3** shows the individual normalized counts of the developmental series). The results reveal that the expression of visual opsins is substantial at 800 dd, corresponding to the developmental stage around first feeding. However, already at 410 dd, before hatching, opsin expression levels increased within the *rh2* and *rh1-1* classes. At 800 dd, rod opsin was at a maximal expression level (**Table 3**). Among the four *rh2* opsin genes, *rh2-3* and *rh2-4* were expressed at higher levels at all stages when compared to *rh2-1* and *rh2-2*. While *lws2* had the highest expression level within the *lws* opsin class, both *lws1* and *lws3* exhibited little or no expression at embryo and alevin stages. Overall, changes in expression levels during development (**Figure 4**) revealed that the largest shift in transcript levels occurred between 410 and 800 dd.

Expression of Visual Opsins in the Developing Eye

The retinal expression patterns of visual opsins in Atlantic salmon after hatching and just before first feeding (555 and 720 dd) were revealed by RNA *in situ* hybridization using opsin class-specific riboprobes (**Figure 5** and **Supplementary Figure 8**). Strong expression of rod opsin (*rh1*) was detected in the central retina after hatching, with expression that spread dorsally and ventrally as development progressed (**Figures 5A1–A3**). Both *sws1* (**Figures 5B1–B3**) and *sws2* (**Figures 5C1–C3**) were also expressed centrally after hatching, with opsin-positive cones spreading dorsally and ventrally in a similar manner to that of *rh1*; however, the number of *sws2*-positive cones were sparse when compared to those expressing *sws1*, especially after hatching. The expression of the four *rh2* genes after hatching was more widespread than the other visual opsin genes, even though *rh2* expression was detected in the central retina (**Figures 5D1–D3**). Before first feeding, *rh2* opsins were also expressed dorsally and ventrally (**Figures 5D1–D3**). For the Lws class, opsin expression was initially located centrally, spreading dorsally, and ventrally as development progressed (**Figures 5E1–E3**), as observed with other visual opsin profiles. For both *rh2* and *lws*

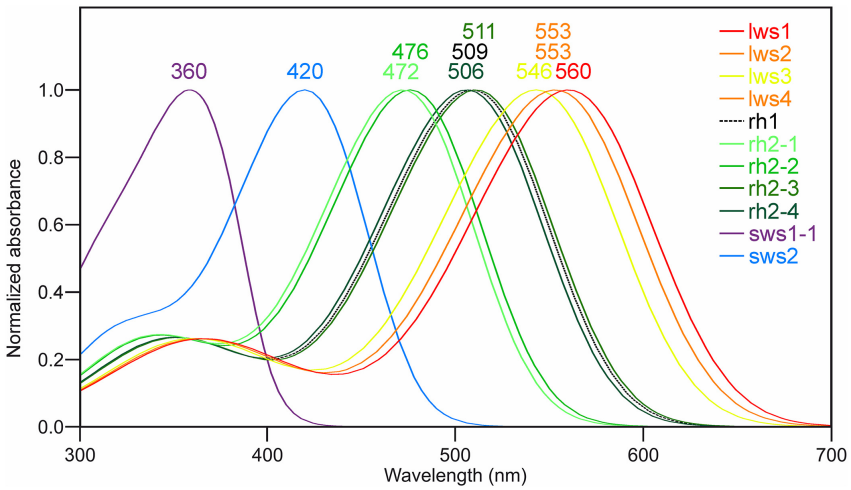

FIGURE 2 | Predicted spectral peaks of absorbance for Atlantic salmon visual photopigments. The schematic shows predicted λ_{max} values using normalized A_1-based rhodopsin templates (Govardovskii et al., 2000) as follows: Sws1 = 360 nm; Sws2 = 420 nm; Rh2-1 = 472 nm; Rh2-2 = 476 nm; Rh2-3 = 511 nm; Rh2-4 = 506 nm; Lws1 = 560 nm; Lws2 = 553 nm; Lws3 = 546 nm; Lws4 = 553 nm, as well as Rh1 = 509 nm.

opsin classes, expression patterns before first feeding were located proximal to the retinal pigment epithelium (**Figures 5D3, E3**).

DISCUSSION

This study presents a comprehensive mapping of visual opsins in salmonids that have undergone an additional round of genome duplication compared to other teleosts. Consistent with the concept of salmonid rediploidization, several visual opsin genes have not been retrained after the Ss4R genome duplication. Nevertheless, salmonids have maintained a broad repertoire of diverse visual opsins, exhibiting at least one representative gene in each of the five main opsin classes. The investigation primarily focused on Atlantic salmon, revealing an advanced array of Rh2 and Lws photopigment genes sensitive to medium and long wavelengths, respectively. Molecular dynamic modeling and tuning site interrogation predictions of the spectral characteristics between opsin types showed the greatest range of variation to be within the Rh2 class of photopigments. Further, expression analyzes showed that opsin expression is dynamic during development, with the *rh1-1* (traditionally responsible for scotopic vision) being the dominant visual opsin expressed post-hatching.

The Complexity of Visual Opsins After Ss4R

The salmonid-specific fourth whole genome duplication, Ss4R, initially provided the common ancestor of all salmonids with a doubling of the complete genome sequence. However, subsequent Ss4R duplicate gene loss was predominated by pseudogenization (Berthelot et al., 2014; Lien et al., 2016) since the genomes of both Atlantic salmon and rainbow trout do not appear to contain the expected doubling of opsin genes compared to teleosts that did not undergo a 4R duplication event (e.g., northern pike) (Lin et al., 2017). In recent years, several genome assemblies of salmonids and a revised genome assembly of northern pike, Atlantic salmon, and rainbow trout have been deposited to Ensembl (Cunningham et al., 2018), which forms the basis here for analyzing salmonid genomes for the presence/absence of visual opsin genes. Indeed, this study identified a number of intact visual opsins, as well as several pseudogenes. As indicated in Lin et al. (2017) and Musilova et al. (2019), there are at least two genes in the Rh1 class for salmonids, but *rh1-2* paralogues have become pseudogenes. The current study showed that there is only one *sws2* gene in all salmonids analyzed and northern pike lack any orthologue of the *sws2* gene class (Lin et al., 2017). By comparison, multiple *rh1*, two *sws1* and two *sws2* paralogue genes were identified in *Cyprinus carpio* (common carp) and *Sinocyclocheilus* spp., i.e., fishes where the common ancestor also underwent a 4R event (Lin et al., 2017). Here, two *sws1* genes were found in all salmonids analyzed; however, in Atlantic salmon and brown trout the second copy of *sws1* seems to have undergone pseudogenization due to presence of indels (e.g., a 6 bp deletion) that would cause in frame protein truncations. The analyzes of the *rh2* opsin genes indicate that salmonids have 3–5 *rh2* genes; synteny analyses (Lin et al., 2017), and a close chromosomal location indicates that these *rh2* genes are tandem duplicated genes and not ohnologues. In northern pike four *rh2* genes are similarly located in an array on the same chromosome. Interestingly, four *rh2* genes were also identified in *C. carpio* and *Sinocyclocheilus* spp. but they do not localize to the same chromosome (Lin et al., 2017), suggesting that these genes either do not derive from a tandem duplication or that sufficient genomic rearrangements have occurred to reposition these *rh2* genes to different chromosomes. Phylogenetic analyzes revealed that *rh2-1*/*rh2-2* and *rh2-3*/*rh2-4* branch together, and as described in zebrafish (Chinen et al., 2003) sequence comparison showed a closer relation of *rh2-3* and *rh2-4* than *rh2-1* and *rh2-2*, indicating that tandem duplication of *rh2-3*/*rh2-4* occurred

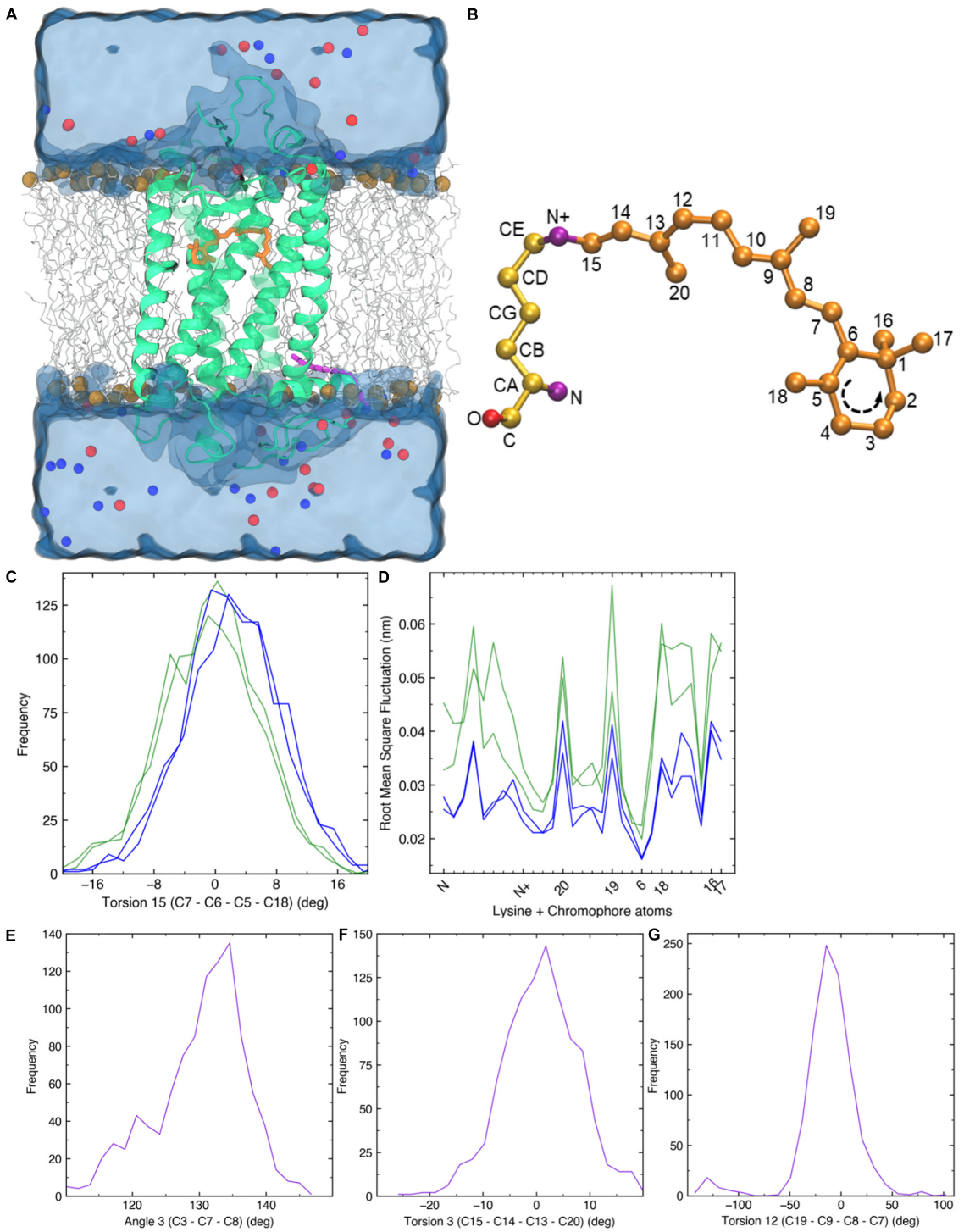

FIGURE 3 | Molecular dynamics simulations. **(A)** A 3D homology structure of Atlantic salmon Rh2-1 cone opsin (green) with the chromophore (orange) bound covalently to K296 of the opsin protein. It is embedded in a phospholipid bilayer (gray, carbon atoms; brown, phosphorus atoms) and surrounded by water molecules (blue). Blue and red spheres indicate positive and negative counter ions, respectively. **(B)** 11-*cis* retinal attached to a lysine residue *via* a Schiff base linkage. **(C)** Frequency distribution of C7–C6–C5–C18 torsion angle 15 (T15) observed in each Rh2 visual photopigment simulation. Blue and green colors indicate spectral sensitivities of each visual photopigment. **(D)** Root mean square fluctuation of 11-*cis* retinal attached to a lysine residue (LYS + RET). Horizontal axis represents atoms along the LYS + RET (see panel **B**). Sequence of β-ionone ring is indicated in **B**. **(E,G)** Frequency distribution of C3–C7–C8 geometric angle 3 (A3), C15–C14–C13–C20 torsion angle 3 (T3), and C19–C9–C8–C7 torsion angle 12 (T12) observed in a Sws2 visual photopigment simulation. Purple color indicates spectral sensitivity of visual photopigments.

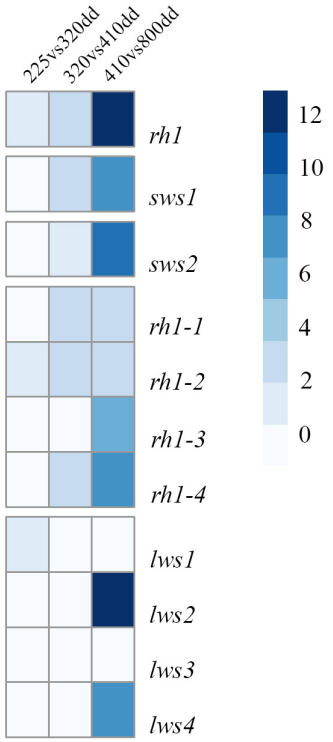

FIGURE 4 | A heatmap of expression levels for individual visual opsin genes in Atlantic salmon. The expression levels identified by RNA sequencing of whole embryos and alevins is presented by logfold2 change. The heatmap shows expression changes observed during development, revealing a significant shift in expression levels from 410 to 800 dd.

TABLE 3 | The mean of normalized counts showing the expression of visual opsins in Atlantic salmon in a developmental series.

	225 dd	320 dd	410 dd	800 dd
rh1-1	1	1	10	30,740
sws1-1	0	1	3	698
sws2	0	0	1	351
rh2-1	9	4	20	211
rh2-2	3	6	22	219
rh2-3	0	0	10	754
rh2-4	0	1	4	513
lws1	0	1	0	2
lws2	0	0	0	1,240
lws3	1	0	0	8
lws4	0	0	2	304

more recently. Coho salmon, rainbow trout and sockeye salmon have an additional *rh2-1* gene, with high sequence similarity, suggesting an even more recent duplication event in these species. Comparative analyzes of the *lws* opsin class showed that there are 3–4 genes in salmonids, with all species seeming to possess intact functional *lws*1 and *lws2* genes that are located close to each other on the same chromosome and with the *sws2* gene in proximity as shown in Lin et al. (2017). Conversely, several salmonid *lws3* and *lws4* genes are not identified at all, present as partial sequences, or has been assigned as a pseudogene. Notable, the updated genomes of Atlantic salmon and rainbow trout (Ensembl version 106) show that *lws3* and *lws4* are located on different chromosomes, while for the other salmonids under investigation *lws4* is not linked currently to a particular chromosome. By comparison, northern pike has four *lws* genes located on the same chromosome, where *lws1* and *lws2* and *lws3* and *lws4* form distinct clades. In contrast to salmonids, there are two *lws* genes in *C. carpio* and *Sinocyclocheilus* spp. located on different chromosomes (Lin et al., 2017).

Spectral Properties of Atlantic Salmon Visual Photopigments

Spectral properties of visual opsins in several salmonids have already been analyzed by microspectrophotometry (MSP) of photoreceptors (Cheng et al., 2006), however the results do not take into account the diversity within the Rh2 and Lws classes. Here, manual interrogation of the Sws1, Rh1 and Lws photopigments (Musilova et al., 2019) and molecular dynamics simulations-based modeling approaches for the Sws2 and four Rh2 visual photopigment (Patel et al., 2018, 2020) were applied to estimate the spectral properties of all photopigments within the five opsin classes of Atlantic salmon. For Sws1 and Rh1, the manual interrogation gave λ_{max} of 360 and 509 nm, respectively, and were in close accordance with the MSP measurements at 361 and 515 nm (Cheng et al., 2006). The molecular dynamics simulations-based modeling of Sws2 gave a λ_{max} of 420 nm while MSP measurements gave a λ_{max} 435 nm (Cheng et al., 2006). Notably, the spectral sensitivity of a photopigment can be altered by a vitamin A_1 to A_2 shift of the chromophore, where the A_2 give higher λ_{max} than A_1 (Bridges, 1972; Hárosi, 1994) and altered ratio of A_1/A_2 has been shown to vary with temperature and daylength in coho salmon (Temple et al., 2006). However, the MSP results indicated that the retinas were primarily based on vitamin A_1 (Cheng et al., 2006) and in the molecular dynamics simulations-based modeling approaches for the Sws2 and four Rh2 the λ_{max} used a standard A_1-based rhodopsin template, indicating that the 15 nm difference in the λ_{max} for Sws2 is not due to different chromophores. When comparing MSP to molecular dynamics approaches, it is possible that modeling predictions are more divergent when estimating λ_{max} values for opsin protein sequences that are less phylogenetically related to the template sequence (e.g., comparing Sws2 to an Rh1 template vs. Rh2 compared to Rh1 that share a higher sequence identity and are more similar in λ_{max} values). The absorbance maximum determined for Rh2 and Lws were 518 and 578 nm, respectively (Cheng et al., 2006) while the diversity within the Rh2 and Lws classes determined by molecular dynamics simulations-based modeling spanned from 472 to 511 and 546 to 560 nm, respectively. These results indicate that the MSP measurements were done on photoreceptor cells with Rh2-3 or Rh2-4 photopigments for the Rh2 class and Lws1 for the Lws class. Further, the 40 nm range within the Rh2 class of photopigments are in accordance with zebrafish where the four Rh2 photopigments span from 467 to 505 nm

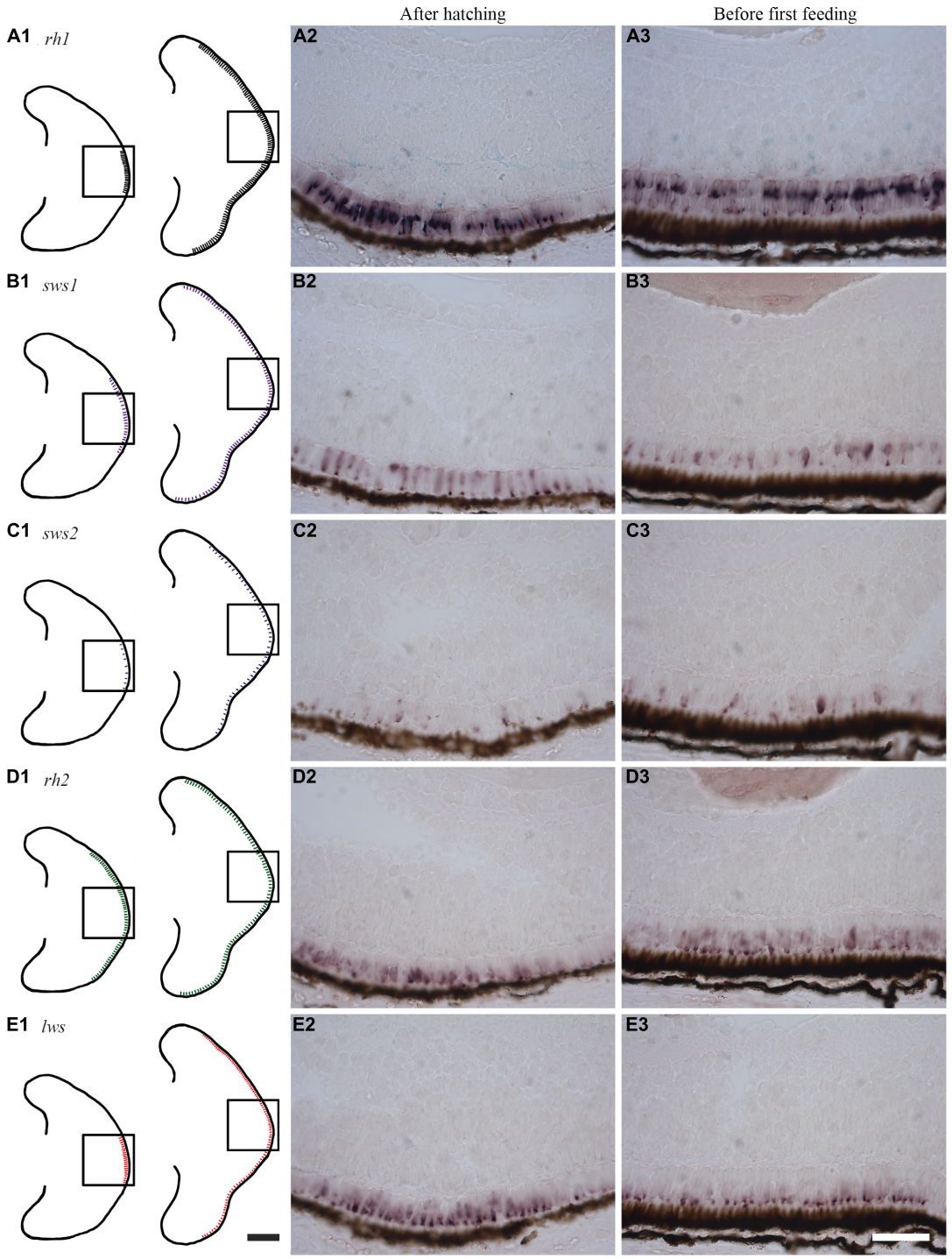

FIGURE 5 | Expression of visual opsins in the developing Atlantic salmon eye. **(A1–E1)** Schematics showing the expression patterns of visual opsins after hatching (555 dd) and before first feeding (720 dd) as obtained by RNA *in situ* hybridization. **(A1–A3)** After hatching, *rh1* is strongly expressed in rod photoreceptor cells in the central retina, with an expression pattern that spreads dorsally and ventrally before first feeding. **(B1–B3)** The single cone opsin *sws1* is expressed in a broader region of the central retina compared to *rh1* at hatching: this expression spreads dorsally and ventrally before first feeding. **(C1–C3)** After hatching, the single cone opsin *sws2* has scattered expression in the central retina. Before first feeding, *sws2*-positive cells are sparse, but they subsequently spread dorsally and ventrally. **(D1–D3)** Probes detecting all four *rh2* genes expressed in double cones reveal that *rh2*-positive cells are the most widely distributed after hatching. Before first feeding, expression levels are highest close to the retinal pigment epithelium (RPE), before spreading dorsally and ventrally. **(E1–E3)** Probes detecting all four *lws genes* (again in double cones) show a central distribution of *lws* before hatching. When approaching first feeding, *lws* expression spreads dorsally and ventrally with expression that is located towards the RPE. Scale bars, 200 μm for schematic drawings and 50 μm for histological sections.

(Chinen et al., 2003; Patel et al., 2018), but the range between the Rh2-1/Rh2-2 and Rh2-3/Rh2-4 branches is greater in Atlantic salmon. As proposed in agnathans, alterations in gene copies and subsequent mutations play an important role in evolution of color vision (Davies et al., 2009). Mutagenesis studies have shown that amino acid position 122 in teleost Rh2 opsins is essential in determining green-shifted λ_{max} (>495 nm) when occupied by Glu (E), and blue-shifted λ_{max} (<495 nm) when occupied by Gln (Q). This E122Q substitution alone accounts for ∼15 nm of determined spectral shift (Chinen et al., 2005; Patel et al., 2018). **Supplementary Figure 4** shows that Atlantic salmon Rh2-1 and Rh2-2 have Q122 whereas Rh2-3 and Rh2-4 have E122. Which likely explains the blue vs. green spectral shift among salmonid Rh2 photopigments. The absorbance maximum of visual opsins in the anadromous Atlantic salmon range from 360 to 569 nm with representatives in all five opsin classes, providing specialized vision for living both in rivers and in the open ocean. In comparison, the benthopelagic Atlantic cod (*Gadus morhua*) lack representatives in the Sws1 and Lws classes, but has a greater repertoire within the Sws2 and Rh2 classes (Valen et al., 2014).

Differential Gene Expression Profiles

Color visual capacity can be determined by several mechanisms, including changes in the type of chromophore used and/or the opsin expressed, the latter of which is influenced by opsin gene duplication or loss, as well as by changes in expression levels as a function of development or change of habitat (Carleton et al., 2020). For example, the gain and loss of UV-sensitive cones in salmonids are well studied in relation to their sea-river migration paths (Allison et al., 2003, 2006; Cheng et al., 2006). Previously, a two-step developmental profile of the duplex retina in Atlantic cod was demonstrated, where development of scotopic vision was concurrent with life-stage transition and diminishing expression of some of the *rh2* genes (Valen et al., 2016). In Atlantic salmon, with a more direct developmental process, the results of this study are consistent with previous findings showing that the salmon retina is duplex from early developmental stages (Cheng et al., 2007) and that rod opsin is the dominantly expressed visual opsin class post-hatching. As described in Chinook salmon (Cheng et al., 2007), the results presented here revealed that early opsin expression in the retina is located centrally, but expands dorsally and ventrally as eye development progresses. For example, *sws1* expression is topographically widely distributed before first feeding, which is in strong contrast to the restricted *sws1* expression profile close to the ciliary marginal zone at the smolt stage of rainbow trout (Allison et al., 2003). The number and distribution of *sws1* expressing cones in the whole retina at early stages indicates that UV light is likely to be very important for vision in rivers and lakes during early development. Unlike the marine larvae of Atlantic halibut (*Hippoglossus hippoglossus*) where *sws1* expression is restricted to the ventral part of the retina where it detects downwelling UV light, the distribution of *sws1* cones in the whole eye of Atlantic salmon suggests that UV light is detected from all directions (Helvik et al., 2001).

Due to high sequence identity between opsin genes within Rh2 and Lws classes, respectively, RNA *in situ* hybridization experiments were designed not to distinguish between different paralogues genes, but for opsin genes from within a class. However, RNA sequencing analyzes were able to resolve specific expression profiles for opsin genes within a class, where opsins were shown to be differentially expressed during development, with important functional implications. For example, *rh2-3* and *rh2-4*, resulting in photopigments that maximally absorb wavelengths above 500 nm, were more highly expressed at first feeding than *rh2-1* and *rh2-2*, with photopigments that were predicted to have λ_{max} 471 and 475 nm. Similarly, the expression levels of *lws1* and *lws3* (with photopigments that maximally absorb at λ_{max} 546 and 560 nm, respectively) are minimal compared to the expression of *lws2* and *lws4* (both photopigment types predicted to have a λ_{max} value at 553 nm). These patterns of differential expression might be a result of distinct expression of opsins within a class during life history transitions, as observed for *sws1* (Allison et al., 2003). As such, further studies that analyze the expression profiles of opsins within both Rh2 and Lws classes through smoltification would be of great scientific and commercial interest. In conclusion, this study describes the opsin repertoire of several species of salmonids, accompanied by more in depth analyzes of spectral tuning and expression profiles of Atlantic salmon photopigment genes.

DATA AVAILABILITY STATEMENT

The sequences of Atlantic salmon visual opsin genes can be found at the National Center for Biotechnology Information (NCBI) GenBank repository, https://www.ncbi.nlm.nih.gov/genbank/, ON456431–ON456441.

ETHICS STATEMENT

Animal facilities, husbandry and sampling procedures were conducted in accordance with Norwegian Food Safety Authority recommendations.

AUTHOR CONTRIBUTIONS

ME did the *in silico* analyzes of the genomes for visual opsins, designed the primers for molecular cloning, did the interpretation of the RNA sequencing data and phylogenetic analyzes, performed the RNA *in situ* hybridization, made figures, and wrote the manuscript. WD and JM interpreted the complexity of the visual opsins, did the phylogenetic analyzes and the manual interrogation of spectral properties, made figures, and wrote and revised the manuscript. DP, JB, DS, and JP designed and performed the spectral modeling of the visual opsins, made figures, and revised the manuscript. RK did the molecular cloning and made the RNA probes. JH designed the study, interpreted the complexity of the visual opsins, the phylogenetic analyzes, RNA sequencing and *in situ* hybridization results, and revised the

manuscript. All authors contributed to the article and approved the submitted version.

FUNDING

This study was funded by the Research Council of Norway ("The effect of narrow banded LED light on development and growth performance" Grant No. 254894 and "Nonvisual light regulation of biological rhythm and life history transformation" Grant No. 315106). DP, JB, and JP were supported by the Center for Modeling Complex Interactions (CMCI) sponsored by the NIGMS under award number NIH P20 GM104420, through a Pilot Grant to JP and DS was also supported in part by NIH R01 EY012146 and NSF DEB 1638567. Computer resources were provided by the Institute for Bioinformatics and Evolutionary Studies Computational Resources Core sponsored by the National Institutes of Health (NIH P30 GM103324). This research also made use of the computational resources provided by the high-performance computing center at Idaho National Laboratory, which is supported by the Office of Nuclear Energy of the U.S. DOE and the Nuclear Science User Facilities under Contract No. DE-AC07-05ID14517.

ACKNOWLEDGMENTS

We thank Hans Øivind Svensvik in Marine Harvest, Tveitevågen, Norway, for providing the eggs and sperm of Atlantic salmon. We also thank Rolf B. Edvardsen and Tomasz Furmanek at the Institute of Marine Research, Bergen, Norway, for bioinformatics support regarding the RNA sequencing analyzes.

SUPPLEMENTARY MATERIAL

The Supplementary Material for this article can be found online at: https://www.frontiersin.org/articles/10.3389/fnana.2022.945344/full#supplementary-material

Supplementary Figure 1 | Amino acid alignment of Rh1-1.

Supplementary Figure 2 | Amino acid alignment of Sws1-1 and Sws1-2.

Supplementary Figure 3 | Amino acid alignment of Sws2.

Supplementary Figure 4 | Amino acid alignment of Rh2-1, Rh2-2, Rh2-3, and Rh2-4.

Supplementary Figure 5 | Amino acid alignment of Lws1, Lws2, Lws3, and Lws4.

Supplementary Figure 6 | Nucleotide alignment of *rh1-2.1* and *rh1-2.2*.

Supplementary Figure 7 | Nucleotide alignment of *sws1-2*.

Supplementary Figure 8 | Extended images of visual opsin expression in the developing Atlantic salmon eye. **(A1–E1)** Visual opsins after hatching (555 dd) and **(A2–E2)** before first feeding (720 dd). Scale bar 200 μm.

Supplementary Table 1 | Primers used for molecular cloning of visual opsins in Atlantic salmon.

Supplementary Table 2 | IDs and chromosome location of visual opsins in salmonids and northern pike.

Supplementary Table 3 | Individual normalized count showing the expression of visual opsins in Atlantic salmon during development.

REFERENCES

Allendorf, F. W., and Thorgaard, G. H. (1984). "Tetraploidy and the evolution of salmonid fishes," in *Evolutionary Genetics of Fishes*, ed. B. J. Turner (Boston, MA: Springer), 1–53. doi: 10.1007/978-1-4684-4652-4_1

Allison, W. T., Dann, S. G., Veldhoen, K. M., and Hawryshyn, C. W. (2006). Degeneration and regeneration of ultraviolet cone photoreceptors during development in rainbow trout. *J. Comp. Neurol.* 499, 702–715. doi: 10.1002/cne.21164

Allison, W. T., Dann, S. G., Helvik, J. V., Bradley, C., Moyer, H. D., and Hawryshyn, C. W. (2003). Ontogeny of ultraviolet-sensitive cones in the retina of rainbow trout (*Oncorhynchus mykiss*). *J. Comp. Neurol.* 461, 294–306. doi: 10.1002/cne.10682

Balon, E. K. (1985). *Early Life Histories of Fishes: New Developmental, Ecological and Evolutionary Perspectives*. Herlin: Springer. doi: 10.1007/978-94-010-9258-6

Berthelot, C., Brunet, F., Chalopin, D., Juanchich, A., Bernard, M., Noel, B., et al. (2014). The rainbow trout genome provides novel insights into evolution after whole-genome duplication in vertebrates. *Nat. Commun.* 5:10. doi: 10.1038/ncomms4657

Bridges, C. D. B. (1972). "The Rhodopsin-Porphyropsin Visual System," in *Photochemistry of Vision*, eds E. W. Abrahamson, C. Baumann, C. D. B. Bridges, F. Crescitelli, H. J. A. Dartnall, R. M. Eakin, et al. (Berlin: Springer), 417–480. doi: 10.1007/978-3-642-65066-6_11

Carleton, K. L., Escobar-Camacho, D., Stieb, S. M., Cortesi, F., and Marshall, N. J. (2020). Seeing the rainbow: mechanisms underlying spectral sensitivity in teleost fishes. *J. Exp. Biol.* 223:jeb193334. doi: 10.1242/jeb.193334

Chan, T., Lee, M., and Sakmar, T. P. (1992). Introduction of hydroxyl-bearing amino acids causes bathochromic spectral shifts in rhodopsin. amino acid substitutions responsible for red-green color pigment spectral tuning. *J. Biol. Chem.* 267, 9478–9480. doi: 10.1016/S0021-9258(19)50115-6

Cheng, C. L., and Flamarique, I. N. (2007). Chromatic organization of cone photoreceptors in the retina of rainbow trout: single cones irreversibly switch from UV (SWS1) to blue (SWS2) light sensitive opsin during natural development. *J. Exp. Biol.* 210, 4123–4135. doi: 10.1242/jeb.009217

Cheng, C. L., Flamarique, I. N., Hárosi, F. I., Rickers-Haunerland, J., and Haunerland, N. H. (2006). Photoreceptor layer of salmonid fishes: transformation and loss of single cones in juvenile fish. *J. Comp. Neurol.* 495, 213–235. doi: 10.1002/cne.20879

Cheng, C. L., Gan, K. J., and Flamarique, I. N. (2007). The ultraviolet opsin is the first opsin expressed during retinal development of salmonid fishes. *Invest. Ophthalmol. Vis. Sci.* 48, 866–873. doi: 10.1167/iovs.06-0442

Chinen, A., Hamaoka, T., Yamada, Y., and Kawamura, S. (2003). Gene duplication and spectral diversification of cone visual pigments of zebrafish. *Genetics* 163, 663–675. doi: 10.1093/genetics/163.2.663

Chinen, A., Matsumoto, Y., and Kawamura, S. (2005). Reconstitution of ancestral green visual pigments of zebrafish and molecular mechanism of their spectral differentiation. *Mol. Biol. Evol.* 22, 1001–1010. doi: 10.1093/molbev/msi086

Cowing, J. A., Poopalasundaram, S., Wilkie, S. E., Robinson, P. R., Bowmaker, J. K., and Hunt, D. M. (2002). The molecular mechanism for the spectral shifts between vertebrate ultraviolet- and violet-sensitive cone visual pigments. *Biochem. J.* 367, 129–135. doi: 10.1042/bj20020483

Cunningham, F., Achuthan, P., Akanni, W., Allen, J., Amode, M. R., Armean, I. M., et al. (2018). Ensembl 2019. *Nucleic Acids Res.* 47, D745–D751. doi: 10.1093/nar/gky1113

Davies, W. I., Collin, S. P., and Hunt, D. M. (2012). Molecular ecology and adaptation of visual photopigments in craniates. *Mol. Ecol.* 21, 3121–3158. doi: 10.1111/j.1365-294X.2012.05617.x

Davies, W. L., Collin, S. P., and Hunt, D. M. (2009). Adaptive gene loss reflects differences in the visual ecology of basal vertebrates. *Mol. Biol. Evol.* 26, 1803–1809. doi: 10.1093/molbev/msp089

Davies, W. L., Cowing, J. A., Carvalho, L. S., Potter, I. C., Trezise, A. E., Hunt, D. M., et al. (2007). Functional characterization, tuning, and regulation of visual pigment gene expression in an anadromous lamprey. *FASEB J.* 21, 2713–2724. doi: 10.1096/fj.06-8057com

Douglas, R., and Djamgoz, M. (1990). *The Visual System of Fish*. Berlin: Springer. doi: 10.1007/978-94-009-0411-8

Eilertsen, M., Drivenes, Ø, Edvardsen, R. B., Bradley, C. A., Ebbesson, L. O. E., and Helvik, J. V. (2014). Exorhodopsin and melanopsin systems in the pineal complex and brain at early developmental stages of *Atlantic halibut* (*Hippoglossus hippoglossus*). *J. Comp. Neurol.* 522, 4003–4022. doi: 10.1002/cne.23652

Evans, B., and Browman, H. (2004). "Variation in the development of the fish retina," in *The Development of Form and Function in Fishes and the Question of Larval Adaptation*, ed. J. J. Govoni (Bethesda, MD: American Fisheries Society), 145–166. doi: 10.47886/9781888569582.ch7

Evans, B. I., and Fernald, R. D. (1990). Metamorphosis and fish vision. *J. Neurobiol.* 21, 1037–1052. doi: 10.1002/neu.480210709

Gorodilov, Y. N. (1996). Description of the early ontogeny of the atlantic salmon, salmo salar, with a novel system of interval (state) identification. *Environ Biol. Fish.* 47, 109–127. doi: 10.1007/BF00005034

Govardovskii, V. I., Fyhrquist, N., Reuter, T. O. M., Kuzmin, D. G., and Donner, K. (2000). In search of the visual pigment template. *Vis. Neurosci.* 17, 509–528. doi: 10.1017/S0952523800174036

Hárosi, F. I. (1994). An analysis of two spectral properties of vertebrate visual pigments. *Vis. Res.* 34, 1359–1367. doi: 10.1016/0042-6989(94)90134-1

Helvik, J. V., Drivenes, Ø, Harboe, T., and Seo, H. C. (2001). Topography of different photoreceptor cell types in the larval retina of Atlantic halibut (*Hippoglossus hippoglossus*). *J. Exp. Biol.* 204, 2553–2559. doi: 10.1242/jeb.204.14.2553

Higgins, D. G., Thompson, J. D., and Gibson, T. J. (1996). Using CLUSTAL for multiple sequence alignments. *Methods Enzymol.* 266, 383–402. doi: 10.1016/S0076-6879(96)66024-8

Hope, A. J., Partridge, J. C., Dulai, K. S., and Hunt, D. M. (1997). Mechanisms of wavelength tuning in the rod opsins of deep-sea fishes. *Proc. R. Soc. London. Ser. B: Biol. Sci.* 264, 155–163. doi: 10.1098/rspb.1997.0023

Hunt, D. M., Dulai, K. S., Partridge, J. C., Cottrill, P., and Bowmaker, J. K. (2001). The molecular basis for spectral tuning of rod visual pigments in deep-sea fish. *J. Exp. Biol.* 204, 3333–3344. doi: 10.1242/jeb.204.19.3333

Janz, J. M., and Farrens, D. L. (2001). Engineering a functional blue-wavelength-shifted rhodopsin mutant. *Biochemistry* 40, 7219–7227. doi: 10.1021/bi002937i

Jerlov, N. G. (1976). *Marine Optics*. Amsterdam: Elsevier Scientific.

Kendall, A. W., Ahlstom, E. H., and Moser, H. G. (1984). "Early life history stages of fishes and their characters," in *Ontogeny and Systematics of Fishes*, eds. H. G. Moser, W. J. Richards, D. M. Cohen, M. P. Fahay, A. W. Kendall, and S. L. Richardson (Lawrence, KS: Allen Press), 11–22.

Kolde, R. (2019). *Pheatmap: Pretty Heatmaps. R package version 1.0.12*. Available online at: https://CRAN.R-project.org/package=pheatmap

Kuraku, S., Meyer, A., and Kuratani, S. (2008). Timing of genome duplications relative to the origin of the vertebrates: did cyclostomes diverge before or after? *Mol. Biol. Evol.* 26, 47–59. doi: 10.1093/molbev/msn222

Langmead, B., and Salzberg, S. L. (2012). Fast gapped-read alignment with Bowtie 2. *Nat. Methods* 9, 357–359. doi: 10.1038/nmeth.1923

Larkin, M. A., Blackshields, G., Brown, N. P., Chenna, R., Mcgettigan, P. A., Mcwilliam, H., et al. (2007). Clustal W and Clustal X version 2.0. *Bioinformatics* 23, 2947–2948. doi: 10.1093/bioinformatics/btm404

Levine, J. S., and MacNichol, E. F. (1982). Color vision in fishes. *Sci. Am.* 246, 140–149. doi: 10.1038/scientificamerican0282-140

Li, H., Handsaker, B., Wysoker, A., Fennell, T., Ruan, J., Homer, N., et al. (2009). The sequence alignment/map format and samtools. *Bioinformatics* 25, 2078–2079. doi: 10.1093/bioinformatics/btp352

Lien, S., Koop, B. F., Sandve, S. R., Miller, J. R., Kent, M. P., Nome, T., et al. (2016). The atlantic salmon genome provides insights into rediploidization. *Nature* 533, 200–205. doi: 10.1038/nature17164

Lin, J.-J., Wang, F.-Y., Li, W.-H., and Wang, T.-Y. (2017). The rises and falls of opsin genes in 59 ray-finned fish genomes and their implications for environmental adaptation. *Sci. Rep.* 7:15568. doi: 10.1038/s41598-017-15868-7

Macqueen, D. J., Primmer, C. R., Houston, R. D., Nowak, B. F., Bernatchez, L., Bergseth, S., et al. (2017). Functional annotation of all salmonid genomes (faasg): an international initiative supporting future salmonid research, conservation and aquaculture. *BMC Genomics* 18:484. doi: 10.1186/s12864-017-3862-8 doi: 10.1186/s12864-017-3862-8

Musilova, Z., Cortesi, F., Matschiner, M., Davies, W. I. L., Patel, J. S., Stieb, S. M., et al. (2019). Vision using multiple distinct rod opsins in deep-sea fishes. *Science* 364, 588–592. doi: 10.1126/science.aav4632

Nei, M., and Kumar, S. (2000). *Molecular Evolution and Phylogenetics*. New York, NY: Oxford University Press.

Partridge, J. C., and Cummings, M. E. (1999). *"Adaptation of Visual Pigments to the Aquatic Environment.," in Adaptive Mechanisms in the Ecology of Vision*. Dordrecht: Springer. doi: 10.1007/978-94-017-0619-3_9

Patel, D., Barnes, J. E., Davies, W. I. L., Stenkamp, D. L., and Patel, J. S. (2020). Short-wavelength-sensitive 2 (Sws2) visual photopigment models combined with atomistic molecular simulations to predict spectral peaks of absorbance. *PLoS Comput. Biol.* 16:e1008212. doi: 10.1371/journal.pcbi.1008212 doi: 10.1371/journal.pcbi.1008212

Patel, J. S., Brown, C. J., Ytreberg, F. M., and Stenkamp, D. L. (2018). Predicting peak spectral sensitivities of vertebrate cone visual pigments using atomistic molecular simulations. *PLoS Comput. Biol.* 14:e1005974. doi: 10.1371/journal.pcbi.1005974

Percie du Sert, N., Hurst, V., Ahluwalia, A., Alam, S., Avey, M. T., Baker, M., et al. (2020). The ARRIVE guidelines 2.0: updated guidelines for reporting animal research. *PLoS Biol.* 18:e3000410. doi: 10.1371/journal.pbio.3000410 doi: 10.1371/journal.pbio.3000410

Rennison, D. J., Owens, G. L., and Taylor, J. S. (2012). Opsin gene duplication and divergence in ray-finned fish. *Mol. Phylogenet Evol.* 62, 986–1008. doi: 10.1016/j.ympev.2011.11.030

Rondeau, E. B., Minkley, D. R., Leong, J. S., Messmer, A. M., Jantzen, J. R., Von Schalburg, K. R., et al. (2014). The genome and linkage map of the northern pike (*Esox lucius*): conserved synteny revealed between the salmonid sister group and the neoteleostei. *PLoS One* 9:e102089. doi: 10.1371/journal.pone.0102089

Saitou, N., and Nei, M. (1987). The neighbor-joining method: a new method for reconstructing phylogenetic trees. *Mol. Biol. Evol.* 4, 406–425.

Sakmar, T. P., Franke, R. R., and Khorana, H. G. (1991). The role of the retinylidene schiff base counterion in rhodopsin in determining wavelength absorbance and schiff base pka. *Proc. Natl. Acad. Sci. U.S.A.* 88:3079. doi: 10.1073/pnas.88.8.3079

Sandbakken, M., Ebbesson, L., Stefansson, S., and Helvik, J. V. (2012). Isolation and characterization of melanopsin photoreceptors of Atlantic salmon (*Salmo salar*). *J. Comp. Neurol.* 520, 3727–3744. doi: 10.1002/cne.23125

Sayers, E. W., Agarwala, R., Bolton, E. E., Brister, J. R., Canese, K., Clark, K., et al. (2019). Database resources of the national center for biotechnology information. *Nucleic Acids Res.* 47, D23–D28. doi: 10.1093/nar/gky1069

Tamura, K., and Nei, M. (1993). Estimation of the number of nucleotide substitutions in the control region of mitochondrial DNA in humans and chimpanzees. *Mol. Biol. Evol.* 10, 512–526.

Tamura, K., Stecher, G., and Kumar, S. (2021). MEGA11: molecular evolutionary genetics analysis version 11. *Mol. Biol. Evol.* 38, 3022–3027. doi: 10.1093/molbev/msab120

Temple, S. E., Plate, E. M., Ramsden, S., Haimberger, T. J., Roth, W. M., and Hawryshyn, C. W. (2006). Seasonal cycle in vitamin A1/A2-based visual pigment composition during the life history of coho salmon (*Oncorhynchus kisutch*). *J. Comp. Physiol. A Neuroethol. Sens. Neural Behav. Physiol.* 192, 301–313. doi: 10.1007/s00359-005-0068-3

Terakita, A. (2005). The opsins. *Genome Biol.* 6:213. doi: 10.1186/gb-2005-6-3-213

Thisse, C., and Thisse, B. (2008). High-resolution *in situ* hybridization to whole-mount zebrafish embryos. *Nat. Protoc.* 3, 59–69. doi: 10.1038/nprot.2007.514

Valen, R., Edvardsen, R. B., Søviknes, A. M., Drivenes, Ø, and Helvik, J. V. (2014). Molecular evidence that only two opsin subfamilies, the blue light- (SWS2) and green light-sensitive (RH2), drive color vision in Atlantic Cod (*Gadus morhua*). *PLoS One* 9:e115436. doi: 10.1371/journal.pone.0115436 doi: 10.1371/journal.pone.0115436

Valen, R., Eilertsen, M., Edvardsen, R. B., Furmanek, T., Rønnestad, I., Van Der Meeren, T., et al. (2016). The two-step development of a duplex retina involves distinct events of cone and rod neurogenesis and differentiation. *Dev. Biol.* 416, 389–401. doi: 10.1016/j.ydbio.2016.06.041

Van Der Spoel, D., Lindahl, E., Hess, B., Groenhof, G., Mark, A. E., and Berendsen, H. J. C. (2005). GROMACS: fast, flexible, and free. *J. Comput. Chem.* 26, 1701–1718. doi: 10.1002/jcc.20291

von Schalburg, K. R., Gowen, B. E., Messmer, A. M., Davidson, W. S., and Koop, B. F. (2014). Sex-specific expression and localization of aromatase and its regulators during embryonic and larval development of *Atlantic salmon*. *Comp. Biochem. Physiol. Part B: Biochem. Mol. Biol.* 168, 33–44. doi: 10.1016/j.cbpb.2013.11.004

Yokoyama, S. (2000). Molecular evolution of vertebrate visual pigments. *Prog. Retin. Eye Res.* 19, 385–419. doi: 10.1016/S1350-9462(00)00002-1

Yokoyama, S. (2008). Evolution of dim-light and color vision pigments. *Annu. Rev. Genomics Hum. Genet.* 9, 259–282. doi: 10.1146/annurev.genom.9.081307.164228

Yokoyama, S., Tada, T., and Yamato, T. (2007). Modulation of the absorption maximum of rhodopsin by amino acids in the C-terminus. *Photochem. Photobiol.* 83, 236–241. doi: 10.1562/2006-06-19-RA-939

Yokoyama, S., Tada, T., Zhang, H., and Britt, L. (2008). Elucidation of phenotypic adaptations: Molecular analyses of dim-light vision proteins in vertebrates. *Proc. Natl. Acad. Sci. U.S.A.* 105:13480. doi: 10.1073/pnas.0802426105

Yokoyama, S., Zhang, H., Radlwimmer, F. B., and Blow, N. S. (1999). Adaptive evolution of color vision of the comoran coelacanth (*Latimeria chalumnae*). *Proc. Natl. Acad. Sci. U.S.A.* 96:6279. doi: 10.1073/pnas.96.11.6279

Conflict of Interest: The authors declare that the research was conducted in the absence of any commercial or financial relationships that could be construed as a potential conflict of interest.

Publisher's Note: All claims expressed in this article are solely those of the authors and do not necessarily represent those of their affiliated organizations, or those of the publisher, the editors and the reviewers. Any product that may be evaluated in this article, or claim that may be made by its manufacturer, is not guaranteed or endorsed by the publisher.

frontiers | Frontiers in Neuroanatomy

ORIGINAL RESEARCH
published: 05 August 2022
doi: 10.3389/fnana.2022.916510

Expression of Opsins of the Box Jellyfish *Tripedalia cystophora* Reveals the First Photopigment in Cnidarian Ocelli and Supports the Presence of Photoisomerases

Anders Garm[1]*, *Jens-Erik Svaerke*[1], *Daniela Pontieri*[1] and *Todd H. Oakley*[2]

[1] Marine Biological Section, University of Copenhagen, Copenhagen, Denmark, [2] Department of Biology, University of California, Santa Barbara, Santa Barbara, CA, United States

Cubomedusae, or box jellyfish, have a complex visual system comprising 24 eyes of four types. Like other cnidarians, their photoreceptor cells are ciliary in morphology, and a range of different techniques together show that at least two of the eye types—the image-forming upper and lower lens eyes—express opsin as the photopigment. The photoreceptors of these two eye types express the same opsin (*Tc LEO*), which belongs to the cnidarian-specific clade cnidops. Interestingly, molecular work has found a high number of opsin genes in box jellyfish, especially in the Caribbean species *Tripedalia cystophora*, most of which are of unknown function. In the current study, we raised antibodies against three out of five opsins identified from transcriptomic data from *T. cystophora* and used them to map the expression patterns. These expression patterns suggest one opsin as the photopigment in the slit eyes and another as a putative photoisomerase found in photoreceptors of all four eyes types. The last antibody stained nerve-like cells in the tentacles, in connection with nematocytes, and the radial nerve, in connection with the gonads. This is the first time photopigment expression has been localized to the outer segments of the photoreceptors in a cnidarian ocellus (simple eye). The potential presence of a photoisomerase could be another interesting convergence between box jellyfish and vertebrate photoreceptors, but it awaits final experimental proof.

Keywords: photopigment, box jellyfish, cubozoa, cnidaria, phototransduction, opsin phylogeny, vision

OPEN ACCESS

Edited by:
Marta Agudo-Barriuso, Biomedical Research Institute of Murcia (IMIB), Spain

Reviewed by:
Lauren Sumner-Rooney, University of Oxford, United Kingdom
Michael L. Firsov, Institute of Evolutionary Physiology and Biochemistry (RAS), Russia
Toshio Takahashi, Suntory Foundation for Life Sciences, Japan

***Correspondence:**
Anders Garm
algarm@bio.ku.dk

Received: *09 April 2022*
Accepted: *24 June 2022*
Published: *05 August 2022*

Citation:
Garm A, Svaerke J-E, Pontieri D and Oakley TH (2022) Expression of Opsins of the Box Jellyfish Tripedalia cystophora Reveals the First Photopigment in Cnidarian Ocelli and Supports the Presence of Photoisomerases. Front. Neuroanat. 16:916510. doi: 10.3389/fnana.2022.916510

INTRODUCTION

Photosensitive organs, eyes and ocelli, have arisen many times in animal evolution (Salvini-Plawen and Mayr, 1977; Nilsson and Pelger, 1994), and recent analyses suggest that this has even happened at least nine times within the cnidarian phylum alone (Picciani et al., 2018; Miranda and Collins, 2019). In almost all known cases, opsins are used as the photopigment initially harvesting photons as a complex including a chromophore, which is most often retinal (Land and Nilsson, 2012). Although opsins diversified dramatically since their origin, many animal eyes employ opsins from two major clades, rhabdomeric opsins, which interact with G-alpha-q, and ciliary opsins, which interact with G-alpha-t, with their expression somewhat

following the morphology of the photoreceptors as their names imply (Shichida and Matsuyama, 2009) [but see (Vanfleteren and Coomans, 1976; Salvini-Plawen and Mayr, 1977) for alternative viewpoints]. Recent studies proved that another clade of opsins, xenopsins, is also used in some cases as photopigments (Vöcking et al., 2017; Döring et al., 2020). Still, other opsins, including peropsins and RGR opsins, are not directly involved in light absorption but work as photoisomerases in vertebrate ciliary photoreceptors to reactivate the opsin–retinal complex (Shichida and Matsuyama, 2009). In rhabdomeric photoreceptors, light absorption does not lead to full dissociation of retinal but to a metarhodopsin complex, which is reactivated through absorption of a second photon.

In cnidarians, few experimental data are available about the details of phototransduction, but molecular studies found some of the components to indicate G-alpha-s phototransduction (Koyanagi et al., 2008; Plachetzki et al., 2010; Liegertová et al., 2015). All examined cnidarian classes express opsins, and especially in hydrozoans and anthozoans, they can be present in high numbers (Picciani et al., 2018; Gornik et al., 2021). *Cladonema radiatum* has 18 opsin genes, and *Hydra vulgaris* has as many as 42 genes (Suga et al., 2008; Macias-Munoz et al., 2019). Based on tissue or whole-body mRNA sequencing, these opsins are expressed in all body parts, but experimental evidence for their functional significance beyond gene expression is lacking in almost all cases. The known cnidarian opsins fall into three distinct clades called cnidops, anthozoan opsins I, and anthozoan opsins II, respectively, but all medusozoan opsins are in the cnidops clade (Vöcking et al., 2017; Gornik et al., 2021). Interestingly, the three clades do not seem to be closely related to each other, indicating an ancient divergence before the origin of Bilateria (Ramirez et al., 2016; Vöcking et al., 2017).

Within cnidarians - cubomedusae (or box jellyfish) - so far represent the only case of true vision with image-forming eyes that probably evolved independently of all other image-forming eyes (Nilsson et al., 2005; Garm et al., 2011; Picciani et al., 2018). These image-forming eyes, the upper and lower lens eyes, share many structural similarities with vertebrate camera-type eyes such as a hemisphere-shaped retina made of ciliary photoreceptors, a single spherical lens at least partly focusing the light onto the retina, and an adjustable pupil in the lower lens eye (Nilsson et al., 2005). Based on electrophysiological work, immunocytochemistry, microspectrophotometry, and *in situ* hybridization, the two lens eyes use opsins as the photopigment (Garm et al., 2007; Ekström et al., 2008; O'Connor et al., 2010; Bielecki et al., 2014; Liegertová et al., 2015). Even though the photoreceptors of all examined cubozoan photoreceptors are ciliary in structure, they do not express ciliary opsins. Instead, all the recovered opsins belong to the before-mentioned clade cnidops, which is so far only found in cnidarians and they express a G-alpha-s phototransduction cascade (Koyanagi et al., 2008; Picciani et al., 2018).

In addition to the two lens eyes, all known species of cubomedusae have two other eye types, the paired pit and the slit eyes, with unknown photopigments (Garm et al., 2008; Garm and Ekström, 2010). The pit eyes are structurally similar to simple ocelli found in many scyphomedusae and hydromedusae (Yamasu and Yoshida, 1973; Weber, 1981; Singla and Weber, 1982) and are putatively non-image forming, directional light meters. The slit eyes are surprisingly complex and contain four different cell types: vitreous cells, non-sensory pigment cells, pigmented photoreceptors, and non-pigmented photoreceptors. The outer segments of the photoreceptors are arranged in an asymmetric pigment groove, which might result in spatial resolution but in the vertical plane only (Garm et al., 2008). Neither pit nor slit eyes have any functional data including no data on the photopigments. The only evidence for them being photosensory comes from morphology.

In this study, we raised antibodies against the three unidentified opsins recently discovered in transcriptomic data from the Caribbean cubozoan, *Tripedalia cystophora* (Nielsen et al., 2019). We used these antibodies to examine expression not only in polyps and medusae of *T. cystophora* but also in the hydromedusa, in *Sarsia tubulosa*, and in the ocellus-carrying rhopalia of the scyphomedusae *Aurelia aurita* and *Cassiopea xamachana*. The antibodies raised against *T. cystophora* opsins only stained the medusae of *T. cystophora* and not the polyps or the tested scyphomedusae and hydromedusae. The expression patterns in *T. cystophora* allowed us to suggest specific functions for each of them.

MATERIALS AND METHODS

Animal Cultures

Polyps and juvenile (bell diameter (BD): 1.5–2.5 mm), sub-adult (BD: 3–5 mm), and adult (BD: 6–8 mm) medusae of *T. cystophora,* Conant 1897, were obtained from cultures at the Marine Biological Section, University of Copenhagen. They were cultured in 250 l tanks with recycled seawater on a 10:14-h light–dark cycle, a temperature of 28–29 °C, and a salinity of 36–37 PSU. Medusae of *Sarsia tubulosa,* Lesson 1843, *Aurelia aurita,* L. 1758, and *Cassiopea xamachana,* Péron and Lesueur 1809, were likewise obtained from cultures at the University of Copenhagen. They were cultured in 150 l tanks with recycled sea water on a 10:14-h light–dark cycle. The temperature and salinity were 5–6°C and 24–26 PSU for *S. tubulosa*, 10–11°C and 24–26 PSU for *A. aurita*, and 24–25°C and 33–34 PSU for *C. xamachana*. All cultures were fed Selco-enriched *Artemia salina* nauplii daily.

Custom-Made Antibodies Against Opsins

The opsins investigated in this study were originally identified from transcriptomics of juvenile and adult medusae of *T. cystophora* (Nielsen et al., 2019). Specific antibodies against three of the recovered opsins were produced in rabbits (Genosphere, Paris, France) using the following three amino acid sequences from their c-terminus:

Opsin 1: RPEQTSVSAPTTQAVTAANA
Opsin 2: ASGVQPEKENTNTVETTREP
Opsin 3: GLDESEIMPTEGQEPDGQPEIT.

Immunostaining Procedure

Each of the three antibodies was used for immune staining in three polyps, 12 juvenile, four sub-adult, and two adult-male medusae of *T. cystophora* (**Figure 1A**). The adult medusae

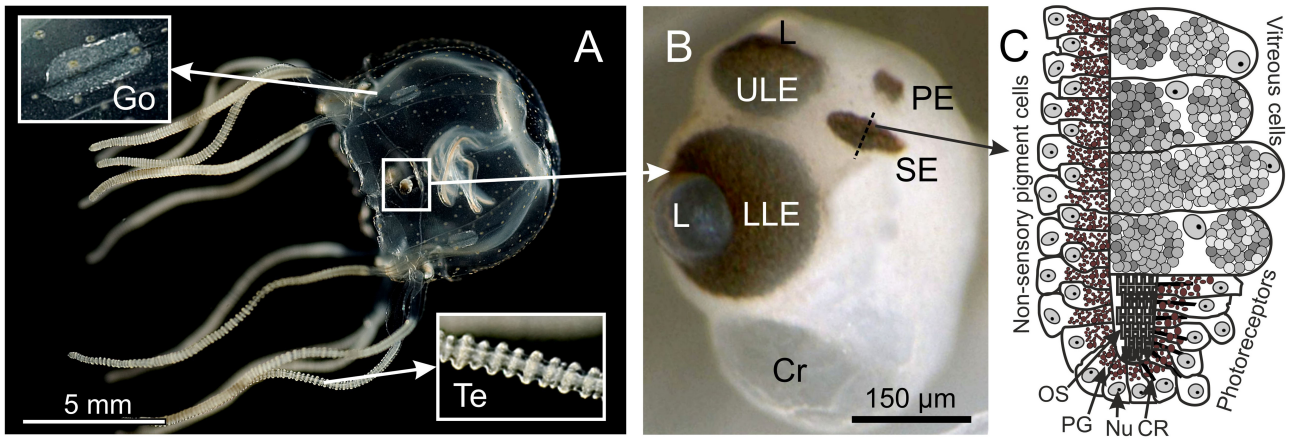

FIGURE 1 | Box jellyfish *T. cystophora*. **(A)** Adult medusa of *T. cystophora* high lighting the paired gonads (Go) and tentacles (Te). **(B)** Close-up of a rhopalium showing the four eye types: upper and lower lens eye (ULE, LLE), slit eyes (SE), and pit eyes (PE). Cr, crystal; L, lens. **(C)** Schematic drawing of a cross section midways in the slit eye [broken line in **(B)**]. Note the asymmetric groove formed by the pigmented cells housing the outer segments of the ciliary photoreceptors. CR, ciliary rootlet; Nu, nucleus; OS, outer segments; PG, pigment granules. **(A)** Modified from Bielecki et al. (2013), **(C)** is modified from Garm et al. (2008).

were dissected into quarters prior to the staining, and their rhopalia were cut off and stained separately (**Figure 1B**). Each quarter contained a pedalium with tentacles and a pair of gonads. Medusae were starved for 24 h prior to fixation/staining to prevent interference from their gut contents. The polyps were likewise starved but for 3 days to maximize their tentacle extension. To prevent the polyps from retracting their tentacles prior to fixation, they were anesthetized in 3.5% $MgCl_2$ in seawater for 60 min prior to fixation. The polyps were kept in a dish containing ∼20 ml seawater, and then, 20 ml of 7% $MgCl_2$ was slowly (over 20 min) titrated into the dish. The three opsin antibodies were additionally tested on three juvenile medusae of *S. tubulosa* (BD: 2 mm), three rhopalial niches of sub-adult *A. aurita* (BD: 3–5 cm), and three rhopalial niches of sub-adult *C. xamachana* (BD: 2–4 cm).

All the materials were initially fixed in 0.1 M phosphate-buffered saline (PBS) with 4% paraformaldehyde and 5% sucrose for an hour on a rocking table at room temperature. Afterward, the tissue samples were washed 4 x 2 times with PBS buffer with triton X and bovine serum albumin (0.1 M PBS with 0.1% Triton X and 0.5% BSA) after 0, 5, 15, and 60 min.

After the last wash, the primary antibodies were added at a concentration of 1:1,000 diluted in 0.1 M PBS with 0.1% Triton X and 0.5% BSA. The incubation with the primary antibodies lasted for 72 h at 5°C in darkness followed by a second series of washes with the same time schedule as the first series. Next, the secondary antibody was added at a concentration of 1:1,000 diluted in 0.1 M PBS with 0.1% Triton X and 0.5% BSA. This incubation lasted 24 h at 5°C in darkness. After 24 h, the material was washed with pure 0.1 M PBS following the schedule above and mounted on glass slides. The material was mounted in glycol using coverslips with wax "feet," sealed with a nail polish, and stored at 5°C in darkness until scanned (always within 5 days after preparation).

Control Preparations

To verify that the obtained staining with the three custom-made antibodies was specific, negative controls and pre-absorption preparations were made. The pre-absorption experiments followed the general staining protocol described above with the exception that the primary antibody was mixed with the corresponding peptide for 60 min before it was included in the protocol. The peptide was diluted 1:500 by weight in 0.1 M PBS. Three juvenile *T. cystophora* medusae were used for each of the three antibody pre-absorption tests.

The negative control experiments also followed the general staining protocol with the exception that the primary antibodies were excluded from the protocol. The materials used for the negative control experiments were three juvenile *T. cystophora* medusae, three juvenile medusae of *S. tubulosa*, three rhopalial niches from *A. aurita,* and two rhopalial niches from *C. xamachana.*

Confocal Laser Scanning Microscopy

The preparations were all scanned on a Leica SP2 microscope using 10X, 40X, or 63X oil immersion objectives. The scan depth varied between 5 and 70 µm with a z-resolution between 0.2 and 1 µm. Both single slides and maximum projections from the scans are used in the illustrations, which were prepared in Corel Graphics Suite 2020. A standard argon laser was used for both fluorescent and transmission scans.

Opsin Phylogeny

We began with the opsin sequences and phylogeny of Picciani et al. (2018) and extracted the entire cnidops clade of opsins plus xenopsins as outgroups from the supplemental file entitled all_0512. We next searched for opsin-like genes in the recently published full genome sequence of the cubozoan *Morbakka virulenta* (Khalturin et al., 2019), using BLAST to retain the *Morbakka* sequences most similar to *T. cystophora* opsins, *Tc*

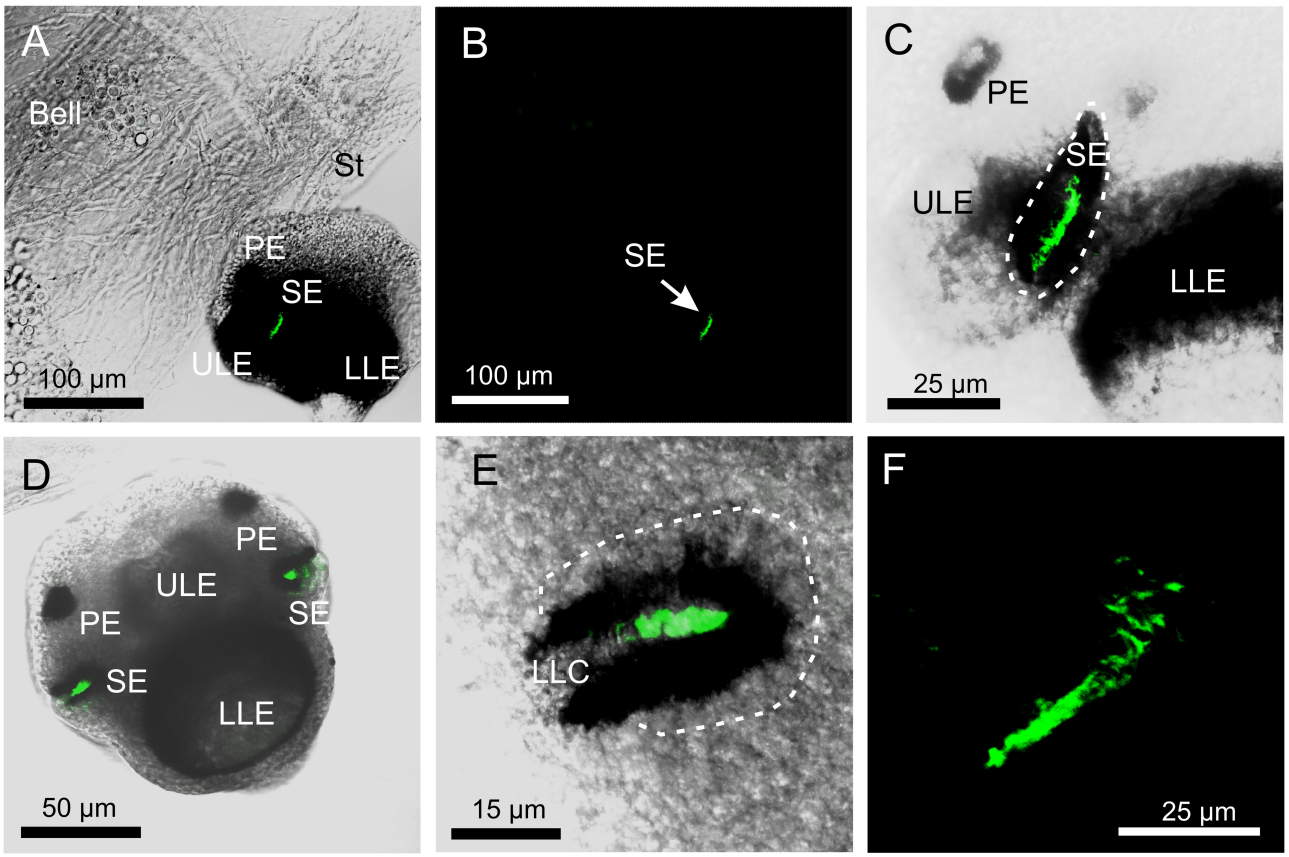

FIGURE 2 | Expression of opsin 1 in *T. cystophora*. **(A)** Overlay of stain with antibody against opsin 1 (green) and transmission showing a rhopalium and parts of bell rim of a juvenile medusa. The retina of the slit eye (SE) is brightly stained. **(B)** The area in (A) only showing the immune stain. Note the complete absence of stain outside the retina of SE. **(C)** Close-up of SE from (A). The entire retina is rather evenly stained. **(D)** A juvenile rhopalium seen frontally showing identical staining in the two-slit eyes. **(E)** Close-up of left SE in (D). Note that the stain is restricted to the photoreceptors outer segments and nor the cell bodies (encircles by broken white line) or the lens-like cells (LLC) are stained. **(F)** Staining of the retina in an adult SE. LLE, lower lens eye; PE, pit eye; ULE, upper lens eye.

LEO, *Tc NEO*, and *Tc GEO*, to represent each of three major groups of known box jelly opsins. After an initial alignment and phylogenetic analysis of all genes, we removed non-opsin GPCR genes of *Morbakka* based on their phylogenetic position and subsequent BLAST searches on all datasets of GenBank. This resulted in retaining two genes from *Morbakka* that fall within the cnidops clade. We then aligned all the cnidops sequences and the xenopsin outgroup sequences using MAFFT and estimated a cnidops phylogeny using IQ-TREE to select the best-fit model.

RESULTS

Opsin 1—*Tc SEO*

The antibody against opsin 1 gave a clear result in *T. cystophora*. There was no stain in the polyps, but all stages of medusae displayed a bright stain in both slit eyes (SE) and no other places (**Figure 2**). Accordingly, we followed our previous nomenclature (Bielecki et al., 2014) and named it *Tripedalia cystophora*slit eye opsin—*Tc SEO*. The stain was located inside the pigment screen in the area matching the outer segments of the photoreceptors (**Figures 1**, **2C–E**). The retina was evenly stained, indicating that the antibodies had attached to all outer segments (**Figure 2C**).

Opsin 2—*Tc GEO*

The antibody against opsin 2 also gave a clear result in *T. cystophora*. Similar to the antibody against opsin 1, it stained the outer segments of the photoreceptors, but in all four eye types (**Figure 3**). Again, following our previous nomenclature, we named it Tripedalia cystophora general eye opsin—*Tc GEO*. The stain against opsin 2 was not as strong as for opsin 1, and the staining of slit eyes was especially weak (**Figures 3B,D,I**). Interestingly, the staining pattern in the outer segments differed when compared to opsin 1 since the stain is not homogeneous but appears as lines. In the upper lens eye (ULE), the lines are 10–30-µm long and 2–4-µm wide in the adults and 5–15-µm long and 2–4-µm wide in the juveniles. Most of the lines in ULE are more or less straight and oriented like the outer segments (**Figure 3G**). In the lower lens eye (LLE), which has the thickest screening pigment, the stain is harder to see. Most lines are seen through the lens of LLE and appear as dots (**Figures 3F,G**). The

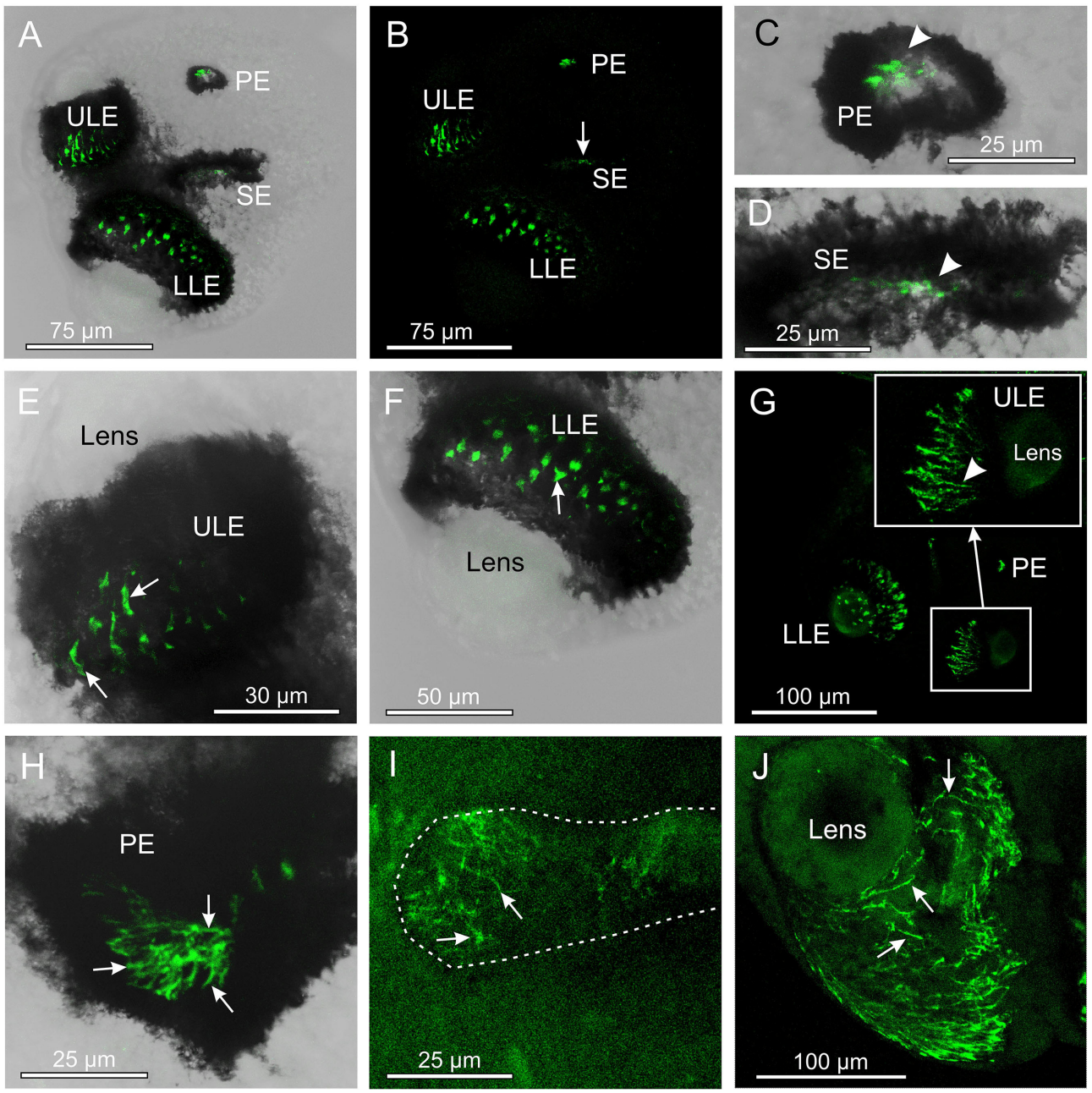

FIGURE 3 | Expression of opsin 2 in *T. cystophora*. **(A)** Overlay between transmission and antibody stain of a juvenile rhopalium. Note that the retina of all eyes is stained. **(B)** The area in (A) only showing the immune stain. The slit eyes (SE) are only weakly stained (arrow). **(C)** Close-up of pit eye (PE) from (A). The stain is only seen inside the pigment screen (arrowhead) which is the outer segments of the photoreceptors. **(D)** Close-up of SE from (A). The stain is again only seen in the outer segments (arrowhead) of the photoreceptors inside the pigment screen. **(E)** Close-up of the upper lens eye (ULE) from (A). Note that the stain in the outer segments is not homogeneous but rather appears as individual lines. **(F)** Close-up of the lower lens eye (LLE) from (A). **(G)** Immuno-stain of a juvenile rhopalium clearly showing the staining pattern as lines following the orientation of the segments in the ULE (insert, arrowhead). **(H)** Stain in an adult PE also showing the expression of opsin 2 as individual lines (arrows). **(I)** The immuno-stain is also weak in the adult SE (outlines by broken white line) and appears as randomly oriented lines (arrows). **(J)** The immune stain in the adult ULE is similar to the juvenile ULE [compare with **(G)**] except for the number of stained lines (arrows) being higher.

dots are 3–4-µm wide in both adults and juveniles. In the pit eyes (PE), the lines seem to have a random orientation crossing each other several times (**Figure 3H**). The single lines are hard to discriminate in juvenile PE, but in adults, they are more easily seen and are ∼0.5-µm wide. In the SE, the stain is uneven with the lateral part of the retina being more stained (**Figures 3D,I**). The lines are also randomly oriented here and 5–10-µm long and ∼0.5-µm wide in the adult SE.

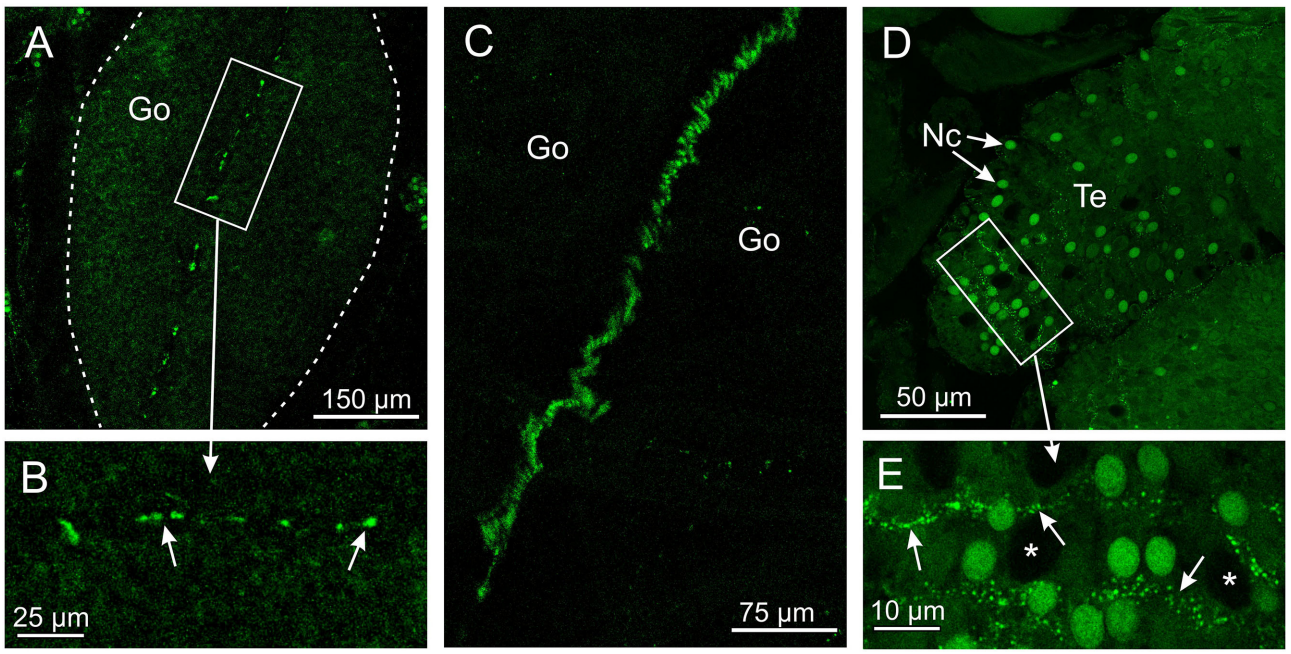

FIGURE 4 | Expression of opsin 3 in *T. cystophora*. **(A)** Punctuated staining is seen along the midline of the immature gonad (Go, framed by broken white line) in the area where the interradial canal and interradial nerve are also situated. **(B)** Close-up of framed area in (A) showing the punctuated staining (arrows). **(C)** The interradial nerve stained with custom-made antibodies raised against *Tripedalia* RFamide. See Nielsen et al. (2019) for details. **(D)** Lines of punctuated staining are also found between the autofluorescent nematocyst (Nc) on the tentacles (Te). **(E)** Close-up of framed area in (C) showing lines of punctuated staining (arrows) between the Nc. Note that the larger nematocysts are not autofluorescent (asterisks).

Opsin 3—*Tc GCO*

The antibody against opsin 3 did not provide as strong a staining pattern in *T. cystophora* as the two other antibodies. The weak stain was seen in two areas and only in the medusa stage. One area is along the midline of the gonads in the area where the interradial nerve is running (**Figures 4A–C**). The stain was not found along the entire midline but appeared as ∼20 elongated dots between 3- and 10-µm long. The other area is between the cnidocytes on the tentacles (**Figures 4D,E**). The stain again appeared as dotted lines but here with dots smaller than 1 µm. We named it *Tripedalia cystophora* gonad and cnidocyte opsin *Tc GCO*.

Control Staining

The pre-absorption tests with the antibody against opsin 1 removed all staining of the SE (**Figures 5A,D**). Similarly, the pre-absorption tests with the antibody against opsin 2 also removed all staining in the rhopalia (**Figures 5B,E**). The weak staining obtained with the antibody against opsin 3 was also absent in the tentacles (**Figures 5C,F**) and in the gonads (not shown) in the pre-absorption tests. Autofluorescent cnidocysts were seen in all three pre-absorption tests (**Figure 5**). The negative control staining without the primary antibodies displayed no stain in the rhopalia, but several autofluorescent cnidocysts were again seen (**Figures 5G,H**).

Stain in *A. aurita*, *C. xamachana*, and *S. tubulosa*

None of the three opsin antibodies provided any specific stain in *A. aurita*, *C. xamachana,* and *S. tubulosa* (**Figure 6**). In *S. tubulosa,* epithelial cells in the middle part of the manubrium did fluoresce in all three cases, but we interpret this as autofluorescence because the same area also has fluorescence in the negative controls (not shown). Furthermore, like for *T. cystophora,* many of the cnidocysts were autofluorescent.

Opsin Phylogeny

In the maximum likelihood phylogeny, the opsin-containing sequence used to create the opsin 1 (*Tc SEO*) antibody clusters closest to the only other ocular opsin known from *Tripedalia*, lens eye opsin (*Tc LEO*) (**Figure 7**). This clade, previously called "Group 2" (Liegertová et al., 2015), also contains sequences from three other cubozoan opsin genes from *Alatina alata* and *Carybdea rastoni*, three opsin genes from the scyphozoans *A. aurita* and *Rhopilema esculentum,* and two opsin genes from the stauromedusae *Haliclystus auricula* and *Lucernaria quadricornis* (**Figure 7**). The sequence of the opsin 3 (*Tc GCO*) gene is found within Group 2 in a sister clade to these ocular opsins and is closely related to an opsin from *A. alata* (**Figure 7**). Interestingly, the sequence of the opsin 2 (*Tc GEO*) gene is only distantly related to the two other opsin genes in this study and was found in a

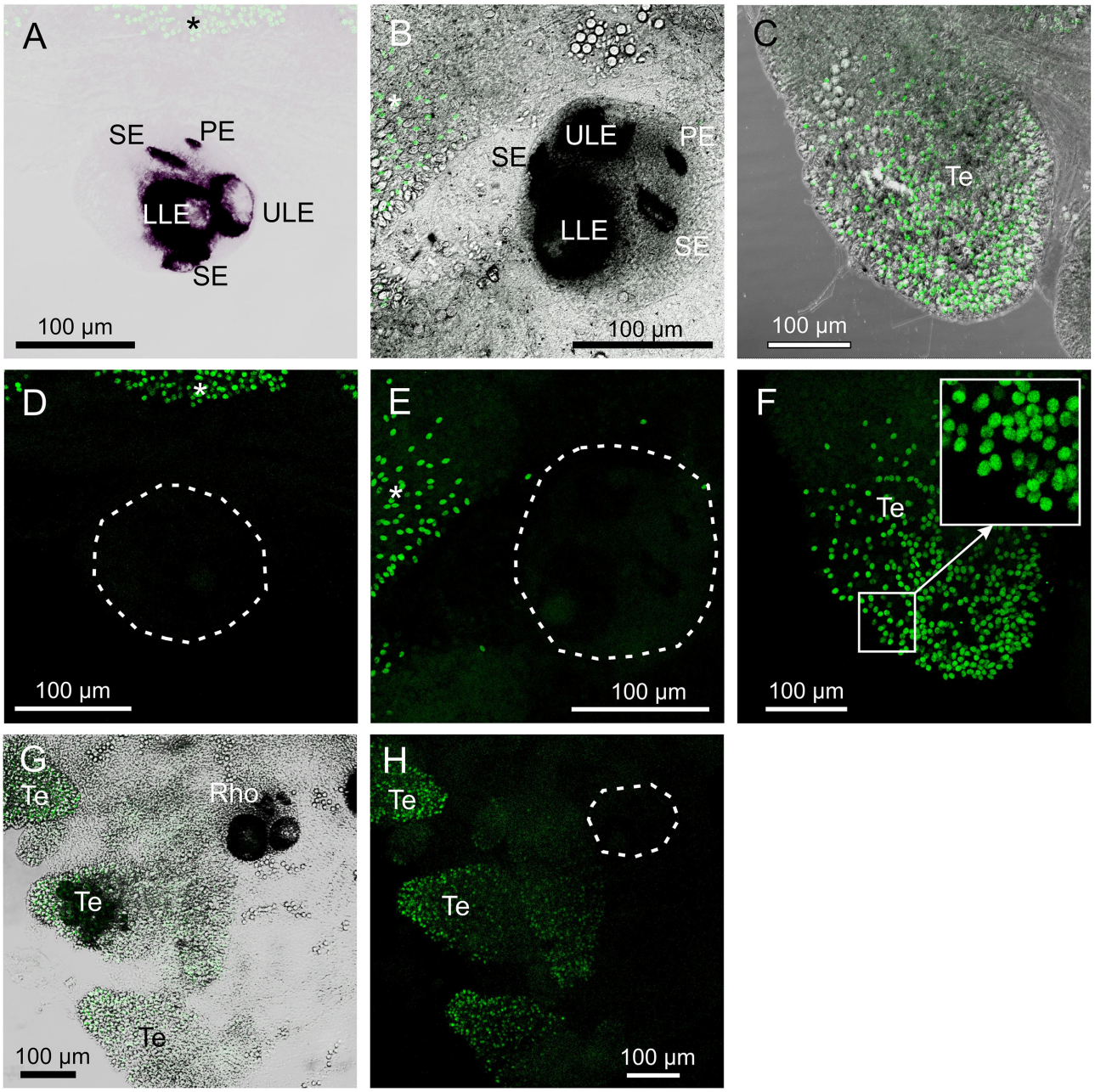

FIGURE 5 | Control staining in *T. cystophora*. **(A,D)** Overlay between transmission and staining and staining alone from pre-absorption test with opsin 1 antibodies. Note the complete absence of staining in the rhopalium including the slit eye (Se). Broken white line in (D) encircles the rhopalium. Asterisks indicate autofluorescent nematocysts. **(B,E)** Overlay between transmission and staining and staining alone from pre-absorption test with opsin 2 antibodies. Note the complete absence of staining in any of the four eye types on the rhopalium [Outlined by broken white line in **(E)**]. Asterisks indicate autofluorescent nematocysts. **(C,F)** Overlay between transmission and staining and staining alone from pre-absorption test with opsin 3 antibodies. Note the absence of punctuated staining between the autofluorescent nematocyst on the tentacle (Te) (insert). **(G,H)** Negative control staining of juvenile medusa. Note the lack of staining in the rhopalium (Rho). Broken white line in **(H)** encircles the rhopalium. The only fluorescence comes from the autofluorescent nematocysts on the Te. LLE, lower lens eye; PE, pit eye; ULE, upper lens eye.

cluster together in a clade previously called Group 1b with other *Tripedalia* opsins and some opsins from scyphomedusae and stauromedusae (see also **Supplementary Figures 1**, **2** and **Supplementary Table 1** for extended phylogenies and *Tripedalia* opsin names).

DISCUSSION

Opsins form the basis of vision in almost all examined eyes, but many animals contain a surprisingly high number of opsin genes, suggesting functional diversification. This is not

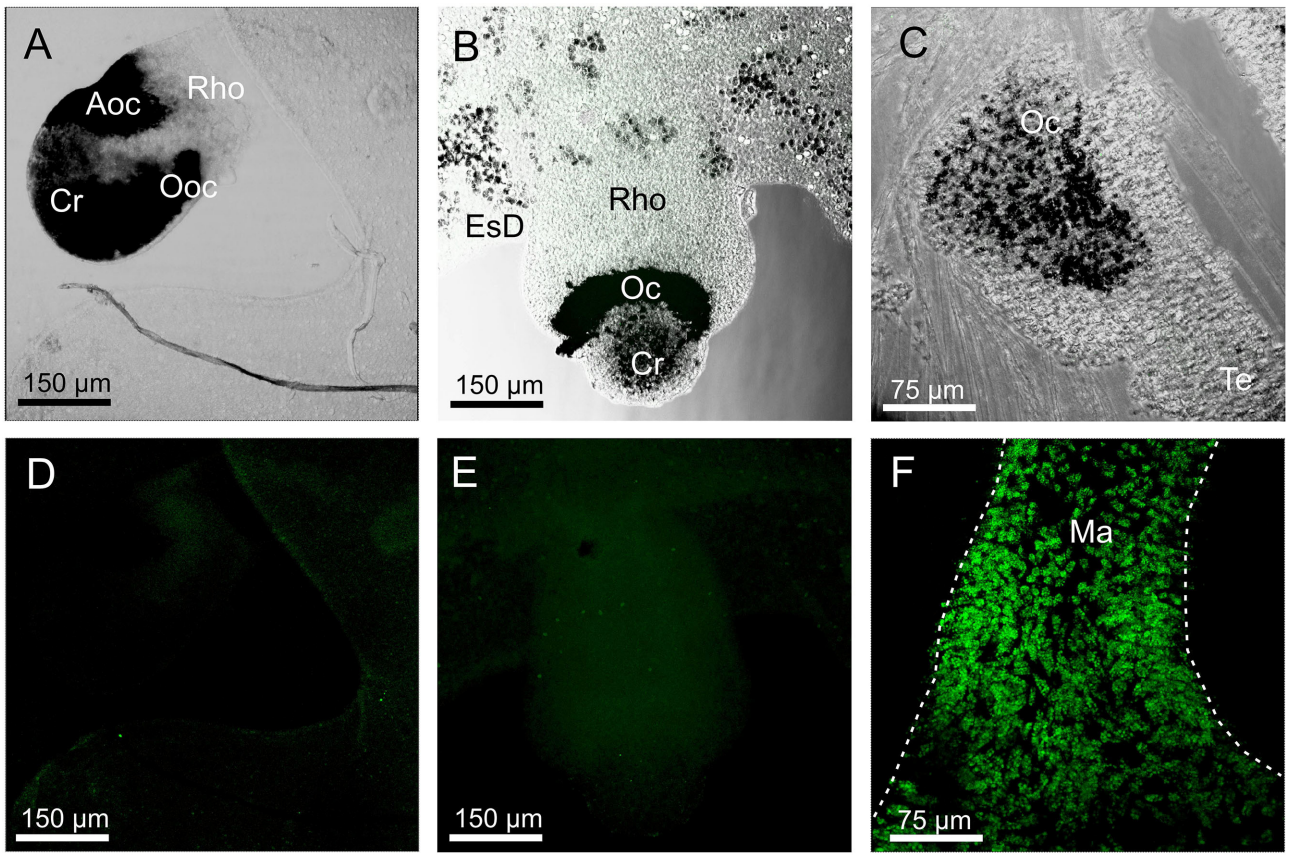

FIGURE 6 | Staining with opsin 1 antibody in other medusae. **(A,D)** Overlay between transmission and staining and staining alone of a rhopalium (Rho) of *Aurelia aurita*. No staining is seen including in the aboral ocellus (Aoc) and the oral ocellus (Ooc). **(B,E)** Overlay between transmission and staining and staining alone of a rhopalium of *Cassiopea xamachana*. No staining is seen including ocellus (Oc). **(C)** Overlay between transmission and staining in the tentacular bulb of *Sarsia tubolosa*. No staining is seen including ocellus (Oc). **(F)** A huge number of autofluorescent cells are found on the middle part of the manubrium (Ma, outlined by broken white line) of *S. tubolosa*. Cr, crystal; EsD, endosymbiotic dinoflagellates; Te, tentacle.

least the case for cnidarians, and here, we used custom-made antibodies to examine the expression patterns of three opsins found in transcriptomic data from the box jellyfish *T. cystophora*. These expression patterns allowed us to suggest functions for each of them, supporting functional diversification, since they are putative visual pigment, photoisomerase, and extraocular photopigment, respectively.

Visual Pigment of the Slit Eyes

The expression pattern of opsin 1 (*Tc SEO*) strongly suggests that this is the photopigment of slit eye photoreceptors. The staining coincides precisely with the known arrangement of the outer segments in the slit eye (Garm et al., 2008). Furthermore, it is a very homogenous stain, which is expected of the photopigments since they are densely packed in the outer segments (Nilsson, 2013). Interestingly, there is a distinct difference in the staining pattern when compared to the anti-opsin stain of putative *Tc LEO* previously obtained from the lens eyes of *T. cystophora* (Ekström et al., 2008). In the photoreceptors of the lens eyes, the opsin antibody stains both the outer segments and the cell bodies where the opsins are synthesized. This is not the case with the slit eye photoreceptors, suggesting that the c-terminus of the opsin (which the opsin 1 (*Tc SEO*) antibodies are raised against) could be hidden from the antibodies prior to opsin entering the outer segments. Two possible explanations for this could be that the c-terminus is folded differently while in the cell body or that the antibodies cannot enter the vesicles which hold the opsin during the transport to the outer segments. The uniform stain of the entire retina also strongly suggests that all photoreceptors express the same opsin and thus that the slit eyes alone do not support color vision, in contrast to an earlier suggestion based on the presence of two morphologically distinct photoreceptor types (Garm et al., 2008). Adding receptor-specific color filters could still result in color vision despite expressing a single opsin only, but there are no indications of such filters in the slit eyes (Garm et al., 2008).

To our knowledge, this is the first study to identify the photopigment of a cnidarian ocellus and thereby also demonstrate that they are opsin based like nearly all other known eyes and ocelli in the animal kingdom (Land and Nilsson, 2012). Several previous molecular studies showed that medusae with ocelli in both Hydrozoa and Scyphozoa have many

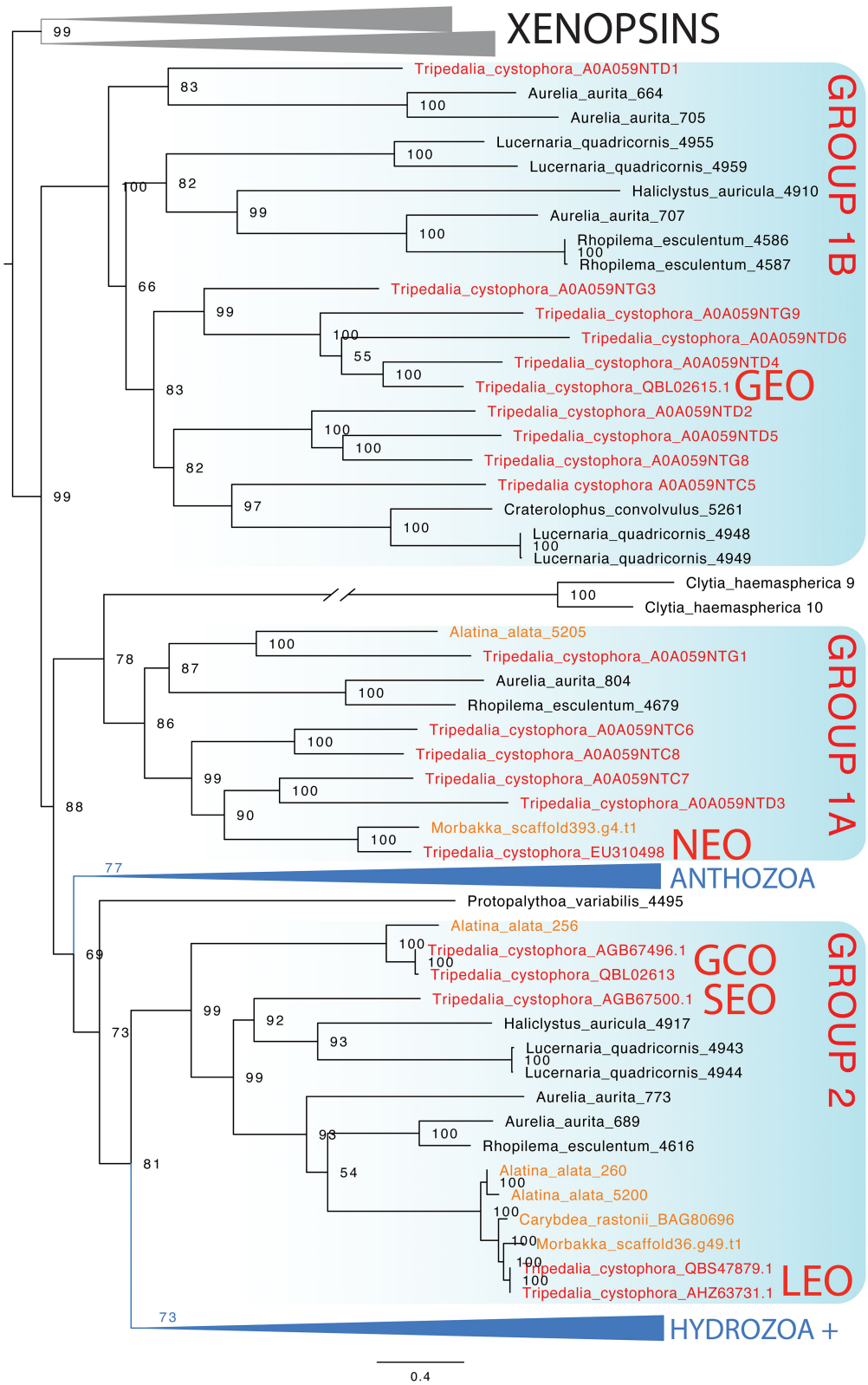

FIGURE 7 | Maximum likelihood phylogenetic analysis of known opsins of the box jellyfish *Tripedalia cystophora*. We combined 21 protein sequences of opsin of *T. cystophora* (red) with other known cnidops, including those of *Alatina alata* (orange), and xenopsins (outgroup in gray), then added putative *Morbakka* opsin

(Continued)

FIGURE 7 | (orange)—for multiple alignments using MAFFT. We then selected the best-fit model in IQ-TREE for likelihood and UFBoot phylogenetic analyses. Illustrated is the bootstrap consensus with numbers at nodes showing bootstrap proportions. Two large clades are collapsed, one containing Anthozoa cnidops, and the other containing mainly Hydrozoa cnidops (see **Supplementary Material** for full phylogeny). Cubozoan opsins fall into three clades, somewhat consistent with previous analyses, which we label here as Group 1a, Group 1b, and Group 2 (Liegertová et al., 2015). Our antibody experiments labeled *Tripedalia cystophora* slit eye opsins—*Tc SEO* (Antibody 1), labeled *Tripedalia cystophora* general eye opsins—*Tc GEO* (Antibody 2), and labeled *Tripedalia cystophora* gonads and cnidocyte opsins—*Tc GCO* (Antibody 3). Note that both *Tc LEO* and *Tc GCO* are represented. These originate from two different studies and putatively represent two different alleles of the same opsin gene.

opsin genes (Suga et al., 2008; Picciani et al., 2018) but their expression in the photoreceptor outer segments has not been shown before. Opsins are associated with the photoreceptors of the hydromedusa *Cladonema radiatum*, but the expression was not seen in the outer segments only in the cell body, leaving the function uncertain. In addition to molecular analyses, the photopigment of cnidarian ocelli was examined in two species of hydromedusae using electrophysiology (Weber, 1982a,b). The spectral sensitivities from those recordings do support the presence of a single opsin in both cases, even though the data were not analyzed to address this.

It is not surprising that the antibody against opsin 1 (*Tc SEO*) did not stain the photoreceptors in the ocelli of the hydromedusae, *S. turbulosa*. In the opsin phylogeny, the hydrozoan opsins cluster outside the cubozoan opsins with the interesting exception of a couple of *Clytia* opsins. This means that the *Sarsia* opsins are likely too different structurally to be recognized by specific antibodies raised against cubozoan opsins, which was confirmed when we compared the sequences of the c-termini (not shown). Our phylogeny did show that opsin 1 (*Tc SEO*) is somewhat closely related to both the *Tripedalia* lens eye opsin (*Tc LEO*) and two opsin genes from *A. aurita*, but no cross-reactions were seen in the lens eyes or the rhopalia of *A. aurita*. Despite this relationship, the c-termini of the opsins are quite different across species. Still, it is interesting that the two known cnidarian ocular opsins cluster closely together, as it could indicate that opsins in this cluster are photoreceptor photopigments. This would pinpoint the most likely candidates for ocular opsins in *A. aurita*, *R. esculentum,* and the putative ocelli of stauromedusae.

Potential Photoisomerase

The staining pattern of the antibody against opsin 2 (*Tc GEO*) is highly interesting. All ocular photoreceptors in the rhopalia of *T. cystophora* seem to be stained, which can indicate one of at least three possibilities: (1) It is the photopigment of a separate type of photoreceptor present in all eyes/ocelli, (2) it is the conserved half of an opsin complex-forming dimer in all ocular photoreceptors, or (3) it is a photoisomerase reactivating the photopigments in all ocular photoreceptors. We found the third option the most likely.

If opsin 2 (*Tc GEO*) is the photopigment of a separate class of photoreceptors, and if it has a different lambda-max value, this could imply color vision in at least the slit eyes and the lens eyes. However, we do not favor this hypothesis. Nothing is known about the physiology of the photoreceptors of the slit eyes, but all available data strongly support the presence of a single photoreceptor type in the lens eyes (Garm et al., 2007; Ekström et al., 2008; O'Connor et al., 2010). Furthermore, the details of the staining patterns indicate that opsin 2 (*Tc GEO*) is situated centrally in the outer segments of the photoreceptors but not in the membrane where the photopigments are normally found.

Dimerization of opsins is a very interesting and highly debated topic, but we do not favor this hypothesis to explain the staining pattern of opsin 2 (*Tc GEO*). Opsins might form dimers similar to the GPCRs involved in insect olfaction (Rützler and Zweibel, 2005; Zhang et al., 2016). The dimerization is potentially important both for successful transportation and integration in the outer segments and for activation of the transduction cascade (Zhang et al., 2016). Still, if opsin 2 (*Tc GEO*) forms heterodimers with opsin 1 (*Tc SEO*) in the slit eyes and LEO in the lens eyes, then we would expect opsin 2 (*Tc GEO*) to be expressed in similar patterns as opsin 1 (*Tc SEO*) and LEO in the slit eye and LLE, respectively, and this is not the case (current results, Ekström et al., 2008).

We hypothesize that opsin 2 (*Tc GEO*) functions as a photoisomerase, reactivating the photopigments in the photoreceptors. Bleaching experiments in another species of box jellyfish, *C. bronzei*, hinted that reactivation does not happen through a light-activated metarhodopsin and thus likely involves a photoisomerase as in vertebrate and cephalopod photoreceptors (Shichida and Matsuyama, 2009; O'Connor et al., 2010; Vöcking et al., 2021). All photoreceptors in *T. cystophora* could use the same photoisomerase, which matches the staining of opsin 2 (*Tc GEO*) we found in all eyes/ocelli. Furthermore, a photoisomerase is likely not bound in the cell membrane but is instead found internally in the cells (Smith and Goldsmith, 1991), which also matches the present staining of opsin 2 (*Tc GEO*). Finally, function as photoisomerase instead of a photopigment is supported by opsin 2 (*Tc GEO*) being in a different evolutionary clade within cnidops, being only distantly related to the known visual opsins in *T. cystophora*.

Perhaps counter to a photoisomerase hypothesis, the extraocular photoreceptors in the rhopalium (Bielecki et al., 2014) and in the tentacles and gonads (current study) are not stained by the opsin 2 (*Tc GEO*) antibody. However, this could also be due to a low amount of opsin/photoisomerase in these cells, resulting in staining that is too weak to be convincingly detected or could indicate that the extraocular opsins are reactivated by a different mechanism.

Extraocular Photoreceptors

The antibody against opsin 3 (*Tc GCO*) only stains structures outside the rhopalium, cells we believe to be extraocular photoreceptors. The neurite-like structures stained in the tentacles are perhaps involved in modulating cnidocyte discharge

based on the light level. In a diversity of polyp stages across cnidarian taxa, the discharge of the nematocytes on the tentacles is influenced by the ambient light (Plachetzki et al., 2012; Picciani et al., 2021). We expect this function to be present in most cnidarians including box jellyfish, which display a strict diurnal rhythm (Garm et al., 2012), and the staining patterns on the tentacles in between the nematocytes are exactly how we would expect the putative opsin-carrying neurons to be arranged. The weak staining also matches an expectation of a low concentration of opsin in extraocular photoreceptors used to detect the time of day (Nilsson, 2013). Furthermore, the presence of the retinal binding residue LY296 supports the function as that of a photoreceptor (Land and Nilsson, 2012).

The stain in the area of the interradial nerve restricted to where it passes the gonad indicates that opsin 3 (*Tc GCO*) might be involved in reproduction. This is supported by juvenile and sub-adult specimens showing no stain in this area. *T. cystophora* has internal fertilization following an actual mating, so light control of gamete release is not a likely function of opsin 3 (*Tc GCO*) (Werner, 1971, 1973). In the hydromedusae, *Clytia hemisphaerica* and *Cladonema radiatum*, specific opsins are also expressed in the gonads and they are involved in gamete maturation (Suga et al., 2008; Artigas et al., 2018). In *C. hemisphaerica,* the system has been characterized in detail, and here, the opsin is expressed in the epidermal cells of the gonads along with a maturation-inducing hormone (MIH). This putatively allows for direct light control of MIH release and thus gamete maturation (Artigas et al., 2018). Little is known about gamete maturation in *T. cystophora* and about what hormones might influence this. If opsin 3 (*Tc GCO*) is involved in gamete maturation, it operates in a different way than in *C. hemispaerica*, since it is not expressed in the gonad as such but rather in the space between the two hemi-gonads in the area of the interradial nerve. Still, personal observation from their natural habitat in the Puerto Rican mangroves shows that medusa size, rather than light level or day length, seems to control when gametes/gonads start to develop, and at least male medusae can carry ripe spermatozeugmata for days (Helmark and Garm, 2019). A third option is that opsin 3 (*Tc GCO*) is not a photoreceptor but has another function, which is yet to be determined.

Opsin Phylogeny

An open question in cnidarian biology is which opsins are expressed in eyes and ocelli of different clades. This is particularly interesting because eyes and ocelli originated multiple times convergently in medusozoa, raising the question of whether the same opsin ortholog is expressed each time. Unfortunately, expression data for cnidarian eyes are mainly missing, but our current gene phylogeny presents some candidates for future tests. Namely, Group 2 opsins contain *Tripedalia* lens eye opsins (*Tc LEO*) and slit eye opsins (*Tc SEO*), raising the possibility that this is a clade of ocular opsins. The clade also contains opsins from *Aurelia* and *Rhopilema*, which we consider to be prime candidates as ocular opsins, even though those scyphozoan eyes may be non-homologous to cubozoan eyes (Picciani et al., 2018). The Group 2 clade also contains opsins from two staurozoans. Some staurozoans have dark pigment spots consistent with their function as photoreceptive organs (Miranda and Collins, 2019). These Group 2 opsins are candidates for expression in these pigment spots.

Our phylogeny of cnidarian opsins focused on *Tripedalia* is consistent with previous studies that found a diverse assemblage of opsins in box jellyfish (Liegertová et al., 2015; Ramirez et al., 2016). Two groups of Tripedalia opsins (Group 1 and Group 2) are distantly related to each other, with Group 2 being related most closely to a large clade of hydrozoan opsins. In our analysis, Group 1 opsins are paraphyletic with Group 1B as the sister group to all the other cnidops. This is a rather surprising result because it implies that 1A and 1B were lost independently from Anthozoa and Hydrozoa. An alternative interpretation is that the gene tree is challenging to root properly. We chose xenopsins as the outgroup to cnidops based on previous studies (Ramirez et al., 2016; Vöcking et al., 2017), and so we do not believe there is a better choice of outgroup opsins. Future studies could explicitly consider gene duplication and loss events when constructing the gene tree.

DATA AVAILABILITY STATEMENT

Data and phylogenetic analyses can be found online at: https://github.com/ostratodd/Tripedalia_opsin_expression_2022.

AUTHOR CONTRIBUTIONS

AG conceptualized the work, designed the experiments, wrote the initial version of the manuscript, and designed the figures. J-ES and DP collected and analyzed the immunocytochemical data. TO performed the phylogenetic analysis. AG and TO financed the work. All authors contributed to the final version.

ACKNOWLEDGMENTS

The authors appreciate the help maintaining the cultures offered by the members of the Sensory Biology Group, University of Copenhagen, Denmark and the help designing the antibodies offered by Frank Hauser, University of Copenhagen, Denmark. AG acknowledges the financial support from the Danish Research Council (DFF, grant# 4181–00398), and TO acknowledges grant #1754770 from the US National Science Foundation (NSF).

SUPPLEMENTARY MATERIAL

The Supplementary Material for this article can be found online at: https://www.frontiersin.org/articles/10.3389/fnana.2022.916510/full#supplementary-material

Supplementary Figure 1 | Maximum likelihood phylogenetic analysis to discover opsins from the genome of *Morbakka*. We searched for opsin-like genes in the recently published full genome sequence of the cubozoan *Morbakka virulenta* (Khalturin et al., 2019), using BLAST to retain the *Morbakka* sequences most similar to *Tripedalia cystophora* opsins *Tc LEO*, *Tc NEO*, and *Tc GEO*, which represent each of the major groups 1a, 1b, and 2. Such similarity searches usually

retain non-opsin GPCR genes. To determine non-opsins, we combined the *Morbakka* genes with our cnidops and xenopsin dataset (see **Figure 7** and **Supplementary Figure 2**) and estimated this phylogeny in IQ-TREE using the best-fit model, illustrated here rooted with a clade of 16 *Morbakka* genes (magenta). These 16 genes are non-opsin GPCRs that we removed for final analyses. The topology of the overall tree shown here is different from the final, probably because adding non-opsin genes to opsins destabilizes the opsin ingroup (Plachetzki et al., 2007). This tree also contains duplicated genes of *Tripedalia cystophora* (black) that were removed before the final analysis. Multiple sequences are very similar to other sequences and are probably allelic variants, but that cannot be determined with certainty without genome sequencing. The scale bar indicates amino acid substitutions per site.

Supplementary Figure 2 | Full phylogenetic tree for our xenopsin + cnidops dataset. See **Supplementary Figure 1** and main text for methodological details. The scale bar indicates amino acid substitutions per site.

REFERENCES

Artigas, Q. O., Lapebie, P., Leclere, L., Takeda, N., Deguchi, R., Jekely, G., et al. (2018). A gonad-expressed opsin mediates light-induced spawning in the jellyfish Clytia. *eLife* 7, e29555. doi: 10.7554/eLife.29555

Bielecki, J., Nachman, G., and Garm, A. (2013). Swimpacemaker response to bath applied neurotransmitters in the cubozoan *Tripedalia cystophora*. *J. Comp. Physiol. A* 199, 785–795. doi: 10.1007/s00359-013-0839-1

Bielecki, J., Zaharoff, A., Leung, N., Garm, A., and Oakley, T. H. (2014). The cubozoan visual system utilizes several opsins. *PLoS ONE 9*, 1–9. doi: 10.1371/journal.pone.0098870

Döring, C. C., Kumer, S., Tumu, S. C., Kourtesis, I., and Hausen, H. (2020). The visual pigment xenopsin is widespread in protostome eyes and impacts the view on eye evolution. *eLife* 9:e55193. doi: 10.7554/eLife.55193

Ekström, P., Garm, A., Pålsson, J., Vihtlec, T., and Nilsson, D. E. (2008). Immunohistochemical evidence for several photosystems in box jellyfish using opsin-antibodies. *Cell Tissue Res.* 333, 115–124. doi: 10.1007/s00441-008-0614-8

Garm, A., Anderson, F., and Nilsson, D. E. (2008). Unique structure and optics of the lesser eyes of the box jellyfish *Tripedalia cystophora*. *Vision Res.* 48, 1061–1073. doi: 10.1016/j.visres.2008.01.019

Garm, A., Bielecki, J., Petie, R., and Nilsson, D. E. (2012). Opposite patterns of diurnal activity in the box jellyfish *Tripedalia cystophora* and *Carybdea sivickisi*. *Biol. Bull.* 222, 35–45. doi: 10.1086/BBLv222n1p35

Garm, A., Coates, M. M., Seymour, J., Gad, R., and Nilsson, D. E. (2007). The lens eyes of the box jellyfish *Tripedalia cystophora* and *Chiropsalmus sp.* are slow and color-blind. *J. Comp. Physiol. A* 193, 547–557. doi: 10.1007/s00359-007-0211-4

Garm, A., and Ekström, P. (2010). Evidence for multiple photosystems in jellyfish. *Int. Rev. Cell. Mol. Biol.* 280, 41–78. doi: 10.1016/S1937-6448(10)80002-4

Garm, A., Oskarsson, M., and Nilsson, D. E. (2011). Box jellyfish use terrestrial visual cues for navigation. *Curr. Biol.* 21, 798–803. doi: 10.1016/j.cub.2011.03.054

Gornik, S. B., Bergheim, B. G., Morel, B., Stamatakis, A., Foulkes, N. S., and Guse, A. (2021). Photoreceptor diversification accompanies the evolution of Anthozoa. *Mol. Biol. Evol.* 38, 1744–1760. doi: 10.1093/molbev/msaa304

Helmark, S., and Garm, A. (2019). Gonadal cnidocytes in the cubozoan *Tripedalia cystophora* Conant, 1897 (Cnidaria: Cubozoa). *J. Morphol.* 280, 1530–1536. doi: 10.1002/jmor.21046

Khalturin, K., Shinzato, C., Khalturina, M., Hamada, M., Fujie, M., Koyanagi, R., et al. (2019). Medusozoan genomes inform the evolution of the jellyfish body plan. *Nat. Ecol. Evol.* 3, 811–822. doi: 10.1038/s41559-019-0853-y

Koyanagi, M., Takano, K., Tsukamoto, H., Ohtsu, K., Tokunaga, F., and Terakita, A. (2008). Jellyfish vision starts with cAMP signaling mediated by opsin-Gs cascade. *Proc. Natl. Acad. Sci. U. S. A.* 105, 15576–15580. doi: 10.1073/pnas.0806215105

Land, M. F., and Nilsson, D. E. (2012). *Animal Eyes*. Oxford: Oxford University Press.

Liegertová, M., Pergner, J., Kozmikova, I., Fabian, P., Pombinho, A. R., Strnad, H., et al. (2015). Cubozoan genome illuminates functional diversification of opsins and photoreceptor evolution. *Sci. Rep.* 5, 1–18. doi: 10.1038/srep11885

Macias-Munoz, A., Murad, R., and Mortazavi, A. (2019). Molecular evolution and expression of opsin genes in *Hydra vulgaris*. *BMC Genomics* 20, 1–19. doi: 10.1186/s12864-019-6349-y

Miranda, L. S., and Collins, A. G. (2019). Eyes in Staurozoa (Cnidaria): a review. *Peer J.* 7, e6693. doi: 10.7717/peerj.6693

Nielsen, S. K. D., Koch, T. L., Wiisbye, S., Grimmelikhuijzen, C. J. P., and Garm, A. (2019). Neuropeptide expression in the box jellyfish *Tripedalia cystophora*—New insights into the complexity of a "simple" nervous system. *J. Comp. Neurol.* 529, 2865–2882. doi: 10.1002/cne.25133

Nilsson, D. E. (2013). Eye evolution and its functional basis. *Vis. Neurosci.* 30, 5–20. doi: 10.1017/S0952523813000035

Nilsson, D. E., Gislén, L., Coates, M. M., Skogh, C., and Garm, A. (2005). Advanced optics in a jellyfish eye. *Nature* 435, 201–205. doi: 10.1038/nature03484

Nilsson, D. E., and Pelger, S. (1994). A pessimistic estimate of the time required for an eye to evolve. *Proc. R. Soc. Lond. B. Biol. Sci.* 256, 53–58. doi: 10.1098/rspb.1994.0048

O'Connor, M., Garm, A., Hart, N. S., Nilsson, D. E., Ekström, P., Skogh, C., et al. (2010). Visual pigments of the box jellyfish species *Chiropsella bronzie*. *Philos. Trans. R. Soc. Lond.* 277, 1843–1848. doi: 10.1098/rspb.2009.2248

Picciani, N., Kerlin, J. R., Jindrich, K., Hensley, N. M., Gold, D. A., and Oakley, T. H. (2021). Light modulated cnidocyte discharge predates the origins of eyes in Cnidaria. *Ecol. Evol.* 11, 3933–3940. doi: 10.1002/ece3.7280

Picciani, N., Kerlin, J. R., Sierra, N., Swafford, A. J. M., Ramirez, M. D., Roberts, N. G., et al. (2018). Prolific origination of eyes in cnidaria with co-option of non-visual opsins. *Curr. Biol.* 28, 2413–2419. doi: 10.1016/j.cub.2018.05.055

Plachetzki, D. C., Degnan, B. M., and Oakley, T. H. (2007). The origine of novel protein interactions during animal opsin evolution. *PLoS Biol.* 5, 1–9. doi: 10.1371/journal.pone.0001054

Plachetzki, D. C., Fong, C. R., and Oakley, T. H. (2010). The evolution of phototransduction from an ancestral cyclic nucleotide gated pathway. *Proc. Biol. Sci.* 277, 1963–1969. doi: 10.1098/rspb.2009.1797

Plachetzki, D. C., Fong, C. R., and Oakley, T. H. (2012). Cnidocyte discharge is regulated by light and opsin-mediated phototransduction. *BMC Biol.* 10, 1–9. doi: 10.1186/1741-7007-10-17

Ramirez, M. D., Pairett, A. N., Pankey, S. M., Serb, J. M., Speiser, D. I., Swafford, A. J., et al. (2016). The last common ancestor of most bilaterian animals possessed at least nine opsins. *Genome Biol. Evol.* 8, 3640–3652. doi: 10.1101/052902

Rützler, M., and Zweibel, L. J. (2005). Molecular biology of insect olfaction recent progress and conceptual models. *J. Comp. Physiol. A* 191, 777–790. doi: 10.1007/s00359-005-0044-y

Salvini-Plawen, L. V., and Mayr, E. (1977). On the evolution of photoreceptors and eyes. *Evol. Biol.* 10 doi: 10.1007/978-1-4615-6953-4_4

Shichida, Y., and Matsuyama, T. (2009). Evolution of opsins and phototransduction. *Philos. Trans. R. Soc. Lond.* 364, 2881–2895. doi: 10.1098/rstb.2009.0051

Singla, C. L., and Weber, C. (1982). Fine structure of the ocellus of *Sarsia tubulosa* (Hydrozoa, Anthomedusae). *Zoomorphology* 100, 11–22. doi: 10.1007/BF00312197

Smith, W. C., and Goldsmith, T. H. (1991). Localization of retinal photoisomerase in the compound eye of the honeybee. *Vis. Neurosci.* 7, 237–249. doi: 10.1017/S0952523800004053

Suga, H., Schmid, V., and Gehring, W. J. (2008). Evolution and functional diversity of jellyfish opsins. *Curr. Biol.* 18, 51–55. doi: 10.1016/j.cub.2007.11.059

Vanfleteren, J. R., and Coomans, A. (1976). Photoreceptor evolution and phylogeny. *J. Zoolog. Syst. Evol. Res.* 14, 157–168. doi: 10.1111/j.1439-0469.1976.tb00934.x

Vöcking, O., Kourtesis, I., Tumu, S. C., and Hausen, H. (2017). Co-expression of xenopsin and rhabdomeric opsin in photoreceptors bearing microvilli and cilia. *eLife* 6, e23435. doi: 10.7554/eLife.23435

Vöcking, O., Leclere, L., and Hausen, H. (2021). The rhodopsin-retinochrome system for retinal re-isomerization predates the origin of cephalopod eyes. *BMC Ecol. Evol.* 21, 215. doi: 10.1186/s12862-021-01939-x

Weber, C. (1981). Structure, histochemistry, ontogenetic development, and regeneration of the ocellus of *Cladonema radiatum* Dujardin (Cnidaria, Hydrozoa, Anthomedusae). *J. Morphol.* 167, 313–331. doi: 10.1002/jmor.1051670306

Weber, C. (1982a). Electrical activities of a type of electroretinogram recorded from the ocellus of a jellyfish, *Polyorchis penicillatus* (Hydromedusae). *J. Exp. Zool.* 223, 231–243. doi: 10.1002/jez.1402230305

Weber, C. (1982b). Electrical activity in response to light of the ocellus of the hydromedusan, *Sarsia tubulosa*. *Biol. Bull.* 162, 413–422. doi: 10.2307/1540993

Werner, B. (1971). Life cycle of *Tripedalia cystophora* Conant (Cubomedusae). *Nature* 232, 582–583. doi: 10.1038/232582a0

Werner, B. (1973). Spermatozeugmen und paarungsverhalten bei *Tripedalia cystophora* (Cubomedusae). *Mar. Biol.* 18, 212–217. doi: 10.1007/BF00367987

Yamasu, T., and Yoshida, M. (1973). Electron microscopy on the photoreceptors of an anthomedusa and a scyphomedusa. *Pub. Seto Mar. Biol. Lab.* 20, 757–778. doi: 10.5134/175744

Zhang, T., Cao, L.-H., Kumar, S., Enemchukwu, N. O., Zhang, N., Lambert, A., et al. (2016). Dimerization of visual pigments *in vivo*. *Proc. Natl. Acad. Sci. U. S. A.* 113, 9093–9098. doi: 10.1073/pnas.1609018113

Conflict of Interest: The authors declare that the research was conducted in the absence of any commercial or financial relationships that could be construed as a potential conflict of interest.

Publisher's Note: All claims expressed in this article are solely those of the authors and do not necessarily represent those of their affiliated organizations, or those of the publisher, the editors and the reviewers. Any product that may be evaluated in this article, or claim that may be made by its manufacturer, is not guaranteed or endorsed by the publisher.

frontiers | Frontiers in Neuroanatomy

TYPE Correction
PUBLISHED 08 September 2022
DOI 10.3389/fnana.2022.1028092

OPEN ACCESS

APPROVED BY
Frontiers Editorial Office,
Frontiers Media SA, Switzerland

*CORRESPONDENCE
Anders Garm
algarm@bio.ku.dk

RECEIVED 25 August 2022
ACCEPTED 26 August 2022
PUBLISHED 08 September 2022

CITATION
Garm A, Svaerke J-E, Pontieri D and Oakley TH (2022) Corrigendum: Expression of opsins of the box jellyfish *Tripedalia cystophora* reveals the first photopigment in cnidarian ocelli and supports the presence of photoisomerases.
Front. Neuroanat. 16:1028092.
doi: 10.3389/fnana.2022.1028092

Corrigendum: Expression of opsins of the box jellyfish *Tripedalia cystophora* reveals the first photopigment in cnidarian ocelli and supports the presence of photoisomerases

Anders Garm[1]*, Jens-Erik Svaerke[1], Daniela Pontieri[1] and Todd H. Oakley[2]

[1]Marine Biological Section, University of Copenhagen, Copenhagen, Denmark, [2]Department of Biology, University of California, Santa Barbara, Santa Barbara, CA, United States

KEYWORDS

photopigment, box jellyfish, cubozoa, cnidaria, phototransduction, opsin phylogeny, vision

A corrigendum on
Expression of opsins of the box jellyfish *Tripedalia cystophora* reveals the first photopigment in cnidarian ocelli and supports the presence of photoisomerases

by Garm, A., Svaerke, J.-E., Pontieri, D., and Oakley, T. H. (2022). *Front. Neuroanat.* 16:916510. doi: 10.3389/fnana.2022.916510

In the published article, there was an error in the legend for **Figure 1** as published. Credits are missing for the picture in **(A)**. The corrected legend appears below.

"Box jellyfish *T. cystophora*. **(A)** Adult medusa of *T. cystophora* high lighting the paired gonads (Go) and tentacles (Te). **(B)** Close up of a rhopalium showing the four eye types: upper and lower lens eye (ULE, LLE), slit eyes (SE), and pit eyes (PE). Cr, crystal; L, lens. **(C)** Schematic drawing of a cross section midways in the slit eye [broken line in **(B)**]. Note the asymmetric groove formed by the pigmented cells housing the outer segments of the ciliary photoreceptors. CR, ciliary rootlet; Nu, nucleus; OS, outer segments; PG, pigment granules. **(A)** Modified from Bielecki et al. (2013), **(C)** is modified from Garm et al. (2008)."

The authors apologize for this error and state that this does not change the scientific conclusions of the article in any way. The original article has been updated.

Publisher's note

References

Bielecki, J., Nachman, G. and Garm, A. (2013). Swim pacemaker response to bath applied neurotransmitters in the cubozoan *Tripedalia cystophora*. *J. Comp. Physiol. A* 199, 785–795. doi: 10.1007/s00359-013-0839-1

Garm, A., Anderson, F., and Nilsson, D. E. (2008). Unique structure and optics of the lesser eyes of the box jellyfish *Tripedalia cystophora*. *Vision Res.* 48, 1061–1073. doi: 10.1016/j.visres.2008.01.019

frontiers | Frontiers in Neuroanatomy

TYPE Mini Review
PUBLISHED 23 September 2022
DOI 10.3389/fnana.2022.994890

OPEN ACCESS

EDITED BY
Antón Barreiro-Iglesias,
University of Santiago de Compostela, Spain

REVIEWED BY
Xandra Pereiro,
University of the Basque Country, Spain

*CORRESPONDENCE
Marta Agudo-Barriuso
martabar@um.es

RECEIVED 15 July 2022
ACCEPTED 02 September 2022
PUBLISHED 23 September 2022

CITATION
Galindo-Romero C, Norte-Muñoz M, Gallego-Ortega A, Rodríguez-Ramírez KT, Lucas-Ruiz F, González-Riquelme MJ, Vidal-Sanz M and Agudo-Barriuso M (2022) The retina of the lab rat: focus on retinal ganglion cells and photoreceptors. Front. Neuroanat. 16:994890. doi: 10.3389/fnana.2022.994890

The retina of the lab rat: focus on retinal ganglion cells and photoreceptors

Caridad Galindo-Romero, María Norte-Muñoz, Alejandro Gallego-Ortega, Kristy T. Rodríguez-Ramírez, Fernando Lucas-Ruiz, María Josefa González-Riquelme, Manuel Vidal-Sanz and Marta Agudo-Barriuso*

Experimental Ophthalmology Group, Instituto Murciano de Investigación Biosanitaria Virgen de la Arrixaca (IMIB-Arrixaca) & Ophthalmology Department, Universidad de Murcia, Murcia, Spain

Albino and pigmented rat strains are widely used in models to study retinal degeneration and to test new therapies. Here, we have summarized the main topographical and functional characteristics of the rat retina focussing on photoreceptors and retinal ganglion cells (RGCs), the beginning and end of the retinal circuitry, respectively. These neurons are very sensitive to injury and disease, and thus knowing their normal number, topography, and function is essential to accurately investigate on neuronal survival and protection.

KEYWORDS

retinal ganglion cells, melanopsin, photoreceptors, topography, electroretinogram

Introduction

Preclinical research in visual sciences is generally conducted in small mammals, mostly rodents and, to a lesser extent, rabbits or pigs. Rabbits are (usually) used to study the anterior part of the eye, the cornea, while rodents are (usually) used to investigate the retina, optic nerve, and retinorecipient areas. Within rodents, rats (*Rattus norvergicus*) and mice (*Mus musculus*) are the preferred species (>70,000 published articles in the last 20 years). Because they are nocturnal animals for specific research questions (i.e., circadian rhythms), diurnal rodents such as squirrels, Nile rats or common degus are also established models.

The layered structure of the retina is highly conserved along vertebrates (Ramón y Cajal, 2021). However, there are some cellular and regional differences, species-specific consequence of environmental and behavioral factors. For instance, rodents are nocturnal and thus their retina is rod-dominated. Most of primates and humans are diurnal, and though rods outnumber cones in the peripheral retina, they are almost absent in the central retina or macula. For color vision, like most mammals, rodents have two types of cones, S-cones (short light wavelength detecting-cones, or blue cones) and L/M-cones (medium-long light wavelength detecting-cones, red-green cones) while primates have three, S-, M-, and L- cones.

Primates are highly social animals and to correctly gauge the mood of their congeners, their vision must have high resolution. Thus, humans and primates have a specialized

retinal area, the macula, with several rows of retinal ganglion cells (RGCs) and an RGC:cone ratio close to 1:1 characteristics that provide high resolution. Within the macula there is a depression, the fovea centralis, where most of retinal layers are missing but the cones, thus optimizing visual acuity. In rats there is no macula or fovea, instead they have a visual streak with higher RGC and L/M-cone densities (Salinas-Navarro et al., 2009; Ortín-Martínez et al., 2010).

Despite these differences, rats and mice are still the model of choice because they offer several advantages. They are small and adaptable, reproduce quickly and are easy to house and handle. In fact, both species have been used for research since the beginning of the 20th century, when the strains most commonly used today were created. Wistar rats (outbred, albino) were developed in 1906, Sprague Dawley (outbred, albino) in 1925, and C57/Bl6 mice (inbred pigmented) in 1921. These strains are now very well characterized genetically and physiologically (Hedrich and Bullock, 2012; Boorman, 2018). Furthermore, there are strains that spontaneously develop diseases such as diabetes, retinitis pigmentosa or glaucoma. In mice, genetic manipulation allows the generation of mutant or transgenic strains that, in many cases, are created to accurately mimic human diseases and pathologies. Genetic engineering is also used in rats but not very frequently.

Even though lack of melanin causes an impaired visual acuity, lower number of ipsilaterally projecting RGCs, defects in the optokinetic nystagmus, and a lower functional response (Lund, 1965; Balkema et al., 1981; Lund, 1986; Dräger and Balkema, 1987; Balkema and Drager, 1991; Prusky et al., 2002; Alarcón-Martínez et al., 2009; Nadal-Nicolás et al., 2012), albino rats are as used as pigmented ones in basic research.

Most retinal diseases proceed with the degeneration of RGCs or photoreceptors. The loss of these neurons may be caused by systemic dysfunctions such as diabetes or stroke, or congenital defects such as retinitis pigmentosa or Leber hereditary optic nerve neuropathy. There are other pathologies of unknown or complex etiology further complicated with risk factors such as glaucoma or age-related macular degeneration. To mimic these diseases there are many rat and mouse models that are either induced, spontaneous or genetically engineered (Shareef et al., 1995; Avilés-Trigueros et al., 2003; Pérez de Lara et al., 2014; Morgan and Tribble, 2015; Urcola et al., 2016; Mrejen et al., 2017; Sánchez-Migallón et al., 2018; Marchesi et al., 2021; Karademir et al., 2022; Subramaniam et al., 2022).

Consequently, the most studied retinal neurons are the photoreceptors and RGCs the beginning and end, respectively, of the neuronal retinal circuitry. Photoreceptors, as their name states, sense the light and transform it into action potentials that finally reach the RGCs which, in turn, send the processed information to the brain where ultimately the vision and non-vision light-induced responses occur.

Here, we compile for the first time the retinal topography and exact numbers of RGCs (vision and non-vision forming) and cone photoreceptors (L and S) and the electroretinographic waves used to study their function in the healthy rat retina.

Retinal ganglion cells

Majority of RGCs are found in the ganglion cell layer (GCL), the innermost layer of the retina sharing location with displaced amacrine cells (50% of the cells in the GCL in rat) and glial cells (astrocytes and microglia, 10% of the cells in the GCL; Nadal-Nicolás et al., 2015, 2018). A small number of RGCs have their somas displaced to the inner plexiform layer (displaced RGCs; Nadal-Nicolás et al., 2014). Regardless of their location, RGCs are a heterogeneous population encompassing more than 40 subtypes according to their gene expression (Rheaume et al., 2018; Tran et al., 2019). Functionally, though, they are classified in two main groups: RGCs that convey vision-forming information and RGCs that send non-vision forming information.

Non-vision forming RGCs are intrinsically photosensitive (ipRGCs) because they express the photopigment melanopsin. Thanks to this pigment they sense light irradiance and regulate the circadian rhythm and the pupillary reflex (Provencio et al., 2000; Berg et al., 2019) ipRGCs, which encompass M1-M6 subtypes, have also some roles in pattern vision (Hattar et al., 2006; Ecker et al., 2010; Schmidt et al., 2011).

RGCs univocal identification is necessary to assess the extent of degeneration after a given insult or disease and to know if an experimental therapy is effective (Avilés-Trigueros et al., 2003; Vidal-Sanz et al., 2017; Sánchez-Migallón et al., 2018), and to do that most groups opt for immunodetection. There are several well-known RGC markers, i.e., proteins that in the retina are only expressed by RGCs. Among them Brn3a (Nadal-Nicolás et al., 2009) and RBPMS (Kwong et al., 2010; Rodriguez et al., 2014) stand out. Brn3a is expressed in vision-forming RGCs and thus it is a great tool to analyze vision and non-vision forming RGCs independently. RBPMS is expressed by all RGCs regardless of their function. Because melanopsin is a protein specifically expressed by ipRGCs, it's immunodetection is the standard protocol to identify them. However, only M1-M3 ipRGCs express melanopsin at high enough levels for immunodetection. For this reason, ipRGCs identified with α-melanopsin antibodies are called melanopsin$^+$ipRGCs (m$^+$ipRGCs).

Using automated tools, our lab first described the total number and topographical distribution of Brn3a$^+$ and m$^+$ipRGCs quantified in retinal flatmounts imaged on the GCL (Nadal-Nicolás et al., 2009; Galindo-Romero et al., 2013), an approach now used by other groups (Geeraerts et al., 2016; Miesfeld et al., 2020; Masin et al., 2021). The total number of Brn3a$^+$RGCs in albino rats (Sprague Dawley strain, SD) is 82,979 ± 1,787 and in pigmented (Pierald Viro Glaxo strain,

PVG) a little higher, 84,818 ± 4,119. The m^+RGC population is similar in both strains (2,047 ± 309 in SD and 2,098 ± 149 in PVG; Nadal-Nicolás et al., 2009; Galindo-Romero et al., 2013). Thus, m^+ipRGCs represent ∼2% of the RGCs.

Topographically both functional subtypes have a complementary distribution (**Figures 1A,B**). While the density of $Brn3a^+$RGCs is higher in the central retina above the optic nerve along the naso-temporal axis, m^+ipRGCs are more abundant in the areas of lowest $Brn3a^+$RGC density.

Because the density of RGCs differs so much from central to peripheral retina (**Figures 1A,B**) to avoid topographic bias when manually quantifying RGCs one should sample standard areas in the central, medial, and peripheral retina (Parrilla-Reverter et al., 2009; Galindo-Romero et al., 2011).

Photoreceptors

Cones and rods are the classical photoreceptors that is photoreceptors with a role in vision, while ipRGCs, which are also photoreceptors, differ from cones and rods in that they send afferents to the brain, as RGCs do, and in that their function is non-visual, as mentioned above.

Phototransduction starts in the photoreceptor outer segments where the opsins are stored. The outer segments face the retinal pigmented epithelium, and thus can be imaged in flatmounts with the vitreal side down. Opsin immunodetection is often used to visualize photoreceptors: rhodopsin (rods), S-opsin (S-cones), and L/M-opsin (L/M-cones). For cones it is possible to quantify each of the outer segments in flatmounts and assess their total numbers (**Figures 1C,D**) in health (Ortín-Martínez et al., 2010) and disease (García-Ayuso et al., 2013; Ortín-Martínez et al., 2015; Vidal-Sanz et al., 2015).

In rats, S-cones, which sense blue light, are more abundant in albino (41,028 ± 5,074; SD strain) than in pigmented animals (27,316 ± 2,235 PVG strain). However, the population of L/M cones, which perceive red-green light, is similar among them (albino: 231,736 ± 14,517; pigmented: 239,939 ± 6,494). S-cones are more abundant in the ventral retina and the extreme periphery, the retinal rims (**Figure 1C**) while the distribution of L/M cones resembles the topography of RGCs (compare panels **A** and **D** in **Figure 1**). Some cones express both opsins, the so-called dual cones. In both strains dual cones are ∼8,000 per retina, and they are mainly found in the retinal rims (Ortín-Martínez et al., 2010).

Rods are very abundant, with an estimated population of 50 million (Nadal-Nicolás et al., 2018). They appear to be homogeneously distributed in the retina, as their outer segments are very dense (García-Ayuso et al., 2013) impeding the discrimination of individual ones, and precluding their automated quantification in flatmounts. Consequently, rod degeneration and neuroprotection are assessed in retinal cross-sections by quantifying the nuclei rows in the outer nuclear layer (Di Pierdomenico et al., 2018).

Function

Since the early days of Gotch in 1903, who was the first to record the eye's response to a flash of light in the frog retina, the electroretinogram (ERG) has been used as a non-invasive technique to assess retinal functionality and to establish more solid diagnoses of retinal pathologies. Numerous studies have characterized the functional response of the rat retina with full-field ERG (Alarcón-Martínez et al., 2009; Gallego-Ortega et al., 2020, 2021).

Depending on the type and intensity of the stimulus specific waves are obtained from specific retinal populations (**Figure 1E**). Very weak light stimuli under scotopic conditions, close to the rod threshold, raises the scotopic threshold response (STR), a slow negative corneal potential. This wave is formed by a positive (pSTR) and a negative (nSTR) component. The STR originates in the innermost part of the retina, where the RGC somas are located (Sieving et al., 1986; Frishman and Steinberg, 1989a,b). Although part of this wave is generated by amacrine cells (Naarendorp and Frumkest, 1991; Saszik et al., 2002), especially the positive component, many studies use the pSTR to assess the functional status of RGCs in albino and pigmented rats (Nadal-Nicolás et al., 2018; Boia et al., 2020; Gallego-Ortega et al., 2020, 2021) and mice (Valiente-Soriano et al., 2019; Norte-Muñoz et al., 2021). In adult rats the pSTR does not exceed 50 microvolts and can be generated with approximately −4.6 to −4 log cd.s/m^2 light pulses.

In response to low-intensity full-field stimuli (intensities between −4 and −2 cd.s/m^2 before the a-wave appears) the retina produces an electrical signal known as the rod response, consisting of a positive deflection of the electrophysiological tracing of about 250 μV amplitude. This response is generated by the rod bipolar cells, because of the decrease in glutamate release by rods and its action on mGluR6 receptors.

By increasing light intensity, the mixed response the best known of all waves, is obtained. The mixed response is the major component of the ERG and is used both clinically and experimentally. It consists mainly of two components: (i) the first to appear is a negative component, the a-wave, generated by the absorption of light in the photoreceptor outer segments and the closure of cGMP-gated cationic channels (Penn and Hagins, 1969; Sillman et al., 1969). In the adult rat the a-wave reaches 200 μV; and (ii) the a-wave is followed by a positive component, called the b-wave. There has been much controversy and theories about the origin of this ERG component, such as the hypothesis that it originates from Müller cells but nowadays everything points to it being generated exclusively by the

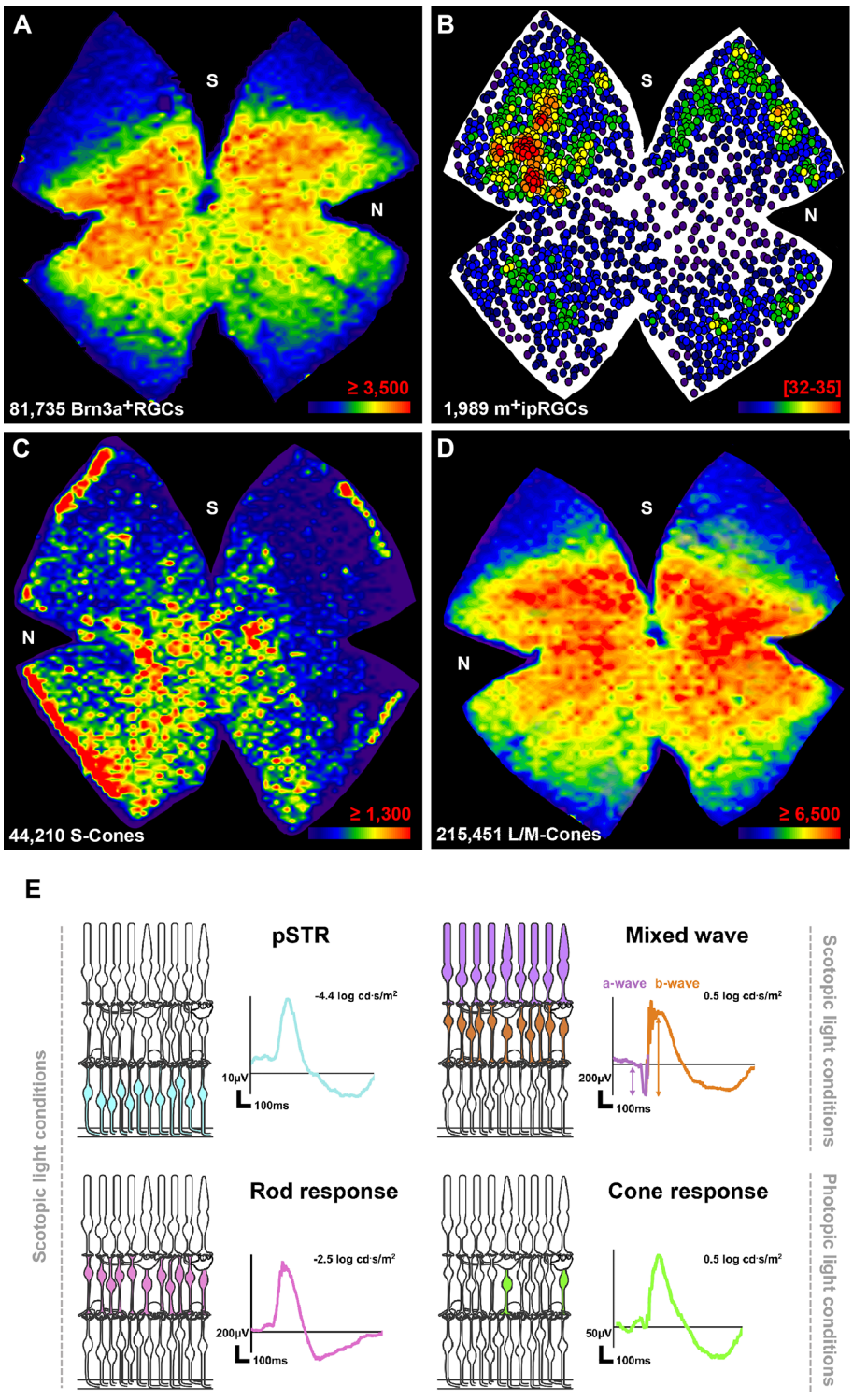

FIGURE 1
Anatomy and function of the healthy albino rat retina. **(A–D)** Distribution of RGCs and cone photoreceptors. Maps showing the topography of Brn3a$^+$RGCs **(A)**, m$^+$ipRGCs **(B)**, S-cones **(C)**, and L/M-cones **(D)** in the same retina from a 2 months old female SD albino rat. After flatmounting the retina each neuronal population was immunoidentified. Next the retina was imaged first vitreal side up (RGCs), and then flipped and imaged vitreal side down (photoreceptors). Then, each neuronal population was automatically quantified (total number shown at the bottom left of each map) and the topographical maps generated. For more details see references in text and below. **(A,C,D)** The distribution of Brn3a$^+$RGCs and cone photoreceptors is visualized with isodensity maps that represent cell density in the retina with a color scale that goes from purple
(*Continued*)

FIGURE 1 (Continued)
(0–500 cells/mm^2) to red (≥3,500 Brn3a$^+$RGCs/mm^2, ≥1,300 S-cones/mm^2, ≥6,500 L/M-cones/mm^2). **(E)** The topography of m$^+$ipRGCs is shown with a neighbor map that represents the number of neighbor cells around a given cell in a radius of 0.22 mm with a color code that goes from purple (0–2 neighbors) to red (32–35 neighbors). Thus, each dot represents one m$^+$ipRGC. Neighbor maps are better than isodensity maps for low density populations. N, nasal; S, superior. **(E)** Electroretinographic waves and their retinal origin. Under scoptopic conditions, the electroretinogram records the pSTR generated from RGCs (blue cells in the retinal drawing), the rod response, generated by rod-bipolar cells (pink cells), and the mixed wave generated by photoreceptors (purple) and ON-center bipolar cells (orange). Under higher light intensities, cone bipolar cells (green) generate the photopic b-wave. These images are original and have been created following our protocols described in: Alarcón-Martínez et al. (2009), Ortín-Martínez et al. (2010), Galindo-Romero et al. (2013), Nadal-Nicolás et al. (2018), and Gallego-Ortega et al. (2020).

ON-center bipolar cells (Masu et al., 1995; Green and Kapousta-Bruneau, 1999; Karwoski and Xu, 1999). At high light intensities (2 cd.s/m^2), the rat b-wave reaches up to 800 microvolts in amplitude.

Under photopic conditions, with a background light of approximately 30 cd/m^2 to eliminate the negative component generated by the hyperpolarization of the photoreceptors, the photopic b-wave emerges. This wave is generated exclusively by the cone pathway and is the result of the depolarization of the bipolar cone cells. In rat at intensities of 2 cd.s/m^2 the photopic b-wave reaches peaks of ∼150 microvolts.

There are other parameters that can be measured with full ERG such as the c-wave, d-wave, and oscillatory potentials, although these are seldom used.

There is some debate regarding retinal function in albino and pigmented rats. Some works describe a lower functional response in albino than pigmented rats (Nadal-Nicolás et al., 2018), while others do not observe a significant difference (Alarcón-Martínez et al., 2009).

Discussion

The rat retina is widely used as a model of central nervous degeneration as well as to study specific ophthalmological diseases. As we have summarized here, its anatomy is well known and at present there are approaches to objectively assess the topography, number, and function of RGCs and photoreceptors, the retinal neurons most sensitive to injury. These automated tools have allowed to determine the fate of RGCs and cone photoreceptors in a variety of degeneration models, as well as their response to neuroprotective therapies (Hernandez et al., 2008; García-Ayuso et al., 2013; Ortín-Martínez et al., 2015; Vidal-Sanz et al., 2015; Millán-Rivero et al., 2018; Boia et al., 2022).

We have described the retina of 2-month-old female rats. Female rats are generally preferred over males because they are smaller and easier to handle. At 2 months of age, rats are young adults and most labs use animals within 2–4 months of age. However, it is important to have in mind that as the rat grows, so does the retina and although the total number of neurons does not change their density does. Retinal size stabilizes around 4–6 months of age and only in very old rats (22 months) there is loss of rods or cones but no of RGCs. Functionally, the highest wave amplitudes are obtained from 2-month-old rats thereafter all amplitudes decrease gradually (Nadal-Nicolás et al., 2018). Therefore, within the same experiment rats should have similar ages.

We show here that is feasible to study vision-forming (Brn3a$^+$) and non-vision forming (melanopsin$^+$) RGCs, and S- and L/M- cones in the same retina. Analyzing all these populations together is a very powerful approach hardly exploited and very useful to work with models that proceed with the death of all these populations, such as ischemia/reperfusion or retinal dystrophies or to assess the different vulnerability of each population to injury. For instance, m$^+$ipRGCs are more resilient to injury or disease than Brn3a$^+$RGCs (Nadal-Nicolás et al., 2015; Valiente-Soriano et al., 2015; Vidal-Sanz et al., 2017) and likewise, the susceptibility of L/M- and S- cones to the same insult differs (Hadj-Saïd et al., 2016; García-Ayuso et al., 2018; Di Pierdomenico et al., 2020).

Brn3a$^+$RGCs and L/M-cones have their highest densities in the dorso-central retina in opposition to S-cones and m$^+$ipRGCs that are densest in the ventral and dorsal periphery, respectively. The area of higher RGC and L/M cone density forms the visual streak (Salinas-Navarro et al., 2009; Ortín-Martínez et al., 2010), the region of the retina specialized to provide the best vision at some point in the visual space located along the naso-termporal axis above the optic nerve. The main characteristic of the visual streak is that it contains a high concentration of RGCs, L-cones, and cone bipolar cells.

Rats are foraging animals as well as prey. Thus, they do not need a central area of high resolution as primates, some birds, and reptiles have, but rather a good vision in the naso-temporal axis in a position that allows the animal to search for food without tilting its head. Furthermore, the high density of blue light-detecting cones in the ventral retina may be a key feature to detect birds of prey, their natural hunters.

In conclusion, although rats are nocturnal animals and their retinas do not have all anatomical features that human retinas have, such as the fovea, they are nonetheless a very good model for preclinical research. Besides the practical advantages of housing and relatively quick and easy breeding and development, there are many established models of ophthalmic disease and neuronal injury and, more importantly, as reviewed here, we have a very precise understanding of their retinal anatomy and function.

Author contributions

CG-R and MN-M: conceptualization, bibliographic search, and graphics. AG-O, KR-R, FL-R, and MG-R: conceptualization and bibliographic search. MV-S: conception and funding. MA-B: conception, funding, writing the first draft of the manuscript. All authors: revising the article critically for important intellectual content. All authors contributed to the article and approved the submitted version.

Funding

This research was funded by the Spanish Ministry of Economy and Competitiveness (project: PID2019-106498GB-I00 (MV-S), by the Instituto de Salud Carlos III, Fondo Europeo de Desarrollo Regional "Una manera de hacer Europa" project: PI19/00071 (MA-B), the RETICS subprograms of Spanish Networks OftaRed RD16/0008/0026 and RD16/0008/0016 (MV-S).

Conflict of interest

The authors declare that the research was conducted in the absence of any commercial or financial relationships that could be construed as a potential conflict of interest.

Publisher's note

All claims expressed in this article are solely those of the authors and do not necessarily represent those of their affiliated organizations, or those of the publisher, the editors and the reviewers. Any product that may be evaluated in this article, or claim that may be made by its manufacturer, is not guaranteed or endorsed by the publisher.

References

Alarcón-Martínez, L., de La Villa, P., Avilés-Trigueros, M., Blanco, R., Villegas-Pérez, M. P., and Vidal-Sanz, M. (2009). Short and long term axotomy-induced ERG changes in albino and pigmented rats. *Mol. Vis.* 15, 2373–2383. Available online at: http://www.molvis.org/molvis/v15/a254.

Avilés-Trigueros, M., Mayor-Torroglosa, S., García-Avilés, A., Lafuente, M. P., Rodríguez, M. E., de Imperial, J. M., et al. (2003). Transient ischemia of the retina results in massive degeneration of the retinotectal projection: long-term neuroprotection with brimonidine. *Exp. Neurol.* 184, 767–777. doi: 10.1016/S0014-4886(03)00298-X

Balkema, G. W., and Drager, U. C. (1991). Impaired visual thresholds in hypopigmented animals. *Vis. Neurosci.* 6, 577–585. doi: 10.1017/s095252380000256x

Balkema, G. W., Pinto, L. H., Drager, U. C., Vanable, J. W., Rodieck, R. W., and Bunt, A. (1981). Characterization of abnormalities in the visual system of the mutant mouse pearl1. *J. Neurosci.* 1, 1320–1329. doi: 10.1523/JNEUROSCI.01-11-01320.1981

Berg, D. J., Kartheiser, K., Leyrer, M., Saali, A., and Berson, D. M. (2019). Transcriptomic signatures of postnatal and adult intrinsically photosensitive ganglion cells. *eNeuro* 6:ENEURO.0022-19.2019. doi: 10.1523/ENEURO.0022-19.2019

Boia, R., Dias, P. A. N., Galindo-Romero, C., Ferreira, H., Aires, I. D., Vidal-Sanz, M., et al. (2022). Intraocular implants loaded with A3R agonist rescue retinal ganglion cells from ischemic damage. *J. Control. Release* 343, 469–481. doi: 10.1016/j.jconrel.2022.02.001

Boia, R., Salinas-Navarro, M., Gallego-Ortega, A., Galindo-Romero, C., Aires, I. D., Agudo-Barriuso, M., et al. (2020). Activation of adenosine A3 receptor protects retinal ganglion cells from degeneration induced by ocular hypertension. *Cell Death Dis.* 11:401. doi: 10.1038/s41419-020-2593-y

Boorman, G. A. (2018). *Boorman's Pathology of the Rat: Reference and Atlas*, Second Edition, eds A. W. Suttie, J. R. Leininger and A. E. Bradley (Virginia, USA: Elsevier). doi: 10.1016/C2010-0-69040-7

Di Pierdomenico, J., Martínez-Vacas, A., Hernández-Muñoz, D., Gómez-Ramírez, A. M., Valiente-Soriano, F. J., Agudo-Barriuso, M., et al. (2020). Coordinated intervention of microglial and Müller cells in light-induced retinal degeneration. *Invest. Ophthalmol. Vis. Sci.* 61:47. doi: 10.1167/iovs.61.3.47

Di Pierdomenico, J., Scholz, R., Valiente-Soriano, F. J., Sánchez-Migallón, M. C., Vidal-Sanz, M., Langmann, T., et al. (2018). Neuroprotective effects of FGF2 and minocycline in two animal models of inherited retinal degeneration. *Invest. Ophthalmol. Vis. Sci.* 59, 4392–4403. doi: 10.1167/iovs.18-24621

Dräger, U. C., and Balkema, G. W. (1987). Does melanin do more than protect from light? *Neurosci. Res. Suppl.* 6, S75–S86. doi: 10.1016/0921-8696(87)90009-0

Ecker, J. L., Dumitrescu, O. N., Wong, K. Y., Alam, N. M., Chen, S. K., LeGates, T., et al. (2010). Melanopsin-expressing retinal ganglion-cell photoreceptors: cellular diversity and role in pattern vision. *Neuron* 67, 49–60. doi: 10.1016/j.neuron.2010.05.023

Frishman, L. J., and Steinberg, R. H. (1989a). Intraretinal analysis of the threshold dark-adapted ERG of cat retina. *J. Neurophysiol.* 61, 1221–1232. doi: 10.1152/jn.1989.61.6.1221

Frishman, L. J., and Steinberg, R. H. (1989b). Light-evoked increases in [K+]10 in proximal portion of the dark-adapted cat retina. *J. Neurophysiol.* 61, 1233–1243. doi: 10.1152/jn.1989.61.6.1233

Galindo-Romero, C., Avilés-Trigueros, M., Jiménez-López, M., Valiente-Soriano, F. J., Salinas-Navarro, M., Nadal-Nicolás, F., et al. (2011). Axotomy-induced retinal ganglion cell death in adult mice: quantitative and topographic time course analyses. *Exp. Eye Res.* 92, 377–387. doi: 10.1016/j.exer.2011.02.008

Galindo-Romero, C., Jiménez-López, M., García-Ayuso, D., Salinas-Navarro, M., Nadal-Nicolás, F. M., Agudo-Barriuso, M., et al. (2013). Number and spatial distribution of intrinsically photosensitive retinal ganglion cells in the adult albino rat. *Exp. Eye Res.* 108, 84–93. doi: 10.1016/j.exer.2012.12.010

Gallego-Ortega, A., Norte-Muñoz, M., Miralles de Imperial-Ollero, J. A., Bernal-Garro, J. M., Valiente-Soriano, F. J., de la Villa Polo, P., et al. (2020). Functional and morphological alterations in a glaucoma model of acute ocular hypertension. *Prog. Brain Res.* 256, 1–29. doi: 10.1016/bs.pbr.2020.07.003

Gallego-Ortega, A., Vidal-Villegas, B., Norte-Muñoz, M., Salinas-Navarro, M., Avilés-Trigueros, M., Villegas-Pérez, M. P., et al. (2021). 7,8-dihydroxiflavone maintains retinal functionality and protects various types of rgcs in adult rats with optic nerve transection. *Int. J. Mol. Sci.* 22:11815. doi: 10.3390/ijms222111815

García-Ayuso, D., Ortín-Martínez, A., Jiménez-López, M., Galindo-Romero, C., Cuenca, N., Pinilla, I., et al. (2013). Changes in the photoreceptor mosaic of P23H-1 rats during retinal degeneration: implications for rod-cone dependent survival. *Invest. Ophthalmol. Vis. Sci.* 54, 5888–5900. doi: 10.1167/iovs.13-12643

García-Ayuso, D., di Pierdomenico, J., Hadj-Said, W., Marie, M., Agudo-Barriuso, M., Vidal-Sanz, M., et al. (2018). Taurine depletion causes iprgc loss and increases light- induced photoreceptor degeneration. *Invest. Ophthalmol. Vis. Sci.* 59, 1396–1409. doi: 10.1167/iovs.17-23258

Geeraerts, E., Dekeyster, E., Gaublomme, D., Salinas-Navarro, M., De Groef, L., and Moons, L. (2016). A freely available semi-automated method for quantifying

retinal ganglion cells in entire retinal flatmounts. *Exp. Eye Res.* 147, 105–113. doi: 10.1016/j.exer.2016.04.010

Green, D. G., and Kapousta-Bruneau, N. V. (1999). A dissection of the electroretinogram from the isolated rat retina with microelectrodes and drugs. *Vis. Neurosci.* 16, 727–741. doi: 10.1017/s0952523899164125

Hadj-Saïd, W., Froger, N., Ivkovic, I., Jiménez-López, M., Dubus, É., Dégardin-Chicaud, J., et al. (2016). Quantitative and topographical analysis of the losses of cone photoreceptors and retinal ganglion cells under taurine depletion. *Invest. Ophthalmol. Vis. Sci.* 57, 4692–4703. doi: 10.1167/iovs.16-19535

Hattar, S., Kumar, M., Park, A., Tong, P., Tung, J., Yau, K. W., et al. (2006). Central projections of melanopsin-expressing retinal ganglion cells in the mouse. *J. Comp. Neurol.* 497, 326–349. doi: 10.1002/cne.20970

Hedrich, H. J., and Bullock, G. (2012). *The Laboratory Mouse*, 2nd Edition, eds H. J. Hedrich, G. Bullock, P. Petrusz and J. Arora (Boston: Elsevier, Academic Press). doi: 10.1016/B978-0-12-336425-8.X5051-1

Hernandez, M., Urcola, J. H., and Vecino, E. (2008). Retinal ganglion cell neuroprotection in a rat model of glaucoma following brimonidine, latanoprost or combined treatments. *Exp. Eye Res.* 86, 798–806. doi: 10.1016/j.exer.2008.02.008

Karademir, D., Todorova, V., Ebner, L. J. A., Samardzija, M., and Grimm, C. (2022). Single-cell RNA sequencing of the retina in a model of retinitis pigmentosa reveals early responses to degeneration in rods and cones. *BMC Biol.* 20:86. doi: 10.1186/s12915-022-01280-9

Karwoski, C. J., and Xu, X. (1999). Current source-density analysis of light-evoked field potentials in rabbit retina. *Vis. Neurosci.* 16, 369–377. doi: 10.1017/s0952523899162163

Kwong, J. M. K., Caprioli, J., and Piri, N. (2010). RNA binding protein with multiple splicing: a new marker for retinal ganglion cells. *Invest. Ophthalmol. Vis. Sci.* 51, 1052–1058. doi: 10.1167/iovs.09-4098

Lund, R. D. (1965). Uncrossed visual pathways of hooded and albino rats. *Science* 149, 1506–1507. doi: 10.1126/science.149.3691.1506

Lund, R. D. (1986). Neurobiology. Pigment and visual projections. *Nature* 321, 203–204. doi: 10.1038/321203a0

Marchesi, N., Fahmideh, F., Boschi, F., Pascale, A., and Barbieri, A. (2021). Ocular neurodegenerative diseases: interconnection between retina and cortical areas. *Cells* 10:2394. doi: 10.3390/cells10092394

Masin, L., Claes, M., Bergmans, S., Cools, L., Andries, L., Davis, B. M., et al. (2021). A novel retinal ganglion cell quantification tool based on deep learning. *Sci. Rep.* 11:702. doi: 10.1038/s41598-020-80308-y

Masu, M., Iwakabe, H., Tagawa, Y., Miyoshi, T., Yamashita, M., Fukuda, Y., et al. (1995). Specific deficit of the ON response in visual transmission by targeted disruption of the mGluR6 gene. *Cell* 80, 757–765. doi: 10.1016/0092-8674(95)90354-2

Miesfeld, J. B., Ghiasvand, N. M., Marsh-Armstrong, B., Marsh-Armstrong, N., Miller, E. B., Zhang, P., et al. (2020). The Atoh7 remote enhancer provides transcriptional robustness during retinal ganglion cell development. *Proc. Natl. Acad. Sci. U S A* 117, 21690–21700. doi: 10.1073/pnas.2006888117

Millán-Rivero, J. E., Nadal-Nicolás, F. M., García-Bernal, D., Sobrado-Calvo, P., Blanquer, M., Moraleda, J. M., et al. (2018). Human Wharton's jelly mesenchymal stem cells protect axotomized rat retinal ganglion cells via secretion of anti-inflammatory and neurotrophic factors. *Sci. Rep.* 8:16299. doi: 10.1038/s41598-018-34527-z

Morgan, J. E., and Tribble, J. R. (2015). Microbead models in glaucoma. *Exp. Eye Res.* 141, 9–14. doi: 10.1016/j.exer.2015.06.020

Mrejen, S., Audo, I., Bonnel, S., and Sahel, J. A. (2017). Retinitis pigmentosa and other dystrophies. *Dev. Ophthalmol.* 58, 191–201. doi: 10.1159/000455281

Naarendorp, F., and Frumkest, T. (1991). The influence of short-term adaptation of human rods and cones on cone-mediated grating visibility. *J. Physiol.* 432, 521–541. doi: 10.1113/jphysiol.1991.sp018398

Nadal-Nicolás, F. M., Jiménez-López, M., Salinas-Navarro, M., Sobrado-Calvo, P., Alburquerque-Béjar, J. J., Vidal-Sanz, M., et al. (2012). Whole number, distribution and co-expression of Brn3 transcription factors in retinal ganglion cells of adult albino and pigmented rats. *PLoS One* 7:e49830. doi: 10.1371/journal.pone.0049830

Nadal-Nicolás, F. M., Jiménez-López, M., Sobrado-Calvo, P., Nieto-López, L., Cánovas-Martinez, I., Salinas-Navarro, M., et al. (2009). Brn3a as a marker of retinal ganglion cells: qualitative and quantitative time course studies in naïve and optic nerve-injured retinas. *Invest. Ophthalmol. Vis. Sci.* 50, 3860–3868. doi: 10.1167/iovs.08-3267

Nadal-Nicolás, F. M., Salinas-Navarro, M., Jiménez-López, M., Sobrado-Calvo, P., Villegas-Pérez, M. P., Vidal-Sanz, M., et al. (2014). Displaced retinal ganglion cells in albino and pigmented rats. *Front. Neuroanat.* 8:99. doi: 10.3389/fnana.2014.00099

Nadal-Nicolás, F. M., Sobrado-Calvo, P., Jiménez-López, M., Vidal-Sanz, M., and Agudo-Barriuso, M. (2015). Long-term effect of optic nerve axotomy on the retinal ganglion cell layer. *Invest. Ophthalmol. Vis. Sci.* 56, 6095–6112. doi: 10.1167/iovs.15-17195

Nadal-Nicolás, F. M., Vidal-Sanz, M., and Agudo-Barriuso, M. (2018). The aging rat retina: from function to anatomy. *Neurobiol. Aging* 61, 146–168. doi: 10.1016/j.neurobiolaging.2017.09.021

Norte-Muñoz, M., Lucas-Ruiz, F., Gallego-Ortega, A., García-Bernal, D., Valiente-Soriano, F. J., de la Villa, P., et al. (2021). Neuroprotection and axonal regeneration induced by bone marrow mesenchymal stromal cells depend on the type of transplant. *Front. Cell Dev. Biol.* 9:772223. doi: 10.3389/fcell.2021.772223

Ortín-Martínez, A., Jimenez-Lopez, M., Nadal-Nicolás, F. M., Salinas-Navarro, M., Alarcon-Martínez, L., Sauve, Y., et al. (2010). Automated quantification and topographical distribution of the whole population of S- and L-cones in adult albino and pigmented rats. *Invest. Ophthalmol. Vis. Sci.* 51, 3171–3183. doi: 10.1167/iovs.09-4861

Ortín-Martínez, A., Salinas-Navarro, M., Nadal-Nicolás, F. M., Jiménez-López, M., Valiente-Soriano, F. J., García-Ayuso, D., et al. (2015). Laser-induced ocular hypertension in adult rats does not affect non-RGC neurons in the ganglion cell layer but results in protracted severe loss of cone-photoreceptors. *Exp. Eye Res.* 132, 17–33. doi: 10.1016/j.exer.2015.01.006

Parrilla-Reverter, G., Agudo, M., Sobrado-Calvo, P., Salinas-Navarro, M., Villegas-Pérez, M. P., and Vidal-Sanz, M. (2009). Effects of different neurotrophic factors on the survival of retinal ganglion cells after a complete intraorbital nerve crush injury: a quantitative *in vivo* study. *Exp. Eye Res.* 89, 32–41. doi: 10.1016/j.exer.2009.02.015

Penn, R. D., and Hagins, W. A. (1969). Signal transmission along retinal rods and the origin of the electroretinographic a-wave. *Nature* 223, 201–205. doi: 10.1038/223201a0

Pérez de Lara, M. J., Santano, C., Guzmán-Aránguez, A., Valiente-Soriano, F. J., Avilés-Trigueros, M., Vidal-Sanz, M., et al. (2014). Assessment of inner retina dysfunction and progressive ganglion cell loss in a mouse model of glaucoma. *Exp. Eye Res.* 122, 40–49. doi: 10.1016/j.exer.2014.02.022

Provencio, I., Rodriguez, I. R., Jiang, G., Pä Hayes, W., Moreira, E. F., and Rollag, M. D. (2000). A novel human opsin in the inner retina. *J. Neurosci.* 20, 600–605. doi: 10.1523/JNEUROSCI.20-02-00600.2000

Prusky, G. T., Harker, K. T., Douglas, R. M., and Whishaw, I. Q. (2002). Variation in visual acuity within pigmented and between pigmented and albino rat strains. *Behav. Brain Res.* 136, 339–348. doi: 10.1016/s0166-4328(02)00126-2

Ramón y Cajal, S. (2021). *La Retina de los Vertebrados*. 1st ed. eds N. Cuenca and P. de la (Villa Madrid: Consejo Superior de Investigaciones Científicas).

Rheaume, B. A., Jereen, A., Bolisetty, M., Sajid, M. S., Yang, Y., Renna, K., et al. (2018). Single cell transcriptome profiling of retinal ganglion cells identifies cellular subtypes. *Nat. Commun.* 9:2759. doi: 10.1038/s41467-018-05134-3

Rodriguez, A. R., de Sevilla Müller, L. P., and Brecha, N. C. (2014). The RNA binding protein RBPMS is a selective marker of ganglion cells in the mammalian retina. *J. Comp. Neurol.* 522, 1411–1443. doi: 10.1002/cne.23521

Salinas-Navarro, M., Mayor-Torroglosa, S., Jiménez-López, M., Avilés-Trigueros, M., Holmes, T. M., Lund, R. D., et al. (2009). A computerized analysis of the entire retinal ganglion cell population and its spatial distribution in adult rats. *Vis. Res.* 49, 115–126. doi: 10.1016/j.visres.2008.09.029

Sánchez-Migallón, M. C., Valiente-Soriano, F. J., Salinas-Navarro, M., Nadal-Nicolás, F. M., Jiménez-López, M., Vidal-Sanz, M., et al. (2018). Nerve fibre layer degeneration and retinal ganglion cell loss long term after optic nerve crush or transection in adult mice. *Exp. Eye Res.* 170, 40–50. doi: 10.1016/j.exer.2018.02.010

Saszik, S. M., Robson, J. G., and Frishman, L. J. (2002). The scotopic threshold response of the dark-adapted electroretinogram of the mouse. *J. Physiol.* 543, 899–916. doi: 10.1113/jphysiol.2002.019703

Schmidt, T. M., Chen, S. K., and Hattar, S. (2011). Intrinsically photosensitive retinal ganglion cells: many subtypes, diverse functions. *Trends Neurosci.* 34, 572–580. doi: 10.1016/j.tins.2011.07.001

Shareef, S. R., Garcia-Valenzuela, E., Salierno, A., Walsh, J., and Sharma, S. C. (1995). Chronic ocular hypertension following episcleral venous occlusion in rats. *Exp. Eye Res.* 61, 379–382. doi: 10.1016/s0014-4835(05)80131-9

Sieving, P. A., Frishman, L. J., and Steinberg, R. H. (1986). Scotopic threshold response of proximal retina in cat. *J. Neurophysiol.* 56, 1049–1061. doi: 10.1152/jn.1986.56.4.1049

Sillman, A. J., Ito, H., and Tomita, T. (1969). Studies on the mass receptor potential of the isolated frog retina1 ii. On the basis of the ionic mechanism. *Vis. Res.* 9, 1443–1451. doi: 10.1016/0042-6989(69)90060-1

Subramaniam, M. D., Chirayath, R. B., Iyer, M., Nair, A. P., and Vellingiri, B. (2022). Mesenchymal stem cells (MSCs) in Leber's hereditary optic neuropathy (LHON): a potential therapeutic approach for future. *Int. Ophthalmol.* 42, 2949–2964. doi: 10.1007/s10792-022-02267-9

Tran, N. M., Shekhar, K., Whitney, I. E., Jacobi, A., Benhar, I., Hong, G., et al. (2019). Single-cell profiles of retinal ganglion cells differing in resilience to injury reveal neuroprotective genes. *Neuron* 104, 1039–1055.e12. doi: 10.1016/j.neuron.2019.11.006

Urcola, J. H., Hernandez, M., and Vecino, E. (2016). Three experimental glaucoma models in rats: comparison of the effects of intraocular pressure elevation on retinal ganglion cell size and death. *Exp. Eye Res.* 83, 429–437. doi: 10.1016/j.exer.2006.01.025

Valiente-Soriano, F. J., Nadal-Nicolás, F. M., Salinas-Navarro, M., Jiménez-López, M., Bernal-Garro, J. M., Villegas-Pérez, M. P., et al. (2015). BDNF rescues RGCs but not intrinsically photosensitive rgcs in ocular hypertensive albino rat retinas. *Invest. Ophthalmol. Vis. Sci.* 56, 1924–1936. doi: 10.1167/iovs.15-16454

Valiente-Soriano, F. J., Ortín-Martínez, A., di Pierdomenico, J., García-Ayuso, D., Gallego-Ortega, A., Miralles de Imperial-Ollero, J. A., et al. (2019). Topical brimonidine or intravitreal bdnf, cntf, or bfgf protect cones against phototoxicity. *Transl. Vis. Sci. Technol.* 8:36. doi: 10.1167/tvst.8.6.36

Vidal-Sanz, M., Galindo-Romero, C., Valiente-Soriano, F. J., Nadal-Nicolás, F. M., Ortin-Martinez, A., Rovere, G., et al. (2017). Shared and differential retinal responses against optic nerve injury and ocular hypertension. *Front. Neurosci.* 11:235. doi: 10.3389/fnins.2017.00235

Vidal-Sanz, M., Valiente-Soriano, F. J., Ortín-Martínez, A., Nadal-Nicolás, F. M., Jiménez-López, M., Salinas-Navarro, M., et al. (2015). Retinal neurodegeneration in experimental glaucoma. *Prog. Brain Res.* 220, 1–35. doi: 10.1016/bs.pbr.2015.04.008

frontiers | Frontiers in Neuroanatomy

TYPE Original Research
PUBLISHED 23 September 2022
DOI 10.3389/fnana.2022.983151

OPEN ACCESS

EDITED BY
Isabel Pinilla,
Hospital Clinico Universitario, Spain

REVIEWED BY
Divya Ail,
Institut de la Vision, France
Patrick W. Keeley,
University of California, Santa Barbara, United States

*CORRESPONDENCE
Concepción Lillo
conlillo@usal.es

RECEIVED 30 June 2022
ACCEPTED 25 August 2022
PUBLISHED 23 September 2022

CITATION
Segurado A, Rodríguez-Carrillo A, Castellanos B, Hernández-Galilea E, Velasco A and Lillo C (2022) Scribble basal polarity acquisition in RPE cells and its mislocalization in a pathological AMD-like model. *Front. Neuroanat.* 16:983151. doi: 10.3389/fnana.2022.983151

Scribble basal polarity acquisition in RPE cells and its mislocalization in a pathological AMD-like model

Alicia Segurado[1,2,3], Alba Rodríguez-Carrillo[2], Bárbara Castellanos[2], Emiliano Hernández-Galilea[3,4], Almudena Velasco[1,2,3] and Concepción Lillo[1,2,3]*

[1]Department of Cell Biology and Pathology, University of Salamanca, Salamanca, Spain, [2]Institute of Neurosciences of Castilla y León (INCyL), University of Salamanca, Salamanca, Spain, [3]Plasticity, Degeneration, and Regeneration of the Visual System Group, Institute for Biomedical Research of Salamanca (IBSAL), Salamanca, Spain, [4]Department of Surgery, Ophthalmology Service, University Hospital of Salamanca, University of Salamanca, Salamanca, Spain

Apicobasal polarity is a hallmark of retinal pigment epithelium cells and is required to perform their functions; however, the precise roles of the different proteins that execute polarity are still poorly understood. Here, we have studied the expression and location of Scribble, the core member of the polarity basal protein complex in epithelial-derived cells, in human and mouse RPE cells in both control and pathological conditions. We found that Scribble specifically localizes at the basolateral membrane of mouse and human RPE cells. In addition, we observed an increase in the expression of Scribble during human RPE development in culture, while it acquires a well-defined basolateral pattern as this process is completed. Finally, the expression and location of Scribble were analyzed in human RPE cells in experimental conditions that mimic the toxic environment suffered by these cells during AMD development and found an increase in Scribble expression in cells that develop a pathological phenotype, suggesting that the protein could be altered in cells under stress conditions, as occurs in AMD. Together, our results demonstrate, for the first time, that Scribble is expressed in both human and mouse RPE and is localized at the basolateral membrane in mature cells. Furthermore, Scribble shows impaired expression and location in RPE cells in pathological conditions, suggesting a possible role for this protein in the development of pathologies, such as AMD.

KEYWORDS

Scribble, cell polarity, epithelium, differentiation, retina, retinal pigment epithelium (RPE), Scribble complex, age-related macular degeneration (AMD)

Introduction

Cell polarity is achieved thanks to the coordinated functions of three protein complexes that are highly conserved in evolution: the Crb and Par complexes (in the apical domain of cells) and the Scribble complex (in the basal domain) (Assémat et al., 2008; Rodriguez-Boulan and Macara, 2014). The correct acquisition of cell polarity is

essential for specific cell and tissue functions (Assémat et al., 2008; Kaplan et al., 2009). The Scribble gene (and the protein) was first identified in *D. melanogaster*, where it was described as a crucial regulator of morphogenesis. It was also identified that mutations in Scribble cause drastic defects in the epithelial organization, resulting in rounded, irregularly shaped cells. In these models, it was also described that Scribble exerted its function by confining the localization of the Crb complex to the apical zone of the cell, excluding it from the basolateral domain and assisting in the correct establishment of the cell-cell adherens junctions (Bilder and Perrimon, 2000; Bilder et al., 2000; Assémat et al., 2008). The mammalian Scribble complex is composed of three proteins, Scribble *(Scribble planar cell polarity protein)*, DLG *(Discs large MAGUK scaffold protein),* and LLGL *(LLGL scribble cell polarity complex component),* and it is associated with the basolateral domain of the epithelial cell membrane, overlapping adherens junctions (Navarro et al., 2005; Qin et al., 2005; Kallay et al., 2006; Humbert et al., 2008). Scribble complex is expressed in numerous mammalian tissues and cell types, although the highest expression levels have been found in epithelial cells (Navarro et al., 2005). Low levels of these proteins have been described in the kidney, skeletal muscle, liver, and lung, while the highest levels are in the intestine, breast, placenta, and skin (Navarro et al., 2005; Assémat et al., 2008; Su et al., 2013). This protein complex has also been localized in the developing mouse retina (Nguyen et al., 2005), the epithelium of the human colon (Gardiol et al., 2006), and it even participates in fundamental processes of the immune response (Barreda et al., 2020). These proteins function cooperatively to establish and regulate cell polarity, junction formation, cell growth, and migration in most epithelial cells (Kallay et al., 2006; Yamanaka and Ohno, 2008; Su et al., 2012).

Malfunctions in the Scribble complex are associated with severe alterations in cell polarity. For example, during development in mammals, point mutations cause the mislocalization of the protein, resulting in perinatal death due to defects in neural tube closure (Robinson et al., 2012; Lei et al., 2013). Mislocalization or loss of Scribble disrupts polarity in human epithelial cells, leading to dysregulation in their function and contributing to tumor development; although they play a role as tumor suppressors in certain epithelial cancers, how Scribble contributes to this anomaly is not yet well-understood (Zhan et al., 2008; Pearson et al., 2011; Feigin et al., 2014; Liu et al., 2017). Furthermore, it causes a delay in tight junction formation and impaired E- cadherin recruitment to the membrane and, as a result, cells undergo an epithelial-mesenchymal transition process (Qin et al., 2005; Yamanaka and Ohno, 2008; Ivanov et al., 2010).

The retinal pigment epithelium (RPE) is a monolayer of epithelial cells that exhibits a marked apicobasal polarity (Bok, 1993; Rizzolo, 1997; Strauss, 2005; Lehmann et al., 2014). The integrity and maintenance of its functions depend on the establishment of this polarity and cell-cell junctions (Rahner et al., 2004; Rizzolo, 2007). As in other epithelial cells, these processes are functionally coupled due to the presence and correct functioning of the polarity complexes. Apical complexes, Par and Crb, have been described in the retina and in the RPE cells (van de Pavert et al., 2004; Luo et al., 2006; Park et al., 2011; Paniagua et al., 2015, 2021), but the expression and localization of the Scribble complex remain largely unexplored. Very few works have dealt with the localization and functions of this complex in the RPE cells. One of them has focused on the expression of the proteins Scribble, DLG, and some adhesion proteins in ocular tissues during the development of the mouse eyecup, particularly on the iris and the cornea (Nguyen et al., 2005). Another one has analyzed the alterations in the localization and functions of some members of the Scribble complex in a model of ocular adenocarcinoma. Both the mislocalization and downregulation of DLG, Scribble, and LLGL proteins seem to be correlated to tumor progression in this mouse model of adenocarcinoma (Vieira et al., 2008).

Then, all these previous works in different epithelial-derived tissues, including the retina, have suggested that the Scribble complex is not only involved in the establishment of the basal domain during development and mature conditions, but its alterations in pathological conditions could also be closely related to a starting point in the progression of diseases depending on the maintenance of apicobasal polarity. Nevertheless, this hypothesis still needs to be deeply explored. In addition, the involvement of the polarity proteins, especially those of the Scribble complex, in aging processes, such as Age-Related Macular Degeneration (AMD), where RPE cell barrier maintenance is compromised, is still largely unknown. Due to the critical nature of polarized pathways in RPE functionality, any anomalies in the organization and/or maintenance of the cell-cell junctions will have a major impact on the capability of the RPE to maintain choriocapillaris and photoreceptors. Moreover, in aging and AMD, these capabilities are compromised.

To better understand these processes, in the present work, we have first analyzed the time-course expression of Scribble in human RPE cells in culture, focusing on the expression and localization of this protein and others related to the polarization of these cells in the different apicobasal compartments over time. We observed not only an increase in the amount of Scribble during RPE development but also the fact that Scribble localizes early at the basal domain during RPE development and gradually acquires a well-defined basolateral pattern as the tissue reaches a fully mature phenotype. Furthermore, the expression of Scribble was compared with that of other elements involved in RPE cell polarity establishment and cell junctions, both in human RPE cells in culture and in tissue-fixed mouse RPE cells, allowing us to establish its precise location in the basolateral membrane of the cells, along with the proteins that define RPE differentiation. Finally, to better understand the potential implications and modifications of

Scribble in pathological conditions of RPE cells, we have analyzed the role of this protein in human RPE cells subjected to experimental conditions that mimic the toxic environment that these cells undergo during the development of AMD. We observed an increase in Scribble expression in those cells, which develop a pathological phenotype, suggesting that this protein could be altered in situations of cellular stress, as occurs in AMD. This experimental model was established by exposing fully differentiated human RPE cells in culture to different concentrations of blood serum obtained from patients with atrophic AMD, exudative AMD, or control in a different timely manner. The results show that in these pathological conditions, both the expression and localization of Scribble get altered from the very beginning of the process, suggesting, as it has been shown in other epithelial tissues anomalies, a possible role in the onset and progress of aging pathologies, such as AMD.

Materials and methods

Animals

All procedures used in this work were in accordance with the guidelines of the European Directive 2010/63/UE and the RD 53/2013 Spanish legislation for the use and care of animals. All details of the study were approved by the Bioethics Committee of the University of Salamanca. For this study, seven 90-day-old adult wild-type C57BL/6J mice were used for *in vivo* immunofluorescence analysis. Animals were euthanized with carbon dioxide before tissue extraction.

Human retinal pigment epithelium cell cultures (hRPE)

For *in vitro* studies, human RPE cells (LONZA) were used in the fourth passage, seeded at a density of 50000 cells/cm^2 on Transwell® polyester membrane inserts with 6.5 mm diameter and 0.4 μm pore size (Corning®) and maintained in RtEBM® Basal Medium (LONZA), supplemented with L-Glutamine, FGF-B, and Gentamicin and Amphotericin-B. During the first 3 days, 2.5% fetal bovine serum (FBS) was also included. The medium was replaced every 3–4 days. To study the Scribble protein expression during RPE cell development and maturation, samples at three different time points of culture were collected: 7, 14, and 21 days in culture (DIC). Subsequently, to study the expression of this protein in pathological conditions, once cells reached 21 DIC, they were incubated with the different types of blood serum obtained from patients with ophthalmological problems.

Human serum samples

All studies have been done in accordance with the Code of Ethics of the World Medical Association (Declaration of Helsinki) for experiments involving humans. Blood serum samples from voluntary patients with atrophic or exudative AMD and control, obtained from the Ophthalmology Service of the University Hospital of Salamanca, were used in this study. The use of human samples was approved by the Clinical Research Ethics Committee of the Institute for Biomedical Research of Salamanca (IBSAL) (PI15/01240; PI18/01536), the Drug Research Ethics Committee of the Regional Ministry of Health of the Junta de Castilla y León, and all the participants signed written informed consent. Clinical evaluation, diagnosis, and the subsequent recruitment of patients were carried out by ophthalmologists from the same hospital service. To be included in the study, patients had to meet the following criteria: (i) age >50 years; (ii) newly diagnosed with AMD; (iii) no previous treatment for AMD; (iv) no abnormalities that could interfere with the study and/or other degenerative diseases. Control sera were obtained from healthy volunteers, based on the same inclusion criteria. Therefore, patients were classified into three groups: (1) *Atrophic or dry AMD*: patients with intermediate, extensive, or large macular drusen (≥125 μm diameter); (2) *Exudative or wet AMD*: patients with choroidal neovascularization and/or its clinical manifestations (e.g., subretinal hemorrhages, retinal pigment epithelium detachments due to subretinal fluid accumulation); (3) *Control*: patients without AMD or any other macular disorder that could confuse the diagnosis. Blood samples were collected from patients at the time of diagnosis, before any treatment. After coagulation, serum was recovered by centrifugation, aliquoted in cryovials, and stored at −80°C until required.

Exposure to human sera

Five serum samples from each group (5 atrophic or dry AMD, 5 exudative or wet AMD, and 5 controls) were used for this study. Briefly, mature confluent hRPE cells cultured in 24-well plates were exposed to different concentrations of the three types of blood serum and in a different timely manner. Separate plates were used for each type of serum, i.e., 5 24-well plates for serum from control patients, 5 for dry AMD serum, and 5 for wet AMD serum. Different concentrations of serum (5 and 10%) were diluted in the usual culture medium. This serum-medium mixture was added to the lower chamber of the Transwell®. 21 DIC cells were culture in this mixture for 3 and 7 days (DWS, *Days with serum*). Cells at the same stage of development, 24 and 28 DIC, respectively, with no serum added were used as a control for each period analyzed (non-serum group in results). Half of each plate (12 wells) was used for immunofluorescence experiments and the other half for western blot analysis. From

this, half of the wells were analyzed at 3 days (DWS) and the other half at 7 days (DWS).

Immunofluorescence labeling

The hRPE cells were fixed with 4% paraformaldehyde (PFA) for 10 min at 4°C. Then, were rinsed in PBS and stored at 4°C until use. For retinal cryosections, eyes were dissected and fixed by immersion for 30 min at 4°C in a solution containing 4% PFA in 0.1 M phosphate buffer at pH 7.4 (PB). The cornea and lens were then removed; retina, RPE, and choroid were further fixed by immersion for two additional hours at 4°C in the same fixative solution and washed in PB. Eyeballs were then cryoprotected in a graded sucrose series, embedded in Tissue-Tek O.C.T (Sakura), and stored at −20°C until sectioning. 14-μm tissue sections were obtained with a cryostat (Microm HM560, Thermo Fisher Scientific) and placed onto Superfrost Ultra Plus® (ThermoFisher Scientific) slides and stored at −20°C until their use. Tissue autofluorescence was quenched with 0.25% sodium borohydride in 0.1 M phosphate-buffered saline, pH 7.4 (PBS) for 10 min at room temperature (RT). Both cells and tissues were then permeabilized in PBS with 0.02% or 0.1% Triton X-100 (PBS-Tx), respectively, and blocked for 1 h in 1% bovine serum albumin (BSA) and 5 % normal serum in PBS-Tx. Next, they were incubated overnight at 4°C with 1% BSA, 2% normal serum in PBS-Tx, and the primary antibodies for Scribble (Santa Cruz Biotechnology, 1:200), CRB2 [custom-made (Paniagua et al., 2015), 2.25 μg/ml], PAR3 (Millipore, 1:250), E-cadherin (Santa Cruz Biotechnology, 1:100), Occludin (Invitrogen, 1:200), and Apo-E (Millipore, 1:200). Subsequently, samples were washed with PBS-Tx and incubated for 1 h at room temperature with 1:750 Alexa fluor-488 and/or Alexa fluor-555 fluorescent secondary antibodies (Life Technologies), and/or Faloidin-FITC (Sigma, 1:500), and the nuclear marker DAPI (Sigma-Aldrich, 1:10,000) in 1% BSA and 2% normal serum in PBS-Tx. Finally, they were washed with PBS-Tx and PBS. Both cells and tissues were cover-mounted using Prolong Gold antifading reagent (Life Technologies) for subsequent microscopic analysis. Negative controls were also performed excluding primary and/or secondary antibodies in the incubation steps.

Image acquisition and analysis

Images were obtained using an inverted Zeiss Axio Observer Z1 microscope (Carl Zeiss Microscopy, UC, USA) with a Zeiss Plan-Apochromat 40x NA 1.3 oil objective and processed with ZEN imagen software (Carl Zeiss Microscopy). To visualize the spatial arrangement of target proteins in cells, a z-stack of 20 images was taken for each field of view. Each set of images taken along the z-axis was transformed using a maximum sum algorithm into a single two-dimensional image called the maximum intensity orthogonal projection using Zen software. Images and projections optimized using Adobe Photoshop CS6 software and pseudo-colored for better comprehension with ImageJ software.

Protein extraction and western blotting

Normal and serum-exposed hRPE cells were lysed in RIPA buffer (Bioscience) with a protease inhibitor cocktail (Sigma-Aldrich). Proteins were dissolved in Laemmli loading buffer and loaded onto an SDS-polyacrylamide gel under reducing conditions. After electrophoresis, proteins were transferred to PVDF membranes, blocked for 1 h at room temperature in Tris-buffered saline-Tween (0.1%) (TBST) with 2% BSA, and immunolabeled overnight at 4°C with primary antibodies for Scribble (Santa Cruz Biotechnology) and β-actin (Sigma-Aldrich) diluted in TBST solution with 2% BSA. After several washes in TBST, membranes were incubated with appropriate secondary antibodies in 5% non-fat dry milk in TBST for 1 h at RT. Membranes were then washed in TBST and developed with Clarity Western ECL Substrate (Bio-Rad) using a chemiluminescent imaging system (MicroChemi 4.2, Berthold Technologies). As negative controls, the PVDF membrane was incubated without the primary or secondary antibodies and both. Protein levels were measured by densitometric analysis using ImageJ software. The optical density obtained from each band was normalized against the corresponding β-actin and relativized vs. the negative control in all groups. Minor brightness adjustments were performed with Adobe Photoshop CS6.

Statistical analysis

For each experiment, samples were obtained from individual wells, so for statistical purposes, each one is considered an independent sample. Half of each plate (12 wells) was used for IF experiments and the other half for WB analysis. From this, half of the wells were analyzed at 3 days (DWS) and the other half at 7 days (DWS). Statistical analyses were performed using Microsoft Excel (2016) (Microsoft Corporation), IBM SPSS Statistics software (version 20.0) (IBM Corp.; Armonk, NY, USA), and GraphPad Prism (version 8) (GraphPad Software, San Diego, California, USA). Samples were initially analyzed using the Kolmogorov-Smirnov test and Levene's test to check for normality of data distribution and homogeneity of variances, respectively. Statistically significant differences were analyzed by one-way ANOVA test followed by Bonferroni's *post-hoc* test in parametric data distribution, as well as the Kruskal–Wallis test, followed by Dunn-Bonferroni's *post-hoc* test was conducted for non-parametric data. A *p-value* of <0.05 (*)

was considered statistically significant and <0.01 (**) highly significant. Data are given as mean ± standard deviation (SD). All experiments were performed independently and at least three times. The complete statistical analysis and data are included in Supplementary material.

Results

Scribble localizes at the basolateral membrane of human retinal pigment epithelium during development

Well-defined circumferential actin belt formation is a determinant process in RPE cells for the acquisition of cell polarity (Miyoshi and Takai, 2008; Pfeffer and Philp, 2014). In these experiments, circumferential actin belt formation has been used then as a reliable indicator of the polarization rate of hRPE cells in culture. In this model, at 7 DIC, most actin filaments appeared as stress fibers. At 14 and especially at 21 DIC, a rearrangement of actin from stress fibers occurred, eventually resulting in a well-defined actin belt that precisely demarcates the cell periphery (Figure 1A). The three time points, 7, 14, and 21 DIC, were then established as checkpoints to define the developmental process of hRPE cells.

To elucidate the precise location of Scribble during the polarization and differentiation of human RPE cells, immunolabeling of hRPE cells during development in culture was performed. Axial and Z-stack images acquired along the Z-axis of immunolabeled hRPE cells in culture allowed us to precisely identify apical and basolateral areas of the cells (Figure 1A). Scribble expressed from day 7 in culture, when it displayed a punctuated pattern, was situated predominantly at the basal area, clearly outlining the irregularly shaped plasma membrane of some cells, which is a typical feature of early developmental stages. Scribble reorganized from the basal to the basolateral zone at 14 DIC. By this time point, there was a higher and more site-specific expression at the plasma membrane, although some cytoplasmic expression patches remained. At 21 DIC, Scribble showed a precisely defined localization in the basolateral domain of the plasma membrane, delineating all the neighboring cells. All hRPE cells at this time point exhibited a regular hexagonal shape, giving rise to the typical cobblestone pattern of a fully developed RPE monolayer. The expression of Scribble during maturation of hRPE cells in culture was also analyzed by western blot (Figure 1B). Scribble was detected at 210 and 175 kDa, two high-molecular weight bands that correspond to the two major isoforms of the Scribble protein produced by alternative splicing. The 175 kDa isoform is considered the canonical sequence. Analyzing this expression, both independently and altogether, Scribble appears from 7 DIC in hRPE cells, increasing from 7 to 21 DIC. The altogether expression of Scribble isoforms did not show statistically significant differences among 7, 14, and 21 DIC ($p = 0.828$; $n = 27$). However, when analyzing the two Scribble isoforms independently, although the 210 kDa isoform showed no significant differences among 7, 14, and 21 DIC ($p = 0.112$; $n = 27$), the 175 kDa isoform exhibited significant differences between 7 and 21 DIC ($p = 0.016$; $n = 27$) (Figure 1C). While the Scribble 210 kDa isoform remains constant throughout the developmental period, the Scribble 175 kDa isoform increases its expression during the maturation of the epithelial monolayer. Together, these data support the findings of the immunofluorescence analyses. Then, Scribble expression in hRPE cell culture increased during development up to 21 DIC and during this same period defined its basolateral localization.

Scribble is located in the basolateral domain of the retinal pigment epithelium of the adult mouse

Expression and localization of Scribble in tissue-fixed RPE of the adult wild-type mouse were determined by immunofluorescence. To define the precise subcellular localization of Scribble in this tissue, double immunofluorescence labeling was performed for Scribble and certain well-known proteins that perform specific functions in this cell type. To identify the basolateral domain of the RPE, the localization of Apolipoprotein E (ApoE), a carrier protein for lipids found in Bruch's membrane, was used as a marker. Double immunofluorescence for Scribble-ApoE showed that these two proteins are co-expressed in the same location, the basolateral domain of the RPE (Figure 2A). Similarly, apical domain-defining proteins that predominantly localize in this area were identified. CRB2 and PAR3 are both core components of the Crb and Par apical polarity complexes, respectively. Double immunofluorescence for Scribble-CRB2 (Figure 2B) and Scribble-PAR3 (Figure 2C) resulted in an opposed localization. Both CRB2 and PAR3 localized in the apical zone of the RPE cells, whereas Scribble defined their basolateral region (Figures 2B,C). In mature RPE cells, phalloidin stains the actin microfilaments that constitute the actin belt organized around the cell-cell adherens junctions. Scribble-Phalloidin double immunolabeling showed actin in an apical arrangement, whereas Scribble exhibited a basolateral localization (Figure 2D). Furthermore, the expression of E-cadherin (Figure 2E) and occludin (Figure 2F), two of the proteins involved in the establishment of adherens and tight junctions in the RPE cells, respectively, was also analyzed. As expected, since these proteins take part in the apical cell-cell junctions of the RPE cells, both were typically located in the apical domain in mature RPE cells, so the double labeling for Scribble and these two proteins highlighted the basolateral

10.3389/fnana.2022.983151

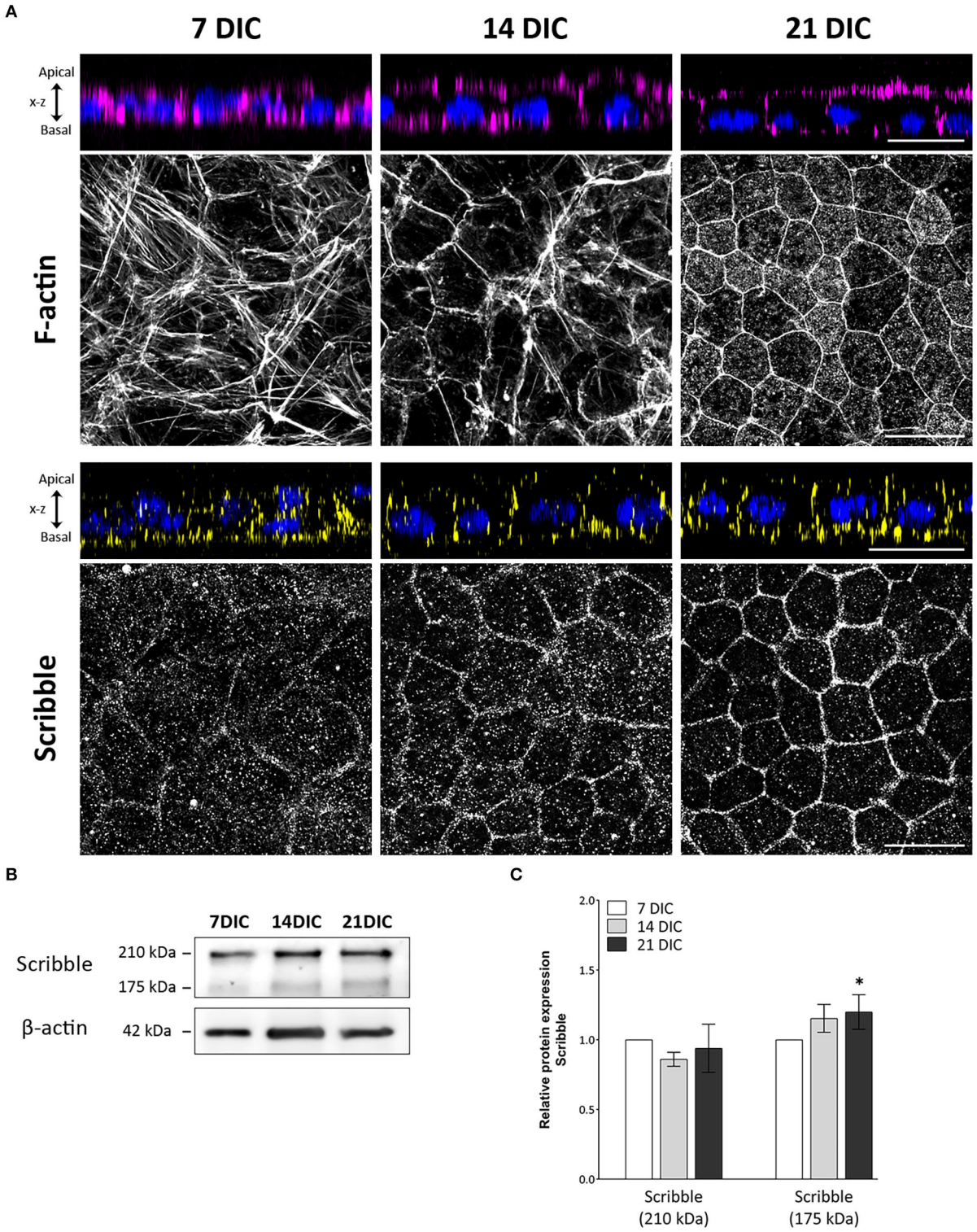

FIGURE 1
Time-course expression pattern of actin and Scribble protein during hRPE cell development in culture. **(A)** Orthogonal views and corresponding z-stack maximum projections showing actin (magenta) and Scribble protein (yellow) localization as hRPE cells gradually form the mature epithelial tissue. DAPI (blue): nuclear labeling. Scale bars: 20 μm. **(B)** Western blot analyses showing expression of Scribble (210 kDa) and Scribble (175 kDa) from 7 to 21 DIC. β-actin was used as loading control. **(C)** Graphical representation of the relative expression of Scribble (210 kDa) and Scribble (175 kDa) during the development of hRPE cells in culture. In both cases, 7 DIC ($n = 9$), 14 DIC ($n = 9$), and 21 DIC ($n = 9$). DIC in **(A–C)**:
(Continued)

FIGURE 1 (Continued)
Days in culture. Data are presented as mean ± sd. *Statistical information*: The Kolmogorov-Smirnov and Levene tests were used to evaluate the normality and homoscedasticity of the sample distribution, respectively. Data were determined to be non-parametrically distributed. The potential significant statistical differences were analyzed by the Kruskal-Wallis test, followed by Dunn–Bonferroni's *post-hoc* test. Asterisks indicate statistical differences. *p-value < 0.05 *vs.* 7 DIC.

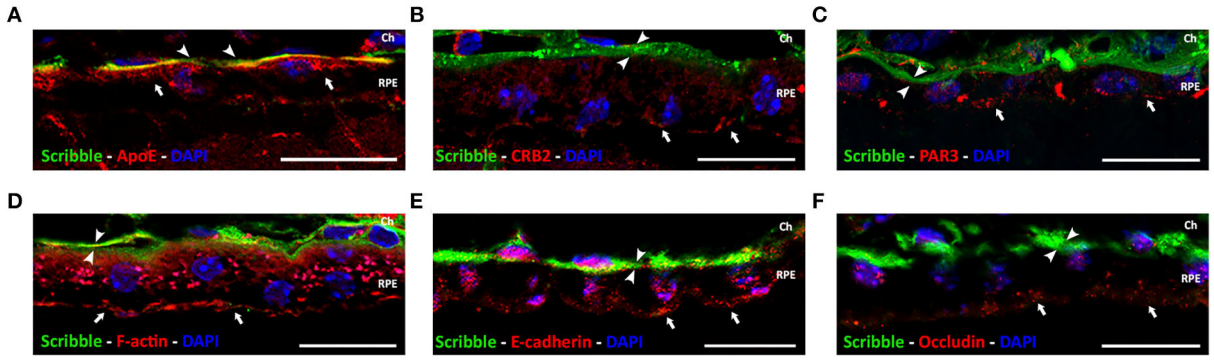

FIGURE 2
Localization of Scribble protein in wild-type adult mouse RPE. Double immunolabeling for Scribble (green, arrowheads) and other proteins (red, arrows): carrier protein for lipids, ApoE **(A)**; apical polarity proteins CRB2 **(B)** and PAR3 **(C)**; F-actin **(D)**; and adherens and tight junctional protein E-cadherin **(E)** and occludin **(F)**, respectively. DAPI (in blue): nuclear labeling. Scale bars: 20 μm. Ch, Choroid; RPE, retinal pigment epithelium.

localization of the latter. Using this approach, it was possible to confirm that, in the mature and functional RPE, Scribble is expressed, localized, and conserved at the basolateral domain of the retinal pigment epithelium of the wild-type adult mouse.

Effects of serum from patients with AMD on actin cytoskeleton integrity

In this work, we have designed an experimental model to mimic, in hRPE cells in culture, the early modifications that RPE cells undergo in a toxic environment such as the early stages of AMD disease. To do this, hRPE cells, once differentiated and polarized at 21 DIC, were exposed basolaterally to serum obtained from patients with atrophic or exudative AMD or control as described in material and methods. The first characteristic analyzed was the organization of the circumferential actin belt. This structure is the most reliable indicator of the polarization state of hRPE cells and provides an insight of the strength and optimal conditions of cultured cells. One of the consequences of the exposure of hRPE cells to patients' blood serum was that actin cytoskeleton of hRPE cells was seriously altered (Figure 3A). Actin filaments of non-treated cells (non-serum) were arranged in the cell periphery, in a regular and well-defined ring, giving a mosaic-like appearance with all the pieces tightly fitting together (Figure 3A). Serum exposure caused a disruption of this organization, triggering an alteration of the cytoskeleton and the generation of stress fibers crossing the cytoplasm of the cells. Cells exposed to serum of control patients (5% and 10% control) showed an enlargement in cell size, as well as multiple stress fibers generation. These findings were more dramatic and visible in cells exposed to serum from patients with dry and especially wet AMD, where larger and more abundant stress fibers were observed (Figure 3A). Orthogonal views of the actin and nuclear immunostaining in the hRPE cells revealed that the monolayer of epithelial tissue observed in the non-treated hRPE cells transformed into a multilayered epithelial organization, especially visible in cells exposed to 10% of control serum and in any of the cultures exposed to serum from patients with dry or wet AMD (Figure 3A). In these cells, nuclei were often observed in clusters and in several layers, revealing that the typical epithelial monolayer of the mature RPE cells was completely disorganized after serum exposure. Spatial arrangement of the actin belt, located continuously in the apical zone of the untreated cells, was altered. In the cells exposed to patients' blood serum, actin labeling became patchy, cracked in appearance, and even disappeared in certain areas of the cell cultures. Stress fibers formation, the disorganized appearance, and the multilayered tissue transformation of RPE cells clearly demonstrated that serum exposure had an evident impact on the integrity of mature hRPE cells in culture. Such effects were observed in both control and patients with dry/wet AMD serum-exposed cells, although they were most prominent in the cultures exposed to serum of the two types of AMD.

10.3389/fnana.2022.983151

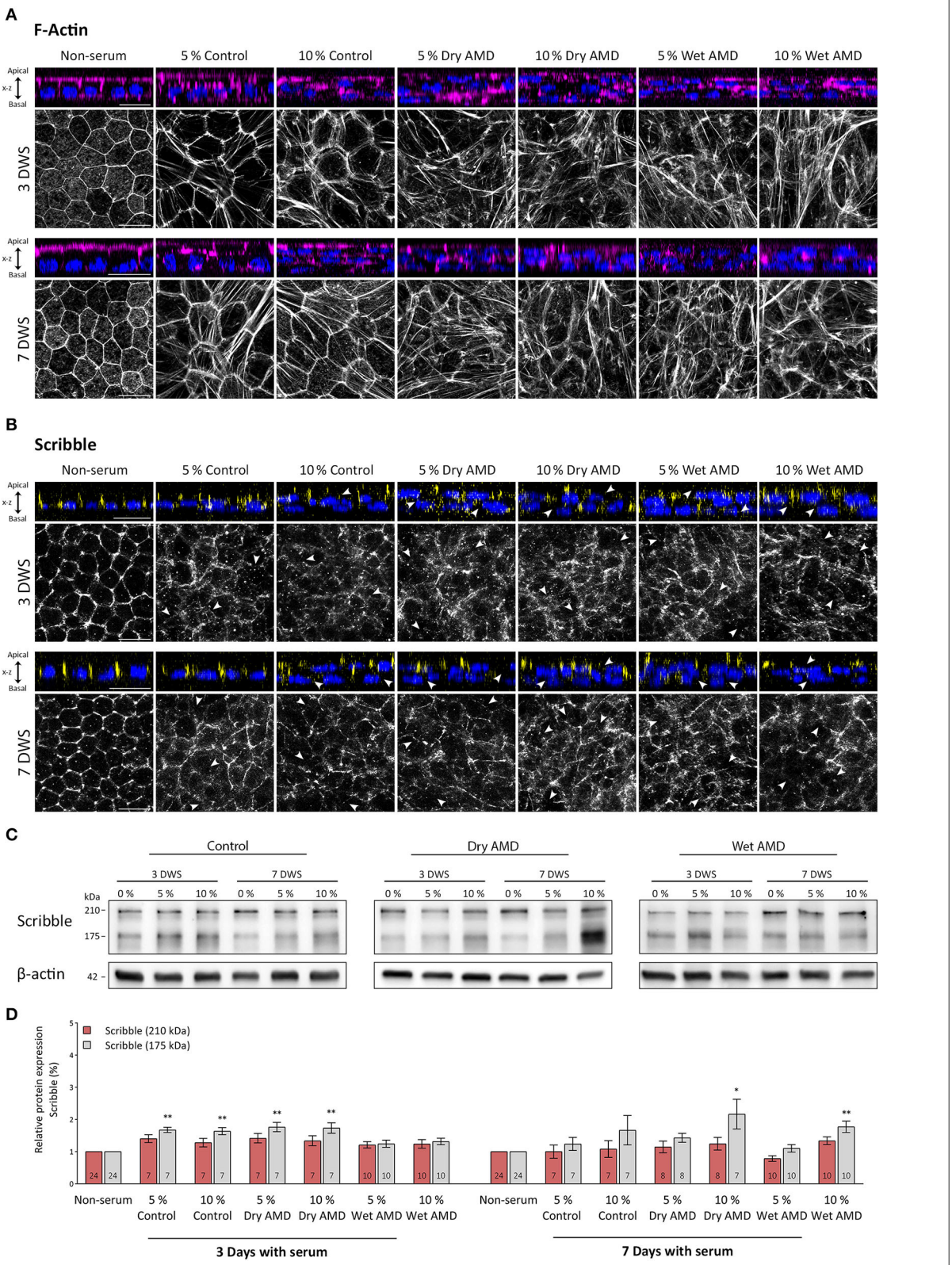

FIGURE 3
Expression pattern of actin and Scribble proteins in hRPE cells after serum exposure. **(A)** Orthogonal views and corresponding z-stack maximum projections showing actin (magenta) in cells without serum and after the serum exposure of both control patients and patients with AMD patients. **(B)** Orthogonal views and corresponding z-stack maximum projections showing Scribble (yellow) in cells without serum and after

(Continued)

FIGURE 3 (Continued)
serum exposure of control patients and patients with AMD. DAPI (blue): nuclear labeling. Scale bars in **(A,B)**: 20 μm. **(C)** Western blot analyses showing expression of Scribble (210 kDa) and Scribble (175 kDa) in cells without serum and after control and AMD patients serum exposure. β-actin was used as loading control. DWS in **(A–C)**: Days with serum. **(D)** Graphical representation of the relative expression of Scribble (210 kDa) and Scribble (175 kDa) in cells without serum and after serum exposure of control patients and patients with AMD. Data are presented as mean ± SD. Arrows in **(B)** point out to areas where Scribble has translocated from the plasma membrane to the cytoplasm. The number within each column corresponds to the number of samples per data. Statistical information: The Kolmogorov-Smirnov and Levene tests were used to assess the normality and homoscedasticity of the sample distribution, respectively. Data were determined to be non-parametrically distributed. The potential significant statistical differences were analyzed by the Kruskal–Walli's test followed by Dunn–Bonferroni's *post-hoc* test. Asterisks indicate statistical differences. *p-value < 0.05; **p-value < 0.01 vs. non-serum group.

Scribble distribution in hRPE cells exposed to serum from patients with AMD

The effects of serum exposure on the expression and localization of Scribble in the hRPE cells were observed soon after this procedure since 3 days after the treatment, the distribution of Scribble was severely affected. In cells without human serum (non-serum), Scribble was found outlining the cell perimeter, showing a regularly well-defined appearance and the typical cobblestone pattern, while disorganization of this pattern was noticeable on serum-treated cells (Figure 3B). In all hRPE cell cultures treated with patients' blood serum, Scribble acquired a patchy pattern and showed a complete disarrangement from the cell membrane (arrows in Figure 3B). Only few patches of the protein remained, outlining the cells' structure. Although only few of the cells exposed to control serum retained Scribble expression in the plasma membrane in a diffuse and disorganized manner, the localization of Scribble (and the organization of the hRPE monolayer, as noted with F-actin labeling) was severely altered since Scribble was completely absent and displaced from the plasma membrane in these serum-treated cells. On the other hand, no clear differences between dry or wet AMD serum-exposed cells were appreciated in relation with the distribution of Scribble (Figure 3B).

Effects of exposure to serum from patients with AMD on scribble expression levels in hRPE cells

The two main Scribble isoforms were detected by western blot in all experimental groups. Serum exposure for 3 days caused a slight increase of the 210 kDa isoform in cells from both control and dry AMD groups, compared with cells of the non-serum group. Interestingly, in wet AMD group cells, the expression was maintained at a similar level as in the non-serum cells (Figures 3C,D). When the exposure time was increased to 7 days, the expression of this protein is maintained at a similar level in all groups, except for a slight decrease in the 5% wet AMD group cells (Figures 3C,D). However, no statistically significant differences in the expression levels of the 210 kDa isoform between the different groups treated with serum were found. On the other hand, we found highly significant differences for the expression of the 175 kDa Scribble isoform among the groups exposed to the serum from different patients ($p = 0.001$; $n = 143$). In contrast to the cells without serum (non-serum) ($n = 24$), this isoform significantly increased its expression level in the cells of the group exposed to control serum at 5% ($n = 7$) ($p = 0.005$) and 10% ($n = 7$) ($p = 0.009$), as well as in the cells exposed to dry AMD serum at 5% ($n = 7$) ($p = 0.003$) and 10% ($n = 7$) ($p = 0.003$); and it is maintained at the same level in the cells exposed to wet AMD serum. As the time of exposure increased up to 7 days, an increment in the expression of this isoform was observed in the 10% dry AMD ($n = 6$) ($p = 0.043$) and 10% wet AMD ($n = 10$) ($p = 0.002$) groups compared with cells that were not exposed to sera. Thus, a very different impact on the expression level of Scribble was evident in hRPE cells depending on the exposure to serum from patients with diverse AMD pathological backgrounds.

Discussion

The RPE is a simple epithelial tissue located in the interface between the neural retina and the choroid, and constitutes the outer blood-retinal barrier of the retina (Strauss, 2005). It is defined by a pronounced apicobasal polarity and robust tight junctions, providing the basis for all the functions it performs (Bok, 1993; Rizzolo, 1997, 2007; Rahner et al., 2004; Strauss, 2005; Lehmann et al., 2014). Apicobasal polarity is an inherent feature in many tissues, which must be perfectly orchestrated (Assémat et al., 2008; Kaplan et al., 2009), and when disrupted, it triggers multiple signaling pathways and molecular processes that ultimately lead to pathology development (Stein, 2002; Mostov et al., 2003; Coradini et al., 2011). In epithelial tissues, cell polarity is established by the coordinated and cooperative action of three evolutionary, highly conserved polarity complexes known as Par, Crb, and Scribble. Apical polarity complexes Par and Crb have been described in the human retina and RPE (van de Pavert et al., 2004; Luo et al., 2006; Park et al., 2011; Paniagua et al., 2015, 2021), but the expression and localization of the Scribble complex remained largely unexplored in this tissue.

Scribble complex in mammals is composed of three proteins: Scribble, DLG, and LLGL, and it is associated to the basolateral domain of the epithelial cell membrane, overlapping adherens junctions (Qin et al., 2005; Kallay et al., 2006). It function cooperatively to establish and regulate cell polarity, junction formation, cell growth, and migration in most epithelial cells (Kallay et al., 2006; Yamanaka and Ohno, 2008; Su et al., 2012).

In the present work, we have defined, for the first time, the precise localization and the expression pattern of Scribble in human RPE cells *in vitro*. Results obtained by Western blot and immunofluorescence during the differentiation process in cultured cells have allowed us to establish the presence of Scribble in human RPE cells as early as 7 DIC, when it was found close to the basal membrane in only a few cells. As RPE tissue reached a mature status (Paniagua et al., 2021), its location changed, acquiring a well-defined location on the basolateral membrane of fully polarized mature RPE cells at 21 DIC. Also, there is much controversy in the literature, as to which is the more characteristic and functional isoform of the Scribble protein since some authors have focused on the 210 kDa isoform (Vieira et al., 2008; Phua et al., 2009; Boczonadi et al., 2014), while others have centered their efforts on the 175 kDa one (Métais et al., 2005; Assémat et al., 2008; Su et al., 2013). Since its function is largely unknown in the RPE, we decided to analyze the expression of the two isoforms in this tissue under different conditions, such as development, and under pathological-simulated conditions to shed light on this issue.

Although Scribble is expressed in a multitude of mammalian cell types and tissues, the highest expression levels have been found in epithelial cells, where it plays a coordinating role together with apical polarity complexes in establishing and regulating apicobasal polarity, junction formation, cell growth, or migration (Navarro et al., 2005; Kallay et al., 2006; Assémat et al., 2008; Yamanaka and Ohno, 2008; Su et al., 2013). In 2005, it was described for the first time the widespread protein expression of Dlg-1 and Scribble in the mouse eye during embryonic and postnatal development (Nguyen et al., 2005). Our results have shown that in adult mouse RPE cells, Scribble localization is restricted to the basolateral domain, as double immunofluorescence labeling for Scribble, and the proteins known to be in the apical side demonstrated that they never colocalized in these cells. Additionally, we have confirmed that the distribution of this protein in the basal domain of the mouse RPE cells is continuous and uniform throughout the cell surface. Other works have shown that high concentrations of Dlg-1 and Scribble seem to be localized at regions known to contain apical junctional complexes in several parts of the eye, in which they often overlap with E- cadherin, N-cadherin, or ZO-1, suggesting they may play different roles in cell adhesion and differentiation. Intriguingly, the distribution of this protein in RPE seems to differ. It has been shown that Scribble colocalizes with Dlg-1, like in most ocular structures, and E-cadherin colocalized with Dlg-1 but not with Scribble, as occurs in the corneal or the lens epithelia. Interestingly, although Scribble colocalizes with ZO-1 in most eye structures, there was only minimal colocalization of the two proteins on the apical surface in this case, and Scribble was also distributed along the basolateral sides of the cells. While the punctate labeling on the apical surface suggested some overlap of these proteins in the tight junctions in RPE, the authors suggested that Scribble could be involved not only in the establishment of tight junctions but also in the organization of cell adhesion complexes in the RPE. This was the first time it was suggested that Dlg and Scribble may not only have functions that are conserved across species, but also may be additionally involved in the regulation of cell adhesion, growth and differentiation in mammalian organ systems, such as the eye (Nguyen et al., 2005). Later, it was found that all the three proteins of the Scribble complex were widely distributed through the adult mouse retina (Vieira et al., 2008). When studying a transgenic mouse, which developed tumors in the RPE, they observed changes in the behavior of these proteins during ocular carcinogenesis, including their mislocalization and downregulation (Vieira et al., 2008). Both the mislocalization and downregulation of Dlg-1, Scribble, and Lgl1 proteins seemed to be correlated to tumor progression in the RPE, due to their role in the onset of epithelial-to-mesenchymal transition (EMT), which was later found to be a common event in more aggressive human tumors (Gardiol et al., 2006; Humbert et al., 2008; Pearson et al., 2011; Elsum et al., 2012; Stephens et al., 2018), which also occurs in age-related macular degeneration (AMD) development (Goldberg et al., 2018). Alterations in Dlg1, Scribble, and Lgl1 functions could promote tumorigenesis by, first, promoting hyperplasia and, second, leading to a loss of cell polarity, thereby reducing cell adhesion and facilitating aggressive overgrowth and invasive behavior (Vieira et al., 2008), suggesting they are involved in pathways that play a major role in cancer development (Zhan et al., 2008; Elsum et al., 2012; Feigin et al., 2014; Pearson et al., 2015).

Age-related macular degeneration (AMD) is a chronic, multifactorial, and highly disabling neurodegenerative pathology of the retina that mainly affects people over 50 years of age (Mitchell et al., 2018). The RPE is located at the core of AMD pathogenesis (Bhutto and Lutty, 2012; Ferrington et al., 2016; Datta et al., 2017). The RPE is damaged in the early stages of pathology, and due to its strategic location, RPE injury affects the choroid and photoreceptors, causing them to degenerate, and, ultimately, leading to blindness (Ach et al., 2015; Gupta et al., 2017; Tarau et al., 2019). Disruption of the epithelial barrier and tight junctions' disassembly is well-documented in AMD. The integrity of tight junctions is necessary for maintenance of cell polarity, whereas correct segregation of the apical and basolateral plasma membrane domains mediated by different protein polarity complexes is essential for their structure and stability (Knust, 2002; Shin et al., 2006). There are different works where blood serum collected directly from

patients suffering from different diseases has been used to simulate *in vitro* certain pathological conditions occurring *in vivo* (Minagar et al., 2003; Sattler et al., 2019; Curtaz et al., 2020). In fact, a modified commercial human serum has also been used to establish a controlled environment that mimics the AMD-like scenario, promoting drusen formation (Johnson et al., 2011), where 10% of human sera was stablished as a preferred concentration to mimic this condition. In the pathological hRPE model used in this work, where cells are exposed to serum obtained from AMD and control patients to generate the experimental conditions that mimic the toxic environment that these cells undergo during the development of AMD, one of the features that indicated anomalies in the cell monolayer was the distribution of F-actin. F-actin cytoskeleton analysis is sufficient to report changes in RPE cultures and identify anomalies in shape and size when these cells are affected (Ach et al., 2015; Müller et al., 2018). The RPE in its normal state has few stress fibers; however, the presence of intracellular stress fibers is a common finding when they are altered (Tarau et al., 2019). In fact, AMD impacts individual RPE cells by cytoskeleton derangement, including separations and breaks around subretinal deposits, thickening, and stress fibers (Ach et al., 2015; Tarau et al., 2019).

Regarding the Scribble complex, it has been linked with the onset and progression of many types of tumors and diseases that primarily result in a loss of polarization and disorganization of the epithelial tissue (Gardiol et al., 2006; Humbert et al., 2008; Pearson et al., 2011; Elsum et al., 2012; Stephens et al., 2018). Scribble was recently identified as a regulator of a transcriptional and signaling pathway of EMT that is involved in tight junction establishment (Elsum et al., 2013) and is also important for tight junction assembly and function in intestinal epithelial cells (Ivanov et al., 2010). Immunofluorescence analysis of Scribble location in serum-exposed cells shows a disorganization of its distribution, which is common in cells exposed to both control and serum from patients with AMD, although a few cells partially preserve its expression at the plasma membrane. Scribble disruption occurs independently from the exposure time or serum concentration employed. Western blot analysis showed increased expression only of the 175 kDa isoform of Scribble after exposure to serum, especially with control and dry AMD serum. After 7 days with serum, the increase was more evident as the cells were exposed to the highest concentration of AMD serum used in this work. It has been shown that, under inflammatory conditions, Scribble acquires an abnormal distribution in the cytoplasm in epithelial cells both *in vitro* and *in vivo* (Ivanov et al., 2010), as it occurs in this hRPE model following the serum exposure. Prior studies in other cell models have shown that mislocalization of the protein or its loss leads to polarity alteration in human epithelial cells, leading to dysregulation of their function (Zhan et al., 2008; Pearson et al., 2011; Feigin et al., 2014). Scribble is considered a tumor suppressor, so when its roles are altered, cell proliferation and tissue overgrowth occur, leading to apicobasal polarity and junctional integrity disruption (Qin et al., 2005; Elsum et al., 2013; Pearson et al., 2015; Saito et al., 2018). Therefore, these data suggest that the Scribble delocalization from the plasma membrane that was observed in our model could be a critical step for the progression of hRPE cells to an EMT process, increasing proliferation and losing apicobasal polarity. Moreover, Scribble is a transcriptional regulator of the EMT process, so the delocalization, together with the increased expression of Scribble, might be the result of the activation of this process.

Conclusion

Apicobasal polarity is an essential feature for the RPE to perform its functions. In this study we have explored both the presence and the alterations of the Scribble protein in this tissue in physiological and pathological conditions. Results obtained have shown for the first time that the polarity protein Scribble is expressed early during the development of this tissue, and that it is precisely located in the basolateral membrane of mature RPE cells soon during this process. Furthermore, we have originally shown that RPE cells exposed to blood serum of both control patients and patients with AMD induces structural changes in the cells, including the cytoskeleton and the Scribble polarity complex, which are reflected on the cell monolayer integrity, especially in cells exposed to the serum of patients with AMD. Alterations in human RPE cells due to AMD serum exposure may be consistent with an epithelial-to-mesenchymal transition process, resembling the one that occurs at the beginning of the human disease, although further studies are required to confirm these findings.

Data availability statement

The raw data supporting the conclusions of this article will be made available by the authors, without undue reservation.

Ethics statement

The studies involving human participants were reviewed and approved by Clinical Research Ethics Committee of the Institute for Biomedical Research of Salamanca (IBSAL) and the Drug Research Ethics Committee of the Regional Ministry of Health of Junta de Castilla y León. The patients/participants provided their written informed consent to participate in this study. The animal study was reviewed and approved by Bioethics Committee of the University of Salamanca.

Author contributions

AS and CL conceived the presented idea. AS, AV, and CL designed the methodology and wrote the original draft. EH-G recruited the patients and obtained the blood serum. AS, AR-C, and BC performed, validated, and carried out the formal analysis of the experiments. AV, EH-G, and CL contributed with funding, resources, and supervision. All authors validated the analysis and completed the review, editing of the manuscript, contributed to the final manuscript, and approved the submitted version.

Funding

This study has been funded by Instituto de Salud Carlos III (ISCIII) through the projects PI15/01240 and PI18/01536 co-funded by the European Union (to CL) and by grants from Consejería de Sanidad de la Junta de Castilla y León (GRS2334/A/21 and GRS2167/1/2020). AS was supported by a pre-doctoral fellowship from Junta de Castilla y León co-financed by the European Social Fund.

Conflict of interest

The authors declare that the research was conducted in the absence of any commercial or financial relationships that could be construed as a potential conflict of interest.

Publisher's note

All claims expressed in this article are solely those of the authors and do not necessarily represent those of their affiliated organizations, or those of the publisher, the editors and the reviewers. Any product that may be evaluated in this article, or claim that may be made by its manufacturer, is not guaranteed or endorsed by the publisher.

Supplementary material

The Supplementary Material for this article can be found online at: https://www.frontiersin.org/articles/10.3389/fnana.2022.983151/full#supplementary-material

References

Ach, T., Tolstik, E., Messinger, J. D., Zarubina, A. V., Heintzmann, R., and Curcio, C. A. (2015). Lipofuscin redistribution and loss accompanied by cytoskeletal stress in retinal pigment epithelium of eyes with age-related macular degeneration. *Invest. Ophthalmol. Visual Sci.* 56, 3242–3252. doi: 10.1167/iovs.14-16274

Assémat, E., Bazellières, E., Pallesi-Pocachard, E., Le Bivic, A., and Massey-Harroche, D. (2008). Polarity complex proteins. *Biochim. Biophys. Acta Biomembranes* 1778, 614–630. doi: 10.1016/j.bbamem.2007.08.029

Barreda, D., Gutiérrez-González, L. H., Martínez-Cordero, E., Cabello-Gutiérrez, C., Chacón-Salinas, R., and Santos-Mendoza, T. (2020). The scribble complex PDZ proteins in immune cell polarities. *J. Immunol. Res.* 2020, 5649790. doi: 10.1155/2020/5649790

Bhutto, I., and Lutty, G. (2012). Understanding age-related macular degeneration (AMD): relationships between the photoreceptor/retinal pigment epithelium/Bruch's membrane/choriocapillaris complex. *Mol. Aspects Med.* 33, 295–317. doi: 10.1016/j.mam.2012.04.005

Bilder, D., Li, M., and Perrimon, N. (2000). Cooperative regulation of cell polarity and growth by Drosophila tumor suppressors. *Science* 289, 113–116. doi: 10.1126/science.289.5476.113

Bilder, D., and Perrimon, N. (2000). Localization of apical epithelial determinants by the basolateral PDZ protein Scribble. *Nature* 403, 676–680. doi: 10.1038/35001108

Boczonadi, V., Gillespie, R., Keenan, I., Ramsbottom, S. A., Donald-Wilson, C., Al Nazer, M., et al. (2014). Scrib:Rac1 interactions are required for the morphogenesis of the ventricular myocardium. *Cardiovasc. Res.* 104, 103–115. doi: 10.1093/cvr/cvu193

Bok, D. (1993). The retinal pigment epithelium: a versatile partner in vision. *J. Cell Sci. Suppl.* 17(Suppl. 17), 189–195. doi: 10.1242/jcs.1993.Supplement_17.27

Coradini, D., Casarsa, C., and Oriana, S. (2011). Epithelial cell polarity and tumorigenesis: new perspectives for cancer detection and treatment. *Acta Pharmacol. Sin.* 32, 552–564. doi: 10.1038/aps.2011.20

Curtaz, C. J., Schmitt, C., Herbert, S.-L., Feldheim, J., Schlegel, N., Gosselet, F., et al. (2020). Serum-derived factors of breast cancer patients with brain metastases alter permeability of a human blood-brain barrier model. *Fluids Barriers CNS* 17, 31. doi: 10.1186/s12987-020-00192-6

Datta, S., Cano, M., Ebrahimi, K., Wang, L., and Handa, J. T. (2017). The impact of oxidative stress and inflammation on RPE degeneration in non-neovascular AMD. *Prog. Retin. Eye Res.* 60, 201–218. doi: 10.1016/j.preteyeres.2017.03.002

Elsum, I., Yates, L., Humbert, P. O., and Richardson, H. E. (2012). The Scribble-Dlg-Lgl polarity module in development and cancer: from flies to man. *Essays Biochem.* 53, 141–168. doi: 10.1042/bse0530141

Elsum, I. A., Martin, C., and Humbert, P. O. (2013). Scribble regulates an EMT polarity pathway through modulation of MAPK-ERK signaling to mediate junction formation. *J. Cell Sci.* 126, 3990–3999. doi: 10.1242/jcs.129387

Feigin, M. E., Akshinthala, S. D., Araki, K., Rosenberg, A. Z., Muthuswamy, L. B., Martin, B., et al. (2014). Mislocalization of the cell polarity protein scribble promotes mammary tumorigenesis and is associated with basal breast cancer. *Cancer Res.* 74, 3180–3194. doi: 10.1158/0008-5472.CAN-13-3415

Ferrington, D. A., Sinha, D., and Kaarniranta, K. (2016). Defects in retinal pigment epithelial cell proteolysis and the pathology associated with age-related macular degeneration. *Progress Retinal Eye Res.* 51, 69–89. doi: 10.1016/j.preteyeres.2015.09.002

Gardiol, D., Zacchi, A., Petrera, F., Stanta, G., and Banks, L. (2006). Human discs large and scrib are localized at the same regions in colon mucosa and changes in their expression patterns are correlated with loss of tissue architecture during malignant progression. *Int. J. Cancer* 119, 1285–1290. doi: 10.1002/ijc.21982

Goldberg, M. F., McLeod, S., Tso, M., Packo, K., Edwards, M., Bhutto, I. A., et al. (2018). Ocular histopathology and immunohistochemical analysis in the oldest known individual with autosomal dominant vitreoretinochoroidopathy. *Ophthalmol. Retina* 2, 360–378. doi: 10.1016/j.oret.2017.08.001

Gupta, T., Saini, N., Arora, J., and Sahni, D. (2017). Age-related changes in the chorioretinal junction: an immunohistochemical study. *J. Histochem. Cytochem.* 65, 567–577. doi: 10.1369/0022155417726507

Humbert, P. O., Grzeschik, N. A., Brumby, A. M., Galea, R., Elsum, I., and Richardson, H. E. (2008). Control of tumourigenesis by the Scribble/Dlg/Lgl polarity module. *Oncogene* 27, 6888–6907. doi: 10.1038/onc.2008.341

Ivanov, A. I., Young, C., Beste, K., Den, C.apaldo, C. T., Humbert, P. O., Brennwald, P., et al. (2010). Tumor suppressor scribble regulates assembly of tight junctions in the intestinal epithelium. *Am. J. Pathol.* 176, 134–145. doi: 10.2353/ajpath.2010.090220

Johnson, L. V., Forest, D. L., Banna, C. D., Radeke, C. M., Maloney, M. A., Hu, J., et al. (2011). Cell culture model that mimics drusen formation and triggers complement activation associated with age-related macular degeneration. *Proc. Natl. Acad. Sci. U. S. A.* 108, 18277–18282. doi: 10.1073/pnas.1109703108

Kallay, L. M., McNickle, A., Brennwald, P. J., Hubbard, A. L., and Braiterman, L. T. (2006). Scribble associates with two polarity proteins, Lgl2 and Vangl2, via distinct molecular domains. *J. Cell. Biochem.* 99, 647–664. doi: 10.1002/jcb.20992

Kaplan, N. A., Liu, X., and Tolwinski, N. S. (2009). Epithelial polarity: interactions between junctions and apical-basal machinery. *Genetics* 183, 897–904. doi: 10.1534/genetics.109.108878

Knust, E. (2002). Regulation of epithelial cell shape and polarity by cell - cell adhesion (Review). *Mol. Membr. Biol.* 19, 113–120. doi: 10.1080/09687680210137219

Lehmann, G. L., Benedicto, I., Philp, N. J., and Rodriguez-Boulan, E. (2014). Plasma membrane protein polarity and trafficking in RPE cells: past, present and future. *Exp. Eye Res.* 126, 5–15. doi: 10.1016/j.exer.2014.04.021

Lei, Y., Zhu, H., Duhon, C., Yang, W., Ross, M. E., Shaw, G. M., et al. (2013). Mutations in planar cell polarity gene SCRIB are associated with Spina Bifida. *PLoS ONE* 8, e69262. doi: 10.1371/journal.pone.0069262

Liu, J., Li, J., Li, P., Wang, Y., Liang, Z., Jiang, Y., et al. (2017). Loss of DLG5 promotes breast cancer malignancy by inhibiting the Hippo signaling pathway. *Sci. Rep.* 7, 42125. doi: 10.1038/srep42125

Luo, Y., Fukuhara, M., Weitzman, M., and Rizzolo, L. J. (2006). Expression of JAM-A, AF-6, PAR-3 and PAR-6 during the assembly and remodeling of RPE tight junctions. *Brain Res.* 1110, 55–63. doi: 10.1016/j.brainres.2006.06.059

Métais, J. Y., Navarro, C., Santoni, M. J., Audebert, S., and Borg, J. P. (2005). hScrib interacts with ZO-2 at the cell–cell junctions of epithelial cells. *FEBS Lett.* 579, 3725–3730. doi: 10.1016/j.febslet.2005.05.062

Minagar, A., Ostanin, D., Long, A. C., Jennings, M., Kelley, R. E., Sasaki, M., et al. (2003). Serum from patients with multiple sclerosis downregulates occludin and VE-cadherin expression in cultured endothelial cells. *Mult. Scler.* 9, 235–238. doi: 10.1191/1352458503ms916oa

Mitchell, P., Liew, G., Gopinath, B., and Wong, T. Y. (2018). Age-related macular degeneration. *Lancet (London, England).* 392, 1147–1159. doi: 10.1016/S0140-6736(18)31550-2

Miyoshi, J., and Takai, Y. (2008). Structural and functional associations of apical junctions with cytoskeleton. *Biochim. Biophys. Acta Biomembranes* 1778, 670–691. doi: 10.1016/j.bbamem.2007.12.014

Mostov, K., Su, T., and ter Beest, M. (2003). Polarized epithelial membrane traffic: conservation and plasticity. *Nat. Cell Biol.* 5, 287–293. doi: 10.1038/ncb0403-287

Müller, C., Charniga, C., Temple, S., and Finnemann, S. C. (2018). Quantified F-actin morphology is predictive of phagocytic capacity of stem cell-derived retinal pigment epithelium. *Stem Cell Rep.* 10, 1075–1087. doi: 10.1016/j.stemcr.2018.01.017

Navarro, C., Nola, S., Audebert, S., Santoni, M. J., Arsanto, J. P., Ginestier, C., et al. (2005). Junctional recruitment of mammalian Scribble relies on E-cadherin engagement. *Oncogene* 24, 4330–4339. doi: 10.1038/sj.onc.1208632

Nguyen, M. M., Rivera, C., and Griep, A. E. (2005). Localization of PDZ domain containing proteins discs large-1 and scribble in the mouse eye. *Mol. Vision* 11, 1183–1199.

Paniagua, A. E., Herranz-Martín, S., Jimeno, D., Jimeno, Á. M., López-Benito, S., Carlos Arévalo, J., et al. (2015). CRB2 completes a fully expressed crumbs complex in the retinal pigment epithelium. *Sci. Rep.* 5, 14504. doi: 10.1038/srep14504

Paniagua, A. E., Segurado, A., Dolón, J. F., Esteve-Rudd, J., Velasco, A., Williams, D. S., et al. (2021). Key role for CRB2 in the maintenance of apicobasal polarity in retinal pigment epithelial cells. *Front. Cell Dev. Biol.* 9, 701853. doi: 10.3389/fcell.2021.701853

Park, B., Alves, C. H., Lundvig, D. M., Tanimoto, N., Beck, S. C., Huber, G., et al. (2011). PALS1 is essential for retinal pigment epithelium structure and neural retina stratification. *J. Neurosci.* 31, 17230–17241. doi: 10.1523/JNEUROSCI.4430-11.2011

Pearson, H. B., McGlinn, E., Phesse, T. J., Schlüter, H., Srikumar, A., Gödde, N. J., et al. (2015). The polarity protein Scrib mediates epidermal development and exerts a tumor suppressive function during skin carcinogenesis. *Mol. Cancer* 14, 169. doi: 10.1186/s12943-015-0440-z

Pearson, H. B., Perez-Mancera, P. A., Dow, L. E., Ryan, A., Tennstedt, P., Bogani, D., et al. (2011). SCRIB expression is deregulated in human prostate cancer, and its deficiency in mice promotes prostate neoplasia. *J. Clin. Invest.* 121, 4257–4267. doi: 10.1172/JCI58509

Pfeffer, B. A., and Philp, N. J. (2014). Cell culture of retinal pigment epithelium: special issue. *Exp. Eye Res.* 126, 1–4. doi: 10.1016/j.exer.2014.07.010

Phua, D. C. Y., Humbert, P. O., and Hunziker, W. (2009). Vimentin regulates scribble activity by protecting it from proteasomal degradation. *Mol. Biol. Cell* 20, 2841–2855. doi: 10.1091/mbc.e08-02-0199

Qin, Y., Capaldo, C., Gumbiner, B. M., and Macara, I. G. (2005). The mammalian Scribble polarity protein regulates epithelial cell adhesion and migration through E-cadherin. *J. Cell Biol.* 171, 1061–1071. doi: 10.1083/jcb.200506094

Rahner, C., Fukuhara, M., Peng, S., Kojima, S., and Rizzolo, L. J. (2004). The apical and basal environments of the retinal pigment epithelium regulate the maturation of tight junctions during development. *J. Cell Sci.* 117, 3307–3318. doi: 10.1242/jcs.01181

Rizzolo, L. J. (1997). Polarity and the development of the outer blood-retinal barrier. *Histol. Histopathol.* 12, 1057–1067.

Rizzolo, L. J. (2007). Development and role of tight junctions in the retinal pigment epithelium. *Int. Rev. Cytol.* 258, 195–234. doi: 10.1016/S0074-7696(07)58004-6

Robinson, A., Escuin, S., Vekemans, K. D., Stevenson, R. E., Greene, N. D. E., Copp, A. J., et al. (2012). Mutations in the planar cell polarity genes CELSR1 and SCRIB are associated with the severe neural tube defect craniorachischisis. *Hum. Mutat.* 33, 440–447. doi: 10.1002/humu.21662

Rodriguez-Boulan, E., and Macara, I. G. (2014). Organization and execution of the epithelial polarity programme. *Nat. Rev. Mol. Cell Biol.* 15, 225–242. doi: 10.1038/nrm3775

Saito, Y., Desai, R. R., and Muthuswamy, S. K. (2018). Reinterpreting polarity and cancer: the changing landscape from tumor suppression to tumor promotion. *Biochim. Biophys. Acta.* 1869, 103–116. doi: 10.1016/j.bbcan.2017.12.001

Sattler, K., El-Battrawy, I., Zhao, Z., Schrottenberg, C., Yücel, G., Lan, H., et al. (2019). Serum of patients with acute myocardial infarction prevents inflammation in iPSC-cardiomyocytes. *Sci. Rep.* 9, 5651. doi: 10.1038/s41598-019-42079-z

Shin, K., Fogg, V. C., and Margolis, B. (2006). Tight junctions and cell polarity. *Annu. Rev. Cell Dev. Biol.* 22, 207–235. doi: 10.1146/annurev.cellbio.22.010305.104219

Stein, M. (2002). Altered trafficking and epithelial cell polarity in disease. *Trends Cell Biol.* 12, 374–381. doi: 10.1016/S0962-8924(02)02331-0

Stephens, R., Lim, K., Portela, M., Kvansakul, M., Humbert, P. O., and Richardson, H. E. (2018). The scribble cell polarity module in the regulation of cell signaling in tissue development and tumorigenesis. *J. Mol. Biol.* 430, 3585–3612. doi: 10.1016/j.jmb.2018.01.011

Strauss, O. (2005). The retinal pigment epithelium in visual function. *Physiol. Rev.* 85, 845–881. doi: 10.1152/physrev.00021.2004

Su, W., Wong, E. W. P., Mruk, D. D., and Cheng, C. Y. (2012). The scribble/Lgl/Dlg polarity protein complex is a regulator of blood-testis barrier dynamics and spermatid polarity during spermatogenesis. *Endocrinology* 153, 6041–6053. doi: 10.1210/en.2012-1670

Su, W.-H., Mruk, D. D., Wong, E. W. P., Lui, W.-Y., and Cheng, C. Y. (2013). Polarity protein complex scribble/Lgl/Dlg and epithelial cell barriers. *Adv. Exp. Med. Biol.* 763, 149–170. doi: 10.1007/978-1-4614-4711-5_7

Tarau, I.-S., Berlin, A., Curcio, C. A., and Ach, T. (2019). The cytoskeleton of the retinal pigment epithelium: from normal aging to age-related macular degeneration. *Int. J. Mol. Sci.* 20, 3578. doi: 10.3390/ijms20143578

van de Pavert, S. A., Kantardzhieva, A., Malysheva, A., Meuleman, J., Versteeg, I., Levelt, C., et al. (2004). Crumbs homologue 1 is required for maintenance of photoreceptor cell polarization and adhesion during light exposure. *J. Cell Sci.* 117, 4169–4177. doi: 10.1242/jcs.01301

Vieira, V., de la Houssaye, G., Lacassagne, E., Dufier, J. L., Jaïs, J. P., Beermann, F., et al. (2008). Differential regulation of Dlg1, Scrib, and Lgl1 expression in a transgenic mouse model of ocular cancer. *Mol. Vis.* 14, 2390–2403.

Yamanaka, T., and Ohno, S. (2008). Role of Lgl/Dlg/Scribble in the regulation of epithelial junction, polarity and growth. *Front. Biosci.* 13, 6693–6707. doi: 10.2741/3182

Zhan, L., Rosenberg, A., Bergami, K. C., Yu, M., Xuan, Z., Jaffe, A. B., et al. (2008). Deregulation of scribble promotes mammary tumorigenesis and reveals a role for cell polarity in carcinoma. *Cell* 135, 865–878. doi: 10.1016/j.cell.2008.09.045

Frontiers in Neuroanatomy

Explores the anatomical organization of nervous systems across all species

Advances our understanding of neuroanatomy - from sub-cellular and connectivity anatomy to immunocytochemistry mapping protein expression patterns.

Discover the latest Research Topics

See more →

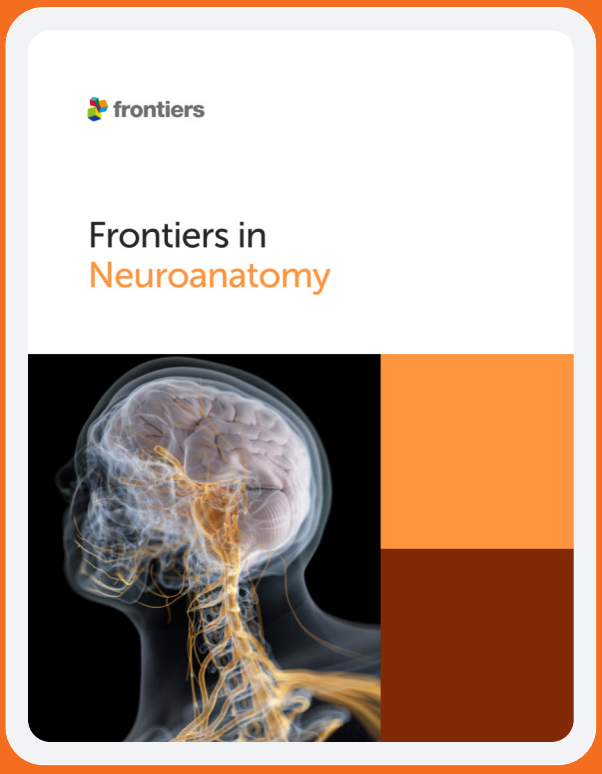

Frontiers

Avenue du Tribunal-Fédéral 34
1005 Lausanne, Switzerland
frontiersin.org

Contact us

+41 (0)21 510 17 00
frontiersin.org/about/contact